Transactions of the ASME

Journal of Heat Transfer

Published Quarterly by The American Society of Mechanical Engineers

VOLUME 105 • NUMBER 3 • AUGUST 1983

The Journal of Heat Transfer (ISSN 0022-1481) is published quarterly for $72 per year by The American Society of Mechanical Engineers, 345 East 47th Street, New York, N Y 10017. Second class postage paid at New York, NY and additional mailing offices. POSTMASTER: Send address changes to The Journal of Heat Transfer, c/o THE AMERICAN SOCIETY OF MECHANICAL ENGINEERS, P.O. Box 3199, Grand Central Station, New York, NY 10163.

CHANGES OF ADDRESS must be received at Society headquarters seven weeks before they are to be effective. Please send old label and new address.

PRICES: To members, $36.00, annually; to nonmembers, $72.00. Single copies, $24.00 each. Add $6.00 for postage to countries outside the United States and Canada.

INDEXED by the Engineering Index, Inc.

ANNOUNCEMENTS

TECHNICAL PAPERS

(contents continued on page 439)

(contents continued)

TECHNICAL NOTES

(contents continued on page 468)

(contents continued)

P. K.-B. Chao[1]
Graduate Student,
Department of Chemical Engineering,
University of Pennsylvania,
Philadelphia, Pa. 19104

H. Ozoe
Associate Professor,
Department of Industrial and Mechanical Engineering,
Okayama University,
Okayama, Japan

S. W. Churchill
Carl V. S. Patterson Professor of Chemical Engineering.
Department of Chemical Engineering,
University of Pennsylvania,
Philadelphia, Pa. 19104

N. Lior
Associate Professor,
Department of Mechanical Engineering and Applied Mechanics
University of Pennsylvania,
Philadelphia, Pa. 19104
Mem. ASME

Laminar Natural Convection in an Inclined Rectangular Box With the Lower Surface Half-Heated and Half-Insulated

The pattern of circulation and the rate of heat transfer were determined experimentally and also by three-dimensional, finite-difference calculations for an inclined 2 × 1 × 1 rectangular enclosure with a 1 × 1 segment of the lower 2 × 1 surface at a uniform temperature, the other 1 × 1 segment and four side walls insulated, and the upper surface at a lower uniform temperature. As contrasted with an enclosure heated and cooled on the horizontal surfaces, a fluid motion occurs and the rate of heat transfer exceeds that for pure conduction for all temperature differences and orientations. The effects of elevation of the heated and insulated segments were investigated, as well as of inclination about the longer dimension. Despite differences in the Prandtl and Rayleigh numbers, the observed and predicted patterns of circulation are in good agreement, and the measured and predicted rates of heat are in qualitative agreement.

Introduction

Natural convection in inclined rectangular enclosures has been studied extensively in recent years owing to its application to solar collectors. In most of the these investigations, the lower surface has been assumed to be at an essentially uniform temperature. However, in real solar collectors the cooling coil or jacket and the edges of the enclosure may produce a significant nonuniformity of temperature on the lower plate.

The effect of nonuniformities in the surface temperature of enclosures has received only limited attention. The most relevant work is that of Chao et al. [1], who investigated theoretically the effect of sawtooth variations in the temperature of the lower surface of 1 × 1 × 2 box inclined about the longer dimension at Ra = 6000 and Pr = 10. All of the variations in surface temperature which were studied produced a stronger circulation and a higher overall Nusselt number than did a uniform temperature. A higher angle of inclination was required for transition from two roll cells with axes in the shorter horizontal dimension to a single circulation with its axis in the longer dimension. Otherwise, the pattern of circulation was unchanged.

Other work on nonuniform surface temperatures is illustrated by the following examples. Chu and Churchill [2] studied, both theoretically and experimentally, the effect of the size and location of an isothermal, horizontal strip in an otherwise insulated vertical surface of a rectangular channel. Hanzawa et al. [3] computed the velocity and temperature fields for laminar flow through a channel with a 1 to 1.2 height-to-width ratio, heated isothermally on the central half of the base with the balance of the walls at a lower uniform temperature. They predicted, and confirmed experimentally, two symmetrical roll cells superimposed on the forced flow. Boehm and Kamyab [4] computed laminar free convection for isothermal heating of alternate, equally wide strips of a large horizontal plate facing upward in an unconfined fluid; the intermediate strips were insulated or at a lower uniform temperature. The Nusselt number for large Ra (with both dimensionless groups based on the average surface temperature and the total area) was found to be higher than for a completely isothermal surface. Torrance and coworkers [5, 6], Greenspan and Schultz [7], and others have studied the effect of a hot spot in the lower surface of an enclosure, as a simulation of a fire. None of these latter six investigations are directly relevant to natural convection in the enclosed air space of a solar collector, or to the work reported herein, owing to the fundamentally different boundary conditions.

In this study, the effect of insulating half of the lower surface was investigated as an exaggerated and presumably bounding case of the nonuniformity due to the individual cooling coils or passages of solar collectors. Three-dimensional, finite difference calculations were utilized to predict the pattern of circulation and the related rates of heat transfer. Photographs of particle paths were used to test the reliability of the computations in predicting the pattern of flow.

Three modes of inclination of the heated surface from the horizontal were investigated, as illustrated in Fig. 1. In (*a*) the shorter horizontal dimension is inclined about the longer dimension as an axis, in (*b*) the insulated end is elevated with the opposite shorter horizontal edge in the same plane as an axis, and in (*c*) the heated end is elevated with the corresponding opposite shorter edge as an axis. It may be noted in advance that cases (*b*) and (*c*) would not be expected to be identical or even symmetrical.

A 2 × 1 × 1 enclosure was chosen for the calculations since greater aspect ratios would exceed the capability of our current computational facilites for such involved three-dimensional behavior. The results, although quantitatively applicable only for solar collectors with rectangular honey-

[1] Presently Senior Staff Engineer, Mobil R&D Corporation, Paulsboro, N.J.

Contributed by the Heat Transfer Division and presented at the AIAA/ASME Fluids, Plasma, Thermophysics, and Heat Transfer Conference, St. Louis, Mo., June 7–11, 1982. Manuscript received by the Heat Transfer Division June 1, 1982. Paper No. 82-HT-72.

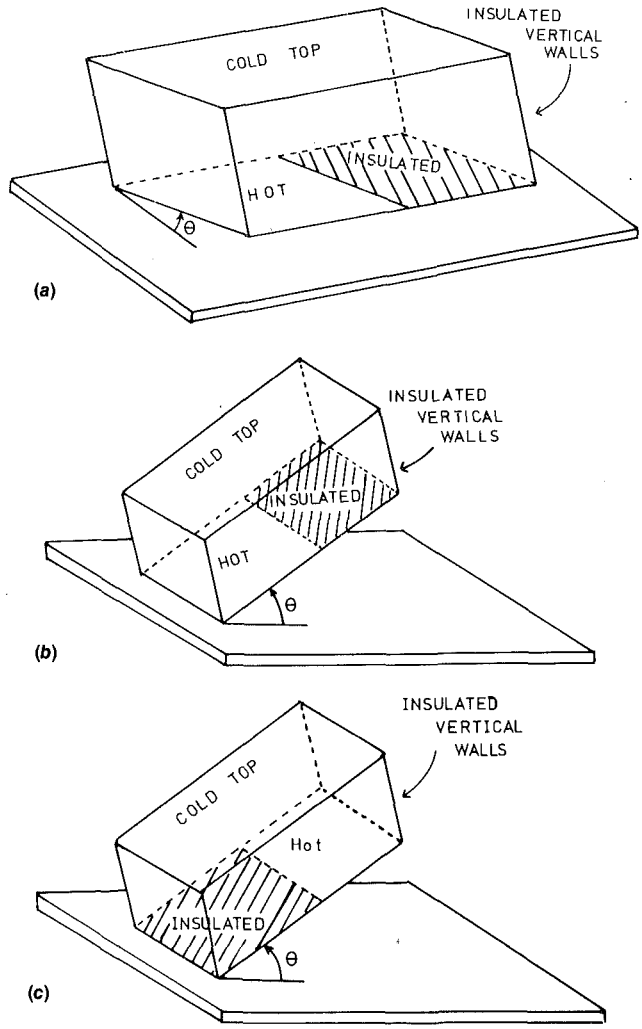

Fig. 1 Schematic drawing of different inclinations of a 2 × 1 × 1 rectangular enclosure with a half-insulated and half-heated lower surface: (a) inclination of the shorter dimension; (b) elevation of the insulated end; (c) elevation of the heated end

combs, nevertheless provide qualitative information on the effect of nonuniform heating on enclosures of large aspect ratio.

Large Prandtl number fluids were used in the experimental work because of difficulties in photographing the patterns of circulation and measuring the rate of heat transfer accurately in air. Extensive experimental work by dozens of investigators (see, Churchill [8]) on natural convection in enclosures has failed to reveal a significant dependence of the Nusselt number on the Prandtl number for a Prandtl number greater than 0.7 and a fixed Rayleigh number. In prior experimental work for rectangular enclosures, Ozoe et al. [9] found the angles of inclination for the minimum and maximum in the Nusselt number to be independent of the Prandtl number. Hence, our calculations were limited to a single Prandtl number, and the experimental fluids were chosen to optimize the experimental precision.

The necessity of a reasonable temperature difference between the heated and cooled plates established a minimum Rayleigh number of about 8000 for the measurements of heat transfer. A Rayleigh number of 25,000 proved necessary for the streakline photography. On the other hand, the maximum Rayleigh number which was feasible computationally was 10,000 for inclinations about the longer dimension as an axis, and 6000 for inclinations about the shorter dimension as an axis. These discrepancies in the range of the Rayleigh number preclude quantitative comparisons of the experimental and computation results. Fortunately, the above cited work of Ozoe et al. [9] also indicates that the qualitative dependence of the flow pattern and the Nusselt number on the Rayleigh number does not change significantly over this range.

Theoretical Model and Calculations

The calculations were for one 1 × 1 segment of the lower surface of the 2 × 1 × 1 enclosure at a uniform, dimensionless temperature U of +0.5. The other 1 × 1 segment, as well as the four side walls, were postulated to be perfectly insulated. The upper surface was at a lower, uniform, dimensionless temperature of −0.5.

The three-dimensional equations for the conservation of mass, energy, and momentum, as simplified by the well-known Boussinesq approximations, were postulated to describe the behavior. This model, its finite difference approximation, and the method of solution were essentially the same as that used by Ozoe et al. [10], and hence will only be outlined in this paper. The introduction of the vector potential and the vorticity permits replacement of the continuity equation and the three equations for the conservation of momentum with three equations for the conservation of vorticity. These equations were then solved in transient form together with the energy equation. The components of the vector potential were calculated from the definition of the vorticity, and the components of the velocity from the definition of the vector potential. A false transient term was added to the elliptic equation relating the vector potential and vorticity in order to obtain a parabolic form. The unknown vorticities at the wall were computed from the velocity gradients. For the numerical calculations, the derivatives in space were approximated by central differences. This scheme is not conservative, but, as previously demonstrated by Chu and Churchill [11], the resulting heat fluxes through all planes extrapolate to the same value for zero grid size. The three-dimensional, alternating-direction implicit method developed

Nomenclature

A = area of upper, cooled surface, m^2
g = acceleration due to gravity, m/s^2
h = grid size as fraction of H
H = height of enclosure, m
k = thermal conductivity, W/m•K
Nu = Nusselt number = $qH/kA(T_l - T_u)$
Pr = Prandtl number = ν/α
q = heat flux, W
Q = dimensionless heat flux = q/q_c
Ra = Rayleigh number = $g\beta(T_l - T_u)H^3/\nu\alpha$
T = temperature, K
U = dimensionless temperature = $(T - 1/2T_l - 1/2T_u)/(T_l - T_u)$
x = distance in long dimension, m
X = dimensionless distance in long dimension = x/H
y = distance in short horizontal dimension, m
Y = dimensionless distance in short dimension = y/H
z = distance from cooled plate, m
Z = dimensionless distance from cooled plate = z/H
α = thermal diffusivity, m^2/s
β = volumetric coefficient of expansion with temperature, K^{-1}
ν = kinematic viscosity, m^2/s
θ = angle of inclination of heated surface, rad

Subscripts

c = by conduction
l = on heated surface
u = on cooled surface

by Brian [12] was used. The matrices were solved iteratively at each time step as required for convergence. The steps in time proceeded until the steady state was closely approached.

The problem considered herein required the following two modifications: (*i*) the condition $\partial U/\partial Z = 0$ was substituted for $U = 0.5$ over the insulated portion of the lower surface, and (*ii*) as illustrated in Fig. 2, the finite difference approximation for the second derivative of U in the Z-direction along the border between the insulated and isothermal segments of the lower surface, was written as

$$\left(\frac{\partial^2 U}{\partial Z^2}\right)_{Z=0.9} = \frac{1}{2}\left[\frac{U_3 - 2U_2 + U_1}{(\Delta Z)^2} + \frac{U_2 - 2U_2 + U_1}{(\Delta Z)^2}\right]$$

$$= \frac{0.5U_3 - 1.5U_2 + U_1}{(\Delta Z)^2} \quad (1)$$

That is, one half of the element was taken to be isothermal at the temperature of the heated segment ($U_3 = 0.5$), while the other half was adiabatic and thus had a surface temperature equal to that of the adjacent grid point in the fluid, U_2. This formulation was found by Chu and Churchill [11] to produce a more rapid convergence to the exact solution as the grid size was reduced, than the use of a single unknown U_3 at the edge of the insulation.

The finite difference computations were carried out on the IBM 360/175 computer of the Department of Physics of the University of Pennsylvania for Pr = 10, Rayleigh numbers of 4000, 6000, and 10,000, and a complete series of inclinations from 0 to π rad. This value was arbitrarily chosen for Pr since, as previously noted, the behavior is known to be unchanged for larger values and only slightly for lower values down to 0.7. These values were chosen for Ra to be above the conductive regime but within the computationally stable regime for a feasible time step. Two grid sizes were used so that the computed heat fluxes could be extrapolated to zero grid size using the Richardson-Gaunt method [13], which has been validated for natural convection by Churchill et al. [14]. These two grid sizes were uniform and equal to 0.1 and 0.2 of the shorter dimension of the enclosure. Since the truncation error of the finite difference formulation was second-order throughout, the mean heat flux for zero grid size was calculated from

$$q_{h=0} = (4q_{h=0.1} - q_{h=0.2})/3 \quad (2)$$

The indicated errors for $h = 0.1$ and $h = 0.2$ were approximately 3 and 13 percent, respectively, as compared to the results obtained by extrapolation to zero grid size.

The resulting heat fluxes for zero grid size were converted to the dimensionless form, $Q = q/q_c$, by dividing by the heat flux for pure conduction with the same boundary conditions. The Nusselt number $\mathrm{Nu} = qH/kA\Delta T$ is herein arbitrarily based on the area of the cooled surface, and hence is less than Q.

The value of the Nusselt number for pure conduction with the same boundary conditions was found from finite difference calculations to be

$$\mathrm{Nu}_c = \frac{q_c H}{kA\Delta T} = 0.69 \quad (3)$$

It follows from equation (3) that

$$\mathrm{Nu} = \frac{qH}{kA\Delta T} = 0.69\,Q \quad (4)$$

Streaklines were computed from the calculated velocity field for a grid size of 0.1, and the results were displayed isometrically and dynamically on a cathode ray tube, as described by Yamamoto et al. [15]. Photographs were taken of static displays. The inaccuracy due to the use of the calculations with $h = 0.1$ for the generation of these displays is sufficiently small so as to produce the qualitatively correct behavior, which is of principal interest.

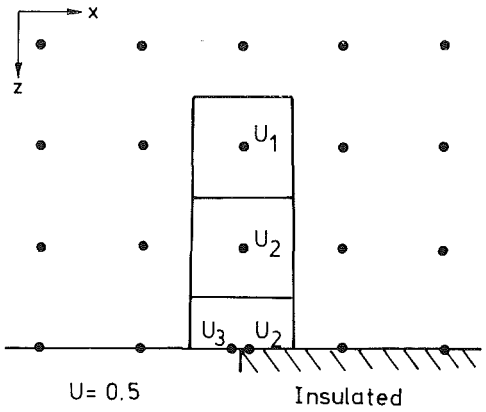

Fig. 2 Finite-difference approximation of the boundary condition at the intersection of the heated and adiabatic segments of the lower surface

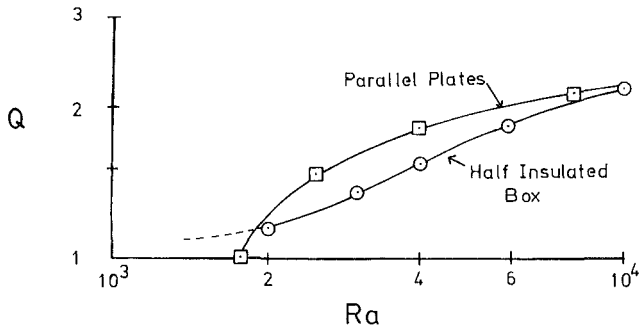

Fig. 3 Computed dimensionless heat flux in a 2 × 1 × 1 rectangular enclosure with a half-heated lower surface as compared with isothermal, infinite, parallel plates

The computed steady-state results were found to be independent of the initial conditions. Hence the steady state for the previous case was usually utilized to save computing time.

Theoretical Results

Heat Transfer Rates.

No Inclination (Heating From Below). The computed, dimensionless, mean heat flux for the half-heated and half-insulated lower surface of the 2 × 1 × 1 enclosure is compared in Fig. 3 with that for infinite parallel plates with isothermal upper and lower surfaces. In the later idealized case, heat transfer is by pure conduction ($Q = 1$) below a Rayleigh number of 1708. For the half-insulated surface the isotherms are not horizontal even for pure conduction. Hence, natural convection occurs for all temperature differences, $Q \to 1$ only as $\mathrm{Ra} \to 0$, and a critical Rayleigh number does not exist. It follows that Q for the half-insulated lower surface exceeds Q for infinite isothermal plates as $\mathrm{Ra} \to 0$. A crossover would also occur, but at a higher Ra, for a 2 × 1 × 1 enclosure with isothermal horizontal surfaces. If the results were plotted in terms of Nu (based on the cooled area) instead of Q, a crossover would not occur, since in this form the doubled area for heating with an isothermal surface overcomes the finite convection with half-heating, even for $\mathrm{Ra} \to 0$.

Inclination of the Shorter Horizontal Dimension About the Longer Dimmension as an Axis. The mean Nusselt number for the cooled surface is plotted in Fig. 4 for a complete range of inclinations of the half-insulated surface from the horizontal and for Rayleigh numbers of 4000, 6000, and 10,000. Nu is seen to go through a minimum at about $2\pi/180$ to $5\pi/180$ rad and a maximum at about $45\pi/180$ rad, and then to decrease to a value slightly above 0.7 at π rad, corresponding to heating from above. Because of the unsymmetrical heating, some convection occurs even in the

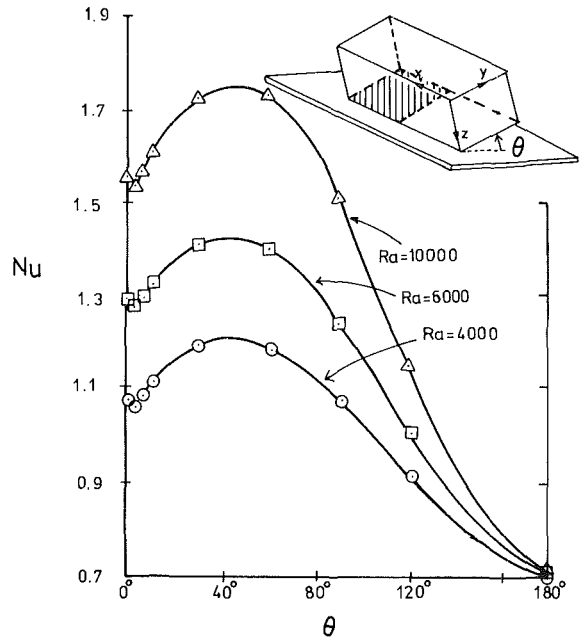

Fig. 4 Predicted mean Nusselt number for inclination of the shorter horizontal dimension (about the longer horizontal dimension as an axis) of a 2 × 1 × 1 rectangular enclosure with a half-heated lower surface

latter limit. The mimimum is attributed to the transition from one mode of circulation to another, as described below.

For a uniform temperature on the lower surface, the mean Nusselt number, as computed by Ozoe et al. [16], varies similarly with the angle of inclination but is approximately one-third higher.

Elevation of the Unheated End of the Enclosure About the Shorter Horizontal Dimension as an Axis. The behavior for this case, as illustrated in Fig. 5, is qualitatively similar to that for inclination about the longer dimensions as an axis. However, the minimum occurs at about $5\pi/180$ rad and the maximum at about $60\pi/180$ rad. The latter value is in close agreement with the prediction of $63.4\pi/180$ rad by Churchill and Ozoe [17]. Again, the mimimum is associated with a transition in the mode of circulation, as described below.

Elevation of the Heated End About the Shorter Horizontal Dimension as an Axis. As illustrated in Fig. 6, a mimimum does not occur for this case. This result is consistent with the absence of a transition in the mode of circulation, as discussed below. The maximum occurs at the somewhat lower angle of about $50\pi/180$ rad.

Streaklines.

Photographs were taken of static displays of the computed streaklines for Ra = 6000 and various inclinations on the cathode ray tube of the Vector General 3404 Graphic Display Unit of the Computer Graphics Laboratory of the School of Engineering and Applied Science of the University of Pennsylvania. Dynamic displays of the streaklines were used to determine the direction and speed of circulation.

Elevation of the Shorter Horizontal Dimension About the Longer Dimension as an Axis. Perspective views of the streaklines as photographed from the cathode ray tube are shown in Fig. 7 for inclination about the longer dimension as an axis (as in Fig. 4). Different viewing angles (not to be confused with the angle of elevation of the enclosure) were used to better elucidate the fluid motion. The heated segment is at $Z=1$ (bottom) and $0\leq X\leq 1$. The Y-axis is inclined.

For no inclination, as shown in Fig. 7(*a*) and somewhat better in Fig. 8(*a*), the motion consists of two symmetrical roll-cells with a 2 × 1 cross section. These roll-cells have a

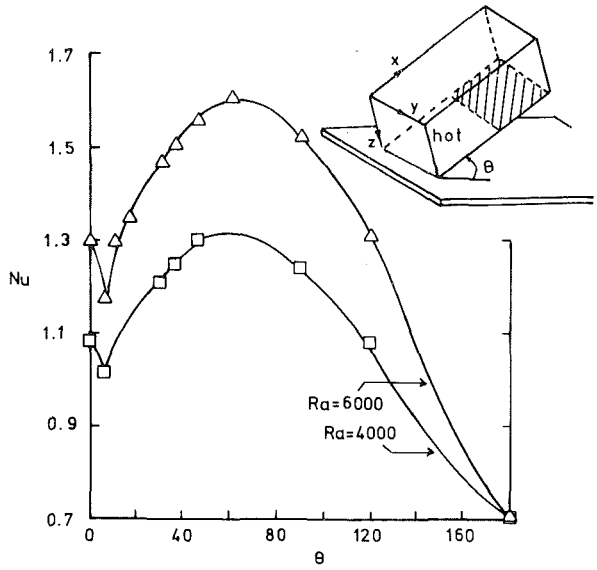

Fig. 5 Predicted mean Nusselt number for elevation of the unheated end (about the shorter horizontal dimensions as an axis) of a 2 × 1 × 1 rectangular enclosure with a half-heated lower surface

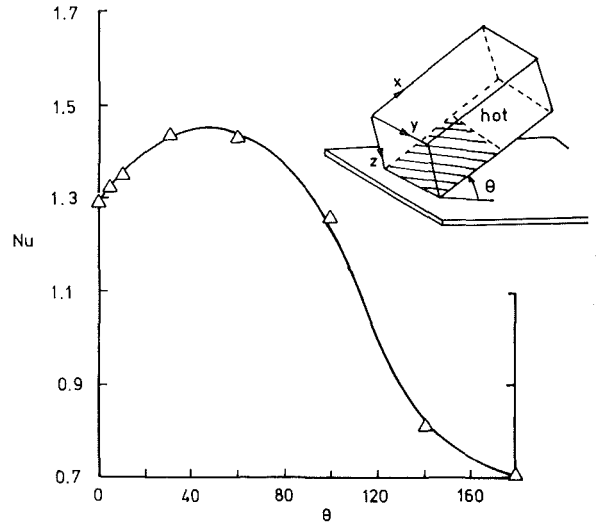

Fig. 6 Predicted mean Nusselt number at Ra = 6000 for elevation of the heated end (about the shorter horizontal dimension as an axis) of a 2 × 1 × 1 rectangular enclosure with a half-heated lower surface

common axis and could be considered to be a single gross roll-cell except that they do not interchange fluid. Their axes are parallel to the shorter dimension (Y-axis) and displaced somewhat from the midplane ($X = 1$) toward the heated end. From the dynamic display, the motion was observed to be upward at the heated end of the enclosure, along the upper, cooled surface ($Z = 0$), downward at the insulated end, and back along the insulated segment ($X>1$) of the lower ($Z=1$) surface.

As the enclosure is inclined about the longer dimension, the two roll-cells become increasingly oblique, distorted, and dissimilar, as illustrated in Figs. 7(*b*), (*c*), (*d*) for $2\pi/180$, $6\pi/180$ and $10\pi/180$ rad, respectively. They retain a common but highly curved axis. For an inclination greater than $10\pi/180$ rad, the plane of separation between the two roll-cells crosses the diagonal plane between the vertical edges of the enclosure, and a gradual transition occurs. Following the transition, the roll-cells are relocated in the left and right hands of the enclosure, as illustrated in Figs. 7(*e*) and (*f*) for $60\pi/180$ and $90\pi/180$ rad, respectively. The portion of the common axis associated with the left hand roll-cell is now nearly parallel to the longer dimensions of the enclosure, but that of the right-hand roll-cell is somewhat oblique.

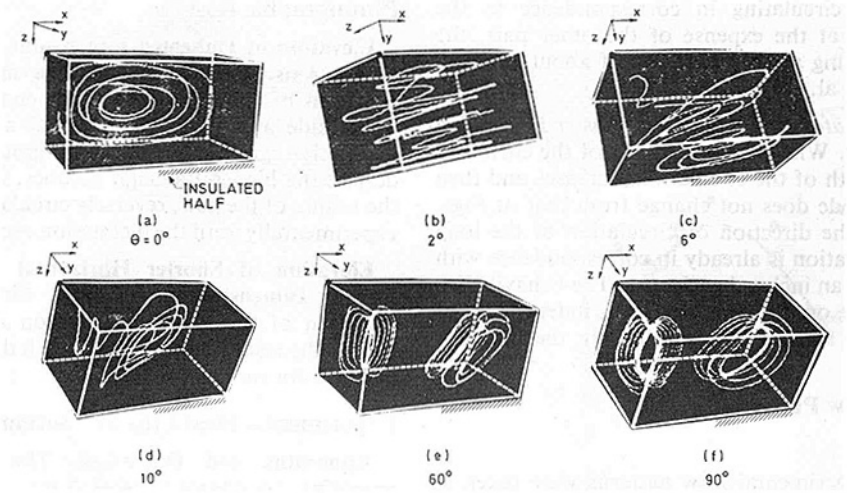

Fig. 7 Perspective view of computed streaklines at Ra = 6000 for inclination of the shorter horizontal dimension (about the longer dimension as an axis) of a 2 × 1 × 1 rectangular enclosure with a half-heated lower surface (heated surface is at $Z = 1$, $X < 1$; angle θ is between the horizontal plane and the X-Y-plane)

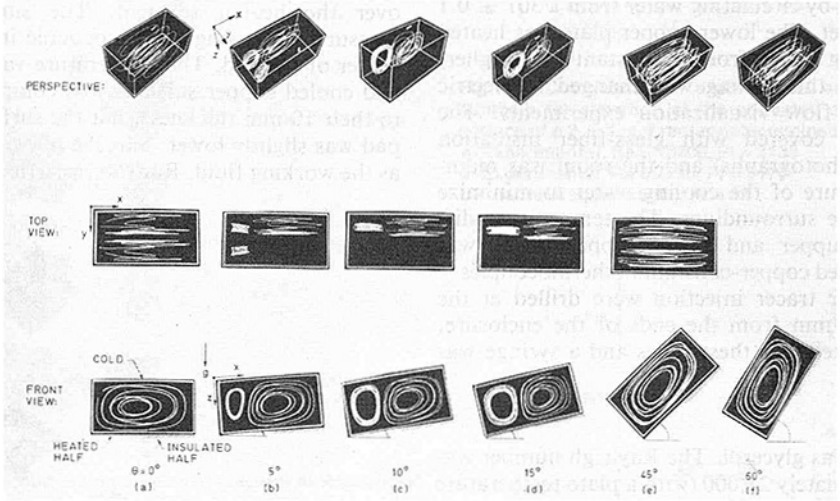

Fig. 8 Perspective, top and front views of computed streaklines at Ra = 6000 for elevation of the unheated end of a 2 × 1 × 1 rectangular enclosure with a half-heated lower surface

This behavior contrasts with that described by Ozoe et al. [16] for a 2 × 1 × 1 box with a uniform surface temperature. In the latter case, the stable motion for a horizontal orientation consists of four roll-cells with 1 × 1 cross sections, and again with axes parallel to the shorter horizontal dimension. These cells are symmetrical with respect to the two vertical midplanes of the enclosures but the direction of circulation of the pair of cells at each end is up along the 1 × 1 end walls and down along the midplane, or the reverse, depending on the initial conditions. Upon inclination about the longer dimension, the four roll-cells retain their integrity, and their symmetry with respect to the 1 × 1 vertical midplane, but become increasingly distorted and unsymmetrical with respect to the 2 × 1 vertical midplane. At an inclination of about $2\pi/180$ rad the plane of separation of the two roll-cells at either end of the enclosure crosses the diagonal plane of that half of the enclosure and a transition of each pair of roll-cells to a single roll-cell with its axis exactly parallel to the longer dimension occurs. The two consolidated roll-cells have a common axis parallel to the longer dimension of the enclosure, and, as contrasted with the half-heated case, are perfectly symmetrical with respect to the vertical 1 × 1 midplane of the enclosure.

Elevation of the Unheated End About the Shorter Horizontal Dimension as an Axis. Photographs for the cathode ray tube of perspective, top and front views are shown in Fig. 8 for several elevations of the unheated end of the enclosure (as in Fig. 5). For this type of elevation, symmetry is maintained with respect to the vertical 2 × 1 midplane. For very small inclinations the two roll-cells of Figs. 7(*a*) and 8(*a*) persist although their common rate of circulation decreases. At an inclination of less than $5\pi/180$ rad two new, small roll-cells are generated at the heated end. These new roll-cells circulate up along the inclined heated surface in correspondence to the buoyant force. Due to the elevation of the unheated end, the circulation of the original roll-cells is in opposition to the buoyant force. Initially, this reverse circulation is maintained by induction from the new roll-cells, but as the inclination is further increased, the new roll-cells grow in size and strength at the expense of the original ones, and the latter eventually vanish, resulting in, as indicated in Fig. 8(*d*) and (*e*), a circulation similar to that for no inclination, but in the opposite direction. The minimum in the rate of heat transfer, as shown in Fig. 5, appears to correspond to the appearance of the two new roll-cells.

For a uniform temperature on the lower surface, whichever

pair of roll-cells is circulating in correspondence to the buoyant force grows at the expense of the other pair, the second pair disappearing at an inclination of about $10\pi/180$ rad (see again, Ozoe et al. [16]).

Elevation of the Heated End About the Shorter Horizontal Dimension as an Axis. When the heated end of the enclosure is elevated, the strength of the circulation increases and then decreases, but the mode does not change from that of Figs. 7(*a*) and 8(*a*), since the direction of circulation of the long roll-cells for no inclination is already in correspondence with the buoyant force for an inclined enclosure. The behavior for a uniform temperature on the lower surface is independent of the elevated end and hence is as described in the previous paragraph.

Photography of Flow Patterns

Apparatus.

Photographs of experimental flow patterns were taken at Okayama University in an enclosure with internal dimensions of 31 × 31 × 62 mm. The upper plate and half of the lower plate were of 10-mm thick copper, resulting in a negligible variation in temperature. The four side walls and the insulated half of the lower plate were plexiglass, also 10-mm thick. The upper plate was cooled by circulating water from a 301 ± 0.1 K bath through a jacket. The lower copper plate was heated similarly by circulating water from a constant (but higher) temperature bath, but the heating was changed to electric resistance during the flow visualization experiments. The entire apparatus was covered with glass-fiber insulation (except when taking photographs) and the room was maintained at the temperature of the cooling water to minimize heat exchange with the surroundings. The temperature difference between the upper and lower copper plates was measured with embedded copper-constantan thermocouples.

Two small holes for tracer injection were drilled at the middle height at 15.5 mm from the ends of the enclosure. Vinyl tubes were inserted into these holes and a syringe was used to inject the tracer.

Conditions.

The working fluid was glycerol. The Rayleigh number was established at approximately 25,000 (with a plate-temperature difference of ~4 K) for each inclination, since this was the lowest value for which it was possible to obtain good photographs without anomalous dispersion of the tracer particles. On the other hand, finite difference calculations were not feasible for such a high Rayleigh number, owing to an inordinate restriction on the time steps. As noted above, prior results for a uniform temperature on the lower surface indicate that this difference in Rayleigh number would not be expected to change the circulation pattern even though the rates of circulation and heat transfer differ considerably. The difference in Prandtl number would be expected to change the rate of circulation but not the pattern.

Ten hours or more were allowed for the enclosure to reach hydrodynamic and thermal equilibrium. A variation of less than 0.1 μV, equivalent to 0.0024K, in the thermocouple readings over the copper plates was used as a further criterion of the attainment of a steady state. (In all cases a unique and nonoscillatory state was observed.) Thereafter, 0.5 ml of a dense dispersion of aluminum particles in glycerol was injected into the enclosure through each of the two holes at a depth of 3 mm. Forty to ninety minutes later, the insulation was removed to permit photographing the traces of these particles. Photographs were taken from both the long and the short sides with $\pi/2$ rad illumination of the whole surface from a projector lamp. ASA 400 black and white film was used with a Nikon f2 Photomic camera having an f3.5 Micro Nikkor lens, at a setting of f11 and an exposure time of 15 s.

Photographic Results

Elevation of Unheated End About the Shorter Dimension as an Axis. Photographs of the aluminum particles for elevation of the right (unheated) end are shown in Fig. 9. These side and front views reveal a circulation pattern in qualitative agreement with the computed streaklines of Fig. 8, despite the higher Rayleigh number. A minor discrepancy is the failure of the new, reversely circulating roll-cells to appear experimentally until the inclination exceeded $5\pi/180$ rad.

Elevation of Shorter Horizontal Dimension About the Longer Dimension as an Axis. Similar photographs for elevation of the shorter dimension are shown in Fig. 10. Again, the results are consistent with the computed streaklines of Fig. 7 for similar conditions.

Experimental Heat Flux Measurements

Apparatus and Operation. The same enclosure and operating conditions were used for the heat flux measurements as for the photographs of particle paths, except that the maintenance of the same surface temperature at different elevations was found to be easier when hot circulating water was used for heating, rather than electricity. The heat flux was measured by placing a heat-flux meter pad over the heated segment. The surface-temperature was measured by a single thermocouple integral with and at the center of the pad. The temperature variation over the heated and cooled copper surfaces was completely negligible owing to their 10-mm thickness, but the surface temperature of the pad was slightly lower. Silicone oil with Pr ≅ 3200 was used as the working fluid. Runs were carried out at Ra = 7790 and

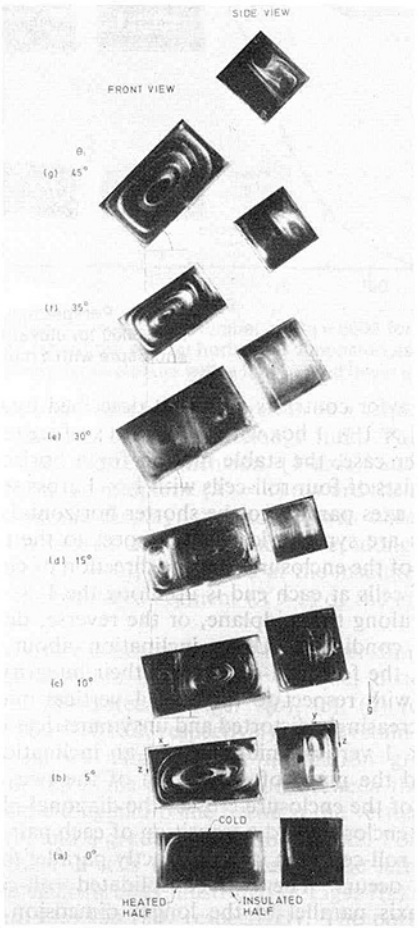

Fig. 9 Photographs of aluminum particles in glycerol at Ra = 25,000 in a 62 × 31 × 31-mm rectangular enclosure with elevation of the unheated end of the half-heated lower surface

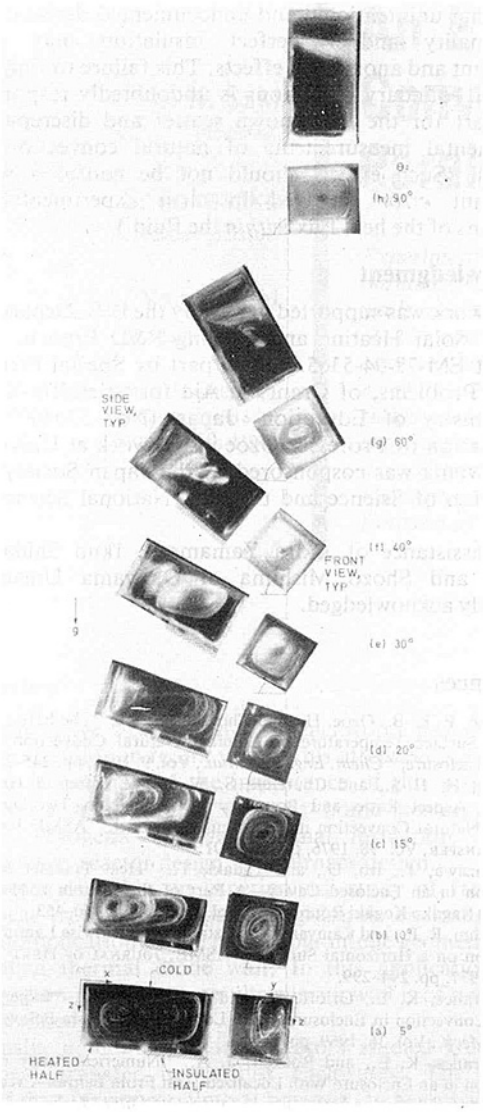

Fig. 10 Photographs of aluminum particles in gylcerol at Ra = 25,000 in a 62 × 31 × 31-mm rectangular enclosure with inclination of the shorter dimension of the half-heated lower surface

13,300. The silicone oil was chosen because of the relatively small variation in its viscosity with temperature. As noted above, the choice of Rayleigh numbers extending upward from the computed range followed from the necessity of a reasonable temperature difference between the plates. Even then, the small temperature differences of 1–2 K precluded the establishment of precise, prechosen values of the Rayleigh number.

Results. The experimentally determined Nusselt numbers for elevation of the unheated end about the shorter horizontal dimension as an axis are compared with the computed values in Fig. 11. The predicted maximum at about $45\pi/180$ rad and minimum at about 2 to $5\pi/180$ rad are both observed. Good qualitative agreement can also be observed between the predictions for Ra = 6000 and Pr = 10, and the measurements for Ra = 7790 and 13,300 and Pr = 3130-3170 for elevations greater than $\pi/6$ rad. The experimental Nusselt numbers for lesser inclinations fall far below the predicted values.

Figure 12 is a similar comparison for elevation of the heated end about the shorter horizontal dimension as an axis. In this case, the measurements confirm the predictions qualitatively, with a maximum at about $45\pi/180$ rad and no minimum, but are much lower at all angles.

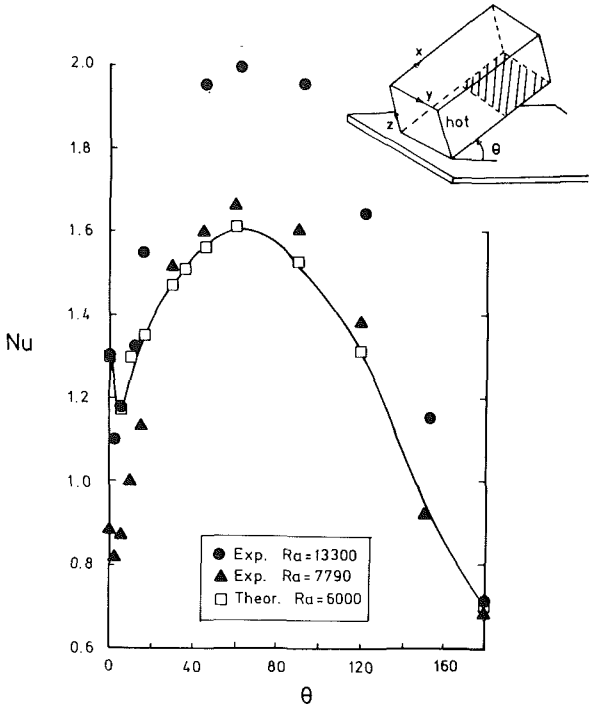

Fig. 11 Comparison of experimental and predicted mean Nusselt numbers for elevation of the unheated end of the half-heated lower surface of a 2 × 1 × 1 rectangular enclosure
● -Experimental, Ra = 13300, Pr = 3130
▲ -Experimental, Ra = 7790, Pr = 3170
□ -Theoretical, Ra = 6000, Pr = 10

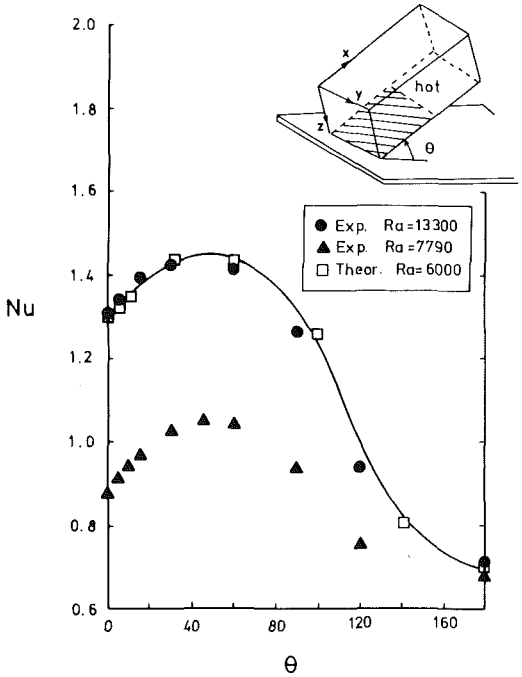

Fig. 12 Comparison of experimental and predicted mean Nusselt numbers for elevation of the heated end of the half-heated lower surface of a 2 × 1 × 1 rectangular enclosure

The foregoing discrepanices are presumed to be due to heat flow along and through the plexiglass section of the lower plate. For elevation of the heated end, this unaccounted heat flow generates a pair of secondary roll-cells with reverse circulation, thereby impeding the pair of primary roll-cells and decreasing the overall rate of convection between the uninsulated half of the high-temperature surface and the cooled surface. As noted previously, the theoretical calculations for perfect insulation do not produce a pair of

secondary roll-cells for elevation of the heated end.

In the case of elevation of the unheated end, heat flow through the plexiglass apparently tends to impede the motion of the original roll-cells above the insulation (as shown on the right-hand side of Fig. 8(*b*), (*c*), and (*d*), and on the right-hand side of the front view in Fig. 9(*c*), (*d*), and (*e*)), thereby decreasing the overall rate of convection. After the original roll-cells vanish, at elevations above $35\pi/180$ rad, the effect of the heat flow through the plexiglass is apparently less improtant.

Conclusions

Insulating a portion of the heated surface of an inclined rectangular enclosure produces significant changes in the mode of circulation and rate of heat transfer relative to a completely isothermal surface. These changes may be of practical importance in solar collectors and in space heating.

The asymmetry due to insulating half of the heated surface results in circulation for all temperature differences and orientations. Thus, there is no critical Rayleigh number for heating from below, and the rate of heat transfer always exceeds that for pure conduction with the same boundary conditions. Some circulation and a rate of heat transfer exceeding that for pure conduction with the same boundary conditions also occur for heating from above. However, the absolute rate of heat transfer with a uniform temperature on the lower plate still exceeds that for half-heating at all inclinations and for all of the Rayleigh numbers which were investigated, primarily because the heated (lower) area is twice as big.

If the Nusselt number were based on the heated area rather than on the cooled area, it would exceed that for surfaces with uniform temperatures for all conditions. This result is in accord with the conclusion reached by Chao et al. [1] that surface temperature variations produce higher heat transfer rates than do uniform temperatures.

The number of roll cells appears to be associated with the area of heating rather than with the total area. Thus, one pair of roll-cells occurred for heating of half of the lower surface as compared to two pairs of roll-cells for uniform heating.

Photographs of particle paths were in good agreement with computed streaklines despite differences in the Rayleigh and Prandtl numbers, thus providing confidence in the computed rates of heat transfer.

Streaklines were found to be invaluable in interpreting the behavior. For example, the variation of the mean Nusselt number with the type and degree of inclination can be explained directly in terms of the changes in strength and mode of the circulation pattern. Specifically, the minimum in the Nusselt number is observed to occur in conjunction with the change in the mode of circulation for elevation of the shorter dimension or the insulated end of the enclosure, whereas no minimum and no change of mode occur for elevation of the heated end at angles greater than $30\pi/180$ rad about the shorter horizontal dimension as an axis. For lesser elevations of the heated end and for elevations of the unheated end the

The experimentally measured heat fluxes are in qualitative agreement with the computed values for elevation of the heated end at angles greater than $30\pi/180$ rad about the shorter horizontal dimension as an axis. For lesser elevations of the heated end and for elevations of the unheated end the experimental values follow the same trends as the predictions but fall significantly lower for the same Ra. This discrepancy is attributed to finite conduction along and through the plexiglass plate comprising the insulated half of the initially lower plate, resulting in a small counter-circulation.

The theoretical results of this investigation and of Chao et al. [1], as well as the above experimental discrepancies, indicate that unintentional and undocumented deviations from isothermality and/or perfect insulation may produce significant and anomalous effects. This failure to simulate the nominal boundary conditions is undoubtedly responsible in large part for the well-known scatter and discrepancies in experimental measurements of natural convection in enclosures. (Such effects should not be confused with the significant *error* involved in most experimental determinations of the heat flux *within* the fluid.)

Acknowledgment

This work was supported in part by the U.S. Department of Energy, Solar Heating and Cooling R&D Branch, through contract EM-78-04-5365. and in part by Special Projects on Energy Problems, of Grants in Aid for Scientific Research, the Ministry of Education, Japan (No. 57040075). The participation of Professor Ozoe in the work at University of Pennsylvania was cosponsored by the Japan Society for the Promotion of Science and the U.S. National Science Foundation.

The assistance of Akira Yamamoto, Ikuo Shida, Akira Mouri, and Shozo Mishima of Okayama University is gratefully acknowledged.

References

1 Chao, P. K.-B., Ozoe, H., and Churchill, S. W., "The Effect of a Non-Uniform Surface Temperature on Laminar Natural Convection in a Rectangular Enclosure," *Chem. Eng. Commun.*, Vol. 9, 1981, pp. 245–254.

2 Chu, H. H.-S., and Churchill, S. W., "The Effect of Heater Size, Location, Aspect Ratio and Boundary Conditions on Two-Dimensional, Laminar Natural Convection in Rectangular Channel," ASME JOURNAL OF HEAT TRANSFER, Vol. 98, 1976, pp. 194–201.

3 Hanzawa, T., Ito, U., and Tadaki, T., "Heat Transfer by Natural Convection in an Enclosed Cavity—A Part of the Bottom is Heated," (in Japanese) Kagaku Kogaki Ronbunshu, Vol. 1, 1975, pp. 450–453.

4 Boehm, R. F., and Kamyab, D., "Established Stripwise Laminar Natural Convection on a Horizontal Surface," ASME, JOURNAL OF HEAT TRANSFER, Vol. 99, 1977, pp. 294–299.

5 Torrance, K. E., Orloff, L., and Rockett, J. A., "Experiments on Natural Convection in Enclosures With Local Heating from Below," *Journal of Fluid Mech.*, Vol. 36, 1969, pp. 21–31.

6 Torrance, K. E., and Rockett, J. A., "Numerical Study of Natural Convection in an Enclosure With Localized Heat From Below—Creeping Flow to the Onset of Laminar Instability," *Journal of Fluid Mech.*, Vol. 36, 1969, pp. 33–54.

7 Greenspan, D., and Schultz, D., "Natural Convection in an Enclosure With Localized Heating from Below," *Computer Methods Appl. Mechanics and Engineering*, Vol. 3, 1974, pp. 1–10.

8 Churchill, S. W., "Free Convection in Layers and Enclosures," *Heat Exchanger Design Handbook*, ch. 2.5.8, edited E. U. Schlunder, Hemisphere Publishing, Washington, D.C., 1983.

9 Ozoe, H., Sayama, H., and Churchill, S. W., "Natural Convection in an Inclined Rectangular Channel at Various Aspect Ratios and Angles—Experimental Measurements," *International Journal of Heat and Mass Transfer*, Vol. 18, 1975, pp. 1425–1431.

10 Ozoe, H., Yamamoto, K., Churchill, S. W., and Sayama, H., "Three-Dimensional, Numerical Analysis of Laminar Natural Convection in a Confined Fluid Heated From Below," ASME JOURNAL OF HEAT TRANSFER, Vol. 98, 1976, pp. 202–207.

11 Chu, H. H.-S., and Churchill, S. W., "The Development and Testing of a Numerical Method for Computation of Laminar Natural Convection in Enclosures," *Computers and Chem. Engrg.*, Vol. 1, 1977, pp. 103–108.

12 Brian, P. L. T., "A Finite Difference Method of High-Order Accuracy for the Solution of Three-Dimensional Transient Heat Conduction," *AIChE Journal*, Vol. 7, 1961, pp. 367–370.

13 Richardson, L. F., and Gaunt, J. A., "The Deferred Approach to the Limit," *Phil. Trans. Roy. Soc.*, London, Ser. A, Vol. 226, 1972, pp. 299–361.

14 Churchill, S. W., Chao, P., and Ozoe, H., "Extrapolation of Finite-Difference Calculations of Laminar Natural Convection in Enclosures to Zero Grid-Size," *Num. Heat Transfer*, Vol. 4, 1981, pp. 39–51.

15 Yamamoto, K., Ozoe, H.,, Chao, P., and Churchill, S. W., "The Computation and Dynamic Display of Three-Dimensional Streaklines for Natural Convection in Enclosures," *Computers and Chem. Engrg.*, Vol. 6, 1982, pp. 161–167.

16 Ozoe, H., Churchill, S. W., Okamoto, T., and Sayama, H., "Three-Dimensional Natural Convection in Inclined Rectangular Enclosures," *Proc. PACHEC '77*, Vol. 1, 1977, pp. 24–31, AIChE, New York.

17 Churchill, S. W., and Ozoe, H., "Correlating Equations for Natural Convection in Enclosures," in preparation.

N. Seki
Professor.

S. Fukusako
Associate Professor.

A. Yamaguchi
Graduate Student.

Department of Mechanical Engineering,
Hokkaido University,
Sapporo 060, Japan

An Experimental Study of Free Convective Heat Transfer in a Parallelogrammic Enclosure

Experimental measurements are presented for free convective heat transfer across a parallelogrammic enclosure with the various tilt angles of parallel upper and lower walls insulated. The experiments covered a range of Rayleigh numbers between 3.4 $\times$ 10^4 and 8.6 $\times$ 10^7, and Prandtl numbers between 0.70 and 480. Those also covered the tilt angles of the parallel insulated walls with respect to the horizontal, ϕ, of 0, ± 25, ± 45, ± 60, and ± 70 deg under an aspect ratio of $H/W = 1.44$. The fluids used were air, transformer oil, and water. It was found that the heat transfer coefficients for $\phi = -70$ deg were decreased to be about 1/18 times those for $\phi = 0$ deg. Experimental results are given as plots of the Nusselt number versus the Rayleigh number. A correlation equation is given for the Nusselt number, Nu, as a function of ϕ, Pr, and Ra.

Introduction

Free convective heat transfer in enclosures has received increasing attention in recent years. This attention is ascribed in part to recognition of the importance of this process in many diverse applications, such as home heating, solar collectors, cryogenic storage, thermal insulation, crystal growth, nuclear reactor design, and furnace design.

This paper describes an experimental study of free convective heat transfer in a parallelogrammic enclosure. An important application of the parallelogrammic geometry is to the so-called thermal diode wall. In this application, the parallelogrammic geometry results when a wall is of a vertical stack of inclined cavities.

Previously, a number of investigators studied free convective heat transfer in various enclosures. The works completed thus far appear almost, however, to be restricted to relatively simple rectangular, cylindrical, and spherical enclosures, even if including ones tilted. Dropkin and Sommerscales [1] performed an experimental study of free convective heat transfer in liquid between two parallel plates at various inclination angles. They determined a power-law form relating the variables Nusselt, Rayleigh, and Prandtl numbers. Free convective heat transfer through inclined fluid layers of high aspect ratio was investigated by Hollands et al. [2], who covered Rayleigh numbers up to 10^5 and inclination angles from 0 to 70 deg measured from the horizontal. Arnold et al. [3] determined free convective heat transfer in a rectangular enclosure of various aspect ratios with Rayleigh numbers ranging up to 10^6. They claimed that the variation of Nusselt number with tilt angle showed a local minimum Nu between 70 and 30 deg, while Nu had a local maximum at 0 deg tilt angle. Hart [4] carried out extensive analytical and experimental investigations of flow regimes in an inclined box. Catton et al. [21] investigated theoretically the free convection heat transfer in a finite, rectangular slot arbitrarily oriented with respect to the gravity vector using the Galerkin method, for the range of parameters: Rayleigh numbers of 3 $\times$ 10^4 to 2 $\times$ 10^6, aspect ratios of 0.1 to 20, and tilt angles of -30 to $+75$ deg. They found that the heat transfer characteristics of the rectangular regions with aspect ratios less than 1 are clearly sensitive to the aspect ratio. Ozoe et al. [5–11] performed experimental and analytical studies pertaining to tilted rectangular channels. In [5], the author reported that the mode of convection in a square box at 90 deg tilt is a single two-dimensional roll with its axis along the long dimension. It was also found in [6] that the Nusselt number takes a minimum value between 0 and 90 deg for low aspect ratios. By the author's explanation, the minimum is caused by a change in the nature of the circulation pattern. Three-dimensional photographs which illustrate the transition between the flow modes as the inclination angle changes were presented in [9]. Randall et al. [12] measured extensively the heat transfer across air in tilted enclosures with Grashof numbers ranging up to 3 $\times$ 10^5. Edwards et al. [22] proposed correlations for free convection through rectangular cells with the aspect ratios (height/width) of 0.25 to 0.125, which are in good agreement with their experimental results including ones for the rectangular honeycombs.

Recently, Nakamura and Asako [13] investigated both analytically and experimentally free convective heat transfer in a parallelogrammic enclosure filled with air. They reported that their analytical results are in good agreement with the experimental ones for the case of one vertical side uniformly cooled, the opposing vertical side uniformly heated, and linear-temperature top and bottom tilted. An experimental study of free convective heat transfer in liquids in parallelogrammic geometries at various aspect ratios was carried out by Maekawa and Tanazawa [14]. They covered a Rayleigh number range of 3 $\times$ 10^3 to 2 $\times$ 10^7 and a Prandtl number range of 7 to 10^4 for tilt angles of 0 to ± 45 deg by using water and silicon oil as testing fluids.

From the foregoing literature survey, it appears that there may be a great lack of information on the heat transfer characteristics of the parallelogrammic geometries.

The objective of this paper is, therefore, to present experimental heat transfer data for a two-dimensional parallelogrammic enclosure which has one vertical side isothermally heated, the opposing vertical side isothermally cooled, and the parallel adiabatic upper and lower walls tilted. Overall heat transfer data for Rayleigh numbers from 3.4 $\times$ 10^4 to 8.6 $\times$ 10^7 were obtained using air, transformer oil, and water as testing fluids. In particular, the effect of the tilt angle and heat flux on the heat transfer characteristics of the parallelogrammic enclosure was extensively investigated.

Contributed by the Heat Transfer Division for publication in the JOURNAL OF HEAT TRANSFER. Manuscript received by the Heat Transfer Division January 13, 1982.

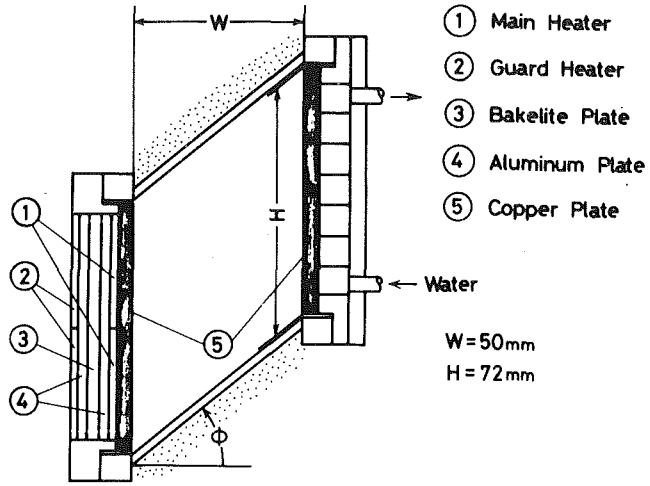

Fig. 1 Schematic diagram of experimental set-up

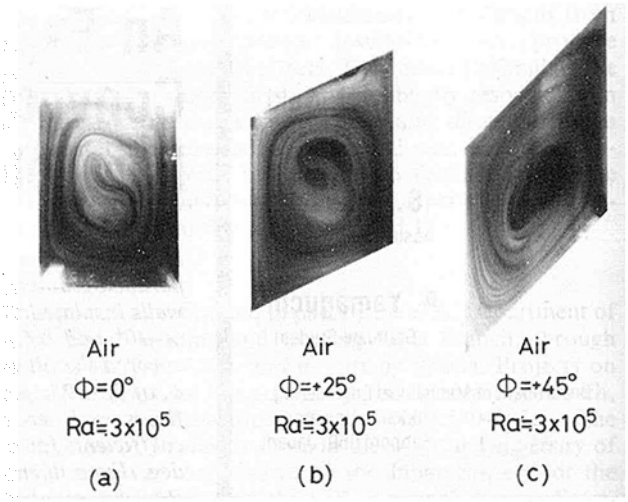

Fig. 2 Visual observations of flow patterns for $\phi \gtreqless 0$

Experimental Apparatus and Procedures

A schematic of the experimental apparatus used is shown in Fig. 1. The apparatus was constructed specially for measuring of heat flux for various tilt angles of parallel upper and lower insulated walls in a parallelogrammic enclosure. It mainly consists of two vertical copper plates, each 72-mm long and 300-mm wide, enclosed with two bakelite plates tilted from the horizontal. The width of the enclosure, W, was maintained at 50 mm giving an aspect ratio $H/W = 1.44$. The front and the back side walls of the enclosure were made of lucite plates to permit the visual observation of flow patterns. One of the two vertical plates was made of a 6-mm thick copper sheet heated by two main foil-type heaters. Guard heaters were mounted on the back side of these main heaters to minimize heat loss to the environment. Each main heater could be individually controlled so that a desired isothermal wall condition was obtained. The other opposing vertical plate was cooled by temperature-controlled water running through a chamber with six baffle-fins inside to guide the water flow, attached to the back surface of the plate. Asbestos sheeting was used as a gasket between the copper and bakelite plates to reduce the thermal conduction between the two.

Surface temperature measurements were obtained from 12 copper-constantan thermocouples of 0.1 mm in diameter penetrating each plate from the rear to the front face. All the thermocouples were calibrated up to 120°C. The output of these thermocouples was continuously recorded on Yokogawa Multiplex Recorders. Maximum temperature variations of less than 0.3°C over the surface of the cold plate and 0.6°C over the surface of the hot plate were obtained at temperature differences up to 31°C. The power to the main heaters was measured by means of an ammeter and voltmeter provided for each heating circuit. The power to the main heaters was increased in steps up to a prescribed temperature. In each run, 3 to 7 hrs were usually required to reach a steady state.

Visual observation of flow patterns were attained from the front side wall with a camera by projecting a light through narrow slits of 2 mm in width on both upper and lower bakelite tilted walls. Polystyrene powder of about 50 μm in diameter, aluminum powder of about 100 μm in equivalent diameter, or cigarette smoke was selectively provided depending on the kinds of fluid employed.

The whole system of the experimental apparatus was wrapped by an insulating material (styrofoam of 50 mm in thickness) and was set in a temperature-controlled room. In the current experiments, the cooled-plate temperature, T_c, was carefully adjusted to $T_c = 2T_\infty - T_h$ in order to minimize the heat loss to the environment, where T_∞ denotes the room temperature and T_h the heated-plate temperature. Each surface was polished to reduce the radiation contribution to the total heat flow. The T_h was, furthermore, ranged to be less than 40°C. The heat transferred by radiation when adopting air as working fluid could be simply calculated using the laws of radiation. The emissivity of 0.08 was used for copper plate. The approximate magnitude of radiative heat transfer was, thus, found to be less than 5 percent of the total heat flux transferred.

Distilled water, transformer oil, and air as testing fluids were employed. The current experiments, thus, covered a range of Rayleigh numbers between 3.4×10^4 and 8.6×10^7 and Prandtl numbers between 0.7 and 480 for an aspect ratio $H/W = 1.44$.

Visual Observation

Qualitative visual observations were carried out to study the effect of the tilt angle of the parallel upper and lower walls insulated on the flow pattern in the current parallelogrammic enclosure. Typical flow patterns under the various tilt angles are shown in Figs. 2 and 3. In these experiments, the flow patterns were stable and two-dimensional flow was attained.

Nomenclature

C_p = specific heat
g = gravitational acceleration
H = length of heated and cooled walls
Nu = Nusselt number, defined in equation (1)
Pr = Prandtl number, defined in equation (3)
q = heat flux from heated wall
Ra = Rayleigh number, defined in equation (2)
T_c = temperature of cooled wall
T_h = temperature of heated wall
T_∞ = temperature of environment
ΔT = temperature difference between heated and cooled walls, $T_h - T_c$
β = coefficient of volumetric expansion
κ = thermal diffusivity
θ = tilt angle in radian, $\pi\phi/180$
λ = thermal conductivity
μ = viscosity
ν = kinematic viscosity
ϕ = tilt angle of insulated upper and lower walls

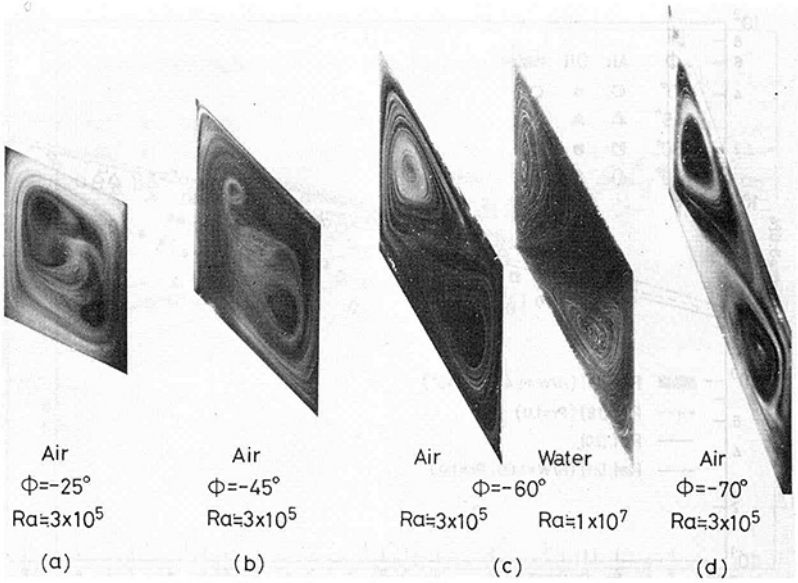

Fig. 3 Visual observations of flow patterns for $\phi < 0$

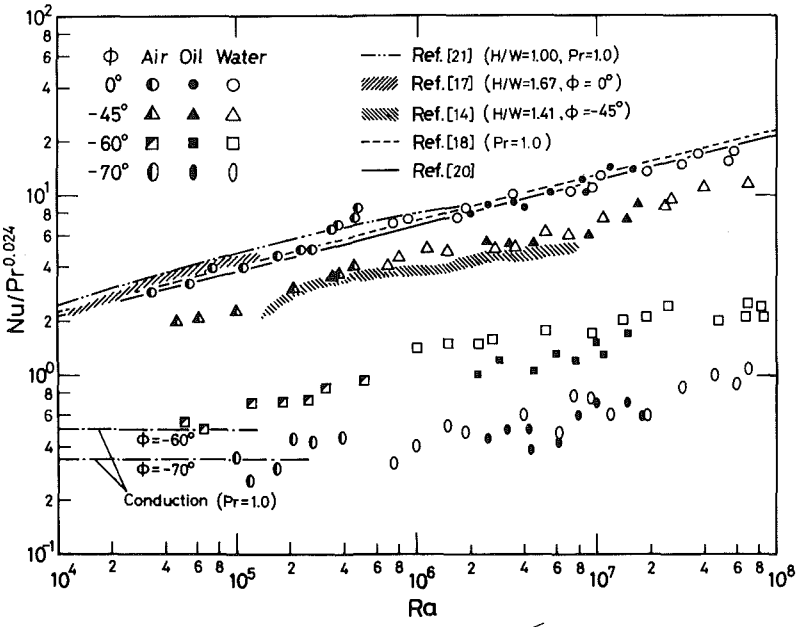

Fig. 4 Heat transfer results for $\phi \leqq 0$

The experimental flow pattern in Fig. 2(*a*) for an orthodox geometry (one vertical side isothermally heated, the opposing vertical side isothermally cooled, and horizontal adiabatic top and bottom), for Ra = 3×10^5 and $H/W = 1.44$, appears to be qualitatively in good agreement with analytical or experimental results of previous investigators [15-20]. The movement of the eddy is upward along the heated wall while downward along the cooled wall. Figures 2(*b*) and 2(*c*) show the flow patterns observed for the positive tilt angles of the parallel upper and lower walls insulated. The flows seem to be qualitatively similar through all of the tilt angles tested.

On the other hand, when the tilt angle of the parallel upper and lower walls insulated is negative, the effect of the inclination on the flow pattern becomes very clear. Figure 3(*b*) shows the flow pattern for $\phi = -45$ deg. It seems that the centers of the twin secondary flows may be observed in the parallelogrammic enclosure. However, the intensity of the eddies are so weak that tracers do not follow it exactly. Figures 3(*c*) and 3(*d*) show the flow patterns for $\phi = -60$ and -70 deg, respectively. The twin secondary flows can be clearly observed. Thus, it appears that the heat transfer performance may be markedly disturbed by the complex mechanism of the flow pattern followed with the retarded velocity in the enclosure.

Results and Discussion

In all, 235 experimental runs were conducted for various temperatures of the heated wall. Measurements were made for the temperature differences, ΔT, between the heated and cooled walls, which varied up to 31°C.

The present study is concerned with the experiments of free convective heat transfer across the parallelogrammic enclosures with the adiabatic parallel upper and lower walls tilted. Guided by dimensional analysis, the effects of various parameters on the heat transfer characteristics of the parallelogrammic enclosure were experimentally evaluated. The following dimensionless clusters which may be relevant in correlating and evaluating the observed results were obtained

$$qW/(\Delta T\lambda), g\beta\Delta TW^3/(\nu\kappa), \mu C_p/\lambda, H/W, \phi$$

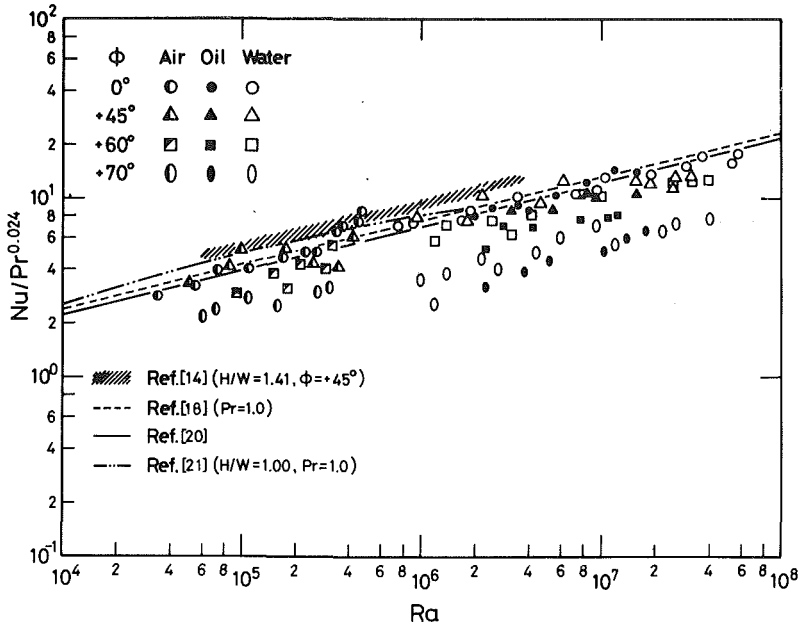

Fig. 5 Heat transfer results for $\phi \gtreqless 0$

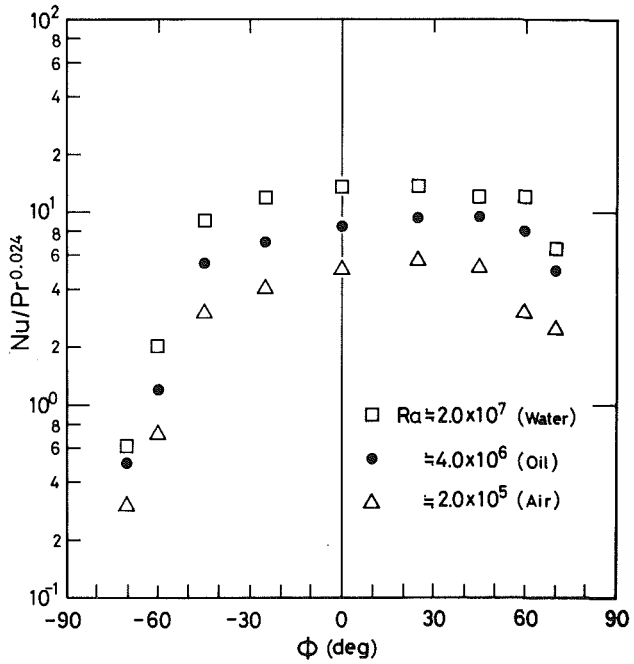

Fig. 6 Effects of tilt angle on heat transfer

where q is the heat flux from the heated wall, W the vertical distance between the heated and cooled walls, ΔT the temperature difference between the heated and cooled walls, g the gravitational acceleration, λ the thermal conductivity, β the coefficient of volumetric expansion of the working fluid, μ the viscosity, ν the kinematic viscosity, κ the thermal diffusivity, C_p the specific heat, H the length of heated or cooled wall, and ϕ the tilt angle of the parallel upper and lower insulated walls. Thus, for the sake of convenience, the Nusselt number, Nu, the Rayleigh number, Ra, and the Prandtl number, Pr, may be conventionally defined as follows

$$\mathrm{Nu} = qW/(\Delta T\lambda) \tag{1}$$

$$\mathrm{Ra} = g\beta\Delta TW^3/(\nu\kappa) \tag{2}$$

$$\mathrm{Pr} = \mu C_p/\lambda \tag{3}$$

The logarithmic plots in Figs. 4 and 5 show the relationship between the Nusselt numbers and Rayleigh numbers for the various tilt angles of the parallel upper and lower insulated walls using air, water, and transformer oil as testing fluids. In calculations of the dimensionless parameters, all the properties were evaluated at the reference temperature, namely, the average temperature of the heated and cooled walls. With a view to generalizing the results, the quantity $\mathrm{Nu}/\mathrm{Pr}^{0.024}$ is plotted on the ordinate in all the figures rather than Nu itself. The choice of $\mathrm{Pr}^{0.024}$ as the scale factor is based on Seki et al. [20], who investigated numerically the effect of Prandtl number on Nusselt number for an aspect ratio of 0.2 and Rayleigh number of 10^5, and evaluated the Prandtl to the 0.024 power using the slope of the relation between the Nu and Pr. In each figure, the experimental data are parameterized by the tilt angles of the parallel upper and lower insulated walls. Aside from the expected trend whereby the Nusselt number increases monotonically with increasing Rayleigh number, it is evident that the tilt angle plays a markedly important role.

Consider first the case when $\phi \leqq 0$. Figure 4 is plots of $\mathrm{Nu}/\mathrm{Pr}^{0.024}$ versus Ra for the negative various angles of inclination tested. The data points for $\phi = -25$ deg are omitted from the figure to avoid crowding and confusion. In the graph, the previous experimental [17] and analytical [18, 20, 21] results for $\phi = 0$ deg are also presented along with the current experimental ones. Hirata et al. [17] investigated experimentally the free convective heat transfer across an enclosed vertical layer of various aspect ratios varied from 0.17 to 25.6 using water as the testing fluid. The experimental data of [17] for $H/W = 1.67$ are entered for comparison in the figure. MacGregor and Emery [18] and Seki et al. [20] studied numerically the free convective heat transfer in an enclosed rectangular cavity with various aspect ratios for a wide range of Prandtl and Rayleigh numbers, and proposed the correlated equations of Nusselt number as functions of Rayleigh number and aspect ratio, (and furthermore Prandtl number in [20]), respectively. As will be seen in Fig. 4, the present experimental results for $\phi = 0$ deg is in good agreement with experimental [17] and analytical ones [18, 20, 21].

From an inspection of Fig. 4, it is seen that the heat transfer rate across the parallelogrammic enclosure is markedly

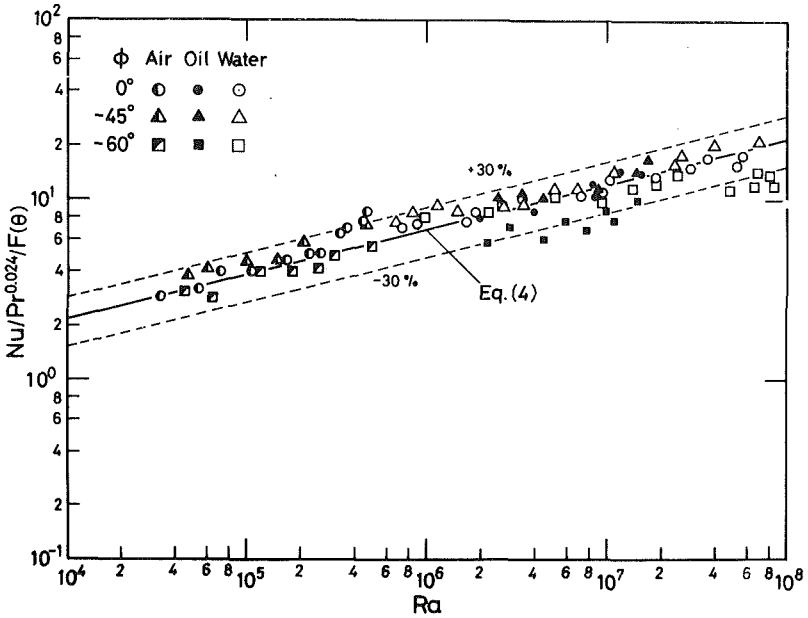

Fig. 7 Correlation of heat transfer results for $\phi \lessgtr 0$

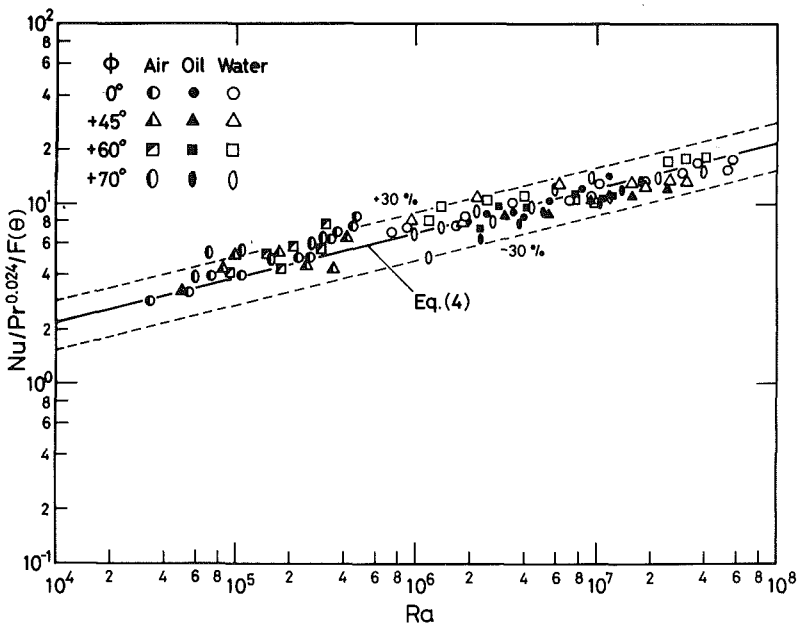

Fig. 8 Correlation of heat transfer results for $\phi \gtrless 0$

decreased with negatively increasing tilt angles of the parallel upper and lower insulated walls. It is clear that the heat transfer coefficients for $\phi = -70$ deg are decreased to be about 1/18 those for $\phi = 0$ deg. Part of this characteristic can be ascribed to the fact that large negative inclination of the parallel upper and lower insulated walls results in a variety of complex retarded flow patterns, as shown in Fig. 3. These may be caused by the condition that the heated surface is situated at the higher level than that of the cooled one. Namely, Fig. 3(*d*) ($\phi = -60$ deg) shows that there are independently two quite weak circular flows, one along the hot wall and the other along the cold wall, which exchange with much difficulty the thermal energy at the central part in the enclosure each other. This fact suggests that the hot fluid is easily trapped above the cold fluid when the heated surface is clear above the top edge of the cooled one. Therefore, it appears that the heat transfer between the two surfaces may be through pure conduction if the Rayleigh number becomes smaller than that of some critical value (the onset of free convection).

It is relevant to consider comparison between the current results and those of Nakamura and Asako [13] and Maekawa and Tanazawa [14]. In [13] the experiments were carried out under the condition of the top and bottom walls having the linear distributions of temperature, respectively. On the other hand, in [14] the tilt angles of the insulated top and bottom walls and the width between the heated and cooled plates were varied so that the relation $H/(W/\cos\phi)$ is uniform. A comparison with $\mathrm{Nu/Pr}^{0.024}$, therefore, is made in Fig. 4 only for $\phi = -45$ deg, because the operating conditions of [13, 14] except one for $\phi = -45$ deg by [14] evidently different from those of the current experiments as mentioned above. As will be seen in Fig. 4, the present experimental results for $\phi = -45$ deg are qualitatively in good agreement with those of [14].

Of interest is that most of the data for both $\phi = -60$ and -70 deg decrease below the value of $Nu/Pr^{0.024} = 1.0$ (assumed $Pr = 1.0$). It is to be noted that in the present study the perpendicular width between the heated and cooled walls is adopted as a reference length. It is, thus, seen that the current experimental results for $\phi = -60$ and -70 deg tend to approach asymptotically the Nusselt numbers for the conduction region ($Nu = \cos\phi$) which are denoted as the dashed lines in the figure.

Attention will now be turned to the case when $\phi > 0$. Figure 5 shows the Nusselt numbers plotted as a function of the Rayleigh number for $\phi = 0$, $+45$, $+60$, and $+70$ deg. The data points for $\phi = +25$ deg are omitted from the figure because of crowding and confusion. Also presented in the figure are the analytical [20] and experimental [14] results along with the current experimental ones for a comparison. It is seen in the figure that the trends from the two sets of experiments for $\phi = +45$ deg are the same, but there are small differences in the level of the Nusselt numbers. From further inspection of Fig. 5, it appears that there may be a trend that the Nusselt number for $\phi > 0$ increases at first with an increase in ϕ, attains a maximum, and then decreases. It is, furthermore, noteworthy that the relative sensitivity of the ϕ to the magnitude of the $Nu/Pr^{0.024}$ for $\phi > 0$ is lower than that for $\phi < 0$.

To investigate more clearly the effect of the tilt angle of the upper and lower walls insulated on the heat transfer performances in a parallelogrammic enclosure, the Nusselt numbers $Nu/Pr^{0.024}$ for air, transformer oil, and water as testing fluids as a function of the tilt angle ϕ are shown in Fig. 6. It is seen that there is a general trend toward lower values of $Nu/Pr^{0.024}$ at both of lower and higher ϕ, which is qualitatively in good accordance with prior experiences [13, 14]. Aside from the characteristics mentioned above, it is of interest that the heat transfer coefficient for $\phi > 0$ increases at first slightly with an increase in ϕ, goes through a maximum at a value of about $\phi \simeq +30$ deg, and then decreases with further increase in ϕ. This phenomenon is probably due to the somewhat complex varieties of the following effects: (*i*) the heat transfer may be promoted by the fact that the heated wall is below the cooled one when $\phi > 0$; (*ii*) the increased actual distance between the heated and cooled walls with positively increasing ϕ may retard the heat transfer across the enclosure.

Finally, all the data entered in Figs. 4 and 5 for $\phi \leqq 0$ deg except for $\phi = -70$ deg and for $\phi \geqq 0$ deg are given on Figs. 7 and 8, respectively, using the plots of $(Nu/Pr^{0.024})/F(\theta)$ versus Ra, where $F(\theta)$ is a function of the tilted angle θ (radian) of the parallel upper and lower walls insulated in a parallelogrammic enclosure. All the dimensionless parameters are computed using properties evaluated at the mean temperature between the heated and cooled walls. Employing the least-squares technique, it appears that the overall correlation of the heat transfer rate may be given as follows

$$Nu = 0.218F(\theta)Pr^{0.024}Ra^{1/4} \tag{4}$$

where for 0 deg $\leqq \phi \leqq +70$ deg, $3.4 \times 10^4 < Ra < 5.8 \times 10^7$, $0.7 < Pr < 480$, and $H/W = 1.44$

$$F(\theta) = 1 + 0.546\theta - 0.781\theta^2 \tag{5}$$

and for -60 deg $\leqq \phi \leqq 0$ deg, $3.4 \times 10^4 < Ra < 8.6 \times 10^7$, $0.7 < Pr < 480$, and $H/W = 1.44$

$$F(\theta) = 1 - 0.754\theta^2 \tag{6}$$

It may be seen that the equation obtained almost correlates the data within a deviation of less than about ± 30 percent, as will be shown in Figs. 7 and 8.

Conclusions

This paper reports the results of an experimental study of free convective heat transfer across a set of parallelogrammic enclosures with constant H/W. Visual observations were made to investigate the effect of the tilt angle of the parallel insulated upper and lower walls on the flow pattern in the enclosure. Based on the experimental data reported in this paper, a mathematical expression has been developed for evaluating the heat transfer coefficient in the parallelogrammic enclosures for fluids of air, transformer oil, and water at various tilt angles of the insulated walls.

The correlative expression for the ranges of the parameters investigated was found to be

$$Nu = 0.218F(\theta)Pr^{0.024}Ra^{1/4}$$

The $F(\theta)$ (θ:radian) is a function of the tilt angle of the parallel insulated upper and lower walls.
For 0 deg $\leqq \phi \leqq +70$ deg, $3.4 \times 10^4 < Ra < 5.8 \times 10^7$, $0.7 < Pr < 480$, and $H/W = 1.44$

$$F(\theta) = 1 + 0.546\theta - 0.781\theta^2$$

For -60 deg $\leqq \phi \leqq 0$ deg, $3.4 \times 10^4 < Ra < 8.6 \times 10^7$, $0.7 < Pr < 480$, and $H/W = 1.44$

$$F(\theta) = 1 - 0.754\theta^2$$

It may be seen that the equation obtained reasonably correlates the measured heat transfer data within a deviation of ± 30 percent. It is also to be noted that the equation is verified for an aspect ratio of $H/W = 1.44$.

References

1 Dropkin, D. J., and Sommerscales, E., "Heat Transfer by Natural Convection in Liquids Confined by Two Parallel Plates Which Are Inclined at Various Angles With Respect to the Horizontal," ASME JOURNAL OF HEAT TRANSFER, Vol. 87, 1965, pp. 77–84.

2 Hollands, K. G. T., Unny, T. E., Raithby, G. D., and Konicek, K., "Free Convective Heat Transfer Across Inclined Air Layers," ASME JOURNAL OF HEAT TRANSFER, Vol. 98, 1976, pp. 189–193.

3 Arnold, J. N., Catton, I., and Edwards, D. K., "Experimental Investigation of Natural Convection in Inclined Rectangular Regions of Differing Aspect Ratios," ASME JOURNAL OF HEAT TRANSFER, Vol. 98, 1976, pp. 67–71.

4 Hart, J. E., "Stability of the Flow in a Differentially Heated Inclined Box," *Journal of Fluid Mechanics*, Vol. 47, 1971, pp. 547–576.

5 Ozoe, H., Sayama, H., and Churchill, S. W., "Natural Convection in an Inclined Square Channel," *International Journal of Heat and Mass Transfer*, Vol. 17, 1974, pp. 401–406.

6 Ozoe, H., Yamamoto, K., and Churchill, S. W., "Natural Circulation in an Inclined Rectangular Channel Heated on One Side and Cooled on the Opposing Side," *International Journal of Heat and Mass Transfer*, Vol. 17, 1974, pp. 1209–1217.

7 Ozoe, H., Sayama, H., and Churchill, S. W., "Natural Convection in an Inclined Rectangular Channel at Various Aspect Ratios and Angles—Experimental Measurements," *International Journal of Heat and Mass Transfer*, Vol. 18, 1975, pp. 1425–1431.

8 Ozoe, H., Yamamoto, K., Churchill, S. W., and Sayama, H., "Three-Dimensional Numerical Analysis of Laminar Natural Convection in a Confined Fluid Heated From Below," ASME JOURNAL OF HEAT TRANSFER, Vol. 98, 1976, pp. 202–207.

9 Ozoe, H., Sayama, H., and Churchill, S. W., "Natural Convection Patterns in a Long Inclined Rectangular Box Heated From Below: Part I, Three-Dimensional Photography," *International Journal of Heat and Mass Transfer*, Vol. 20, 1977, pp. 123–129.

10 Ozoe, H., Yamamoto, K., and Sayama, H., "Natural Convection Patterns in a Long Inclined Rectangular Box Heated From Below: Part II, Three-Dimensional Numerical Results," *International Journal of Heat and Mass Transfer*, Vol. 20, 1977, pp. 131–139.

11 Ozoe, H., Yamamoto, K., and Churchill, S. W., "Three-Dimensional Natural Convection in an Inclined Channel With a Square Cross-Section," *AIChE Journal*, Vol. 25, 1979, pp. 709–716.

12 Randall, K. R., Mitchell, J. W., and El-Wakil, M. M., "Natural Convection Heat Transfer Characteristics of Flat Plate Enclosures," ASME JOURNAL OF HEAT TRANSFER, Vol. 101, 1979, pp. 120–125.

13 Nakamura, H., and Asako, Y., "Heat Transfer in a Parallelogrammic

Enclosure (1st Report, Heat Transfer by Free Convection)," *Transactions JSME*, Vol. 46, 1980, pp. 471-481.

14 Maekawa, T., and Tanazawa, I., "Natural Convection Heat Transfer in a Parallelogrammic Enclosure," 17th National Heat Transfer Symposium of Japan, A317, 1980, pp. 160-162.

15 Emery, A., and Chu, N. C., "Heat Transfer Across Vertical Layers," ASME JOURNAL OF HEAT TRANSFER, Vol. 87, 1965, pp. 110-114.

16 Wilkes, J. O., and Churchill, S. W., "The Finite-Difference Computation of Natural Convection in a Rectangular Enclosure," *AIChE Journal*, Vol. 12, 1966, pp. 161-166.

17 Hirata, M., Nishiwaki, N., Miyashita, H., and Itoh, M., "Heat Transfer Across an Enclosed Vertical Layer of Relatively Low Height/Thickness Ratio," *Proceedings of the JSME 1967 Semi-International Symposium*, Tokyo, 1967, pp. 13-18.

18 MacGregor, R. K., and Emergy, A. F., "Free Convection Through Vertical Plane Layers—Moderate and High Prandtl Number Fluids," ASME JOURNAL OF HEAT TRANSFER, Vol. 91, 1969, pp. 391-403.

19 Seki, N., Fukusako, S., and Inaba, H., "Visual Observation of Natural Convective Flow in a Narrow Vertical Cavity," *Journal of Fluid Mechanics*, Vol. 84, 1978, pp. 695-704.

20 Seki, N., Fukusako, S., and Inaba, H., "Heat Transfer in an Enclosed Rectangular Cavity with a Relatively Small Aspect-Ratio," *Bulletin of the Faculty of Engineering*, Hokkaido University, No. 87, 1978, pp. 75-84.

21 Catton, I., Ayyaswamy, P. S., and Clever, R. M., "Natural Convection Flow in a Finite, Rectangular Slot Arbitrarily Oriented With Respect to the Gravity Vector," *International Journal of Heat and Mass Transfer*, Vol. 17, 1974, pp. 173-184.

22 Edwards, D. K., Arnold, J. N., and Wu, P. S., "Correlations for Natural Convection Through High L/D Rectangular Cells," ASME JOURNAL OF HEAT TRANSFER, Vol. 101, 1979, pp. 741-743.

Natural Convection Heat Transfer Between Bodies and Their Spherical Enclosure

R. E. Powe
Associate Vice President
for Research,
Mississippi State University,
Mississippi State, Miss. 39762
Mem. ASME

R. O. Warrington, Jr.
Associate Professor
of Mechanical Engineering,
Montana State University,
Bozeman, Mont. 59717

The natural convective heat transfer phenomena which occur between a body and its spherical enclosure have been experimentally investigated. Bodies of several different shapes were employed, so the results should have broad applicability. New temperature field and heat transfer results, in the form of natural convection from cubical inner bodies to a spherical enclosure, have been combined with previously available enclosure data. By considering all of the data combined, trends in the behavior of the convective heat transfer phenomena have been established, thus enabling a much more reliable analysis of enclosed body problems than is now possible. A very general heat transfer correlation has been developed which predicts the natural convection heat transfer from spheres (concentric and eccentric), cylinders, and cubes to a spherical enclosure with an average deviation of less than 12 percent. Although these results are strictly valid only for a spherical outer body, they should give a preliminary indication of expected behavior for other shapes.

Introduction

For many years, the problem of natural convection from a body to a surrounding fluid of infinite extent has received a great deal of attention. In recent years, considerable interest has been shown in the problem of natural convection in confined fluids, as is evidenced by the rapidly increasing number of publications in the literature on this subject. Accurate prediction of such heat transfer rates, which can now only be roughly approximated, is required in many engineering design problems. Since natural convection flow fields are buoyancy driven due to thermal effects, the thermal fields and hydrodynamic fields are very closely coupled, and a knowledge of the flow field is essential to the complete understanding of the heat transfer phenomena. The unusual stability conditions associated with this problem are also of fundamental interest in the fields of heat transfer and fluid mechanics.

The first experimental studies of natural convection in simple enclosures which began to given an understanding of the basic heat transfer and flow phenomena were those of Eckert and Carlson [1] and Elder [2] for rectangular cavities and that of Brooks and Ostrach [3] for a horizontal cylinder. Experimental investigations of enclosed body geometries have been limited to spherical and cylindrical shapes. For air contained between long horizontal concentric cylinders, flow visualization studies have been conducted by Bishop et al. [4, 5], Powe et al. [6], Grigull and Hauf [7] and Lis [8]. Liu et al. [9] have extended both flow and heat transfer studies to include other fluids, such as water and silicone oils. The first experimental studies of natural convection in air contained between concentric spheres were conducted by Bishop et al. [10, 11], and these have recently been extended to cover a variety of fluids [12, 13]. Heat transfer results have also been obtained for slight perturbations from the concentric sphere geometry. Eccentric spheres have been studied by Weber et al. [14], while McCoy et al. [15] have considered a vertical cylinder within a spherical enclosure. More recently approximate solutions to natural convection problems in enclosures have been made by Raithby and Hollands [16–19]. Their generalized integral method has been applied to a wide variety of geometries including spheres (concentric and eccentric) and cylinders. Their method can be adapted to thick boundary layers and turbulent boundary layers.

The purpose of the current paper is to consider in detail the natural convection heat transfer phenomena which occur between a body and its spherical enclosure. This will be accomplished by combining new heat transfer results with the previously available data. New temperature field and heat transfer results will be presented for a body of cubical shape inside the spherical enclosure. By considering all the data combined, trends in the behavior of the convective phenomena can be established, and this should enable a more reliable analysis of enclosed body problems than is now possible.

Apparatus and Procedure

The heat transfer apparatus consisted of a cooled outer sphere enclosing a heated inner body which was either spherical, cylindrical, or cubical in shape. The different geometries and the test fluids used with each geometry are listed in Table 1. All of the inner bodies were concentrically located within the enclosing sphere, and, in addition, the spheres with outer diameters of 11.4, 13.9, 17.8, and 22.8 cm were also located eccentrically within the spherical test space with eccentricity ratios $[e/(r_o - r_i)]$ from $+0.75$ to -0.75. (The positive eccentricities are measured upward from the concentric sphere position.) The new data presented are the cubical inner bodies with side lengths of 6.39, 10.64, and 12.56 cm and a Prandtl number range of .706 (air) to 10,690 (96 percent glycerin).

The sperical outer body was 25 cm in diameter and was surrounded by a 35.6-cm sphere. Cooling water from a closed system flowed between the spheres and maintained the outer body at a constant temperature. Five thermocouple probes, located in a common vertical plane at 0, 40, 80, 120, and 160 deg from the upward vertical, were used to obtain the temperature profile data. The inner bodies were maintained at a constant temperature by condensing Freon-11 on the inner surface. The inner body temperature was controlled by varying the power to cartridge heaters within the inner bodies which changed the saturation conditions of Freon-11.

The heat transfer by natural convection was measured by subtracting the support stem conduction losses and the radiation, in the case of air, from the total power input to the

Contributed by the Heat Transfer Division for publication in the JOURNAL OF HEAT TRANSFER. Manuscript received by the Heat Transfer Division Aug. 20, 1981.

Table 1 Geometries and test fluids used with spherical enclosure

Inner body (cm)	Air	Water	20CS	350 CS	Gly.	r_i/r_o	L/r_i	L/R_i	$b_{(cm)}$
Spherical inner bodies [Bishop [11], Scanlan [12]]									
Diameter									
						0.40	1.50	1.50	15.95
10.16	×					0.50	1.00	1.00	19.94
12.70	×					0.50	1.00	1.00	19.94
15.24	×					0.60	0.67	0.67	23.93
20.32	×					0.80	0.25	0.25	31.93
8.89		×				0.36	1.81	1.81	13.97
11.43		×	×	×		0.46	1.18	1.18	17.96
13.97		×	×	×		0.56	0.79	0.79	21.95
17.78		×	×	×		0.71	0.40	0.40	27.94
22.86		×	×	×		0.92	0.09	0.09	35.92
Cylindrical inner bodies [Weber [14], McCoy [15]]									
Diameter × length									
11.43 × 17.15		×				0.46	0.98	0.81	23.67
11.43 × 22.23			×			0.46	0.84	0.63	28.75
13.97 × 18.11		×	×	×		0.56	0.66	0.58	26.10
13.97 × 22.38		×	×	×		0.56	0.55	0.44	30.35
17.78 × 20.32		×				0.71	0.34	0.32	30.48
17.78 × 20.53		×				0.71	0.28	0.25	32.69
22.86 × 23.70		×				0.92	0.07	0.07	36.73
Cubical inner bodies [new data]									
Side length									
6.39	×	×	×	×	×	0.26	2.67	2.15	12.78
10.64	×	×	×	×	×	0.43	1.10	0.89	21.29
12.56		×	×	×	×	0.50	0.75	0.60	25.12

inner bodies. The radiation was measured with the test space evacuated (less than 10 microns). The support stem was 1.29 cm in diameter and was insulated so that the conduction losses were estimated by one-dimensional heat transfer from the inner body to the outer body. Temperature profiles were obtained for each fluid/geometry combination using the five thermocouple probes mentioned above. For the cubical inner bodies, temperature profiles were obtained on a vertical plane normal to the cube surface and on a vertical plane through the cube diagonal. Each probe was attached to a micrometer probing mechanism which could advance the probe and indicate its position to within 0.003 cm. For each heat transfer data point and temperature profile the total power input and inner and outer body temperatures were recorded. The apparatus and procedure are described more fully in [12, 14, 15], as are the potential measurement errors. To minimize the impact of such measurement errors, all data presented are for temperature differences large enough that the conduction regime is not encountered, as verified by the temperature profiles.

Nomenclature

a = any characteristic length
A_i = inner body surface area
b = distance traveled by the boundary layer on the inner body
c_1, c_2 = empirically determined constants
c_p = specific heat at constant pressure
D = cylinder or sphere diameter
e = eccentricity, positive upward from the concentric sphere position
g = acceleration of gravity, $9.81 \frac{\text{m}}{s^2}$
Gr_a = Grashof number, $\rho^2 g\beta(T_i - T_o)a^3/\mu^2$
h = average heat transfer coefficient, $\bar{h} = q_{\text{conv}}/A_i\Delta T$
H = total cylinder height
k = thermal conductivity
k_{eff} = effective thermal conductivity
L = gap width or hypothetical gap width, $R_o - R_i$
Nu_a = Nusselt number, $\bar{h}a/k$
Pr = Prandtl number, $c_p\mu/k$
Q = ratio of $q_{\text{conv}}/q_{\text{cond}}$
$\bar{Q}$ = heat transfer normalized by the conduction between concentric spheres
q_{cond} = heat transfer by conduction
q_{conv} = heat transfer by convection
Ra_a = Rayleigh number, $\rho^2 g\beta(T_i - T_o)a^3 c_p/\mu k$
Ra_a^* = modified Rayleigh number, $\text{Ra}_a^* = \text{Ra}_a(L/R_i)$
r_i = inner body radius, except for cubes where it is half the side length
R_i = inner body radius for the spheres, but for the cylinders and cubes it is hypothetical radius of an inner sphere of a volume equal to that of the cylindrical or cubical inner body
r_o = outer body radius
$r(\theta)$ = distance from the center of the inner body to the surface of the outer body
$r_o(\theta)$ = distance from the center of the outer body to the surface of the outer body
T = local temperature
T_{am} = Arithmetic mean temperature, $T_{am} = (T_i + T_o)/2$
T_i = inner body temperature
T_o = outer body temperature
ΔT = temperature difference, $\Delta T = T_i - T_o$
β = thermal expansion coefficient
ν = dynamic viscosity
θ = angular temperature probe location measured from upward vertical axis (all probes in common vertical plane)
ρ = density

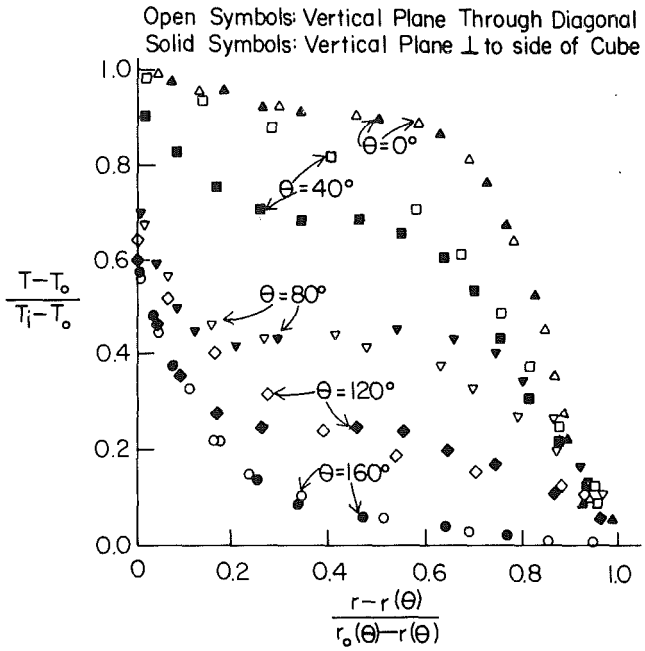

Fig. 1 Comparison of the diagonal and perpendicular planes for the 12.56 cm cube and glycerin, PR = 9205

Results

Temperature Profiles. Temperature profiles were obtained for each of the inner geometry/fluid combinations marked in Table 1. No eccentric sphere profiles are represented here since the temperature profiles for the eccentric spheres were the same as the temperature profiles for the concentric spheres with the following exceptions [14]:

(*i*) Negative eccentricities enhanced the convective motion (higher temperature at the same angular position).

(*ii*) Positive eccentricities promoted corner eddies and produced a tendency toward pure conduction.

Only steady flow temperature profiles are presented in the following figures.

Previous work (11–15) has shown that the temperature profile is independent of the temperature difference between the inner and outer bodies for a given inner geometry and approximately the same Prandtl number. The temperature profiles for the cubical inner bodies, with the exception of $\theta = 40$ deg, were also insensitive to the vertical plane through which the profile was taken. The temperature at $\theta = 40$ deg was consistently higher for the diagonal plane than the plane perpendicular to the side of the cube because of the increased area for heating the test fluid. These trends can be seen in Fig. 1.

All of the profiles exhibit five regions that have been defined by previous investigators [11–15]. These regions are: steep gradient regions adjacent to the body surfaces; a region of small temperature gradients; and inner and outer transition regions. The temperature gradient at the inner body is larger than that at the outer surface because the area is smaller, and the resistance to heat transfer is higher. The region near $\theta = 160$ deg is generally stagnant with conduction as the primary mode of heat transfer.

The effects of Prandtl number on the temperature profiles for the spherical, cylindrical, and cubical inner bodies are shown in Figs. 2–4, respectively. With the exceptions of Fig. 2 and the water data in Fig. 3, all of these temperature profiles represent unpublished data. Common to all of these figures is the tendency for the temperature in the region of small temperature gradients to increase with increasing Prandtl number. The thickening of the boundary layers (on both the inner and outer bodies), due to an increase in Prandtl number, increased the radial extent of both the inner and outer body transition regions.

Temperature inversions were prevalent in most of the profiles. These inversions were first noted by Liu [9] and are caused by the high angular transport of heat relative to the radial transport. Previous researchers [12] have found that inversions always occur for at least one angular position when $Ra_L > 5.10^5$. The angular extent and magnitude of these inversions tends to increase with increasing Prandtl number.

The last temperature profiles presented, Fig. 5, compare the profiles for the different inner body types at approximately the same Prandtl number and L/R_i. At $\theta = 0$ deg the magnitude of the temperature is greater for the cylinder, followed by the sphere, and then the cube. This would be expected since the heating length of the inner geometries are also in this order. At $\theta = 40$, 80, and 120 deg, the cube temperatures are higher. One notable fact is the similarity of the temperature profiles, particularly when one considers the radically different inner geometries that are represented.

None of the profiles presented here have exhibited a reordering of the magnitudes of the temperature. Previous work [11–15] has shown that for small L/R_i the temperatures at the lower angular positions (higher θ) in the test space can be higher than the temperatures at the higher angular positions (lower θ). This was postulated to be due to multicellular flow patterns in the gap. For the cubical inner bodies tested, only a slight reordering of the $\theta = 0$ and 40 deg profiles were noted, and this was generally in the vertical plane through the cube diagonal.

The different behavior of the $\theta = 0$ deg profiles was found by Bishop [11] to be the result of a corner eddy near the top of the inner body. This same behavior for cylinders was determined by McCoy [15] to be caused by the inability of the high-speed flow layer adjacent to the inner body to extend completely into the upper portion of the gap. The flow separated from the inner surface near the junction of the cylinder and its hemispherical end. This behavior for the cubes is also caused by the high-speed flow separating from the inner body at the top edge of the cube.

Heat Transfer. One of the primary objectives of this investigation was to determine the relationship between the Nusselt number and the following independent parameters: Rayleigh or Grashof number, Prandtl number, and an appropriate geometric parameter. Previous analyses [11, 12, 14, 15] of the enclosure heat transfer data have shown that correlations of the form

$$Q = \frac{q_{\text{conv}}}{q_{\text{cond}}} = \frac{k_{\text{eff}}}{k} = C_l \text{Ra}^{C_2} \tag{1}$$

or

$$Q = C_1 \text{Ra}^{*C_2} \tag{2}$$

could correlate concentric and eccentric sphere data, and cylindrical data extremely well. The geometric effect is accounted for in q_{cond} and the Prandtl number effect is accounted for in the Rayleigh number. These same investigators [11, 12, 14, 15] used a volume weighted mean temperature to evaluate the fluid properties.

The major difficulty with the above equations is that q_{cond} and the volume weighted mean temperature must be evaluated numerically for most enclosure geometries. Comparisons of the heat transfer correlations were made using both the volume weighted mean temperature and the arithmetic mean temperatures for the spherical and cubical inner geometries. There was little difference in the overall heat transfer correlations. The difference in the average deviation for the

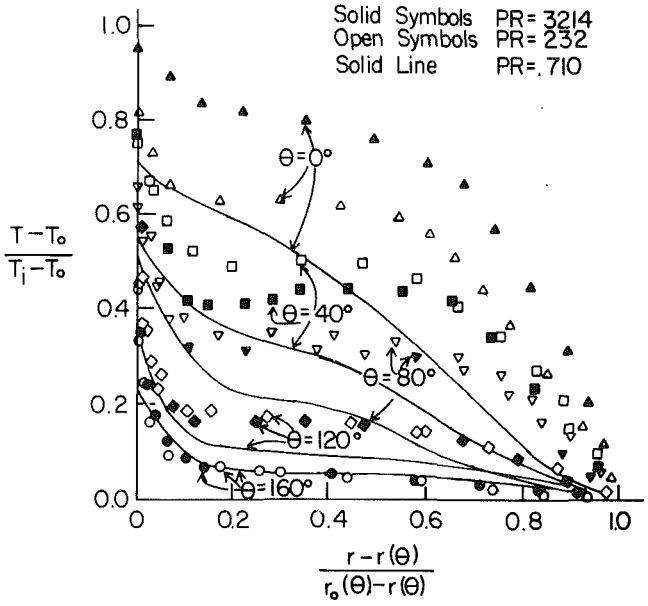

Fig. 2 Prandtl number effect on the temperature profiles for the 13.97 cm sphere (15.24 cm for air), 20 CS and 350 CS fluids

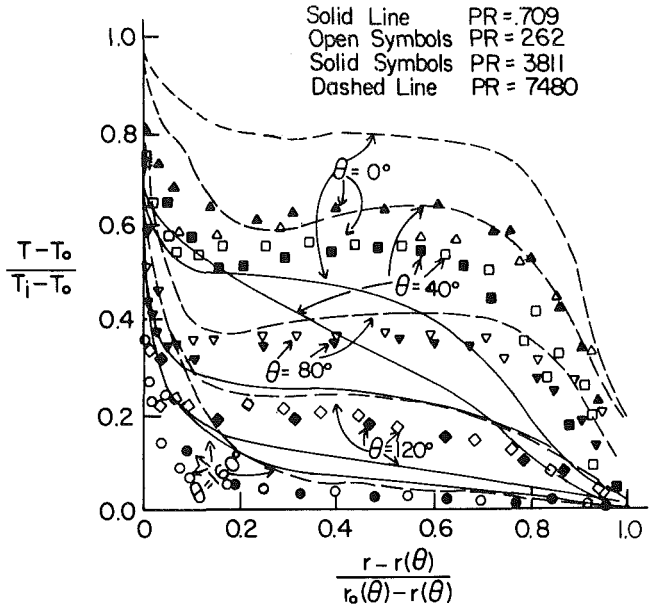

Fig. 4 Prandtl number effect on the temperature profiles for the 10.64 cm cube and air, 20 CS, and glycerin

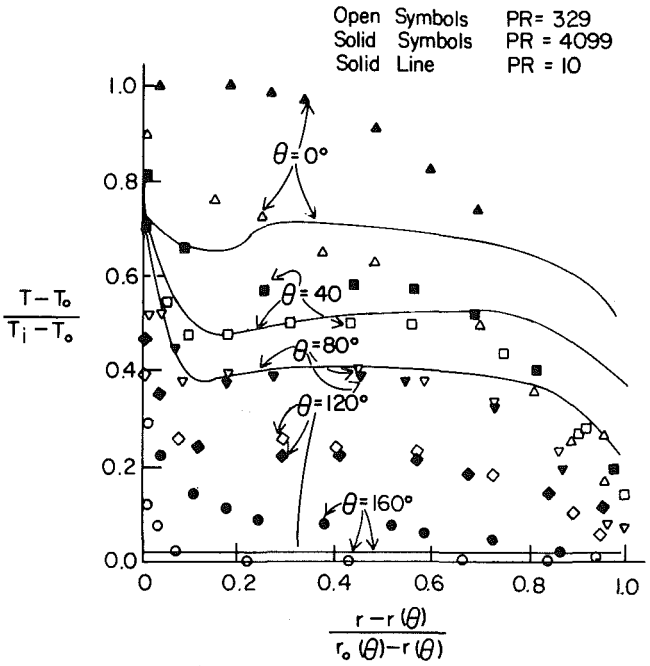

Fig. 3 Prandtl number effect on the temperature profiles for the 13.97 by 18.11 cm cylinder and water, 20 CS and 350 CS fluids

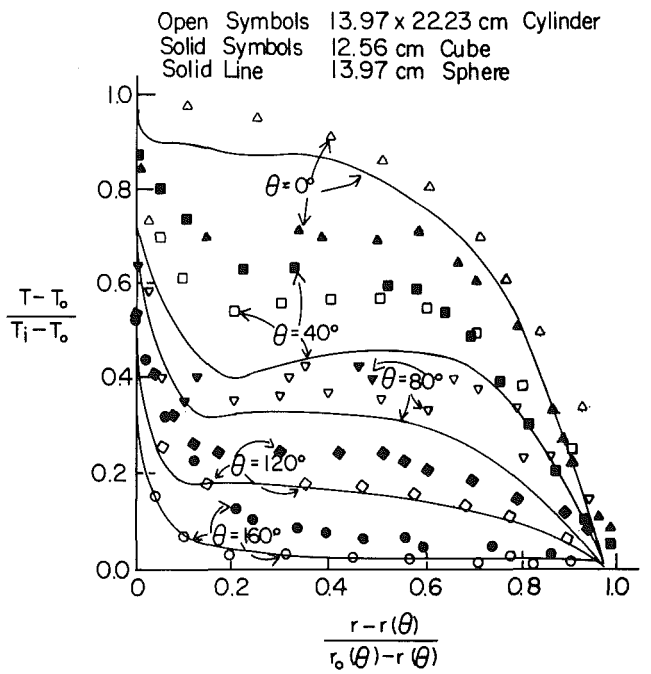

Fig. 5 Comparison of the different inner geometries for 350 CS fluid, PR = 3300

spherical inner bodies was less than 1 percent (advantage to the volume weighted mean temperature). The difference for the cubical inner bodies was less that 2 percent (advantage to the arithmetic mean temperature). With very little difference between the two, the arithmetic mean temperature has been used to evaluate the fluid properties.

Other correlations that were used in this study to correlate the heat transfer data were

$$\mathrm{Nu}_L = C_1 \mathrm{Ra}_L^{C_2} \quad (3)$$

$$\mathrm{Nu}_L = C_1 \mathrm{Ra}_L^{*C_2} \quad (4)$$

$$\mathrm{Nu}_b = C_1 \mathrm{Ra}_b^{C_2} \quad (5)$$

and

$$\mathrm{Nu}_b = C_1 \mathrm{Ra}_b^{*C_2} \quad (6)$$

The length term, L, is defined as a hypothetical gap width, $(R_o - R_i)$, where R_o is the radius of the outer sphere, and R_i is the inner body radius for the spheres; for the cylinders and cubes it represents a hypothetical radius of an inner sphere of a volume equal to that of the cylindrical or cubical inner body. The length term b is the distance "traveled" by the boundary layer on the inner body assuming no boundary layer separation. This distance, which was first proposed by Lienhard [20], is defined as $b = \pi D/2$ for spheres, $b = H + D[\pi/2 - 1]$ for cylinders, and $b = 2$ (cube length) for cubes. Let us first address the heat transfer data for the

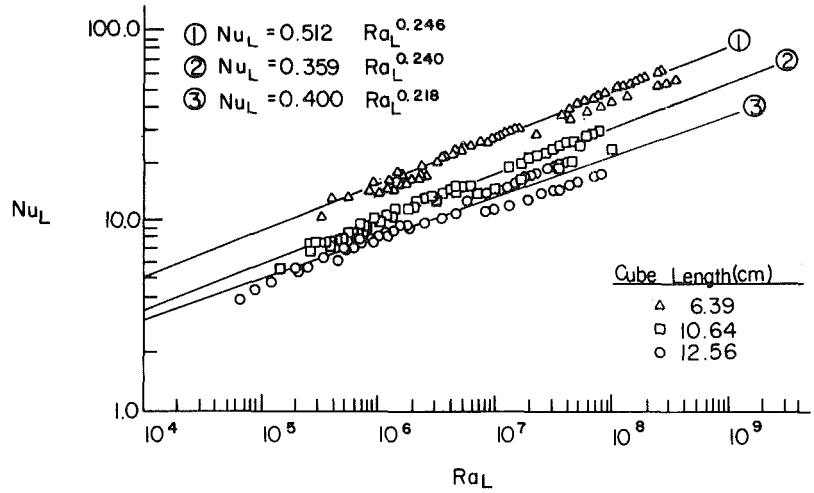

Fig. 6 Heat transfer correlations for all of the cube data and each individual inner body

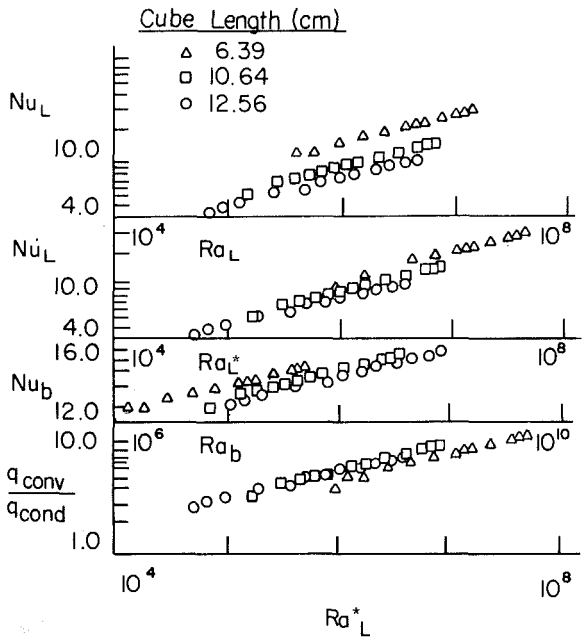

Fig. 7 Various correlation schemes for the cube data and glycerin

cubical inner body as this data has not been previously presented.

Equation (3) is plotted in Fig. 6 along with all of the cubical inner body heat transfer data. The lack of scatter for any given inner body indicates very little Prandtl number influence; however, there is still a large geometric effect. Figure 7 shows the decrease in this geometric effect as different correlation equations are plotted. Although only the glycerin data and the cubical inner bodies are represented in Fig. 7, the same trends were observed for the other fluid/geometry combinations. The conduction solution for the cube-sphere geometry ($q_{c_o} n^d$) was obtained using standard finite differences. The curved surface was approximated by taking the closest mesh point, thus perturbing the actual region so that it coincided with the Cartesian grid. The extrapolated Leibmann or successive over-relaxation was used to solve the difference model.

In general, equations (1) and (6) gave approximately the same average percent deviation for the cubical geometry, and equations (3) and (4) were considerably worse. The best single parameter correlation is

$$N_{u_b} = 0.582\ \mathrm{Ra}_b^{*0.235} \tag{7}$$

which has an average percent deviation of 7.13. All of the empirical constants in this investigation were determined by using a standard least-squares curve fitting technique. In general, the Prandtl number/geometric effects can be seen to increase as the modified Rayleigh number increases, and this could be due to boundary layer separation effects at the higher Rayleigh numbers [13].

All of the spherical enclosure data in Table 1 are plotted in Fig. 8 with every other data point eliminated to reduce the clutter in the figure. Again, there is a definite increase in the effects of the Prandtl number/geometry as the Rayleigh number increases. The individual correlations presented for each inner body geometry in Fig. 8 had average percent deviations of 16.30, 12.99, and 10.02 for the spheres, cylinders, and cubes, respectively.

The best single parameter correlation for all of the heat transfer data was

$$\mathrm{Nu}_b = 0.744\mathrm{Ra}_b^{*0.222} \tag{8}$$

which has an average percent deviation of 13.05 and 81.44 percent of the data were within ±20 percent of the equation. Other correlations for the cubical inner geometry and for all of the enclosure data are presented in Table 2.

Equations with more than one independent correlating parameter were, of course, more accurate. The best correlation for all of the enclosure data was

$$\mathrm{Nu}_b = 0.664\mathrm{Ra}_b^{*0.222}\left[\frac{L}{R_i}\right]^{0.165}\mathrm{Pr}^{0.018} \tag{9}$$

which has an average percent deviation of 11.83.

Conclusions

The results presented in the previous section represent temperature profiles and heat transfer correlations for the natural convection heat transfer from several inner geometries to a spherical enclosure. The dimensionless temperature profiles for the different inner body types displayed remarkable similarity. The prominent features of the spherical and cylindrical temperature profiles discussed by previous investigators were also found to be true for the cubical inner bodies despite their radically different shape.

The correlations presented are unambiguous and represent

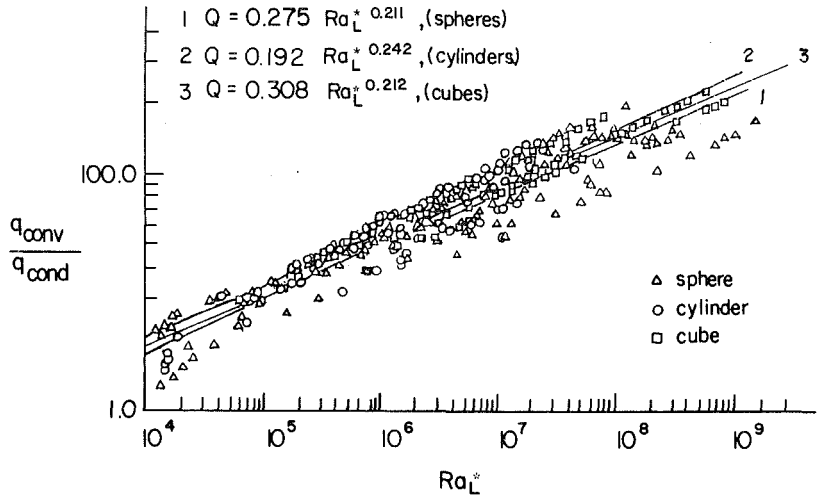

Fig. 8 Heat transfer correlations for all of the spherical enclosure data and each inner body type (only 50 percent of the data points represented)

Table 2 Correlations for the enclosure data

Fluid	Equation number	Empirical constants C_1	C_2	Average deviation	percent of data within ±20% of equation
Spherical inner bodies (concentric)					
All	(2)	.275	.211	16.27	73.8
	(7)	.985	.205	14.01	72.3
	(5)	.200	.271	20.72	59.3
Spherical inner bodies (eccentric)					
All	(7)	1.997	.174	16.27	67.4
	(5)	.156	.294	26.20	52.0
Cylindrical inner bodies					
All	(2)	.192	.242	12.99	77.7
	(7)	.564	.238	13.13	78.9
	(5)	.155	.287	13.52	79.3
Cubical inner bodies					
All	(2)	.308	.212	10.02	91.1
	(7)	.582	.235	7.13	94.4
	(5)	.235	.272	12.38	84.9
All the spherical enclosure data					
All	(2)	.257	.219	14.89	77.42
	(7)	.744	.222	13.05	81.44
	(5)	.180	.280	18.77	62.81
Air	(2)	.390	.187	6.78	99.0
	(7)	.258	.284	5.07	100.0
	(5)	.148	.312	4.49	100.0
Water	(2)	.247	.215	15.31	75.4
	(7)	.965	.205	14.34	72.0
	(5)	.147	.283	13.63	78.7
20 cs	(2)	.226	.236	9.75	92.2
	(7)	.276	.276	8.22	95.5
	(5)	.104	.319	8.66	90.9
350 cs	(2)	.222	.236	8.83	94.7
	(7)	.265	.282	7.35	92.5
	(5)	.133	.315	7.72	94.0
Glycerin	(2)	.265	.221	7.39	97.4
	(7)	.474	.246	3.49	100.0
	(5)	.134	.315	9.84	87.2

the data with a high degree of accuracy, considering the wide Prandtl number range and the geometries studied. The correlations based on the hypothetical gap width and the boundary layer length are, in addition to being unambiguous, very simple to employ. The correlations involving the conduction solutions, while accurate and unambiguous, would require a substantial computational effort if the correlations were extrapolated to other inner body geometries.

The correlations developed by Raithby and others [16–19] have been used to correlate the spherical and cylindrical enclosure data. Their work, which has an excellent physical basis, also requires some computational effort and, in the case

of cubical inner bodies, would require some modification. In general, the heat transfer by natural convection from an arbitrary inner body to a spherical enclosure can be approximated with a great deal of confidence by using equation (8) or equation (1). For very small values of L/R_i, it is probable that the parameter q_{conv}/q_{cond} would be the superior dependent correlating parameter. An extension of these correlations to a different enclosure geometry will require additional experimental work.

References

1 Eckert, E. R. G., and Carlson, W. O., "Natural Convection in an Air Layer Enclosed Between Two Vertical Plates With Different Temperatures," *International Journal of Heat and Mass Transfer*, Vol. 2, 1961, pp. 106–120.

2 Elder, J. W., "Laminar Free Convection in a Vertical Slot," *Journal of Fluid Mechanics*, Vol. 23, No. 1, 1965, pp. 77–98.

3 Brooks, I. H., and Ostrach, S., "An Experimental Investigation of Natural Convection in a Horizontal Cylinder," *Journal of Fluid Mechanics*, Vol. 44, No. 3, 1970, pp. 545–561.

4 Bishop, E. H., and Carley, C. T., "Photographic Studies of Natural Convection Between Concentric Cylinders," *Proceedings of the 1966 Heat Transfer and Fluid Mechanics Institute*, Stanford University Press, 1966, pp. 63–78.

5 Bishop, E. H., Carley, C. T., and Powe, R. E., "Natural Convective Oscillatory Flow in Cylindrical Annuli," *International Journal of Heat and Mass Transfer*, Vol. 11, 1968, pp. 1741–1752.

6 Powe, R. E., Carley, C. T., and Bishop, E. H., "Free Convective Flow Patterns in Cylindrical Annuli," ASME JOURNAL OF HEAT TRANSFER, Vol. 91, 1969, pp. 310–314.

7 Grigull, U., and Hauf, W., "Natural Convection in Horizontal Cylindrical Annuli," *Proceedings of the Third International Heat Transfer Conference*, Vol. 2, AIChE, 1966, pp. 182–195.

8 Lis, J., "Experimental Investigation of Natural Convection Heat Transfer in Simple and Obstructed Horizontal Annuli," *Proceedings of the Third International Heat Transfer Conference*, Vol. 2, AIChE, 1966, pp. 196–204.

9 Liu, C. Y., Mueller, W. K., and Landis, F., "Natural Convection Heat Transfer in Long Horizontal Cylindrical Annuli," *International Development in Heat Transfer*, pt. V, pp. 976–984.

10 Bishop, E. H., Kolflat, R. S., Mack, L. R., and Scanlan, J. A., "Convective Heat Transfer Between Concentric Spheres," *Proceedings of the 1964 Heat Transfer and Fluid Mechanics Institute*, Stanford University Press, 1964, pp. 69–80.

11 Bishop, E. H., Mack, L. R., and Scanlan, J. A., "Heat Transfer by Natural Convection Between Concentric Spheres," *International Journal of Heat and Mass Transfer*, Vol. 9, 1966, pp. 649–662.

12 Scanlan, J. A., Bishop, E. H., and Powe, R. E., "Natural Convection Heat Transfer Between Concentric Spheres," *International Journal of Heat and Mass Transfer*, Vol. 13, 1970, pp. 1857–1872.

13 Yin, S. H., Powe, R. E., Scanlan, J. A., and Bishop, E. H., "Natural Convection Flow Patterns in Spherical Annuli," *International Journal of Heat and Mass Transfer*, Vol. 16, 1973, pp. 1785–1795.

14 Weber, N., Powe, R. E., Bishop, E. H., and Scanlan, J. A., "Heat Transfer by Natural Convection Between Vertically Eccentric Spheres," ASME JOURNAL OF HEAT TRANSFER, Vol. 95, No. 1, 1973, pp. 47–52.

15 McCoy, C. T., Powe, R. E., Bishop, E. H., Weber, N., and Scanlan, J. A., "Free Convection Between a Vertical Cylinder and a Spherical Enclosure," *Proceedings of the Fifth International Heat Transfer Conference*, Paper No. NC 3.5, Vol. 3, Tokyo, 1974, pp. 105–109.

16 Raithby, G. D., and Hollands, K. G. T., "A General Method of Obtaining Approximate Solutions to Laminar and Turbulent Free Convection Problems," *Advances in Heat Transfer*, 1975, Vol. 11, Academic Press, pp. 265–315.

17 Raithby, G. D., Pollard, A., Hollands, K. G. T., and Yovanovich, M. M., "Free Convection Heat Transfer from Spheroids," ASME JOURNAL OF HEAT TRANSFER, Vol. 98, No. 3, 1976, pp. 452–458.

18 Raithby, G. D., and Hollands, K. G. T., "Laminar and Turbulent Free Convection from Elliptic Cylinders, with a Vertical Plate and Horizontal Circular Cylinder as Special Cases," ASME JOURNAL OF HEAT TRANSFER, Vol. 98, No. 1, 1976, pp. 72–80.

19 Raithby, G. D., and Hollands, K. G. T., "Analysis of Heat Transfer by Natural Convection (or Film Condensation) for Three Dimensional Flows," *Sixth International Heat Transfer Conference*, Paper No. NC-1, Vol. 2, Toronto, 1978, pp. 187–192.

20 Leinhard, J., "On the Commonality of Equations for Natural Convection From Immersed Bodies," *International Journal of Heat and Mass Transfer*, Vol. 16, 1973, pp. 2121–2123.

Heat Transfer From a Heated Pool to a Melting Miscible Substrate

I. Catton
Mem. ASME

W. A. Brinsfield

S. M. Ghiaasiaan

School of Engineering and Applied Science, University of California, Los Angeles, Calif. 90024

Melting a miscible substrate by a heated overlying pool of higher density is studied experimentally. The heated pool is either carbon tetrachloride or diiodomethane, and the substrate is frozen benzene. By performing the experiments with heated pools of different densities the effects of pool-to-substrate temperature differences and pool-density to melt-density ratios on melting heat transfer are independently studied. Heat transfer rates are reported as a function of both temperature difference and density ratio. A model is postulated and compared with experimental results. The downward heat flux is found to be essentially independent of temperature differences, while being an increasing function of the density ratio between the pool and the melting solid for large density rations. For low-density ratios a buoyant plume analysis was used to obtain a correlation.

Introduction

Some nuclear reactor core catcher concepts envision use of layers of material soluble in a core melt. Examples are crucibles or ladles, frequently called sacrificial beds, consisting of refractory materials such as alumina, borax, or MgO brick. Hypothetical situations have been envisioned in which, following a core melt down, molten fuel, such as UO_2, contacts a solid boundary of a sacrificial bed material which, when molten, is miscible in the overlying pool. Understanding of how the melt front advances into the sacrificial layer is essential if one is to properly lay out the geometry of the crucible and design a heat removal system for post accident heat removal.

The aim of this work is to describe the heat transfer between the molten pool and the sacrificial material when the melt density is less than the density of the pool. The hydrodynamics governing the heat transfer process are driven primarily by the density difference. Density-driven motion of the type of interest here is due to Rayleigh-Taylor instabilities. Rayleigh-Taylor instabilities have been used in the past to explain many physical phenomena, such as minimum film boiling, maximum nucleate boiling heat flux, as well as film boiling. A brief review of past work leading up to this study follows.

In 1950, Taylor [1] discussed the instability of a horizontal interface between two immiscible fluids of infinite depth. He showed that the irregularities at the interface grew if the acceleration was directed from the heavier fluid to the less dense fluid. A great deal of work on this type of instability followed. It has been used to describe certain aspects of nuclear weapons, as well as film boiling. Only the work relevant to the problem under study is reviewed here. For a more general discussion, see the work by Taghavi-Tafreshi [2]. Zuber [3], in 1959, used a Rayleigh-Taylor instability mechanism for immiscible fluids to predict minimum and maximum heat fluxes for pool boiling. He proposed that near the minimum heat flux the bubbles would be released in a square grid with spacing bounded between the fastest growing and critical Taylor wavelength.

The problem of melting of a flat layer of a solid has been extensively studied by many investigators. In the melting process, the heat transfer mode in the liquid is either by conduction or convection. The Stephen problem involves heat transfer by conduction through the liquid phase. An account of this problem and the analytical solution of Neumann are given by Carslaw and Jaeger [4], while a numerical solution of the same problem is given by Murray and Landis [5]. A majority of solids, when melted from above, exhibit this kind of heat transfer behavior.

To date only limited knowledge in the subject area of melt front advance rate is available, although the effect has been explicitly mentioned in the literature [6, 7]. Baker and Faw [8] have looked at heat transfer from a horizontal layer of internally heated liquid to an immiscible melting solid and found that measured heat fluxes and melting rates were consistent with a model based upon downward heat transfer by conduction through a nearly stagnant liquid layer and upward heat transfer augmented by natural convection. Some questions about the thickness of the stagnant layer were not answered by their work. A study by Taghavi-Tafreshi et al. [9] used a frozen layer of olive oil under a heated pool of water. They were able to use the hydrodynamics of a Rayleigh-Taylor instability to develop a predictive model that gave very good comparison with their data.

Farhadieh and Baker [10] were the first to measure heat transfer between a heated pool and melting miscible material. They used water soluble wax and an aqueous salt solution heated internally by a planar heater suspended in the pool. The temperature difference between the pool and the substrate was held fixed by means of the heater, while the initial density of the pool was varied. Their results indicate that the downward heat transfer coefficient, h, increases with the density ratio $\delta\rho/\rho_m$, where

$$\delta\rho = \rho_s - \rho_m$$

Although their work offers insight into the phenomena of heat transfer to a miscible substrate from a overlying pool, little information was given as to the dependence of the heat flux upon the temperature difference between the pool and the substrate. The Rayleigh-Taylor instability problem for miscible fluids with a thin layer of low density fluid on the bottom was solved by Taghavi-Tafreshi and Dhir [11].

Similar work by Boger and Westwater [12] and Yen [13, 14, 15] for very low R ($R < 1.03$) was carried out by melting ice by heating from above. Boger and Westwater found that the heat transfer to the ice could be correlated with a properly defined Rayleigh number. This is in contrast with the work of Yen [15] who found the heat transfer to be independent of the imposed temperature difference. The continuous variation in density from the melting interface to the heated surface and very low density ratio cause different physical processes than those of interest here.

In an effort to further understand the effect of the melting

Contributed by the Heat Transfer Division and presented at the ASME Winter Annual Meeting, Washington, D.C., November 15-20, 1981. Manuscript received by the Heat Transfer Division November 30, 1981. Paper No. 81-WA/HT-31.

Table 1

Property	Remarks	Benzene	CCl_4	CH_2I_2
Density	Pure substance, gm/cm^3	0.88 (@ 5.5C)	1.58 (@20C)	3.3 (@ 20C)
Heat capacity	Pure substance, cal/gm-deg cm^2	0.402 (@ 5.5C)	0.200 (@ 25C)	0.119 (@ 25C)
Viscosity	At melting temperature, cm^2/s	9.33×10^{-3}	----------	----------
Heat of fusion	cal/gm	30.19	----------	----------

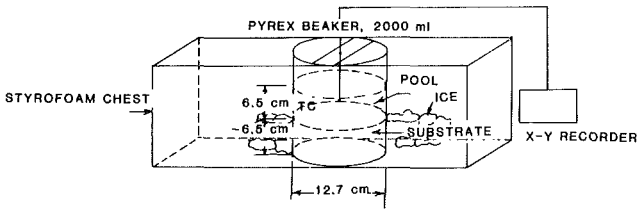

Fig. 1 Test apparatus

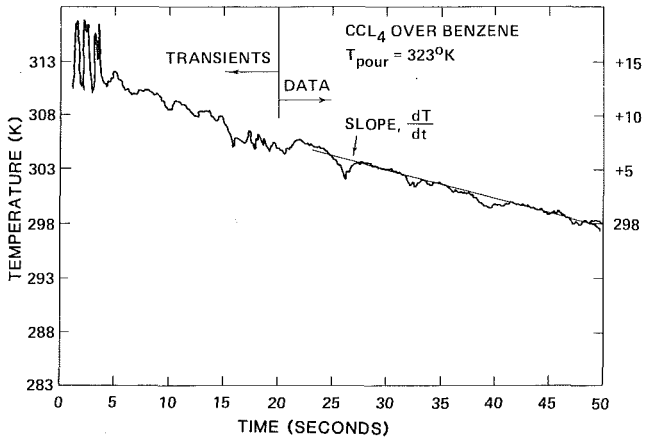

Fig. 2 A typical temperature-time plot for an experimental run

process on heat transfer to the melt, the present study was undertaken. This study involves a heated liquid layer over a solid substrate. The liquid layer and the melted solid are dissimilar and hence have different thermophysical properties, but the two media, upon melting of the solid, are mutually miscible. The density of the liquid layer is greater than that of the melted solid, and hence the two dissimilar liquid layers are gravitationally unstable. When gravitationally unstable, the liquid system overturns and the two layers intermix, with the resultant convective currents causing thermal mixing of the layers. This double mixing process has been dubbed "convective mixing" by Farhadieh and Baker. No indication as to the wavelength spacing expected within a melting system was given. In the present study, attention is focused on the affects of variation in density and temperature on the melting rate and downward heat transfer during a cooling process. Preliminary observations indicate that the quasi-static cooling approach of Taghavi-Tafreshi et al. [9] is applicable here. Attempts are made to correlate the data with expressions based upon density driven instability processes.

Experimental Work

Materials. After some preliminary studies, materials for the experiments were chosen. A number of requirements had to be met. The density ratio had to be large enough to span the range expected for a core melt, namely from one to approximately three or four. The materials had to be mutually miscible, so that surface tension would plan a negligible role. The freezing process for the substrate materials was also important as cracks formed upon freezing were unacceptable. The fluids had to be manageable in the laboratory, which imposed certain toxicity requirements as well as temperature requirements on the selection process. Because of these requirements, a number of materials were considered before the final selection was made.

Benzene was decided upon for the frozen substrate layer because of its availability, low density, and relatively high freezing point. Carbon tetrachloride (CCl_4) or diiodomethane (CH_2I_2) constituted the heated liquid pool. These two liquids were chosen on the basis of their infinite solubility in benzene and the wide range of density ratios they offered. Table 1 contains the thermophysical properties of the fluids used that are needed for this work.

Apparatus. A 2000-ml Pyrex glass breaker was chosen as the container for the fluids. The inside diameter of the beaker was 12.7 cm, with a wall thickness of 0.32 cm. The Pyrex beaker was chosen because it offered good benzene. The breaker was placed in a styrofoam chest and surrounded by ice to eliminate sideward melting of the benzene due to radial conduction through the glass wall. A 13.0-cm by 2.54-cm piece of bakelite, 0.32-cm thick, was placed over the top of the beaker. Type K chromel-alumel thermocouple wire was passed through a 3-mm o. d., 20 cm long glass tube, which in turn was passed through a 0.32-cm dia hole drilled through the center of the bakelite cover and into the liquid pool. The thermocouple was connected to a Houston model x-y recorder upon which the temperature time profile could be recorded.

Nomenclature

A = area
C_p = molar heat capacity
c_p = specific heat
D = diameter
f = friction factor
g = gravitational constant
h = heat transfer coefficient
h_{sf} = latent heat of fusion
K = thermal conductivity
L = depth of solution
M = mass
$\dot{m}$ = mass flow
P = pressure
q = heat flux
R = density ratio
T = temperature
t = time
$\dot{x}$ = melt front advance rate
z = distance

Greek Letters

ΔT = temperature difference between pool and melting temperature of substrate
δ = melt layer thickness
λ = wavelength
μ = dynamic viscosity
ν = kinematic viscosity
ρ = density

Subscripts

c = cell
e = exit
H = heater
i = inlet
j = jet
L = loss
m = melt
o = initial value
r = raw
s = solution
∞ = initial value, pure solution

Only one thermocouple was found to be necessary because of the uniformity of pool temperature. Figure 1 shows a sketch of the test apparatus.

Procedure. 1000 ml of benzene was frozen in the Pyrex beaker by placing the beaker containing the benzene on top of a slab of dry ice. This considerably slowed the freezing process and eliminated thermal cracking. Bubbles of dissolved gas formed in the benzene during the freezing process were scraped off of the surface approximately every 30 min with a thin metal rod. The resulting surface was quite smooth and free of depressions. After the benzene was frozen, the beaker was placed inside the styrofoam chest and surrounded by ice up to the level of the benzene. The chest was then put into a refrigerator and the temperature of the frozen slab was allowed to stabilize at the refrigerator temperature. The inside temperature of the refrigerator was constant with time and adjusted to 273 K. This resulted in approximately 5.5 K of subcooling in the slab. The pool solution was then heated to the desired temperature. When this temperature was reached, the chest containing the beaker of frozen substrate was removed from the refrigerator and the thermocouple connected to the recorder. The position of the thermocouple was adjusted to approximately 3 cm from the surface of the substrate. The recorder was started and the heated solution poured quickly into the center of the beaker on top of the 6.5-cm thick layer of frozen benzene. Enough pool solution was used to give a depth of 6.5 cm. The mean temperature of the pool was then recorded as a function of time. The experiments were terminated after approximately 2 min. This kept the pool from nearing its freezing temperature and also eliminated the effects of melting due to axial heat conduction through the glass walls of the beaker. After termination of the experiment, the liquid was poured off and the remaining solid was inspected for any pattern which might indicate the existence of a melting pattern that could result from a Rayleigh-Taylor instability. The amount of liquid poured off was measured in a graduate cylinder, and the difference between the initial final pool volume was noted as an estimate of the amount of benzene melted during the experiment. The liquid weight was also recorded. The change in the thickness of the frozen layer was also noted as a check on the amount of benzene melt added to the pool.

Data Reduction. To obtain the net heat flux, q, across the melt layer when the slab is at its melting temperature, heat losses were subtracted from the observed raw heat flux, q_r.

The heat losses to the surrounding area were determined experimentally. To do this, the slab of frozen benzene was replaced by a disk of insulating material (bakelite) of the same thickness, 6.5 cm, as the benzene slab. The loss of ethalpy of the heated pool in this situation was then noted. The procedure was as follows.

1 The Pyrex beaker, without the insulating disk, was placed within the styrofoam chest, surrounded by ice up to the same level as in the experiments, and the entire apparatus was then placed in the refrigerator and allowed to chill to the refrigerator temperature, as in the actual runs.

2 The chilled apparatus was then removed from the refrigerator and the insulating disk inserted into the beaker. The thermocouple was adjusted to the same height as for the actual runs.

3 A heated pool of either CCl_4 or CH_2I_2 was then formed over the insulating disk and the temperature-time history recorded as before. The volume of this pool was the same as the initial volume used in the data runs. The initial density was also the same.

The heat loss experiment was performed with different initial pool temperatures corresponding to the pool temperature used for the actual runs. The heat loss from the pool, normalized to the pool horizontal area, q_L, was calculated using the expression

$$q_L = \rho_\infty L_\infty C_{p_\infty} \frac{dt_L}{dt} \tag{1}$$

where ρ_∞, L_∞, and $C_{p\infty}$ are density, pool depth and heat capacity evaluated after the initial transients have decayed. The raw heat flux, q_r, was calculated using the expression

$$q_r = \rho_s c_{ps} L_s \frac{dT}{dt} \tag{2}$$

The final density of the pool was measured and averaged to obtain a mean density. The mean density was used in calculating heat fluxes. For the CCl_4 runs, the mean density was found to remain fairly constant, and a value of $\rho_s = 1510$ kg/m was used as the solution density for all CCl_4 runs. CH_2I_2 is expensive and was reused. As a result, the initial densities of the CH_2I_2 pools were different for each run made. Actually the density of the solution changes with time as more liquid benzene is added. The error introduced by using a mean ρ_s, however, is as small or smaller than the error made when trying to calculate an instantaneous value of the solution density. This is because the solution density is a function of the melt front which could not be optically measured with great accuracy. The error in ρ_s should be less than 10 percent.

After the mean solution density was calculated, the specific heat, c_{ps}, was determined. As mentioned earlier, the specific heat of the pool is a function of the pool temperature and was evaluated at the temperature, T_s, of the pool. For the CCl_4 runs, the specific heat of the solution was approximated to be that of the pure CCl_4 at the temperature, T_s. Again, because of the addition of benzene to the solution, this is not exactly correct. Since the duration of the experiment was short (2 min) and the amount of benzene added was sufficiently small compared to the pool volume, this was felt to be a good assumption. The error introduced from this approximation was estimated to be ± 5 percent. However, for the CH_2I_2 runs, the addition of benzene was non-negligible. In these cases, the weight percent of benzene in the solution at its mean solution density, ρ_s, was determined. The specific heat of the solution was then weighted accordingly between the specific heat of a pure CH_2I_2 solution at temperature, T_s, and the specific heat of a pure solution of benzene at temperature, T_s. Some error was introduced via this method, but it was felt that this was an improvement over the case of a solution of pure CH_2I_2 alone.

A value of dT_s/dt was picked directly from the temperature-time plot of the experiment. A typical temperature-time plot is shown in Fig. 2. Data was taken at a time after the initial transients had died out. The initial transient only lasted for 3 or 4 s. The amount of benzene melt was small compared to that melted during the total run time of 2 min. Errors incurred while emptying the beaker were similarly small. The time, t, after the pouring of the heated solution into the beaker, was approximately the same for each run. A best fit slope was superimposed upon the temperature time plot at this time, and the slope was calculated.

The depth of the solution, L_s, at time, t, was calculated from the expression

$$L_s(t) = L_0 + \dot{x}\, t \tag{3}$$

where L_0 is the initial depth of the solution at time $t = 0$ ($L_0 = 6.5$ cm) and $\dot{x}$ is the melt front advance rate. The advance rate could not accurately be measured through optical means, and was therefore calculated from heat transfer considerations. The calculated value was then compared to the mean advance rate determined at the end of the experiment by measuring the change in substrate layer thickness. These

Table 2 Data for heat transfer from carbon tetrachloride to benzene

Run number	Solution density ρ_s, kg/m^3	Mean pool temperature T_s, K	Raw heat flux q_r, W/m^2	Heat loss to surroundings q_L, W/m^2	Heat of melting q', W/m^2	Corrected heat flux q', W/m^2	Heat transfer coefficient h, W/m^2 – k
1	1510	295.00	23278.6	3077.3	16579.7	20222.2	1225.6
2	1510	282.00	25916.3	2260.9	22608.7	23655.4	6758.7
3	1510	293.50	23236.7	2847.0	16998.4	20389.7	1359.3
4	1510	318.00	33996.8	6322.1	18170.7	27674.8	700.6
5	1510	309.50	22441.3	3077.3	13732.7	19384.9	625.3
6	1510	299.80	25539.5	3077.3	17542.7	22483.1	1055.5
7	1510	282.50	27214.2	2260.9	23697.3	24953.3	6238.3
8	1510	308.40	32196.5	6322.1	18547.5	25874.4	865.4
9	1510	310.50	24534.7	4479.9	14109.5	20096.6	628.0
10	1510	329.25	30940.5	6322.1	14737.5	24618.4	485.1
11	1510	304.25	25288.3	4061.2	15826.1	21227.1	824.4
12	1510	307.75	29726.3	6322.1	16872.8	23404.2	800.1

Table 3 Data for heat transfer from diiodomethane to benzene

Run number	Solution density ρ_s, kg/m^3	Mean pool temperature T_s, K	Raw heat flux q_r, W/m^2	Heat loss to surroundings q_L, W/m^2	Heat of melting q', W/m^2	Corrected heat flux q', W/m^2	Heat transfer coefficient h, W/m^2 – k
1	2890	292.4	62969.5	5861.5	48441.3	57317.3	4123.5
2	2630	300.0	59075.8	5317.2	41826.1	53758.5	2500.4
3	2160	295.3	49278.6	9211.0	32740.8	40067.7	2385.0
4	2130	292.2	47938.9	9211.0	32782.6	38727.9	2826.9
5	2130	298.5	55223.7	15323.7	39070.9	40570.1	2028.5
6	2130	286.3	45384.9	4057.0	37471.9	41323.7	5297.9
7	2120	293.5	49236.8	9211.0	33368.8	40025.8	2668.4

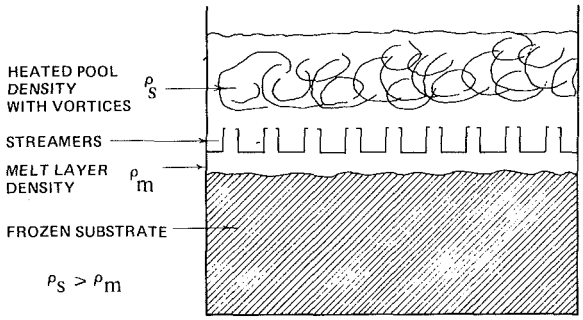

Fig. 3 Observed physical situation (heated pool overlying a melting miscible substrate)

values were found to compare reasonably well. The calculation of $\dot{x}$ was as follows:

(*i*) An initial guess was made for $\dot{x}$, and L_s was calculated at time, t, using equation (3).

(*ii*) The raw heat flux, q_r, was then calculated from equation (2). The heat loss per unit area at time t, q_L, was calculated from equation (1) for the corresponding initial pool temperature and subtracted from q_r to give an initial value for q, the net heat flux. In other words,

$$q = q_r - q_L \tag{4}$$

(*iii*) The melt front advance rate was calculated from the heat flux required to change the benzene from a subcooled solid to a liquid at its melting temperature and the heat flux required to raise the liquid temperature to the mean pool temperature. The heat flux per unit area required to raise the benzene to its melting temperature is denoted as q', where

$$q' = \dot{x}[h_{sf} + c_{p_m}(T_m - T_{sc})]\rho_{\text{solid}} \tag{5}$$

where T_{sc} is the subcooled temperature of the substrate. The heat flux required to raise the melt layer temperature to that of the pool is then the difference between net heat flux and the melting heat flux. In symbols, this is expressed by the following equation

$$q - q' = \dot{x}\rho_m c_{p_m}(T_s - T_{\text{film}}) \tag{6}$$

where T_{film} is some mean melt layer temperature. This temperature was assumed to be the melting temperature of benzene. Defining $h^*_{sf} = h_{sf} + c_{p_m}(T_m - T_{sc})$ and solving equation (5) and (6) simultaneously for $\dot{x}$ yields

$$\frac{q'}{h^*_{sf}\rho_m} = \dot{x} = \frac{q - q'}{\rho_m c_{p_m}(T_s - T_{\text{melt}})} \tag{7}$$

multiplying both sides by ρ_m, and bringing the q' terms together, leads to

$$q'\left[\frac{1}{h^*_{sf}} + \frac{1}{c_{p_m}(T_s - T_{\text{melt}})}\right] = \frac{q}{c_{p_m}(T_s - T_{\text{melt}})} \tag{8}$$

Finally, solving for q

$$q = q'\left[\frac{c_{p_m}(T_s - T_{\text{melt}})}{h^*_{sf}} + 1\right] \tag{9}$$

The term $c_{p_m}(T_s - T_{\text{melt}})/h^*_{sf}$ can be recognized as a form of the Jakob number, Ja.

(*iv*) With equation (9), and an initial value of q, the melting heat flux can be calculated. This gives

$$q' = q\left[\frac{c_{p_m}\left(T_s - T_{\text{melt}}\right)}{h^*_{sf}} + 1\right]^{-1} \tag{10}$$

(*v*) After arriving at a value for q', a new value of the melt front advance rate was calculated, using equation (15). Solving for $\dot{x}$ yields

$$\dot{x} = \frac{q'}{h_{sf}\rho_m} \tag{11}$$

(*vi*) If this value for $\dot{x}$ was more than 10 percent different

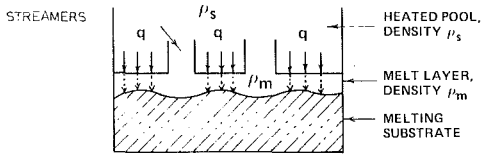

(*a*) Heat is transferred only through the melt layer and not through the area covered by the jets. $\rho_S \geq \rho_m$, heat flux = q.

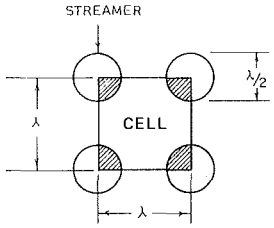

(*b*) Streamers are located on the corners of a square cell, side length-λ. The streamer diameter $D_1 - \lambda$. The shaded portions of the streamers are considered as within the cell.

Fig. 4 Heat transfer through melt layer: (*a*) invertical section; (*b*) horizontal section

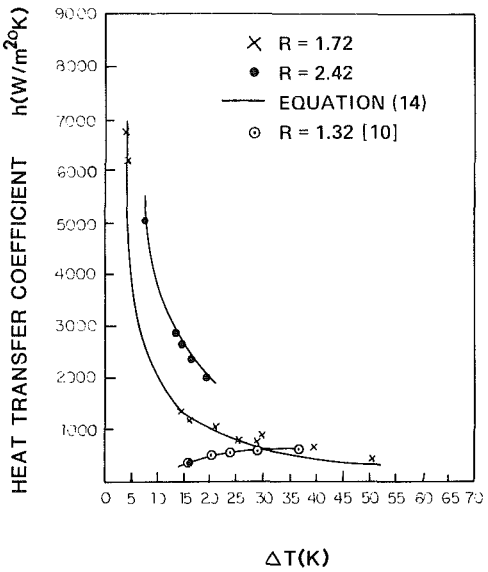

Fig. 5 The measured heat transfer coefficient dependence on temperature difference at constant density ratio

than the original guess, then the process was repeated until the convergence criteria was met. With some experience, the first guess for $\dot{x}$ could be estimated very well, and only one or two iterations were necessary.

(*vii*) After the final value of $\dot{x}$ was obtained, it was compared to the mean value of $\dot{x}$ to be sure that the method of calculation was reasonable. The mean value was determined by noting the change in substrate layer depth at experiment termination and dividing the change in thickness by the total time of the experiment. Because the melt front advance rate calculated from equation (11) is more or less an instantaneous value, and the mean advance rate is an average, it was not expected that the numerical values of the two would be the same. However, they should close and this was indeed the case.

(*viii*) Using the final value of $\dot{x}$ arrived at from the iterative process in steps (*i*) through (*vi*), a final value for q was calculated from equation (10).

Table 2 contains the data obtained from the CCl_4 Benzene experiments. The data from the CH_2I_2 Benzene experiments are given in Table 3.

Analysis

It was noted by Farhadieh and Baker [10] that the melting system of miscible materials of different densities is highly sensitive to the density difference between the pool and the melt material. As the density ratio increases, an increase in heat transfer was noted. This is due to the establishment of large convection cells within the pool, caused in turn by the gravitational instability of the two materials owing to their different densities. These cells mix the pool, and enhance the heat transfer. The melting process itself is characterized by needlelike liquid streamers, or jets, of the substrate material which penetrates into the overlying pool. These streamers are swept away as they rise into the convection cells.

Preliminary observations made in this study also indicated a thin layer of melted substrate between the frozen layer and the overlying heated liquid. It is from this layer that the streamers rise. The streamers are arranged in a systematic pattern across the surface of this thin liquid layer. The presence of two liquid layers, plus observation of the systematic arrangement of streamers, leads to the assumption that the observed physical process is governed by Rayleigh-Taylor instability with zero surface tension. Figure 3 is a sketch of the observed process.

A model for heat transfer from a heated pool should include effects of the ratio of pool density to melt layer density as well as temperature difference. Conduction takes place across the thin layer of melt material and into the frozen substrate, while melting some of the frozen substrate. The melt layer thickens until it becomes gravitationally unstable. The instability results in motion that leads to jets of buoyant fluid being bled off the melt layer. The process reaches an equilibrium state where the melt rate equals the bleed off rate. A sketch of this process is shown in Fig. 4(*a*).

Using an expression for λ obtained by Taghavi-Tafreshi and Dhir [11]

$$\lambda = 2\left(\frac{2R}{R-1}\right)\left(\frac{\nu^2_m}{g}\right)^{1/3} \tag{12}$$

in an analysis similar to that of Berenson [16] for film boiling, an expression for the heat transfer coefficient between the pool and the melt layer-solid substrate interface was found to be

$$h = C\frac{\rho_m h^*_{sf}}{\Delta T}\left(g\nu_m\,(R-1)\right)^{1/3} R^{2/3} \tag{13}$$

where

$$h^*_{sf} = h_{sf} + C_{pm}\,(T_m - T_{sc}).$$

Details of this derivation are given by Brinsfield [17]. The calculated numerical constant was found to be much too large. By adjusting the coefficient to fit the data, the following expression was obtained for the heat transfer coefficient

$$h = 0.0078\frac{\rho_m h^*_{sf}}{\Delta T}\left(g\nu_m\,(R-1)\right)^{1/3} R^{1/3} \tag{14}$$

This leads to an expression for heat flux

$$q = 0.0078\,\rho_m h^*_{sf}\left(g\nu_m\,(R-1)\right)^{1/3} R^{2/3} \tag{15}$$

that is independent of ΔT. A comparison of the resulting heat transfer coefficient with measured data is shown in Fig. 5. The inverse relationship of h with ΔT, which results in the heat flux being independent of ΔT, is clearly shown. Data from [10] for low R are also shown. Note that the physical processes are quite different and the heat transfer coefficient

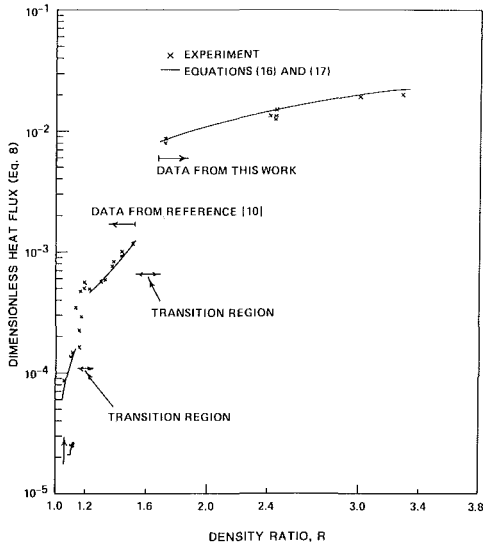

Fig. 6 A comparison of data with the results of curve fitting

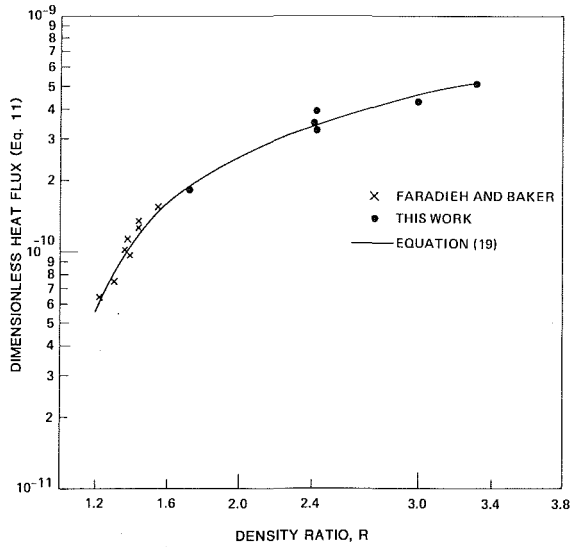

Fig. 7 Results of dimensional analysis

rather than heat flux is almost independent of the temperature difference.

Another approach to obtaining a model, based on Abramovich [18], is to balance vertical momentum leaving in the jet against buoyance forces. The result is

$$\frac{q}{\rho_m h_{sf}^* (g\nu_m)^{1/3}} = 3.759\, y^{5/2} \frac{(R-1)^{1/3}}{(R+1)^{1/2}} R^{2/3} \tag{16}$$

where y is a parameter relating jet diameter to the wavelength, λ, $Dj = y\lambda$. The parameter was adjusted to fit available data and found to be

$$\left.\begin{aligned} y &= (10.88\,R - 9.54) \times 10^{-2} && R < 1.12\ [10] \\ y &= (3\,R - .025) \times 10^{-2} && 1.12 < R < 1.55\ [10] \\ y &= (R + 8.1) \times 10^{-2} && 1.7 < R \end{aligned}\right\} \tag{17}$$

The data from this work and that of Farhadieh and Baker [10] taken at $\Delta T = 21\,^{\circ}\mathrm{C}$ is reproduced to within plus or minus 10 percent using equations (16) and (17). The results of this fitting are shown in Fig. 6.

The data generated in this work clearly shows a lack of dependence on temperature difference. Farhadieh and Baker's data however suggest that at low R, the curve fits for y given above underestimate the true value of y. In part this could be because heating from above stabilizes and at low R, the effect will become apparent. Property variation, however, cannot fully explain the differences.

The data shown in Fig. 6 show two discontinuities or transitions. The first occurs at about $R = 1.2$ and is probably real. The second occurring somewhere between $R = 1.5$ and $R = 1.7$ could be because the viscosity dependence in the models (Rayleigh-Taylor or buoyant plume) is incorrect. The kinematic viscosity of the fluid used in the Farhadieh and Baker experiments is two orders of magnitude larger than that of the fluid used in this work. Using dimensional analysis to correct the viscosity dependence yields

$$\frac{q}{\rho_m h_{sf}^{*3/2}} = \left[\frac{h_{sf}^*}{(g\nu_m)^{2/3}}\right]^{4/10} y(R) \frac{(R-1)^{1/3}}{(R+1)^{1/2}} R^{2/3} \tag{18}$$

with $y(R)$ determined to match experiment. Obtaining $y(R)$ and rearranging, yields

$$\frac{q(g\nu_m)^{4/15}}{\rho_m h_{sf}^{*19/10}} = 44.3 \times 10^{-11} \frac{(R-1)^{1/3}}{(R+1)^{1/2}} R^{2/3}\left(1.125 - \frac{1}{R}\right) \tag{19}$$

for $1.2 < R < 3.3$. This expression fits the data to within plus or minus 10 percent over the entire range. The results of the fit are shown in Fig. 7.

Discussion

A number of interesting physical phenomena were noted during the course of the experimental investigation. Large-scale convective currents were observed in the pool as a result of lighter benzene rising through the heavier overlying pool. These currents kept the pool well mixed so that there was little or no thermal gradient within the pool. Because the fluids used in the experiments were mutually miscible, stratification in the pool was neither expected nor observed. The pool temperature varied only with time and not with location in the pool.

Qualitative observations of the wavelength of the melt layer disruptions were made by noting the spacing between the striations on the surface of the melting material at the conclusion of the experiment. The wavelength was found to be 5–10 mm, decreasing slightly with increasing density ratio. This is in approximate agreement with equation (4). The melt front advance rate was observed to increase with increasing density ratio and decreased with decreasing temperature difference. The advance of the overlying pool into the substrate was fairly uniform over its entire surface when a smooth flat surface was used at the outset. However, if cracks or depressions were formed during the freezing process, they would be selectively attached causing local rapid erosion rates leading to enhanced melting rates. This observation is important to nuclear reactor core catcher design using bricks of refractory material.

Two approaches were taken to modeling the process. Each approach was in a limited way successful. The data from this work and that of Farhadieh and Baker [10] could not, however, be brought together. The process by which the melt layer enters the pool is a complicated one. In particular accounting for viscous effects is complicated. This lead to a more empirical approach that lead to a correlation of both sets of data for R < 1.2. A different process occurs at the lower density ratios and further study is needed.

From the analysis and the data presented within this work, several useful conclusions can be drawn. These are listed below.

(*i*) Melting of a less dense material placed underneath a

heavier heated liquid has been shown to be governed by Rayleigh-Taylor Instability.

(*ii*) If the fluids are miscible, the analysis of jets, or streamers, rather than bubbles, placed a Rayleigh-Taylor wavelength apart, appears to agree favorably with observations.

(*iii*) A model based upon jets placed a Rayleigh-Taylor wavelength apart predicts the behavior of heat fluxes with density ratio and the lack of ΔT dependence.

(*iv*) The heat flux, for the density ratios investigated, is independent of ΔT at density ratios above 1.5. The heat flux increases with increasing density ratio.

(*v*) An empirical correlation has been given which predicts heat fluxes that are within $\pm$ 10 percent of the observed values.

Based upon work done by Farhadieh and Baker [10], and the data presented herein, some areas for further research are indicated. Chief among these is the investigation of the heat flux with the density ratio range near 1.2, which is suspected of being a transition range between temperature dependent and temperature independent heat flux. Work also is required in the very low density range ($R < 1.01$), and for low ΔT($<$ 10 K). The freezing process within the overlying pool could be an important factor in core catcher concepts, and should be studied. The effects of cracks within the substrate material also require attention, as this may affect the design of some core catchers.

Acknowledgments

Support from NSF Grant MEA 81-105542 and NRC Contract 03-80-101 is gratefully acknowledged.

References

1 Taylor, G. I., "The Instability of Liquid Surfaces When Accelerated In a Direction Perpendicular to their Planes, Part I," *Proc. Royal Soc.*, A-201, 1950, p. 192.

2 Taghavi-Tafreshi, K., "Study of Thermal and Hydrodynamic Processes Associated With Melting of Horizontal Substrate," M.S. thesis, UCLA, 1978.

3 Zuber, N., "Hydrodynamic Aspects of Boiling Heat Transfer," AECU-4439, *Physics and Mathematics*, 1959.

4 Carslow, J. S., and Jaeger, J. C., *Conduction of Heat in Solids*, Clarendon Press, Oxford, 1959.

5 Murray, W. E., and Landis, F., "Numerical and Machine Solution of Transient Heat Conduction Problems Involving Melting or Freezing," ASME Transactions, Vol. 81, No. 106, 1959.

6 Project Management Corp., Clinch River Breeder Reactor Plant PSAR.

7 Werle, H., "Experiments for the Diffusion of a Volume Heated Melt In a Soluble Bed," Karlsruhe Nuclear Research Center, ERUFNR-1446, February 1977.

8 Faw, R. E., and Baker, L. Jr. "Post Accident Heat Removal: Part II," *Nuc. Sci. Engr.*, Vol. 61, No. 2, Oct. 1976.

9 Taghavi-Tafreshi, K., et al., "Thermal and Hydrodynamic Phenomena Associated With Melting of Horizontal Substrate Placed Beneath a Heavier Miscible Fluid," JOURNAL OF HEAT TRANSFER.

10 Farhadieh, R., and Baker, L., Jr., "Heat Transfer Phenomenology of a Hydrodynamically Unstable Melting System," JOURNAL OF HEAT TRANSFER, Vol. 100, No. 2, May 1978, p. 305.

11 Taghavi-Tafreshi, K., and Dhir, V. K., "Taylor Instability In Boiling, Melting and Condensation or Evaporation," *International Journal of Heat and Mass Transfer*, Vol. 23, 1980, pp. 1433–1445.

12 Boger, D. V., and Westwater, J. W., "Effect of Buoyancy on the Melting and Freezing Process," JOURNAL OF HEAT TRANSFER, Vol. 89, 1967, pp. 81–89.

13 Yen, Y. C., "Onset of Convection In a Layer of Water Formed by Melting Ice From Below," *The Physics of Fluids*, Vol. 11, 1968, pp. 1263–1270.

14 Yen, Y. C., and Galea, F., "Onset of Convection In a Water Layer Formed by Melting Ice," *The Physics of Fluids*, Vol. 12, 1969, pp. 509–516.

15 Yen, Y. C., "On the Effect of Density Inversion as Natural Convection in a Melted Water Layer," *Chem. Eng. Symposium Series*, Vol. 65, 1969, pp. 245–253.

16 Berenson, P. J., "Film Boiling Heat Transfer From a Horizontal Surface," ASME Paper No. 60-WA-147, 1961.

17 Brinsfield, W. A., "Heat Transfer From a Heated Pool To a Melting Miscible Substrate," M.S. thesis, UCLA, 1979.

18 Abramovich, G. N., *The Theory of Turbulent Jets*, MIT Press, Cambridge, Mass., 1963.

Free Convection in a Vertical Annulus With Constant Heat Flux on the Inner Wall

M. Keyhani

F. A. Kulacki[1]
Mem. ASME

R. N. Christensen

Department of Mechanical Engineering,
The Ohio State University,
Columbus, Ohio 43210

Heat transfer measurements are presented for free convection in a vertical annulus wherein the inner cylinder is at constant surface heat flux and the outer cylinder is at constant temperature. Overall heat transfer data are corrected for thermal radiation in the annulus. Rayleigh numbers span the conduction, transition and boundary layer regimes of flow, and average heat transfer coefficients are obtained with air and helium as the working fluids. The range of Rayleigh number is $10^3 < Ra < 2.3 \times 10^6$; the radius ratio is 4.33; and the aspect ratio (cylinder length divided by annular gap) is 27.6. Energy transferred by thermal radiation varies with Rayleigh number and working fluid. With air, thermal radiation can account for up to 50 percent of the heat transfer. With helium, radiation can account for up to 30 percent of the heat transfer rate. The results of the study provide data relevant to the design and performance assessment of spent fuel packages as part of the National Waste Terminal Storage Program for nuclear waste isolation.

1 Introduction

This paper presents results of an experimental study of free convection in a vertical annulus where the inner wall is at constant heat flux and the outer wall is at constant temperature. Additionally, the aspect ratio for the annulus is large ($L/r_o - r_i >> 1$), and the radius ratio is significantly greater than unity ($K = 4.33$). This combination of geometrical parameters will serve to extend the very few published studies for the vertical annulus with a constant heat flux wall. Also, the present results, in combination with results of previous studies, can serve to form a limiting-case correlation for heat transfer from a nuclear fuel rod bundle to the interior of its canister in either storage or disposal.

For a vertical annulus with both walls at constant temperature, the numerical work of de Vahl Davis and Thomas [1], Thomas and de Vahl Davis [2], and the experimental work of Nagendra, Tirunarayanan, and Ramchandran [3] provide results for Nusselt numbers and flow fields that can serve as a basis for qualitative comparison with results of the present work. The experimental work of Sheriff [4] provides data for the case of a constant heat flux inner wall and a radius ratio close to unity.

de Vahl Davis and Thomas [1] have presented finite difference calculations of free convection in a vertical annulus for $0.5 \le Pr \le 5$, $1 \le K \le 4$, $1 \le H \le 20$, and $Ra \le 2 \times 10^5$. Results for laminar axisymmetric flows were presented for $Pr = 1$. For $Ra < 10^5$, unicellular flow exists, while at larger Ra, multicellular flow was observed. Local heat transfer coefficients on the inner wall were found to increase with radius ratio, but decrease with increasing aspect ratio. Average heat transfer coefficients for $H = 15$ and $K = 1$ were found to agree with the results of Eckert and Carlson [5] for $2 \times 10^4 \le Ra \le 10^5$ in vertical plane layers. At $H = 5$ and $K = 1$, overall Nusselt numbers were somewhat larger than the measurements reported by Emery [5] for a vertical plane layer at $Ra = 2 \times 10^5$. A correlation of the form

$$Nu = f(Pr,K)Ra^{0.3}H^{-1/3} \tag{1}$$

was proposed by de Vahl Davis and Thomas for overall heat transfer coefficients. The function $f(Pr,K)$ was found to be related to the flow field and type of fluid.

Thomas and de Vahl Davis [2] extended the work of de Vahl Davis and Thomas to provide correlation equations for heat transfer for several ranges of Ra. They found that the flow field is strongly dependent on Ra and cavity geometry, whereas the effect of Pr is small. They obtained correlations for the overall Nusselt number for three different flow regimes. The conduction and boundary layer regimes were delimited by the following

Conduction Regime:	$Ra/H \le 400$ ($H > 5$, $Pr = 1$)
	$Ra/H \le 1000$ ($H = 1$)
Boundary Layer Regime:	$Ra/H \ge 3000$ ($H \le 5$, $Pr = 1$)
	$Ra/H \ge 8000$ ($H = 1$)

In all cases, the radius ratio was found to weakly affect the limits of the various flow regimes.

Heat transfer correlations for average Nusselt numbers developed by Thomas and de Vahl Davis were

Conduction Regime:

$$Nu = 0.595Ra^{0.101}Pr^{0.024}H^{-0.052}K^{0.505} \tag{2}$$

Transition Regime:

$$Nu = 0.202Ra^{0.294}Pr^{0.097}H^{-0.264}K^{0.423} \tag{3}$$

Boundary Layer Regime:

$$Nu = 0.286Ra^{0.258}Pr^{0.006}H^{-0.238}K^{0.442} \tag{4}$$

These correlations were developed for $1 \le K \le 10$, $1 \le H \le 33$, $0.5 \le Pr \le 10^4$ and $Ra \le 2 \times 10^5$. It was also found that with moderate aspect ratio, the flow field takes the form of a single cell up to a certain Rayleigh number. As the Rayleigh number is increased, this motion becomes unstable and a multicellular mode rapidly develops.

The experimental work of Sheriff [4] considered free convection in a vertical annulus with the thermal boundary conditions as in the present study. His correlation for average Nusselt number is

$$Nu = 0.25Ra^{0.30}H^{-0.25} \tag{5}$$

where $10^5 \le Ra \le 10^8$. Sheriff's experimental data included three radius ratios, $K = 1.23$, 1.10, and 1.03, with aspect ratios

[1] Present address: Department of Mechanical and Aerospace Engineering, University of Delaware, Newark, Del. 19711

Contributed by the Heat Transfer Division for publication in the JOURNAL OF HEAT TRANSFER. Manuscript received by the Heat Transfer Division May 13, 1982.

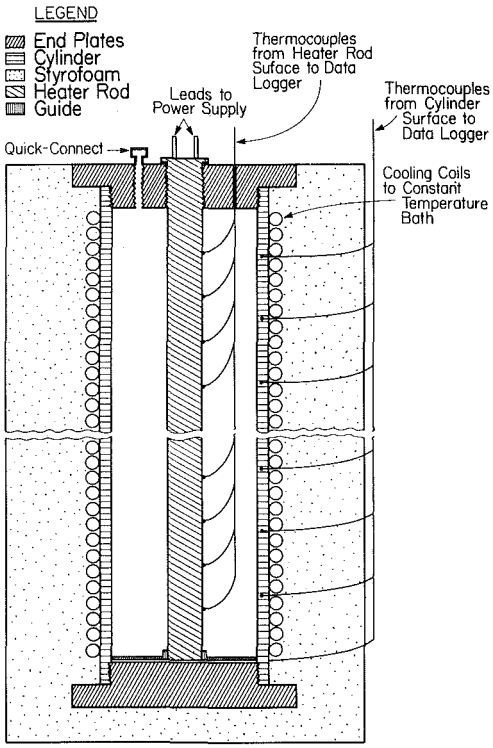

Fig. 1 Schematic of experimental apparatus and instrumentation

of $H = 38$, 76, and 228, respectively. The working fluid (CO_2) was pressurized to extend the range of Rayleigh numbers. In order to correct for the effects of thermal radiation, Sheriff conducted some preliminary tests at a pressure of about 26 mm Hg to ensure no convection. From the temperature drop across the annulus and the temperature gradient along the heater, the radial and axial heat loss by conduction was calculated. The remainder of the heat transferred was assumed to be thermal radiation.

Landis and Yanowitz [8] studied transient and steady free convection in a long vertical rectangular cell with constant heat flux on one of the vertical walls. Air, water, and silicone oil were used over a range of Rayleigh numbers of 900 to 2×10^6. Both temperature and velocity profiles were obtained,

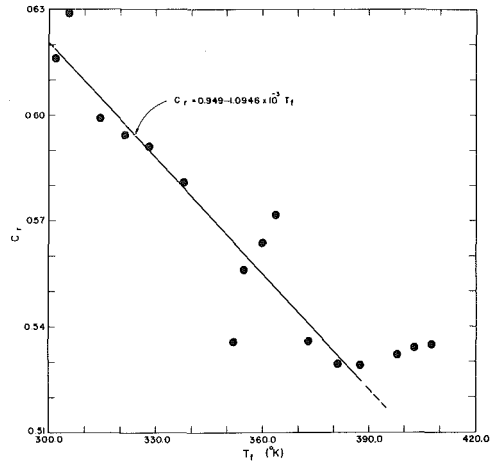

Fig. 2 Overall thermal conductance for radiative transport in the annulus

along with overall heat transfer coefficients. In the heat transfer data, the effects of thermal radiation were determined by rotating the cell to a horizontal position and evacuating the system to about 5-mm *Hg*. At this pressure, the Rayleigh number was an order of magnitude below the value for the onset of convection. The hot wall was then heated to various power levels and conduction heat transfer was subtracted from the power input. The results pertinent to the present work are the correlation for Nusselt number

$$\mathrm{Nu} = 0.194\mathrm{Ra}^{*0.218} \tag{6}$$

where $H = 20$ and $2 \times 10^3 \leq \mathrm{Ra}^* \leq 10^7$. In terms of the conventional Rayleigh number based on the midheight temperature difference, equation (6) becomes

$$\mathrm{Nu} = 0.123\mathrm{Ra}^{0.279} \tag{7}$$

over the range $2 \times 10^3 \leq \mathrm{Ra} \leq 1.5 \times 10^6$.

2 Experimental Apparatus

The major components of the experimental apparatus are the outer cylinder, end plates, heater rod, cooling jacket, pressure control, and power supply with associated controls and instrumentation. Figure 1 presents a schematic of the

Nomenclature

c_p = specific heat at constant pressure, J/kg-°C
C_r = thermal conductance for radiation, equation (9)
g = constant of gravitational acceleration, m/s^2
Gr = Grashof number, $\frac{g\beta}{\nu^2} l^3 \Delta T$
Gr* = modified Grashof number $\frac{g\beta}{k\nu^2} l^4 q_c$
h = convective heat transfer coefficient, $q_c/\Delta T$, W/m^2-°C
H = aspect ratio of cylinder, L/l
k = thermal conductivity, W/m-°C
K = radius ratio, r_o/r_i
l = length scale, $r_o - r_i$, m
L = height of annulus or layer, m
Nu = Nusselt number based on gap, hl/k
Pr = Prandtl number, $\frac{\nu}{\alpha}$
q = heat flux based on inner cylinder area, W/m^2
r = radius, m
Ra = Rayleigh number, Gr Pr
Ra* = modified Rayleigh number, Gr*Pr
T = temperature, °K
T_f = mean temperature of the medium, $\frac{T_{MR} + T_{MC}}{2}$, °K
ΔT = characteristic temperature difference, $T_{MR} - T_{MC}$, °K
x = coordinate measuring distance along rod from top, m
W = power, W

Greek Symbols

α = thermal diffusivity, $k/\rho c_p$, m^2/s
β = isobaric coefficient of thermal expansion, °K^{-1}
ν = kinematic viscosity, m^2/s
ρ = density, kg/m^3
σ = Stephan-Boltzman constant, W/m^2 – °K^4

Subscripts

c = convection
C = cylinder
i = inner wall
M = mean value
MC = mean value on cylinder
MR = mean value on rod
O = outer
r = radiation
R = rod

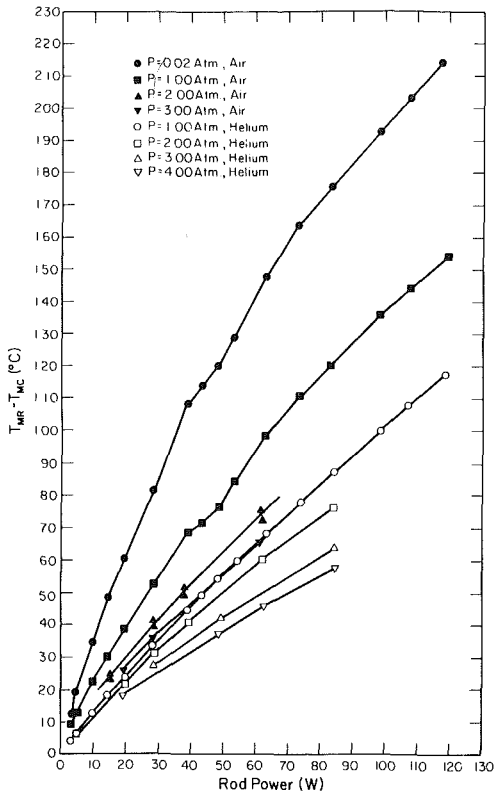

Fig. 3 Temperature difference across the annulus as a function of total rod power

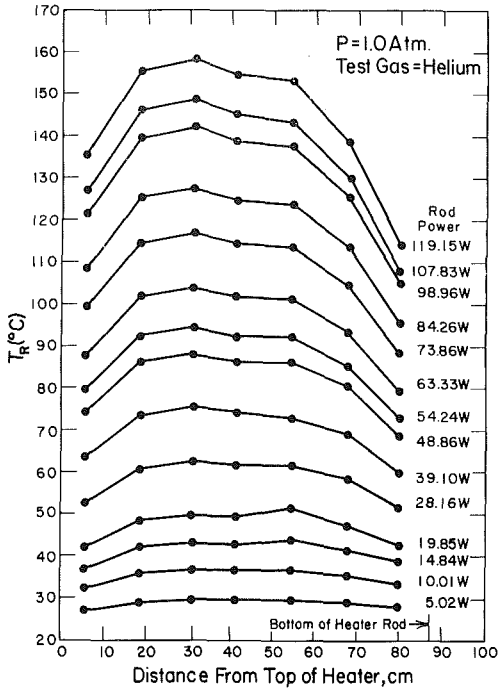

Fig. 5 Temperature distribution on rod surface at atmospheric pressure

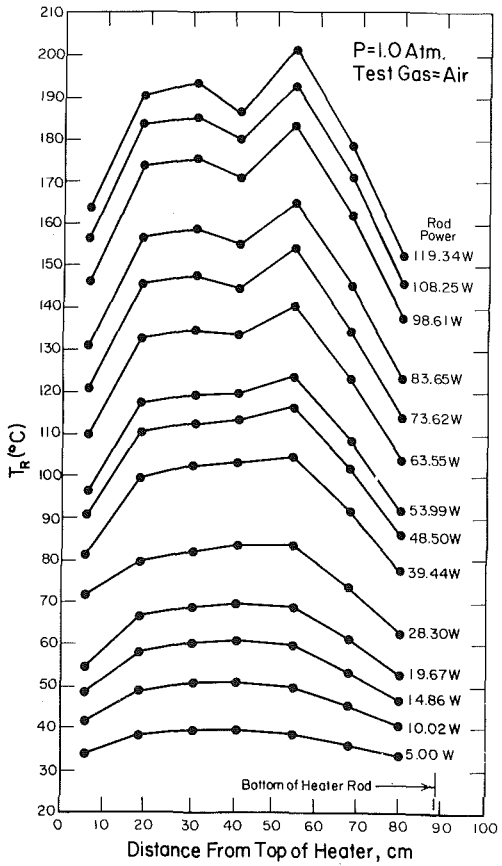

Fig. 4 Temperature distribution on rod surface at atmospheric pressure

apparatus and instrumentation. A detailed description of the apparatus is given in [9].

The outer cylinder is made of carbon steel and is 8.26-cm i.d. × 9.53-cm o.d. × 92.17 cm. A cooling coil wound in a double pass arrangement is soldered to the outer surface to maintain a constant temperature on the surface of the cylinder. The inner cylinder is a 1.91-cm dia cartridge heater with an effective heated length of 87.6 cm and is designed to provide uniform electrical power dissipation per unit length. It comprises a nickel-chromium wire wound around a magnesium oxide core with a 0.05-cm sheath of Incoloy.

To determine surface temperature on the outer wall, 32 thermocouples are potted into 0.32-cm deep holes drilled through the outside surface. Owing to the thermal conductivity of the steel, the inside surface temperature of the cylinder was 3×10^{-4} °C/W greater than the thermocouple output. For the maximum heat transfer rate of 120 W, the overall temperature difference was 0.04°C.

No attempt was made to measure the end losses via axial conduction on the cylinder wall. However, the ratio of thermal resistances in the axial direction to that in the radial direction is of the order of 10^4. This implies that the assumption of radial heat flow through the cylinder wall is a reasonable one.

Surface temperatures on the heater rod were monitored with thermocouples inserted through the end plate and affixed to the surface of the heater rod. Temperature data were recorded with a high sensitivity voltmeter and multichannel data logger.

3 Results

Results obtained in the present work include temperature distributions on the surface of the heater rod and heat transfer coefficients for free convection and combined free convection and thermal radiation for Rayleigh number from 10^3 to 2.3×10^6. This range of Rayleigh number spans the conduction to boundary layer regimes of convection as defined in the study of Thomas and de Vahl Davis [2]. In all cases, a correction for

thermal radiation in the annulus is applied in the calculation of the coefficient for free convection. This correction includes the effects of surface emissivities, radiative view factors, and axial conduction losses along the inner cylinder through the top plate.

The correction for thermal radiation was obtained by operating the apparatus at 15-mm *Hg* over a range of power input. At this pressure, heat transfer is by conduction and radiation. Since the Rayleigh number ($Ra < 80$) is well within the conduction regime as specified by Thomas and de Vahl Davis, the following relations were used to correct overall heat transfer coefficients for thermal radiation

$$h_r = C_r(T_{MR}^2 + T_{MC}^2)(T_{MR} + T_{MC}) \tag{8}$$

$$C_r = \frac{q - q_{\text{conduction}}}{\sigma(T_{MR}^4 - T_{MC}^4)} \tag{9}$$

$$h = h_{\text{total}} - h_r \tag{10}$$

In equation (9), $q_{\text{conduction}}$ is obtained from the correlation given by Thomas and de Vahl Davis. Values of C_r include view factors and emissivity effects and are presented in Fig. 2. An equation of the form

$$C_r = 0.946 - (1.095 \times 10^{-3})T_f \tag{11}$$

adequately describes the data for $300 \leq T_f \leq 390$K. In applying equation (11), one takes into account the temperature dependence of the emissivity for the range of values of C_r in the present work, as well as the effects of axial conduction losses along the inner cylinder through the top plate.

The temperature on the outer cylinder was held constant, although the mean value varied from run to run. A typical value was 24.8°C with a standard deviation of 0.3°C.

Experimental data for air and helium are summarized in Figs. 3 to 5. Figure 3 contains the difference of mean temperatures on the inner and outer walls of the annulus for pressures from 0.02 atm to 4.0 atm. Temperature distributions on the inner cylinder for air at 1.0 atm are contained in Fig. 4. Despite the variation of temperature in the axial direction, the standard deviation of mean values ranges from 5 to 12 percent of mean values. The data for helium exhibit a somewhat smoother variation along the axial direction, with a standard deviation of 3–11 percent of mean values (Fig. 5).

Temperature distributions on the inner cylinder at different Rayleigh numbers is presented in Fig. 6. For truly conductive heat transfer, the temperature distribution on the constant heat flux wall should be constant. As can be seen in Fig. 6, for $Ra = 1.1 \times 10^3$, the temperature distribution on the inner cylinder is nearly constant. As the Rayleigh number is increased to 5×10^3, the temperature increases from the bottom to the top of the inner wall, which is indicative of a unicellular flow. The thermocouple nearest the top of the annulus does not show this increase. This is partly due to conduction losses along the inner cylinder which is estimated to be less than 3.0 percent of the power input for all runs in the present work. This conduction loss is estimated over and above that already included in the radiation correction.

In the transition regime, as defined by Thomas and de Vahl Davis ($1.1 \times 10^4 \leq Ra \leq 8.3 \times 10^4$ for $H = 27.6$), the temperature distribution on the hot wall does not follow the same trend as in the conduction regime. Thomas and de Vahl Davis and other investigators have shown that for the same aspect ratio and radius ratio, as the Rayleigh number is increased, the streamlines shift toward the top of the cavity. This could partially explain the slight drop in temperature in the upper third of the hot wall at $Ra = 2.61 \times 10^4$. At $Ra = 1.4 \times 10^5$, temperatures at the midsection are nearly uniform,

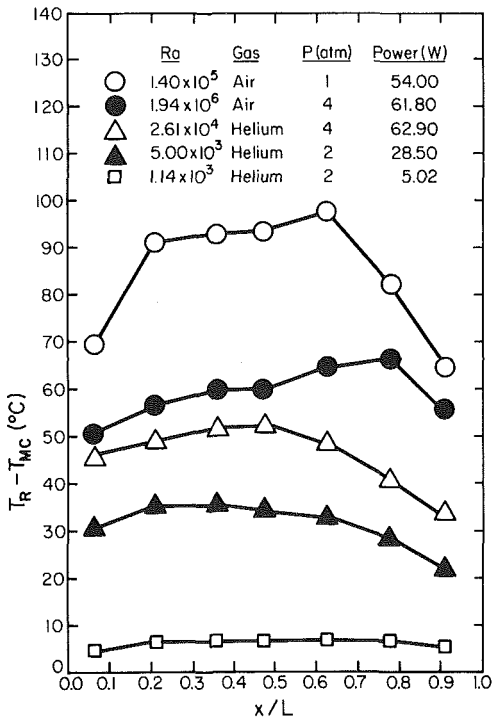

Fig. 6 Local temperature differences on inner cylinder for several Rayleigh numbers

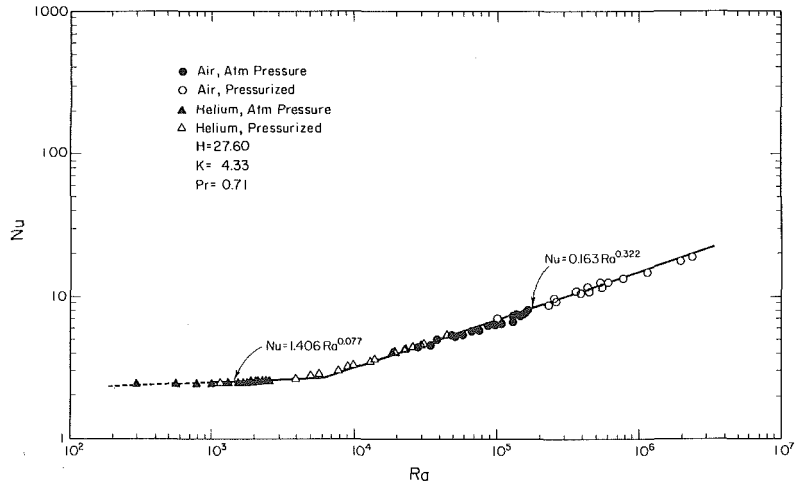

Fig. 7 Average Nusselt number as a function of Rayleigh number (values are corrected for radiation effects)

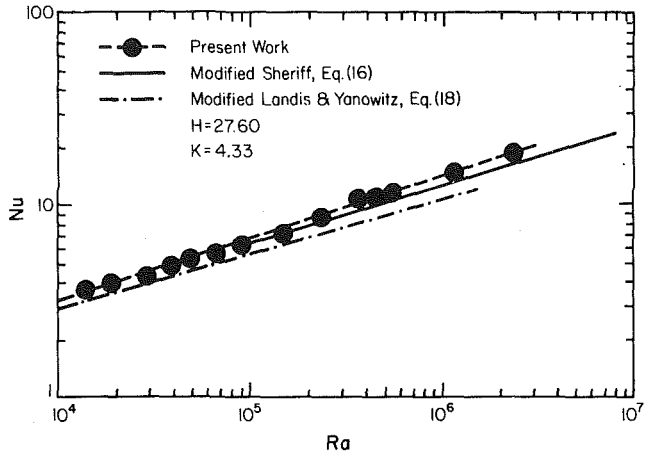

Fig. 8 Present results with modified correlations of Sheriff [16] and Landis and Yanowitz [18]

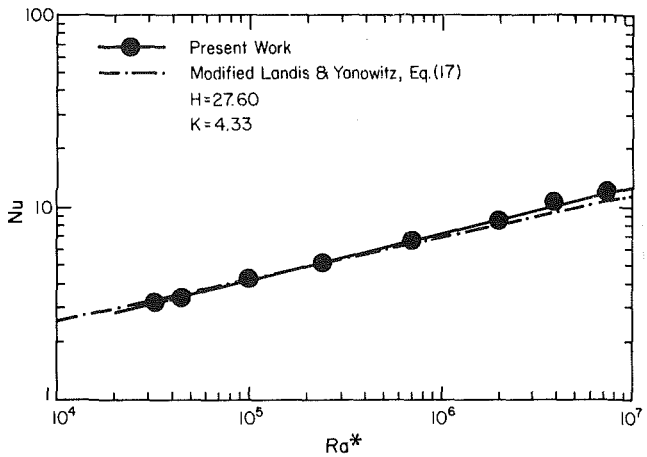

Fig. 9 Average Nusselt numbers in terms of modified Rayleigh number

and decrease on the ends. However, for $Ra = 1.95 \times 10^6$, which is in the boundary layer regime, the behavior is completely different. Temperatures generally increase from the top of the heater to the bottom, except at the bottom 20 percent, where a decrease in temperature is observed. At this Rayleigh number, it is possible that either a multicellular flow has developed or transition to turbulent flow has been initiated. Reference [9] contained a complete tabulation of temperature data.

When the experimental data are reduced to a Rayleigh number based upon the length scale $r_o - r_i$, the difference of mean temperature, $T_{MR} - T_{MC}$, and a Nusselt number for convection only, it is possible to correlate the results in the form $Nu = \text{Constant} \times Ra^m$. The present data permit a correlation for two regimes of heat transfer. These are

$$Nu = 1.406Ra^{0.077} \tag{12}$$

for $10^3 \leq Ra \leq 6.6 \times 10^3$, and

$$Nu = 0.163Ra^{0.322} \tag{13}$$

for $6.6 \times 10^3 \leq Ra \leq 2.3 \times 10^6$.

In terms of the modified Rayleigh number, equations (12) and (13) become

$$Nu = 1.37Ra^{*0.072}, \quad 2.6 \times 10^3 \leq Ra^* \leq 1.8 \times 10^4 \tag{14}$$

and

$$Nu = 0.253Ra^{*0.244} \quad 1.8 \times 10^4 \leq Ra^* \leq 4.21 \times 10^7 \tag{15}$$

Correlations in terms of the conventional Rayleigh number are presented in Fig. 7.

The present results give Nusselt numbers about 10 percent higher than those of Thomas and de Vahl Davis in the conduction regime for $H = 27.6$ and $K = 4.33$. This level of agreement should be expected because most of the temperature profiles on the hot wall in the conduction regime could be approximated as constant temperature with a small standard deviation. However, the Nusselt number in the conduction regime should be higher than those reported by Thomas and de Vahl Davis, owing to the difference in thermal boundary conditions on the inner wall. In the boundary layer regime, however, present results give a much larger Nusselt number than those of Thomas and de Vahl Davis. For example, at $Ra = 10^4$ and 2×10^5, present Nusselt numbers are 16 and 44 percent higher. This large difference is to be expected due to the different thermal boundary condition on the inner wall and the limitation of the numerical computations to laminar flow.

Heat transfer across the annulus by thermal radiation, as a fraction of the total heat transfer varies with Ra and the test gas. With air, thermal radiation accounts for up to 50 percent of the total, while for helium thermal radiation accounts for up to one-third of the total. Total Nusselt numbers are tabulated in [9].

The experimental uncertainty in the present result is based on uncertainties in the thermophysical properties, temperatures, and geometrical factors. For the Rayleigh number, the total uncertainty amounts to 6 to 8 percent and for Nusselt numbers 8 to 10 percent. These uncertainties do not include the previously mentioned standard deviation of mean temperature values on the cylinder. Also, the scatter of the data points for the thermal conductance for radiation is neglected. However, the procedure used in the present study for radiation correction seems to be an improvement over that used by other investigators [4, 8]. In the present study, no attempt was made to obtain an emissivity for the surfaces and use that value for radiation correction. In effect, the procedure used in the present study, can be interpreted as follows. For a given experiment with convective heat transfer present, the same mean temperature on the hot surface is reproduced in the vacuum condition. While the outer cylinder temperature is held at nearly the same value as that with convection present. Then the power input to the heater at vacuum condition with conduction heat transfer across the annulus deducted from it is taken as the radiation and axial conduction loss effects. However, the variability of the data points for c_r (see Fig. 2) results in a maximum uncertainty of about 5 percent in the radiation correction.

End losses due to axial conduction in the inner cylinder through the top plate amounts to 3 percent of total applied power. As mentioned previously, this amount of axial conduction loss is estimated over and above what is already included in the radiation correction. The losses through the bottom plate are considered nil, since the heater rod is separated from it by a small space to allow for thermal expansion. The variation of the temperature on the outer cylinder from its mean value, for the majority of the experiments is about 1 percent of the temperature drop across the annulus. Furthermore, this variation from the mean temperature is mostly in the midsection of the outer cylinder, where a small portion of the heat is being transferred. Therefore, this variation is not considered in the estimation of the uncertainties for the Nusselt and Rayleigh numbers.

4 Discussion and Conclusion

A comparison of the present results to those in the literature is difficult since no equivalent study exists. However, it is possible to modify the results of Sheriff [4] and Landis and Yanowitz [8], whose studies involved thermal boundary

conditions similar to those of the present work. In order to modify their results for a comparison with the present results, the correlation reported by Thomas and de Vahl Davis [2] has been used. For the boundary layer regime, they reported the Nusselt number dependence on the radius ratio and aspect ratio as $K^{0.442}$ and $H^{-0.238}$, respectively. Assuming that this same dependence holds for the constant heat flux boundary condition, one can modify Sheriff's results to the following

$$\mathrm{Nu} = 0.239 K^{0.442} H^{-0.25} \mathrm{Ra}^{0.30} \tag{16}$$

where the leading factor in equation (16), 0.239, has been obtained by formally setting $C K^{0.442} = 0.25$ (see equation (5)) for a K value equal to the average of 1.23, 1.10, and 1.03. Similarly, the correlations reported by Landis and Yanowitz, equations (6) and (7), can be modified for $H = 20$ and $K = 1$. These become

$$\mathrm{Nu} = 0.396 H^{-0.238} K^{0.442} \mathrm{Ra}^{*0.218} \tag{17}$$

and

$$\mathrm{Nu} = 0.251 H^{-0.238} K^{0.442} \mathrm{Ra}^{0.279} \tag{18}$$

Although Thomas and de Vahl Davis report a Prandtl number dependence of $\mathrm{Pr}^{0.006}$ for air ($\mathrm{Pr} = 0.71$), carbon dioxide ($\mathrm{Pr} = 0.76$), and Water ($\mathrm{Pr} = 6$), the effect on equations (16) and (18) would be less than 1 percent.

The assumption that the dependences of the Nusselt number on aspect and radius ratios are the same for the present case, as well as for the constant temperature case, implies that the effect of geometric parameters is independent of the boundary conditions. This claim is partially substantiated by the close agreement on the aspect ratio effect reported by Thomas and de Vahl Davis and by Sheriff. Therefore, the effects of the difference in the boundary conditions are expected to appear in the exponent of the Rayleigh number as well as in the leading constant of the correlation.

A graphical comparison of the present results with those of Sheriff, equation (16), and Landis and Yanowitz, equation (18), is presented in Fig. 8 for $10^5 \leq \mathrm{Ra} \leq 2 \times 10^6$. The present results are from 5.3 percent to 11.3 percent higher than those reported by Sheriff. In general, the comparison of the two results is considered satisfactory. For $10^4 \leq \mathrm{Ra} \leq 1.5 \times 10^6$, the present results are from 8.4 percent to 27.5 percent higher than the modified correlation of Landis and Yanowitz.

The present results, in terms of the modified Rayleigh number, are presented in Fig. 9 along with the modified Landis and Yanowitz correlation, equation (17). In the region of the overlap of the two, i.e., $2 \times 10^4 \leq \mathrm{Ra}^* \leq 10^7$, the comparison of the two is considered satisfactory. At $\mathrm{Ra} = 2 \times 10^4$, the modified Landis and Yanowitz correlation gives Nusselt numbers 5 percent greater than the present, while at $\mathrm{Ra} = 10^7$ present results are 10.7 percent higher than the modified Landis and Yanowitz correlation.

From the generally satisfactory comparison of the present results with those of the modified Sheriff correlation ($K = 1.03$, 1.13, and 1.23, $H = 38$, 76, and 226, and $\mathrm{Pr} = 0.76$) and the modified Landis and Yanowitz correlations ($H = 20$, $K = 1$, and $\mathrm{Pr} = 0.71$, and 1420), it can be concluded that the power-law dependence of the aspect and radius ratios in the overall Nusselt number for the case of both walls at constant temperature can be used for the case where the inner wall is at constant heat flux. There is a slight difference in the power-law dependence on the Rayleigh number in the three sets of results, and this can be attributed to normal experimental scatter. Present results, equations (14) and (15), with the power-law dependence of aspect and radius ratios as reported by Thomas and de Vahl Davis [2] are

$$\mathrm{Nu} = 0.78\ \mathrm{Ra}^{*0.072} H^{-0.052} K^{0.505} \tag{19}$$

for $2.6 \times 10^3 \leq \mathrm{Ra}^* \leq 1.8 \times 10^4$, and

$$\mathrm{Nu} = 0.291\ \mathrm{Ra}^{*0.244} H^{-0.238} K^{0.442} \tag{20}$$

for $1.8 \times 10^4 \leq \mathrm{Ra}^* \leq 4.21 \times 10^7$. The limits on aspect and radius ratios are as reported by Thomas and de Vahl Davis.

Present results indicate that the hot wall boundary condition has a significant effect upon the overall heat transfer. In the boundary layer regime, present results yield overall Nusselt numbers up to 44 percent higher than those obtained from the numerical study of Thomas and de Vahl Davis [2] for the isothermal wall condition. A comparable conclusion was reached by MacGregor and Emery [10] for the vertical cavity case.

Acknowledgment

We gratefully acknowledge the support of the U.S. Department of Energy, Office of Nuclear Waste Isolation, under Contract ONWI/E512-03900 to the Ohio State University Research Foundation.

References

1 de Vahl Davis, G., and Thomas, R. W., "Natural Convection Between Concentric Vertical Cylinder," *High Speed Computing in Fluid Dynamics, Physics of Fluids, Supplement II*, 1969, pp. 198-207.

2 Thomas, R. W., and de Vahl Davis, G., "Natural Convection in Annular and Rectangular Cavities. A Numerical Study," *Proceedings, Fourth International Heat Transfer Conference*, Paris, Vol. 4, Paper NC 2.4, Elsevier, Amsterdam, 1970.

3 Nagendra, H. R., Tirunarayanan, M. A., and Ramachandran, A., "Free Convection Heat Transfer in Vertical Annuli," *Chemical Engineering Science*, Vol. 5, 1970, pp. 605-610.

4 Sheriff, N., "Experimental Investigation of Natural Convection in Single and Multiple Vertical Annuli with High Pressure Carbon Dioxide," *Proceedings, Third International Heat Transfer Conference*, Chicago, Vol. 2, 1966, pp. 132-138.

5 Eckert, E. R. G., and Carlson, W. O., "Natural Convection in an Air Layer Enclosed Between Two Vertical Plates with Different Temperatures," *International Journal of Heat and Mass Transfer*, Vol. 2, 1969, p. 106.

6 Emery, A. F., "The Effect of a Magnetic Field Upon the Free Convection of a Conducting Fluid," ASME JOURNAL OF HEAT TRANSFER, Vol. 85, 1963, pp. 119-124.

7 Emery, A., and Chu, N. C., "Heat Transfer across Vertical Layers," ASME JOURNAL OF HEAT TRANSFER, Vol. 87, 1965, pp. 110-116.

8 Landis, F., and Yanowitz, H., "Transient Natural Convection in a Narrow Vertical Cell," *Proceedings, Third International Heat Transfer Conference*, Chicago, Vol. 2, 1966, pp. 139-151.

9 Keyhani, M., Kulacki, F. A., and Christensen, R. N., "Convective Heat Transfer Within Spent Fuel Canisters—An Experimental Laboratory Study," Office of Nuclear Waste Isolation, Battelle Memorial Institute, Columbus, ONWI-229, Jan. 1981.

10 MacGregor, R. K., and Emery, A. F., "Free Convection Through Vertical Plane Layers-Moderate and High Prandtl Number Fluids," ASME JOURNAL OF HEAT TRANSFER, Vol. 91, 1969, pp. 391-403.

Onset of Convection in a Horizontal Layer of Cold Water

J. C. Mollendorf
Associate Professor,
Mechanical and Aerospace Engineering,
State University of
New York at Buffalo,
Amherst, N.Y. 14260
Mem. ASME

K. H. Jahn
Quality Control Supervisor,
Dupont/Sorvall,
Newton, Conn. 06470

Parabolic, cubic, and higher order expressions have been used in previous investigations to relate temperature to density in the vicinity of the density extremum. Another equation of state, based on the careful measurement of the density variations of both pure and saline water, has been used here to determine the onset of convection in a horizontally confined layer of water near its density extremum. The simplicity of this equation gives rise to a minimum number of problem particular parameters, and relatively easily allows for the inclusion of both pressure and salinity level effects (neglecting saline diffusion). The boundaries are considered to be rigid-rigid and of infinite thermal capacity. Present numerical results are compared with those previously calculated using other density relationships, including that embodied in the linear Oberbeck-Boussinesq approximation. Density extremum effects are seen to be stabilizing, with critical Rayleigh numbers calculated to be about 10 percent below those obtained using a parabolic density-temperature relationship and quite close to those found using a fifth-order polynomial. There is an associated increase in calculated wave number with the inclusion of density extremum effects.

Introduction

For a horizontal fluid layer confined between rigid boundaries, the fluid motion resulting from an adverse density gradient has become known as Benard convection. Mallinson [1] presents a summary of investigations of this flow phenomena. He indicates that when Benard [2], in 1900, first investigated the resulting fluid motion for a viscous fluid heated from below, he noted that for small temperature differences a stable motionless state occurs. On increasing this temperature difference, the configuration eventually became unstable and then settled into a regular pattern of hexagonal cells. Schmidt and Milverton [3], and Silverton [4] later verified this observation and showed that as this temperature difference is further increased the flow can be described as turbulent. They defined a critical Rayleigh number at which convection commences as $\mathrm{Ra}_c = \beta g d^3 (T_h - T_c)/\alpha\nu$.

With this definition of the critical Rayleigh number, for rigid horizontal boundaries, Silverton [4] experimentally obtained the value of $\mathrm{Ra}_c = 1700 \pm 51$. His data indicated that a sudden change in Nusselt number could be interpreted as the indication of fluid motion.

More recent observations by Leontiev and Kirdyashkin [5] demonstrate the progression through differing stable states as the Rayleigh number is increased. Observing a 4-mm-thick layer of ethylene glycol, they noted a roll motion just before the development of steady-state polygonal cells at $\mathrm{Ra} \simeq 10^4$. Upon increasing the Rayleigh number to $\mathrm{Ra} \simeq 10^5$, they found that a further change to rolls occurred, with a corresponding increase in flow complexity. Further increases in flow complexity were noted up to $\mathrm{Ra} \simeq 10^6$, the limit of their experiment.

Similarly, Malkus [6], working in distilled water and acetone, in an earlier study, had already noted up to six flow transitions in the Rayleigh number range of from 10^3 to 10^6. His findings were experimentally confirmed by Willis and Deardoff [7], contradicting the idea of a single change from laminar to turbulent flow, as had been suggested from earlier observations. In addition to this experimental work, considerable attention has also been given to the theoretical analysis of the stability problem, that is, the prediction of the conditions under which the initially motionless state becomes unstable.

The analysis generally consists of an examination of the growth of the Fourier components of a small disturbance, or perturbation. Lord Rayleigh [8] was the first to analytically investigate the horizontal layer, and derived a set of equations defining an eigenvalue problem, which when solved would determine the minimum value of the Rayleigh number for which motion occurs. For rigid horizontal boundaries, Low [9] first solved the governing equations and arrived at $\mathrm{Ra}_c = 1706$. Reid and Harris [10] in 1958 obtained a more accurate estimate of the critical Rayleigh number for rigid boundaries and reported $\mathrm{Ra}_c = 1707.8$ and $a = 3.117$, where a is the nondimensional wave number (i.e., $a = 2\pi d/\lambda$, where λ is the physical wavelength and d is the perpendicular distance between parallel horizontal plates).

However, the second part of the Oberbeck-Boussinesq approximation of a linear density-temperature relationship, as used in all these earlier works, cannot be accurately applied to fluids, which exhibit a density extremum. Water is one such fluid. Pure water exhibits a density extremum at around 4°C at one atmosphere. As an improvement, the parabolic expression

$$\rho = \rho_{\max}[1 - \gamma(T - T_{\max})^2] \tag{1}$$

was used by Debler [11], Tien [12], and Veronis [13]. Veronis [13], using $\gamma = 7.68 \times 10^{-6}/(°\mathrm{C})^2$ and $T_{\max} = 4°\mathrm{C}$, reported that he found equation (1) to be very accurate near 4°C. However, at 14°C, an error of 10 percent or 100,000 ppm resulted, with larger errors expected at higher temperatures. Since this expression is only claimed to be accurate for temperatures from 0–8°C, it represents a major limitation to the analysis of such fluids. It should be noted, moreover, that small changes in density can give rise to significant flow modifications.

Sun, Tien, and Yen [14], in an effort to extend the range of applicability, expanded equation (1) to include an additional cubic term. That is

$$\rho - \rho_{\max} = -\rho_{\max}[\gamma_1(T - T_{\max})^2 + \gamma_2(T - T_{\max})^3] \tag{2}$$

They claim to have thereby increased the range of applicability of the equation of state to temperatures from 0–30°C. In experimental work aimed at verifying their theoretical predictions of Ra_c, Sun, Tien, and Yen [14] report,

Contributed by the Heat Transfer Division and presented at the 21st ASME/AIChE National Heat Transfer Conference, Seattle, Washington July 24–28, 1983. Manuscript received by the Heat Transfer Division October 25, 1982.

within the "experimental error," complete agreement with the analytical results presented by them for both melting from above and below.

In a later study, Sun and Tien [15] attempted to extend the use of equation (2) from the earlier stability work to the derivation of a heat transfer correlation for water near the density extremum in terms of the Nusselt number. They based their approach on the work of Nakagawa [16]. Nakagawa found that the critical Rayleigh number obtained from the linear stability analysis could be used to estimate the heat transfer rate for finite amplitude convection. Sun and Tien [15] report that the correlation thus obtained was found to be accurate for Rayleigh numbers up to five to ten times its critical value.

Yen [17], in 1974 further investigated the effect of a density extremum on free convective heat transfer in porous horizontal layers heated from below. He found that the effect of a density extremum on the heat transfer rate was significant, and in fact, that for small ΔT, it causes the heat transfer rate, at its largest deviation, to be only half as large as for nondensity extremum conditions.

In order to obtain more accurate results, Merker, Wass, and Grigul [18] used a fifth-order polynominal in temperature to represent the density vartiation and found calculated Ra_c to be about 10 percent below those found using a parabolic density relation.

The purpose of the present work is to apply a simple and accurate density relationship to the problem of determining the effect of a density extremum on the critical Rayleigh number for the onset of convection in a horizontal layer of water in the vicinity of its density extremum. This relationship will be described in more detail in the analysis. The following analysis is for both pure and saline water in the absence of mass diffusion for rigid-rigid boundaries of infinite thermal capacity.

Analysis

The governing equations of continuity, force momentum, and energy balance, with the body force, $-\rho g\hat{k}$, vertically downward may be written as

$$\nabla \cdot \mathbf{V} = 0 \tag{3}$$

$$\rho \frac{D\mathbf{V}}{D\tau} = \mu \nabla^2 \mathbf{V} - \nabla p - \rho g \hat{k} \tag{4}$$

$$\frac{Dt}{D\tau} = \alpha \nabla^2 t \tag{5}$$

The formulation proceeds, as usual, by considering the various flow and transport variables to be the sum of baseflow (denoted by bars) and disturbance quantities (denoted by primes) as follows: $u = \bar{u} + u'$, $v = \bar{v} + t'$, $w = \bar{w} + w'$, $t = \bar{t} + t'$, $\rho = \bar{\rho} + \rho'$, $p = \bar{p} + p'$, where $u' << \bar{u}$, $v' << \bar{v}$, etc.

The temperature excess ratio is further defined as $\phi = (t - t_2)/(t_1 - t_2) = (\bar{t} - t_2)/(t_1 - t_2) + t'/(t_1 - t_2) = \bar{\phi} + \phi'$ and upon introducing the one dimensional, steady conduction "base flow," $\bar{\phi} = 1 - z/d + \phi'$ where $\bar{u} = 0$, $\bar{v} = 0$, $\bar{w} = 0$. $\bar{\rho} = \rho_h(z)$ and $\bar{p} = p_h(z)$ and $\bar{\phi} = 1 - z/d = (\bar{t} - t_2)/(t_1 - t_2)$.

Considering first the sum of the body force and pressure term in the z-direction

$$-\rho g - \frac{\partial p}{\partial z} = -g\rho_h(z) - g\rho'$$

$$-\frac{\partial p_h(z)}{\partial z} - \frac{\partial p'}{\partial z} = -g\rho' - \frac{\partial p}{\partial z} \tag{6}$$

where $\partial p_h/\partial z = -g\rho_h$.

The equations, linearized in disturbance quantities, u', v', and w' become

$$\nabla \cdot \mathbf{V}' = \tag{7}$$

$$\rho \frac{\partial \mathbf{V}'}{\partial \tau} = \mu \nabla^2 \mathbf{V}' - \nabla p' - \rho' g \hat{k} \tag{8}$$

$$\frac{\partial \phi'}{\partial \tau} - \frac{w'}{d} = \alpha \nabla^2 \phi' \tag{9}$$

The density equation to be used in this analysis was developed by Gebhart and Mollendoft [19] for both pure and saline water. The density variation is fitted in the temperature,

Nomenclature

a = disturbance wavenumber, $2\pi d/\lambda$
d = distance between horizontal surfaces
$\frac{D}{D\tau} \equiv \frac{\partial}{\partial \tau} + u\frac{\partial}{\partial x} + v\frac{\partial}{\partial y} + w\frac{\partial}{\partial z}$
$f = f(x,y)$ = disturbance amplitude function,
$F = F(z,R)$ = see equation (13d)
g = gravitational acceleration
Gr = Grashof number, see equation (19)
$\hat{i}, \hat{j}, \hat{k}$ = unit vectors in the x, y, z-directions, respectively
K = see equation (13c)
p = pressure
Pr = fluid Prandtl number
q = $q(s,p)$, see equation (10)
$R \equiv (t_m - t_2)/(t_1 - t_2)$
Ra = Rayleigh number, see equation (19)
s = salinity
t = temperature
$T \equiv t/t_m$
u,v,w = velocity components in x, y, z-directions
$\mathbf{V} \equiv u\hat{i} + v\hat{j} + w\hat{k}$
$W = W(z)$ = velocity distrubance amplitude function
x,y,z = Cartesian coordinates, where z is vertically upward
α = thermal diffusivity
$\alpha(s,p)$ = see equation (10)
β = volumetric coefficient of thermal expansion
γ = is given in equation (1)
γ_1, γ_2 = is given in equation (2)
$\theta = \theta(z)$ = temperature disturbance amplitude function
λ = disturbance wavelength
μ = fluid absolute viscosity
ν = fluid kinematic viscosity
ρ = fluid density
σ = temporal amplification factor
τ = time
$\phi \equiv (t - t_2)/(t_1 - t_2)$

Subscripts

c = critical or onset of motion
h = hydrostatic condition
m or max = maximum density condition
1 = pertains to lower boundary
2 = pertains to upper boundary

Superscripts

$-$ = base flow or undisturbed condition
$'$ = disturbance imposed upon baseflow

salinity, and pressure ranges to 20°C, 40°/oo and 1,000 bars absolute. The density relation is

$$\rho(t,s,p)=\rho_m(s,p)\{1-\alpha(s,p)\,|\,t-t_m(s,p)\,|^{q(s,p)}\} \tag{10}$$

where ρ_m and t_m are the density and temperature at the extremum at the existing pressure and salinity levels. Equation (10) is found to agree with the correlation of Kell [20] to about 2.00 ppm to 20°C, where $\rho_m = 99.972$ Kg m^{-3} at $t_m = 4.0293$°C, $\alpha = 9.297173 \times 10^{-6}$ and $q(0,1) = 1.894816$.

Next ρ is expanded in a Taylor series about $\bar{\rho} \equiv \rho_h(z)$, i.e., about $t(z)$ to obtain $\rho = \bar{\rho} + (t-\bar{t})\,\partial\rho/\partial t\,|_{t=\bar{t}}$ + higher order terms. From equation (10)

$$\frac{\partial\rho}{\partial t} = \pm\rho_m\alpha q\,|\,t-t_m\,|^{q-1} \tag{11}$$

where the plus sign is taken for $t < t_m$ and the minus sign for $t > t_m$. By introducing the disturbance quantities and linearizing in t', one finds

$$\rho' = \pm\rho_m\alpha q\,|\,\bar{t}-t_m\,|^{q-1}t' + \text{ higher order terms} \tag{12}$$

Neglecting higher-order terms and further substitution yields

$$\rho' = \pm\rho_m\alpha q(t_1-t_2)\,|\,t_1-t_2\,|^{q-1}\left|1-\frac{z}{d}-R\right|^{q-1}\phi' \tag{13a}$$

where

$$R=\frac{t_m-t_2}{t_1-t_2}. \tag{13b}$$

Letting

$$K=\alpha q(t_1-t_2)\,|\,t_1-t_2\,|^{q-1} \tag{13c}$$

and

$$F(z,R)=\pm\,|\,1-z/d-R\,|^{q-1} \tag{13d}$$

equation (13) becomes

$$\rho'/\rho_m = KF(z,R)\phi' \tag{14}$$

The reference density in (8) and (9) is taken as ρ_m. By eliminating u', v', and p' from equations (8) and (9) one obtains

$$\left(\frac{\partial}{\partial\tau}-\nu\nabla^2\right)\nabla^2 w' = gKF(z,R)\left(\frac{\partial^2\phi'}{\partial x^2}+\frac{\partial^2\phi'}{\partial y^2}\right) \tag{15}$$

$$\left(\frac{\partial}{\partial\tau}-\alpha\nabla^2\right)\phi' = \frac{w'}{d} \tag{16}$$

Generalizing, $x,y,z/d = x,y,z$; $\tau/d^2/\alpha = \tau$, and $w'/\alpha/d = w'$ allows equations (15) and (16) to be rewritten in nondimensional form as

$$\left(\frac{\partial}{\partial\tau}-\mathrm{Pr}\,\nabla^2\right)\nabla^2 w' = gK(d^3/\alpha^2)F(z,R)\left(\frac{\partial^2\phi'}{\partial x^2}+\frac{\partial^2\phi'}{\partial y^2}\right) \tag{17}$$

$$\left(\frac{\partial}{\partial\tau}-\nabla^2\right)\phi' = w' \tag{18}$$

Equation (17) can be rearranged in terms of the following Rayleigh number definition

$$R_a \equiv \left(\frac{g\alpha q(t_1-t_2)\,|\,t_1-t_2\,|^{q-1}d^3}{\nu^2}\right)\mathrm{Pr} \equiv \mathrm{Gr}\ \mathrm{Pr} \tag{19}$$

Following a similar approach as that presented by Chandrasekhar [21] one may postulate the form of disturbance quantities as $w' = f(x,y)\,W(z)\,e^{\sigma\tau}$ and $\phi' = f(x,y)\,\theta(z)\,e^{\sigma\tau}$, where σ being real corresponds to stationary forms of motion whose amplitude may change with time, depending upon its value.

For solid, impervious surfaces of infinite thermal capacity, the physical boundary conditions are ϕ', u', v', $w' = 0$ at $z = 0,d$. By separation of variables, from equations (17) and (18), it is found that

$$f_{xx}+f_{yy}+a^2 f=0 \tag{20}$$

and

$$(\sigma-D^2+a^2)\theta = W \tag{21}$$

where $D = \partial/\partial z$, and a^2 is the separation constant. With this result, equations (17) and (18) become

$$\left[\frac{\sigma}{\mathrm{Pr}}-(D^2-a^2)\right](D^2-a^2)W = a^2\mathrm{Ra}F\theta \tag{22}$$

$$(\sigma-D^2+a^2)\theta = W \tag{23}$$

The equations governing the marginal state of neutral stability are obtained for $\sigma = 0$, that is $(D^2-a^2)^2 W = -a^2\,\mathrm{Ra}\,F\,\theta$ and $(D^2-a^2)\theta = -W$ where $W(0) = W(1) = W'(0) = W'(1) = \theta(0) = \theta(1) = 0$ or finally

$$(D^2-a^2)^3\theta = -a^2\mathrm{Ra}\,F\ \theta \tag{24}$$

Chandrasekhar [21], for the classical Benard problem, reports

$$(D^2-a^2)^3\theta = -a^2\mathrm{Ra}\theta \tag{25}$$

The present formulation (24) differs from the classical Benard result (25) only in the definition of the Rayleigh number, Ra, and in the presence of $F(z,R)$ as defined in (13*d*).

Debler [11], Tien [12], and Veronis [13], with the introduction of a parabolic density relation, found that a term similar to the $F(z,R)$ described in this analysis modifies equation (25). In present notation their result is

$$F=(1-z-R) \tag{26}$$

Since a difference in the definition of the Rayleigh number does not effect stability, but only the interpretation of the physical conditions to which the results apply, Sun, Tien, and Yen [14] modified their Rayleigh number by multiplying it by $(1-R)$, and f was correspondingly dividing by $(1-R)$. The result is a redefined Rayleigh number and the following modified forcing function

$$F((1-z-R)/(1-R) \tag{27}$$

In this way, the physical interpretation of the critical Rayleigh number was retained so as to be identical to the classical Benard interpretation. That is, for large negative values of R, $F \simeq 1$, and the Oberbeck-Boussinesq results are recovered. Also, for $R \to 1$, $F \to \infty$, leading to unconditional stability.

Various stability regimes can be delineated in terms of R. When two new variables are defined such that $T_1 = t_1/t_m$ and $T_2 = t_2/t_m$, the definition of R becomes $R = (1-T_2)/(T_1-T_2)$. Figure 1 then shows the variation of R with T_1, and T_2 and presents a means of conveniently determining whether the density gradient in the fluid layer is negative (stable), locally positive (potentially unstable), or positive (potentially unstable) for boundary temperatures t_1 and t_2. These three regimes correspond to $-\infty \le R \le 0$, $0 < R < 1$ and $1 \le R \le \infty$, respectively.

The function, $F(z,R)$, in this work was also modified in a similar manner as was done by Sun, Tien, and Yen [14] to retain the ordinary Oberbeck-Boussinesq interpretation of Ra_c at large $R<0$

$$F(z,R)=\pm\left|\frac{1-z-R}{1-R}\right|^{q-1} \tag{28}$$

which is + when $t < t_m$ and − when $t > t_m$. Correspondingly, the Rayleigh number also was modified to absorb the term $|\,1-R\,|^{q-1}$, the inverse of the term modifying $F(z,R)$. It is interesting to note that equation (28) reduces exactly to equation (27) as used by Sun, Tien, and Yen [14], when $q=2$, and to the Boussinesq result, that is $F(z,R)=1$, when $q=1$.

The effect of pressure and salinity (neglecting saline diffusion) up to a maximum of 1,000 bars and 40°/oo may now easily be incorporated into the analysis simply by adjusting the value of q. Pure water at one atmosphere is represented by $q = 1.89816$. At 1,000 bars pressure and $s = 0$, $q = 1.58295$.

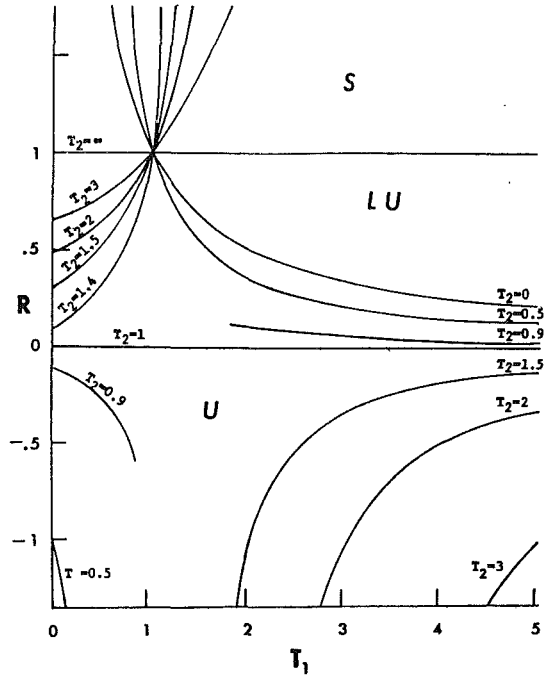

Fig. 1 The variation of R with $T_1 = t_1/t_m$ for the various values of $T_2 = t_2/t_m$ Note: S = density gradient negative (stable), LU = density gradient locally positive (potentially unstable), U = density gradient positive (potentially unstable).

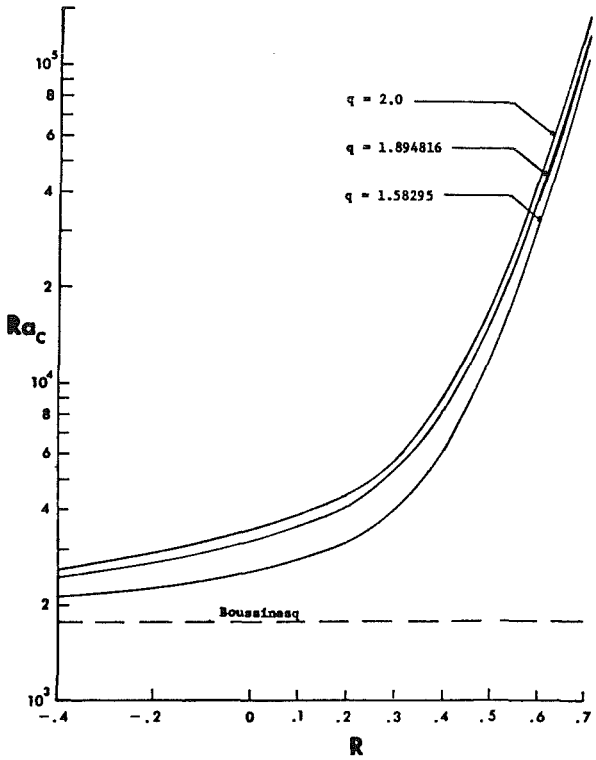

Fig. 2 The variation of Ra_c with R for various q(s,p)

Numerical Solution

The solution of equation (24) constitutes both an eigenvalue problem, as well as a two point boundary value problem. Expanding (24) yields

$$(D^2 - a^2)(D^2 - a^2)(D^2 - a^2)\theta = -a^2 \mathrm{Ra}\ F\ \theta \tag{29}$$

or

$$(D^2 - a^2)(D^2 - a^2)(\theta'' - a^2\theta) = -a^2 \mathrm{Ra}\ F\ \theta \tag{30}$$

or

$$\theta'''' - 3a^2\theta'' + 3a^2\theta'' - a^6\theta + a^2 \mathrm{Ra}\ F\theta = 0 \tag{31}$$

where primes indicate differentiation with respect to z/d.

The boundary conditions at 0 and 1 are

$$\begin{aligned} \theta &= 0 \\ \theta'' &= 0 \\ \theta''' &= a^2\theta' \end{aligned} \tag{32}$$

This expression can now be integrated and solved numerically, by specifying a, the nondimensional wave number, and guessing $\phi'(0)$, $\phi''''(0)$, and the critical Rayleigh number. Solutions satisfying the boundary conditions were found using a predictor-corrector method for numerical integration along with the "shooting method" and automatic interval subdivision.

Numerical Results

The critical Rayleigh number was computed for rigid-rigid boundary conditions for a range of R from -60 to 0.7. Sun, Tien, and Yen [14] obtained their results by the method developed by Chandrasekhar [20] and employed a series of successive approximations. A comparison between their results and those presented herein for $q = 2$ in Table 1 shows agreement to within 1 percent when R is less than 0.5, but an increasing overestimation of about 10 percent in both Ra_c and a as R approaches 0.7.

When $q = 1.894816$ the critical Rayleigh number, as obtained by Debler [11], Tien [12], Veronis [13], and Sun, Tein, and Yen [14] is modified downward by approximately 8.5 percent as R becomes greater than 0.1 (see Table 1). Since all solutions must eventually converge to the Oberbeck-Boussinesq limit, the difference becomes smaller as R becomes negative. It was also found that pressure and salinity level effect the onset of convection. Figure 2 illustrates the numerical results, which are given in Table 1. It shows that when $q(0,100) = 1.58295$, the critical Rayleigh number for a give R decreases by as much as 33 percent from Ra_c at one bar and $s = 0$, or $q(0,1) = 1.894816$.

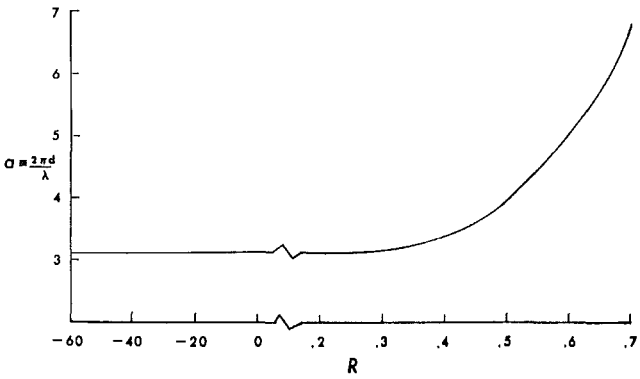

Fig. 3 The variation of a at Ra_c *with* R for $2.0 \le q(0,p) \le 1.58295$

Figure 3 shows the variation of the critical wave number, a_c, with respect to R. It is interesting to note that within the level of accuracy of the present analysis, no variation in a_c could be found at a given R, when q was changed over the range of from 2 to 1.58295 (see Table 1).

For the Oberbeck-Boussinesq case, that is $q = 1$, it was found that a minimum or critical Rayleigh number of $Ra_c = 1707.8$ occurred at $a = 3.117$. This is the same result as reported by Reid and Harris [10] to within the number of

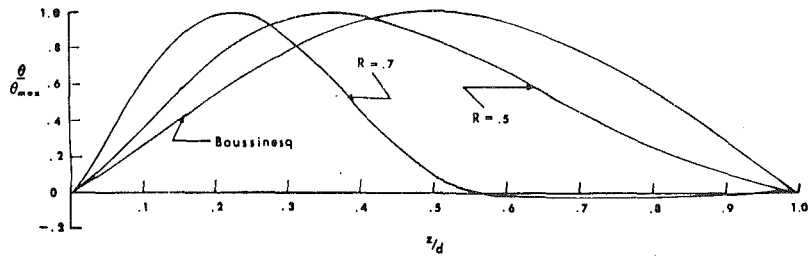

Fig. 4 The variation of the eigenfunction, θ, with R

Table 1 The variation of Ra_c *versus* R with q, where $q = 2$ corresponds to a parabolic form of the equation of state as presented by Debler [11], Tien [12] and Veronis [13]; $q = 1.894816$ to the equation of state as presented by Gebhart and Mollendorf [19] for pure water at 1 bar pressure; and $q = 1.58295$ represents pure water at 1000 bars pressure.

R	a $(2 \le q \le 1.58295)$	Ra_c $(q=2)$	Ra_c $(q=1.894816)$	Ra_c $(q=1.58295)$
−60.0	3.120	1,722	1,721	1,716
− 6.0	3.120	1,831	1,825	1,783
− 3.0	3.120	1,951	1,924	1,846
0.0	3.126	3,390	3,172	2,587
0.1	3.130	3,798	3,524	2,794
0.2	3.140	4,461	4,105	3,163
0.3	3.175	5,715	5,229	3,945
0.4	3.325	8,778	8,030	6,076
0.5	3.995	18,663	17,083	12,955
0.6	5.095	46,110	42,210	32,018
0.7	6.775	145,510	133,176	100,952

digits quoted. Furthermore, a plot of the eigenfunctions tabulated by Reid and Harris was found to coincide exactly with the eigenfunctions calculated here for $q = 1$ shown in Fig. 4.

Conclusions

The density relation used here offers some advantages over the various cubic, parabolic, and higher order relationships set forth by previous investigators when dealing with water in the vicinity of the density extremum. For example, it permits the calculation of pressure and salinity level effects in the absence of saline diffusion. It is also considerably simpler than, for example, a fifth-order polynomial. Accordingly, the present results agree well with those obtained by Merker, Wass, and Grigul [18] inasmuch as the calculated Ra_c are both about 10 percent below results obtained using a parabolic density relation. The calculated effect of increased salinity and pressure level is to destabilize, and all of the present results tend toward the Oberbeck-Boussinesq limit of 1708 for large negative R. The calculated critical wave number is found to increase with increasing R and to be essentially independent of the value of q, for the range of values considered here.

Acknowledgments

The authors gratefully acknowledge support for this research from the National Science Foundation (ENG 7727945).

References

1 Mallinson, G. D., "Natural Convection-State-of the Art," Structures and Materials Report 330, Department of Supply, *Australian Defence Scientific Service*, Aeronautical Research Laboratories, 1969.

2 Benard, H., "Les Tourbillons Cellulaires de une Nappe Liquide," *Revue generale des Sciences Pures et appliquees*, Vol. 11, 1900, pp. 1261-71 and 1309-23.

3 Schmidt, R. J., and Milverton, S. W., "On the Instability of a Fluid When Heated From Below," *Proc. Roy. Soc.*, Ser. A, Vol. 152, 1935, pp. 586-594.

4 Silverton, P. L., "Warmedurchgang, in Waagerechten Flussigkeits-schichten," pt. 1, *Forsch. Ing. Wes.* Vol. 24, 1958, pp. 29-32 and 59-69.

5 Leontiev, A. I., and Kirdyashkin, A. G., "Experimental Study of Flow Patterns and Temperature Fields in Horizontal Free Convection Liquid Layers," *International Journal of Heat and Mass Transfer*, Vol. 11, 1968, pp. 1461-66.

6 Malkus, W. V. R., "Discrete Transitions in Turbulent Convection," *Proc. Roy. Soc.*, Ser. A., Vol. 225, 1954, pp. 185-95.

7 Willis, G. E., and Deardoff, "Confirmation and Renumbering of the Discrete Heat Flux Transitions of Malkus," *Phys. Fluids*, Vol. 10, No. 9, 1967, pp. 1861-1866.

8 Rayleigh, Lord, "On Convection Currents in a Horizontal Layer of Fluid When the Higher Temperature is on the Under Side," *Phil. Mag.* Vol. 32, No. 192, 1916, pp. 529-546.

9 Low, M. A., "On the Criterion for Stability of a Layer of Viscous Fluid Heated From Below," *Proc. Roy. Soc.* Ser. A, Vol. 225, 1954, pp. 196-212.

10 Reid, W. H., and Harris, D. L., "Some Further Results on the Benard Problem," *Phys. Fluids*, Vol. 1, No. 2, 1958, pp. 102-110.

11 Debler, W. R., "On the Analogy Between Thermal and Rotational Hydrodynamic Stability," *Journal of Fluid Mech.*, Vol. 24, 1966, p. 165.

12 Tien, C., "Thermal Instability of a Horizontal Layer of Water Near 4°C," *AIChE Journal*, Vol. 14, No. 4, 1968, pp. 652-653.

13 Veronis, G., "Penetrative Convection," *Astrophysical Journal*, Vol. 137, 1963, pp. 641-663.

14 Sun, Z. S., Tien, C., and Yen, Y. C., "Thermal Instability of a Horizontal Layer of Liquid with Maximum Density," *AIChE Journal*, Vol. 15, No. 6, 1969, pp. 910-915.

15 Sun, Z. S., and Tien, C., "Free Convection Heat Transfer of a Layer of Liquid Heated from Below - The Effect of Maximum Density," *International Journal of Heat and Mass Transfer*, Vol. 13, 1970, pp. 505-509.

16 Nakagawa, Y., "Heat Transport by Convection," *Physics Fluids*, Vol. 3, 1960, pp. 82.

17 Yen, Y. C., "Effects of Density Inversion on Free Convective Heat Transfer in Porous Layer Heated from Below," *International Journal of Heat and Mass Transfer*, Vol. 17, 1974, pp. 1349-1356.

18 Merker, G. P., Wass, P., and Grigul, U., "Onset of Convection in a Horizontal Water Layer With Maximum Density Effect," *International Journal of Heat and Mass Transfer*, Vol. 22, 1979, pp. 505-515.

19 Gebhart, B., and Mollendorf, J. C., "A New Density Relation for Pure and Saline Water," *Deep-Sea Research*, Vol. 24, 1977, pp. 1-18.

20 Kell, G. S., "Thermodynamic and Transport Properties of Fluid Water," *Water: A Comprehensive Treatise*, edited by F. Franks, Plenum Press, New York, 1972.

21 Chandrasekhar, S., *Hydrodynamic and Hydromagnetic Stability*, Oxford at the Clarendon Press, 1961.

Natural Convection Along a Vertical Wavy Surface

L. S. Yao
Department of Mechanical and Aerospace Engineering,
Arizona State University,
Tempe, Ariz. 85287
Mem. ASME

A transformation method is applied to study the natural convection along irregular vertical surfaces. A sinusoidal surface is used as a specific example to demonstrate the advantages of the transformation method, and to elucidate the heat transfer mechanism near such surfaces. The numerical results show that the frequency of the local heat transfer rate is twice that of the wavy surface. The amplitude of the oscillating local Nusselt number gradually decreases downstream where the natural convection boundary layer grows thick.

1 Introduction

Since the work of Schmidt and Beckman [1], natural convection has been one of the most important research topics in heat transfer. A vast amount of literature is now available for different heating conditions, for various kinds of geometries, and for a variety of fluids. Comprehensive reviews can be found in [2, 3]. However, very few studies which illustrate the effects of complex geometries on natural convection have been reported. In general, it is not easy to study a heat transfer problem associated with a complex geometry, even with the help of modern computers.

In this paper, simple transformation is proposed to transform a complex geometry into a simple shape for which the equations of natural convection can be solved by methods previously developed. The transformation itself is rather simple, but it can handle very complex geometries. The equations in transformed space are more complicated than their original forms, but the effort required to solve the transformed equations numerically is about the same as that for the original equations, if one ignores the complication of arranging the computational grid to fit the complex geometry. Sometimes an analytical solution, which is unlikely to be discovered from the original set of equations, can be obtained from the transformed equations.

In the next section, the analysis is carried out for the natural convection along a vertical surface of arbitrary shape. Then a numerical solution is provided for a sinusoidal wavy surface in order to elucidate the effects of complex geometries on natural convection. The sinusoidal wavy surface can be viewed as an approximation to many practical geometries for which natural convective heat transfer is of interest. A familiar example is a cooling fin, often treated in elementary texts. Cooling fins have a larger heat transfer area than a flat surface; therefore, they are better heat transfer devices. Very few texts mention the geometric effects of fins on the heat transfer coefficient. Another example is a machined-roughed surface for heat transfer enhancement. Numerous data have been obtained which show the heat transfer coefficient is indeed larger due to the induced turbulent mixing. In this paper, we will show that an induced fluid motion normal to the surface can contribute to a heat transfer enhancement, even for the condition of laminar flow. Another example, only remotely related to the problem considered in this paper, is the interface between concurrent or countercurrent two-phase flow. Such an interface is always wavy and the momentum transfer across it is by no means similar to that across a smooth, flat surface, and neither is the heat transfer. Therefore, the wavy interface can have an important effect on the condensation process.

Contributed by the Heat Transfer Division for publication in the JOURNAL OF HEAT TRANSFER. Manuscript received by the Heat Transfer Division October 1, 1982.

2 Analysis

The physical model considered is a semi-infinite vertical wavy plate. The surfaces of the plate can be described by

$$\bar{y} = \bar{\sigma}(\bar{x}) \tag{1}$$

The characteristic length associated with the wavy surface is l. The temperature of the wavy surface is held at T_w, which is warmer than the ambient temperature T_∞. The mathematical formulation outlined below is for arbitrary $\bar{\sigma}$. Later a numerical solution is provided for a sinusoidal wavy surface to elucidate explicitly the geometric effect on natural convection.

The dimensional governing equations are the Navier-Stokes equations and the energy equation in two-dimensional Cartesian coordinates $(\bar{x}, \bar{y})$ (see Fig. 1). The dimensionless form of the equations, after ignoring terms of small orders in Gr, are

$$\frac{\partial \hat{u}}{\partial x} + \frac{\partial \bar{v}}{\partial r} = 0 \tag{2a}$$

$$\hat{u}\frac{\partial \hat{u}}{\partial x} + \hat{v}\frac{\partial \hat{u}}{\partial r} = -\frac{\partial P}{\partial x} + \mathrm{Gr}^{1/4} \cdot \sigma' \cdot \frac{\partial P}{\partial r}$$

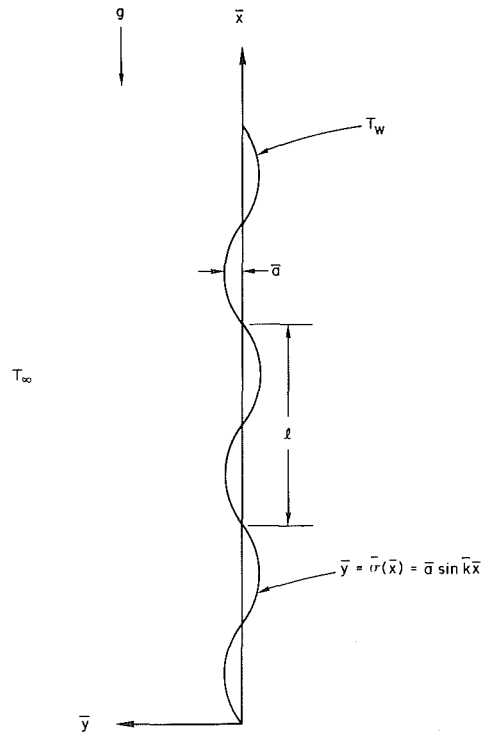

Fig. 1 Physical model and coordinates

$$+\Theta+(1+\sigma'^2)\frac{\partial^2\hat{u}}{\partial x^2} \tag{2b}$$

$$\sigma''\hat{u}^2+\sigma'\Theta=\sigma'\frac{\partial P}{\partial x}-\mathrm{Gr}^{1/4}\cdot(1+\sigma'^2)\cdot\frac{\partial P}{\partial r} \tag{2c}$$

$$\hat{u}\frac{\partial\Theta}{\partial x}+\hat{v}\frac{\partial\Theta}{\partial r}=\frac{1+\sigma'^2}{\mathrm{Pr}}\frac{\partial^2\Theta}{\partial r^2} \tag{2d}$$

where

$$x=\frac{\bar{x}}{l},\ r=\frac{\bar{v}-\bar{o}}{l}\cdot\mathrm{Gr}^{1/4} \tag{3a}$$

$$P=\frac{\bar{p}\cdot l^2}{\rho\nu^2\mathrm{Gr}} \tag{3b}$$

$$\hat{u}=\frac{\bar{u}l}{\nu\mathrm{Gr}^{1/2}},\ \hat{v}=\frac{(\bar{v}-\sigma'\bar{u})\cdot l}{\nu\mathrm{Gr}^{1/4}} \tag{3c}$$

$$\Theta=\frac{T-T_\infty}{T_w-T_\infty} \tag{3d}$$

$$\sigma'=\frac{d\bar{\sigma}}{d\bar{x}}=\frac{d\sigma}{dx} \tag{3e}$$

and

$$\mathrm{Gr}=\frac{\rho g l^3(T_w-T_\infty)}{\nu^2} \tag{3f}$$

The key step is to transform the irregular wavy surface into a flat surface by use of equation (3*a*). The transformed coordinates (x, r) are not orthogonal, but a regular rectangular computational grid can be easily fitted in the transformed coordinates. It is also worthwhile to point out that (u, v) are the velocity components parallel to ($\bar{x}$, $\bar{y}$) and are not parallel to nor perpendicular to the wavy surface. The convection induced by the wavy surface is explicitly described in equations (2). Equation (2*c*) indicates that the pressure gradient along the r-direction is $0(\mathrm{Gr}^{-1/4})$. This implies that the lowest-order pressure gradient along the x-direction can be determined from the inviscid-flow solution. For the current problem this pressure gradient is zero. Equation (2*c*) also shows that $\mathrm{Gr}^{1/4}\cdot\partial P/\partial r$ is 0(1) and is determined by the left-hand side of the equation. Elimination of $\partial P/\partial r$ between equations (2*b*) and (2*c*) results in three equations which can be solved for u, v, and Θ. These equation, in the parabolic coordinates (x, y) are

$$(4x)\frac{\partial u}{\partial x}+2u-y\frac{\partial u}{\partial y}+\frac{\partial v}{\partial y}=0, \tag{4a}$$

$$(4x)u\frac{\partial u}{\partial x}+(v-yu)\frac{\partial u}{\partial y}+\left(2+\frac{4x\sigma'\sigma'''}{1+\sigma'^2}\right)\cdot u^2=\frac{\Theta}{1+\sigma'^2}+(1+\sigma'^2)\frac{\partial^2 u}{\partial y^2} \tag{4b}$$

$$(4x)u\frac{\partial\Theta}{\partial x}+(v-yu)\frac{\partial\Theta}{\partial y}=\frac{1+\sigma'^2}{\mathrm{Pr}}\frac{\partial^2\Theta}{\partial y^2} \tag{4c}$$

where

$$x=\frac{\bar{x}}{l},\ y=\frac{r}{(4x)^{1/4}}=\frac{\bar{y}-\bar{o}}{\left(4\dfrac{\nu^2\bar{x}}{\beta g\Delta T}\right)^{1/4}},$$

$$u=\frac{\hat{u}}{(4x)^{1/2}}=\frac{\bar{u}}{(4\beta g\Delta T\bar{x})^{1/2}},\qquad v=(4x)^{1/4}\hat{v}=\frac{\bar{v}-\bar{o}'\bar{u}}{\left(\dfrac{\beta g\Delta T\nu^2}{4\bar{x}}\right)^{1/4}} \tag{5}$$

Equation (4*b*) is identical to the momentum equation along the wavy surface. For a slightly curved surface, say $\sigma\sim\mathrm{Gr}^{-1/4}$, the curvature effects become small and are negligible. The lowest-order equations are then reduced to those for a flat plate. For a wavy surface of finite amplitude, the curvature effects are important and cannot be ignored.

The associated boundary conditions are

(*i*) On the wavy surface ($y=0$):

$$\Theta=1 \quad \text{(constant temperature)} \tag{6a}$$

$$u=v=0 \tag{6b}$$

(*ii*) Matching with the quiescent free stream ($y\to\infty$):

$$\Theta\to 0 \quad \text{and} \quad u\to 0 \tag{6c}$$

It should be noted that condition (6*b*) is equivalent to the no-slip/no-penetrability condition on the solid wavy surface, since u and v are linearly independent.

A numerical solution of equations (4) by a finite-difference method is straightforward, since the computational grids can be fitted to the body shape in (x, y) coordinates. The central difference scheme is used for the diffusion terms, and the forward difference scheme is adopted for the convection terms. The singularity at $x=0$ has been removed by the scaling. Therefore, the computation can be started at $x=0$, and then marches downstream.

At every x-station, the computations are iterated until the difference of the results of two successive iterations becomes negligible, say 10^{-4}. After several tries, the y-grid size was fixed at 0.02, and the x-grid size at 0.025. By comparing the results for different grid size, the conclusion is reached that the accuracy of the numerical results is much better than 1 percent.

In the next section, numerical results are presented for $\sigma=\alpha\ \mathrm{Sin}\ 2\pi x$ to demonstrate the advantages of the transformation method, and to elucidate the geometric effects on the natural convection. For other shapes of the surface, a similar computation can be carried out by simply inputting the appropriate function for σ.

Nomenclature

a = amplitude of wave
g = gravitational acceleration
Gr = Grashof number, equation (3*f*)
l = wave length
Nu = Nusselt number
P = pressure
Pr = Prandt number = one
s = distance measured along the surface from the leading edge
T = temperature
u,v = velocity components
x,y = coordinates
ν = kinematic viscosity
α = dimensionless amplitude of wave = a/l
β = thermal expansion coefficient
σ = surface geometry function, Fig. 1

Superscripts

– = dimensional quantity
' = derivative with respect to x

Subscripts

w = surface
∞ = free stream

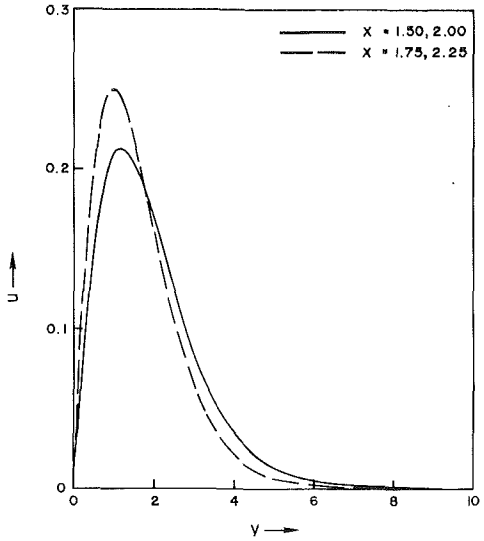

Fig. 2 Axial velocity profiles (α = 0.1)

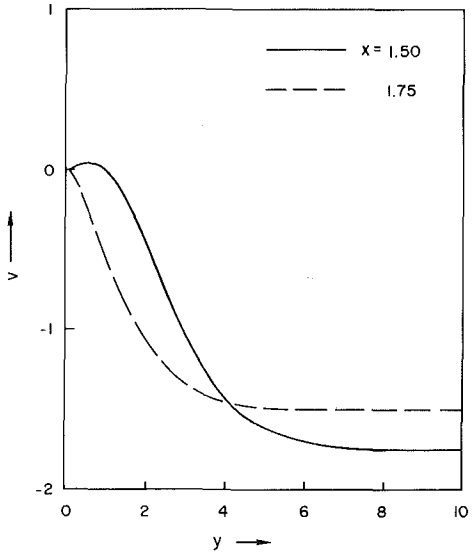

Fig. 3 Normal velocity profiles (α = 0.1)

3 Results and Discussion

The velocity component, u, is plotted for $\alpha = 0.1$ in Fig. 2. The nodes of the sinusoidal waves are at $x = 1.5$, and 2 while $x = 1.75$ is the trough, and $x = 2.25$ is the crest. The velocity profiles at the trough and the crest differ only slightly, and cannot be distinguished in Fig. 2. It is obvious that the boundary layer is thicker near the nodes than near the trough and the crest. It should be remembered that u is not the velocity component parallel to the wavy surface. Its magnitude alone cannot determine the local heat transfer rate.

The velocity component, v, is given in Fig. 3 for $x = 1.5$ and 1.75, respectively. The difference between the profiles at $x = 1.5$ (node) and $x = 2.0$ (node) is indistinguishable in the scale of Fig. 3; this is also true for the profiles at $x = 1.75$ (trough) and $x = 2.25$ (crest). It also should be noticed that v is not normal to the wavy surface, but is normal to the $\bar{x}$-axis. The significance of the distribution of v is that the magnitude of the local heat transfer rate is directly determined by the direction of the velocity component normal to the wavy surface, and v contains a major part of this normal velocity component. The local heat transfer rate is large when the normal velocity is approaching the surface; it is small when the convective stream moves away from the surface. The heat transfer mechanism along a wavy surface is different from that along a flat surface, and is modified by the fluid motion normal to the surface.

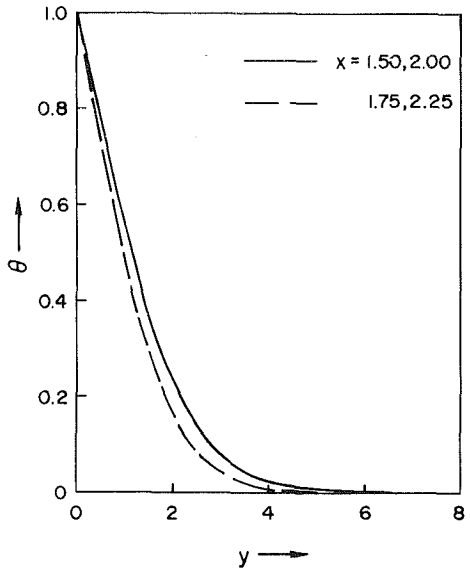

Fig. 4 Temperature distribution (α = 0.1)

The temperature distributions along the y-direction are given in Fig. 4. Since the y-direction is not normal to the wavy surface, the temperature gradient determined from Fig. 4 has to be corrected by the local curvature before the heat transfer rate can be calculated. The local Nusselt number, defined in terms of $T_w - T_\infty$, thermal conductivity, k, and the wave length, can be expressed as

$$\mathrm{Nu}(4x/\mathrm{Gr})^{1/4} = -(1+\sigma'^2)^{1/2}\,\frac{\partial\Theta}{\partial y}\;\Big|_{y=0} \tag{7}$$

Equation (7) is plotted in Fig. 5 for $\alpha = 0.1$ and α and $\alpha = 0.3$. Near the leading edge, the magnitude of the local heat transfer rate depends on the slope of the wavy surface, so it is mainly controlled by the stream motion induced by the buoyancy force parallel to the surface. Downstream the heat transfer rate varies according to the orientation of the surface. For the portion of the wavy surface parallel to the gravitational force, the velocity is larger and so is the heat transfer rate. The wavelength of the local heat transfer rate is half of that of the wavy surface. The peak of the heat transfer rate after one wavelength from the leading edge is shifted slightly upstream from the trough and the crest due to the convection effect. The magnitude of the variation of the heat transfer rate decreases downstream as expected, since the natural convection boundary layer grows thick. The wavy surface effect in a viscous layer is mainly due to the diffusion process. This effect becomes small when the amplitude of the wavy surface is completely covered in the boundary layer. For $\alpha = 0.1$, the curve actually approaches a constant which is slightly below the value, 0.5671, for the flat plate.

The total Nusselt number can be obtained by integrating equation (7). It is

$$\overline{\mathrm{Nu}}/\mathrm{Gr}^{1/4} = \frac{1}{s}\int_0^x \left[\frac{1+\sigma'^2}{(4x)^{1/4}}\cdot\frac{\partial\Theta}{\partial y}\right]_{y=0} dx \tag{8}$$

and

$$s = \int_0^x (1+\sigma'^2)^{1/2}\cdot dx \tag{9}$$

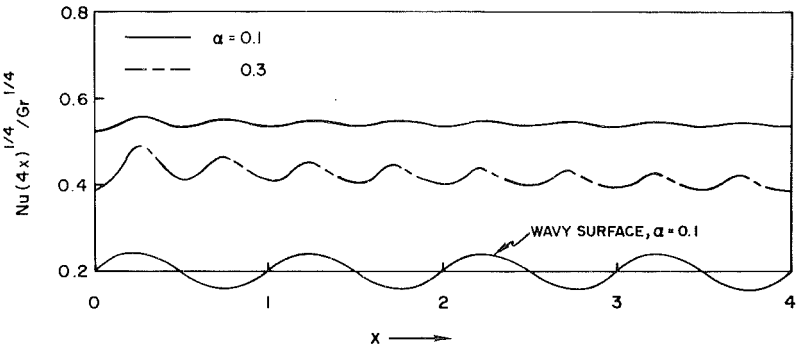

Fig. 5 Local heat transfer rate

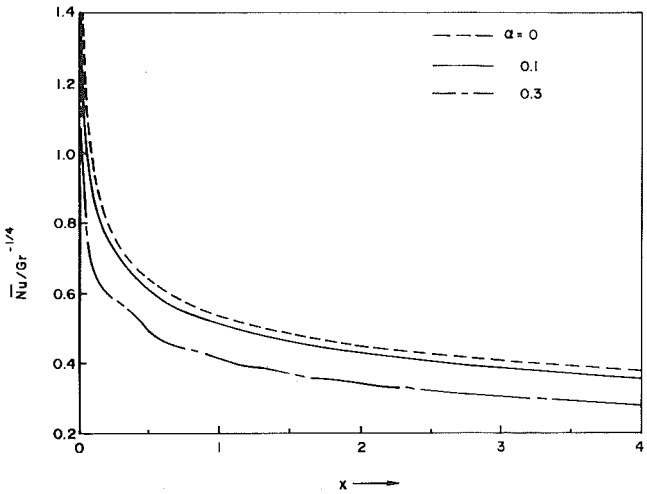

Fig. 6 Averaged heat transfer rate

Equation (8) is plotted in Fig. 6. The curve corresponding to $\alpha = 0$ is for a vertical flat plate. For $\alpha = 0.3$, the wavy variation of the total Nusselt number can be observed only near the leading edge, and gradually disappears downstream. The total Nusselt number for a sinusoidal wavy surface is constantly smaller than that of the corresponding flat plate. The total heat transfer rate for a wavy surface, considering a larger heat transfer area, is about the same as that of a flat plate.

References

1 Schmidt E., and Beckman, W., "Das Temperatur and Geschwindigkeitsfeld vor einer Warmeabgebenden senkrenchten Platte bei naturlicher Konvection," *Tech. Mech. u. Thermodynamic*, Bd. 1. No. 10, Oct. 1930, pp. 341–349.

2 Ostrach, S., "Laminar Flows With Body Forces," *Theory of Laminar Flows, High-Speed Aerodynamics and Jet Propulsion*, Vol. 4, edited by F. K. Moore, Princeton, 1964, pp. 28.

3 Gebhart, B., "External Natural Convection Flows," *Applied Mechanics Reviews*, Vol. 22, 1969, pp. 691.

Evaporation of Water From a Horizontal Surface by Natural Convection

E. M. Sparrow
Fellow ASME

G. K. Kratz

M. J. Schuerger

Department of Mechanical Engineering,
University of Minnesota,
Minneapolis, Minn. 55455

Experiments were performed to measure the mass transfer coefficients for natural convection evaporation from a horizontal water layer. Owing to the latent heat requirements of the evaporation process, the temperature of the water layer is depressed relative to the ambient temperature. This gives rise to a buoyancy which overpowers the oppositely directed buoyancy associated with the concentration gradient of the water vapor. The experiments encompassed two orders of magnitude in the Rayleigh number and, in addition, the effects of two geometrical parameters were investigated. One of these is the size of a horizontal annular frame which surrounds the water containment pan, while the other is the step caused by the difference between the water level and the height of the pan sidewall. Both the presence of the frame and of the step decrease the mass transfer coefficient. Narrow frames give rise to a sharp decrease, but further enlargements of frame size have little additional effect. The step-height effect was found to be independent of both the Rayleigh number and the frame size, enabling a universal correlation. Furthermore, for all of the investigated steps and frames, $Sh \sim Ra^{0.205}$.

Introduction

Despite the recent outpouring of research on natural convection [1], relatively few natural convection problems involving simultaneous heat and mass transfer have been investigated. There is a wide range of applications in which such simultaneous natural convection transfers occur, both in technological processes such as humidification and evaporative cooling and under quiescent conditions in the natural environment (e.g., calm-day evaporation from bodies of water). In this paper, fundamental experiments are described on natural convection evaporation from the surface of a horizontal water layer, a situation where vapor flows from the surface to the environment and heat flows in the opposite direction.

The problem to be studied here possesses certain special features because the surface-to-ambient temperature and concentration differences respectively tend to induce oppositely directed natural convection motions. In the present experiments, there were no heating elements situated within the water layer, so that the energy required to sustain the evaporation was drawn from the surroundings. Correspondingly, the equilibrium temperature of the water layer is lower than that of the ambient air. The depression of the surface temperature makes for a buoyancy-driven downflow from the ambient toward the surface. On the other hand, the relatively high concentration of water vapor near the surface makes for an upflow (since water vapor is less dense than air). For all conditions encountered during the present experiments, the density of the air-water vapor mixture adjacent to the water surface was greater than the ambient density, so that downflow prevailed.

The horizontal water layers investigated here were contained in circular pans. All told, five pans were employed to obtain a range of diameters which yielded a fiftyfold variation in the Rayleigh number, Ra, which was one of the three investigated parameters.

To physically motivate the other parameters, it is relevant to picture the pattern of fluid flow induced by the evaporating circular water layer. The aforementioned downflow from the ambient is caused to change direction by the blocking action of the water surface, and this sets up a radial outflow toward the outer perimeter of the water layer. Depending on the height to which the pan was originally filled and the duration of the evaporation period, the water level may be lower than the height of the sidewall of the containment pan. Under these conditions, the radially outflowing fluid which moves along the water surface encounters a steplike barrier as it approaches the perimeter of the layer. This step is a source of hydrodynamic resistance which can diminish the velocities and, thereby, decrease the rate of evaporation.

The effect of the step was systematically explored during the course of the experiments. A set of data runs was made in which, for each run, the pan was initially overfilled so that the average step height for the overall duration of the run was zero. Other sets of runs were carried out for selected initial fill levels and durations so as to obtain a range of step heights. On a dimensionless basis, the step height, Δ, was characterized by the ratio Δ/R, where R is the radius of the pan.

In certain of the envisioned applications, the containment pan may be built into a horizontal surface, with the plane of the surface being continuous with the open top of the pan. Accordingly, another investigated geometrical factor was the presence of a horizontal annular frame which surrounds the pan and is coplanar with the upper edge of the pan sidewall. Such a frame is an additional source of hydrodynamic resistance for the radially outflowing fluid and, thereby, may decrease the rate of evaporation. Five different frame sizes were investigated characterized by the ratio D_F/D, where D_F and D are, respectively, the diameters of the frame and the pan.

The experimental data yielded the dimensionless mass transfer coefficient (the Sherwood number) as a function of the three independent parameters, Ra, Δ/R, and D_F/D. In the presentation of results, the separate and combined effects of these parameters on the Sherwood number will be set forth and discussed.

From a survey of the literature, it appears that the only prior paper dealing with natural convection evaporation of water from a horizontal surface is that of Boelter, Gordon, and Griffin [2]. In those experiments, the water layer was heated, so that the temperature- and concentration-related buoyancies aided each other and created an upflow – in

Contributed by the Heat Transfer Division for publication in the JOURNAL OF HEAT TRANSFER. Manuscript received by the Heat Transfer Division July 30, 1982.

contrast to the downflow of the present operating conditions. Neither the effects of step nor frame were investigated. Aiding conditions also characterized the experiments of Wragg and Nasiruddin [3], who studied electrochemical mass transfer from a heated horizontal electrode. An analysis by Pera and Gebhart [4] dealt with simultaneous natural convection heat and mass transfer on a semi-infinite horizontal plate on which the flow direction was from the free edge toward the interior.

Experiments on simultaneous natural convection heat and mass transfer are reported in [5] and [6] for vertical surfaces and in [7] for spheres.

It is interesting to cite a subtle relationship between the present work and literature information for simultaneous forced convection heat and mass transfer, which is summarized in Table 9 of [8]. For all the laboratory-type experiments listed in the table (entries 1–4, 8, and 14), the mass transfer coefficient, K, was related to the forced convection velocity, U, via the relation, $K = C_1 + C_2 U$. The constant, C_1, which can be construed as a natural convection asymptote (i.e., $U = 0$), ranged from 0 to 31.4 (m/h). This large scatter indicates that accurate natural convection results are not likely to be obtained as a limiting case of forced convection correlations.

It is also relevant to take note of prior work on the effects of edge-adjacent framing of horizontal surfaces for either pure natural convection heat transfer [9, 10] or mass transfer [11]. Without exception, it was found that framing decreases the heat or mass transfer coefficients. In [11], the effect of a vertical step situated at the edges of a horizontal plate was also explored, and a reduction in the transfer coefficients was encountered.

For simultaneous natural convection heat and mass transfer, the transfer coefficients are not related to those for either pure heat transfer or pure mass transfer by the oft-used heat/mass transfer analogy. Therefore, the extensive natural convection literature for pure heat transfer and pure mass transfer on horizontal surfaces is not directly relevant here.

Experimental Apparatus and Procedure

A particularly noteworthy feature of the experiments was the laboratory room in which they were performed. The walls, ceiling, and floor of the room are insulated with 46 cm of cork, and there is no ductwork or vents. It is situated in a basement, is windowless, and is away from external walls (i.e., a room within a room). The total volume of the room is 70 m^3, and it contains various objects having a large aggregate heat capacity. The combination of the thermal isolation and large heat capacity makes for unusual thermal stability, and the moisture absorbing capability of the cork walls stabilizes the humidity.

Lighting was never turned on either during or several hours prior to a data run, and any in-room measurements (i.e., humidity and mass) were made by flashlight. Thermal stratification, as detected by a vertical array of thermocouples, was negligible. When possible, instrumentation was located in a service area outside the laboratory, and it was never entered during a data run.

The intrinsic characteristics of the laboratory and the aforementioned precautions made it an optimal site for natural convection evaporation experiments.

Apparatus. As was already noted, five pans of circular planform were employed during the course of the experiments, with respective diameters, $D = 8.89$, 12.82, 16.32, 22.18, and 30.68 cm, and a cylindrical side wall that was 2.54 cm in height for all cases. The pans were fabricated from 0.0635-cm thick galvanized steel.

Each pan was equipped with three thermocouples whose junctions were positioned approximately midway between the bottom of the pan and the surface of the water. One of the junctions was situated at the center of the circular planform, while the other two were halfway between the center and the outer perimeter – about 180 deg apart. The thermocouples were led into the pan through a small aperture at the intersection of the bottom and side walls, with copper oxide cement used as a sealant. Chromel-constantan wire was used for the thermocouples because it has the highest sensitivity ($\sim 60 \mu V/°C$) among all common thermocouple wire and because it is inert to water. Similarly, Teflon was chosen for the wire insulating material because of its inertness to water. The thermocouples had been calibrated prior to their installation.

The use of three thermocouples had been shown to be adequate for the determination of the temperature in the water layer by means of preliminary experiments in which one of the larger pans was equipped with ten thermocouples. Among the three thermocouples, the overall variation in emf during any reading sequence was $4\mu V$ or less ($\sim 0.07°C$).

The research program included both data runs with unframed pans and data runs in which the pans were surrrounded by a horizontal annular frame whose upper face

Nomenclature

A_s = area of evaporating surface
C = coefficient in equation (23)
$c_{p,a}$ = specific heat of air
D = diameter of containment pan
D_F = outer diameter of annular frame
$\mathfrak{D}$ = mass diffusion coefficient
g = acceleration of gravity
H_1 = water depth at start of run
H_2 = water depth at end of run
$\bar{H}$ = mean water depth, $\frac{1}{2}(H_1 + H_2)$
H^* = depth at no-step condition
h = enthalpy per unit mass
K = mass transfer coefficient, equation (11)
M_1 = mass at start of run
M_2 = mass at end of run
ΔM = evaporated mass
M^* = mass at no-step condition
p = pressure
p_{sat} = saturation pressure
p_{tot} = total pressure
R = radius of containment pan
Ra = Rayleigh number, equation (14)
Sc = Schmidt number
Sh = Sherwood number, $KR/\mathfrak{D}$
Sh_0 = Sherwood number for no-step case
T = temperature
W = specific humidity
Δ = mean step height, $(H^* - \bar{H})$
μ = viscosity
ν = kinematic viscosity, $\mu/\tilde{\rho}$
ρ = density
ρ_a = partial density of air
ρ_{liq} = density of liquid water
ρ_s = mixture density at water surface
ρ_{sat} = saturation density
$\rho_{wv,s}$ = partial density of water vapor at water surface
$\rho_{wv,\infty}$ = partial density of water vapor in ambient
ρ_∞ = mixture density in ambient
$\tilde{\rho}$ = mean mixture density, $\frac{1}{2}(\rho_s + \rho_\infty)$
$\Delta\tau$ = duration of run
ϕ_∞ = relative humidity in ambient

Subscripts

a = air
db = dry-bulb state
f = saturated liquid
fg = change due to vaporization
g = saturated vapor
s = at the water surface
wb = wet-bulb state
wtr = temperature of liquid water
wv = water vapor
∞ = in the ambient

is coplanar with the upper edge of the pan sidewall. The frames were fabricated from a 0.635-cm-thick rigid composite consisting of a styrofoam core sandwiched between stiff, smooth-surfaced cardboard. If D_F denotes the outer diameter of the annulus and D is the inner diameter (i.e., equal to the pan diameter), then the investigated frames may be characterized by $D_F/D = 1$ (no frame), 1.25, 1.5, 3, and 5.

The two smaller frames ($D_F/D = 1.25$ and 1.5) did not require external support to keep them in place, tightness of the fit at the pan-frame interface being sufficient. For the two larger frames, support was provided by styrofoam pillars which were part of a boxlike structure on which the pan itself was positioned.

During the entire duration of a data run and during a preparatory period preceding the run, the pan rested on the platform of a balance which was used to read the changes of mass. The balance was an Ohaus triple-beam type, with a smallest scale division of 0.1 g and a capacity of 2835 g. For the unframed case and for the two smaller frames, the pan rested on a 2.54-cm-thick styrofoam pad which, in turn, rested on the balance platform. Care was taken that neither the pad nor the platform inadvertently functioned as de facto frames. For the two larger frames, the aforementioned boxlike support structure rested on the platform.

Various items of instrumentation have already been mentioned, and the other measurement tools used in the experiments will now be described. The ambient temperature was measured by a vertical array of three shielded thermocouples situated to the side of the pan, about 60 cm from its center. The lowermost thermocouple was positioned at the same height as the pan surface, while the middle and upper thermocouples were displaced above it by 45 and 90 cm, respectively. Typical overall variations among the three ambient thermocouples were 2–3 μV (0.03–0.05°C). A 1-μV digital voltmeter was employed to read the emf's of both the water-layer and ambient-air thermocouples. The voltmeter was situated in the service area adjacent to the laboratory, as was the barometer used for measuring the ambient pressure.

Owing to the critical nature of the humidity measurement, a special psychrometric unit was designed and fabricated. It consisted of a 76-cm length of 7.6-cm dia plexiglass tube fitted at its downstream end with a fan which operates in the suction mode. The fan and the tube cross-sectional area were chosen to yield an airflow velocity which provides near equality of the psychrometric wet-bulb temperature and the thermodynamic wet-bulb temperature ([12], Fig. 10.6). Wet- and dry-bulb thermometers, which could be read to 0.1°F or better, were inserted radially into the tube through corked apertures in the cylindrical wall. The thermometer bulbs were positioned at the tube centerline, with the dry-bulb thermometer upstream of the wet-bulb thermometer (the separation distance was thirty thermometer diameters).

For the humidity measurement, the psychrometric unit was positioned about half a meter to the side of the pan and about 20 cm below the level of the pan surface.

Experimental Procedure. As was noted in the Introduction, the equilibrium temperature of the evaporating water layer is below the ambient air temperature. If the pan were to be filled with water at a temperature that is different from the equilibrium value, a waiting period must be allowed. During this period, evaporation and heat transfer will occur in the transient mode until the equilibrium temperature is reached. At that point, all processes become steady (provided, of course, that the ambient temperature and water vapor concentration are constant). In view of the foregoing, each data run consisted of two parts – an equilibration period and the data run proper.

Each data run began with the placement of a clean empty pan on the platform of the balance. The pan was then carefully leveled with respect to the horizontal. Next, water at a temperature equal to the expected equilibrium value was poured into the pan and, when the pan was approximately half full, the horizontal leveling was checked and, if necessary, readjusted (a rare event). The filling was then continued and, when the pan was almost full, any irregularities in the meniscus were broken up with the aid of a toothpick. Water was then added very carefully until the meniscus just disappeared. The detection of the moment of disappearance was greatly aided by viewing the reflection of one of the overhead lights of the room in the meniscus.

The disappearance of the meniscus corresponds to the situation in which the surface of the water is perfectly flat and is coplanar with the upper edges of the cylindrical sidewall of the pan. Since there is no step between the water level and the side wall, this situation will be referred to as the no-step condition. The reading of the balance corresponding to the no-step condition is recorded and serves as a reference mass.

The pan is then overfilled with water to accommodate the expected evaporation during the equilibration period. In particular, the extent of the overfilling was governed by the desired initial condition for the data run proper. One of these is that the pan be in an overfilled state at the start of the run so that the average step height (i.e., the average of the beginning and ending step heights) for the run be zero. The other initial state for the data run is the zero-step condition. The amount of overfilling needed to attain either of these conditions was based on evaporation rates determined in prior experiments.

The equilibration period ranged from 3 to 6 hrs. At the end of the period, various measurements were made to initiate the data run proper. The mass indicated by the balance was recorded, and the wet- and dry-bulb temperatures were measured. Then, the laboratory was sealed and, after a brief waiting period, the temperatures of the water layer and the ambient air were recorded, as was the barometric pressure.

The duration of the data run was governed by various considerations. For the smaller pans, the run had to be long enough so that the change in mass due to evaporation was sufficiently large to be measured accurately. Also, for these same pans, overly lengthy runs were avoided to limit the extent of the variation of the step height during the run. For the larger pans, run times were more freely selected, with the one proviso that possible initial transients be of short duration compared with the run time. Such transients might have been induced when the laboratory was entered at the start of the run to measure the mass and wet/dry-bulb temperatures.

In general, the range of the run times extended from 10 to 24 hrs. At the end of the run, all of the measurements made at the beginning of the run were repeated. In some runs, periodic measurements were made of the temperatures in the water layer and in the ambient air and of the barometric pressure – all with meters situated outside the laboratory.

The range of relative humidities encountered during the experiments was 16–40 percent, while the ambient air temperature ranged from 23–26.5°C. The depression of the water temperature below the ambient temperature was from 3–6°C.

Data Reduction

The objective of the data reduction procedure was to evaluate the mass transfer coefficient, the Sherwood number, the Rayleigh number, and the mean step height. The other parameter of the experiments, the frame ratio, D_F/D, was available from direct measurement. It is relevant to note that the density difference which appears in the Rayleigh number will be evaluated including both the effects of temperature and of the composition of the air—water vapor mixture. Therefore, no additional temperature or humidity parameters are needed to characterize the results.

Two of the key quantities in the data reduction are the partial density of the water vapor and the density of the air-water vapor mixture. Numerical values of these quantities are needed both at the water surface and in the ambient. Their determination involves the use of a number of standard thermodynamic relationships.

In this connection, W_{wb} and W_{db} denote the specific humidities corresponding to the wet-bulb and dry-bulb states. Furthermore, in accordance with standard notation, h_f and h_g represent the enthalpies of saturated liquid water and of saturated water vapor, while h_{fg} is the latent heat of evaporation. Also p_{sat} and p_{tot} are, respectively, the saturation pressure of water vapor and the system total pressure.

Then, from any standard thermodynamics text (e.g., [13], pp. 396–397),

$$W_{wb} = 0.622\{p_{\text{sat}}(T_{wb})\}/\{p_{\text{tot}} - p_{\text{sat}}(T_{wb})\} \tag{1}$$

$$W_{db} = \{W_{wb}h_{fg}(T_{wb}) + c_{p,a}(T_{wb} - T_{db})\} / \{h_g(T_{db}) - h_f(T_{wb})\} \tag{2}$$

where the temperatures at which the various h's are evaluated are indicated in the parentheses.

With the measured values of wet-bulb temperature and total pressure and with a table look-up for p_{sat} at T_{wb}, equation (1) yields W_{wb}. Then, using W_{wb} and with all other quantities on the right-hand side of equation (2) known from direct measurement or table look-ups, W_{db} is determined. Furthermore, if $p_{wv,\infty}$ denotes the actual partial pressure of water vapor in the ambient

$$W_{db} = 0.622p_{wv,\infty}/(p_{\text{tot}} - p_{wv,\infty}) \tag{3}$$

which enables $p_{wv,\infty}$ to be found. Then, the relative humidity, ϕ_∞, in the ambient follows as

$$\phi_\infty = p_{wv,\infty}/\{p_{\text{sat}}(T_{db})\} \tag{4}$$

Next, the partial density of water vapor in the ambient is obtained from

$$\rho_{wv,\infty} = \phi_\infty \rho_{\text{sat}}(T_{db}) \tag{5}$$

To find the partial density of air (subscript a) in the ambient, the partial pressure $p_{a,\infty}$ is first calculated from

$$p_{a,\infty} = p_{\text{tot}} - p_{wv,\infty} \tag{6}$$

Then, with $p_{a,\infty}$ and T_∞ ($\simeq T_{db}$), $\rho_{a,\infty}$ is evaluated from the perfect gas law. With both $\rho_{wv,\infty}$ and $\rho_{a,\infty}$ known, the ambient mixture density ρ_∞ follows as

$$\rho_\infty = \rho_{wv,\infty} + \rho_{a,\infty} \tag{7}$$

It may be noted that in all steps subsequent to equation (4) the measured values of T_{db} (psychrometric unit) and T_∞ (ambient air thermocouples) could have been used interchangeably. The differences between T_{db} and T_∞ were typically about 0.05°C, with a consequent uncertainty in the Sherwood number of 0.1 percent or less.

Next, let the subscript, s, denote the surface of the evaporating water layer, with T_{wtr} representing the measured water temperature. Then

$$\rho_{wv,s} = \rho_{\text{sat}}(T_{wtr}), \quad p_{wv,s} = p_{\text{sat}}(T_{wtr}) \tag{8}$$

$$p_{a,s} = p_{\text{tot}} - p_{wv,s} \tag{9}$$

The perfect gas law is then employed to find $\rho_{a,s}$ using $p_{a,s}$ and T_{wtr} as input. Then, for the mixture density

$$\rho_s = \rho_{wv,s} + \rho_{a,s} \tag{10}$$

The mass transfer coefficient, K, and the Sherwood number will now be considered. In this regard, let ΔM represent the mass of water evaporated from the surface area, A_s, during a data run of duration, $\Delta\tau$. With these, the mass transfer coefficient is defined as

$$K = (\Delta M/A_s\Delta\tau)/(\rho_{wv,s} - \rho_{wv,\infty}) \tag{11}$$

and its dimensionless counterpart, the Sherwood number, is

$$\text{Sh} = KR/\mathfrak{D} \tag{12}$$

in which $\mathfrak{D}$ is the binary diffusion coefficient. If note is taken of the Schmidt number $\text{Sc} = \nu/\mathfrak{D}$, then equation (12) becomes

$$\text{Sh} = (KR/\nu)\text{Sc} \tag{13}$$

For the air-water vapor mixture, Sc = 0.6 (Table 10.1 of [12] and Table 7 of [14]).

Attention will now be focused on the Rayleigh number. Since the natural convection is driven by the density difference $(\rho_s - \rho_\infty)$, it is appropriate that this quantity appears in the Rayleigh number. Thus

$$\text{Ra} = \{g\bar{\rho}(\rho_s - \rho_\infty)R^3/\mu^2\}\text{Sc} \tag{14}$$

where

$$\bar{\rho} = \tfrac{1}{2}(\rho_s + \rho_\infty) \tag{15}$$

The mixture viscosity, μ, that appears in the Rayleigh and Sherwood numbers ($\nu = \mu/\bar{\rho}$) is not known to high accuracy [14], but it was estimated to depart by less than 0.3 percent from that for pure air for the conditions of the experiments. In view of this, μ was evaluated as that for pure air, as the average of the values in the ambient and at the water surface.

The final quantity to be evaluated is the average step height Δ. In this regard, let M^* denote the mass measured for the no-step condition, while M_1 and M_2 respectively correspond to the masses measured at the beginning and end of the data run. The corresponding depths of water are

$$H^* = M^*/\tfrac{1}{4}\pi D^2\rho_{\text{liq}}, H_1 = M_1/\tfrac{1}{4}\pi D^2\rho_{\text{liq}}, H_2 = M_2/\tfrac{1}{4}\pi D^2\rho_{\text{liq}} \tag{16}$$

The mean water depth for the data run was then determined from

$$\bar{H} = \tfrac{1}{2}(H_1 + H_2) \tag{17}$$

and, with this, the mean step height is

$$\Delta = H^* - \bar{H} \tag{18}$$

Results and Discussion

As was noted in the Introduction, the response of the Sherwood number to three parameters – Ra, D_F/D, and Δ/R – was investigated. The approach employed to identify the separate effects of these parameters will now be discussed. For a given frame size characterized by D_F/D, two sets of experiments were performed. In one set, the mean step height was zero, while in the other set, various nonzero step heights were investigated. In both sets, the Rayleigh number was varied systematically by making use of the different pan diameters described earlier. Such two-set experiments were carried out for three of the investigated five D_F/D values – $D_F/D = 1$, 1.5, and 3. The correlation of the step-height effect obtained from these data was found to be independent of both D_F/D and Ra. Therefore, only one set of experiments was performed for each of the other two frames, $D_F/D = 1.25$ and 5.

Figure 1 has been prepared to illustrate the results obtained from the two sets of experiments carried out for a given D_F/D. The figure pertains specifically to $D_F/D = 1$ (no frame), but it is very similar to the corresponding graphs for $D_F/D = 1.5$ and 3. In the figure, the Sherwood number is plotted as a function of the Rayleigh number, with the circle and square data symbols representing the zero and nonzero step conditions, respectively. The five distinct clusters of data correspond to the five pan diameters. For the nonzero step case, the range of Δ/R for each data cluster is indicated.

As expected, the Sherwood number increases regularly with

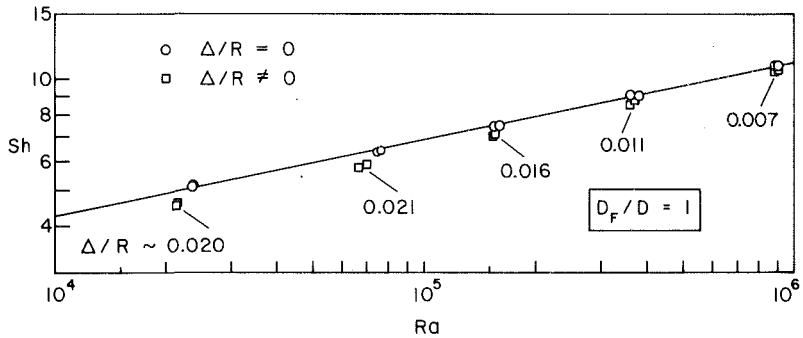

Fig. 1 Sherwood number results for the zero and nonzero step conditions, $D_F/D = 1$ (no frame)

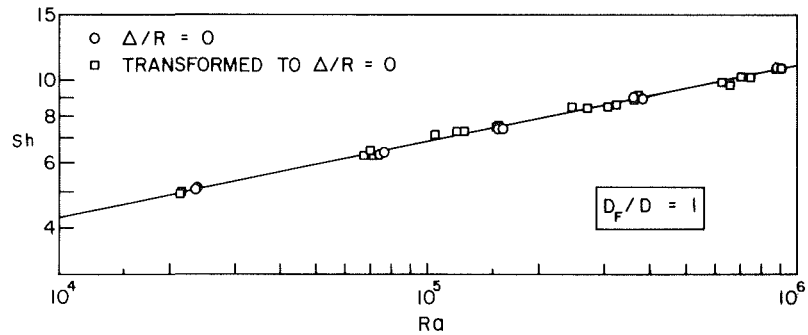

Fig. 2 Demonstration of the validity of the step-effect correlation, $D_F/D = 1$

the Rayleigh number. For the no-step case, a power-law representation $\mathrm{Sh} = C\mathrm{Ra}^n$ has been fit to the data by means of least squares (the constants C and n will be presented later). The straight line shown in the figure depicts the least-squares fit, and it is seen to be an excellent representation of the no-step data. The plotted data for the nonzero step case depend both on Ra and Δ/R (it being a practical impossibility to set a common Δ/R value) and, therefore, a representation of the form $\mathrm{Sh} = C\mathrm{Ra}^n$ is inappropriate

It is of particular importance to note that the presence of a step decreases the Sherwood number relative to that for no step. Furthermore, the larger the step, the greater the reduction of the Sherwood number.

The procedure used to quantify the effect of the step will now be described. Consider any one of the data points for $\Delta/R \neq 0$. For the Rayleigh number for that point, the Sherwood number for the *no-step case* was calculated from the aforementioned least-squares fit. If Sh is now used to denote the Sherwood number for arbitrary Δ/R and Sh_0 corresponds to $\Delta/R = 0$, then the step-effect ratio

$$(\mathrm{Sh}_0 - \mathrm{Sh})/Sh_0 \tag{19}$$

was evaluated at the point in question. Next, by this same procedure, the step-effect ratio was calculated for each of the $\Delta/R \neq 0$ points in Fig. 1. The ratio was then evaluated for each of the $\Delta/R \neq 0$ data points for the $D_F/D = 1.5$ and 3 frame configurations. All told, 45 values of the ratio were determined.

Then, these 45 points were plotted in a graph of $(\mathrm{Sh}_0 - \mathrm{Sh})/\mathrm{Sh}_0$ versus Δ/R, where Δ/R ranged between 0 and 0.072. Careful examination of the points showed that they were randomly distributed with respect to both Ra and D_F/D, but that they could be well correlated by the representation

$$(\mathrm{Sh}_0 - \mathrm{Sh})/\mathrm{Sh}_0 = 3.84(\Delta/R) \tag{20}$$

where 3.84 is an adjusted constant (i.e., the only adjusted constant) determined via least squares.

Equation (20) may be employed to illustrate the magnitude of the step effect. For example, if $\Delta/R = 0.01$, there is a 4 percent reduction in the Sherwood number, while if $\Delta/R = 0.05$, the reduction is 19 percent – which is not insignificant.

Attention is now turned to illustrating the degree of excellence of the global correlation (20). To this end, (20) is rearranged in the form

$$\mathrm{Sh}_0 = \mathrm{Sh}/(1 - 3.84(\Delta/R)) \tag{21}$$

This equation is, in effect, a means of transforming a Sherwood number, Sh, corresponding to step height, Δ/R, to a no-step Sherwood number, Sh_0. Equation (21) has been employed in preparing Fig. 2, which is the counterpart of Fig. 1 ($D_F/D = 1$), and Figs. 3 and 4, which pertain, respectively, to $D_F/D = 1.5$ and 3.

In Fig. 2, the circle data points and the least-squares straight line are the very same as those of Fig. 1. The square data points correspond to those of Fig. 1 for $\Delta/R \neq 0$ but have been transformed to $\Delta/R = 0$ by equation (21). There are additional square data points in Fig. 2, over and beyond those of Fig. 1, which were obtained in supplementary runs. These data, originally for $\Delta/R \neq 0$, have also been transformed to $\Delta/R = 0$ with the aid of equation (21).

Inspection of Fig. 2 shows that the transformed data points are in excellent agreement with the actual $\Delta/R = 0$ data (circle symbols). Indeed, the transformed data appear to be as well represented by the least-squares line as are the original $\Delta/R = 0$ data on which the line was based. This finding lends strong support to the validity of equations (21) and (20).

Further affirmations of these equations are provided by Figs. 3 and 4. In Fig. 3, which pertains to the $D_F/D = 1.5$ frame configuration, the $\Delta/R = 0$ data and the least-squares line which fits them are shown. The square points are $\Delta/R \neq 0$ data that have been transformed to $\Delta/R = 0$ by equation (21). Once again, the transformed data are very well represented by the least-squares line for the actual $\Delta/R = 0$ data.

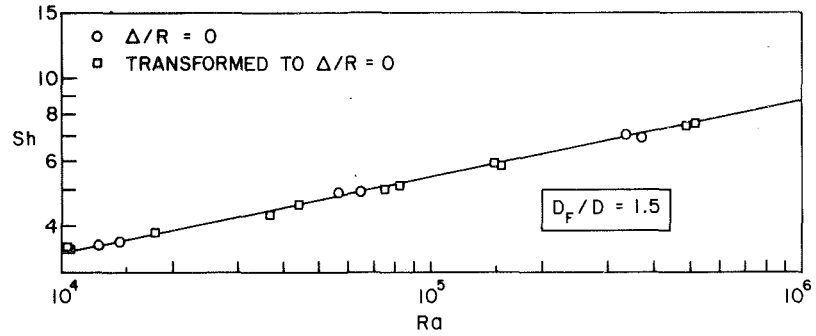

Fig. 3 Demonstration of the validity of the step-effect correlation, $D_F/D = 1.5$

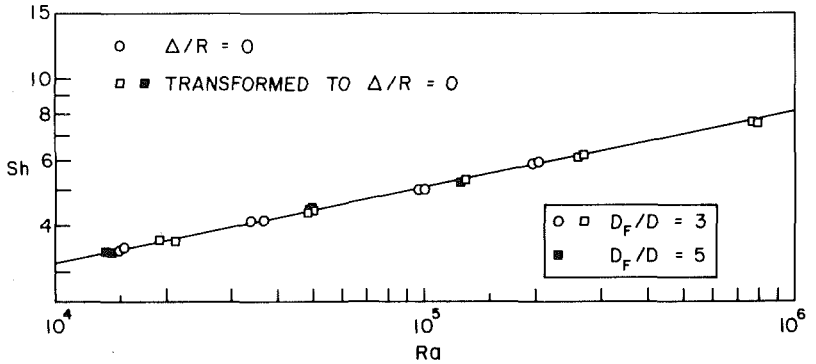

Fig. 4 Demonstration of the validity of the step-effect correlation, $D_F/D = 3$

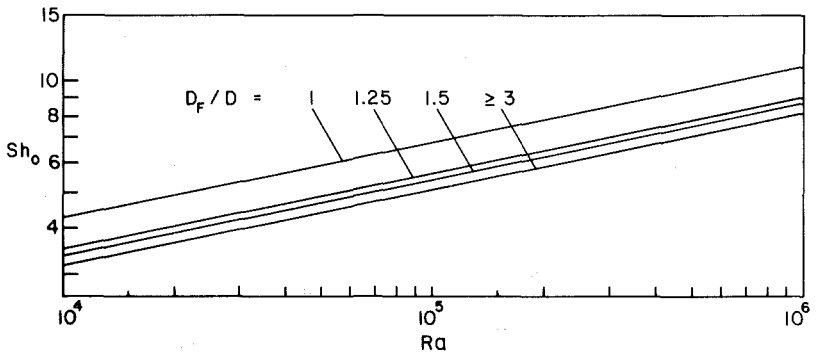

Fig. 5 Sherwood numbers for the no-step condition for the no-frame and framed configurations

A similar story is told in Fig. 4 by the circle and square data symbols for $D_F/D=3$ and by the least-squares line. Another interesting feature of Fig. 4 is the data for the $D_F/D=5$ frame configuration. As seen in the figure, these data are coincident with those for $D_F/D=3$. The coincidence of the data for $D_F/D=3$ and 5 not only occurs subsequent to transformation, as seen in Fig. 4, but also was observed in the original $\Delta/R\neq 0$ data (the Δ/R values were virtually identical for the contiguous $D_F/D=3$ and $D_F/D=5$ data). Thus, there appears to be no further effect of the frame beyond $D_F/D=3$.

In view of the foregoing, the step height effect is very well correlated by equation (20) for the step heights Δ/R encountered here (i.e., between zero and 0.072), independent of the Rayleigh number and the frame size ratio D_F/D. For what follows, it is convenient to write equation (20) as

$$\mathrm{Sh} = (1 - 3.84(\Delta/R))\mathrm{Sh}_0 \tag{22}$$

The dependence of the no-step Sherwood number, Sh_0, on the Rayleigh number and D_F/D will now be correlated. Once this has been accomplished, the procedure for finding Sh for given values of Δ/R, D_F/D, and Ra is first to determine Sh_0 corresponding to the given D_F/D and Ra, and then to calculate Sh from equation (22).

With regard to the Rayleigh number dependence of Sh_0, it may be noted that the exponents n of the power law $\mathrm{Sh} = C\mathrm{Ra}^n$ fitted to the $\Delta/R=0$ data were found to be 0.206, 0.202, and 0.206, respectively, for $D_F/D=1$, 1.5, and 3. In addition, the n value for the $D_F/D=1.25$ data, transformed to $\Delta/R=0$, was 0.207. Furthermore, the transformed data for $D_F/D=5$ coincided with those for $D_F/D=3$ and, therefore, share the same n value. The near coincidence of these n values is worthy of note and suggests that a common exponent, $n=0.205$, be used for all cases. Indeed, the lines plotted in Figs. 1–4 correspond to the $n=0.205$ exponent.

Thus, in view of the foregoing, the no-step Sherwood numbers can be represented as

$$\mathrm{Sh}_0 = C\mathrm{Ra}^{0.205} \tag{23}$$

where C, is a function of the frame diameter ratio D_F/D. Equation (23) has been plotted in Fig. 5 for the investigated D_F/D, and the values of the coefficient, C, are listed in Table 1. Both the figure and the table indicate that the presence of

Table 1 Values of the coefficient C of equation (23)

$D_F D$	C	C/C(no frame)
1	0.645	1
1.25	0.531	0.823
1.5	0.511	0.792
≥3	0.480	0.744

the frame decreases the Sherwood number. Relatively narrow frames (e.g., $D_F/D=1.25$) give rise to substantial reductions (~18 percent), but further enlargements of the frame do not lead to significant additional decreases. When $D_F/D \geq 3$, the Sherwood number is independent of D_F/D and is about 25 percent lower than the no-frame value. This insensitivity is believed due to the fact that the velocities adjacent to the outer portions of large frames are virtually zero.

Concluding Remarks

The present research appears to be the first systematic experimental investigation of natural convection evaporation from a horizontal water layer whose temperature is below that of the ambient air. The temperature depression of the water is due to the latent heat requirements of the evaporation process. A downward-directed flow from the ambient toward the water surface is induced by the surface-to-ambient temperature difference, and this flow overpowers the oppositely directed buoyancy associated with the concentration gradient of the water vapor.

The focus of the experiments is to determine the Sherwood number (i.e., the dimensionless mass transfer coefficient) as a function of three independent parameters. One of these is the Rayleigh number, Ra, which was varied over a range of nearly two orders of magnitude, primarily by the use of five containment pans of different diameter. The second parameter is the size of a horizontal annular frame which surrounds the pan and is coplanar with the upper edge of the pan sidewall. The frame size was characterized by the ratio, D_F/D.

The third parameter is the difference between the level of the water in the pan and the height of the pan sidewall. This difference is termed the step height Δ and, in dimensionless terms, is reported as the ratio Δ/R.

The presence of the step was found to decrease the Sherwood number, the effect being quantified by the relation

$$\mathrm{Sh} = (1 - 3.84(\Delta/R))\mathrm{Sh}_0 \tag{22}$$

applicable for all values of Ra and D_F/D investigated here. In equation (22), Sh denotes the Sherwood number for an arbitrary step height, and Sh_0 is the zero-step Sherwood number. For all frames, Sh_0 displayed a universal dependence on the Rayleigh number over the investigated range ($10^4 \leq \mathrm{Ra} \leq 10^6$)

$$\mathrm{Sh}_0 = C\mathrm{Ra}^{0.205} \tag{23}$$

where the coefficient, C, depends on D_F/D and is listed in Table 1.

To find Sh for given values of Δ/R, D_F/D, and Ra, the first step is to find Sh_0 from equation (23) and Table 1, after which Sh is calculated from equation (22).

The Sherwood number decreases due to the presence of the frame and is especially sensitive to narrow frames. Enlargements of the frame beyond $D_F/D=3$ do not cause additional reductions in the Sherwood number.

The final correlation of the data should be accurate to better than 5 percent. It is also worth reiterating that since the density difference which appears in the Rayleigh number was evaluated including both the effects of temperature and of the composition of the air-water vapor mixture, no additional temperature or humidity parameters are needed to characterize the results.

Acknowledgment

Scholarship support accorded to Gunther K. Kratz by the Studienstiftung des Deutschen Volkes is gratefully acknowledged.

References

1 Eckert, E. R. G., "Heat Transfer—A Review of 1980 Literature," *International Journal of Heat and Mass Transfer*, Vol. 24, 1981, pp. 1863–1902.

2 Boelter, L. M. K., Gordon, H. S., and Griffin, J. R., "Free Evaporation Into Air of Water From a Free Horizontal Quiet Surface," *Industrial and Engineering Chemistry*, Vol. 38, 1946, pp. 596–600.

3 Wragg, A. A., and Nasiruddin, A. K., "Ionic Mass Transfer by Free Convection With Simultaneous Heat Transfer," *Electrochimica Acta*, Vol. 18, 1973, pp. 619–627.

4 Pera, L., and Gebhart, B., "Natural Convection Flows Adjacent to Horizontal Surfaces Resulting From the Combined Buoyancy Effects of Thermal and Mass Diffusion," *International Journal of Heat and Mass Transfer*, Vol. 15, 1972, pp. 269–278.

5 Adams, J. A., and McFadden, P. W., "Simultaneous Heat and Mass Transfer in Free Convection With Opposing Body Forces," *AIChE Journal*, Vol. 12, 1966, pp. 642–647.

6 De Leeuw Den Bouter, J. A., De Munnik, B., and Heertjes, P. M., "Simultaneous Heat and Mass Transfer in Laminar Free Convection From a Vertical Plate," *Chemical Engineering Science*, Vol. 23, 1968, pp. 1185–1190.

7 Mathers, W. G., Madden, A. J. Jr., and Piret, E. L., "Simultaneous Heat and Mass Transfer in Free Convection," *Industrial and Engineering Chemistry*, Vol. 49, 1957, pp. 961–968.

8 Pruckner, E., "Warme- und Stoffubertragung an fliessende Oberflachengewasser," *Fortschritt-Berichte der VDI-Zeitsechriften*, Reihe 6, Nr. 78, VDI-Verlag, Dusseldorf, 1981.

9 Restrepo, F., and Glicksman, L. R., "The Effect of Edge Conditions on Natural Convection from a Horizontal Plate," *International Journal of Heat and Mass Transfer*, Vol. 17, 1974, pp. 135–142.

10 Hatfield, D. W., and Edwards, D. K., "Edge and Aspect Ratio Effects on Natural Convection From the Horizontal Heated Plate Facing Downwards," *International Journal of Heat and Mass Transfer*, Vol. 24, 1981, pp. 1019–1024.

11 Lau, K. S., "The Effect of Edge Conditions on Laminar Natural Convection Adjacent to a Horizontal Plate," M.S. thesis, Department of Mechanical Engineering, University of Minnesota, 1978.

12 Threlkeld, J. L., *Thermal Environmental Engineering*, Prentice-Hall, Englewood Cliffs, N. J., 1970.

13 Reynolds, W. C., and Perkins, H. C., *Engineering Thermodynamics*, 2d ed., McGraw-Hill, New York, 1977.

14 Mason, E. A., and Monchick, L., "Survey of the Equation of State and Properties of Moist Air," in *Humidity and Moisture*, edited by A. Wexler, Vol. 3, Reinhold, New York, 1965.

Numerical Study of Transient High Rayleigh Number Convection in an Attic-Shaped Porous Layer

D. Poulikakos
Mechanical Engineering Department,
University of Illinois at Chicago,
Chicago Ill. 60680

A. Bejan
Assoc. Mem. ASME

Mechanical Engineering Department,
University of Colorado,
Boulder, Colo. 80309

Scaling arguments and numerical analysis are used to document the transient and steady-state regimes of natural convection in a triangular porous layer cooled from above (along the sloping wall). The numerical simulations are conducted in the high Rayleigh number domain, Ra = 100, 1000, where Ra is the Darcy-modified Rayleigh number based on height, H. The scale analysis predicts the existence of distinct thermal boundary layers if $Ra^{1/2}(H/L) > 1$, where H/L is the height/length geometric ratio of the attic-shaped porous layer. The numerical simulations confirm the scaling results, as well as the prediction that the flow consists primarily of an elongated horizontal counterflow driven by the cold wall. In addition, the numerical solutions show the presence of a Bénard-type instability at high enough Rayleigh numbers. For example, if H/L = 0.2, the instability is present when Ra > 620; this critical Rayleigh number is found to increase as H/L increases.

1 Introduction

The objective of this paper is to document the transient and steady-state, high Rayleigh number regime in an attic-shaped porous layer heated from below and cooled along the upper sloped wall (Fig. 1). The interest in this natural convection phenomenon is fueled by both practical and theoretical considerations. From a practical standpoint, the attic-shaped, or horizontal-wedge, porous layer is a central component in modern insulations and in geothermal systems. Horizontal layers with perfectly parallel surfaces have been studied extensively [1]; however, in most applications the differentially heated surfaces are not perfectly horizontal and, as documented in this study, the flow and heat transfer mechanism differs fundamentally from the classical Bénard convection phenomenon.

From a theoretical standpoint, the attic geometry offers a unique opportunity to study the competition between two fundamentally different phenomena, convection caused by heating from below and convection caused by cooling from the side. The former is possible only above a certain (critical) Rayleigh number, while the latter is present even in the limit $Ra \to 0$, and its intensity increases monotonically as Ra increases [1]. In an attic-shaped porous layer, the coexistence of these two mechanisms is made possible by the slope of the upper wall (Fig. 1): this wall cools the porous layer from above and, at the same time, from the side.

In an earlier study [2], the present authors relied on asymptotic analysis [3] to show that in the limit $H/L \to 0$ (Ra arbitrary but fixed) the flow consists of a single cell—a horizontal counterflow—driven by the sloped wall. In the same study, the single-cell flow was used as model for an approximate analysis [4] of the boundary layer regime (high Ra, H/L small but fixed). Thus, an additional objective of the present study is to test the validity of the limiting flow regimes proposed theoretically in [2]. Numerically, it is found that at a high enough Rayleigh number the single-cell counterflow falls victim gradually to a very interesting Bénard-type instability.

2 Mathematical Formulation

Consider the two-dimensional triangular porous layer shown in Fig. 1(*a*) where the top surface (T_C) is colder than the bottom (T_H). Of interest is the transient flow and heat transfer triggered by the sudden imposition of the temperature difference, $T_H - T_C$ across a wedge layer initially at T_H. According to the Darcy flow model and the homogeneous porous medium model, the equations governing the conservation of mass, momentum, and energy at every point in the porous medium are

$$\frac{\partial u}{\partial x} + \frac{\partial v}{\partial y} = 0 \tag{1}$$

$$u = \frac{-K}{\mu}\frac{\partial P}{\partial x} \tag{2}$$

$$v = -\frac{K}{\mu}\left(\frac{\partial P}{\partial y} + \rho g\right) \tag{3}$$

$$\sigma\frac{\partial T}{\partial t} + u\frac{\partial T}{\partial x} + v\frac{\partial T}{\partial y} = \alpha\left(\frac{\partial^2 T}{\partial x^2} + \frac{\partial^2 T}{\partial y^2}\right) \tag{4}$$

where u, v, x, y, P, and T are the fluid velocity components, the coordinates of each point, the fluid pressure, and temperature, respectively. Properties μ, ρ, α, and K represent the fluid viscosity, fluid density, effective thermal diffusivity based on the thermal conductivity of the fluid/porous matrix composite (k) divided by the "ρc_p" of the fluid, and permeability of the porous medium, respectively. Parameter σ appearing in equation (4) is the heat capacity ratio of the fluid saturated porous matrix to that of fluid [1]

$$\sigma = [\phi(\rho c_p)_f + (1-\phi)(\rho c_p)_m]/(\rho c_p)_f \tag{5}$$

For moderate temperature differences, as encountered in saturated porous insulations and in grain storage facilities, the Boussinesq approximation is appropriate

$$\rho \cong \rho_0[1 - \beta(T - T_0)] \tag{6}$$

Combining this statement with equations (2, 3) and eliminating the pressure P, we obtain a single equation for momentum conservation

$$\frac{\partial u}{\partial y} - \frac{\partial v}{\partial x} = -\frac{Kg\beta}{\nu}\frac{\partial T}{\partial x} \tag{7}$$

In the next section, pure scaling arguments are used to determine the relevant time and length scales of the transient and steady-state regimes in a porous wedge subjected to

Contributed by the Heat Transfer Division for publication in the JOURNAL OF HEAT TRANSFER. Manuscript received by the Heat Transfer Division August 23, 1982.

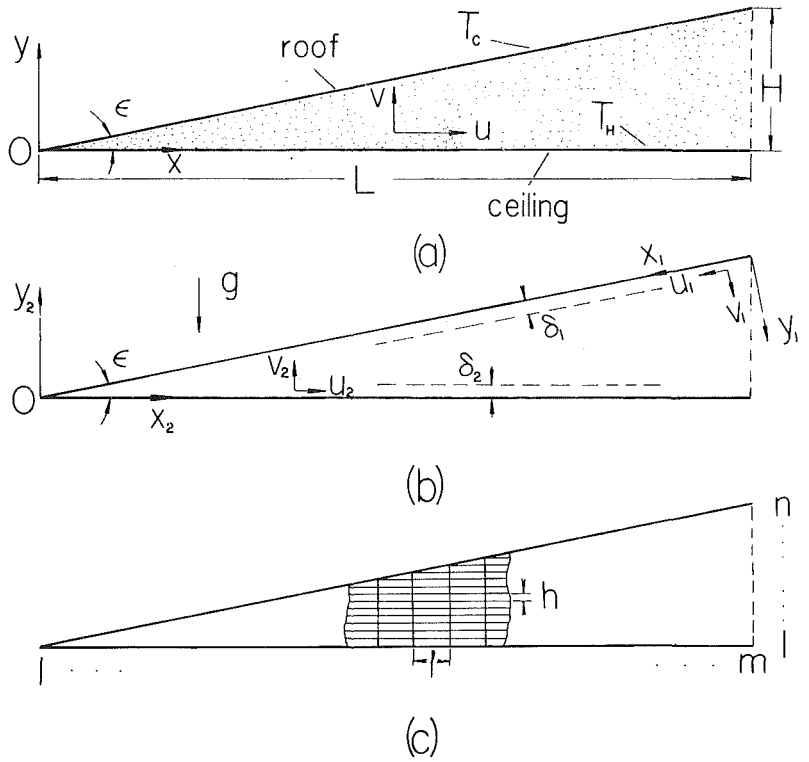

Fig. 1(*a*) Schematic of an attic space filled with fluid saturated porous medium; (*b*) boundary layer development; (*c*) grid used for numerical solutions

sudden cooling along its tilted wall, while the horizontal wall is maintained at the initial temperature.

3 Scale Analysis

A theoretical understanding of the transient behavior of the porous system is most valuable, especially with regard to interpreting the numerical results presented later in this paper. Scale analysis is an effective means to acquire such theoretical understanding: it has been shown that the proper identification of the various time scales of a transient internal flow (as in Fig. 1(*a*)) makes it possible to predict theoretically the basic flow features which survive in the steady state [5]. In addition to its fundamental value, knowledge of the transient behavior has practical relevance because most real-life porous insulations are designed to function under time-varying conditions.

(*a*) Boundary Layer Growth Along the Top Wall. Consider the top wall coordinate system, $x_1 - y_1$ shown in Fig. 1(*b*): the conservation statements for mass momentum and energy are

$$\frac{\partial u_1}{\partial x_1} + \frac{\partial v_1}{\partial y_1} = 0 \tag{8}$$

$$\frac{\partial u_1}{\partial y_1} - \frac{\partial v_1}{\partial x_1} = \frac{Kg\beta}{\nu}\left(\frac{\partial T}{\partial x_1}\cos\epsilon - \frac{\partial T}{\partial y_1}\sin\epsilon\right) \tag{9}$$

$$\sigma\frac{\partial T}{\partial t} + u_1\frac{\partial T}{\partial x_1} + v_1\frac{\partial T}{\partial y_1} = \alpha\left(\frac{\partial^2 T}{\partial x_1^2} + \frac{\partial^2 T}{\partial y_1^2}\right) \tag{10}$$

where u_1, v_1 are the velocity components parallel and per-

Nomenclature

c_p = fluid specific heat at constant pressure
g = gravitational acceleration
H = vertical dimension
k = thermal conductivity of fluid/porous matrix combination
K = permeability
L = horizontal dimension
Nu = Nusselt number, equation (47)
P = pressure
Q = net heat transfer rate, W/m
Ra = Rayleigh number based on H, equation (15)
t = time
T = temperature
u = horizontal velocity component
v = vertical velocity component
x = horizontal coordinate
y = vertical coordinate

Greek Symbols

α = thermal diffusivity $k/(\rho c_p)$
β = coefficient of thermal expansion
δ = boundary layer thickness, and length of conduction-dominated tip region
ϵ = angle, Fig. 1(*a*)
μ = viscosity
ν = kinematic viscosity $\nu = \mu/\rho$
ρ = fluid density
σ = heat capacity ratio, equation (5)
ψ = stream function

Subscripts

C = cold
H = hot
m = pertaining to the porous matrix, equation (5)
f = pertaining to the fluid, equation (5)
o = pertaining to an average temperature between the top and bottom walls
1 = pertaining to the top wall, Fig. 1(*b*)
2 = pertaining to the bottom wall, Fig. 1(*b*)

pendicular to the tilted top wall. Since the fluid is initially motionless, the cooling effect provided by the top wall propagates downward into the porous medium by pure conduction. The energy equation (10) with $\sigma\Delta T/t \sim \alpha\,\Delta T/\delta_1^2$ indicates that the top wall develops a thermal boundary layer whose thickness, δ, grows in time

$$\delta_1 = (\alpha t/\sigma)^{1/2} \tag{11}$$

Note that in natural convection through a porous medium the thermal and velocity boundary layers have the same length scale.

Assuming that in the beginning the thermal layer, δ_1, is sufficiently slender ($\delta_1 < L\epsilon$), the balance "diffusion-buoyancy" in the momentum equation (9) yields the u_1 velocity scale

$$u_1 = \frac{Kg\beta\ \Delta T\epsilon}{\nu} \tag{12}$$

It is also assumed that the attic shape is shallow enough so that $\sin\epsilon \sim \epsilon \sim H/L$. As time passes the boundary layer thickness, δ_1, continues to grow until the heat transfer from the porous layer to the wall is balanced by the energy convected into the top wall region by the fluid sinking through the layer. At this point the energy equation (10) expresses a balance between convection and diffusion in the y_1 direction

$$u_1 \frac{\Delta T}{L} \sim \alpha \frac{\Delta T}{\delta_1^2} \tag{13}$$

The boundary layer thickness scale (11) and the velocity scale (12) along with equation (13) imply that the growth of the boundary layer along the tilted wall ends at time of order

$$t_{1_f} \sim \frac{L^2\sigma}{\alpha \mathrm{Ra}} \tag{14}$$

where Ra is the Darcy modified Rayleigh number based on the height of the enclosure

$$\mathrm{Ra} = \frac{Kg\beta\Delta TH}{\nu\alpha} \tag{15}$$

Combining expressions (11) and (14), we learn that the final thickness of the boundary layer along the top wall is of order

$$\delta_{1_f} \sim L\mathrm{Ra}^{-1/2} \tag{16}$$

It is worth noting that the energy balance between conduction and convection, equation (13), implies that the $\sigma\partial T/\partial t$ term has become negligible, in other words, the top wall boundary layer has reached steady state.

The final thickness of the top thermal boundary layer, equation (16), can be compared with the vertical dimension of the cavity, H. Thus, when $\delta_{1_f} < H$, we expect the presence of a distinct thermal boundary layer along the top wall in the steady state. Combining this condition with equation (16) yields the criterion for the existence of a distinct thermal boundary layer along the tilted wall of the porous layer

$$\epsilon\mathrm{Ra}^{1/2} > 1 \tag{17}$$

Finally, it is worth keeping in mind that the foregoing length and time scales follow from the assumption that, before reaching its terminal thickness δ_{1_f}, the boundary layer along the top wall is slender

$$\delta_1 < L\epsilon \tag{18}$$

This assumption was made in the discussion that preceded equation (12). Using equation (16) the slenderness condition, $\delta_{1_f} < \epsilon L$, reduces to criterion (17), which means that if the boundary layer is distinct, it is also slender.

(*b*) Development of a Layer Along the Bottom Wall. The equations governing the heat and fluid flow along the bottom wall are

$$\frac{\partial u_2}{\partial x_2} + \frac{\partial v_2}{\partial y_2} = 0 \tag{19}$$

$$\frac{\partial u_2}{\partial y_2} - \frac{\partial v_2}{\partial x_2} = -\frac{Kg\beta}{\nu}\frac{\partial T}{\partial x_2} \tag{20}$$

$$\sigma\frac{\partial T}{\partial t} + u_2\frac{\partial T}{\partial x_2} + v_2\frac{\partial T}{\partial y_2} = \alpha\left(\frac{\partial^2 T}{\partial {x_2}^2} + \frac{\partial^2 T}{\partial {y_2}^2}\right) \tag{21}$$

The new notation (u_2, v_2, x_2, y_2) is defined in Fig. 1(*b*). The rest of the quantities appearing in equations (19–21) have been defined earlier.

In the beginning, the cold wall drives a stream of thickness $\delta_1 \sim \sqrt{\alpha t/\sigma}$ and velocity $u_1 \sim Kg\beta\Delta T\epsilon/\nu$. This stream is colder than the rest of the fluid in the enclosure and, as a result, after reaching the $x_2 = 0$ corner of the wedge it has no choice but to move horizontally to the right along the bottom wall (Fig. 1(*b*)). From mass conservation, $u_1\delta_1 \sim u_2\delta_2$, hence

$$u_2\delta_2 \sim \frac{Kg\beta\Delta T\epsilon}{\nu}\sqrt{\frac{\alpha t}{\sigma}} \tag{22}$$

After a short time, t, the horizontal intrusion layer advances a distance $\sigma/t \sim u_2/l$ along the bottom wall. At this point, the momentum equation (20) expresses a buoyancy-convection balance

$$\frac{u_2}{\delta_2} \sim \frac{Kg\beta}{\nu}\frac{\Delta T}{l} \tag{23}$$

Combining expressions (22) and (23) yields the "short time" velocity and boundary layer thickness scales

$$u_2 \sim \mathrm{Ra}^{2/3}\frac{\epsilon^{1/3}\alpha^{5/6}\sigma^{1/6}}{H^{2/3}t^{1/6}} \tag{24}$$

$$\delta_2 \sim \left(\frac{\mathrm{Ra}}{H}\right)^{1/3}\left(\frac{t\epsilon\alpha}{\sigma}\right)^{2/3} \tag{25}$$

At steady state, the energy extracted by the horizontal intrusion layer from the bottom wall (of order $k\Delta T/\delta_2$) is balanced by the enthalpy convected away by the fluid in the layer. Then, the energy equation (21) expresses a balance between the diffusion and convection terms

$$\frac{u_2}{L} \sim \frac{\alpha}{{\delta_2}^2} \tag{26}$$

Combining this statement with expressions (24) and (25) yields an estimate for the time when the bottom intrusion layer reaches steady state

$$t_{2_f} \sim \left(\frac{L^6H^8}{\mathrm{Ra}^8\epsilon^{10}}\right)^{1/7}\frac{\sigma}{\alpha} \tag{27}$$

At and beyond this point in time, the velocity and boundary layer thickness scales are

$$u_{2_f} \sim \left(\frac{\mathrm{Ra}^6\epsilon^4\alpha^7}{H^6L}\right)^{1/7} \tag{28}$$

$$\delta_{2_f} \sim \left(\frac{L^4H^3}{\mathrm{Ra}^3\epsilon^2}\right)^{1/7} \tag{29}$$

Comparing the new time scale, t_{2_f}, (equation 27) with the time, t_{1_f}, (equation 14) needed by the top boundary layer to reach steady state, we learn that the bottom wall layer develops faster than the top wall layer if

$$\frac{t_{2_f}}{t_{1_f}} < 1 \tag{30}$$

or

$$\epsilon\mathrm{Ra}^{1/2} > 1 \tag{31}$$

which is identical to criterion (17) necessary for the existence

of the top layers. Hence, the thermal layer along the bottom wall develops always faster than the layer along the top wall.

4 Numerical Solutions

An extensive series of numerical simulations was performed in order to determine the actual flow and temperature patterns and to verify the scaling results developed in the preceding section. It was assumed that the fluid saturating the wedge-shaped porous matrix is originally motionless and isothermal (T_H), as in the transient scale analysis of section 3. The porous layer is suddenly cooled from the top by decreasing the temperature of the sloping wall. Throughout the numerical simulation, the temperature of the horizontal wall is maintained at the initial level, T_H.

The numerical solution is aided by introducing the streamfunction, ψ, defined as

$$u = \frac{\partial \psi}{\partial y} \tag{32}$$

$$v = -\frac{\partial \psi}{\partial x} \tag{33}$$

Taking H, α/H, and $\Delta T = T_H - T_C$ as reference units for length, velocity, and temperature variation, the following dimensionless variables are introduced

$$\hat{x} = x/H,\ \hat{y} = y/H,\ \hat{t} = \frac{t}{\sigma H^2/\alpha},\ \hat{u} = \frac{u}{\alpha/H}$$
$$\hat{v} = \frac{v}{\alpha/H},\ \hat{\psi} = \frac{\psi}{\alpha},\ \hat{T} = \frac{T - T_C}{T_H - T_C} \tag{34}$$

The corresponding dimensionless form of the governing equations and boundary conditions is

$$\hat{u} = \frac{\partial \hat{\psi}}{\partial \hat{y}} \tag{35}$$

$$\hat{v} = -\frac{\partial \hat{\psi}}{\partial \hat{x}} \tag{36}$$

$$\left(\frac{\partial^2}{\partial \hat{x}^2} + \frac{\partial^2}{\partial \hat{y}^2}\right)\hat{\psi} = -\mathrm{Ra}\frac{\partial \hat{T}}{\partial \hat{x}} \tag{37}$$

$$\frac{\partial \hat{T}}{\partial \hat{t}} + \frac{\partial (\hat{u}\hat{T})}{\partial \hat{x}} + \frac{\partial (\hat{v}\hat{T})}{\partial \hat{y}} = \frac{\partial^2 \hat{T}}{\partial \hat{x}^2} + \frac{\partial^2 \hat{T}}{\partial \hat{y}^2} \tag{38}$$

$\hat{v} = 0$, $\hat{\psi} = 0$, and $\hat{T} = 1$ at $\hat{y} = 0$

$\hat{u} = 0$, $\hat{\psi} = 0$ and $\dfrac{\partial \hat{T}}{\partial \hat{x}} = 0$ at $\hat{x} = L/H$ (the center of symmetry of the attic) (39)

$\hat{v} = \dfrac{H}{L}\hat{u}$, $\hat{\psi} = 0$ and $\hat{T} = 0$ at $\hat{y} = \dfrac{H}{L}\hat{x}$

The effect of the two dimensionless groups, Ra and H/L, is determined by conducting a sequence of numerical experiments for different values of Ra and H/L and by comparing the resulting flow patterns and temperature fields.

The numerical solution of equations (35–39) was accomplished based on a finite difference method and the observation that, due to the symmetry of the problem, only the left half of the problem needs to be calculated. The fluid region of interest was covered with m vertical and n horizontal grid lines; the grid fineness $m = n = 41$ was found to be adequate for the present solution. As shown in Fig. 1(*c*), rectangular meshes of size $l \times h$ were chosen such that $h/l = H/L$; consequently, the uppermost grid-point on each vertical grid line coincided with the top wall of the enclosure. Except for the nonlinear terms, all spatial derivatives in the governing differential equations (35–38) were approximated at the interior points using the central difference formula [6]. The successive overrelaxation method [6] was employed to calculate from equation (37) the streamfunction for a known temperature distribution. To integrate equation (38) in time, we used a function subprogram [7] able to handle an equation of the general form

$$\frac{\partial \phi}{\partial t} = -\frac{\partial (u\phi)}{\partial x} - \frac{\partial (v\phi)}{\partial y} + C\frac{\partial M}{\partial x} + D\left(\frac{\partial^2}{\partial x^2} + \frac{\partial^2}{\partial y^2}\right)\phi \tag{40}$$

We used a computationally stable upwind-differencing scheme [6, 7] to approximate the first two terms of the right-hand side of equation (40). The term multiplied by D was approximated by a central differencing scheme, and the constant C was set equal to zero.

The effect of fluid motion on the heat transfer between the two walls of the attic was evaluated by computing the Nusselt number

$$\mathrm{Nu} = \frac{Q}{kL(T_H - T_C)/H} \tag{41}$$

where k and Q are the thermal conductivity of the fluid/porous matrix composite and the overall heat transfer rate

$$Q = -\int_{0^+}^{L} k\left(\frac{\partial T}{\partial y}\right)_{y=0} dx \tag{42}$$

The heat transfer integral (42) blows up in the $x = 0$ corner if the two surfaces (T_H, T_C) are in direct thermal contact. However, since in a real system the walls near the tip of a shallow triangular enclosure reach a temperature between T_H and T_C, the corner region does not contribute significantly to Q. If the length of this inert (isothermal) region is δ, the overall heat transfer rate is finite: under these circumstances equations (41) and (42) yield

$$\mathrm{Nu} = -\frac{H}{L}\int_{\delta/H}^{L/H}\left(\frac{\partial \hat{T}}{\partial \hat{y}}\right)_{\hat{y}=0} d\hat{x} \tag{43}$$

Equation (43) was integrated numerically for each instant in time until steady state was reached within prescribed error. In order to be able to *comparatively* discuss the evolution of Nu in time and the influence of Ra and H/L on the heat transfer rate, δ/L was set equal to 0.1 throughout the present study. Note that for δ/L values much smaller than 0.1 the Nusselt number calculated using equation (43) would be dominated by conduction through the tip region. It was felt that for a meaningful discussion of the convective heat transfer effect, δ/L should be large enough to remove from the picture the unrealistically large conduction effect (see Fig. 8(*b*)).

It is worth mentioning that in the development of the numerical solution, the authors also experimented with nonuniform grids: the use of such grids did not improve the solution significantly in view of the added complications. Most importantly, the use of alternative techniques did not widen noticeably the range of Ra amenable to a stable numerical solution.

The integral shown in equation (43) was evaluated also along the top wall and compared with the corresponding result from the bottom wall. In all cases, the agreement was better than 2 percent.

Another possible item of concern is the false diffusion effect implicit in the upwind-differencing scheme. One of the peculiarities of the false diffusion argument is that it is based on the assumption that the central difference is accurate and that the upwind scheme may be judged in this frame of reference. In fact, however, the central difference scheme is accurate only in the low Ra regime. In the high Ra regime where convection is important, the so-called false diffusion coefficient is actually a desirable addition, for it actually

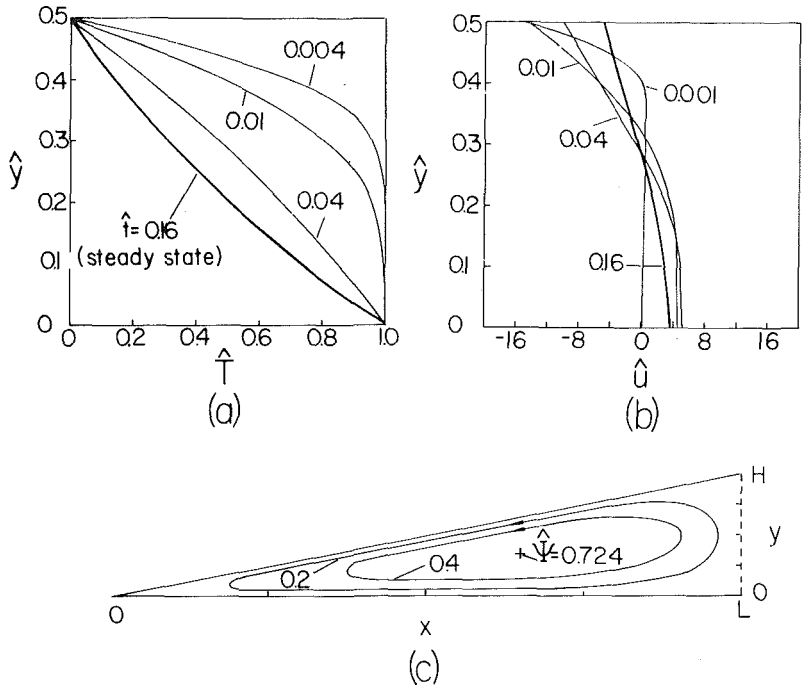

Fig. 2 Numerical results for $H/L = 0.2$, Ra = 100: (*a*) temperature profile at $x = L/2$; (*b*) horizontal velocity profile at $x = L/2$; (*c*) steady-state streamline pattern

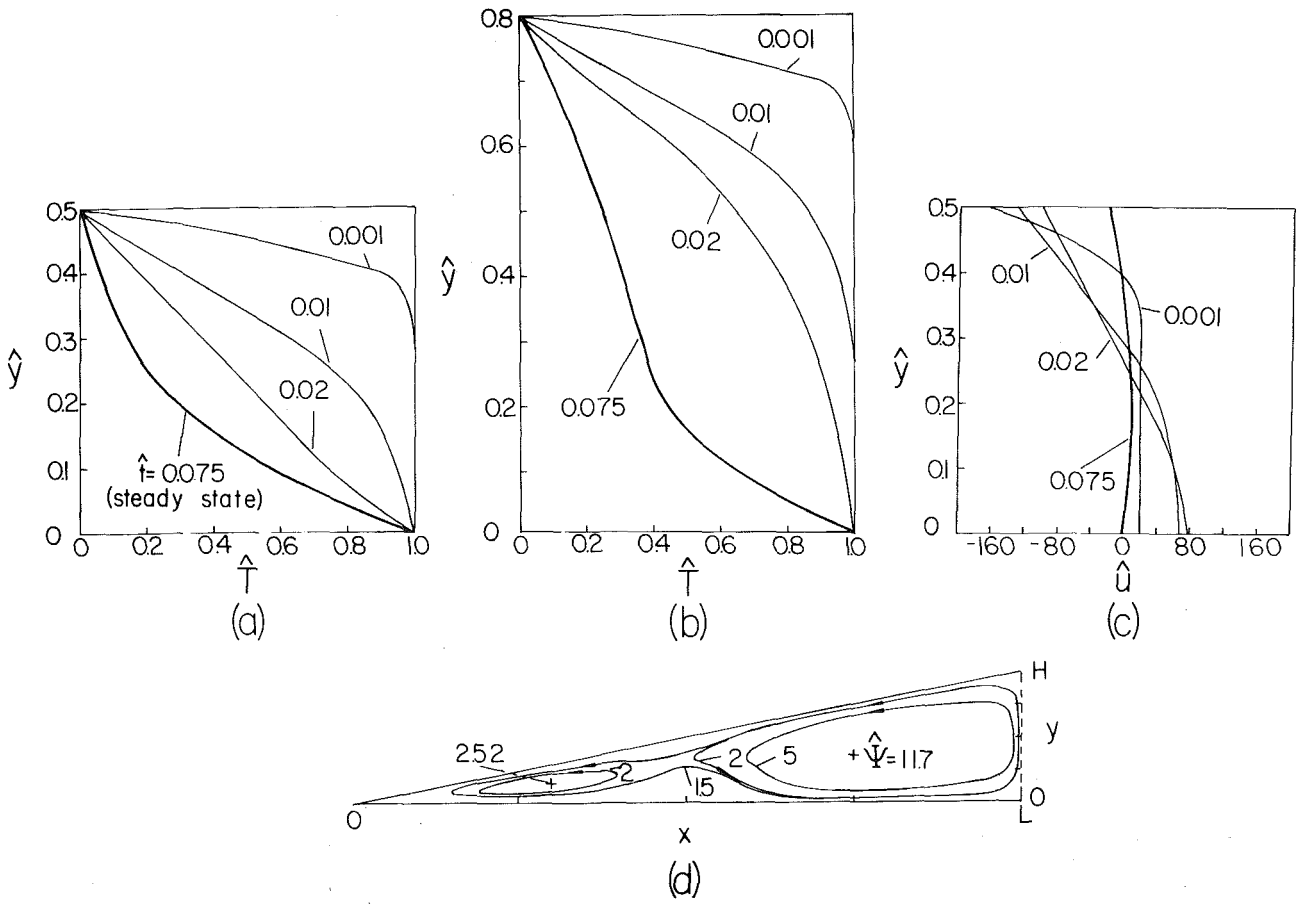

Fig. 3 Numerical results for $H/L = 0.2$, Ra = 1000: (*a*) temperature profile at $x = L/2$; (*b*) temperature profile at $x = 0.8\,L$; (*c*) horizontal velocity profile at $x = L/2$; (*d*) steady-state streamline pattern

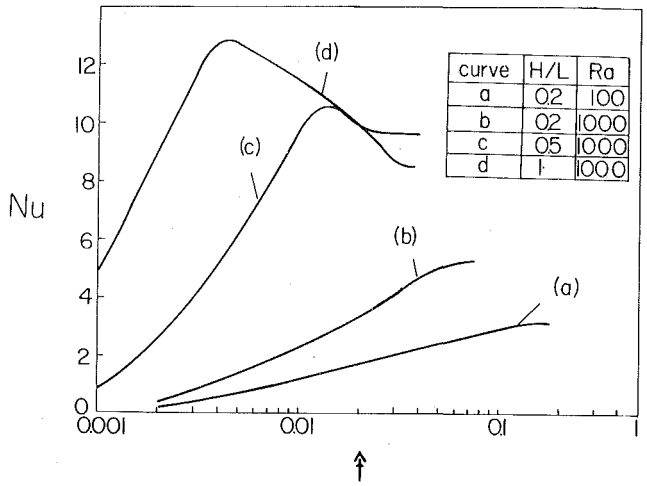

Fig. 4 The Nusselt number approach to steady state

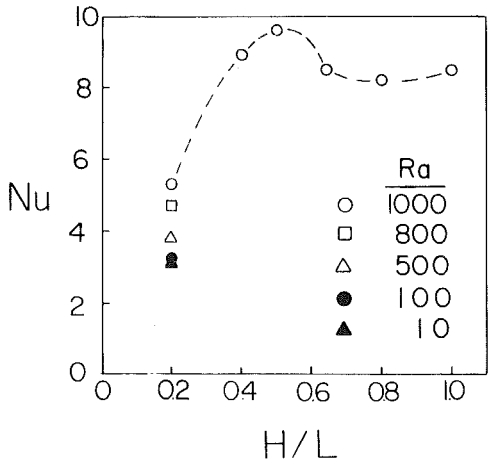

Fig. 5 The Nu dependence on H/L and Ra in the steady state

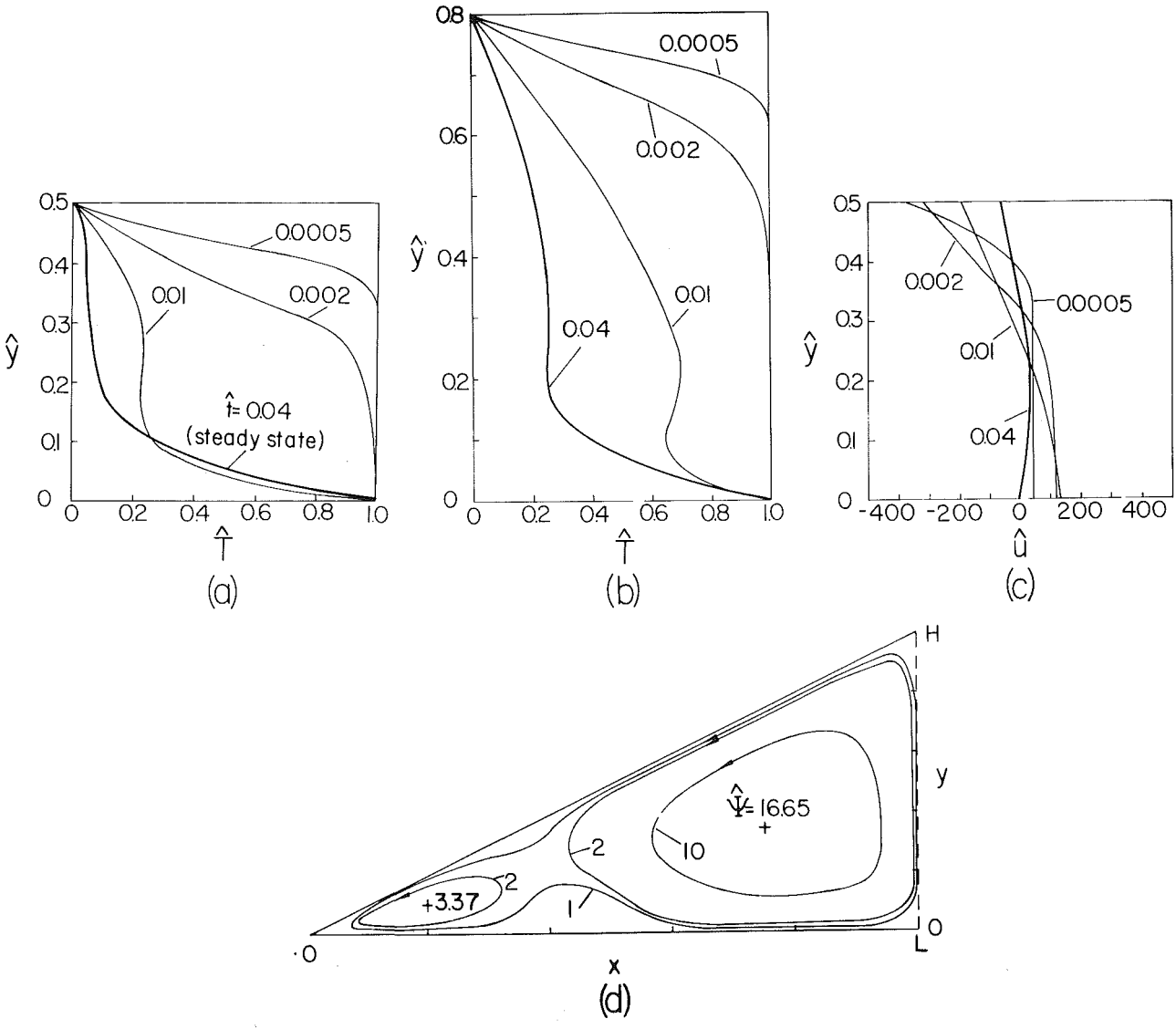

Fig. 6 Numerical results for $H/L = 0.5$, Ra = 1000: (*a*) temperature profile at $x = L/2$; (*b*) temperature profile at $x = 0.8\ L$; (*c*) horizontal velocity profile at $x = L/2$; (*d*) steady-state streamline pattern

tends to correct the wrong effects that would otherwise follow from the central difference scheme. This is shown thoroughly in Patankar [11] for one one-dimensional flow model (for simplicity). Since our study is concerned with a relatively high Ra regime, one would expect the numerical results to be fairly accurate. It is also true that the false diffusion effect depends on the angle at which the flow crosses the mesh. deVahl Davis and Mallinson [12] reported an approximate expression which shows that the false diffusion is most serious when the angle is 45 deg or $H/L = 1$. In our study, we only report one critical Ra for $H/L = 0.2$, which is considerably smaller than $H/L = 1$ and, therefore, the false diffusion should not influence the result as much as in the $H/L = 1$ case.

5 Results and Discussion

(a) The Effect of Rayleigh Number. The results of these numerical experiments are shown in Figs. 2–5. For each value of Rayleigh number, we report the evolution and approach to steady state of the temperature and the horizontal velocity evaluated at $\hat{x} = (L/2)/H$. We also show the streamline pattern in the steady state and the evolution of the Nusselt number from $\hat{t} = 0$, until steady state is reached. The geometric aspect ratio of the enclosure is fixed at $H/L = 0.2$ throughout this phase of the study.

In the case of Ra = 100 the sudden cooling of the top wall initiates a counterclockwise circulation in the enclosure (see Fig. 2(*c*)). The velocities are initially highest near the roof of the attic, which is the surface driving the flow. At the same time, the body of fluid saturating the porous matrix and residing outside the top wall layer is displaced slowly to the right in a "uniform flow" fashion. Steady state is reached at a dimensionless time, $\hat{t} \approx 0.16$.

The temperature distribution departs gradually from the initial isothermal pattern and reaches steady state in the manner shown in Fig. 2(*a*)). In agreement with the velocity profile plotted in Fig. 2(*b*), in the early stages of the transient experiment, the temperature gradient is much steeper close to the top wall of the cavity. The steady-state temperature profile indicates that for Ra = 100 the heat transfer across the attic space is dominated by conduction, as in the asymptotic regime of [2].

The steady-state flow pattern is ruled by the counterclockwise cell shown in Fig. 2(*c*). During the transient phase of the experiment, the Nusselt number approaches monotonically a steady-state value that is very close to the

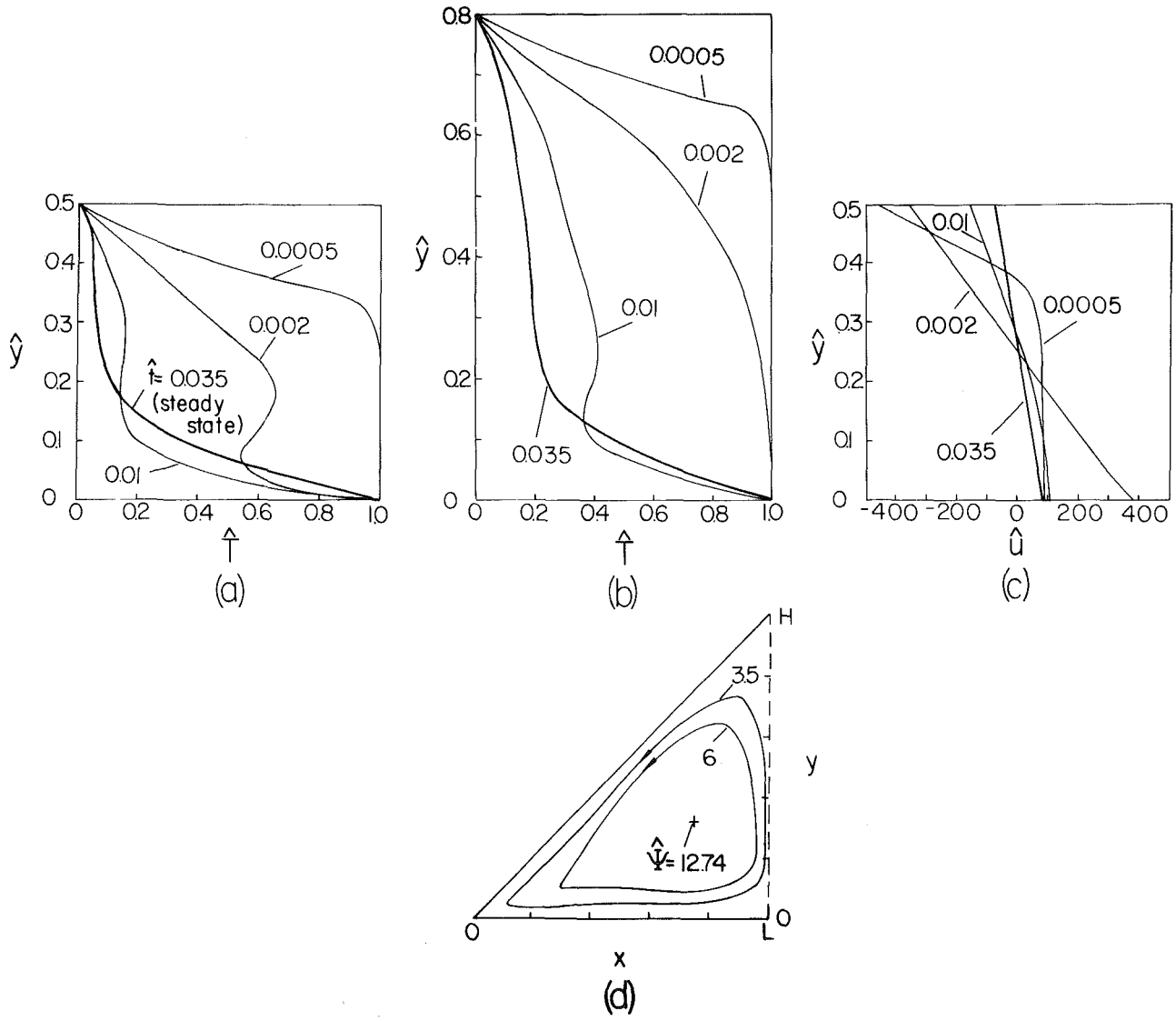

Fig. 7 Numerical results for $H/L = 1.0$, Ra = 1000: (*a*) temperature profile at $x = L/2$; (*b*) temperature profile at $x = 0.8\ L$; (c) horizontal velocity profile at $x = L/2$; (*d*) steady-state streamline pattern

pure conduction estimate: a summary of transient Nusselt results is presented in Fig. 4 (note log $\hat{t}$ on the abscissa). A conduction-dominated flow was also found in the case of Ra = 10, which, for the sake of brevity, is not shown. The steady-state value of the Nusselt number for the Ra = 10 case is practically identical to the pure conduction limit (Fig. 5). The results of this first numerical experiment are in excellent agreement with the scaling criterion (17), which in this case yields $\epsilon Ra^{1/2} \sim 2$: since $\epsilon Ra^{1/2}$ is of order one, no boundary layers are expected to survive in the steady state. The peaks in the Nu versus $\hat{t}$ curves are similar to those observed routinely in enclosures heated from the bottom or from the side.

The highest Rayleigh number investigated in this study was Ra = 1000. The manner in which the temperature field approaches steady state indicates the presence of a sizeable convective effect during the early part of the transient experiment (Figs. 3(*a*), 3(*b*)). In the steady state, the temperature field departs noticeably from the pure conduction limit, as convection plays an increasing role in the heat transfer across the porous wedge (Figs. 3(*a*), 3(*b*), 4, and 5). The shape of the steady-state temperature distribution at $\hat{x} = 0.8\ L/H$ shown in Fig. 3(*b*) indicates the existence of two thermal boundary layers along the walls of the cavity near its center of symmetry ($x = L/H$). Near the tip (left end) of the enclosure, the two boundary layers merge, yielding the steady-state temperature distribution shown in Fig. 3(*a*) ($x = 0.5\ L/H$). The velocity distribution shows once again that the flow is initiated in the close vicinity of the top wall (Fig. 3(*c*)). The steady-state flow pattern (Fig. 3(*d*)) proves that at this high Rayleigh number (Ra = 1000) the fluid saturating the porous medium develops a thermal instabiilty of the Bénard type [1, 8–10]. Hence, the flow in the enclosure is dominated by two counterclockwise cells, the one closer to the tip of the attic being the weaker of the two. The two cells accentuate the role of convection as a heat transfer mechanism (see Fig. 4, curve *b* and Fig. 5). The scaling criterion (17) of the previous section is once more satisfied, as $Ra^{1/2}\ \epsilon \sim 6$ is not significantly higher than one. The time in which steady state is reached, $\hat{t} = 0.075$, is of the same order of magnitude as the dimensionless time defined by equation (14)

$$\hat{t} \sim (L^2\sigma/\alpha Ra)/(\sigma H^2/\alpha) \sim 0.025$$

Finally, the critical Rayleigh number at which the thermal instability first appears was calculated numerically by examining numerous streamline patterns while increasing the Rayleigh number

$$Ra_{crit} = 620, \quad \text{for} \quad H/L = 0.2$$

Since in the case of a horizontal porous layer with perfectly parallel walls $Ra_{crit} \cong 40$ [1], the present study shows that the asymptotic (counterflow) pattern of [2] has the effect of inhibiting the Benard instability. As shown next, the stabilizing effect of the counterclockwise main flow is enhanced as H/L increases, i.e., as the main flow becomes stronger.

(*b*) The Effect of Aspect Ratio. Two additional experiments were carried out in order to determine how seriously the aspect ratio, H/L, affects the flow pattern and temperature field in the enclosure. During these experiments, we assigned to the Rayleigh number the highest value achieved in this study, Ra = 1000.

Figure 6 shows the numerical results for an attic-shaped layer with $H/L = 0.5$. Thinking in terms of keeping the temperature difference, ΔT, across the layer as well as the enclosure height, H, constant, this new aspect ratio ($H/L = 0.5$) is representative of an enclosure with shorter horizontal wall than the one studied before ($H/L = 0.2$). The temperature variation (Fig. 6(*a*), 6(*b*)) shows that the thermal layering structure first observed during the transient part of

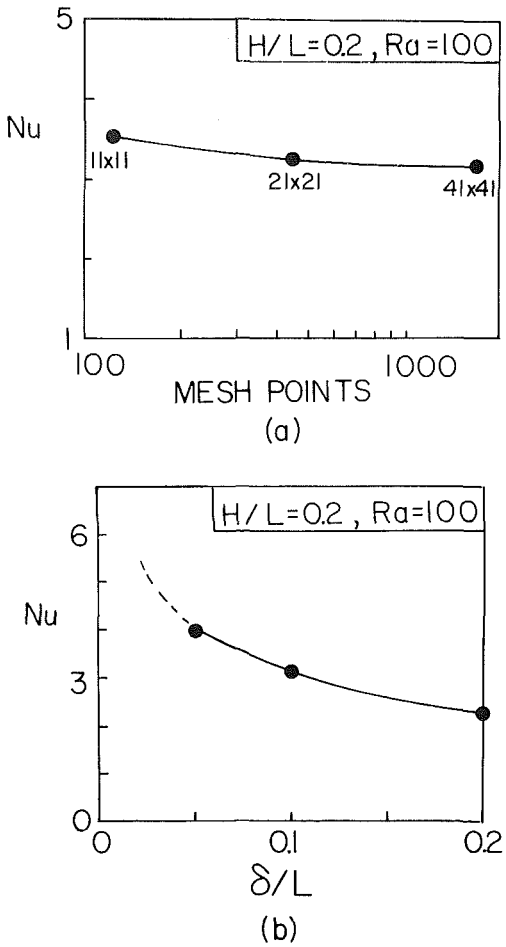

Fig. 8 Testing the accuracy of the numerical scheme: (*a*) the effect of grid fineness; (*b*) the effect of truncating the conduction-dominated tip region of length, δ

the experiment ($t = 0.01$) prevails in the steady state. The thermal boundary layer along the horizontal (bottom) wall is significantly sharper than the one in the close vicinity of the tilted wall. This indicates that, except for a layer adjacent to the bottom wall, the fluid saturating the porous layer is at a temperature very close to the temperature of the top wall.

The velocity variation and steady-state streamline pattern shown in Figs. 6(*c*), 6(*d*) reveal again the presence of Bénard tendency superimposed on the counterclockwise main counterflow. An interesting feature of these numerical results is that the Nusselt number does not approach steady state monotonically but in an *oscillatory* fashion. Figure 4 (curve c) shows Nu first rising to a peak value (at $\hat{t} = 0.014$) and subsequently decaying to the steady-state value of Nu = 8.5 for $\hat{t} > 0.04$. The peak in the Nu(t) curve indicates the time of most intense heat transfer across the attic. According to the scaling criterion (17), $\epsilon Ra^{1/2} \sim 16 > 1$ correctly predicts the presence of distinct thermal layers along the two walls.

Increasing the aspect ratio to $H/L = 1.0$ has a serious effect on the streamline pattern. As shown in Fig. 7(*d*), the steepness of the top wall forces the two cells to merge. The weak cell which was located close to the tip of the wedge in the previous experiments ($H/L = 0.2$ and 0.5) does not appear any more, and the steady-state circulation is dominated by one large counterclockwise cell which "sweeps" the entire length of the cavity. The temperature and velocity fields (Figs. 7(*a*), 7(*b*), 7(*c*)) display similar characteristics, as in the case of $H/L = 0.5$, and the Nusselt number approaches steady state in oscillatory manner again.

It is worth noting that the analytical model proposed for the

boundary layer regime in [2] is not confirmed by the present numerical simulations. In [2], the boundary layer regime was thought to consist of a thin fluid layer moving along the top wall, in counterflow with a "core" moving slowly to the right in Fig. 1. The numerical results shown here in Figs. 3, 6, and 7 demonstrate that *both* walls are lined by thin fluid layers moving in counterflow, in accordance with the scale analysis presented in the first part of this paper.

Figure 5 summarizes the effect of aspect ratio, H/L, on convective heat transfer. It is apparent that the existence of Bénard type of thermal instabilities drastically enhances the heat transfer through the enclosure. Increasing the aspect ratio enough to force the two convective cells to merge decreases the heat transfer and has an insulating effect. This finding shows the limitations of criterion (17), according to which increasing the numerical value of the dimensionless group $\epsilon \mathrm{Ra}^{1/2}$ enhances the convective contribution to heat transfer. Also, Fig. 5 shows that increasing the values of Ra for a fixed aspect ratio, H/L, leads to increasingly higher Nusselt numbers, in agreement with conclusions based on scaling arguments.

Figures 8(*a*) and 8(*b*) illustrate the degree to which the present heat transfer results depend on the numerical method. Figure 8(*a*) shows that the 41 × 41 grid used in this study captures the asymptotic value of the Nusselt number. Figure 8(*b*) shows the dependence of Nu on the conduction dominated tip region of length, δ, which has been removed from the present heat transfer calculations. It is apparent that the tip length, $\delta/L = 0.1$, used throughout this study eliminates effectively the high heat transfer rate associated purely with the tip.

Acknowledgment

This work was supported in part by N. S. F. Grant No. MEA-82-07779.

References

1 Cheng, P., "Heat Transfer in Geothermal Systems," *Advances in Heat Transfer*, Vol. 14, 1979, pp. 1-105.

2 Bejan, A., and Poulikakos, D., "Natural Convection in an Attic-Shaped Space Filled With Porous Material," ASME JOURNAL OF HEAT TRANSFER, Vol. 104, 1982, pp. 241-247.

3 Walker, K. L., and Homsy, G. M., "Convection in a Porous Cavity," *Journal of Fluid Mechanics*, Vol. 87, 1978, pp. 449-474.

4 Ostrach, S., "Natural Convection in Enclosures," *Advances in Heat Transfer*, Vol. 8, 1972, pp. 161-227.

5 Patterson, J., and Imberger, J., "Unsteady Natural Convection in a Rectangular Cavity," *Journal of Fluid Mechanics*, Vol. 100, 1980, pp. 65-86.

6 Roache, P. J., *Computational Fluid Dynamics*, Hermosa Publishers, Albuquerque, New Mexico, 1976.

7 Chow, C. Y., *An Introduction to Computational Fluid Mechanics*, John Wiley and Sons, New York, 1979.

8 Bénard, H., "Les Tourbillons Cellulaires dans une Nappe Liquide Transportant de la Chaleur par Convection en Régime Permanent," *Annales de Chimie et de Physique*, Vol. 23, 1901, pp. 62-144.

9 Rayleigh, Lord, "On Convective Currents in a Horizontal Layer of Fluid When the Higher Temperature of Fluid is on the Underside," *Phil. Mag.*, Vol. 32, 1916, pp. 529-546.

10 Chandrasekhar, S., *Hydrodynamic and Hydromagnetic Stability*, Oxford University Press, 1961.

11 Patankar, S., *Numerical Heat Transfer and Fluid Flow*, Hemisphere, 1980, pp. 105-109.

12 de Vahl Davis, G., and Mallinson, G. D., "False Diffusion in Numerical Fluid Mechanics," *University of New South Wales, School of Mech. and Ind. Engin. Rept.*, 1972/FMT/1.

Heat Transfer in Porous Media Heated From Above With Evaporation, Condensation, and Capillary Effects

K. S. Udell
Department of Mechanical Engineering,
University of California, Berkeley,
Berkeley, Calif. 94720
Assoc. Mem. ASME

Heat and mass transfer characteristics of a sand-water-steam system heated at the top and cooled at the bottom were studied. It was found that at steady-state conditions the system segregated into three regions. The top region was conduction-dominated with the voids containing a stationary superheated steam. The middle region was convection-dominated, nearly isothermal, and exhibited an upward flow of the liquid by capillary forces and a downward flow of steam due to a slight pressure gradient. The bottom portion contained a stationary compressed liquid and was also conduction dominated. The length of the two-phase convection zone was evaluated through the application of Darcy's equations for two-phase flow and correlations of relative permeabilities and capillary pressure data. The model was in excellent agreement with the observed results, predicting a decreasing two-phase zone length with increasing heat flux. The thermodynamics of the two-phase zone were also analyzed. It was found that the vapor phase was in a superheated state as described by the Kelvin equation for vapor pressure lowering. Also, it was evident that the liquid must also be superheated for thermodynamic equilibrium to result. A stability analysis demonstrated that the superheated liquid can exist in an unconditionally stable state under conditions typical of porous systems. The degree of liquid superheat within the two-phase zone of these experiments was obtained.

Introduction

Heat transfer in porous media with phase change is a topic which draws broad interest due to the many applications. Examples of this phenomenon are geothermal reservoir performance prediction, thermally enhanced oil recovery, nuclear waste disposal, food drying, and porous insulation moisture transport. In many of these systems, the effective pore radii are small, thereby accentuating the significance of capillary pressure effects. Capillary pressures contribute to liquid phase transport in two-phase regions as well as modify the thermodynamic equilibrium conditions for the liquid-vapor system as predicted by the Kelvin equation for vapor pressure lowering.

Studies of heat transfer in porous media involving phase change and capillary effects have been reported in the literature. Gomaa and Somerton [1] have shown that the apparent thermal conductivity of a sand containing water and steam phases can be several times larger than for the sand containing only one phase. Earlier work has been reported by researchers in soil science. Boyoucos [2], Winterkorn [3], and Taylor and Cavazza [4] studied the effects of temperature gradients and capillary forces on moisture movement in porous media. A summary of the efforts of Soviet authors in the mathematical description of heat and mass transfer in capillary-porous media has been given by Luikov [5]. Similar studies have been reported by Sahota and Pagni [6], Eckert and Faghri [7], and Ogniewicz and Tien [8, 9].

Experiments were conducted by Hansen, Breyer, and Riback [10] using glass and copper beads as the porous media and performed over a wide range of heat fluxes. Their results also showed an enhancement of the heat transfer due to a heat pipe effect. Su [11] also conducted experiments exhibiting the effect of capillary-evaporation-condensation heat transfer enhancement. Most recently, Bau and Torrance [12] heated water saturated porous media from the bottom to temperatures above saturation. The work presented in this paper was performed in order to evaluate the heat and mass transfer mechanism present within a partially saturated, capillary driven porous medium from an experimental as well as theoretical viewpoint. The thermodynamics of the phase behavior within the two-phase system and the hydrodynamics of the liquid and vapor migration will be analyzed.

Experimental Study

Experiments were conducted using two different sand grain sizes contained in a 25.4-cm long, 5.4-cm i.d. fiberglass tube as shown in Fig. 1. Ottawa sands of 20-28 and 65-100 mesh were chosen because of the spherical grain shape and nearly pure silica composition. The sand core was heated from the top by a nichrome wire coil imbedded in a copper block. An identical copper block heater was used to control the bottom temperature and was cooled by heat transfer to the environment. The heater temperatures were held constant through the use of two variable set-point temperature controllers. Fifteen chromel-alumel thermocouples were placed along the sand pack centerline at 1.6 cm intervals. The core was separated from the top and bottom heaters by fired lava thermal conductivity standards in order to facilitate heat flux measurements. The core holder, standards, and heaters were placed in a hydraulic press and loaded to approximately 2500 N to insure thermal contact between the standards and the sand pack. This load also provided a seal between the standards and the core holder separated by O-rings.

Five individually controlled heater tapes were wrapped around the core holder at 5.1 cm intervals. Thermocouples were placed between each heater tape and the core holder on opposite sides. Individual heater tape power levels were adjusted periodically during the experiments such that the

Contributed by the Heat Transfer Division for publication in the JOURNAL OF HEAT TRANSFER. Manuscript received by the Heat Transfer Division August 23, 1982.

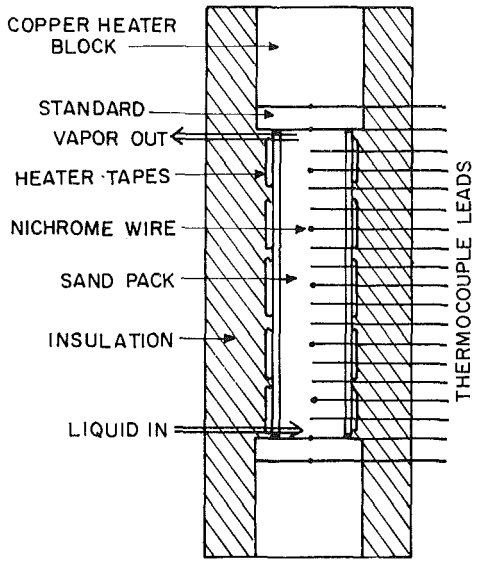

Fig. 1 *Experimental apparatus*

average core holder outside temperature at each of the five locations matched the sand pack centerline temperature. This procedure prevented radial heat flux within the sand pack and insured one-dimensional heat and mass transfer within the core holder. This condition was experimentally verified by measuring the heat fluxes across the top and bottom thermal conductivity standards. These fluxes matched within 4.3 percent for all experiments reported.

During the packing of the core, a pneumatic vibrator was pressed to the side of the core holder to obtain a minimum porosity. The porosity was determined from the core holder volume, the mass of the sand pack and the sand grain density. Prior to each experiment, air within the core holder was removed using a vacuum pump. Distilled water was then allowed to flow into the core until the sand pack was completely saturated. Before heating, a permeability test was run. The core was then brought to saturation temperature using the top and bottom heaters as well as the heating tapes. The temperatures of the heaters were then set such that the axial heat flux was downward; thus, the potential for intra-sand pack natural convection was eliminated. The fluid pressure was controlled during heating by a pressure regulator set slightly above atmospheric pressure. As the water evaporated, steam was bled off, condensed and collected in a graduated cylinder in order to obtain the average sand pack water pore volume fraction. Steady-state conditions were determined from the stabilization of all temperature and pressure data, as well as the absence of flow of steam in the bleed-off line. Cementation reported by other researchers [12] was avoided by the use of distilled water as the working fluid and by conducting all experiments on each sand pack within a span of two days to reduce the effect of silica dissolution. No evidence of cementation was observed during disassembly of the experiments.

Experimental Results

From these experiments, it was found that at steady-state conditions, three distinct regions appeared as shown in Fig. 2. The top region was above the steam saturation temperature with the temperature distribution being linear with respect to distance from the top standard. The bottom region, where measured temperatures were less than the saturation temperature, also exhibited a linear temperature profile. These results are expected for conduction-dominated heat transfer.

Thermal conductivities of these zones were calculated and compared to those reported by Gomaa and Somerton [1]. The thermal conductivities obtained from the liquid zone temperature profiles were 3.87 W/(m•K) and 2.48 W/(m•K) for the coarse and fine grain sands, respectively. These values compare reasonably well with the conductivity reported for a brine saturated 20-28 mesh Ottawa sand of 3.2 W/(m•K) [1]. On the other hand, the measured values of thermal conductivity of the vapor zone were 1.25 and 1.05 for the coarse and fine grain sand. Gomaa and Somerton report a conductivity of .45 W/(m•K) for a dry steam saturated 20-28 mesh Ottawa sand. This discrepancy will be discussed in a later section.

The region separating the top and bottom conduction zones was nearly isothermal with each measured temperature within 1°C of the saturation temperature as illustrated in Fig. 2. Since the temperature gradient in this region was small, the dominant mode of heat transfer was convection. It was deduced from conservation of energy and mass principles that there existed an upward mass flux of the liquid phase from the bottom to top of this isothermal zone due to capillary pressure differences. The heat flux at the top of this zone balanced the evaporation rate of the water with the resulting steam flowing counter current to the liquid flux. The potential for the vapor flow was a slight pressure gradient (decreasing pressure from top to bottom). The condensation rate of the steam at the

Nomenclature

a = constant in van der Waal's equation
b = constant in van der Waal's equation
f = nondimensional capillary pressure
f' = derivative of f with respect to s
g = gravitational constant
h_{fg} = enthalpy of evaporation
k = permeability
k_r = relative permeability
p = pressure
p_c = capillary pressure
$\tilde{p}_l$ = nondimensional liquid pressure
$\tilde{p}_v$ = nondimensional vapor pressure
q = downward heat flux
R = gas constant
r_e = effective meniscus radius
S = entropy
s = scaled liquid saturation
s_{li} = irreducible liquid saturation
T = temperature
v = fluid velocity
V = specific volume
x = distance from bottom of two-phase zone

Greek Symbols

β = liquid/vapor kinematic viscosity ratio
δ = nondimensional distance from bottom of two-phase zone
δ_l = length of two-phase zone
ϵ = sand porosity
μ = fluid dynamic viscosity
ν = fluid kinematic viscosity
ρ = fluid density
σ = vapor-liquid interfacial tension
Φ = fluid potential
ϕ = chemical potential
$\psi(T)$ = constant of integration
ω = nondimensional convective heat flux

Subscripts

b = vapor bubble
l = liquid phase
o = saturation conditions
v = vapor phase

Table 1 Summary of experimental conditions and results

Experiment	Grain size Mesh	Grain size dia. range (μm)	Porosity	Permeability (m^2)	Heat flux (w/m^2)	Two phase zone length (cm)	ω	δ_l	Top temp. °C	Bottom temp. °C
1.1	20-28	833-589	.33	1.39×10^{-12}	2260	7.7	1.52	.025	170.6	48.5
1.2	20-28	833-589	.33	1.39×10^{-12}	1660	8.7	1.12	.029	174.6	72.4
2.1	65-100	208-149	.38	6.41×10^{-12a}	1990	12.8	.282	.084	173.0	60.6
2.2	65-100	208-149	.38	6.41×10^{-12a}	1510	13.6	.224	.089	175.6	73.8
2.3	65-100	208-149	.38	6.41×10^{-12a}	1520	13.7	.226	.090	175.4	81.1
Su[11]	65-100	208-149	.38	6.41×10^{-12}	1210	20.1	.180	.132	112.1	86.7

[a]The permeabilities of Su[11] were assumed for identical grain sizes and porosity.

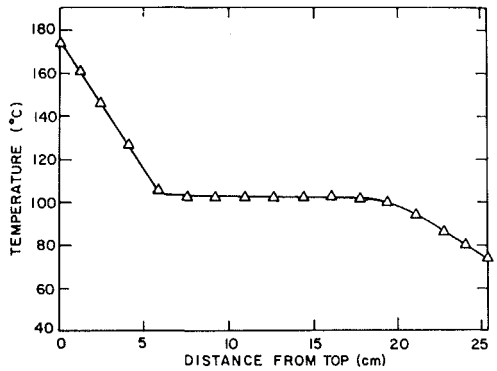

Fig. 2 Temperature profile of 65-100 mesh Ottawa sand: porosity of 38 percent, average saturation of 51 percent (by volume), heat flux of 1510 w/m^2

bottom of this zone balanced the heat flux to the liquid bottom region. Thus, the mass flux of the liquid, which was equal to the downward mass flux of the vapor, was simply equal to the heat flux divided by the heat of vaporization. This mode of heat transfer is analogous to the familiar heat pipe phenomenon.

The length of the two-phase zone was observed to decrease with increasing heat flux as shown in Table 1. The values for the two-phase zone length were obtained by extrapolating the linear profiles of the top and bottom zones to the temperature of the two-phase zone as shown in Fig. 2. This procedure results in approximate values of the true zone length, since the transitions from the conduction dominated zones to the convection region were smooth rather than abrupt. Also, the discrete nature of the temperature data precludes the availability of sufficient data at the transition points to accurately define an end of the constant temperature zone. It is also clear from the data given in Table 1 that the two-phase convection zones of the finer grain sand were longer than those of the coarser grain sand at comparable heat fluxes.

Hydrodynamic Analysis

The results of the experimental work presented in the previous section describe in a relatively general manner the macroscopic heat and mass transfer mechanisms characteristic of the porous system under study. From those experiments, it was concluded that in the central, two-phase zone a countercurrent flow of the liquid phase and vapor phase existed. The analysis of the hydrodynamics within that region can be approached through the application of flow in porous media considerations.

The superficial velocities of the liquid and vapor phases within the system shown in Fig. 3 can be expressed by the following representations of Darcy's Law for two-phase flow.

$$v_l = \frac{-\rho_l k k_{rl}}{\mu_l}\frac{d\Phi_l}{dx} \tag{1}$$

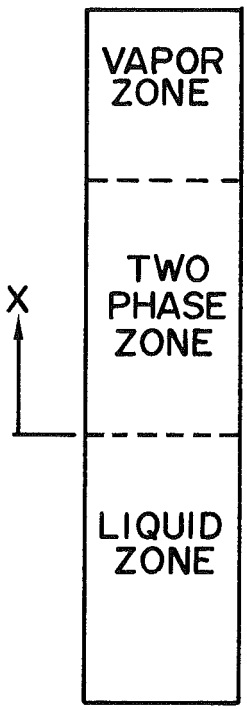

Fig. 3 Coordinate system

$$v_v = \frac{\rho_v k k_{rv}}{\mu_v}\frac{d\Phi_v}{dx} \tag{2}$$

where the liquid potential ($\Phi_{l,v}$) is defined by

$$\Phi_{l,v} \equiv \frac{p_{l,v}}{\rho_{l,v}} + gx \tag{3}$$

The variables k_{rl} and k_{rv} are the relative permeabilities of the liquid and vapor phases, respectively. The relative permeabilities account for the decreases in the mobility of one phase due to the presence of the second phase. Thus, each relative permeability varies in value from unity, if only that phase exists, to zero if the phase is immobile. The relative permeability of a particular phase is a function of the saturation of that phase as well as the interfacial tensions and viscosities of the two fluids.

The difference between the vapor and liquid pressure is defined as the capillary pressure, p_c.

$$p_c = p_v - p_l \tag{4}$$

The capillary pressure is the result of the effects of the interfacial tension between the two phases and can be evaluated by the expression given below.

$$p_c = \frac{2\sigma}{r_e} \tag{5}$$

The effective or mean meniscus radius, r_e, is defined by

$$\frac{2}{r_e} = \frac{1}{r_1} + \frac{1}{r_2} \tag{6}$$

where r_1 and r_2 are principal radii of curvature.

From the system under consideration, the upward liquid mass flux must equal the downward vapor mass flux.

$$\dot{m}_l = -\dot{m}_v \tag{7}$$

Since the two-phase zone is isothermal, the downward heat flux, q, must equal the vapor mass flux multiplied by the heat of evaporation.

$$-\dot{m}_v h_{fg} = q \tag{8}$$

By incorporating (8) and (7) into (1) and (2), and solving for the pressure gradients, the following result.

$$\frac{dp_v}{dx} = \frac{\nu_v q}{h_{fg} k r_{rv} k} - \rho_v g \tag{9}$$

$$\frac{dp_l}{dx} = \frac{-\nu_l q}{h_{fg} k r_{rl} k} - \rho_l g \tag{10}$$

Equation (9), subtracted from (10) results in the capillary pressure gradient.

$$\frac{dp_c}{dx} = \frac{q}{k h_{fg}} \left(\frac{\nu_v}{k r_{rv}} + \frac{\nu_l}{k r_{rl}} \right) + (\rho_l - \rho_v) g \tag{11}$$

Equation (11) can be nondimensionalized to give

$$\frac{df}{d\delta} = \omega \left(\frac{1}{k_{rv}} + \frac{\beta}{k_{rl}} \right) + 1 \tag{12}$$

where

$$f = \frac{p_c}{\sigma} \left(\frac{k}{\epsilon} \right)^{1/2}$$

$$\omega = \frac{-q \nu_v}{k h_{fg} (\rho_l - \rho_v) g}$$

$$\delta = \frac{x (\rho_l - \rho_v) g}{\sigma} \left(\frac{k}{\epsilon} \right)^{1/2}$$

$$\beta = \frac{\nu_l}{\nu_v}$$

$$s = \frac{s_l - s_{li}}{1 - s_{li}}$$

In defining s, the liquid saturation is scaled to include only mobile liquid saturations.

If it is assumed that the capillary pressure is a function only of s,

$$\frac{df}{d\delta} = \frac{df}{ds} \frac{ds}{d\delta} \tag{13}$$

Thus, the following first-order, linear differential equation can be integrated once f, k_{rv}, and k_{rl} are specified.

$$\frac{d\delta}{ds} = \frac{f'}{1 + \omega \left(\frac{1}{k_{rv}} + \frac{\beta}{k_{rl}} \right)} \tag{14}$$

Equation (14) was also obtained by Ogniewicz and Tien [9]. Equations (9) and (10) can be written in a nondimensional form by incorporating (14).

$$\frac{d\tilde{p}_v}{ds} = \frac{\omega f' / k_{rv}}{1 + \omega \left(\frac{1}{k_{rv}} + \frac{\beta}{k_{rl}} \right)} \tag{15}$$

$$\frac{d\tilde{p}_l}{ds} = \frac{-\omega \beta f' / k_{rl}}{1 + \omega \left(\frac{1}{k_{rv}} + \frac{\beta}{k_{rl}} \right)} \tag{16}$$

where

$$\tilde{p}_v = \frac{(p_v - p_{vo})}{\sigma} \left(\frac{k}{\epsilon} \right)^{1/2}$$

$$\tilde{p}_l = \frac{(p_l - p_{lo})}{\sigma} \left(\frac{k}{\epsilon} \right)^{1/2}$$

The pressures p_{vo} and p_{lo} are the vapor and liquid pressures at $\delta = 0$, respectively.

The vapor and liquid relative permeabilities reported by Fatt and Klikoff [13] can be represented by the following expressions:

$$k_{rl} = s^3 \tag{17}$$

$$k_{rv} = (1 - s)^3 \tag{18}$$

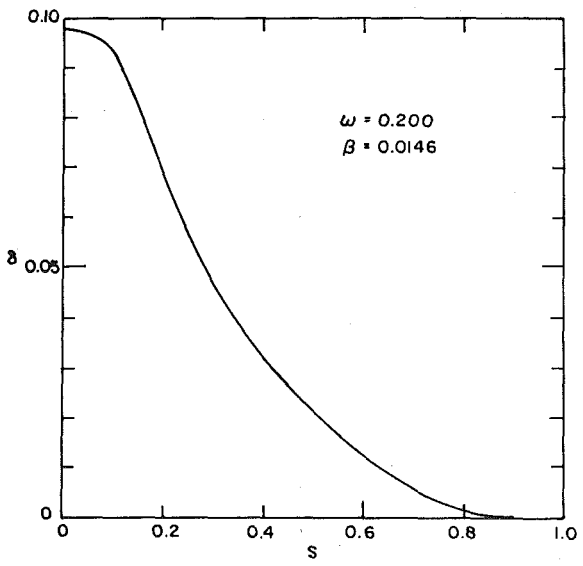

Fig. 4 Two-phase zone saturation profile for conditions similar to Fig. 2

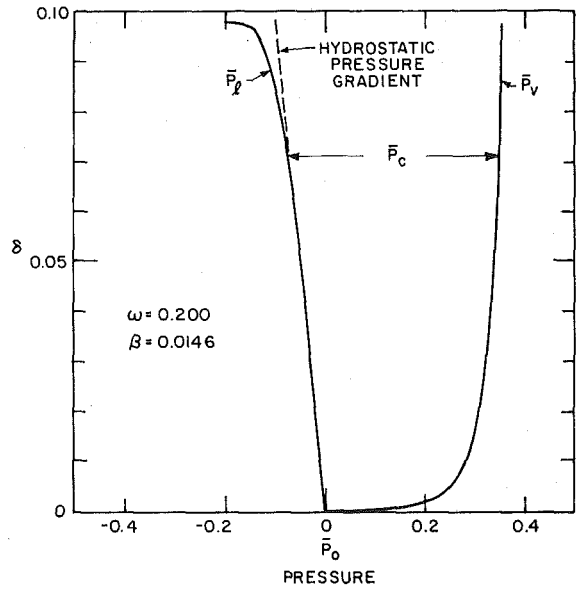

Fig. 5 Two-phase zone pressure profiles for conditions similar to Fig. 2

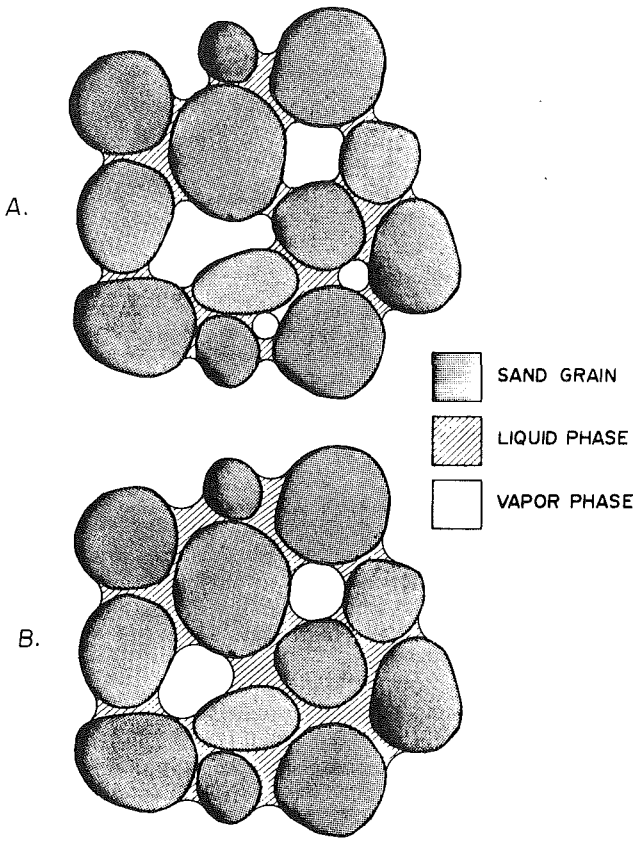

Fig. 6 Sand grain-liquid-vapor geometry: (*a*) near top of two-phase zone; (*b*) near bottom of two-phase zone

These forms of relative permeability are also suggested by Wyllie [14]. Imbibition capillary pressure data obtained by Leverett [15] was correlated well by the cubic polynomial of equation (19).

$$f = 1.417(1-s) - 2.120(1-s)^2 + 1.263(1-s)^3 \qquad (19)$$

The appropriate conditions at the bottom of the two-phase zone are

$$s \simeq 1 \quad \text{at} \quad \delta = 0 \qquad (20)$$

$$\bar{p}_v = 0 \quad \text{at} \quad \delta = 0 \qquad (21)$$

$$\bar{p}_l = 0 \quad \text{at} \quad \delta = 0 \qquad (22)$$

Given the correlations (17), (18), and (19) and the above boundary conditions, equations (14), (15), and (16) were integrated numerically for the saturation and pressure profiles. For conditions similar to those of Fig. 2, the profiles of Figs. 4 and 5 result.

As illustrated by Fig. 4, the saturation gradients near the top and bottom of the two-phase zone are high relative to those of intermediate locations. This is due to low liquid and vapor phase relative permeabilities at the end points. Since the vapor phase relative permeabilities at the bottom are small, the assumption of $s = 1$ at $\delta = 0$ can be justified although lesser saturations must exist in the real system. In fact, for $s \geq .9$ at $\delta = 0$, the results obtained from this analysis will remain nearly unaltered. The effects of the low endpoint relative permeabilities are also shown in Fig. 5 as high liquid and vapor pressure gradients. These large gradients account for a major portion of the total pressure drop. The liquid phase pressure variation is basically due to the hydrostatic pressure gradient, with additional loss due to low liquid saturations near the top. It is also clear from this figure that the vapor phase pressure loss is dominant, which is expected for low values of β.

Also of interest is the capillary pressure profile shown as the difference between the vapor and liquid pressures in Fig. 5. Implied in this figure is the condition of $p_{vo} = p_{lo}$ at $\delta = 0$, resulting from zero capillary pressure for $s = 1$ from equation (19). This condition was specified *a priori* in the correlation of equation (19) in order to insure that the limiting value of δ for $\omega \to 0$ be equal to the capillary suction height through the integration of equation (14). As in the saturation calculation, the pressure calculations are insensitive to the exact specification of s at $\delta = 0$ for $s \geq .9$, since the vapor relative permeabilities are small. The variation of the capillary pressures as shown in Fig. 5, in conjunction with the expression given in equation (5), allows a qualitative description of the macroscopic geometry of the two-phase system. Near the top of the two-phase zone, the capillary pressure is large thus the effective meniscus radius must be small. Conversely, the smaller capillary pressures near the bottom imply larger radii. Thus the geometries illustrated in Figs. 6(*a*) and 6(*b*) must exist. Near the top of the two-phase zone (Fig. 6(*a*)), the effective meniscus radius will approach the smallest radius of the smallest pore conditional on a funicular wetting phase distribution (connected wetting phase). A further decrease in r_e results in an immobile pendular-ring (disconnected wetting phase) distribution ($s = 0$). Near the bottom the meniscus radius, r_e will approach the largest radius of the largest pore as shown in Fig. 6(*b*).

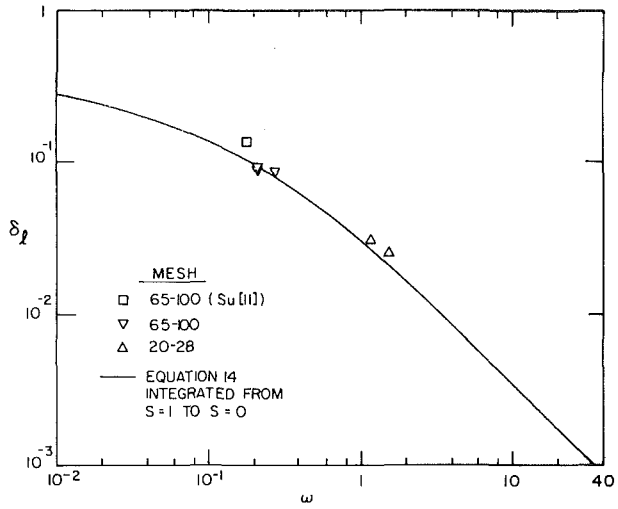

Fig. 7 Height of two-phase zone versus heat flux

Calculations were performed over a wide range of ω. The results of those calculations, shown with data obtained from experiments, are illustrated in Fig. 7. The length of the two-phase zone, δ_l, is shown to decrease with increasing ω. In all cases, δ_l was obtained from integrating equation (14) from $s = 1$ to $s = 0$. The match of the experimental data with the model is excellent considering the lack of accuracy in obtaining the two-phase zone lengths. The limiting conditions are $\delta_l \to .56$ for $\omega = 0$ (from the data of Leverett [15]) and $\delta_l \to 0$ as $\omega \to \infty$.

Thermodynamic Analysis

If the countercurrent flow of the vapor and liquid phase is to occur, a capillary pressure discontinuity must exist between the two phases within the convection zone. This pressure difference introduces a question as to the thermodynamic states of the liquid and vapor, which are in thermodynamic equilibrium locally. If the liquid phase is taken to be a saturated liquid, the vapor, which is in contact with the liquid but at higher pressure due to interfacial tension, would thus be a supercooled vapor, since the temperatures are equal. Due to the extremely unstable nature of supercooled vapors, one

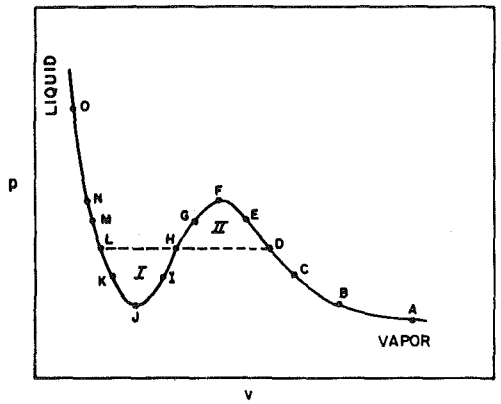

Fig. 8 Illustration of van der Waal's equation

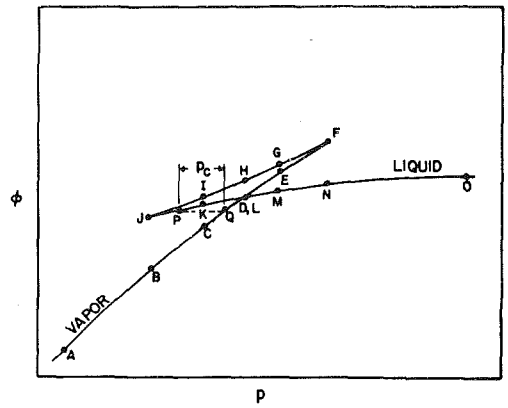

Fig. 9 Chemical potential of possible states at constant temperature

would not expect this state in a system with extremely high specific surface area as well as large numbers of nucleation sites. On the other hand, if the vapor were in a saturated state, the liquid phase would exist at a lower pressure because of the capillary pressure discontinuity. Therefore, the liquid state would be defined as superheated. Superheated liquids are metastable and become unstable if nucleation sites such as rough walls or liquid impurities are present. Both types of nucleation sites exist in abundance in most porous systems. Thus, one would not expect this state to exist either. The resolution of the question of thermodynamic states can be facilitated by the reexamination of the thermodynamics of phase change from fundamental principles.

The state of a fluid can be defined through the use of van der Waal's equation

$$p = \frac{RT}{v-b} - \frac{a}{v^2} \tag{23}$$

Equation (16) is shown at constant temperature in Fig. 8. The line segment JKLMNO in Fig. 8 corresponds to the liquid phase, whereas ABCDEF describes the vapor phase. The joining segment FGHIJ is an imaginary state since $\partial p/\partial v > 0$.

The condition necessary for thermodynamic equilibrium between two phases is the equality of the chemical potential (ϕ) of each. The chemical potential can be obtained from the Gibbs-Duhem relation.

$$d\phi = SdT + vdp \tag{24}$$

Integration along an isotherm results in

$$\phi = \int vdp + \psi(T) \tag{25}$$

where $\psi(T)$ is a constant of integration which is a function only of temperature. Equation (25) is shown qualitatively in Fig. 9. As the pressure of a liquid is decreased, the chemical potential of that liquid also decreases as defined by the segment ONML. At point L, an incremental decrease in pressure may result in one of two different possibilities, either the state defined by the path LJ or a phase transition to the vapor line segment ABCD. From the principle of minimum Gibbs free energy, the chemical potential of a substance must also be at a minimum. Thus, the higher chemical potential path LJ corresponds to an unstable state, that of a superheated liquid. The phase transition of a liquid to a vapor occurs then at point D,L. This is shown in Fig. 8 as a constant pressure increase in specific volume from point L to point D. The condition of equal chemical potential of the vapor and liquid in thermodynamic equilibrium results in the requirement that areas I and II be equal in Fig. 8. The boundaries of the vapor dome at a given isotherm are thus defined [16].

Within the two-phase zone of the sand pack, the liquid and vapor phases are in contact and at the same temperature, but exist at different pressures due to the effect of interfacial tension. This pressure difference is equal to the capillary pressure as given by equation (4). If the condition of thermodynamic equilibrium between the liquid and vapor phases is to be met, each phase must have the same chemical potential. Since the liquid pressure must be less than the vapor pressure, the only possible states are a superheated liquid phase and a corresponding superheated vapor phase, points P and Q, respectively, in Fig. 9. Keenan [17] reached the same conclusion for a liquid in a capillary tube in equilibrium with its vapor. The thermodynamic state of each phase is defined by the temperature and capillary pressure difference.

The question of the stability of the liquid phase can be resolved by postulating the existence of a vapor bubble within the liquid of a pore resulting from molecular energy fluctuations of the order of vapor energy. The pressure in the bubble can be determined from a force balance given by

$$p_b = p_l + \frac{2\sigma}{r_b} \tag{26}$$

The pressure of the vapor which is in thermodynamic equilibrium with the liquid phase in the two-phase porous system can be expressed by the combination of equations (4) and (5).

$$p_v = p_l + \frac{2\sigma}{r_e} \tag{27}$$

If the bubble radius (r_b) is less than the effective liquid-vapor meniscus radius (r_e), the bubble pressure will be greater than the vapor pressure. The state of the vapor therefore corresponds to a point on the line segment CQD above point Q in Fig. 9. Since that state results in a higher Gibbs energy than the superheated liquid state, the bubble will collapse back into the liquid phase. All bubbles thus formed will collapse unless the bubble radius equals the effective meniscus radius, which is the equilibrium condition. It is of interest to note that the effective meniscus radius is identical to the critical bubble radius used to establish the stability of a bubble within a superheated liquid. In a porous system, the effective liquid-vapor meniscus radius is generally larger than the radius of any bubble which could physically form within the pore containing the liquid. Therefore, the superheated liquid within that pore is unconditionally stable.

Given the foregoing description of the states of the vapor and liquid phases, the thermodynamic states can be quantified. The chemical potential of the vapor is given by

$$\phi_v = \phi_o - \int_{p_v}^{p_o} v_v dp_v \tag{28}$$

where ϕ_o and p_o are the chemical potential and pressure at

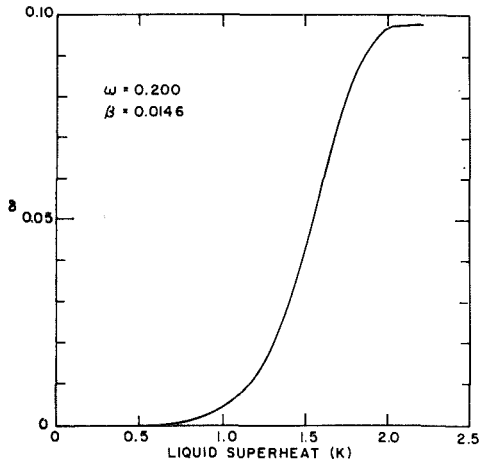

Fig. 10 Two-phase zone liquid superheat profile for conditions similar to Fig. 2

saturation. Assuming that the vapor specific volume can be accurately represented by the ideal gas law, integration of equation (28) can be performed resulting in the following.

$$\phi_v = \phi_o - \mathrm{RT}ln\frac{p_o}{p_v} \tag{29}$$

The superheated liquid chemical potential can be written as

$$\phi_l = \phi_o - \int_{p_l}^{p_o} v_l d\rho_l \tag{30}$$

Assuming that the change in the liquid specific volume can be neglected for the pressure differences, equation (30) becomes

$$\phi_l = \phi_o - (p_o - p_l)v_l \tag{31}$$

Since the liquid and vapor are in thermodynamic equilibrium, the right-hand sides of equations (29) and (31) can be equated resulting in the following

$$\mathrm{RT}ln\frac{p_o}{p_v} = (p_o - p_l)v_l \tag{32}$$

Through the use of equation (27), equation (32) can be rewritten as the following familiar Kelvin equation for vapor pressure lowering.

$$\frac{2\sigma}{r_e} = \rho_l \mathrm{RT}ln\frac{p_o}{p_v} - (p_o - p_v) \tag{33}$$

Equations (27) and (32) can be combined differently to obtain the equation for liquid pressure lowering.

$$p_o - p_l = \rho_l \mathrm{RT}ln\frac{p_o}{p_l + \dfrac{2\sigma}{r_e}} \tag{34}$$

The degree of superheat corresponding to conditions of Fig. 7 can be evaluated at each location. From equation (32), p_o was calculated by an iterative procedure given p_l and p_v at δ. The actual temperature was assumed to be the saturation temperature referenced to p_o. The saturation temperature corresponds to p_l. The liquid superheat, defined as the difference between the actual temperature and the saturation temperature, is shown as a function of δ in Fig. 11. For these conditions, superheat of 2 K and less are expected in the two-phase zone. The calculated actual temperature change from the bottom to top of this zone was 0.72 K, which agrees with measured temperatures. For lower permeabilities, the superheat was found to be higher since a larger p_c resulted.

Discussion

The experiments and analyses of this study describe many of the predominate interactions within a capillary-porous, two-phase system. Unlike bottom heating studies, instabilities due to buoyancy effects were eliminated, resulting in a stable, well-defined system, conducive to fundamental understanding. Since the two-phase zone was nearly isothermal and one-dimensional, the heat transfer analysis reduced to a two-phase, countercurrent flow analysis, driven primarily by capillarity and vapor pressure gradients. The description of the counterflow phenomena required the use of relative permeability and capillary pressure correlations. The form of these correlations are difficult to justify theoretically due to the extreme complexity of the porous medium geometry. Thus, the fact that these correlations predict observed phenomena must suffice for justification pending further investigation.

The extension of this analysis to similar bottom heating experiments conducted by Bau and Torrance [12] was attempted with only qualitative success, although it is clear that capillary pressure gradients did influence those results. Their observation of less than 1 K bottom superheat at the onset of two-phase boiling is supported by this analysis, and can be explained simply by the nucleation sites present at all vapor-liquid contacts: the r_e at those sites equal to (or for the observed phase change, larger than) the critical bubble radius.

The discrepancy between the vapor zone thermal conductivities measured in this work and the conductivities reported by Gomaa and Somerton [1] can be explained in part by the presence of superheated liquid in a pendular ring distribution at the grain contact points. The presence of superheated water at these locations will significantly increase the sand pack conductivity by decreasing the contact resistances. Also, the bed porosity and permeability reported by Gomaa and Somerton [1] were slightly higher implying increased grain-grain contact resistance.

The use of imbibition capillary pressures rather than drainage capillary pressures in the correlation of equation (19) follows from the thermodynamic analysis. Since the drainage data implies the locations of meniscus radii at the pore throats (resulting in the observed higher capillary pressures), the system would be thermodynamically unstable for a steam-water system. On the other hand, the imbibition data imply that the local meniscus radius corresponds to the largest r_e within the pore volume which was shown to be stable.

Conclusions

Several conclusions resulting from this research can be drawn and are summarized below:

1 For a sand-water-steam system heated from above such that the top temperature exceeds the saturation temperature and cooled at the bottom to a temperature below saturation, three regions will result if the pore diameters are sufficiently small: (*a*) a liquid, conduction-dominated region at the bottom, (*b*) a two-phase, isothermal, convection-dominated transition zone, and (*c*) a conduction-dominated vapor zone at the top.

2 The transfer of heat in the convection zone is due to the vaporization of the liquid at the top of the zone, the downward flow of a steam phase to the bottom due to a vapor pressure gradient; condensation and the upward flow of the liquid due to capillary pressure gradients.

3 The length of the two-phase zone increases with decreasing heat flux, limited by the capillary suction height as the heat flux approaches zero, and a length approaching zero as the heat flux becomes very large.

4 Both vapor and liquid within the two-phase zone are superheated, the liquid being unconditionally stable with the

effective meniscus radius equivalent to the critical bubble radius.

Acknowledgments

The assistance of M. W. Burr in performing the experiments is acknowledged. Funding for this research was provided by the California Institute of Mining and Mineral Resources, the College of Engineering, University of California, Berkeley, and Union Oil Company.

References

1 Gomaa, E. E., and Somerton, W. H., "The Behavior of Multifluid-Saturated Formations, Part II: Effect of Vapor Saturation—Heat Pipe Concept and Apparent Thermal Conductivity," SPE Paper 4896-B, Presented at the Society of Pet. Engineers California Regional Meeting, San Francisco, Calif., Apr. 1974.

2 Boyoucos, G. J., "The Effect of Temperature on the Movement of Water Vapor and Capillary Moisture in Soils," *Journal of Agriculture Research*, Vol. 5, 1915, pp. 141–172.

3 Winterkorn, H. F., "Fundamental Similarities Between Electro-Osmotic and Thermo-Osmotic Phenomena," *Highway Research Board Proceedings*, Vol. 27, 1947, pp. 443–455.

4 Taylor, S. A., and Cavazza, L., "The Movement of Soil Moisture in Response to Temperature Gradients," *Soil Science Society of America Proceedings*, Vol. 18, No. 4, 1954, pp. 351–365.

5 Luikov, A. V., "Systems of Differential Equations of Heat and Mass Transfer in Capillary-Porous Bodies," *International Journal of Heat and Mass Transfer*, Vol. 18, 1975, pp. 1–14.

6 Sahota, M. S., and Pagni, P. J., "Heat and Mass Transfer in Porous Media Subject to Fires," *International Journal of Heat and Mass Transfer*, Vol. 22, 1979, pp. 1069–1081.

7 Eckert, E. R. G., and Faghri, M., "A General Analysis of Moisture Migration Caused by Temperature Differences in an Unsaturated Porous Medium," *International Journal of Heat and Mass Transfer*, Vol. 23, 1980, pp. 1613–1623.

8 Ogniewicz, Y., and Tien, C. L., "Analysis of Condensation in Porous Insulation," *International Journal of Heat and Mass Transfer*, Vol. 24, 1981, pp. 421–429.

9 Ogniewicz, Y., and Tien, C. L., "Porous Heat Pipe," Paper 79-1093, AIAA 14th Thermophysics Conference, Orlando, Fla., June 1979.

10 Hansen, D., Breyer, W. H., and Riback, W. J., "Steady-State Heat Transfer in Partially Liquid Filled Porous Media," ASME JOURNAL OF HEAT TRANSFER, Aug. 1970.

11 Su, H. J., "Heat Transfer in Porous Media with Fluid Phase Change," Ph.D. thesis, University of California, Berkeley, 1981.

12 Bau, H. H., and Torrance, K. E., "Boiling in Low-Permeability Porous Materials," *International Journal of Heat and Mass Transfer*, Vol. 25, No. 1, pp. 45–55, 1982.

13 Fatt, I., and Klikoff, W. A., "Effect of Fractional Wettability on Multiphase Flow Through Porous Media," AIME Technical Note #2043, AIME Transactions, Vol. 216, 1959, p. 246.

14 Wyllie, M. R. J., "Relative Permeability," ch. 25, *Petroleum Production Handbook*, Vol. 2, edited by Frick, McGraw-Hill, New York, 1962.

15 Leverett, M. C., "Capillary Behavior in Porous Solids," *AIME Transactions*, Vol. 142, 1941, p. 152.

16 Callen, H. B., *Thermodynamics*, John Wiley & Sons, Inc., New York, 1960, p. 152.

17 Keenan, J. H., *Thermodynamics*, John Wiley & Sons, Inc., London, 1941, p. 437.

Single-Blow Transients in Packed-Bed Storage Units With Solid-Phase Conduction by Crump's Numerical Inversion of Laplace Transforms

P. -C. Lu
Department of Mechanical Engineering
University of Nebraska-Lincoln
Lincoln, Nebraska 68588
Mem. ASME

A robust and fast scheme for the numerical inversion of Laplace transforms, recently established by Crump, is applied to the linear problem of two-phase (solid-and-fluid) response of a packed-bed thermal storage unit during a single-blow operation, with solid conduction in the flow direction properly considered (while neglecting the conduction and energy storage in the fluid). The scheme is shown to be capable of handling implicit solutions in the transformed domain, which are themselves to be calculated numerically on a computer. The numerical results compare very well with those obtained by other methods of attack. The comparison also discloses some rather large errors in a set of data generated by a finite difference scheme as reported in the literature.

Introduction

Heat transfer from a fluid stream to a packed-bed thermal storage unit (as well as the related problem of transpiration cooling of porous slabs) has been treated numerically by many authors for the single-blow application of the fluid throughflow, employing either the *single-phase model* or the two-phase model *with the solid conduction neglected*. On the other hand, in works of a more general scope (e.g., [1-4]), the bed (or slab) is regarded as being semi-infinite in the flow direction, or subjected to rather unrealistic entrance conditions, or both. In the literature, we count only four works that deal with beds (or slabs) of finite dimension in the flow direction, with proper boundary conditions at the entrance, and with heat conduction (as well as energy storage) in the solid phase accounted for. In [5], Burch et al. calculated numerically (by finite difference) one example for a moderate value of the interphase Biot number, B. The present author, in [6], attempted an asymptotic investigation of the problem of Burch et al. for, among other cases, large values of B. The "single-phase" model treated by many authors (including Burch et al.), where it is "assumed" that the solid and the fluid share the same temperature distribution, was demonstrated in [6] to be the outer limit of the solutions as $B \to \infty$. A corresponding analysis of the inner limit in [6] revealed the existence of a thermal boundary layer near the entrance, in which the fluid temperature deviates drastically from the "single-phase" prediction. A similar analysis, with extensive numerical data, is carried out for time-varying flow rates in [7]. Finally, in [8], the influence of the thermal boundary layer (near the entrance) on the outer region farther away and the "reflected" influence on the boundary layer were investigated in great detail (for large B and single-blow flow rate).

In the present paper, we will attack the problem of [5-8], with unrestricted values of B, using a new scheme of numerical inversion of Laplace transforms proposed recently (1976) by Crump [9]. The procedure calls for an application of the Laplace transform. The problem in the transformed (complex) domain is then solved numerically on a computer. Numerical inversion following Crump is then employed to yield the solution in the physical domain.

The foregoing procedure, using the Laplace transforms for beds of finite dimension with solid conduction accounted for has already been outlined by Moreland [3] (albeit with unrealistic boundary conditions). Unfortunately, with only numerical-inversion schemes of the older generation available, Moreland [3] reported merely some limited results (no temperature histories were generated at all); both the speed and robustness of these schemes being rather deficient. In addition, Hiep [4] even outlined the procedure for the more complicated case with the conduction and energy storage in the fluid considered (but again with unrealistic boundary conditions). Using the same inversion scheme are Moreland [3], Hiep presented numerical data on the temperature history, but only for beds with semi-infinite dimensions in the flow direction.

This new generation of numerical inversion, which culminates in Crump's work [9], started its development in 1968 with the appearance of a paper [10] by Dubner and Abate. The method is then improved and execution time shortened by Simon, Stroot, and Weiss [11]. In the final version due to Crump [9], the numerical rate of convergence is further improved.

To demonstrate the power of Crump's scheme, our results are to be compared with data from three different sources: the finite difference solutions from [5], the two-term matched asymptotics from [8], and the yet-to-be-published data from [12] which employs an integro-differential formulation first reported in [6].

The Problem

Referring to Burch et al. [5][1], it can be shown that the equations governing the heat transfer in a packed-bed storage unit are

Contributed by the Heat Transfer Division for publication in the JOURNAL OF HEAT TRANSFER. Manuscript received by the Heat Transfer Division July 8, 1982. Paper No. 82-HT-9.

[1] With corrective modifications displaying the void fraction β. The discrepancies can be absorbed by redefining certain parameters; see footnote 2.

$$\frac{\partial^2 T_m}{\partial x^2} + \frac{h_v}{(1-\beta)K_m} \cdot (T_f - T_m) = \frac{1}{\alpha_m} \frac{\partial T_m}{\partial t} \tag{1}$$

$$-\rho_f V_0 C_f \frac{\partial T_f}{\partial x} = h_v (T_f - T_m) \tag{2}$$

where subscripts m and f denote, respectively, the porous medium (solid bed) and the fluid. Roughly speaking, equations (1) and (2) state the fact that there is no flow for $t<0$, and the solid is initially in thermal equilibrium with the stationary fluid filling it; for $t \geq 0$, fluid from a reservoir at T_{f_0} flow through the porous medium and exits, across a thermal boundary layer, into another *reservoir* still maintained at the initial temperature [5]. The mass flux $\rho_f V_0$ sets up a convective mechanism in equation (2) for $t \geq 0$. The initial condition to be enforced is

$$t=0: \; T_m = T_i, \text{ a constant} \tag{3}$$

No initial condition is enforceable on T_f since equation (2) ignores the energy storage (and heat conduction) in the fluid. Within the present scope, it is possible to have a thermal front propagating from $x=0$ to $x=L$. Before its arrival the true initial value of T_f prevails in the fluid; after its arrival, the theoretically predicted T_f-value takes over. To investigate the singularity associated with the discontinuity (if any) across this front belongs to some other (more general) study.

The boundary condition for the porous bed at the exit face, beyond which the initial (fluid) temperature prevails is

$$x=L: \; -K_m \frac{\partial T_m}{\partial x} = h(T_m - T_i) \tag{4}$$

At the entrance, there are two boundary conditions:

$$x=0: \; \rho_f V_0 C_f (T_{f_0} - T_f) = (1-\beta) h_f (T_{f_0} - T_m) \tag{5}$$

$$-K_m \frac{\partial T_m}{\partial x} = h_f (T_{f_0} - T_m) \tag{6}$$

where the first condition expresses the energy transfer (by convection) from the oncoming stream to the inlet face of the bed, and the second represents that (by conduction) from the inlet face to the interior of the solid medium [5]. (Although these boundary conditions (from [5]) are much more realistic, they are still deficient in that the variation of the fluid temperature before the entrance and after the exit is truncated. Future work can be done to improve the situation, if the energy storage and heat conduction in the fluid are considered, and if the range of investigation is extended beyond $0<x<L$.) Clearly, the thermal link between the solid and the fluid at the entrance is represented by h_f; that at the exit, h; and that (interphase) in the range $0<x<L$, h_v.

Introducing dimensionless quantities, as explained in the Nomenclature, into equations (1-6) yields[2]

$$\frac{\partial^2 \theta}{\partial \zeta^2} + \mathrm{B}(\nu - \theta) = \frac{\partial \theta}{\partial \tau'} \tag{7}$$

$$-g \frac{\partial \nu}{\partial \zeta} = \mathrm{B}(\nu - \theta) \tag{8}$$

$$\tau' = 0: \; \theta = 0 \tag{9}$$

$$\zeta = 0: \; \nu - 1 = S(\theta - 1) \tag{10}$$

$$gS(\theta - 1) = \frac{\partial \theta}{\partial \zeta} \tag{11}$$

$$\zeta = 1: \; \frac{\partial \theta}{\partial \zeta} + b\theta = 0 \tag{12}$$

where (in dimensionless terms) θ and ν are, respectively, the solid and fluid temperatures (above T_i); ζ is the distance in the flow direction across the bed; τ', the time; B, the interphase Biot number; g, the mass flow rate; and where S and b represent the thermal interaction at the bounding faces of the bed.

The Transformed Domain

Applying the Laplace transform

$$\bar{f}(p) = \int_0^\infty e^{-p\tau'} \cdot f(\tau') d\tau' \tag{13}$$

to our system, equations (7-12), we have

$$\frac{d^2 \bar{\theta}}{d\zeta^2} + \mathrm{B}(\bar{\nu} - \bar{\theta}) = p\bar{\theta} \tag{14}$$

$$-g \frac{d\bar{\nu}}{d\zeta} = \mathrm{b}(\bar{\nu} - \bar{\theta}) \tag{15}$$

[2] Note that, although the forms of equations (7-12) are exactly the same as in [5-7], B, S, and g are here modified by factors involving β. Our present belief is that, conceptually speaking, β should be displayed.

Nomenclature

a = real part of p
B = modified interphase Biot number, $(h_v L^2/K_m)/(1-\beta)$
b = hL/K_m
C = specific heat capacity, J/K•kg
C_1, C_2, C_3 = complex coefficients
E = error bound
$f(\ )$ = a function
$G_n(\ )$ = a sequence of functions, see equation (25)
g = $(L\rho_f V_0 C_f/K_m)/(1-\beta)$
h = exit heat transfer coefficient, W/m²•K
h_f = entrance heat transfer coefficient
h_v = effective volumetric (per unit volume of solid plus fluid) heat transfer coefficient between the two phases in the bed, W/m³•K
K = thermal conductivity, W/m•K
L = length of bed in the flow direction, m
M, M' = finite (real) numbers
p = complex parameter in a Laplace transform
S = $(1-\beta)h_f/(\rho_f V_0 C_f)$
T = temperature, K
T_{f_0} = temperature of *entering* fluid, far ahead of the entrance, K
t = time, s
V_0 = throughflow velocity upstream of bed, m/s
x = coordinate in the flow direction originating from the entrance, m
$Z, Z_1, Z_2 Z_3$ = complex numbers, see equations (20) and (21)
α = thermal diffusivity, m²/s
β = void fraction of bed
ν = $(T_f - T_i)/(T_{f_0} - T_i)$
ω = imaginary part of p
ρ = density, kg/m³
τ' = $\alpha_m t/L^2$
τ_0' = a fixed value of τ'
θ = $(T_m - T_i)/(T_{f_0} - T_i)$
Υ = a chosen time value
ζ = x/L
$\bar{(\ )}$ = Laplace transform of
Im( ) = imaginary part of
Re( ) = real part of

Subscripts

f = fluid stream
i = initial value
m = porous medium (solid bed)

$$\zeta=0:\ \frac{d\bar{\theta}}{d\zeta}-Sg\bar{\theta}=-\frac{Sg}{p} \tag{16}$$

$$(g\bar{\nu}=)g\left(1+\frac{p}{\mathrm{B}}\right)\bar{\theta}-\frac{g}{\mathrm{B}}\frac{d^2\bar{\theta}}{d\zeta^2}$$

$$=Sg\bar{\theta}-\frac{Sg}{p}+\frac{g}{p} \tag{17}$$

$$\zeta=1:\ \frac{d\bar{\theta}}{d\zeta}+b\bar{\theta}=0 \tag{18}$$

Eliminating $\bar{\nu}$, we obtain

$$\frac{g}{\mathrm{B}}\frac{d^3\bar{\theta}}{d\zeta^3}+\frac{d^2\bar{\theta}}{d\zeta^2}-g\left(1+\frac{p}{\mathrm{B}}\right)\frac{d\bar{\theta}}{d\zeta}-p\bar{\theta}=0 \tag{19}$$

subject to the boundary conditions (16-18).

Depending on the roots of the characteristic equation

$$\left(\frac{g}{\mathrm{B}}\right)Z^3+Z^2-g\left(1+\frac{p}{\mathrm{B}}\right)Z-p=0 \tag{20}$$

one can write down explicit forms of $\bar{\theta}$. For instance, if equation (20) yields three distinct roots[3], we would have

$$\bar{\theta}=C_1e^{Z_1\zeta}+C_2e^{Z_2\zeta}+C_3e^{Z_3\zeta} \tag{21}$$

where C_1, C_2, and C_3 are to be obtained algebraically by way of the boundary conditions (16-18).

For each ζ-value, and for each p chosen by the subroutine executing Crump's numerical scheme for the inversion of equation (13), a computer package will solve equation (20), and another will determine C_1, C_2, and C_3. When $\bar{\theta}(p)$ is calculated for enough p-values demanded by Crump's scheme, it will be inverted to yield $\theta(\tau')$ for the given ζ. Similarly, $\nu(\tau')$ is to be obtained by inverting

$$\bar{\nu}(p)=\left(1+\frac{p}{\mathrm{B}}\right)\bar{\theta}-\frac{1}{\mathrm{B}}\frac{d^2\bar{\theta}}{d\zeta^2} \tag{22}$$

Crump's Numerical Inversion

Since both $\theta(\tau')$ and $\nu(\tau')$ in the present problem approach certain finite steady distributions as $\tau'\to\infty$, we can restrict ourselves in equation (13) to cases where $|f(\tau')|\le M$, where M is a finite number. Then, the inversion formula

$$f(\tau')=\frac{1}{2\pi i}\int_{a-i\infty}^{a+i\infty}e^{p\tau'}\bar{f}(p)dp \tag{23}$$

would require only an integration along a vertical line at a (which is real) as long as $a>0$. Thus, writing $p=a+i\omega$ on this line, we have

$$f(\tau')=\left(\frac{e^{a\tau'}}{\pi}\right)\int_0^\infty[\mathrm{Re}\{\bar{f}(p)\}\cos\omega\tau'-\mathrm{Im}\{\bar{f}(p)\}\sin\omega\tau']d\omega \tag{24}$$

To perform the integration in equation (24) numerically, Crump introduces the following functions for $n=0$, 1, 2, ...

$$G_n(\tau')=f(\tau')e^{-a\tau'},\ 2n\Upsilon\le\tau'<2(n+1)\Upsilon \tag{25}$$

And for τ' outside of the interval from $2n\Upsilon$ to $2(n+1)T$, $G_n(\tau')$ is generated by the condition that they be periodic in $-\infty<\tau'<\infty$ with period 2Υ. Then, $G_n(\tau')$ are expanded into Fourier series and summed up over n. It is shown in [9] that the result can be written as

$$\sum_{n=0}^{\infty}G_n(\tau')=\frac{1}{\Upsilon}\left\{\frac{1}{2}\bar{f}(a)+\sum_{m=1}^{\infty}\left[\mathrm{Re}\left\{\bar{f}\left(a+\frac{m\pi i}{\Upsilon}\right)\right\}\cos\frac{m\pi\tau'}{\Upsilon}-\mathrm{Im}\left\{\bar{f}\left(a+\frac{m\pi i}{\Upsilon}\right)\right\}\sin\frac{m\pi\tau'}{\Upsilon}\right]\right\}$$

[3] The roots are practically distinct when the relative deviations of both their real and imaginative parts are respectively larger than, say, 10^{-4}.

Concentrating on the interval from 0 to 2Υ, we remember that

$$G_0(\tau')\equiv f(\tau')e^{-a\tau'}$$

So, to compute f at a desired instant τ_0' in the interval $(0, 2\Upsilon)$, we have

$$f(\tau_0')=\frac{e^{a\tau_0'}}{\Upsilon}\left\{\frac{1}{2}\bar{f}(a)+\sum_{m=1}^{\infty}\left[\mathrm{Re}\left\{\bar{f}\left(a+\frac{m\pi i}{\Upsilon}\right)\right\}\cos\frac{m\pi\tau_0'}{\Upsilon}-\mathrm{Im}\left\{\bar{f}\left(a+\frac{m\pi i}{\Upsilon}\right)\right\}\sin\frac{m\pi\tau_0'}{\Upsilon}\right]\right\}-E \tag{26}$$

where

$$E=e^{a\tau_0'}\sum_{n=1}^{\infty}G_n(\tau_0')$$

$$=e^{a\tau_0'}\sum_{n=1}^{\infty}\exp[-a(2n\Upsilon+\tau_0')]f(2n\Upsilon+\tau_0')$$

(for $0<\tau_0'<2\Upsilon$). For $|f(\tau')|\le M'$ in $(0, 2\Upsilon)$ where $M'\le M$,

$$E\le M'/(e^{2a\Upsilon}-1)\sim M'e^{-2a\Upsilon}$$

and the relative error becomes

$$E/M'\le e^{-2a\Upsilon} \tag{27}$$

In summing the series of equation (26), Crump recommends the use of Wynn's epsilon algorithm[4] based on Padé approximants [13-14] for accelerated convergence. The actual choice of Υ and a (which is not very influential) can be decided by systematic trial runs[5].

From the previous paragraph, it is obvious that the Gibbs phenomenon associated with summation of the Fourier series will generate numerical trouble whenever $f(\tau')$ jumps. In the present problem, this happens only at $\tau'=0$. Thus, we expect the computation to (*i*) converge only in the mean at $\tau'=0$, (*ii*) overshoot the true solution at $\tau'=0^+$; (*iii*) oscillate numerically and converge at a very slow rate near $\tau'=0$.

The phenomenon, however, is not particularly bothersome. In the first place, we know that for our problem

$$\lim_{\tau'\to0}\theta=0$$

$$\lim_{\tau'\to0}\nu=(1-S)\exp(-\mathrm{B}\zeta/g) \tag{28}$$

In the second, for all practical purposes, $\theta<0.005$ can be neglected; making it unnecessary to go below (say) $\tau'=0.005$ in the computation.

Finally, as a footnote, we may mention that (if more correct digits at smaller τ' are required) equation (7) can be simplified by noting equation (28):

$$\frac{\partial^2\theta}{\partial\zeta^2}-B\theta+\mathrm{B}(1-S)\cdot\exp(\mathrm{B}\zeta/g)=\frac{\partial\tau'}{\partial\theta} \tag{29}$$

This approximate equation for very small times can be solved under conditions (9), (11), and (12), by applying (for example) a generalized finite Fourier transform.

Numerical Results

Figure 1 shows a plot of θ (solid curves) and ν (crossed curves) versus ζ for $\mathrm{B}=5$, $g=1$, $S=0.4$, and $b=1$. In generating this plot, roughly 3 min are spent on an IBM 360/370 computer, using Crump's scheme with 13 terms summed in equation (26). In contrast, a similar generation in [8] (which uses *approximate* formulas) required about 5 min; in [12], on the order of 35 min. (The computing time is not available in [5].) Using the same scale for plotting, Fig. 1. is

[4] This algorithm is akin to Shanks' transformation (of high order) [14].

[5] Crump recommends $\Upsilon=0.8\cdot\tau_0'$; we did not always find this choice optimal, especially for small values of τ_0'.

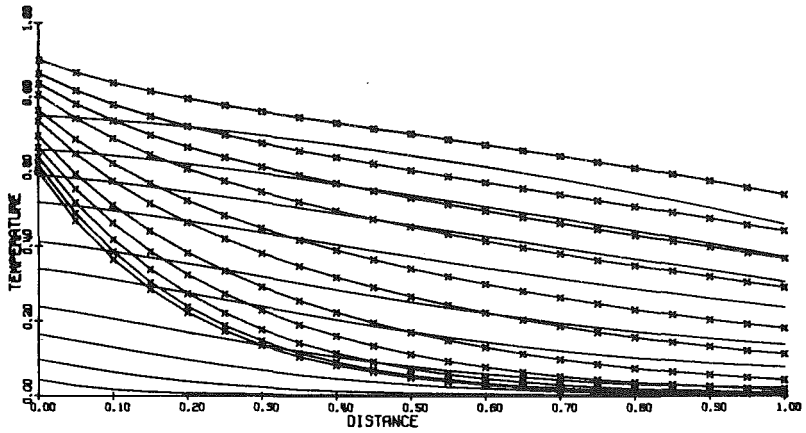

Fig. 1 Solid temperature θ (solid curves) and fluid temperature ν (crossed curves) versus distance ζ (B = 5, g = 1, S = 0.4, and b = 1). τ' values (from top down): for $\theta -$ ≥ 3, = 1, 0.7, 0.5, 0.3, 0.2, 0.1, 0.05, 0.02, 0.005; for $\nu -$ ≥ 3 = 1, 0.7, 0.5, 0.3, 0.2, 0.1, 0.05, 0.02, 0.005, ≤ 0.001.

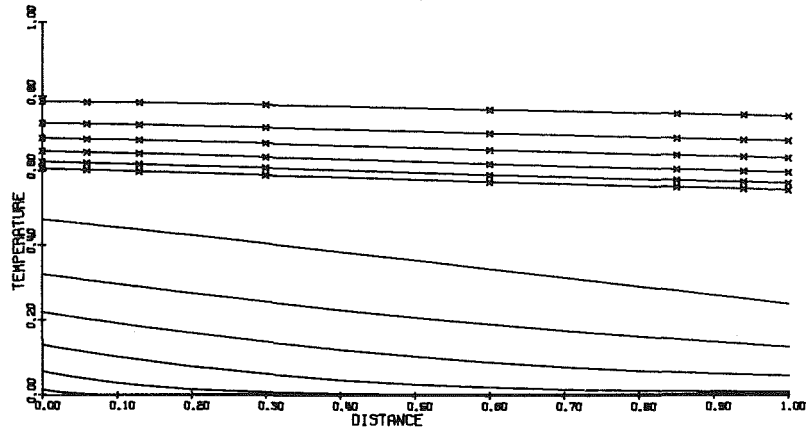

Fig. 2 Solid temperature θ (solid curves) and fluid temperature ν (crossed curves) versus distance ζ (B = 0.1, g = 1, S = 0.4, and b = 1). τ' values (from top down): for θ___ ≥ 3, = 1, 0.7, 0.3, 0.1, 0.02, 0.001, for ν___ ≤ 3 = 0.7, 0.3, 0.1, 0.02, ≤ 0.001.

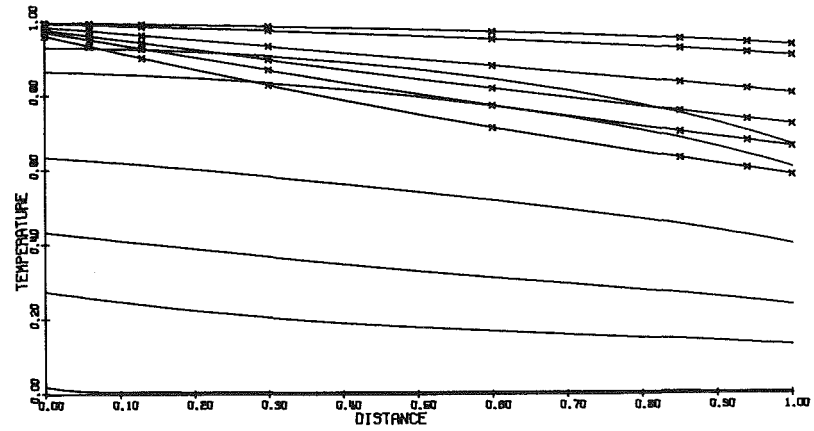

Fig. 3 Solid temperature θ (solid curves) and fluid temperature ν (crossed curves) versus distance ζ (B = 5, g = 10, S = 0.04, and b = 1). τ' values (from top down): for θ___ ≥ 3, = 0.5, 0.2, 0.1, 0.05, 0.001, for ν___ ≥ 3 = 0.5, 0.2, 0.1, 0.05, ≤ 0.001.

"identical" with the corresponding data in [12]. However, a digit by digit comparison with [12] shows the following for θ: (*i*) for $\tau' \geq 3$, the present calculation reproduces data in [12] to four significant digits; (*ii*) for $0.3 \leq \tau' < 3$, three reliable significant digits; (*iii*) for $\tau' = 0.3$, three digits form $\zeta = 0$ to 0.85, and two digits beyond $\zeta = 0.85$; (*iv*) for $\tau' = 0.2$, three digits from $\zeta = 0$ to 0.1, and two digits beyond $\zeta = 0.1$; (*v*) for $0.005 \leq \tau' < 0.02$, two digits where $\theta \geq 0.002$, and one digit where $\theta < 0.002$; (*vi*) for $\tau' = 0.001$, on digit where $\theta \geq 0.002$. (A similar comparison on ν is omitted here.) Since it is not likely that an engineering task will demand a simulation for $\tau' < 0.005$, we regard the present calculation to be satisfactory. In view of the short computing time needed, we can go one step further and recommend the present approach as a viable simulation tool in preliminary design work, not only for the present problem, but also for similar and more complex (but linear) tasks.

In comparing the present data (and, for all practical

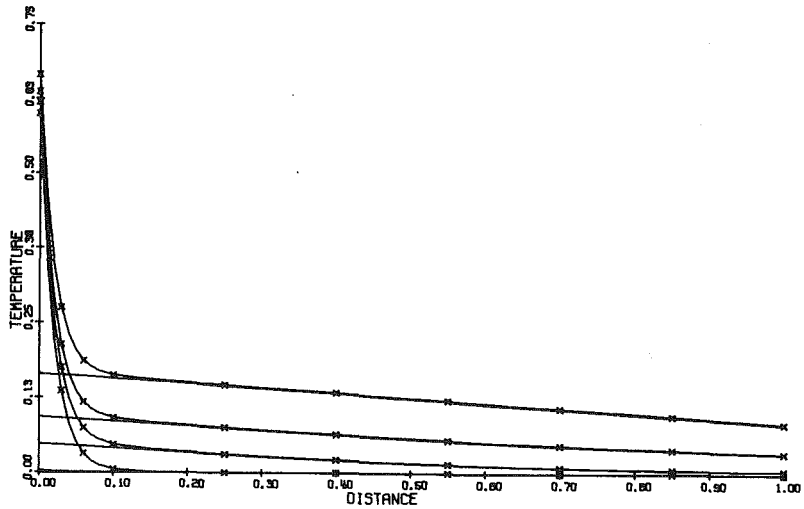

Fig. 4 Solid temperature θ (solid curves) and fluid temperature ν (crossed curves) versus distance ζ (B = 5, $g = 0.1$, $S = 0.4$, and $b = 1$). τ' values (from top down): for θ___ ≥ 3, = 0.7, 0.2, 0.001; for ν___ ≥ 3, = 0.7, 0.2, ≤ 0.001.

purposes, those of [12]) with those in [5] and [8], it is seen that data from [8], considering their approximate nature, are amazingly serviceable; while data from [5] are somewhat worse than expected, especially at $\tau' = 0.1$. (Since there is no detailed description in [5], it is impossible to tell whether its worse-than-expected result at $\tau' = 0.1$ is due to rough grids, numerical errors, mistakes in transposing data, or simply bad draftsmanship[6].)

Extensive calculations have been performed for a variety of combinations of parameter values; they all check very well (almost identical plots) against data from [12]. Figures 2–4 represent some samples from these calculations, where solid curves represent θ, and crossed ones indicate ν. In Fig. 2, we see that, as B decreases, the solid and fluid temperatures do not evolve into a common range anymore; and the fluid stream tends to keep within a narrow range of uniformity. In Fig. 3, a similar trend is showing up, owing to fast speed with which the fluid passes through the bed. Finally, Fig. 4 displays the trend when the rate of fluid flow becomes small. The asymptotic case with $g \to 0$ although not treated in [6], can be handled rather easily by going back to the governing system, equation (7-12). It is easily seen that there should be a thermal boundary layer in the fluid phase near the entrance, and an outer region farther downstream. In the outer region, $\nu \equiv \theta$ while the "one-phase" temperature evolves as a purely conductive process. All these, of course, are closely reflected in Fig. 4.

Acknowledgment

Mr. Zeng-Hwa Yang, Graduate Assistant, was very helpful in the numerical work. Financial support from the Research Council of the University of Nebraska-Lincoln is gratefully acknowledged.

[6] Data from [5] are only available in miniscaled plots.

References

1 Creswick, F. A., "A Digital Computer Solution of the Equations for Transient Heating of a Porous Solid Including the Effects of Longitudinal Condition," *Industrial Mathematics*, 1957, pp. 61–69.

2 Howard, C. P., "The Single-blow Problem Including the Effects of Longitudinal Conduction," ASME Paper No. 64-GTP-11, 1964.

3 Moreland, F. E., "Solution of the Single-blow Problem With Longitudinal Conduction by Numerical Inversion of Laplace Transforms," MS thesis, United States Naval Postgraduate School, Monterey, Calif., 1964.

4 Hiep, D. D., "Transient Heat Transfer in Porous Media," MS thesis, United States Naval Postgraduate School, Monterey, Calif., 1964.

5 Burch, D. M., Allen, R. W., and Peavy, B. A., "Transient Temperature Distributions Within Porous Slabs Subjected to Sudden Transpiration Heating," ASME JOURNAL OF HEAT TRANSFER, Vol. 98, 1976, pp. 221–225.

6 Lu, P. -C., "Perturbation Solutions of Transient Heat Transfer to a Porous Medium From a Fluid Stream," ASME JOURNAL OF HEAT TRANSFER, Vol. 103, 1981, pp. 159–164.

7 Lu, P. -C., and Hon, T. -L., "Single-Phase Response of a Packed-Bed Thermal Storage Unit to a General Variation in the Rate of Throughflow," *Proceedings of the Third Miami International Conference on Alternative Energy Sources*, to be published by Hemisphere Publishing Corp., Washington, D.C. (also, *Proceedings of Condensed Papers*, University of Miami, Coral Gables, Fla., 1980, pp. 105–107.)

8 Lu, P. -C., "Matched Asymptotic Expansion in Transient Solid-Fluid Response of Packed-Bed Thermal Storage Units," *Alternative Energy Sources*, IV *(Proceedings of the Fourth Miami International Conference on Alternative Energy Sources)*, Ann Arbor Science, Ann Arbor Mich., 1982, pp. 229–252; (also *Proceedings of Condensed Papers*, University of Miami, Coral Gables, Fla., 1981, pp. 19–21.)

9 Crump, K. S., "Numerical Inversion of Laplace Transforms Using a Fourier Series Approximation," *Journal of the Association for Computing Machinery*, Vol. 23, 1976, pp. 89–96.

10 Dubner, H., and Abate, J., "Numerical Inversion of Laplace Transforms by Relating Them to the Finite Fourier Cosine Transform," *Journal of the Association for Computing Machinery*, Vol. 15, 1968, pp. 115–123.

11 Simon, R. M., Stroot, M. T., and Weiss, G. H., "Numerical Inversion of Laplace Transforms with Application to Percentage Labeled Mitoses Experiments," *Computers and Biomedical Research*, Vol. 5, 1972, pp. 596–697.

12 Lu, P. -C., and Yang, Z. -H., "Numerical Prediction of Transient Single-blow Responses in Fluid-Solid Heat Exchange via an Integro-Differential Formulation," presented in the 16th Southeastern Seminar on Thermal Sciences, Apr. 19-21, 1982, Miami Beach, Fla.; to appear in the *Proceedings*.

13 Macdonald, J. R., "Accelerated Convergence, Divergence, Iteration, Extrapolation, and Curve Fitting," *Journal of Applied Physics*, Vol. 35, 1964, pp. 3034–3041.

14 Hemming, R. W., *Numerical Methods for Scientists and Engineers*, 2d ed., McGraw-Hill, New York, 1973.

T. Hung Nguyen

P. Vasseur

L. Robillard

B. Chandra Shekar

Department of Civil Engineering,
Ecole Polytechnique,
Université de Montréal,
Montréal, Quebec, Canada, H3C 3A7

Combined Free and Forced Convection of Water Between Horizontal Concentric Cylinders

This paper presents a theoretical study of combined free and forced laminar convection of a mass of water confined between two horizontal concentric cylinders with constant surface temperatures and subject to an externally-imposed constant pressure gradient along the axial direction. The governing system of differential equations is solved, within the Boussinesq approximation, by perturbation and finite difference methods, and the solutions are obtained in terms of the various characteristic parameters of the problem. Essentially, it is found that the flow pattern and the wall shear stress in the axial direction are significantly affected by the Prandtl and the Rayleigh numbers. Thus, the axial flow shows a tendency to develop in two or even three jets, depending on the Rayleigh number. The occurrence of the inversion of density, for water at 4°C, was found to modify completely the convective, or secondary flow, but to have little effect on the main, or axial, flow.

Introduction

Laminar flow heat transfer in annular passages is encountered in a wide variety of engineering situations, such as heat exchangers designed for chemical process, food industries, and biomedical applications. In most physical situations, mixed convection, i.e., combined free and forced convection, is present and much research remains to be done to understand the resulting interaction. In fact, previous theoretical as well as experimental studies were mainly concerned with either pure free convection or pure forced convection. For example, free convection within horizontal cylindrical annuli has been studied analytically [1, 2] and numerically [3–5] by many authors under various boundary conditions, while the laminar forced convection has been considered by Hatton and Quarmby [6] and Lundberg et al. [7], respectively. Recently, theoretical solutions for the mixed convection in horizontal concentric annuli have been obtained by Mojtabi and Caltagirone [8] and Hattori [9], who found that the secondary flows at high Rayleigh number can strongly distort the temperature and axial velocity profiles and significantly increase the average Nusselt number. Both studies were concerned with the effects of the Rayleigh number on the mixed convection of a fluid characterized by a linear density profile and fixed Prandtl numbers of .7 and 1, respectively.

In the present study, we consider the problem of combined free and forced convection of water contained between two isothermal concentric cylinders with an externally imposed constant pressure gradient along the axial direction. Our interest is due not only to the common occurrence of water in nature and technology, but also to its particular density profile and its wide range of Prandtl number. For example, as the temperature increases from 0 to 150°C, its Prandtl number decreases from 14 to 1 while its density reaches a maximum at 4°C. Past studies on the free convection of water [10–14] have in fact demonstrated that the effect of density inversion on the flow pattern, temperature distribution, and the Nusselt number was unexpectly large. In the present study, we shall investigate the interaction between the free and forced convection in terms of the various governing parameters of the problem. In particular, attention will be focused on the effects of Prandtl number, Rayleigh number, and density inversion on the fluid motion and the wall shear stress.

Mathematical Statement of the Problem

The geometry of the problem is shown in Fig. 1. The inner and outer cylinders, of radii r_i' and r_o', are maintained at temperatures T_i' and T_o', respectively. It is assumed that the externally imposed axial pressure gradient is constant, and the velocity profile in the fluid fully developed. All fluid properties, except the density in the buoyancy force, are taken to be constant and evaluated at the arithmetic mean temperature of the two cylinders, this assumption being valid when the temperature difference between the two cylinders is small enough. To determine the buoyance force, the following equation of state will be used

$$\rho' = \rho_r' \left[1 - \sum_{n=1}^{N} \beta_n' (T' - T_r')^n \right] \tag{1}$$

The governing equations of the present problem, using the Oberbeck-Boussinesq approximation [15, 16] and neglecting viscous dissipation and compressibility effects, then reduce to the following nondimensional system.

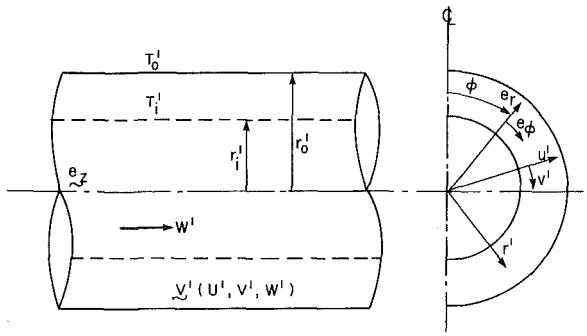

Fig. 1 Flow geometry and coordinate system

Contributed by the Heat Transfer Division for publication in the JOURNAL OF HEAT TRANSFER. Manuscript received by the Heat Transfer Division July 9, 1982. Paper No. 82-HT-13.

$$\frac{\partial \omega}{\partial t} = \mathrm{Pr}\,\nabla^2\omega - \left(U\frac{\partial \omega}{\partial r} + \frac{V}{r}\frac{\partial \omega}{\partial \phi}\right)$$

$$-\mathrm{Pr}\left(\frac{\cos\phi}{r}\frac{\partial}{\partial \phi} + \sin\phi\frac{\partial}{\partial r}\right)\sum_{n=1}^{N}\mathrm{Ra}_n T^n \tag{2}$$

$$\frac{\partial T}{\partial t} = \nabla^2 T - \left(U\frac{\partial T}{\partial r} + \frac{V}{r}\frac{\partial T}{\partial \phi}\right) \tag{3}$$

$$\frac{\partial W}{\partial t} = \mathrm{Pr}\,\nabla^2 W + K\mathrm{Pr} - \left(U\frac{\partial W}{\partial r} + \frac{V}{r}\frac{\partial W}{\partial \phi}\right) \tag{4}$$

where the stream function, Ψ, and the vorticity, ω, are defined respectively by

$$U = \frac{1}{r}\frac{\partial \Psi}{\partial \phi}, \quad V = -\frac{\partial \Psi}{\partial r} \tag{5}$$

$$\nabla^2\Psi = -\omega \tag{6}$$

Other notations are defined in the Nomenclature, and the following nondimensional variables and parameters will be used

$$r = r'/r_i', \qquad z = z'/r_i', \qquad t = t'\alpha' r_i'^2,$$

$$U = U' r_i'/\alpha', \qquad V = V' r_i'/\alpha', \qquad W = W'/W_m', \tag{7}$$

$$p = p' r_i'^2/\alpha'^2\rho_r', \quad \mathrm{Pr} = \nu'/\alpha' \qquad \mathrm{Re} = \frac{W_m' r_i'}{\nu'},$$

$$\mathrm{Ra}_n = \frac{g' r_i'^3}{\nu'\alpha'}\beta_n'(T_i' - T_r')^n, \quad T = (T' - T_o')/(T_i' - T_o')$$

and $K = 8/(R^2 + 1 - (R^2 - 1)\,1n^{-1}\,R)$ is related to the externally imposed constant pressure gradient according to the classical forced flow theory (see, for instance, [8]).

For the case of isothermal rigid boundaries, and due to the symmetry of the flows with respect to a vertical plane passing through the axis of the cylinders, we need only to consider the half space $0 \le \phi \le \pi$ with the following boundary conditions

$$\text{at } t = 0 \qquad \Psi = \frac{\partial \Psi}{\partial r} = W = T = 0, \forall\, r, \forall\, \phi \tag{8}$$

for $t > 0$,

$$r = 1, \qquad \Psi = \frac{\partial \Psi}{\partial r} = W = 0, \quad T = 1 \tag{9}$$

$$r = R, \qquad \Psi = \frac{\partial \Psi}{\partial r} = W = 0, \quad T = 0 \tag{10}$$

$$\phi = 0, \pi, \quad \Psi = \frac{\partial^2 \Psi}{\partial \phi^2} = \frac{\partial W}{\partial \phi} = \frac{\partial T}{\partial \phi} = 0 \tag{11}$$

Methods of Solution

Perturbation Analysis. In the case of weak convection, equations (2-4) can be solved by the perturbation method. Also, the density can be approximated by a second-degree polynomial

$$\frac{(\rho' - \rho_r')}{\rho_r'} = -\beta_1'(T' - T_r') - \beta_2'(T' - T_r')^2 \tag{12}$$

where the coefficients β_1' and β_2' are functions of T_r' and can be chosen such that this equation is accurate to within a few percent over a temperature range of 10°C [17]. It should be noted that this limitation is largely compensated by the fact that, on the basis of this equation of state, one can predict all the essential features associated with the nonlinearity as well as the inversion of the density by introducing just one more parameter as compared to the classical case of a linear density profile.

From the above equation of state, it is appropriate to define a nonlinear Rayleigh number

$$\hat{\mathrm{Ra}} = \mathrm{Ra}_2 \tag{13}$$

together with a second parameter, namely the inversion parameter

$$\gamma = \frac{\mathrm{Ra}_1}{\mathrm{Ra}_2} = -2\frac{(4°\mathrm{C} - T_o')}{(T_i' - T_o')} \tag{14}$$

which essentially indicates the position of the maximum density with respect to the cavity walls.

The steady-state solutions for U, V, and T have already been obtained in the past, solving the governing equations (2), (3), (5), and (6) by a perturbation method in the form of powers series of $\hat{\mathrm{Ra}}$ [17]. The value of the axial velocity, W, may be obtained in a similar way as

$$W = \sum_{m=1}^{\infty}\hat{\mathrm{Ra}}^{m-1} W_m \tag{15}$$

By substituting equation (15) into equation (4) and equating terms of the same order in $\hat{\mathrm{Ra}}$, we readily obtain the following hierarchy of linear inhomogeneous equations.

Nomenclature

A = size parameter, $g' r_i'^3/\alpha^2$
$\mathbf{e}_i, \mathbf{e}_\phi, \mathbf{e}_z$ = unit vectors in the cylindrical coordinate system
g' = gravitational acceleration
p = pressure
Pr = Prandtl number, ν'/α
r, ϕ, z = cylindrical coordinates
$\mathfrak{R}$ = ratio of mean shear stresses on the inner an outer cylinders, $|\bar{\tau}_{zi}|/|\bar{\tau}_{zo}|$
R = radius ratio, r_o'/r_i'
Ra = Rayleigh number, $g'\beta_1' r_i'^3(T_i' - T_o')/\nu'\alpha'$
$\hat{\mathrm{Ra}}$ = nonlinear Rayleigh number, $g'\beta_2' r_i'^3(T_i' - T_o')^2/\nu'\alpha'$
Ra_n = nth Rayleigh number
Re = Reynolds number, $W_m' r_i'/\nu'$
T = temperature
t = time
U, V, W = velocity components in the r-, ϕ-, and z-directions, respectively
$\mathbf{V}$ = total velocity
W_m^* = mean velocity of the forced convection

Greek Symbols

α' = thermal diffusivity
β_n' = volumetric coefficient of expansion (see equation (1))
γ = inversion factor $\mathrm{Ra}_1/\mathrm{Ra}_2$
ν' = kinematic viscosity
ρ' = density
Ψ = stream function
ω = vorticity
τ_ϕ = local wall shear stress in the ϕ-direction, $\tau_\phi = \partial v/\partial r$
τ_z = local wall shear stress in the z-direction, $\tau_z = \mathrm{Re}\,\mathrm{Pr}\,\partial W/\partial r$
τ_z^* = wall shear stress due to pure forced convection

Subscripts

i = inner cylinder
m = mean value
o = outer cylinder
r = reference state
MAX = maximum value
MIN = minimum value

Superscript

' = denotes dimensional variables
$-$ = refers to average value
* = refers to pure forced convection

$$\nabla^2 W_m = \sum_{i=1}^{m} \frac{1}{r\,\mathrm{Pr}} \left[\frac{\partial W_{m-i}}{\partial r} \frac{\partial \Psi_i}{\partial \phi} - \frac{\partial W_{m-i}}{\partial \phi} \frac{\partial \Psi_i}{\partial r} \right], \quad m>1 \tag{16}$$

where

$$W_1 = -\frac{K}{4}\left[(r^2-1) - \frac{(R^2-1)\ln r}{\ln R} \right] \tag{17}$$

subject to the following boundary conditions

$$\begin{aligned} W_m &= 0 \quad \text{at} \quad r = 1, R \\ \frac{\partial W_m}{\partial \phi} &= 0 \quad \text{at} \quad \phi = 0, \pi \end{aligned} \tag{18}$$

The above system can be solved successively to any desired order. However, as the recurrence proceeds, the algebraical expressions become rapidly cumbersome, details of the interaction between the various parameters are lost and no additional physical insight is gained by the inclusion of further terms. We therefore limit expansion (15) to third-order terms such that

$$W = \sum_{m=1}^{3} \hat{\mathrm{Ra}}^{m-1} W_m \tag{19}$$

Using the method of separation of variables, one can solve successively the hierarchy of equations (16-18) and obtain solutions of the form

$$W_m = \sum_{i,j,k} C_m(i,j,k)\, r^{i-m} \ln r^{j-1} \cos(k-1)\phi \tag{20}$$

where the summations are over indices i, j, and k, and the coefficients A_m (i, j, k) B_m (i, j, k) and C_m (i, j, k) are, in general, functions of the parameters Pr, R, and γ. Readers interested in these coefficients, which have been stored in a computer memory to save space, are invited to write to the authors. A detailed discussion on the range of validity of the perturbation solutions can be found in the paper by Nguyen, Vasseur and Robillard [17].

Numerical Analysis. In the preceeding section, the perturbation solutions up to the third-order terms have been derived for the case of small free convection effects on a predominantly forced flow. This type of analysis has the advantage to yield a through qualitative understanding of the problem. However, to study the case of strong convection lying beyond the range of applicability of the above perturbation solutions, the system of equations (2-4) have been solved numerically, using a two-dimensional alternating direction procedure (A.D.I.) similar to that used by Mallison and de Vahl Davis [18]. The first and second derivative were approximated by central differences and the time derivatives by a first-order forward difference. The finite difference forms of the equations were written in conservative form for the advective terms in order to preserve the transportive property [19]. The stream function equation (6) was solved by the method of successive overrelaxation (S.O.R.) which was then used to obtain the velocities and the wall vorticity. The major disadvantage of the S.O.R. method is the take of choosing the optimum relaxation coefficient for a given situation. For the present problem it was found that a relaxation factor of 1.8 was an optimum value and the iterative procedure was repeated until the following condition was satisfied

$$\mathrm{Max} \left| \frac{\Psi_{i,j}^{n+1} - \Psi_{i,j}^{n}}{\Psi_{i,j}^{n+1}} \right| \leq 0.5 \times 10^{-3}$$

where the subscripts (n) and $(n+1)$ indicate the values of the nth and $(n+1)$th iterations, respectively. A useful method for checking the convergence of the steady-state solution was to compare the average Nusselt number for the inner and outer cylinder.

Several different mesh sizes have been used, the choice depending largely on the size of the cavity. The mesh size in the r-direction ranged from $\Delta r = 1/18$ to $1/30$. In the ϕ-direction, a mesh size of $\Delta\phi = \pi/18$ to $\pi/30$ was chosen. Typical values of the time step were 0.0001 and 0.0005. The total time steps ranged from 1600 to 2500 and the corresponding computing time was from 530 to 680 s on the IBM 360/70 computer.

In order to verify the consistency of the present numerical study, the first cases considered were those corresponding to already published results on fluids with linear temperature - density relationship. A full description of the results obtained and a discussion on the accuracy of the present numerical procedure are presented in [11]. When considering the temperature range 0-20°C, the equation of state of water, equation (1), can be approximated by a fourth-order polynomial [20] with an error of less than one unit at the last digit of the tabulated data of Landolt-Börnstein [21].

In order to save computing time, the perturbation solutions for Ψ, W, and T for a low Rayleigh number were used as the initial guesses to start the numerical procedure. After the new solutions converged completely, they were used as initial guesses for the next computation. Thus, the numerical computation proceeded in turn to the calculation for higher Rayleigh number. Computing time was found to increase gradually with increasing Rayleigh number. To expedite plotting of the results, a CALCOMP 563 automatic plotter was used.

Results and Discussion

Before presenting the results, it should be noted that the mixed convection considered here can be separated into two parts. The first one is the natural convection flow in the (r, ϕ) plane, arising from the temperature difference between the two cylinders. The second one is the axial flow along the annulus. In fact, as the problem is independent of the z-coordinate, the axial velocity, W, has no effect on the free convection that arises in the (r, ϕ) plane. Inversely, while this latter moves the fluid particles around, it does disturb the distribution of the axial velocity within the annular space. This "one way" interaction between free and forced convection is expressed by the fact that equations (2-3) are independent of W while equation (4) is governed by both the free and forced terms. Therefore, all previous existing solutions of equations (2) and (3), for pure natural convection within isothermal annuli (see for instance [22-24]), can be directly applied to the present problem by simply computing, from equation (4), the axial velocity profile, W, from the existing results for U and V. In particular, the results of [11], concerning the effect of density inversion on the natural convection of cold water within a horizontal annulus, will be used to study the influence of this phenomena on W. Finally, it should be noted that equation (4) does not depend explicitely on the Reynolds number as in the case of [8]. This results from the way the axial velocity, W, has been normalized in the present study.

In order to verify the consistency of the present numerical study, the first cases considered were those corresponding to already published results. The influence of natural convection on the forced flow between horizontal concentric cylinders has been studied recently by Mojtabi and Caltagirone [8] for the case of a fluid with linear temperature-density relationship. Results for the axial velocity, W, were obtained for Pr = 0.7, Re = 2, R = 2 and Rayleigh numbers, Ra, varying between 0 and 10^4. The current analysis reproduced most of their results with a precision of about 2 percent. Furthermore,

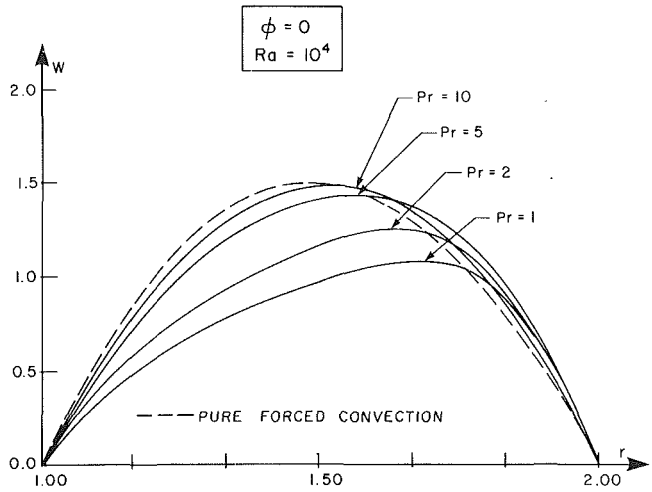

Fig. 2(*a*) Axial velocity distributions at ϕ = 0 deg as a function of Prandtl number Pr for Ra = 10^4 and R = 2

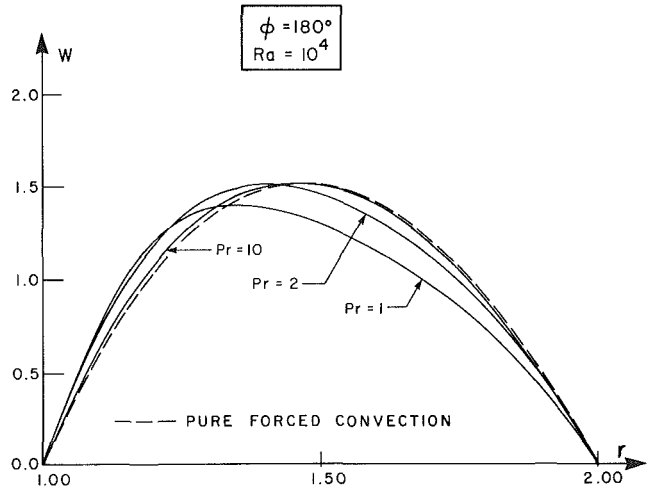

Fig. 2(*b*) Axial velocity distributions at Φ = 180 deg as a function of Prandtl number Pr for Ra = 10^4 and R = 2

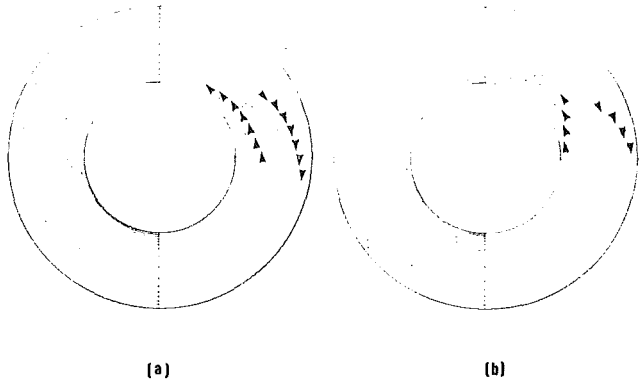

Fig. 3 Streamlines and isovelocities for R = 2, Pr = 1.0. The values of Ra, Ψ_{MAX}, $\Delta\Psi$, W_{MAX}, and ΔW are (*a*) Ra = 5 × 10^3, Ψ_{MAX} = 9.60, $\Delta\Psi$ = 1.20, W_{MAX} = 1.54, ΔW = 0.11; (*b*) Ra = 5 × 10^4, Ψ_{MAX} = 29.0, $\Delta\Psi$ = 3.63, W_{MAX} = 1.58, and ΔW = 0.11.

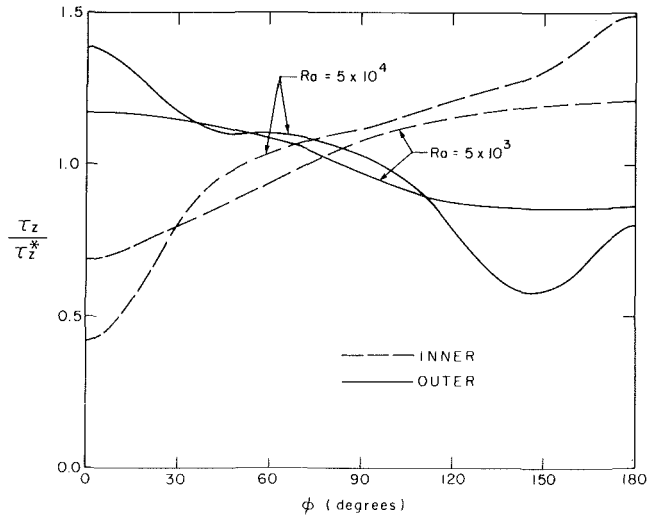

Fig. 4 Angular variation of the ratio of local wall shear stress to shear stress due to pure forced convection for R = 2 and Pr = 1.0

the flow patterns predicted by the numerical study were also compared with the perturbation solution, equation (20), for various combinations of R, Ra, and Pr. Essentially, it was found that both solutions were in good agreement when $\overline{Nu} < 1.2$ (corresponding, for example, to the case Pr = 1, R = 2 and Ra $\simeq 3 \times 10^3$). A discussion on the validity of the present perturbation solution is given in [17].

The results presented below cover the case of water with a temperature between 0 and 150°C. Within this range, the Prandtl number varies between approximately 14 and 1, while the water density passes through a maximum at about 4°C. The influence of the Prandtl number on the axial velocity, W, has not been considered by Motjabi and Caltagirone [8] and will be first discussed here for the case of a fluid with a linear equation of state. Then the effect of the inversion of density, which occur for water at a temperature in the vicinity of 4°C, will be considered.

The effect of the Prandtl number, Pr, on the axial velocity, W, at ϕ = 0 and 180 deg is illustrated in Figs. 2(*a*) and 2(*b*), respectively for the case Ra = 10^4 and R = 2. The dotted line on this graph indicates the axial velocity profile in the case of pure forced convection. It is seen that as the Prandtl number is increased the values of the axial velocity tend toward those predicted by the pure forced convection theory. This result can be predicted from equation (4), where the convective term, representing the interaction between the free and forced motion, is proportional to Pr^{-1} and therefore becomes negligible for Pr > 10. The axial velocity profile is then practically the same as that of pure forced convection. It is also noted that, for a given Prandtl number, the influence of the natural convection on the axial velocity, W, is stronger at ϕ = 0 deg than at ϕ = 180 deg. For the position $\phi = \pi/2$ the results obtained, but not presented here, were very close to those predicted by the pure forced convection theory. A similar trend has been observed by Mojtabi and Caltagirone [8] while studying the effect of the Rayleigh number on the axial velocity, W.

Figure 3 shows typical results obtained for annuli with radius ratio R = 2, Prandtl number Pr = 1.0 and Rayleigh numbers Ra = 5 × 10^3 and 5 × 10^4, respectively. The problem under consideration being symmetrical with respect to a vertical axis, the streamlines for the flow pattern resulting from the natural convection in the (r, ϕ) plane, are represented on the right half of the cavity and the isovelocities, for the axial flow in the z-direction, on the left half. To expedite plotting of the results, an auxiliary computer program was used to locate points lying on specified streamlines and isovelocities. The behaviour of the streamlines, resulting from the natural convection, has been

discussed extensively in the past and are presented here for reference only. Attention will be focused on the flow pattern in the axial direction. The corresponding angular variation of the wall shear stress, τ_z, normalized to the pure forced convection shear stress, τ_z', is presented in Fig. 4.

In the absence of natural convection (i.e., Ra = 0), the pure forced flow in the axial direction is characterized by isovelocities in the (r, ϕ)-plane, consisting of concentric circles. The effect of the natural convection on this basic flow pattern is depicted on Fig. 3. When the convective motion is relatively small ($Ra = 5 \times 10^3$), Fig. 3(*a*) shows that the streamlines have the well-known kidney shape and the cell occupy the whole cavity, having its center at about 80 deg. The effect of the free convection is to reduce the speed of the axial flow at the top and to increase it at the bottom of the inner cylinder. The opposite effect is observed on the outer cylinder. A region of maximum velocity, having its center at about 80 deg, may also be observed in the flow pattern. As a result, Fig. 4 shows that the angular variation of the wall shear stress in the axial direction is now not constant, as in the case of a pure forced flow, but is maximum at the top of the outer cylinder and the bottom of the inner one, and minimum at the bottom of the outer cylinder and the top of the inner one. As the Rayleigh number is increased, it is seen from Fig. 3(*b*) that the convective cell is moving up, its intensity is enhanced, and a region of stagnant fluid is appearing at the bottom of the cavity. The flow pattern for the axial velocity is now considerably perturbated by the convective motion. Thus the region of maximum velocity is moving up and a second jet is developed with a maximum of velocity at the bottom of the cavity. As a result it is seen from Fig. 4 that the shear stress on the outer cylinder passes through a minimum at about 150 deg rather than at the bottom of the cylinder, the zone of lower velocity gradient being now located between the two jets.

From the equilibrium of the forces acting in the axial direction, it may be shown that the mean shear stresses, $\bar{\tau}_{zi}$ and $\bar{\tau}_{zo}$, on the inner and the outer cylinder, respectively, are related to the axial pressure gradient by the following relationship

$$|\bar{\tau}_{zi}| + R\,|\bar{\tau}_{zo}| = K\frac{(R^2-1)}{2} \tag{21}$$

The values of $\bar{\tau}_{zi}$ and $\bar{\tau}_{zo}$ have been evaluated numerically, using Simpson's rule and a three-point, finite difference approximation for $\partial W/\partial r$, for various values of the Rayleigh number, Ra. It was found that for $R = 2$ and $Ra \leq 5 \times 10^4$ the above equation was satisfied with an error of less than 2 percent.

Furthermore, it is seen from equation (21) that, for a given radius ratio, R, and axial pressure gradient, $\partial p/\partial z = -K\,\mathrm{Re}\,\mathrm{Pr}^2$, the sum of the shear stresses on the inner and outer cylinders remains constant, independently of the Rayleigh, Prandtl, and Reynolds numbers. On the other hand the ratio of the mean shear stresses on the inner and outer cylinder, $\Re = |\bar{\tau}_{zi}|/|\bar{\tau}_{zo}|$ is a function of the natural convection, that is of the Rayleigh and Prandtl numbers. In the limit of pure forced convection, (Ra = 0), it may be shown that this ratio is given by

$$\Re = -\frac{R(1-R^2+2\ln R)}{1-R^2(1-2\ln R)} \tag{22}$$

i.e., $\Re = 1.268$ when $R = 2$. For values of Ra different from zero, the numerical results obtained, Fig. 5 show, that this ratio is increasing with increasing Ra and decreasing Pr. For instance it was found that for $Ra = 3 \times 10^4$ and Pr = 1, $\Re$ = 1.415. This result indicates that the repartition of the total stress in the axial direction between the two cylinders is affected, although, as a whole, the total shear remains constant in order to balance the pressure gradient. As a consequence of the perturbation brought by the free convection on the shear stress, less flow rate is required to produce the same amount of shear.

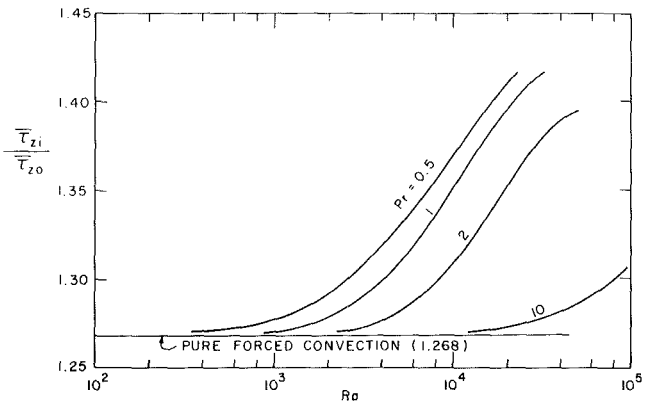

Fig. 5 Ratio of the average shear stresses on the inner or outer cylinders as a function of Rayleigh number, Ra, and Prandtl number, Pr

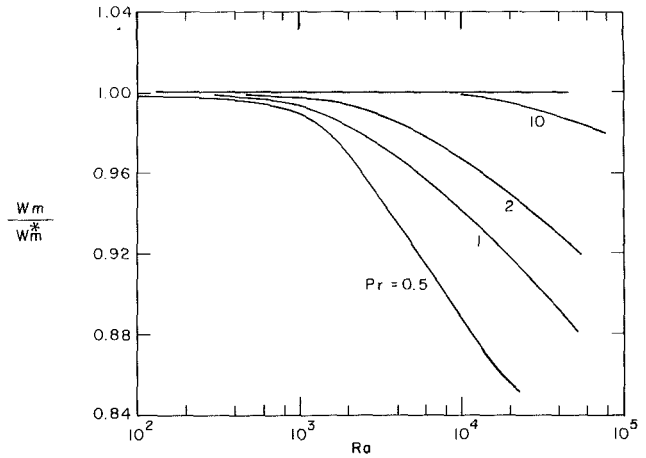

Fig. 6 Space average velocity, W_m, as a function of Rayleigh number, Ra, and Prandtl number, Pr

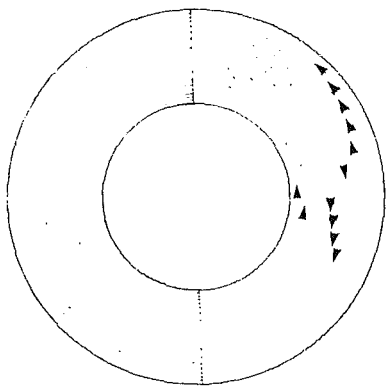

Fig. 7 Streamlines and isovelocities for $R = 2$, Pr = 11.65, $\hat{\mathrm{Ra}} = 2400$, $\gamma = -0.77$, $\Psi_{MAX} = 0.89$, $\Psi_{MIN} = -5.20$, $\Delta\Psi = 0.89$, $W_{MAX} = 1.50$, $\Delta W = 0.107$

Figure 6 shows the space average velocity, W_m, normalized with respect to the space average velocity, W_m^* for pure forced convection, as a function of the Rayleigh number, Ra, for various Prandtl numbers, Pr. It is seen that the effect of the natural convection is to reduce the rate of axial flow in the annulus. Thus, for $Ra = 10^5$ and Pr = 1, a decrease of about 15 percent in the rate of mass flow may be observed.

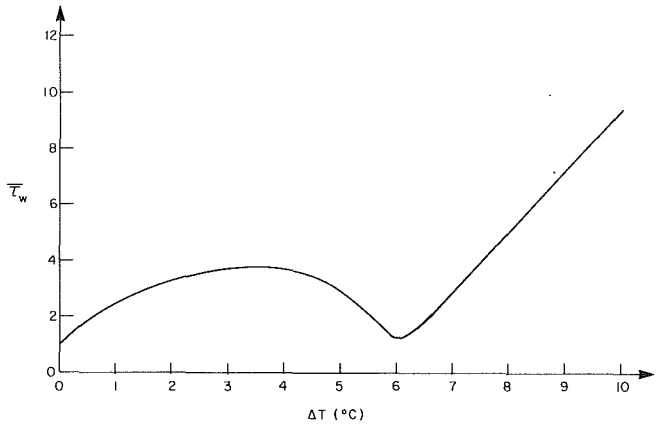

Fig. 8 Variation of angular wall shear stress in term of the applied temperature difference between the boundaries for R = 2.6, A = 2.2 × 10^9, and Re = 1.0

However, it is noticed that this trend becomes less important with increasing Prandtl numbers.

The natural convection of cold water between two horizontal concentric cylinders with density inversion of water at 4°C has been extensively studied in the past both numerically [11] and theoretically [17]. The flow pattern and heat transfer were observed to be both strongly affected by the fact that the density of water reaches a maximum value at about 4°C. Essentially, it was found that, under certain conditions, the flow in each half cavity was bicellular, in contrast to the unicellular flow obtained for a fluid without maximum density effect, and as a result the heat transfer occurred primarily by conduction. A typical result showing the effect of this particular convective flow field on the axial velocity, W, is depicted in Fig. 7 for the case $\hat{\text{Ra}}$ = 2400, radius ratio R = 2 and inversion parameter $\gamma = -0.77$. It is seen that the resulting isovelocities for the axial flow are now very close to that predicted by the pure forced convection theory, i.e., they are almost concentric circles. This is due to the fact that water, for this temperature range, has a relatively high Prandtl number (Pr > 10) which strongly reduces the effects of the free convection on the forced motion, as discussed above. Furthermore, the effects of the density inversion is to reduce the intensity of the free convection across the annulus, and consequently its influence on the forced motion along the axial direction.

Figure 8 shows the relationship between the average wall shear stress, $\bar{\tau}_w$, on the outer cylinder and ΔT, the temperature difference between the outer and inner cylinders. Here, the normalized shear stress has been defined has $\bar{\tau}_w = (\bar{\tau}_\phi^2 + \tau_z^2)^{1/2}/\tau_z^*$, where τ_ϕ and τ_z are the shear components acting along the ϕ- and z-directions, and τ_z^* is that due to the pure forced flow. The results of Fig. 7 were obtained for a cavity with size parameter, $A = 2.2 \times 10^9$, radius ratio, R = 2.6, inner cylinder tempeature, $T_i = 0$°C, and outer cylinder temperature, T_o, varying between 0 and 10°C (i.e., $\Delta T \equiv T_o$). This figure reveals that $\bar{\tau}_w$ does not increase monotonously from pure forced flow condition value ($\bar{\tau}_w$ = 1.0) with increasing ΔT as one could expect from common fluids having a linear density-temperature relationship. In fact, $\bar{\tau}_w$ increases monotonously with T_o only when a single large convective eddy occupies the major portion of the gap as in the case $T_o \leq 4$°C and $T_o \geq 7$°C. After reaching a peak value at $T_o \simeq 4$°C a minimum value of $\bar{\tau}_w$ is observed at about $T_o \simeq 6$°C. This temperature corresponds to a situation in which two convective vortices of approximately equal strength exist in the gap. Under this circumstance, the velocity gradient near the walls is small, and the value of the shear stresses in the ϕ-direction reaches a minimum. It must be mentioned that the behavior of the Nusselt number under these circumstances follows a similar trend as reported in [11].

Conclusion

The mixed convection of water confined between two isothermal concentric cylinders and subject to an externally imposed constant pressure gradient along the axial direction has been investigated, using both perturbation and numerical methods. The results obtained may be summarized as follows:

1 The axial velocity in the annulus may be strongly affected by the natural convection flow. Thus, by increasing the Rayleigh number, the flow rate in the axial direction is reduced and the maximum axial velocity is located more or less at the center of the convective cell. Decreasing the Prandtl number amplifies these effects for a given Rayleigh number.

2 In the presence of an inversion of density, the fluid motion inside each half of the cavity consists of two counterrotating helical paths, the relative sizes of which essentially depend on the inversion parameter, γ. However this more complex convective motion has little effect on the main flow.

Acknowledgment

This work was supported by the National Research Council of Canada through grants NRC A-9201 and NRC A-4197. The authors wish to gratefully thank Ecole Polytechnique for providing necessary time on IBM 360/70.

References

1 Mack, L. R., and Bishop, E. H., "Natural Convection Between Horizontal Concentric Cylinders for Low Rayleigh Numbers," *Quarterly Journal of Mechanics and Applied Mathematics*, Vol. 21, 1968, pp. 223-241.

2 Huetz, J., and Petit, J. P., "Natural and Mixed Convection in Concentric Annular Spaces Experimental and Theoretical results for Liquid Metals," 5th International Heat Transfer Conference, Tokyo, Vol. 3, 1974, pp. 169-172.

3 Powe, R. E., Carley, C. T., and Carruth, S. L., "A Numerical Solution for Natural Convection in Cylindrical Annuli," ASME JOURNAL OF HEAT TRANSFER, Vol. 93, 1971, pp. 210-220.

4 Kuehn, T. H., and Goldstein, R. J., "Experimental and Theoretical Study of Natural Convection in the Annulus Between Horizontal Concentric Cylinders," *Journal of Fluid Mechanics*, Vol. 74, 1976, pp. 695-719.

5 Charrier-Mojtabi, M. C., Mojtabi, A., and Caltagirone, J. P., "Numerical Solutions of a Flow Due to Natural Convection in Horizontal Cylindrical Annulus," ASME JOURNAL OF HEAT TRANSFER, Vol. 101, No. 1, 1979, pp. 171-173.

6 Hatton, A. P., and Quarmby, A., "Heat Transfer in the Thermal Entry Length with Laminar Flow in an Annulus," *International Journal of Heat and Mass Transfer*, Vol. 5, 1962, pp. 973-979.

7 Lundberg, R. E., McCuen, P. A., and Reynolds, W. C., "Heat Transfer in Annular Passages Hydrodynamically Developed Laminar Flow With Arbitrarily Prescribed Wall Temperatures or Heat Fluxes," *International Journal of Heat and Mass Transfer*, Vol. 6, 1963, pp. 495-501.

8 Mojtabi, A., and Caltagirone, J. P., "Analyse du transfert de chaleur en convection mixte laminaire entre deux cylindres coaxiaux horizontaux," *International Journal of Heat and Mass Transfer*, Vol. 23, 1980, pp. 1369-1375.

9 Naozo Hattori, "Combined Free and Forced-Convection Heat-Transfer for Fully Developed Laminar Flow in Horizontal Concentric Annuli (Numerical Analysis)," JSME *Transactions*, Vol. 45, 1979, pp. 227-239.

10 Vasseur, P., and Robillard, L., "Transient Natural Convection Heat Transfer in a Mass of Cold Water Cooled through 4°C," *International Journal of Heat and Mass Transfer*, Vol. 23, 1980, pp. 1195-1205.

11 Vasseur, P., Robillard, L., and Chandra Shekar, "Numerical Study On Natural Convection Heat Transfer With Density Inversion of Water Within a Horizontal Cylindrical Annulus," *20th ASME/AICHE* National Heat Transfer Conference, Milwaukee, Wis., August 2-5, 1981, HTD-Vol. 16, pp. 81-89.

12 Robillard, L., and Vasseur, P., "Transient Natural Convection Heat Transfer of Water with Maximum Density Effect and Supercooling," ASME JOURNAL OF HEAT TRANSFER, Vol. *103*, *1981*, pp. 528-534.

13 Seki, N., Fukusako, S., and Nakaoha, M., "Experimental Study on Natural Convection Heat Transfer With Density Inversion of Water Between Two Horizontal Concentric Cylinders," ASME JOURNAL OF HEAT TRANSFER, Vol. 97, 1975, pp. 556-561.

14 Saitoh, T., and Hirose, K., "Thermal Instability of Natural Convection

Flow over a Horizontal Ice Cylinder Encompassing a Maximum Density Point," ASME JOURNAL OF HEAT TRANSFER, Vol. 102, 1980, pp. 261–267.

15 Gray, D. D., and Giorgini, A., "The Validity of the Boussinesq Approximation for Liquids and Gases," *International Journal of Heat and Mass Transfer*, Vol. 19, 1976, pp. 545–551.

16 Chandra Shekar, S., *Hydrodynamic and Hydromagnetic Stability*, Oxford University Press, 1961.

17 Nguyen, T. Hung, Vasseur, P., and Robillard, L., "Natural Convection Between Horizontal Concentric Cylinders With Density Inversion of Water for Low Rayleigh Numbers," *International Journal of Heat and Mass Transfer*, Vol. 25, No. 10, 1982, pp. 1559–1568.

18 Mallison, G. D., and de Vahl Davis, D., "The Method of the False Transient for the Solution of Coupled Elliptic Equations," *Journal of Computational Physics*, Vol. 12, 1973, pp. 435–461.

19 Roache, P., *Computational Fluid Dynamics*, Hermosa Publishers, 1976.

20 Fujii, T., "Fundamentals of Free Convection Heat Transfer," *Progress in Heat Engineering*, Vol. 3, 1974, pp. 66–67.

21 Landbolt-Börnstein, "Zahlenwerte Und Funktionen," Springer-Verlag, II, No. 1, 1971, pp. 36–37.

22 Crawford, L., and Lemlich, R., "Natural Convection in Horizontal Concentric Annuli," *IEC Fundamentals*, Vol. 1, 1962, pp. 260–264.

23 Bishop, E. H., and Carley, C. T., "Photographic Studies of Natural Convection Between Concentric Cylinders," *Proceedings Heat Transfer Fluid Mechanics*, 1966, pp. 63–78.

24 Grigull, U., and Hauf, W., "Natural Convection in Horizontal Cylindrical Annuli," Third International Heat Transfer Conference, Chicago, 1966, pp. 182–195.

An Interferometric Investigation of Separated Forced Convection in Laminar Flow Past Cavities

W. Aung
Director,
Heat Transfer Program,
National Science Foundatoin,
Adjunct Professor,
Mechanical Engineering Department,
Howard University,
Washington, D. C. 20059
Mem. ASME

This study concerns the separated, laminar forced convection in cavities located on a flat plate in a low-speed wind tunnel. Temperature profiles and local heat transfer coefficients are measured by means of a Mach-Zehnder interferometer. With all walls maintained at a uniform temperature, experiments are conducted for cavity aspect ratios (length divided by depth) w/s = 4 and w/s = 1 at different Reynolds numbers. Results show that the temperature distribution outside of the cavity is little influenced by flow in the cavity. The local heat transfer distribution on the cavity floor attains a maximum value that is located between the midpoint of the cavity floor and the downstream wall. Everywhere on the cavity floor, the local heat transfer is substantially less than the value upstream of the cavity. Compared with attached flow obtained by setting the cavity depth to zero, the average heat transfer on the cavity floor is more than a factor of two lower for w/s = 4 and more than an order of magnitude lower for w/s = 1. The average Nusselt number on the cavity floor is correlated by an equation of the form, $\overline{Nu}_s = C(Re_s)^m$, where m is nearly 1/2 and C varies with the aspect ratio. Downstream of the cavity, the local heat transfer is less than the value that would prevail if the cavity depth was set equal to zero.

Introduction

The present paper is concerned with the flow of a fluid over a heated cavity or cut-out, as shown in Fig. 1. A boundary layer flow approaches a cavity of rectangular profile. A separated shear layer is formed across the open face of the cavity and reattaches on the downstream vertical wall. Some of the fluid in the shear layer enters the reverse flow in the cavity while the rest of the fluid passes downstream. The dividing streamline separates the fluid that reverses from that which flows downstream. Following reattachment, an attached boundary layer redevelops. The flow is everywhere laminar and all walls are maintained at a constant temperature.

The separated forced convection situation described above is frequently encountered in engineering applications. They include solid propellent rockets where certain combustion characteristics can lead to the formation of cavities in which the flow is laminar, and electronic systems where cavities are formed in the spaces between discrete circuit devices. In the latter situation, the heat generation in the device is partially transferred directly from each device to the cooling fluid flowing past it, but a significant portion of the heat transfer occurs from the cavity walls. Notwithstanding the engineering importance of the fluid flow and heat transfer in rectangular cavities, the prediction of the associated heat transfer process is not yet generally possible. Most of the currently available information does not cover situations that are commonly encountered in practice. In addition, there is no unanimity concerning the relation that governs the average Nusselt number in cavity flows.

The earliest study of the heat transfer in laminar flow past cavities appears to have been undertaken by Chapman [1] who performed an analysis for laminar flow by assuming that the heat transfer from the cavity is completely governed by the shear layer; that is, the shear layer is assumed to cover a "dead-air" or isothermal region. By treating the shear layer as having zero initial thickness and by neglecting the reattachment zone, Chapman obtained a similarity solution for the temperature distribution in the shear layer. He then derived a relation for the wall heat transfer by applying an overall volume energy balance, leading to an expression in which the average Nusselt number in the entire reverse flow region is related to the Reynolds number (based on the cavity length) raised to the 1/2 power, in qualitative agreement with the form of the $\overline{Nu}_L$ versus Re_L relationship for attached laminar thermal boundary layer. Chapman found that the quantitative value of $\overline{Nu}_L$ is 56 percent of the attached flow value. That is,

$$\frac{\overline{Nu}_L}{\overline{Nu}_{fp,L}} = 0.56 \tag{1}$$

Since

$$\overline{Nu}_{fp,L} = 0.595\sqrt{Re}_L, \qquad \text{for Pr} = 0.72$$

therefore

$$\overline{Nu}_L = 0.333\sqrt{Re}_L, \qquad \text{for Pr} = 0.72 \tag{2}$$

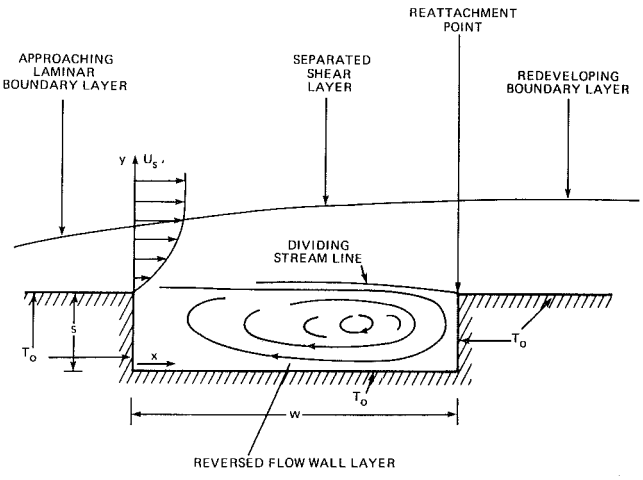

Fig. 1 Two-dimensional cavity and qualitative flow structure

Contributed by the Heat Transfer Division and presented at the 21st ASME/AIChE National Heat Transfer Conference, Seattle, Washington, July 24-28, 1983. Manuscript received by the Heat Transfer Division June 2, 1982.

Early experiments on the pressure field and the heat transfer in cavities were conducted by Larson [2] and by Nicoll [3] for high-speed flows up to hypersonic velocities. Using wedge- and cone-shaped models in laminar flow with small initial shear layer thickness (of the order of 10 percent of the cavity length), they both found that Chapman's theory correctly predicted the average heat transfer. The local heat transfer on most of the cavity floor was found to be small, amounting to as low as 10 percent of the attached flow value, but the overall average value was enhanced to 0.56 of the attached flow result by high heat transfer rates near the reattachment location. In the vicinity of the reattachment point, the local heat transfer coefficient is as much as three times that of attached flow. Following reattachment, the redeveloping laminar boundary layer is thickened as compared with nonseparated flow, and the heat transfer is comparatively lower. Thus, across the reattachment zone, the local heat transfer increases from a small value that is governed by the reverse flow in the cavity, to a high value dictated by the reattachment process, and then abruptly drops to a value somewhat less than the corresponding attached flow value.

While the aforementioned experiments have confirmed Chapman's theory, the inclusion of the reattachment zone data has cast some doubt on the validity of the comparison. Further, the effect of the aspect ratio of the cavity has not been resolved.

An experimental study by Yamamoto, Seki, and Fukusako [4] deals with the heat transfer characteristics in rectangular cavities where the bottom walls are heated at a uniform heat flux while the other two cavity walls are insulated. A momentum boundary layer develops along an unheated upstream plate. Results on flow visualization, pressure measurement, and local heat transfer coefficients are presented for both laminar and turbulent flow, with aspect ratios (w/s) ranging from 1 to 25. The study thus is concerned with both the open cavity, where the shear layer bridges the open face of the cavity, and the closed cavity where the shear layer reattaches to the cavity floor. Their laminar flow study was conducted at free stream velocities of 1.1 and 1.3 m/s at aspect ratios of 1 and 5, respectively. A correlation, valid for $\mathrm{Pr} = 0.72$ and $\mathrm{Re}_w \leq 0.7 \times 10^4$ approximately, was obtained for the average Nusselt number on the cavity floor and this is of the form

$$\overline{\mathrm{Nu}}_w = 0.427\ \mathrm{Re}_w^{1/3} \tag{3}$$

The most striking difference between this latest correlation for laminar separated flow and the standard correlation for heat transfer in the attached laminar boundary layer is in the exponent for the Reynolds number. In attached boundary layer flow, the exponent is 1/2 as in the case also for separated flow with zero initial boundary layer thickness (see equation (2)). This suggests an as yet not understood influence of the upstream boundary layer and perhaps a range for the value of the index, depending on the properties of the approaching flow. Haugen and Dhanak [5], studying the heat transfer to a turbulent boundary layer flow approaching rectangular cavities also found that the index of the Reynolds number is different from that for attached flow for which $\overline{\mathrm{St}}_{fp} \propto \mathrm{Re}_L^{0.8}$. Haugen and Dhanak, on the other hand, found the following correlation

$$\overline{\mathrm{St}}_w\,[3(1 + w/s)]^{0.5} = 0.365(\delta/w)^{-0.14}\mathrm{Re}_w^{-0.25} \tag{4}$$

The preceding comments indicate that the heat transfer problem in separated flow is in need of further study. This is also supported by a recent review by Aung and Watkins [6] pointing out the confusion prevailing in heat transfer correlations for separated forced convection, particularly in relation to the functional relationship between the $\overline{\mathrm{Nu}}$ or $\overline{\mathrm{St}}$ and Re. The situation alluded to in the foregoing comments and more fully illustrated in [6] would suggest that it was probably invalid to assume that any universal functional relation between $\overline{\mathrm{Nu}}$ and Re, such as the 1/2 power relation indicated in equation (2) for laminar flow, would exist.

The scope of the present paper is confined to laminar flow where the cavity walls are maintained at a uniform temperature. This boundary condition was chosen in order to reduce difficulties caused by heat leakage as was encountered in the study in [4]. Two aspect ratios of $w/s = 1$ (the 1:1 cavity) and $w/s = 4$ (the 4:1 cavity) were chosen for study. Temperature distributions were measured using a low-speed wind tunnel together with a Mach-Zehnder interferometer. Though no measurement was undertaken with respect to the velocity field inside the cavity, there is much that is already known about the structure of flow in this class of problem. One of the first papers dealing with the flow inside cavities was that by Charwat, Dewey, Roose, and Hitz [7], while two of the latest were by Yamamoto et al. [4], and Sinha, Gupta, and Oberai [8]. The latter studies are concerned wholly or in part with laminar flow past rectangular cavities. From these previous studies, it is possible to deduce that for $w/s = 1$ the flow in the cavity consists of a single laminar eddy that occupies the entire cavity. For $w/s = 4$, the flow is still characterized by a single elongated eddy, but the eddy center is displaced towards the downstream cavity wall (see Fig. 1).

Nomenclature

c_p = heat capacity of air
d = characteristic length
h = local heat transfer coefficient; $-\dfrac{k}{(T_0 - T_\infty)}\left(\dfrac{\partial T}{\partial y}\right)_0$
$\bar{h}$ = average heat transfer coefficient
k = thermal conductivity of air
$\overline{\mathrm{Nu}}$ = average Nusselt number in the separated region, $\dfrac{\bar{h}d}{k}$
Pr = Prandtl number
Re = Reynolds number, $\dfrac{U_s d}{\nu}$
s = depth of cavity
$\overline{\mathrm{St}}$ = Stanton number in the separated region, $\dfrac{\bar{h}}{\rho c_p U_s}$
T = temperature
T_∞ = free-stream temperature
U_s = free-stream velocity
w = width of cavity
x, y = coordinates defined in Fig. 1
$y_{1/2}$ = value of y where temperature difference is 50 percent of maximum temperature difference

Greek Letters

ρ = density
δ = boundary layer thickness just upstream of cavity
ν = kinematic viscosity

Subscripts

fp = parameter for the equivalent flat plat
L = parameter defined using the length of the shear layer or cavity length
max = maximum value
o = wall value
s = parameter defined using height of cavity
w = parameter defined using length of cavity

This flow situation persists up to $w/s = 7$ or 8. This so called open cavity flow is distinct from closed cavity flow that prevails for larger values of w/s where the shear layer reattaches to the cavity floor. These studies also confirm the earlier studies of Goldstein, Eriksen, Olsen, and Eckert [9], and Mueller and O'Leary [10] that deal with the transitional flow and reattachment mechanisms. For the cavities of concern here, it is generally known that the pressure within the cavity is relatively uniform spatially.

Experimental Method

In the present study, heat transfer information was obtained in a low-speed wind tunnel by means of a Mach-Zehnder interferometer. In order to reduce the influence of natural convection, the heated constant temperature cavity models were located on the upper wall of the test section in the wind tunnel. The wind tunnel, shown schematically in Fig. 2, is 3.53 m in length and is rectangular in cross-section with a working area at the test section of 15-cm width × 20-cm height × 61-cm length. The suction fan is a Dayton 2C 962 squirrel cage blower with a rated capacity of 490 cfm. Its speed is varied by means of a voltage regulator. Except for the test section, the remaining components of the wind tunnel are constructed of 0.30-cm thick sheet metal. The side walls and bottom plate of the test section are made of 1.27-cm plexiglas. A detachable plug, attached by screws, is provided at the bottom plate through which probes are inserted for the measurement of free-stream temperature and velocity. Windows of optical quality are provided on the side walls of the cavity and its vicinity.

The heated cavity model is composed of three aluminum sections. Two of them, each 30.5-cm length, are fixed relative to each other thus forming a backstep of 1.27-cm height. This backstep thus formed the upstream vertical wall for the cavity. Each of these two sections is provided with hot water channels and a plexiglas cover and is heated by water recirculated from a constant temperature water bath. Thermocouples are located in each aluminum section to indicate wall temperatures. Removable pins are provided along the centerline of the cavity for scaling in interferogram analysis and for camera focusing. The downstream cavity wall is formed by an additional aluminum plate of 1.27-cm thickness. By using two plates of different lengths, cavities measuring 1.27 cm × 1.27 cm and 1.27 cm × 5.08 cm are obtained. The cross section of the air flow area at the test section is 15-cm wide by 20-cm high.

The Mach-Zehnder interferometer has been described extensively in the literature and will not be further elaborated on. The interferograms in the present study are recorded on 35-mm photographic film using a Nikon-F camera. A 1/4-s exposure time is used throughout. The processed negative film is then analyzed with the aid of a toolmaker's microscope, or in cases where only the local heat transfer coefficient is desired, by directly measuring the slope of the fringe at the wall. The heat transfer coefficients obtained by both methods are in excellent agreement.

The free-stream velocity in the wind tunnel is measured with an impact tube through a "Barotron" pressure transducer. The emf's from thermocouples are recorded by a Honeywell precision self-balancing multipoint potentiometer. Further details of the experimental procedure and interferogram evaluation techniques may be found in the thesis in [11]. The present interferometric measurement is accurate to ± 7 percent for the temperature.

Discussion of Results

Interferograms for the 1:1 cavity are presented in Fig. 3, while those for the 4:1 cavity are given in Fig. 4. All experiments are conducted with $\Delta T_w \approx 18°C$ with $s = 1.27$ cm. Air flows from left to right across the field of view. (The interferograms have been inverted so that the heated cavity now appears to be underneath the airflow. In the wind tunnel, the cavity is mounted on the top wall of the test section, so that the air flow lies below.) As the free-stream velocity increases, the shear layer becomes increasingly unstable and the thermal fluctuation associated with the process of transition to turbulence can be observed through the interferometer. This striking capability of the interferometric technique was used in a previous study dealing with the backstep [12]. It is shown there that transition first occurs near the reattachment point. As the velocity increases, the transition point moves upstream. This phenomenon is also observed with the cavity, with shear layer transition coming about at a lower velocity for the cavity of higher aspect ratio. Thus, the limiting velocity for completely laminar flow is lower for the 4:1 cavity as compared with the 1:1 cavity.

Inspection of Figs. 3 and 4 suggests the insensitivity of the upper portion of the shear layer to the presence of the cavity. Throughout most of the cavity, the fluid temperature as indicated by the vertical fringes is seen to be quite uniform and is close to the wall temperature. The exception is the vicinity of the downstream vertical wall in the case of the 4:1 cavity. This characteristic of laminar separated flow is in direct contrast with those in transitional separated flow [12] and turbulent separated flow [13, 14]. In transitional flow, Aung and Goldstein's measurements [12], also using the interferometric technique, show that in the case of a backstep the temperature drop across the reverse flow adjacent to the downstream step wall averages about 40 percent of the total temperature difference between the wall and the free stream. For turbulent flow, the figure amounts to 50 percent [13] but locally the temperature drop across the wall layer can be much

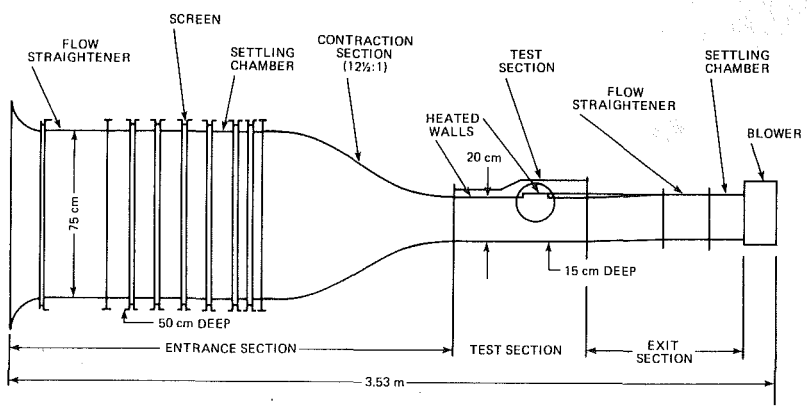

Fig. 2 Low-speed wind tunnel

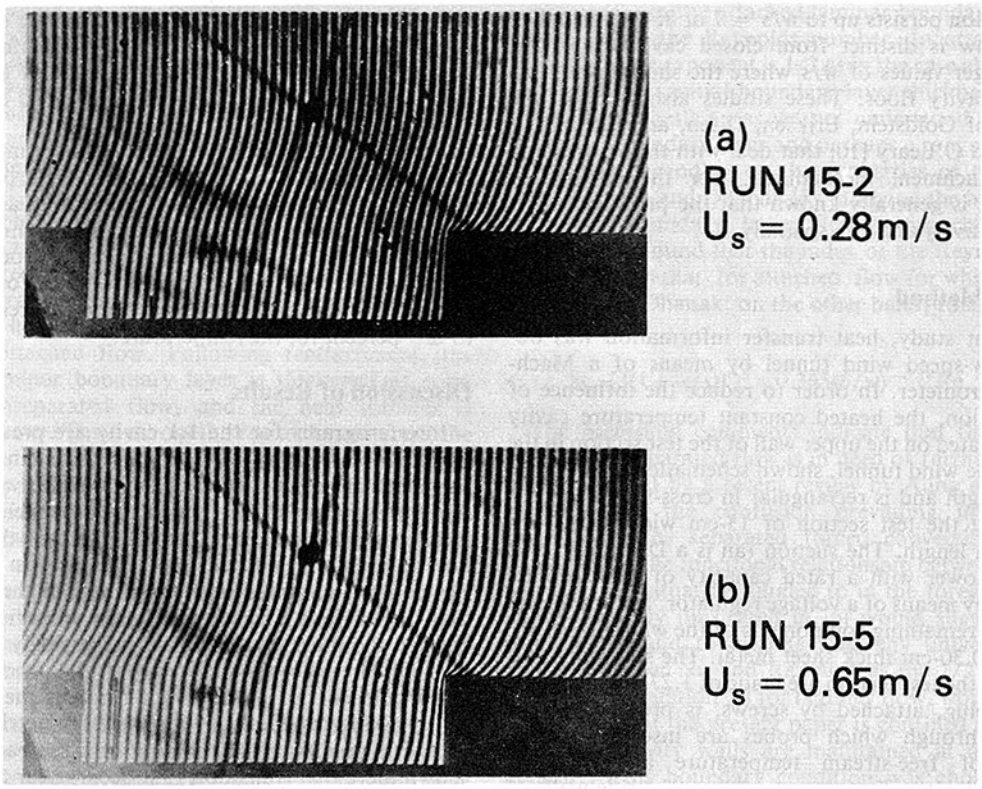

Fig. 3 Interferograms for the 1:1 cavity (air flows from left to right)

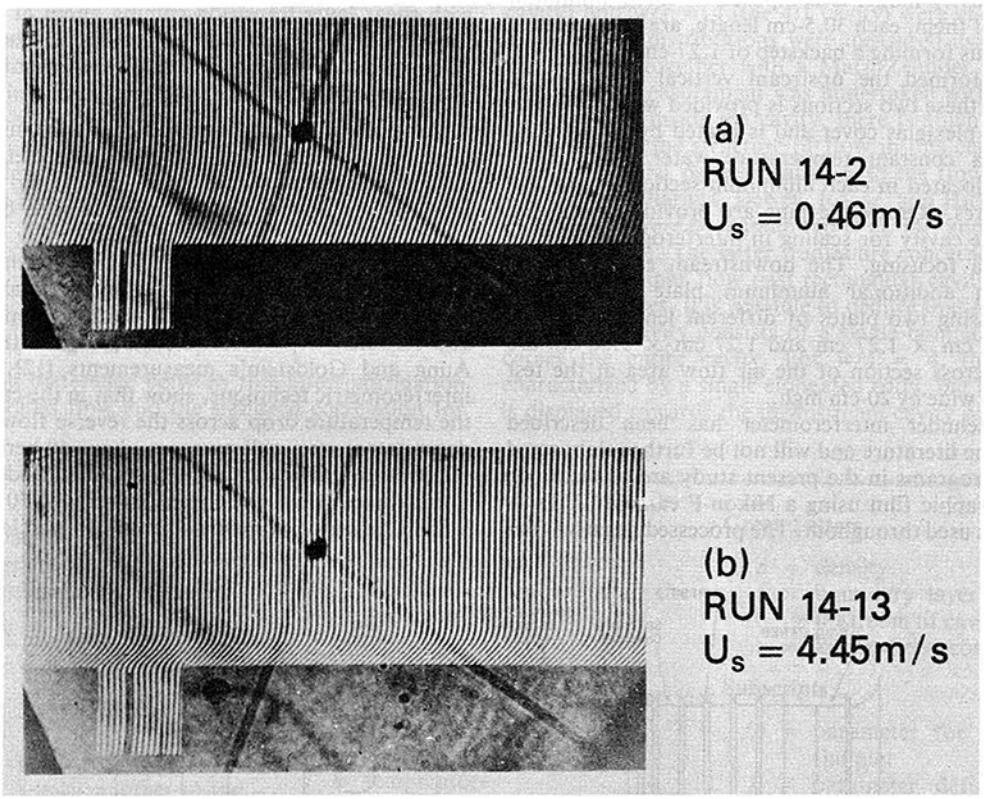

Fig. 4 Interferograms for the 4:1 cavity (air flows from left to right)

higher [13, 14], being as much as 80 percent of the total temperature drop. It is clear from the quantitative results presented in Figs. 5 that the temperature drop across the recirculating wall layer, taken to be roughly given by the temperature drop from the wall ($y/s = 0$) up to the midheight of the cavity ($y/s = 0.5$), amounts to no more than 5 percent of the total temperature for the 1:1 cavity, and no more than about 10 percent for the 4:1 cavity. Figures 5(*a*) and 5(*b*) also display the capability of the Mach-Zehnder interferometer in acquiring spatially continuous data. Note that the parameter Gr/Re_s^2, where Gr is the Grashoff number based on the cavity depth and the temperature difference between the core fluid

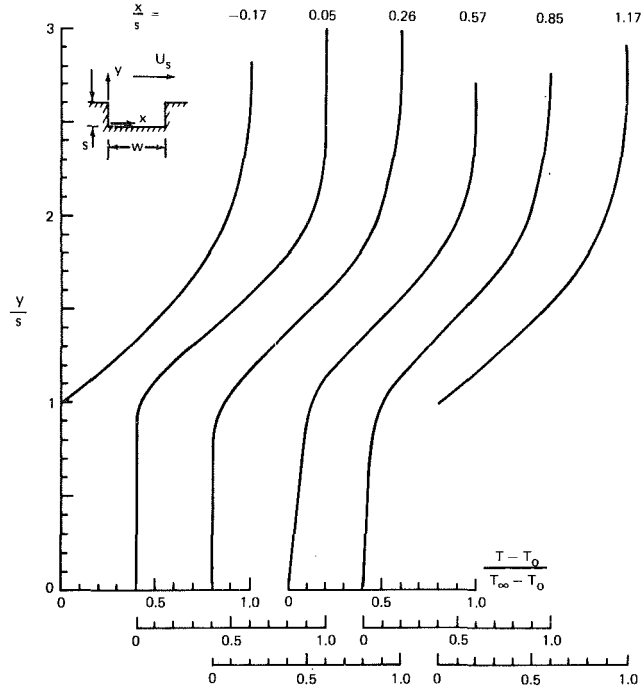

Fig. 5(*a*) Temperature distributions for the 1:1 cavity (Run 14-2)

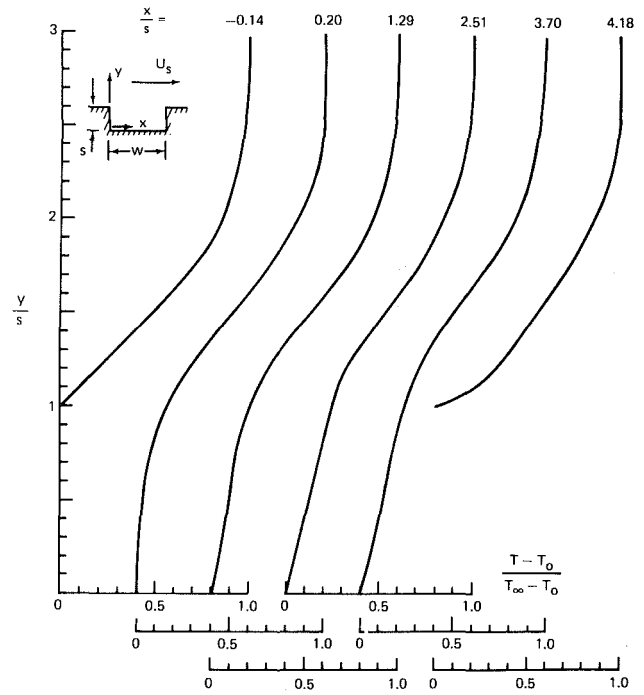

Fig. 5(*b*) Temperature distributions for the 4:1 cavity (Run 15-2)

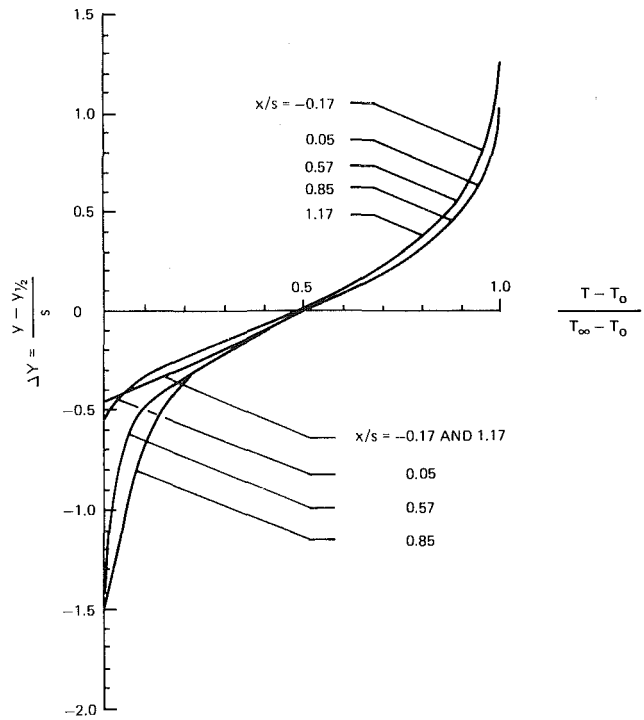

Fig. 6(*a*) Alternative representation of temperature distributions for the 1:1 cavity (Run 14-2)

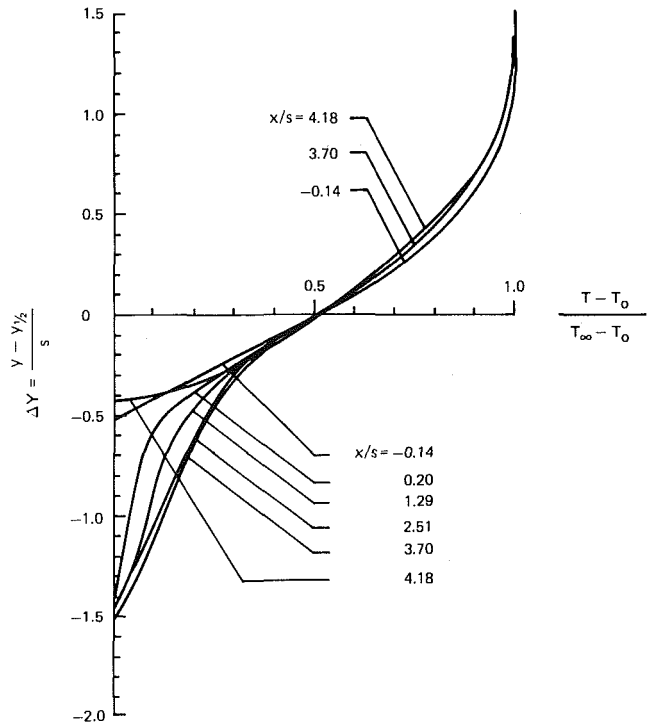

Fig. 6(*b*) Alternative representation of temperature distributions for the 4:1 cavity (Run 15-2)

and the walls of the cavity, attains a maximum value of about 0.005 indicating negligible buoyance effects in the present experiments.

Figures 3-5 all suggest an intriguing self-similarity in the temperature profiles that invites further investigation. Inasmuch as the initial shear layer thickness is not negligible in the present study, the results cannot be plotted using Chapman's similarity variable [1], which is of the form $\eta = (y-s)\,(\mathrm{Re}_x)^{1/2}/x$. For convenience, the dimensionless distance is defined as shown in Figs. 6(*a*) and 6(*b*), where $1.45 < y_{1/2}/s \leq 1.5$. Plotted in this manner, the temperature distributions appear similar and deviate little from the upstream profile for $\Delta Y > -0.2$ approximately. This region is joined with the wall layer adjacent to the floor of the cavity through a "core" where the temperature increases in the negative x-direction. (Note that $y_{1/2}$ is a function of x.)

Local heat transfer coefficients on the cavity floor are evaluated from the interferograms and shown as a function of distance in Figs. 7 and 8. Typically, a maximum in the heat transfer is present and is located near the midpoint of the

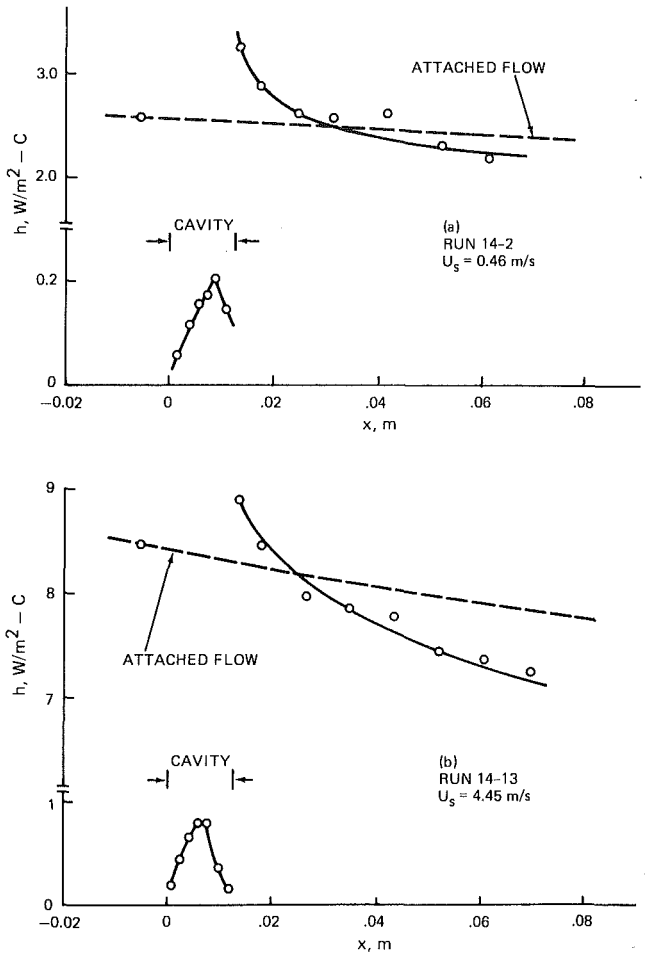

Fig. 7 Local heat transfer coefficient for the 1:1 cavity

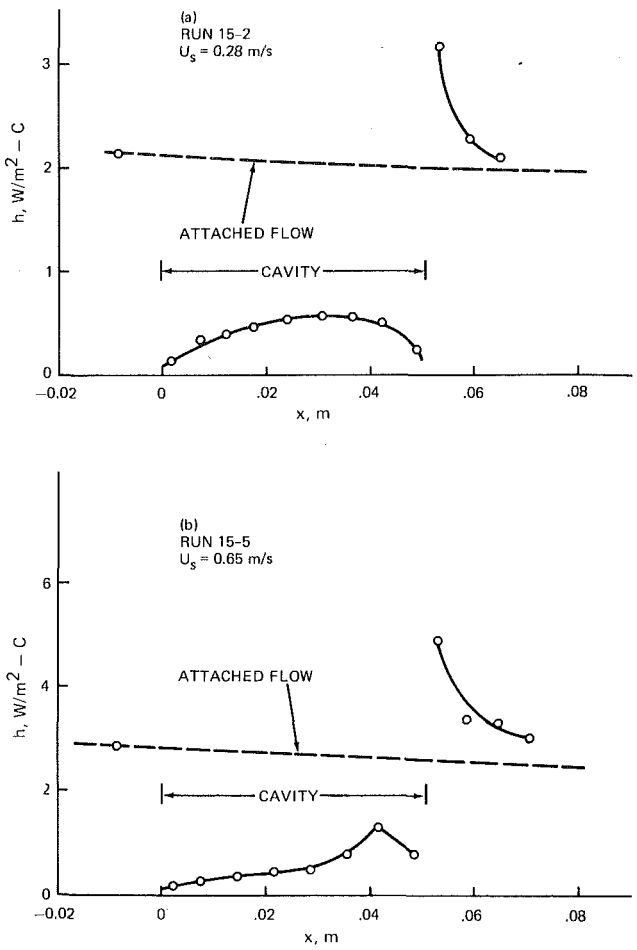

Fig. 8 Local heat transfer coefficient for the 4:1 cavity

cavity floor for the 1:1 cavity and near the downstream wall for the 4:1 cavity. The location of the maximum coincides approximately with the axial location of the center of the eddy, as shown in Fig. 1, but are contrary to results obtained with supersonic flow [2, 3] or when only the cavity floor was heated [4]. These authors' experimental data show a minimum in the heat transfer coefficient near the center of the cavity. In addition, Nicoll's data for cavity aspect ratios of 2.5 and 5 indicate that the minimum heat transfer coefficient on the cavity floor is about 15 percent of the attached flow value, irrespective of the aspect ratio or the Reynolds number. The present study show that the magnitude of the maximum heat transfer coefficient as well as the average value, is highly sensitive to both the aspect ratio and the Reynolds number, as Table 1 indicates. This table further shows that the maximum heat transfer coefficient, when normalized by the average value on the cavity floor, is only mildly sensitive to either the Reynolds number or the aspect ratio.

Each of the graphs in Figs. 7 and 8 contains a dashed line indicating the attached boundary layer flow results. This line is obtained by noting that the present test section carries an unheated starting length. Hence, strictly speaking, the local heat transfer coefficient variation with distance is not given by a relation of the type (see p. 319 of [15])

$$h \propto \bar{x}^{-1/2}$$

where $\bar{x}$ is measured from the origin of the upstream plate, which is typical of boundary layer flow with a simultaneous development of the momentum and thermal boundary layers. However, in the situation under consideration in this study, it can be readily proved that the above functional relation is

Table 1 Maximum heat transfer coefficient on the cavity floor

(h is in W/m^2-C)

Run No.	w/s	Re_s	h_{max}	$\bar{h}$	$h_{max}/\bar{h}$
14-2	1	348	0.20	0.13	1.54
14-13	1	3313	0.77	0.46	1.67
15-2	4	211	0.56	0.43	1.4
15-5	4	490	1.14	0.63	1.81

very nearly true, since our focus is restricted to the relatively narrow region 45 cm $\leq \bar{x} \leq$ 56 cm, being roughly the region traversed by the light beam of the interferometer. Assuming that the cavity has only negligible influence on the local heat transfer coefficient upstream of it, the attached flow curve is constructed using the measured value upstream of the cavity.

It is seen from Figs. 7 and 8 that the local heat transfer coefficient on the floor of the 1:1 cavity is at least an order of magnitude less than the corresponding local attached flow value. For the 4:1 cavity the attached flow curve is at least a factor of 2 higher. Specifically, the heat transfer on the cavity floor is about 25 and 6 percent, respectively, for the 4:1 cavity and the 1:1 cavity. Following reattachment on the downstream vertical wall the heat transfer coefficient is seen to increase by an order of magnitude (note the change in the vertical scale in Figs. 7 and 8). It then rapidly decreases in the downstream direction, the asymptote being lower than – in the case of the 1:1 cavity – the attached flow value that would be obtained if the cavity depth had been set to zero. Thus, flow separation at the cavity has been shown to be capable of

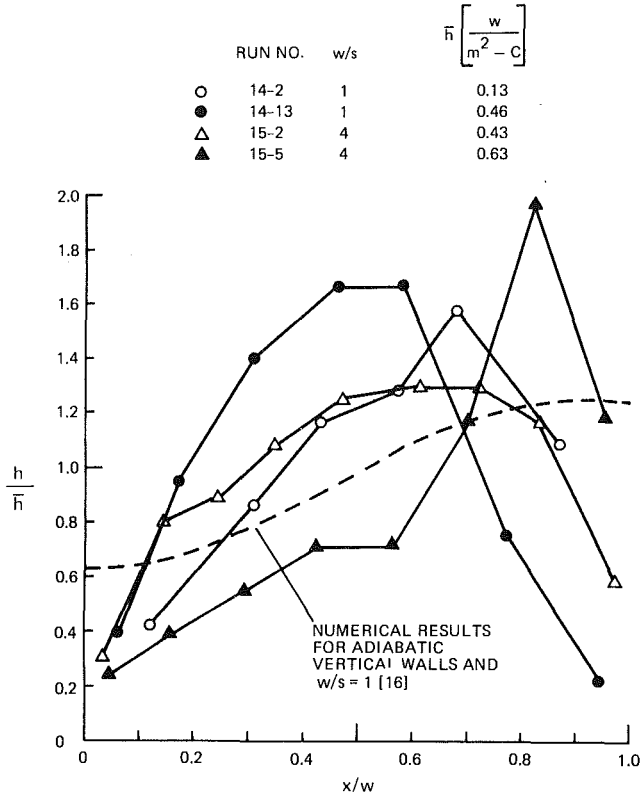

Fig. 9 Normalized local heat transfer distribution on the cavity floor

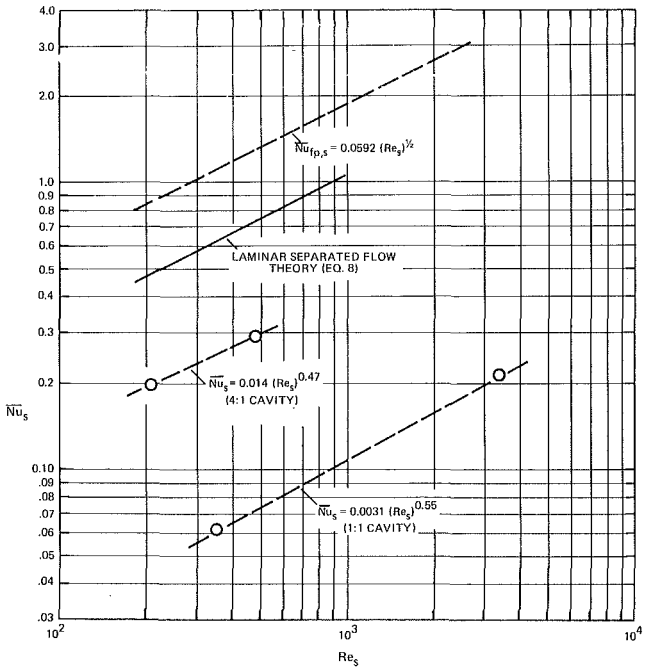

Fig. 10 Dimensionless correlation of average heat transfer on cavity floor

thickening the boundary layer thereby increasing its resistance to heat transfer.

In order to examine the lcoal heat transfer distribution on the cavity floor, the local value is normalized by the average and plotted against the normalized distance along the cavity floor. The result is given in Fig. 9. Except for the existence of the maxima, no other common feature is observed, illustrating the point that even for these relatively "simple" open cavities (where the shear layer spans the open face of the cavity) the analytical description of the local heat transfer still is not an easy task. Humphrey and Jacobs [16] recently performed a numerical calculation for the free-forced convection heat transfer from a 1:1 cavity located on the wall of a channel. The approaching velocity profile is parabolic and all walls of the geometric configuration are adiabatic except for the cavity floor which is maintained at a uniform temperature. The Reynolds number based on the average velocity at the channel entrance and the cavity width is 300. The result for the nonbuoyant forced convection case is shown by the dashed line in Fig. 9. The predicted peak in the heat transfer is smaller than values measured for the 1:1 cavity, and lies very close to the downstream wall of the cavity.

The streamwise average Nusselt number is shown plotted against the Reynolds number in Fig. 10. The data are correlated by the equations

$$\overline{Nu}_s = 0.0031\,(Re_s)^{0.55},\ w/s = 1 \quad (5)$$

$$\overline{Nu}_s = 0.014\,(Re_s)^{0.47},\ w/s = 4 \quad (6)$$

Again, note that the average heat transfer pertains only to the cavity floor; no data were obtained for the two vertical walls of the cavity. From laminar boundary layer theory, the theoretical attached flow results can be easily derived. An expression that applies approximately is

$$\overline{Nu}_{fp,s} = 0.0592\,(Re_s)^{1/2},\ w/s = 0 \quad (7)$$

This equation is also plotted in Fig. 10. By comparison, the heat transfer from the cavity is significantly lower. In fact, the smaller the aspect ratio, the greater is the departure from attached flow. Thus, the heat transfer from the floor of the 1:1 cavity is only about 25 percent of that for the larger cavity. Though the scope of the present study is limited, the implication of a vanishing heat transfer on the cavity floor as the cavity aspect ratio diminishes is unmistakable. There are two ways that w/s can diminish. First, consider the case of constant depth, s. When w is decreased until it is very nearly zero, we have what is tantamount to an insulated gap from which the heat transfer is zero. Secondly, when w is constant, w/s can diminish by letting s increase. When s is extremely large, then irrespective of the magnitude of w, the heat transfer from the floor of the cavity is zero by virtue of the large thermal path involved. These two physical situations are illustrated by the trend of the experimental data in Fig. 10. In view of these comments, Chapman's theory, represented by equation (2), cannot be expected to apply in the present study but is nevertheless shown on Fig. 10 for completeness. The curve plotted is obtained by combining equations (1) and (7), giving

$$\overline{Nu}_s = 0.0332\,(Re_s)^{1/2} \quad (8)$$

It should be mentioned that although this equation does not quantitatively describe the present experimental results, the theory is close to predicting the exponent of the Reynolds number. In equations (5) and (6), the exponent is 0.55 and 0.47, respectively, which average to be 0.51, very nearly equal to the predicted value of 0.50.

Clearly, it is desirable to combine equations (5) and (6) to gain a general correlation that is independent of the aspect ratio, w/s. This, however, is out of the scope of the present study. The general correlation would require additional data for other aspect ratios and for other initial boundary layer thicknesses. In spite of this, an estimate of the effect of the initial boundary layer thickness can be made using the present data. To this end, the thickness of the momentum boundary layer just prior to separation is evaluated by first obtaining the thermal boundary layer thickness at that location. This is accomplished by noting the point on the dimensionless temperature profile (Fig. 6) where 99 percent of the free-

stream value is attained. Having the thickness of the thermal boundary layer, the momentum boundary layer thickness can easily be obtained by a relation given on p. 318 of Eckert and Drake [15]. The ratio, δ/w, can be plotted against the parameter, $\bar{X}$, where

$$\bar{X} = \overline{\mathrm{St}}[A(1 + w/s)]^{0.5}$$

This group is suggested by equation (4). For laminar flow, A is 2. The resulting plot is not indicated here; however, within the narrow ranges of δ/w in this study, no clear functional dependency of $\bar{X}$ on δ/w is evident. Certainly, the dependency is at most a mild one, as is the case for turbulent flow. Note that in laminar supersonic flow past rectangular open cavities, the upstream boundary layer thickness has been found to be the primary scaling parameter for the heat transfer rate at the downstream recompression corner as well as for the entire cavity surface [17].

Conclusions

The separation, reattachment, and redevelopment of laminar fluid layers are complicated phenomena. The present experimental study, while not focused on providing a complete description of these phenomena, is aimed at yielding a fundamental understanding of a number of properties of such flows. The nearly similar temperature profiles along the cavity length is an intriguing aspect that should perhaps motivate further study in which this property is exploited. The average Nusselt number appears to be related to the Reynolds number raised to a power very close to 0.5. This finding is at variance with the observation made by Yamamoto et al. For the 4:1 cavity, the average heat transfer on the cavity floor is about 25 percent of the attached flow value, while for the 1:1 cavity the figure is about 6 percent. It is impossible to discern from the present data what the upper limit of the average heat transfer is, if the cavity aspect ratio should be increased continuously until $w/s = 7$ or 8, the limit of open cavity flow. The eventual change of the flow structure accompanying the transition from an open cavity to a closed cavity, where the shear layer reattaches to the cavity floor, will have to be considered. In the redevelopment region, though the heat transfer appears to suffer a permanent deficit when compared with attached flow, the information available is insufficient to provide a guide as to how to calculate the local heat transfer in this region. Finally, the relative insensitivity of the average Stanton number to the initial boundary layer thickness is interesting, but may only reflect the narrow ranges of the present data. The information furnished in this paper may be used as a basis to construct a more general and complete theory governing the type of heated flows depicted here.

Acknowledgment

The author expresses his appreciation for a number of enlightening discussions with Professor Richard J. Goldstein. The experiments in this paper were carried out at the Heat Transfer Laboratory, Department of Mechanical Engineering, University of Minnesota.

References

1 Chapman, D. R., "A Theoretical Analysis of Heat Transfer in Regions of Separated Flow," NACA TN 3792, 1956.

2 Larson, H. K., "Heat Transfer in Separated Flows," *J. Aerospace Sci.*, Vol. 26, 1959, pp. 731-738.

3 Nicoll, K. M., "A Study of Laminar Hypersonic Cavity Flows," *AIAA Journal*, Vol. 2, No. 9, 1964, pp. 1535-1541.

4 Yamamoto, H., Seki, N., and Fukusako, S., "Forced Convection Heat Transfer on Heated Bottom Surface of a Cavity," ASME JOURNAL OF HEAT TRANSFER, Vol. 101, 1979, pp. 475-479.

5 Haugen, R. L., and Dhanak, A. M., "Heat Transfer in Turbulent Boundary-Layer Separation Over a Surface Cavity," ASME JOURNAL OF HEAT TRANSFER, Vol. 89, 1967, pp. 335-340.

6 Aung, W. and Watkins, C. B., Jr., "Heat Transfer Mechanisms in Separated Forced Convection," *Turbulent Forced Convection in Channels and Bundles—Theory and Applications to Heat Exchangers and Nuclear Reactors*, edited by S. Kakac and D. B. Spalding, Hemisphere Publishing Corp., 1979, pp. 233-256.

7 Charwat, A. F., Dewey, C. F., Roos, J. N., and Hitz, J. A., "An Investigation of Separated Flows—Part II: Flow in the Cavity and Heat Transfer," *J. Aerospace Sci.*, Vol. 28, 1961, pp. 513-527.

8 Sinha, S. N., Gupta, A. K. and Oberai, M. M., "Laminar Separating Flow Over Backsteps and Cavities," *AIAA Journal*, Vol. 20, 1981, pp. 370-375.

9 Goldstein, R. J., Eriksen, V. L., Olson, R. M. and Eckert, E. R. G., "Laminar Separation, Reattachment and Transition of Flow Over a Downstream Facing Step," ASME *Journal of Basic Engineering*, Vol. 92, 1970, pp. 732-741.

10 Mueller, T. J., and O'Leary, R. A., "Physical and Numerical Experiments in Laminar Incompressible Separating and Reattaching Flows," AIAA Paper No. 70-763, 1970.

11 Aung, W., "Heat Transfer in the Separated Region Beyond a Rearward-Facing Step," Ph.D. thesis, University of Minnesota, 1969.

12 Aung, W. and Goldstein, R. J., "Temperature Distribution and Heat Transfer in a Transitional Separated Shear Layer," Paper No. FC 1.5, *Heat Transfer, Proceedings of 4th International Heat Transfer Conference*, Versailles, France, 1970.

13 Aung, W., and Goldstein, R. J., "Heat Transfer in Turbulent Separated Flow Downstream of a Rearward-Facing Step," *Isreal J. of Tech.*, Vol. 10, No. 1-2, 1972, pp. 35-41.

14 Seban, R. A., "Heat Transfer to a Turbulent Separated Flow of Air Downstream of a Step in the Surface of a Plate," ASME JOURNAL OF HEAT TRANSFER, Vol. 86, 1964, pp. 259-264.

15 Eckert, E. R. G., and Drake, R. M. Jr., *Analysis of Heat and Mass Transfer*, McGraw-Hill Book Co., 1972.

16 Humphrey, J. A. C. and Jacobs, E. W., "Free-Forced Laminar Flow Convective Heat Transfer from a Square Cavity in a Channel with Variable Inclination," *International Journal of Heat and Mass Transfer*, Vol. 24, No. 10, 1981, pp. 1589-1597.

17 Lamb, J. P., "Analysis and Correlation of Convective Heat Transfer Measurements for Open Cavities in Supersonic Flow," presented at AIAA 15th Thermophysics Conference, July 14-16, 1980, Snowmass, Colo., Paper No. AIAA-80-1526.

Analysis of Coolant Entrance Boundary Shape of Porous Region to Control Cooling Along Exit Boundary

R. Siegel
Fellow ASME

A. Snyder

National Aeronautics and Space Administration, Lewis Research Center, Cleveland, Ohio 44135

A cooled porous region has a plane surface exposed to a specified spatially varying heat flux. The coolant leaves the region through this surface, and it is desired to control the flow distribution to maintain a specified uniform surface temperature. This is accomplished by having the coolant entrance surface shaped to provide in the region the necessary variation of path length and, hence, flow resistance. The surface shape at the coolant entrance is found by solving a Cauchy boundary value problem. An exact solution is obtained that will deal with a wide variety of heating distributions for both two- and three-dimensional shapes.

Introduction

Surfaces such as those of arc electrodes, turbine blades, rocket nozzles, and reentry bodies, must often be protected from large imposed heat fluxes. A possible cooling technique is to use a porous wall material and force coolant through it so that it leaves the wall through the surface exposed to the heat load. For the present analysis, the design requirements are that the surface exposed to the heat load is plane, and that it is at a uniform temperature as dictated by material strength considerations. The heating at this surface is spatially nonuniform; to deal with the heating variation, the coolant exit flow must also vary along the surface. This can be achieved by using the flow resistance through the porous region to properly distribute the coolant. The interior surface of the porous region, which is adjacent to the coolant reservoir, is given a shape such that the necessary flow resistance is provided along paths through the region, which is of uniform porosity. The shape of the interior surface must be designed to yield the required temperature and heat flux conditions along the flat external surface. The surface temperature depends on both the convective cooling within the porous region and the redistribution of energy by heat conduction in the metallic porous matrix.

The flow through the porous region is governed by Darcy's law, and local thermal equilibrium is assumed between the coolant and the porous metallic matrix. The flow can be compressible (perfect gas) or incompressible, and the fluid viscosity can depend on temperature. For these conditions a heat transfer theory has been derived in [1] and further developed and applied in [2–4]. The energy differential equation is elliptic in type. The conditions that both temperature and heat flux are imposed along one boundary (the coolant exit boundary) means that the boundary conditions are of the Cauchy type. In the previous work [2–4] the unknown curved boundary was at the coolant exit and hence there was a strong coupling between the surface shape and the regulation of coolant flow. In the present situation the coolant exit surface is required to be plane, so that the flow must be regulated by shaping the inlet surface. Unless the porous region is very thin, this provides only weak flow control. As a result, the present mathematical formulation is not well posed [5, 6], and a method of analysis is required that is different from the previous work. The mathematics reflects the physical condition in that it is not possible to find interior surface shapes that can deal with arbitrary heating distributions along the flat external boundary. However, as will be shown, it is possible with the present solution method to obtain a variety of well-defined shapes for heating conditions of practical interest. These shapes will be illustrated and discussed for two- and three-dimensional porous regions. A quite general class of shapes is obtained for two-dimensional slabs and three-dimensional rectangular prisms.

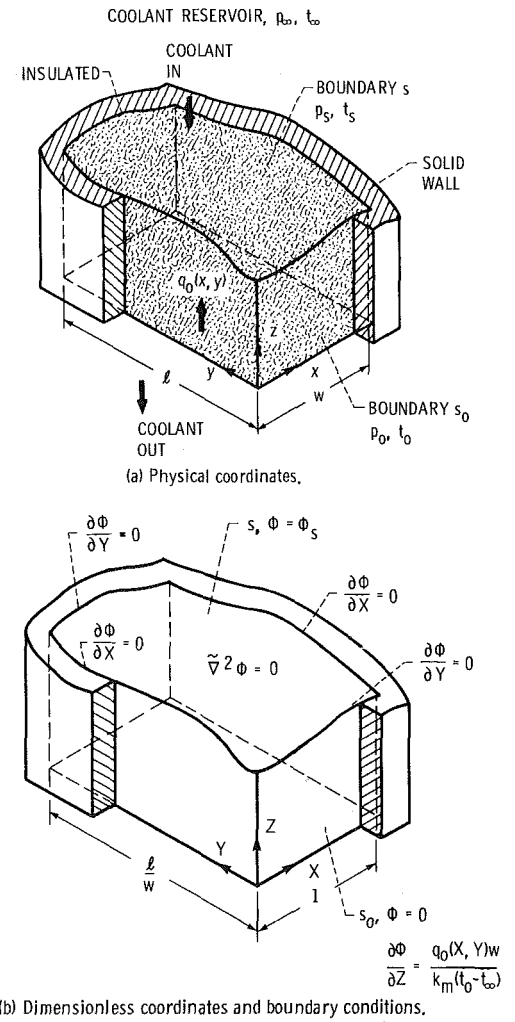

Fig. 1 Three-dimensional porous insert with heating imposed on flat side

Contributed by the Heat Transfer Division for publication in the JOURNAL OF HEAT TRANSFER. Manuscript received by the Heat Transfer Division March 31, 1982.

A few results are also given for axisymmetric heating at the base of a cylindrical region.

Analysis

The three-dimensional porous region is shown in rectangular coordinates in Fig. 1. The upper and lower boundaries are porous, while the four side boundaries are insulated and are impervious to flow. Coolant from the upper reservoir at p_∞, t_∞ is pumped into the porous region through the curved boundary, s, and flows out of the region through the flat boundary, s_o, which is at uniform pressure, p_o. Along this flat boundary is imposed a nonuniform heat flux, $q_o(x,y)$. The spatial distribution of coolant flow moving downward through the flat lower boundary is to be regulated to carry away this heat load and maintain the flat surface at uniform temperature. This is accomplished by properly designing the shape of the upper surface, thereby providing the required variation in local flow resistance through the porous region. The shape of the upper surface is to be obtained by the analysis.

General Equations and Boundary Conditions. The general flow and energy relations needed between pressure, coolant flow, temperature, and imposed heat flux have been developed in [1-4] where they were applied to other types of boundary value problems. The relations required here will now be briefly summarized; they account for both compressible and incompressible flow, and a coolant viscosity that is a function of temperature. The general equations are Darcy's law for flow through a porous medium

$$\mathbf{u} = \frac{-\kappa}{\mu(t)} \nabla p \tag{1}$$

(κ is constant in the present analysis) conservation of mass,

$$\nabla \cdot \mathbf{u} = 0 \text{ incompressible flow} \tag{2a}$$

$$\nabla \cdot (\rho \mathbf{u}) = 0 \text{ compressible flow} \tag{2b}$$

energy conservation for thermal equilibrium between solid and coolant,

$$\nabla \cdot \mathbf{q} = 0 \text{ where } \mathbf{q} = -k_m \nabla t + \rho \mathbf{u} c_p t \tag{3}$$

and the perfect gas law for compressible coolant

$$p = \rho R t \tag{4}$$

The boundary conditions along the coolant inlet surface, s, are (upper surface in Fig. 1)

$$p = p_s = p_\infty = \text{constant} \tag{5}$$

$$k_m \mathbf{n}_s \cdot \nabla t = \rho c_p (t - t_\infty) \mathbf{n}_s \cdot \mathbf{u} \tag{6}$$

Along the side boundaries

$$\mathbf{n} \cdot \mathbf{u} = 0 \tag{7a}$$

$$\mathbf{n} \cdot \mathbf{q} = 0 \tag{7b}$$

Along the coolant exit surface, s_o, of the medium (the flat lower surface in Fig. 1)

$$p = p_o = \text{constant} \tag{8}$$

$$t = t_o = \text{constant} \tag{9}$$

$$-k_m \frac{\partial t}{\partial z}\bigg|_0 = q_o(x,y) \tag{10}$$

Potential Function Relations. In [1-4] the unknown curved boundary was at the coolant exit, and hence the boundary conditions were different than in the present study in which the coolant exit surface is to remain plane. However, by following the basic ideas in the previous work, the relations that follow can be developed. The key element is that the spatial distributions of temperature, coolant flow and heat flow within the medium can all be expressed in terms of a potential function $\phi(X,Y,Z)$ that is obtained by solving Laplace's equation $\tilde{\nabla}^2 \phi = 0$ in the region, subject to boundary conditions that will be described.

The temperature distribution in the medium is related to $\phi(X,Y,Z)$ by

$$T(X,Y,Z) = 1 + (T_o - 1) e^{-\phi(X,Y,Z)} \tag{11}$$

This form results from fixing the arbitrary level in ϕ such that at the lower boundary ($Z = 0$)

$$\phi(X,Y,0) = 0 \tag{12}$$

Then $T(X,Y,0) = T_o$ where T_o is a specified quantity. At the upper boundary, equation (11) yields

$$\phi_s = ln\left(\frac{T_o - 1}{T_s - 1}\right) \tag{13}$$

Nomenclature

A, A_1, A_2 = shape coefficients in cosine heating function
B, B_1, B_2 = amplitudes of cosine heating functions
C_o, C_n = Fourier coefficients
c_p = specific heat at constant pressure
F, G = arbitrary functions
J = Bessel function of the first kind
K_1, K_2 = constants
k_m = effective thermal conductivity of porous material
L = aspect ratio, l/w
l = width in y-direction of porous region
M = for incompressible flow, $M = (1/2)(\mu/\mu_\infty)(t_\infty/t)$; for compressible flow, $M = \mu/\mu_\infty$
n = normal direction; index in Fourier series
P = for incompressible flow, $P = p/p_\infty$; for compressible flow, $P = (p/p_\infty)^2$
p = pressure
Q = dimensionless heat flux, $qw/k_m(t_o - t_\infty)$; $Q_{\text{ref}} = q_{\text{ref}} w/k_m(t_o - t_\infty)$
q = heat flow rate per unit area
R = gas constant
r = radial coordinate; r_o, outer radius of cylinder
s = curved surface of porous region
T = temperature ratio, t/t_∞
t = absolute temperature
u = coolant velocity
w = width of porous region in the x-direction
X,Y,Z = Cartesian coordinates, $x/w, y/w, z/w$
x,y,z = Cartesian coordinates

Greek Symbols

κ = permeability of porous material
λ = parameter, $\rho_\infty c_p \kappa p_\infty / 2\mu_\infty k_m$
μ = coolant viscosity
ξ = dummy variable of integration
ρ = coolant density
Φ_s = dimensionless potential, $\phi_s k_m(t_o - t_\infty)/wq_{\text{ref}}$ or $\phi_s k_m(t_o - t_\infty)/r_o q_{\text{ref}}$
ϕ = potential function
$\tilde{\nabla}^2$ = $\partial^2/\partial X^2 + \partial^2/\partial Y^2 + \partial^2/\partial Z^2$

Subscripts

ref = reference value
s = at shaped coolant entrance surface
o = at flat boundary exposed to heat load (except in C_o and r_o)
∞ = conditions in coolant reservoir

where T_s and ϕ_s are uniform over s as obtained by the analysis. The temperature, T_s, is not a specified quantity, but depends on the coolant flow and thus on the pumping pressure and coolant viscosity. It is found from the relation

$$P_o = 1 + \frac{1}{\lambda}\int_{T_s}^{T_o} \frac{MT}{1-T}\,dT \tag{14}$$

where P_o is known, and M accounts for the viscosity variation with temperature. Along the side walls the boundary conditions in terms of ϕ are

$$\mathbf{n}\cdot\bar{\nabla}\phi = 0 \tag{15}$$

By expressing t in terms of ϕ, the remaining boundary condition, equation (10), becomes

$$\left.\frac{\partial\phi}{\partial Z}\right|_0 = \frac{q_o(X,Y)\,w}{k_m(t_o - t_\infty)} \equiv Q_o(X,Y) \tag{16}$$

Figure 1(*b*) summarizes the conditions on ϕ. The shape of the upper surface at constant ϕ_s must be found to satisfy the dual boundary conditions (12) and (16) along the lower surface at $Z = 0$.

Free Boundary Solution in Two-Dimensions. For ease in the development, two-dimensional results will be considered first; quantities do not vary with Y in this instance. The solution to $\bar{\nabla}^2\phi = 0$ subject to dual boundary conditions at $Z = 0$ is a Cauchy problem and the first thought might be to use a product solution obtained by standard methods. However, as will be shown by the following short development, this is not the type of solution that is desired for a poorly posed problem; therefore, a special type of solution is required.

If $Q_o(X)$ in equation (16) is expanded in a Fourier cosine series

$$Q_o(X) = C_o + \sum_{n=1}^{\infty} C_n \cos(n\pi X) \tag{17}$$

where $C_o = \int_0^1 Q_o(X)\,dX$ and $C_n = 2\int_0^1 Q_o(X)\cos(n\pi X)\,dX$ then the solution to $\bar{\nabla}^2\phi = 0$ satisfying equations (12) and (16), and the zero derivative conditions at the side boundaries $X = 0$ and 1 is

$$\phi(X,Z) = C_o Z + \sum_{n=1}^{\infty} \frac{C_n}{n\pi}\cos n\pi X \sinh n\pi Z \tag{18}$$

The desired $Z_s(X)$ coordinates of the upper boundary can then be found by solving (by some implicit scheme) equation (18) evaluated at S where ϕ_s is known from equation (13)

$$\phi_s = C_o Z_s + \sum_{n=1}^{\infty} \frac{C_n}{n\pi}\cos n\pi X \sinh n\pi Z_s \tag{19}$$

As is characteristic of a Cauchy problem for an elliptic partial differential equation, this product solution is not well behaved [5]. For large n, the hyperbolic sine in equation (19) will grow exponentially with Z_s. As a result, for ϕ_s values corresponding to reasonable thicknesses of the porous material it is only possible to approximate $Q_o(X)$ by at most a few harmonics without the calculated upper boundary becoming irregular; the use of even a few additional harmonics would require a very small Z_s for the series type of solution to properly converge.

The difficulty in applying equation (19) arises from the higher harmonics that are introduced by approximating the imposed $Q_o(X)$ as a Fourier series. When approximating even a smooth function (in practice $Q_o(X)$ would usually be smooth) by a finite series, small irregularities are introduced. In the series solution for Z_s these higher harmonics are magnified by $\sinh(n\pi Z_s)/n\pi$, thus artificially yielding an irregular upper surface of the porous region. It is more desirable to obtain a solution that can deal directly with $Q_o(X)$ as a smooth function, rather than in the form of a finite Fourier series. This solution is found by using the two-dimensional results in [7] that satisfy $\bar{\nabla}^2\phi = 0$ in the upper half plane. The $\phi(X,Z)$ is given in terms of two arbitrary functions f and g

$$\phi = f(X+iZ) + g(X-iZ) \tag{20}$$

where

$$f(X+iZ) = \frac{1}{2}\phi_o(X+iZ) - \frac{1}{2}i\int_0^{X+iZ}\left(\frac{\partial\phi}{\partial Z}\right)_0(\xi)\,d\xi \tag{21}$$

$$g(X-iZ) = \frac{1}{2}\phi_o(X-iZ) + \frac{1}{2}i\int_0^{X-iZ}\left(\frac{\partial\phi}{\partial X}\right)_0(\xi)\,d\xi \tag{22}$$

The sum of (21) and (22) yields

$$\phi(X,Z) = \Re e[\phi_o(X+iZ)] + \frac{1}{2i}\int_{X-iZ}^{X+iZ}\left(\frac{\partial\phi}{\partial Z}\right)_0(\xi)\,d\xi \tag{23}$$

To utilize equation (23) let the width of the present geometry correspond to one half-period of a periodic function boundary condition along the X axis. Then

$$Q_o(X) = \left.\frac{\partial\phi}{\partial Z}\right|_0 = K_1 + F(\cos\pi X) \quad 0 \le X \le 1 \tag{24}$$

where K_1 is a constant and F is *any* function. The solution is then (since $\phi = 0$ along $Z = 0$)

$$\phi(X,Z) = K_1 Z + \frac{1}{2i}\int_{X-iZ}^{X+iZ} F(\cos\pi\xi)\,d\xi \tag{25}$$

A function of $\cos\pi X$ that can be used to approximate a wide variety of heating variations with X along $Z = 0$ is $1/(1 + A\cos\pi X)$ where A is a constant such that $-1 < A < 1$. This function is normalized so that the imposed heat flux equals a reference value q_{ref} at $X = 0$ and increases with X to reach $(1 + B)q_{\text{ref}}$ at $X = 1$. This gives

$$\frac{Q_o(X)}{Q_{\text{ref}}} = \frac{q_o(X)}{q_{\text{ref}}} = 1 - \frac{B(1-A)}{2A}\left(1 - \frac{1+A}{1+A\cos\pi X}\right) \tag{26}$$

Equation (26) is arranged into the form of equation (24) and then substituted into equation (25) to obtain after integration

$$\frac{\phi_s k_m(t_o - t_\infty)}{wq_{\text{ref}}} \equiv \Phi_s = Z_s\left[1 - \frac{B(1-A)}{2A}\right] + \frac{B\sqrt{1-A^2}}{4\pi A} \times ln\left\{\frac{\left[\sqrt{\frac{1+A}{1-A}}(\cosh\pi Z_s + \cos\pi X) + \sinh\pi Z_s\right]^2 + \sin^2\pi X}{\left[\sqrt{\frac{1+A}{1-A}}(\cosh\pi Z_s + \cos\pi X) - \sinh\pi Z_s\right]^2 + \sin^2\pi X}\right\} \tag{27}$$

For various Φ_s values this was evaluated to find surface shapes $Z_s(X)$ corresponding to a variety of heating distributions obtained by using various A and B values. The shapes of the porous region will be presented and discussed in the next section. For small A the above relations reduce to heating described by a single cosine harmonic (the same result as given by equation (19) with $n = 1$)

$$\frac{q_o(X)}{q_{\text{ref}}} = 1 + \frac{B}{2}(1 - \cos\pi X) \tag{28}$$

$$\Phi_s = \left(1 + \frac{B}{2}\right)Z_s - \frac{B}{2\pi}\cos\pi X \sinh\pi Z_s \tag{29}$$

Free Boundary Solution for Three-Dimensional Prism. The previous two-dimensional solution can be used

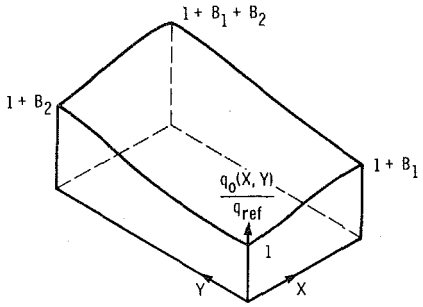

Fig. 2 Heat flux distribution imposed on surface of porous region with rectangular cross section

to obtain an unknown boundary solution in three dimensions. This is done by superposition of two solutions. This is possible because for each part of the solution $\phi = 0$ at $Z = 0$, and ϕ has zero normal derivatives at all four sides; thus the boundary conditions are preserved during the superposition. By adding a Y variation, the heating function in equation (26) becomes

$$\frac{q(X,Y)}{q_{\text{ref}}} = 1 - \frac{B_1(1-A_1)}{2A_1}\left[1 - \frac{1+A_1}{1+A_1\cos(\pi X)}\right] - \frac{B_2(1-A_2)}{2A_2}\left[1 - \frac{1+A_2}{1+A_2\cos(\pi\ Y/L)}\right] \tag{30}$$

As is shown in Fig. 2 this function is unity at the origin, increases to $1 + B_1$ and $1 + B_2$ at the adjacent corners, and reaches $1 + B_1 + B_2$ at the corner diagonally from the origin.

The solution of $\nabla^2\phi = 0$ is

$$\phi(x,y,z) = K_2 z + \frac{1}{2i}\int_{x-iz}^{x+iz} F\left[\cos\left(\frac{\pi\xi}{w}\right)\right]d\xi + \frac{1}{2i}\int_{y-iz}^{y+iz} G\left[\cos\left(\pi\frac{\beta}{l}\right)\right]d\beta \tag{31}$$

From equation (16) the derivative of ϕ in the Z-direction at $Z = 0$ must have the form of equation (30), so the K_2, F, and G are determined by satisfying this boundary condition. Then the integration of equation (31) yields, after placing the results in dimensionless form

$$\Phi_s = \frac{\phi_s k_m (t_o - t_\infty)}{w q_{\text{ref}}} = Z_s\left[1 - \frac{B_1(1-A_1)}{2A_1} - \frac{B_2(1-A_2)}{2A_2}\right] + \frac{B_1\sqrt{1-A_1^2}}{4\pi A_1} ln\left[\left\{\left[\sqrt{\frac{1+A_1}{1-A_1}}(\cosh \pi Z_s + \cos \pi X) + \sinh \pi Z_s\right]^2 + \sin^2 \pi X\right\} \Big/ \left\{\left[\sqrt{\frac{1+A_1}{1-A_1}}(\cosh \pi Z_s + \cos \pi X) - \sinh \pi Z_s\right]^2 + \sin^2 \pi X\right\}\right]$$

$$+ \frac{LB_2\sqrt{1-A_2^2}}{4\pi A_2} ln\left[\left\{\left[\sqrt{\frac{1+A_2}{1-A_2}}\left(\cosh \pi\frac{Z_s}{L} + \cos \pi\frac{Y}{L}\right) + \sinh \pi\frac{Z_s}{L}\right]^2 + \sin^2 \pi\frac{Y}{L}\right\} \Big/ \left\{\left[\sqrt{\frac{1+A_2}{1-A_2}}\left(\cosh \pi\frac{Z_s}{L} + \cos \pi\frac{Y}{L}\right) - \sinh \pi\frac{Z_s}{L}\right]^2 + \sin^2 \pi\frac{Y}{L}\right\}\right] \tag{32}$$

Results for $Z_s(X,Y)$, the surface shape of the porous region, are given in the next section.

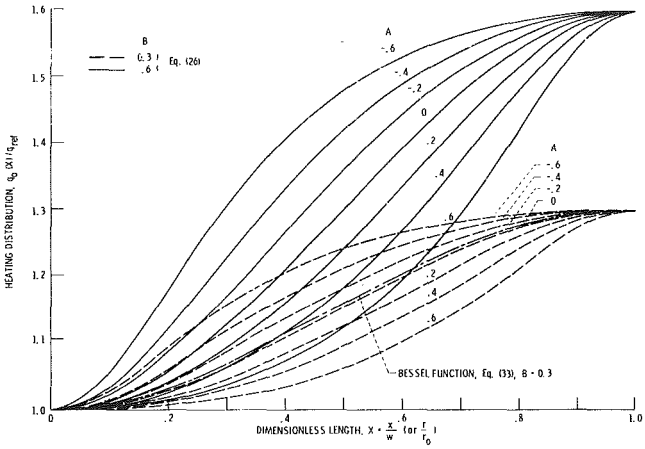

Fig. 3 Imposed heating distributions for various A and B

Axisymmetric Solution. By proper choice of the A value in equation (26) it is possible to obtain a two-dimensional heating function that has the same shape as a portion of the zeroth-order Bessel function, J_o. This will be used to illustrate the effect of a cylindrical geometry, as shown in Fig. 7, as compared with a two-dimensional slab. The heating variation at $z = 0$ in Fig. 7 is selected to be,

$$\frac{q_o(r/r_o)}{q_{\text{ref}}} = 1 + \frac{B}{1 - J_o(\gamma_1)}\left[1 - J_o\left(\gamma_1\frac{r}{r_o}\right)\right] \quad 0 \le r \le r_o \tag{33}$$

where γ_1 is the first zero of J_1. A product solution for $\nabla^2\phi = 0$ in cylindrical coordinates yields for this heating function

$$\Phi_s = \frac{\phi_s k_m (t_o - t_\infty)}{r_o q_{\text{ref}}} = \left[1 + \frac{B}{1 - J_o(\gamma_1)}\right]\frac{z_s}{r_o} - \frac{B}{\gamma_1[1 - J_o(\gamma_1)]} J_o\left(\gamma_1\frac{r}{r_o}\right)\sinh\left(\gamma_1\frac{z_s}{r_o}\right) \tag{34}$$

Results for the surface shape z_s/r_o as a function of r/r_o will be shown in the next section and compared with the two-dimensional geometry.

Results and Discussion

Shapes of the porous region will be presented first for a two-dimensional geometry with heating distributions given by equation (26). The distributions are shown in Fig. 3; the amplitude of the variation is B, and A adjusts the rate at which the variation occurs. Each combination of A and B was inserted into equation (27) and a table of Φ_s calculated for X and Z_s values. Then $Z_s(X)$ values can be interpolated at constant Φ_s values, where Φ_s is the physical parameter determining the average thickness of the porous region (note that when the heating is uniform, $B = 0$, the region thickness is $Z_s = \Phi_s$).

As might be expected it is not possible to obtain coolant inlet surface shapes that can control the flow to deal with any heat flux variation at the coolant exit. The inlet surface shape variation with X must be more pronounced than the heating variation in order to produce the required coolant distribution along the exit surface. This is especially true for a thick region (large Φ_s) as the coolant velocities will tend to equalize while passing through the porous region (this is physically why the problem is poorly posed). For a sufficiently thin region (very small Φ_s) it is usually possible to find a shape that will deal with the imposed heating distributions $q_o(X)$ shown in Fig. 3. As Φ_s is increased, however, the behavior of equation (27) is illustrated in Fig. 4 where for a typical A and B the Φ_s is plotted as a function of Z_s at each X. Above a certain Φ_s (about 0.54 in this example) the Z_s values become multivalued and a solution does not exist.

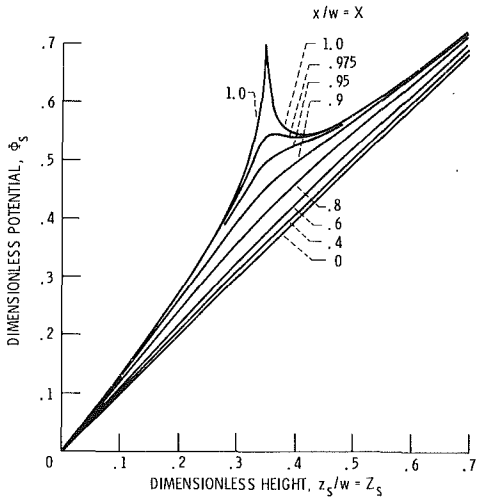

Fig. 4 Typical example of behavior of Φ_s with X and Z_s; parameters $A = 0.6$, $B = 0.3$

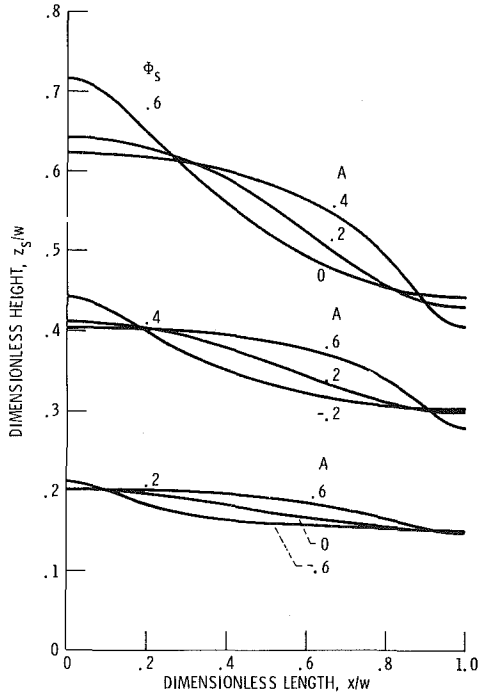

(a) Effect of parameter A for amplitude B = 0.3.

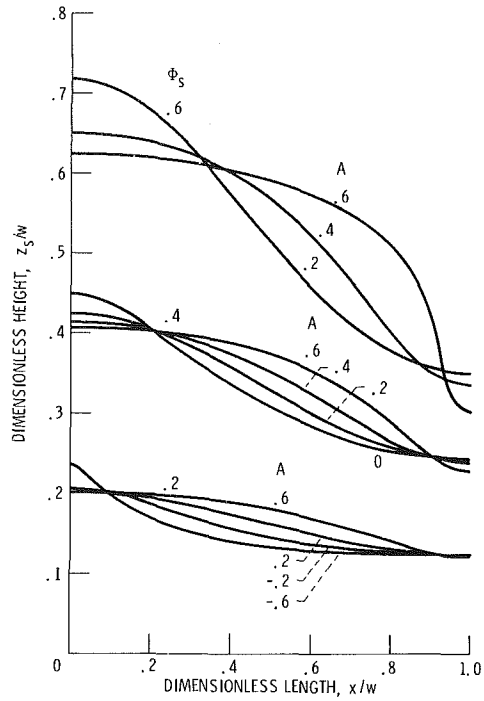

(b) Effect of parameter A for amplitude B = 0.6.

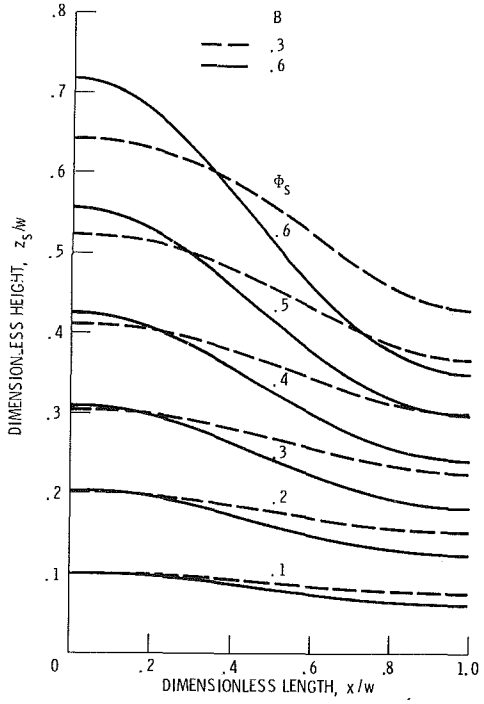

(c) Heating parameter A = 0.2.

Fig. 5 Effect of various parameters on the shape of the porous surface

Figure 5 gives the shape of the porous region for heating amplitudes $B = 0.3$ and 0.6, and for various shape factors A and thicknesses (Φ_s values); these shapes correspond to the heating distributions in Fig. 3. Since the imposed heating increases with x, the thickness of the region decreases with x to allow an increased amount of coolant to flow to the regions of high heat flux along $z = 0$. For a fixed shape parameter, A, the contour of the upper surface has a more extreme variation as the thickness (Φ_s parameter) is increased; this is required because the flow distribution tends to equalize before reaching the coolant exit surface at $z = 0$ where the heating is imposed. It is noted that solutions do not exist for all A values; for example, in Fig. 5(*a*), for a thick medium, $\Phi_s = 0.6$, there are no solutions for either negative A or for $A = 0.6$. For a moderate heating variation, $A = 0.2$, solutions exist for all the Φ_s values shown. To better illustrate the effect of Φ_s a set of curves for this A value and $B = 0.3$ and 0.6 is given in Fig. 5(*c*).

For three-dimensional rectangular porous inserts, results are shown in Fig. 6 for two values of l/w as calculated from equation (32). The heating distribution at the base of the region is given by equation (30) and is illustrated by Fig. 2. At $x = y = 0$ the $q/q_{\text{ref}} = 1$, and for the B values in Fig. 6 the $q/q_{\text{ref}} = 1.3$ at $x = 0, y = l$ and at $x = w, y = 0$. At $x = w, y = l$ the $q/q_{\text{ref}} = 1.6$; hence the smallest thickness of the porous region will be at this corner. The figure shows the region configuration for three Φ_s values for a square cross section, and for a rectangular cross section of aspect ratio $l/w = 2$. For this aspect ratio the configuration exhibits a somewhat locally two-dimensional behavior.

Figure 7 gives results for the shape of the upper surface of a cylindrical porous region heated at its base. The solid curves

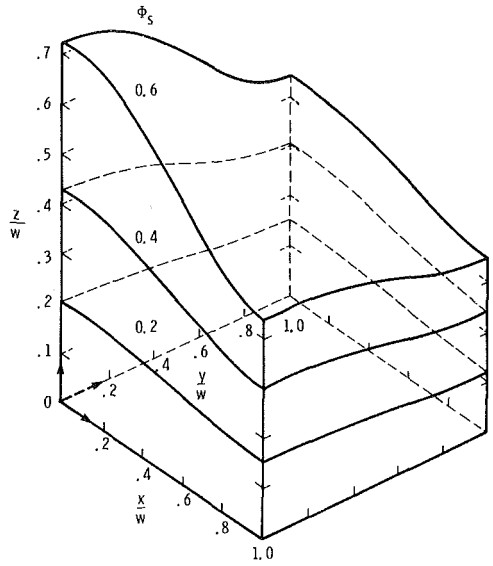

(a) Square cross section, $\ell/w = 1$.

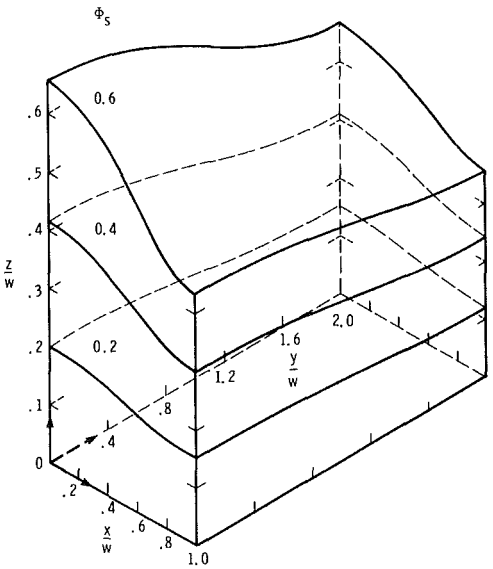

(b) Rectangular cross section, $\ell/w = 2$.

Fig. 6 Surface contours for three Φ_s values: heating parameters $A_1 = A_2 = 0.2, B_1 = B_2 = 0.3$

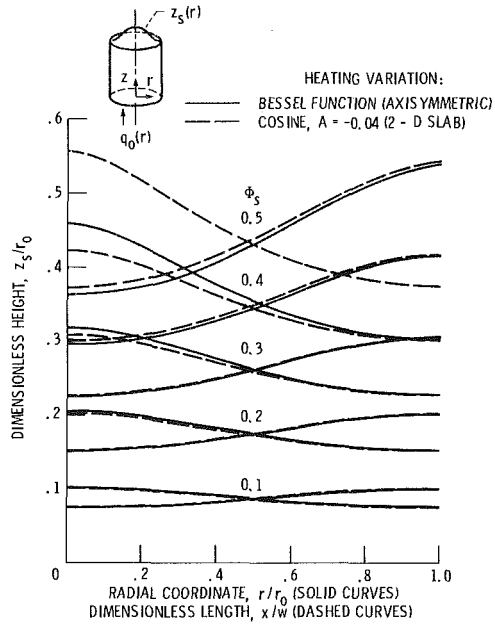

Fig. 7 Axisymmetric surface shapes compared with two-dimensional slab for same heating distribution, $B = \pm 0.3$

are for heating in a Bessel function variation. The curves that decrease from left to right correspond to equation (33) with a positive amplitude, $B = 0.3$; this variation is plotted in Fig. 3. If a negative amplitude of -0.3 is imposed, and the heating distribution normalized so that the reference heat flux is at $r = r_o$ (the heating distribution then ranges from $q(r)/q_{\text{ref}} = 1.3 \rightarrow 1.0$ as $r/r_o = 0 \rightarrow 1.0$), the resulting surface shapes are the curves rising from left to right in Fig. 7. It is found in Fig. 3 that the Bessel function heating variation agrees very well with equation (26) when $A = -0.04$. Using this A, results were computed for a two-dimensional slab, equation (27), and a comparison of the resulting dashed lines in Fig. 7 with the solid lines shows the effect of a cylindrical geometry.

When heating is increasing with r or x, the cylindrical geometry has a greater increase of total heating than the slab case since the cylindrical area is increasing as r^2. This causes the solid curves to drop more rapidly near the origin than the dashed curves. As a result, a solution exists for $\Phi_s = 0.5$ for the slab but not for the cylinder. When heating is decreasing with r or x (curves that are rising from left to right) there is little difference between the two geometries.

Concluding Remarks

The required shape of a porous section of a wall is investigated that will regulate the coolant flow distribution through the porous material and thereby provide desired heat transfer characteristics. One surface of the porous region is to be kept plane. This surface is exposed to a spatially nonuniform heat flux and is to be maintained at a uniform design temperature. The coolant distribution is regulated by the shape of the other wall boundary. The specification of both heat flux and temperature at one surface causes the required region shape to depend on a Cauchy boundary value solution of an elliptic partial differential equation. Solutions are found in two- and three-dimensions for this inherently unstable type of problem. Shapes are given for a variety of heating distributions and average region thicknesses.

Acknowledgment

The authors would like to acknowledge the help of Dr. William F. Ford of the Lewis Research Center in the analysis of this problem.

References

1 Siegel, R., and Goldstein, M. E., "Analytical Solution for Heat Transfer in Three-Dimensional Porous Media Including Variable Fluid Properties," NASA TN D-6941, Sept. 1972.

2 Siegel, R., "Shape of Porous Cooled Region for Surface Heat Flux and Temperature Both Specified," *International Journal of Heat and Mass Transfer*, Vol. 16, No. 9, 1973, pp. 1807-1811.

3 Siegel, R., "Analysis of Shape of Porous Cooled Medium for Imposed Surface Heat Flux and Temperature," NASA TN D-7176, March 1973.

4 Snyder, A., and Siegel, R., "Determination of Boundary Shape of Cooled Porous Region," ASME JOURNAL OF HEAT TRANSFER, Vol. 104, No. 4, Nov. 1982, pp. 722-727.

5 Chester, C. R., *Techniques in Partial Differential Equations*, McGraw-Hill, New York, 1971, pp. 73-74.

6 Shercliff, J. A., "Reflections of a New Editor," *Journal of Fluid Mechanics*, Vol. 106, May 1981, pp. 349-356.

7 Morse, P. M., and Feshbach, H., *Methods of Theoretical Physics, Part I*, McGraw-Hill, New York, 1953, p. 689.

N. V. Suryanarayana
Professor.

T. Scofield[1]
Graduate Student.

R. E. Kleiss[2]

Department of Mechanical Engineering
and Engineering Mechanics,
Michigan Technological University,
Houghton, Mich. 49931

Heat Transfer to a Fluid in Radial, Outward Flow Between Two Coaxial Stationary or Corotating Disks

An experimental study of heat transfer rates to air flowing radially outward between two coaxial, corotating disks was made. Heat transfer data were obtained for five mass flow rates with stationary disks and four mass flow rates and five rotational speeds with rotating disks. Rotation of the disks slightly decreased the average Nusselt numbers compared with the average Nusselt numbers without rotation at the highest speed of rotation (600 rmp), but at lower speeds no consistent trends were observed. The average Nusselt numbers, with and without rotation, can be related as $\overline{Nu} = 0.0529\ Re^{0.71}$ *and the local Nusselt number as* $Nu = 0.124\ Re^{0.608}$.

Introduction

Heat transfer to a fluid in radial flow between disks is of engineering significance in situations such as electrical machinery, rotating heat exchanger, certain types of turbines, etc. Outward flow is quite complex; entry conditions are uncertain; the fluid may be attached at entry or a separation bubble may exist; with stationary disk, there is an adverse pressure gradient as a result of decreasing velocity in the radial direction and the possibility of separation exists; a flow that starts as turbulent flow, may revert to laminar flow. With rotating disks, the radial component of velocity decreases but the tangential component increases, and the conditions under which the flow will be laminar or turbulent are yet to be established.

The purpose of the present study was to experimentally determine the heat transfer rates to an incompressible fluid in outward radial flow between a heated disk and a coaxial, insulated disk, with the disks either stationary or corotating. For the conditions employed in the experiments – flow rates and geometry – measurements of velocity fluctuations with a hot film anemometer indicated that the flow was turbulent with turbulence intensities of up to 40 percent (turbulence intensity related to local mean velocity). There do not appear to be many studies relating to heat transfer rates in turbulent, radial flow. Kapinos [1] and Kapinos et al. [2] have given an analytical treatment with assumed velocity profiles – 1/7 power law – and shear stresses. His analysis is limited to those cases where Reynolds analogy is applicable, with the temperature of the disk varying as the square of the radius and the thermal boundary layer being much less than half the gap between the disks. Here again no details regarding the development of the thermal boundary are given. Owen et al. [5] reports heat transfer results at rotational speeds higher than employed in the present study; a discussion of their results is included under Results and Discussion.

Experimental Apparatus

Figures 1, 2, and 3 give the details of the experimental set up. The building air supply was the source of fluid for the experiments. After passing through an air filter and regulator, the building air supply was routed through a pressure regulator to a 300-L reservoir. From the reservoir, the air passed through a second regulator and then through an orifice plate flow meter built in accordance with ASME recommendations [6]. The pressure drop across the orifice plate was measured with an inclined mercury manometer for pressure drops up to 200 mm and with a U-tube mercury manometer for higher pressure drops. With three pressure regulators and a reservoir in the air line, there was virtually no variation in the pressure drop across the orifice flow meter, indicating a constant mass flow rate. The pressure of air at inlet to the orifice plate was measured with a mercury manometer.

As a check on the calibration of the orifice flow meter, the mass flow rate obtained by the orifice plate measurements were compared with the mass flow rate obtained by velocity measurements. For this purpose, the velocities at the outlet of a long 25.4-mm-dia tube were measured at 7 radial locations, using a micrometer traversing mechanism with a hot film anemometer sensor. The mass flow rates determined by the two methods differed by 0.38 percent, 0.39 percent, and 1.6 percent for three mass flow rates in the range employed in the experiments.

Air entered the top disk through a 2-m long, 41.3-mm i.d., 5.08-mm-o.d. steel tube, flared to 70-mm dia at the inlet to the top insulated disk.

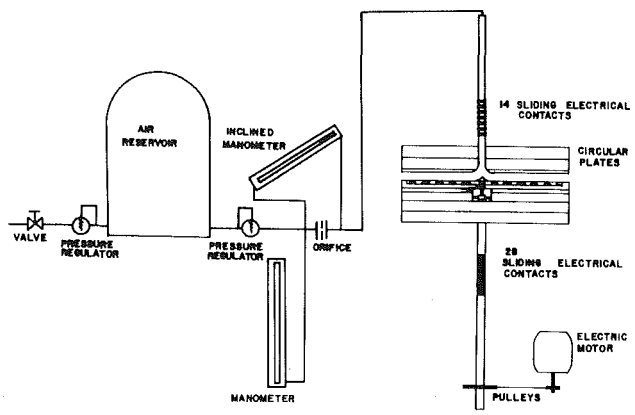

Fig. 1 Schematic of experimental set up

[1] Present address: Cummins Diesel, Columbus, Ind.

[2] Present address: Hewlett Packard, Loveland, Colo.

Contributed by the Heat Transfer Division for publication in the JOURNAL OF HEAT TRANSFER. Manuscript received by the Heat Transfer Division March 1, 1983.

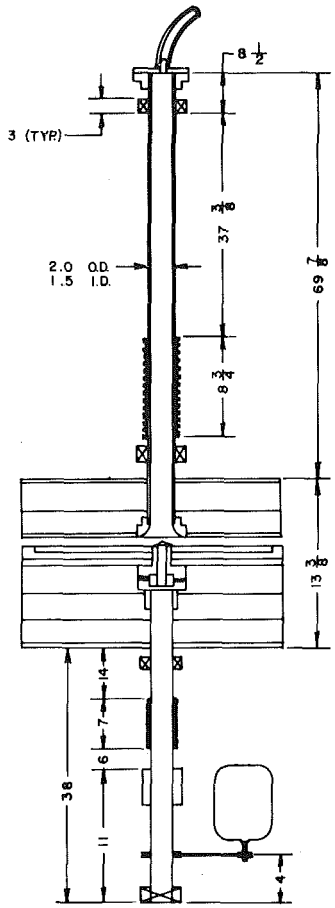

Fig. 2 Details of rotating assembly (all dimensions in inches)

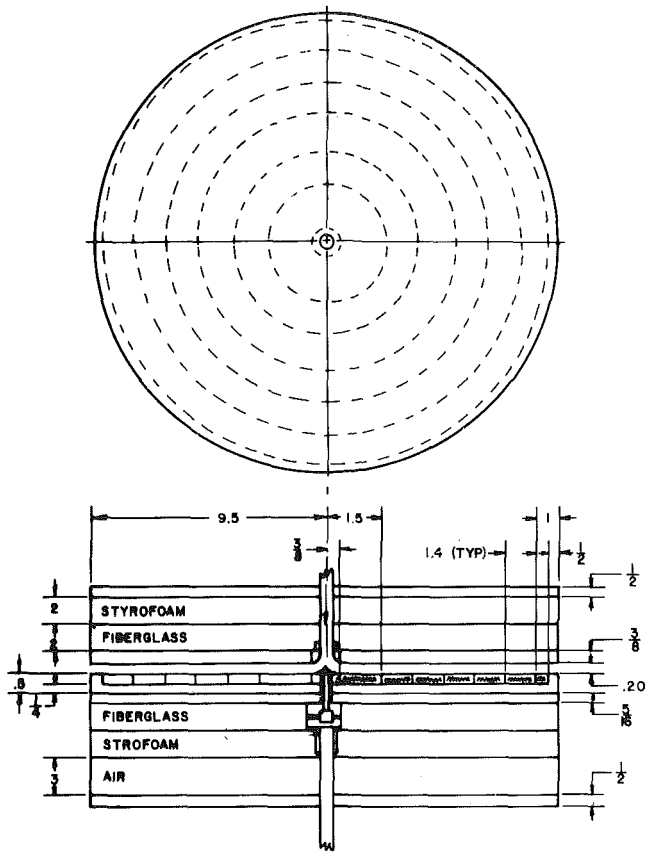

Fig. 3 Heated and insulated disks (all dimensions in inches)

The heated disk was made of seven annular rings of 6-mm thick steel plates. The innermost disk had a radius of 38.1 mm, and each of the five subsequent rings had a radial length of 35.6 mm. The seventh ring, which was used as a guard ring, had a radial length of 12.5 mm. Thus the effective diameter of the heated disk was 431.8 mm. Each ring was separated from its neighboring rings with a 0.005-in. thermoplastic insulation strip. With this arrangement and the temperatures of adjacent rings maintained within 0.5°C, the heat transfer rate from one ring to the adjacent rings is estimated to be less than 1.5 percent of the heat transfer rate from the ring to the air in the worst case with the maximum temperature difference between two adjacent rings and the minimum heat transfer rate from the ring to the air.

Concentric rectangular grooves – 3-mm deep, 0.6–0.7-mm wide (depending on the size of the wire to be embedded), and separated by 1–1.4-mm-thick wall were cut on the underside of the rings. Each ring had about 20 such concentric slots in a radial length of 36 mm. Glass insulated nicrome resistance wire – 22 to 30 g – was embedded in the grooves using Sauereisen high-temperature cement.

Each ring was provided with two 30-gage, copper-constantan thermocouples, diametrically opposite to each other and at the average radius of the ring. The thermocouples were passed through a hole in the ring with the junction brazed to the surface.

The heated plate was placed over a polycarbonate plastic sheet suitably recessed to receive the heated plate. An 8-mm-thick steel disk supported the plastic sheet. The steel backing plate was attached to a hollow shaft and insulated with 50-mm-thick fiberglass insulation followed by 50-mm-thick styrofoam sheet. Towards the lower end of the shaft 21 pairs of slip rings were provided. Of these, 14 pairs were made of 3-mm-wide copper rings for the thermocouples and the rest by a prefabricated slip ring assembly for the supply of electrical power to the heating elements. Stationary copper strips acting

Nomenclature

a = half gap
c_b = constant pressure specific heat
h = local heat transfer coefficient
$\bar{h}$ = average heat transfer coefficient
j = thermal conductivity
$\dot{m}$ = mass rate of flow
N_u = local Nusselt number ($h\,2a/k$)
$\overline{N_u}$ = Average Nusselt number ($\bar{h}\,2a/k$)
q_{pl} = heat transfer rate from the heated plate
$Re_r = \dfrac{\omega r_a 2a}{\nu}$
Re_m = mass flow Reynolds number ($\dot{m}/4\pi\mu a$)
r_a = average radius
r_e = exit radius
r_i = inlet radius
T_e = temperature of air at exit
T_i = temperature of air at inlet
T_w = temperature of heated plate
U_{av} = integrated mean velocity
μ = viscosity
ν = kinematic viscosity (μ/ρ)
ρ = density
ω = angular rotational speed

as brushes made contact with the slip rings. Copper-constantan wires were connected to each pair of slip rings. The shaft was supported by one bearing below the insulation and by a second thrust bearing at the bottom of the shaft. The electrical leads to each heating element were connected suitably through a double pole, double throw knife switch so that in one position the current passed through a 50-mv shunt, and in the other, bypassed the shunt. Each heating element was independently connected to a variac.

The top, insulated, unheated disk of 9-mm-thick aluminum was provided with six thermocouples corresponding to one set of thermocouples in the outer six rings of the heated disk. The top disk was supported by three pins at the outer edge of the disks. These pins served to adjust the gap between the disks and to drive the entire assembly as one unit by the variable speed electrical motor.

Close to the entry of the air to the top disk, the tube was provided with a 305-mm-long cross piece so that the air entered the disk with the same angular velocity as the disks in all cases. The hollow steel tube attached to the top disk was supported by two bearings and carried the slip rings to monitor the signal from the thermocouples attached to the top disk.

In earlier experiments to measure velocity profiles and fluctuations, it was found that it was extremely difficult to obtain uniform radial flow without a central cone attached to the bottom disk. In this set-up a teflon cone, 44.5-mm dia and 5-mm high was installed at the center of the heated disk. This cone could be moved 2 mm in any direction, as necessary, to obtain uniform radial flow.

Experimental Procedure

The procedure for obtaining heat transfer data consisted of: (*a*) establishing heat transfer rates across the insulation, (*b*) obtaining heat transfer with the disks stationary corresponding to mass flow Reynolds numbers (Rem) of 5,000, 10,000, 15,000, 20,000, and 25,000, and (*c*) obtaining heat transfer rates with the disks rotating at 200, 375, 450, 525, and 600 rpm. At each of these rotational speeds, measurements were made at four mass flow rates corresponding to mass flow Reynolds numbers of 10,000, 15,000, 20,000, and 25,000.

To obtain the heat transfer rates across the insulation, the heated disk was insulated on the top side with the same insulation as was provided on the bottom side. The disk was then heated till all the rings were at a uniform temperature, within 0.2°C. The power supply to each of the rings then gave the heat transfer rates from the rings across the insulation. These measurements were made for two values of the disk temperature corresponding to differences of 40 and 66°C between the temperature of the disk and the surrounding air. The heat transfer rate from the rings across the insulation was linearly proportional to the temperature difference between the rings and the surrounding air. When the disks were rotated, the insulation losses increased with the rotational speed in a nonlinear way. Interpolated values were used to determine the heat transfer rate across each ring for any given speed. The heat transfer rate from the top unheated disk across the insulation per degree temperature difference between the disk and the surroundings was assumed to be the same as that from the heated disk.

Heat Transfer Rates – Stationary Disks

With the gap between the disks adjusted at 5 mm, the air flow was adjusted for the maximum flow rate employed in the experiment. The position of the central cone at the bottom disk was adjusted to yield swirl-free flow. This was verified by measuring the maximum velocity at exit at several azimuthal positions with a hot film anemometer. These velocities were within ± 1 percent of the average of the maximum values. When the cone was so adjusted for the highest mass flow rate, it remained swirl-free at lower flow rates.

The flow rate was then adjusted to yield nominal Rem of 5,000 and the electrical power to each of the heating elements continuously adjusted until steady state with uniform temperature was attained. Steady state was assumed to have been attained when the temperature of the rings did not change by more than 0.1°C in less then 15 min. Uniform temperature of the disk was assumed to have been attained when the temperatures of the rings were within ± 0.5°C. The heated disk was maintained at a nominal temperature of 80°C with the inlet air at about 25°C. Typically if took about 4 hrs to reach steady state starting from cold plates.

Temperature profiles of air at the exit of the sixth heated ring were obtained at four azimuthal locations 90 deg apart. A 26-gage, copper-constantan thermocouple was fixed to a thin copper strip and traversed by a micrometer traversing arrangements. Temperature of air was obtained at seven axial locations, in a distance of 5 mm. The minimum distance between the thermocouple and the plates was ~ 0.6 mm.

After steady state was reached, three sets of measurements, each set approximately 30 min after the previous set, were recorded.

The procedure for obtaining the heat transfer measurements with rotating disks was essentially the same as for stationary disks. After fixing the air flow rate, measurements were recorded at each of the five rotational speeds employed in the tests. Temperature profile of air at exit could not be obtained because of the pins at the outer edge of disks. A total of 24 sets of measurements for 4 different values of mass flow rates 6 rotational speeds at each of these mass flow rates were obtained.

Data Analysis

Heat transfer to air in the case of stationary disks was determined by two methods: by measuring the value of the electrical power input and subtracting the heat transfer rate across the insulation, and by determining the difference in the rate of enthalpy flow out and in. To determine the enthalpy flow rate at exit of the sixth ring, the average temperature obtained by the temperature traverse was used as the mean bulk temperature. The heat transfer rates obtained by the two methods were within 1 percent for Rem of 15,000 and 20,000, within 5 percent for Rem of 10,000 and 25,000 but differed by 14 percent for the lowest Rem 5,000. In all computations, heat transfer rate to air was computed on the basis of electrical power input.

Average Nusselt number based on the average heat transfer coefficient was computed using the logarithmic temperature difference as

$$\bar{h} = \frac{q_{\mathrm{pl}}}{\pi(r_e^2 - r_i^2)(T_e - T_i)} \ln\left(\frac{T_w - T_i}{T_w - T_e}\right)$$

With heat transfer rate from each of the rings and the mass flow rate of air known, the temperature of air at exit of each of the rings was determined. From these values the average heat transfer coefficients for r_i = 22 mm and r_e = 38.1 mm, 73.7 mm, 109.2 mm, 144.8 mm, 180.3 mm, 215.9 mm – the outer radii of each of the six heated rings-were determined. In a similar manner, knowing the heat transfer rate from each of the rings to the air and the inlet and exit temperatures at radii corresponding to the inner and outer radii of each ring, the heat transfer coefficients from each of the rings were also determined. These heat transfer coefficients averaged over the radial length of 35.6 mm for each ring ($r_e - r_i$) will, hereafter, be referred to as local heat transfer coefficients and the Nusselt numbers based on them as local Nusselt numbers. The

average and local heat transfer coefficients for rotating disks were also determined in the same way.

Results and Discussion

In the expression used for determining the heat transfer coefficient, q_{pl} is the total heat transfer rate from the heated disk or ring to the air. the major part of the heat transfer takes place by convection to the adjacent air but a smaller part by radiation from the heated disk to the insulated disk by radiation and back to air by convection from the insulated disk. Radiation heat transfer rates from each heated ring to the insulated top plate were estimated by dividing the upper insulated plate into the same number of rings as the heated plate. Using the appropriate shape factors, the radiosities and the heat transfer rates from each of the rings were then computed. An emissivity of 0.2 for the aluminum insulated plate and 0.6 for the polished steel plate were employed. These computations showed that such radiation heat transfer rate accounted for approximately 4–9 percent of the total heat transfer rate.

For a meaningful representation of the experimental results, one should establish the appropriate dimensionless parameters. The convective heat transfer coefficient may be treated as

$$\bar{h} = \bar{h}(\rho, \mu, c_p, k, r_i, r_e, a, \omega, \dot{m})$$

From this relationship, one may obtain several dimensionless parameters such as the Nusselt number, Prandtl number, Reynolds number, length ratios such as r_e/r_i, r_i/a, etc. It seems appropriate to choose the gap between the disks as the characteristic length to form the Nusselt number. As for the Reynolds number, the choice of a characteristic velocity or length is not readily apparent. If the mass flow Reynolds number ($\dot{m}/4\pi\mu a$) is employed, its value remains constant irrespective of the radii at inlet and exit and the influence of the continuously decreasing velocity in the radial direction cannot be shown without explicitly including the geometric ratio, r_e/r_i. The influence of the inlet and exit radii may be accounted for by recognizing their influence on the radial component of the velocity. The average radial velocity continuously decreases in the direction of flow and the characteristic velocity may be taken as the integrated mean velocity defined by

$$U_{av} = \frac{1}{r_e - r_i}\int_{r_i}^{r_e} \frac{\dot{m}}{4\pi a\rho}\frac{dr}{r} = \frac{\dot{m}}{4\pi a\rho}\frac{\ln(r_e/r_i)}{r_e - r_i}$$

Thus the Reynolds number may be defined by $\rho U_{av} 2a/\mu$. The effect of rotation may be accounted for by the rotational Reynolds number defined by $\omega r_a 2a/\nu$ where r_a represents the average radius so that the Rotational Reynolds number is based on the average tangential velocity of the disk.

The average Nusselt numbers corresponding to r_i = 22 mm, and r_e/r_i values of 1.72, 3.32, 4.92, 6.52, 8.12, and 9.73 are shown in Fig. 4 for stationary disks. This plot includes data from earlier experiments [3]. As can be expected the Nusselt number increases with Reynolds number. However, the higher Reynolds numbers correspond to low values of r_e/r_i where the thermal boundary layer is still developing and the high heat transfer coefficients are the combined result of high average velocity and developing thermal boundary layer. In passing, it may be mentioned that in radial flow considered here, there is no such thing as fully developed velocity profile except in the case of creeping flow for large values of r_e/r_i. From this plot it is easily perceived that a relation of the type $\overline{Nu} = c\,Re^m$ will represent the experimental data. A least square fit of the data gave the relation

$$\overline{Nu} = 0.0332\,Re^{0.782} \quad (1)$$

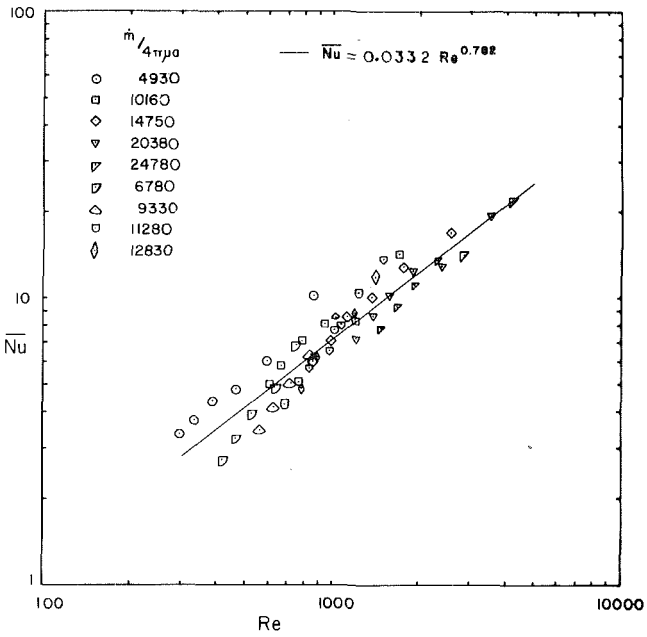

Fig. 4 Average Nusselt numbers – stationary disks

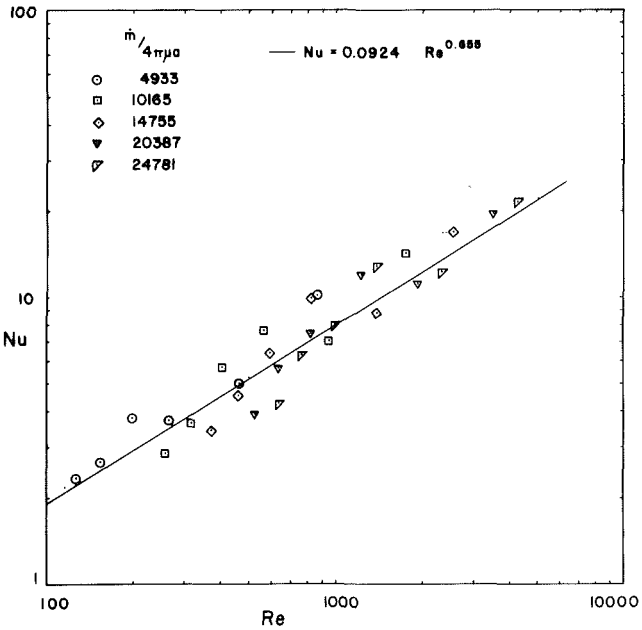

Fig. 5 Local Nusselt numbers – stationary disks

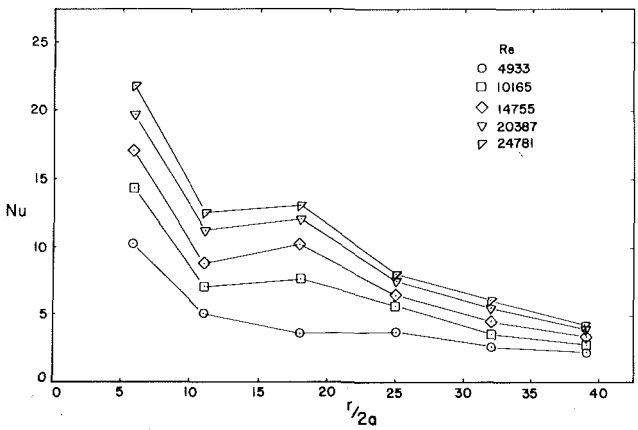

Fig. 6 Local Nusselt numbers – stationary disks

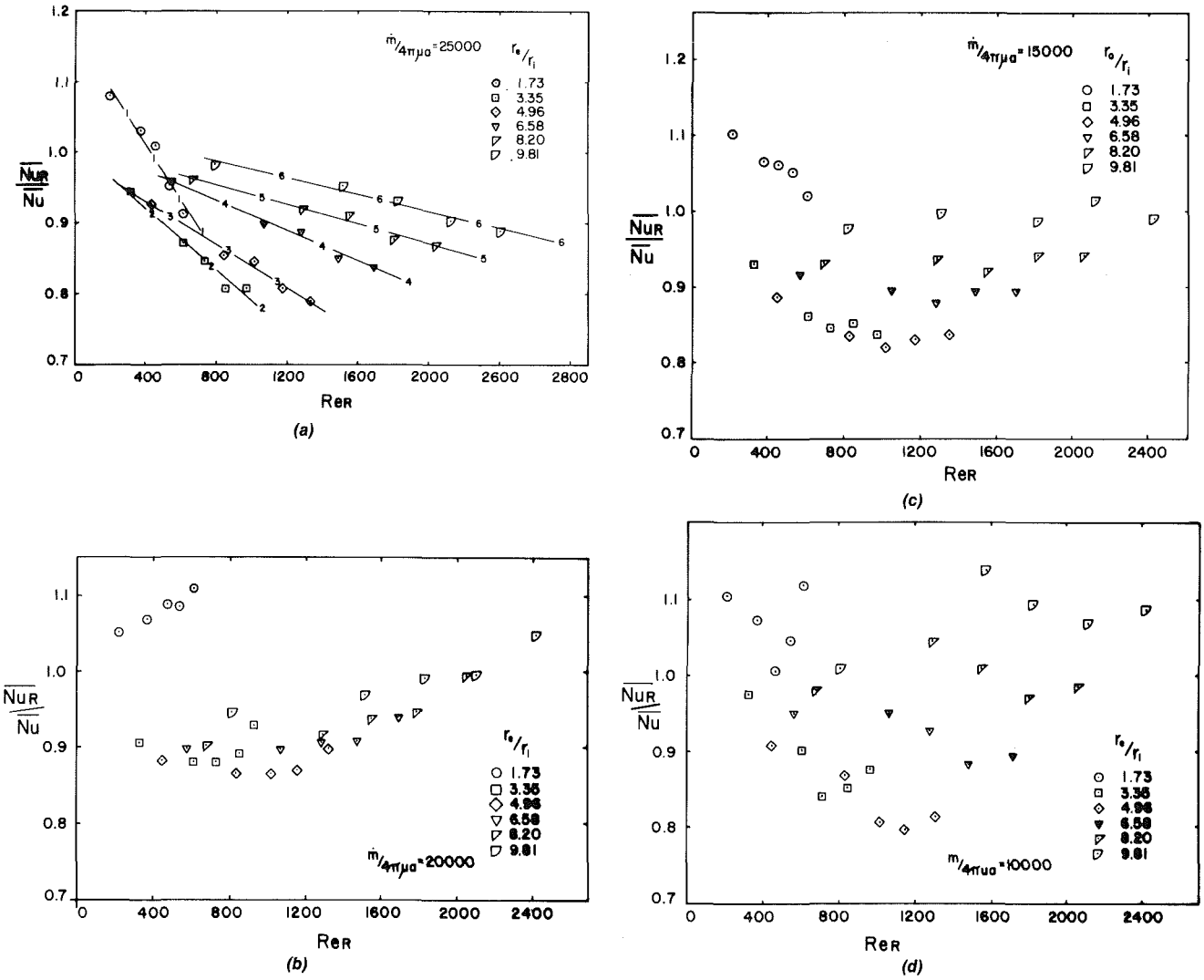

Fig. 7 Effect of rotation on average nusselt numbers

If we denote the expected value of the Nusselt number for a given value of Re by $\overline{\text{Nu}}$, and the actual experimental value of the Nusselt number of $\overline{\text{Nu}}$e, the deviation of the experimental value may be expressed as $D = (\overline{\text{Nu}} - \overline{\text{Nu}}\text{e})/\overline{\text{Nu}}$. The spread of data may then be indicated by $\sqrt{\Sigma D^2/N}$ where N is the total number of experimental values. In the present case, the value of $\sqrt{\Sigma D^2/N}$ is 0.17.

The local Nusselt numbers (based on the heat transfer coefficient from each ring), and Reynolds number is shown in Fig. 5 as a log-log plot. All these values may be correlated by the relation

$$\text{Nu} = 0.0924\ \text{Re}^{0.655} \tag{2}$$

In this case the value of $\sqrt{\Sigma D^2/N}$ is 0.19. Figure 6 shows the local Nu plotted against the dimensionless radius $r/2a$ for the five mass flow rates. This shows that the heat transfer coefficient decreasing with increasing radius except at $r/2a$ = 17 for mass flow Reynolds numbers greater than 10,000, and $r/2a$ = 25 for mass flow Reynolds number of 5,000. But as only one experimental set up was used in the experiment, it would be premature to draw any conclusions. It may be caused by an yet undetermined source of experimental uncertainty or by some fluid flow phenomena. Some preliminary experimental and computational work carried out here have indicated the possibility of flow separation and reattachment. It is possible that the higher Nu values occur where reattachment takes place. Further systematic study should be made before such a trend is confirmed. (The lines in this figure are for visual convenience only and do not indicate any correlation or analysis.)

Effect of Rotation

To show the effect of rotation the ratio of $\overline{\text{Nur}}/\overline{\text{Nu}}$ is shown plotted against Rer in Fig. 7. Figure 7(*a*) shows the data for all the six rotational speeds employed in this experiment, for the highest mass flow rate. The lines marked 1-1, 2-2, etc., show the number of rings over which the heat transfer coefficient is averaged. This particular figure shows some consistent trends. For the first ring the heat transfer coefficient initially increases, but with an increase in rotational speed, it decreases. From the second ring onwards, the heat transfer rate decreases with increasing speed but there is a continuous reduction in the rate of such decrease. Before attempting to draw any further conclusions, one may study Fig. 7(*b*)–7(*d*) showing the effect of rotation for other mass flow rates. From these figures, it can be concluded that no general trends can be established to indicate the effect of rotation. It is also seen that the heat transfer coefficients with rotation are in the general range of ± 15 percent of those with stationary disks for the same value of Re. Keeping in mind the spread of data with stationary disks, all $\overline{\text{Nu}}$ – for both stationary and rotating disks – are shown plotted in Fig. 8. In this figure, the dot

(.) represents the mean of all Nu at a given Re and the vertical line through the dot the range of values. All these values may be correlated by

$$\overline{\mathrm{Nu}} = 0.0529\ \mathrm{Re}^{0.71} \tag{3a}$$

The value of $\sqrt{\Sigma D^2}/N$ is 0.176. Equation (1) representing the best fit of data for stationary disks is also shown in Fig. 8. The analyses given in [1] and [2] are for both plates heated and are not directly useful for comparison with the present experimental results. Owen et al. [5] have given experimental results of heat transfer rates to air flowing between a rotating heated disk and coaxial insulated disk. The mass flow rates and rotational speeds are much higher than those employed in the present experiments. In their discussion regarding the effect of rotation, they give the relation developed for stationary disks by Haynes and Owen

$$\frac{\bar{h} r_e}{k} = 0.0145\left(\frac{\dot{m}}{2\mu a}\right)^{0.8}$$

or

$$\overline{\mathrm{Nu}} = 0.0631\ (\mathrm{Rem})^{0.8}\ 2a \tag{3b}$$

This correlation and equation (3*a*) are shown in Fig. 9. The two equations do not agree with each other either in the trends or in actual values. It must be pointed out that Equation 3(*b*) will predict the same heat transfer coefficient, irrespective of the values of r_i and r_e, for given mass flow rate and gap. This is unlikely to be the case. On the other hand, equation (3*a*) being based on the integrated mean value of the velocity, attempts to take into account the effect of the values or r_i and r_e. They also state that for values of $\mathrm{Rem}/(\omega \mathrm{re}^2/\nu) > 1.7$, rotation does not have a significant effect on the convective heat transfer results. In the present study, the value of $\mathrm{Rem}/(\omega \mathrm{re}^2/\nu)$ was as low as 0.05, and even at this value rotation does not appear to increase the heat transfer rates significantly.

The local Nusselt numbers with rotating disks are shown in Figs. 10(*a*)-10(*d*). From these figures, no consistent trends can be discerned. The effect of rotation appears to be to slightly reduce the heat transfer coefficients up to 20 percent for dimensionless radii in the range 2.5 to 4.1 and to increase the heat transfer coefficients for larger radii. At a radius of 9.0, the increase in the heat transfer coefficient is of the order of 10–50 percent over the value with stationary disks.

Figures 11 shows all the local heat transfer coefficients – with and without rotation – similar to Fig. 8. All of these values can be correlated by the equation

$$\mathrm{Nu} = 0.124\ \mathrm{Re}^{0.608} \tag{4}$$

Equation (2) representing the best fit experimental data for stationary disks is also shown in the figure. The value of $\sqrt{\Sigma D^2}/N$ is 0.187 for equation (4).

To determine if the flow was turbulent or laminar, some measurements of velocity fluctuations were made with a hot film anemometer at radii of 125 mm and 200 mm. The mass rates of flow corresponded to Rem of 7000–8300. Turbulence intensities (referenced to local average velocity) of 4–9 percent at a distance of 0.005 in (0.127 mm) and in the range 13–25 percent at a distance of 0.2 in. (5 mm) when the gap between the disks was 0.25 in. (6.3 mm). Because of these high turbulence intensities, the flow in the present study may be taken as turbulent. From an inspection of the velocity profiles at two different radii, it was also observed that, for the conditions of flow in the present experiments, possibility of separation exists.

From Fig. 7 and 10, no consistent trends relative to the effect of rotation are observed. Comparison with the results of Owen et al. [5] show a lack of consistent trends. Figure 6

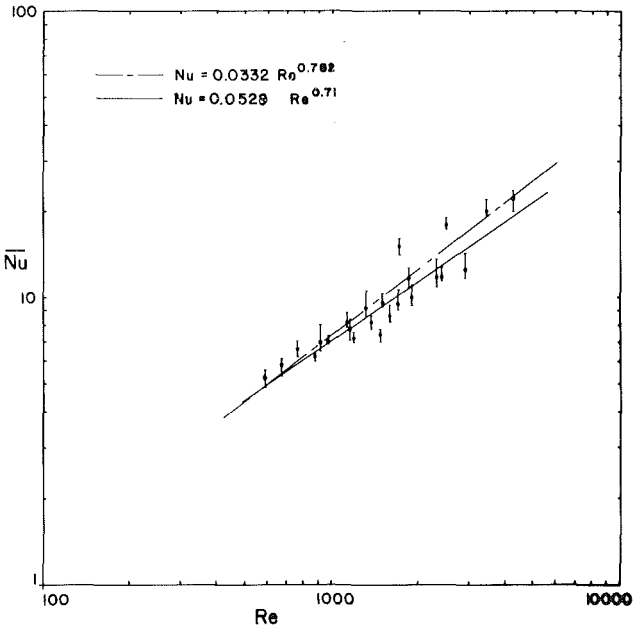

Fig. 8 Average Nusselt numbers – stationary and rotating disks

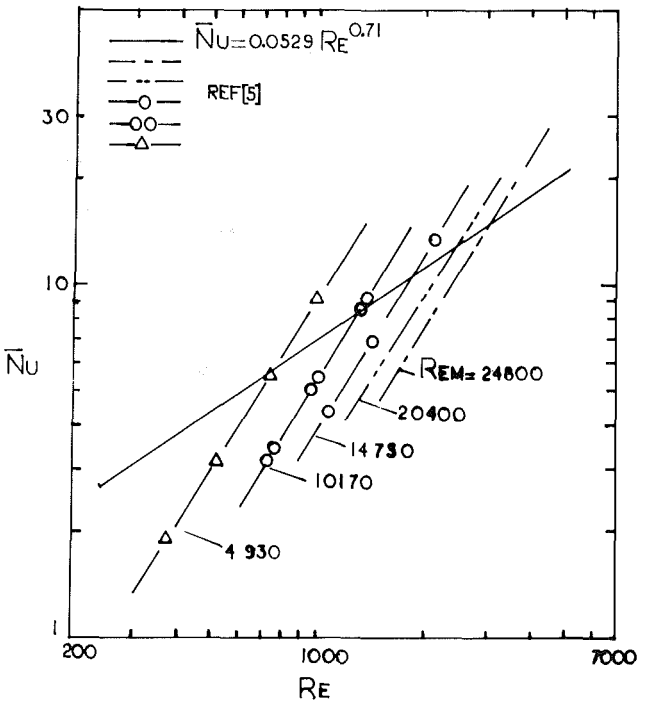

Fig. 9 Comparison of results with reference [5]

shows some unusual trends. All these point out to the need for more extensive experimental and analytical studies to explain all the observed phenomena. This should include studies to define the flow field and local heat transfer rates over a wide range of the appropriate variables. The variables should include the gap ratio $(2a/r_i)$, the ratio of inlet to exit radii (r_e/r_i), the mass flow Reynolds number (Re*m*), rotational Reynolds number (Re*r*) and possibly different inlet conditions (square or rounded entry) and uniform temperature or heat flux. Because of the large number of variables, a systematic study is called for.

The uncertainty in the heat transfer coefficient is estimated at 5 percent. The nonuniformity of the surface temperature

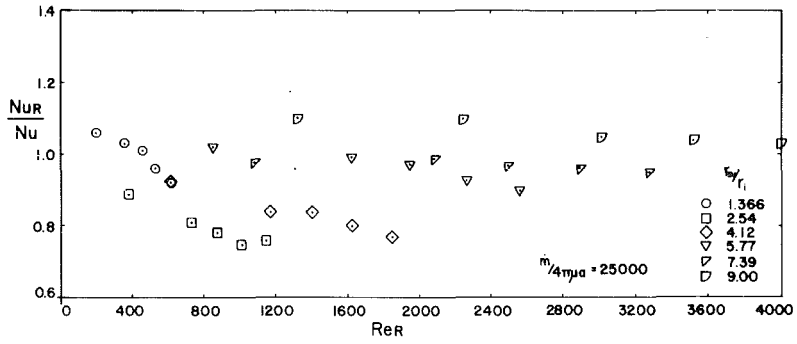

(a)

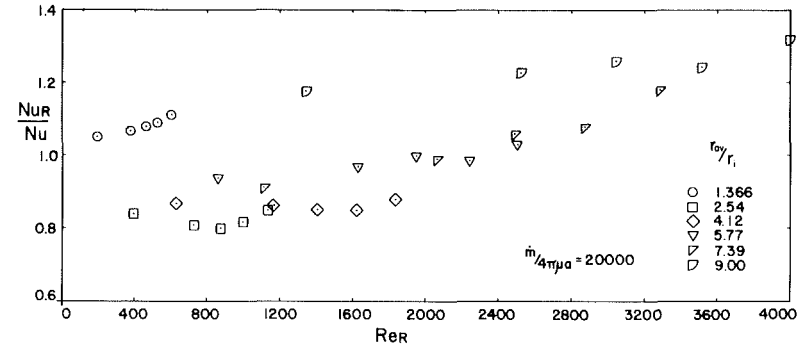

(b)

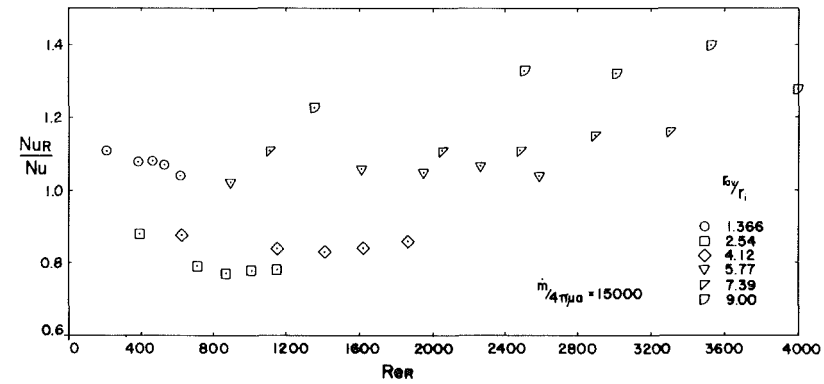

(c)

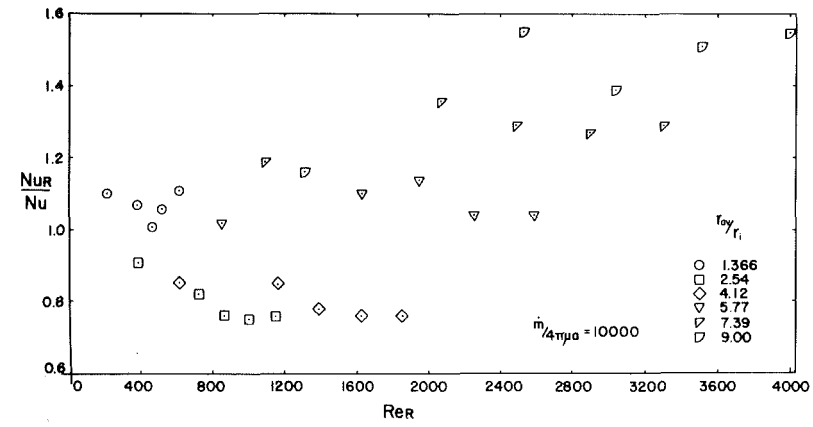

(d)

Fig. 10 Effect of rotation on local Nusselt numbers

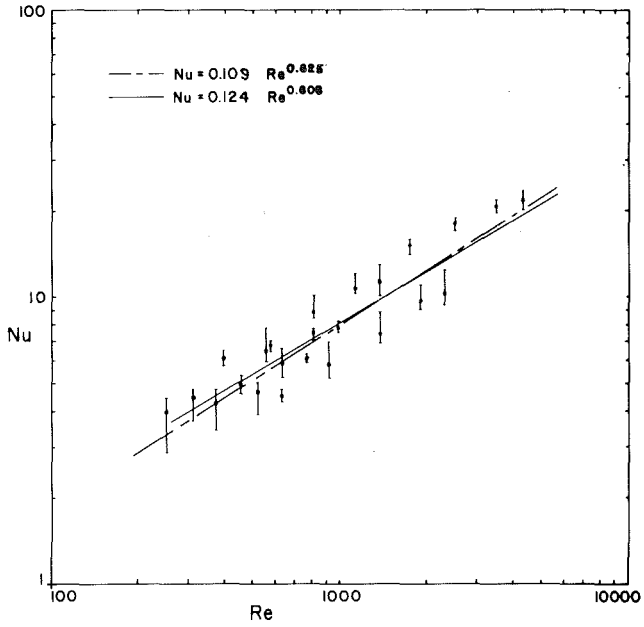

Fig. 11 Local Nusselt numbers – stationary and rotating disks

defined as $\Delta\ (T_w - T_i)/T_w - T_i$ was estimated at less than 4 percent. The variation in the gap between the disks as a fraction of the gap was 2 percent. Details of experimental set up, data, etc., are available in [4].

Acknowledgments

The study was made possible by the support of the National Science Foundation through their grant Eng. 77-11249.

References

1 Kapinos, V. M., "Heat Transfer From a Disc Rotating in a Housing with a Radial Flow of Coolant," *Journal Eng. Phy.*, Vol. 8, 1965, pp. 35–38.

2 Kapinos, V. M., Pubtovalvou, V. N., and Rudko, A. P., "Heat Transfer During the Flow of a Medium from the Center to the Periphery Between Two Rotating Disks," *Heat Transfer Soviet Research*, Vol. 5, No. 1, 1973, pp. 1–9.

3 Suryanarayana, N. V., and Kleiss, R. E., "Heat Transfer to an Incompressible Fluid in Radial Turbulent Flow Between Two Co-axial Disks," Michigan Technological University Report, 1981.

4 Suryanarayana, N. V., and Scofield, T., "Heat Transfer to an Incompressible Fluid in Radially Outward, Turbulent Flow Between Two Coaxial, Corotating Disks," Michigan Technological University Report, 1982.

5 Owen, J. M., Haynes, C. M., and Bayley, F. J., "Heat Transfer from an Air Cooled Rotating Disk," *Proc. Royal Soc. A.336*, London, 1974, pp. 453–473.

6 Fluid Meters, Their Theory and Application, ASME, New York, 1959.

Maldistributed Inlet Flow Effects on Turbulent Heat Transfer and Pressure Drop in a Flat Rectangular Duct

E. M. Sparrow
Fellow ASME

N. Cur

Department of Mechanical Engineering,
University of Minnesota,
Minneapolis, Minn. 55455

The effects of flow maldistribution caused by partial blockage of the inlet of a flat rectangular duct were studied experimentally. Local heat transfer coefficients were measured on the principal walls of the duct for two blockages and for Reynolds numbers spanning the range between 6000 and 30,000. Measurements were also made of the pressure distribution along the duct, and the fluid flow pattern was visualized by the oil-lampblack technique. Large spanwise nonuniformities of the local heat transfer coefficient were induced by the maldistributed flow. These nonuniformities persisted to far downstream locations, especially in the presence of severe inlet flow maldistributions. Spanwise-average heat transfer coefficients, evaluated from the local data, were found to be enhanced in the downstream portion of the duct due to the flow maldistribution. However, at more upstream locations, where the entering flow reattached to the duct wall following its separation at the sharp-edged inlet, the average coefficients were reduced by the presence of the maldistribution.

Introduction

Typically, in pipe- or duct-flow experiments, efforts are made to obtain inlet velocity distributions which either are uniform or are congruous with respect to the symmetry lines of the cross section. In practice, however, the flow supplied to the inlet cross section of a tube or duct may be highly maldistributed. This may occur when the flow is delivered to the duct via a piping system which contains bends, changes of cross section, valves, blockages, or combinations of these perturbating features. Maldistributed flows may not only be nonuniformly and unsymmetrically distributed over the inlet cross section, but the maldistribution may set up pockets of recirculating flow (i.e., backflow) in the duct.

In the case of the circular tube, the heat transfer ramifications of a maldistributed inlet flow have been investigated experimentally for a variety of causal factors (e.g., bends, unsymmetrical blockages, and mixing), and [1–3] are representative of the available literature. On the other hand, the impact of an initial flow maldistirbution on the heat transfer characteristics of rectangular ducts does not appear to have been investigated heretofore. It is the purpose of this paper to report on an experimental investigation of turbulent heat transfer in a flat rectangular duct in the presence of an inlet section flow maldistribution.

The experiments were performed with a high aspect ratio duct (aspect ratio = 18.3) with a view toward approximating a parallel-plate channel. In planning the experimental program, it was decided to work with a severe maldistribution. To create the maldistribution, a portion of the inlet cross section of the duct was blocked, as is illustrated in the center diagram of Fig. 1. The diagram is a head-on view looking at the duct inlet from an upstream vantage point. The duct cross section, of height H and width W (W/H = 18.3), is bounded by the two principal walls and by the side walls. A thin plate served as the blockage. The presence of the blockage causes the flow entering the duct to pack to one side of the inlet cross section. Owing to the inability of the entering flow to turn sharply and fill the space downstream of the blockage, a low-velocity recirculation zone is set up in that space. On the other hand, the flow passing through the unconstricted portion of the inlet section streams in a jetlike manner through the duct, spreading in response to wall friction and momentum exchange with the recirculation zone.

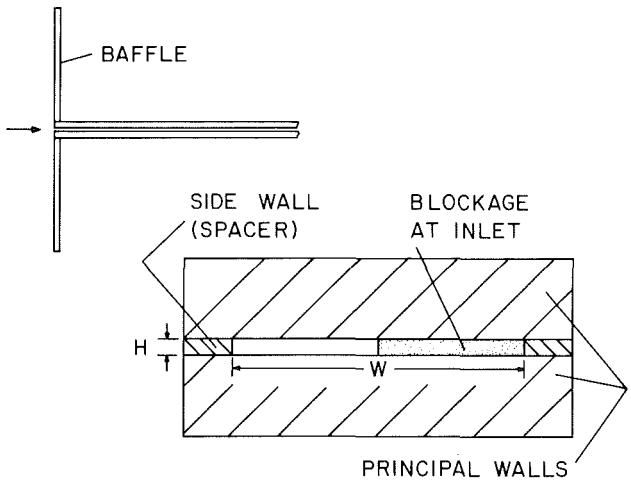

Fig. 1 Duct inlet configuration

The diagram at the upper left of Fig. 1 is a side view which shows the upstream portion of the duct set into a large baffle plate such that the exposed end faces of the duct walls are flush with the upstream face of the baffle. Owing to the presence of the baffle plate and with the system operating in the suction mode, the entire space upstream of the baffle serves as a plenum from which flow is drawn into the duct inlet.

Experiments were performed for two blockage ratios, respectively 1/4 and 1/2 of the total cross section of the duct. The unblocked case, which can be regarded as a baseline case against which the maldistribution-affected results may be compared, was investigated earlier [4]. For each blockage ratio, experiments were carried out for four Reynolds numbers spanning the range from 6000 to 30,000.

Contributed by the Heat Transfer Division for publication in the JOURNAL OF HEAT TRANSFER. Manuscript received by the Heat Transfer Division September, 16, 1982.

In addition to the degree of maldistribution (blockage ratio) and the Reynolds number, the thermal boundary conditions were also varied during the course of the experiments. In one set of experiments, the two principal walls of the duct were maintained at the same uniform temperature, while in a second set one of the principal walls was isothermal and the other principal wall was adiabatic. In all of the experiments, the side walls were adiabatic.

Local heat transfer coefficients were measured at 13 points across the span (i.e., the width) of the duct at each of 21 axial measuring stations. These measurements permitted the evaluation of spanwise-average heat transfer coefficients at the 21 axial stations, and it is these spanwise-average results that will be compared with those for the nonmaldistributed flow.

In addition to the heat transfer measurements, two types of fluid-flow-related results were obtained and will be presented. One of these is the axial pressure distributions in the presence of inlet section blockage. The other is the pattern of fluid flow that is created in the duct due to the blockage. The oil-lampblack technique [5] was used for the flow visualization.

The Experiments

Test Section. As shown in Fig. 1, the test section was made up of two principal walls which formed the upper and lower bounding surfaces of the flow cross section and of two side walls which served as spacers to separate the principal walls. These walls defined a flow cross section of width $W = 8.13$ cm (3.20 in.) and height $H = 0.445$ cm (0.175 in.), with a resulting hydraulic diameter $D_h = 0.842$ cm (0.332 in.). The wall thicknesses shown in the figure are to scale with respect to H and W. In the streamwise direction, the active length of the test section was equal to about $22D_h$.

Instead of heat transfer experiments, the experiments that were actually performed involved mass transfer. According to the analogy between the two processes, the measured mass transfer coefficients can be readily converted to heat transfer coefficients. For the mass transfer studies, either one or both of the principal walls (depending on the desired boundary conditions) were recessed so as to accommodate a layer of naphthalene which was implanted by a casting process. The two principal walls which housed the naphthalene were each fabricated from a solid block of aluminum. On each of the walls that participated in the mass transfer process, the spanwise width of the exposed naphthalene surface was precisely equal to the duct cross-section width, W. The streamwise length of the naphthalene surface has already been noted in the preceding paragraph. There was no mass transfer at the exposed upstream edges of the duct walls, since the edges were metallic.

Two test setups were employed. In one, one of the principal walls housed a naphthalene layer which bounded the flow, while the other wall was an aluminum plate whose surface had been carefully polished. In the other setup, the flow was bounded by naphthalene surfaces in both walls. According to the heat/mass transfer analogy, a naphthalene surface corresponds to an isothermal surface in the counterpart heat transfer experiment, while a metallic surface corresponds to an adiabatic surface. Thus, the setup where the surfaces of both principal walls were of naphthalene corresponded to a symmetrically heated isothermal-walled channel, while the setup with only one naphthalene surface corresponded to unsymmetric heating.

For each data run, a fresh naphthalene layer was cast into each of the mass-transfer-participating walls. The change in the duct height due to naphthalene sublimation during the course of a data run was about 1 percent.

For the determination of the axial pressure distribution in the duct, eight pressure taps were installed along the spanwise centerline of the aluminum plate which served as the non-participating principal wall for the unsymmetric mass transfer experiments. The locations of the taps will be evident from the pressure distribution results to be presented later.

Other Apparatus Components and Instrumentation. For the identification of other components, it is convenient to follow the path of the airflow through the apparatus. Air drawn from the temperature-controlled laboratory room entered the test-section duct via the partially blocked inlet. After traversing the axial length of the duct, the air encountered an abrupt enlargement (area ratio ~ 9.5) as it discharged into a long transition section whose function was to bridge between the flat rectangular cross section of the test section and the circular piping of the downstream air-handling system. The piping system leading from the transition section conveyed the air to a flowmeter (a calibrated rotameter), a control valve, and then to a blower situated in a service corridor adjacent to the laboratory. The naphthalene-laden blower exhaust was vented outside the building.

The partial blockage of the inlet was accomplished by affixing a 0.0254-cm (0.010-in.) thick stainless-steel plate to the face of the baffle by means of pressure-sensitive tape. The choice of a thin plate was made to ensure a sharply defined flow separation; the plate was sufficiently thick so as not to deform under the forces exerted by the airflow.

The instrumentation used in the experiments will now be described. The local mass (heat) transfer coefficients were determined from measurements of the contour of the naphthalene surface made both before and after each data run. For the contour measurements, the naphthalene test surface, housed in the aluminum plate (i.e., the duct wall) into

Nomenclature

A = area of unblocked inlet
A_b = blocked area of inlet
A_i = open inlet area with blockage in place
$\mathfrak{D}$ = naphthalene-air diffusion coefficient
D_h = hydraulic diameter
H = duct height, Fig. 1
K_{xy} = local mass transfer coefficient, equation (8)
$\bar{K}_x$ = spanwise-average mass transfer coefficient, equation (10)
$\dot{M}$ = mass transfer rate per unit length
$\dot{m}$ = mass transfer rate per unit area
P = duct perimeter
p = pressure
p_∞ = pressure upstream of inlet
$\dot{Q}$ = volume flow rate, $\dot{w}/\rho$
Re = Reynolds number, $4\dot{w}/\mu P$
Sc = Schmidt number
Sh_{xy} = local Sherwood number, $K_{xy}D_h/\mathfrak{D}$
$\overline{\mathrm{Sh}}_x$ = spanwise-average Sherwood number, $\bar{K}_x D_h/\mathfrak{D}$
V_i = velocity based on inlet cross section, equation (11)
W = duct width, Fig. 1
$\dot{w}$ = net flow rate in forward direction
x = axial coordinate
y = transverse coordinate
δ = sublimation depth
μ = air viscosity
ν = air kinematic viscosity
ρ = mean air density
ρ_∞ = air density upstream of inlet
ρ_{nb} = bulk density of naphthalene vapor
ρ_{nw} = density of naphthalene vapor at wall
ρ_s = density of solid naphthalene
τ = duration of data run

which it had been cast, was positioned, via pins and clamps, on the bed of a coordinate table. The table permitted controlled, precisely measurable travel in two perpendicular horizontal directions, and this enabled a sensor tip, similar to that of a dial gage, to be traversed over the naphthalene surface. The vertical movements of the tip were converted to electrical signals which were read and printed out by a digital voltmeter. The final digit of the printout corresponds to 10^{-5} in.

The outputs of the test-section pressure taps were conveyed by plastic tubing to a selector switch, the output of which was fed to the terminals of a Baratron solid-state, capacitance-type pressure meter with a resolution of 10^{-4} mm Hg. The Baratron output was read with a digital voltmeter.

The temperature of the air entering the test section was measured by an ASTM-certified 0.1°F thermometer. In a selected number of data runs ($\sim$ 10), a calibrated copper-constantan thermocouple was cast into the naphthalene so that the thermocouple junction lay in the surface exposed to the airflow. In no case did the run-average value of the thermometer readings differ by more than 0.1°C (0.2°F) from the run-average value of the embedded thermocouple readings. This difference introduces an uncertainty of no more than 1 percent in the mass transfer results.

Further information about the apparatus and experimental procedure are available in [6].

Flow Visualization. As was noted in the Introduction, the flow visualization was performed using the oil-lampblack technique. According to this technique, a suitable mixture of oil and lampblack is applied to a surface, which is then exposed to the airflow whose characteristics are to be studied. Ideally, under the action of the forces exerted by the fluid, the mixture will move along the surface, following the paths of the fluid particles that pass adjacent to the surface.

Lampblack is a fine black powder which mixes readily with oil. The fluidity of the mixture can be regulated by the selection of the viscosity of the oil and by the proportions of the oil and the lampblack powder. The fluidity has a profound effect on the extent of the resolution that can be achieved with the oil-lampblack technique. A stiff mixture will not respond to the low velocities while a very fluid mixture will be blown away by a high velocity stream so that, in either of these cases, little information is obtained.

In the present instance, owing to the complexity of the flow, mixtures of different fluidities had to be used for different parts of the duct surface in order to accommodate the extremes of high and low velocity. To enhance the visualization, the mixture was applied to the surface in a variety of patterns. These patterns included a sequence of dots, one or more parallel lines, or a complete coating of a specific portion of the surface.

The mixture was applied only to the lower principal wall of the duct, since sagging and dripping would have occurred had the mixture been applied to the upper principal wall. For all the visualization runs, the surface of the lower wall that bounded the airflow was covered with white, plasticized contact paper in order to provide the highest possible contrast for the black streak lines induced on the surface by the flow. Furthermore, to permit direct observation of the movement of the oil-lampblack mixture during the visualization runs, a specifically fabricated plexiglass plate was used as the upper wall of the duct.

Visualization runs were performed for the same range of Reynolds numbers as that for the mass transfer runs. With the blockage in place, there were pockets of very low velocity flow. In those regions, even the mixture of highest fluidity responded very sluggishly even at the highest Reynolds number. Therefore, in order to obtain the clearest possible flow patterns for the blockage cases, all of the detailed visualization runs were made at the highest Reynolds number, namely, about 30,000.

For the presentation of the flow patterns, direct ink tracings of the streak lines were made by overlaying tracing paper atop the white contact paper used to coat the duct wall.

Data Reduction

Two types of mass transfer coefficients were evaluated from the experimental measurements. One of these is the local coefficient K_{xy} at a position x,y on the principal walls of the duct, where x is the axial coordinate (in the flow direction) and y is the spanwise coordinate (across the width W). The other is the spanwise-average coefficient, $\bar{K}_x$, at an axial station x. The dimensionless counterparts of these coefficients are the Sherwood numbers, Sh_{xy} and $\overline{\mathrm{Sh}}_x$, defined as

$$\mathrm{Sh}_{xy} = K_{xy} D_h / \mathfrak{D}, \quad \overline{\mathrm{Sh}}_x = \bar{K}_x D_h / \mathfrak{D} \tag{1}$$

In turn, these Sherwood numbers are the analogues of the Nusselt numbers, Nu_{xy} and $\overline{\mathrm{Nu}}_x$,

$$\mathrm{Nu}_{xy} = h_{xy} D_h / k, \quad \overline{\mathrm{Nu}}_x = \bar{h}_x D_h / k \tag{2}$$

For duct flows, it is standard to employ the difference between the wall and bulk temperatures (concentrations) as the basis of the heat (mass) transfer coefficient. In conventional situations where the flow is in the forward direction at all points of the cross section (i.e., no recirculation or backflow), the evaluation of the bulk temperature (concentration) in terms of the flow rate, $\dot{w}$, and the heat (mass) added to the flowing fluid is straightforward. For instance, for mass transfer, if $\dot{M}(x)$ denotes the mass of naphthalene vapor added to the airflow per unit time and per unit axial length at x, and if $\dot{Q} = \dot{w}/\rho$ is the volume flow rate of the air (ρ = air density), then

$$d\rho_{nb} = \dot{M}(x)\,dx/\dot{Q} \tag{3}$$

represents the increase in the bulk density (i.e., concentration) of the naphthalene vapor in an axial length, dx.

When there is a backflow in a portion of the cross section, as in the present instance, equation (3)—or its heat transfer counterpart—can continue to serve as the definition of the bulk concentration (or temperature) provided that $\dot{Q}$ is associated with the *net* flow rate, $\dot{w}$, in the forward direction. In the steady state, the net forward flow, $\dot{w}$, is a constant from cross section to cross section despite possible differences in the extent of the backflow. Furthermore, with ρ evaluated at the axial-mean pressure in the test section, the extreme variation of $\dot{Q}$ along the test section was about 1 percent in the present experiments. Thus, $\dot{Q}$ will be regarded as independent of x. With this, equation (3) may be integrated from $x = 0$ to $x = x$ to yield the bulk concentration of the naphthalene vapor

$$\rho_{nb}(x) = \int_0^x \dot{M}(x)\,dx/\dot{Q} \tag{4}$$

where the condition $\rho_{nb} = 0$ at $x = 0$ has been employed.

The determination of $\rho_{nb}(x)$ from equation (4) requires $\dot{M}(x)$ as input. The surface contour measurements made before and after a data run, when differenced, yielded the distribution of local sublimation depths, $\delta\,(x,y)$, on each participating wall. With these, the local rates of mass transfer, $\dot{m}\,(x,y)$, per unit time, and unit surface area follow as

$$\dot{m}(x,y) = \rho_s \delta(x,y)/\tau \tag{5}$$

in which ρ_s is the density of solid naphthalene, and τ is the duration of the data run. If 1 denotes the upper principal wall and 2 denotes the lower principal wall, then

$$\dot{M}_1(x) = \int_0^W \dot{m}_1(x,y)\,dy, \quad \dot{M}_2(x) = \int_0^W \dot{m}_2(x,y)\,dy \tag{6}$$

and

$$\dot{M}(x) = \dot{M}_1(x) + \dot{M}_2(x) \tag{7}$$

When both walls participated in the mass transfer process, the contributions of $\dot{M}_1$ and $\dot{M}_2$ to $\dot{M}$ were typically within 2–3 percent of each other, while when only one wall participated, either $\dot{M}_1$ or $\dot{M}_2 = 0$, depending on the test configuration employed.

With the foregoing as background, the evaluation of the mass transfer coefficients will now be described. For the local coefficient, K_{xy}

$$K_{xy} = \dot{m}(x,y) / (\rho_{nw} - \rho_{nb}(x)) \tag{8}$$

For one participating wall, $\dot{m}(x,y)$ was taken directly from equation (5), while in the case of two participating walls

$$\dot{m}(x,y) = \tfrac{1}{2}(\dot{m}_1(x,y) + \dot{m}_2(x,y)) \tag{9}$$

There were occasional differences between $\dot{m}_1$ and $\dot{m}_2$ in the five percent range, but for the most part agreement was in the 2–3 percent range. For the spanwise-average coefficient

$$\bar{K}_x = \{\dot{M}(x)/nW\} / (\rho_{nw} - \rho_{nb}(x)) \tag{10}$$

where $\dot{M}(x)$ is from equation (7), and $n = 1$ when one wall participates in the mass transfer process and $n = 2$ when both walls participate.

The bulk vapor density, ρ_{nb}, that appears in equations (8) and (10) has been thoroughly discussed. For ρ_{nw}, the naphthalene density at the wall, the Sogin vapor pressure--temperature relationship [7] was used along with the perfect gas law.

The mass transfer coefficients from equations (8) and (10) were introduced into the Sherwood number definitions of equation (1). The diffusion coefficient, $\mathcal{D}$, appearing there was evaluated from the identity $\mathcal{D} = \nu/\mathrm{Sc}$, where Sc is the Schmidt number for naphthalene diffusion in air (equals to 2.5 [7]), and ν is the kinematic viscosity of air.

Attention will now be turned to the pressure distribution measurements. For the unblocked inlet, the axial pressure distributions were linear, and the corresponding friction factors were in excellent agreement with conventional relationships. The pressure distributions corresponding to the maldistributed inlet flow were dominated by inertial effects. Therefore, a pressure loss coefficient, rather than a friction factor, is more suitable for their presentation. Also, it was found that a relatively compact presentation could be achieved using a velocity V_i based on the actual open area A_i of the inlet with the blockage in place, i.e.,

$$V_i = \dot{w}/\rho_\infty A_i \tag{11}$$

where ρ_∞ is density of the air upstream of the inlet. With this, the pressure distributions were expressed in the form

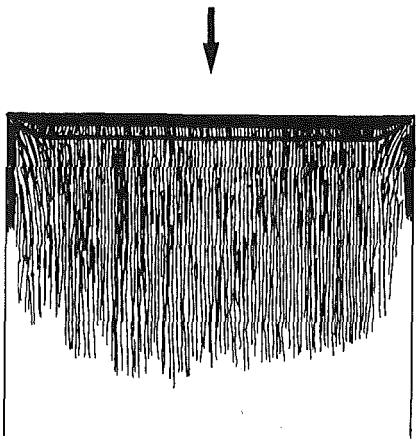

Fig. 2 Flow visualization pattern corresponding to a blockage-free inlet (Re = 21,000)

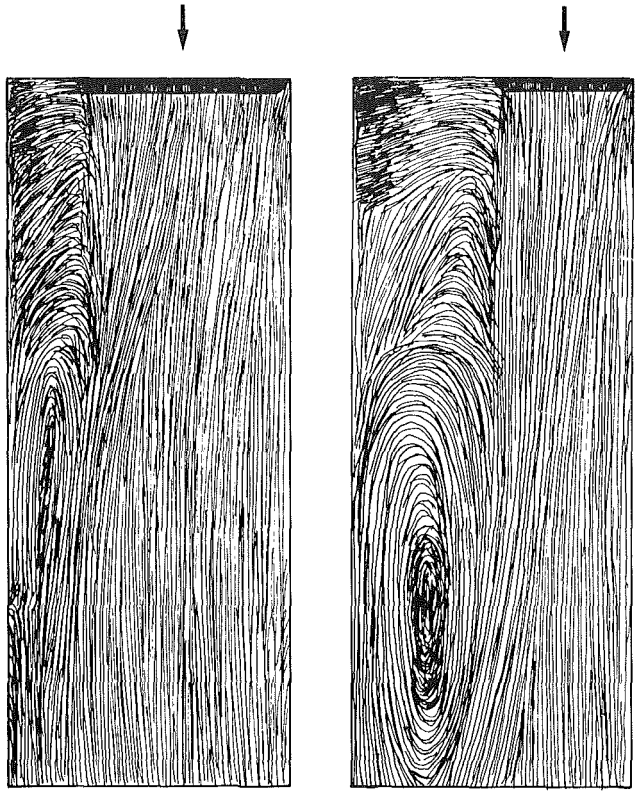

Fig. 3 Flow visualization patterns corresponding to the 1/4 and 1/2 inlet blockages, left- and right-hand diagrams, respectively

$$(p_\infty - p(x)) / \tfrac{1}{2}\rho_\infty V_i^2 \tag{12}$$

with p_∞ denoting the pressure upstream of the inlet.

The results were parameterized by the Reynolds number defined in the standard manner for a rectangular duct

$$\mathrm{Re} = 4\dot{w}/\mu P \tag{13}$$

where P, the perimeter, is equal to $(2W + 2H)$.

Results and Discussion

The presentation of results will begin with the flow visualization patterns, then goes to the local and spanwise-average heat transfer coefficients, and concludes with the pressure distributions.

Fluid Flow Patterns. The flow visualization diagrams now to be presented are direct tracings of the oil-lampblack streaks and are, therefore, true renderings of the pattern of fluid flow. The first case for which results are to be presented is that in which there is no blockage. In this case, the flow passes through a sharp-edged inlet as it enters the duct. Owing to its inability to turn the sharp corner at the inlet, the flow separates from the duct wall. Within the separation bubbles that are formed adjacent to each principal wall, the flow recirculates such that the fluid adjacent to the wall moves upstream, opposite to the mainflow direction. Downstream of the separation bubble, the flow reattaches to the wall.

These events are chronicled in the representative oil-lampblack pattern that is shown in Fig. 2, which is a plan view looking down at the lower wall of the duct. Two horizontal black bands can be seen in the figure. The sharply defined narrow band marks the reattachment of the separated flow, and the separated region and its recirculating flow are located fore of the reattachment. The array of short vertical lines that populate the separated region[1] are lines of backflow (i.e.,

[1] In mass transfer runs of purposely long duration, fine, parallel stria were observed in this region.

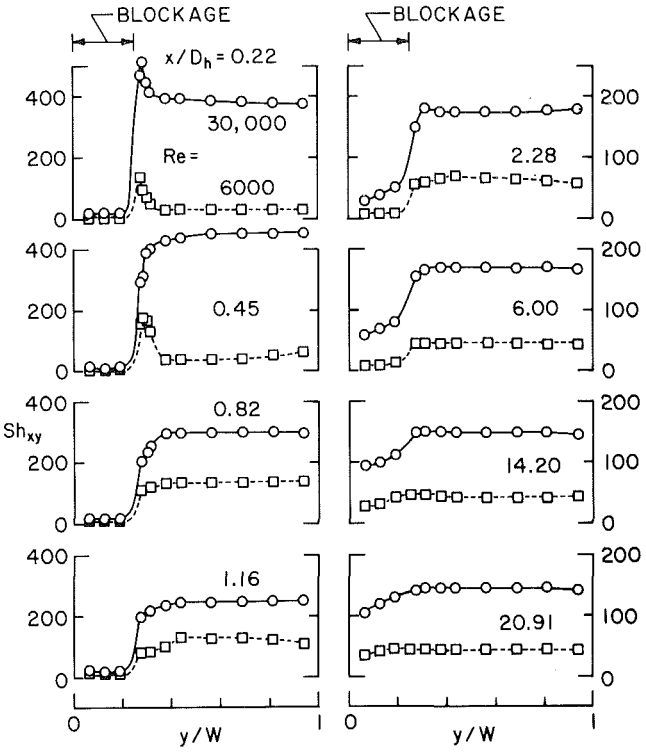

Fig. 4 Spanwise and axial distributions of the local Sherwood number for the 1/4 blocked inlet

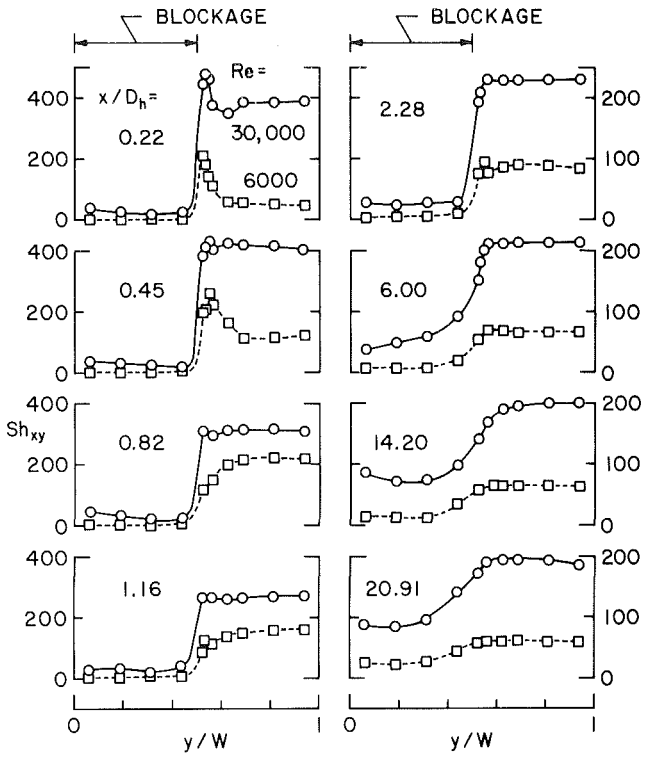

Fig. 5 Spanwise and axial distributions of the local Sherwood number for the 1/2 blocked inlet

opposite to the mainflow direction). The backflow lines terminate in a broad black band situated immediately adjacent to the duct inlet. This black band is the result of an accumulation of the oil-lampblack mixture that was pushed toward the inlet by the backflow.

It is noteworthy that the reattachment line is, for the most part, straight and parallel to the duct inlet—indicating that the separation is two-dimensional over most of the duct width. However, near the inlet and adjacent to the side walls, there is clear evidence of three-dimensional motions.

Attention may now be directed to Fig. 3, which shows, respectively, at the left and at the right, the flow visualization patterns corresponding to the ¼ and ½ blocked inlets. In both cases, the blockage is situated at the left side of the duct inlet. The flow which passes through the unblocked portion of the inlet creates an inlet-adjacent visualization pattern identical to that already discussed in connection with Fig. 2, and no further elaboration is needed. The novel features of Fig. 3 relate, therefore, to the presence of the blockage.

Behind the blockage and over a substantial distance downstream of it, the velocities are very low (as noted from visual observations) and a well-defined recirculation loop is not in evidence. Rather, the expected recirculating eddy with its clearly defined eye is situated farther downstream. In the case of the ¼ blockage, the eddy appears to have closed well ahead of the downstream end of the duct and a fully forward flow, albeit not necessarily fully developed, appears to have been established. For the ½ blockage case, the eye of the eddy is positioned forward of the exit section, but the closure of the eddy occurs downstream of the duct exit. In neither case is there a tendency for the entering flow to spread rapidly into the space behind the blockage.

The ramifications of these fluid flow events will be evident during the presentation of the heat transfer and pressure drop results.

Heat (Mass) Transfer Results. In view of the analogy between the two processes, the phrases *heat transfer* and *mass transfer* will be used interchangeably during the forthcoming presentation. In particular, the Sherwood numbers that will be presented can be regarded as Nusselt numbers. According to the analogy, these Nusselt numbers correspond to a Prandtl number of 2.5, since the Schmidt number for the mass transfer results is 2.5. These Nusselt numbers can, however, be generalized to apply to other Prandtl numbers by using the conventional Pr^m scaling, where m may be selected between ⅓ and 0.4.

To obtain numerical values of the Sherwood number to higher accuracy than can be read from the forthcoming figures, reference may be made to [6].

Local Sherwood Number Results. Space limitations permit only a representative sample of the total collection of local-coefficient results to be presented here, but the full complement of results is available in [6].

Figure 4 conveys distributions of the local Sherwood number for the case of the ¼ blockage with mass transfer at both principal walls. The figure consists of eight graphs, each of which corresponds to a specific axial station starting with the first measurement station, $x/D_h = 0.22$, and ending with the last measurement station, $x/D_h = 20.91$. These eight stations were selected from among the twenty-one measurement stations at which data were collected.

In each graph, the local Sherwood number, Sh_{xy}, is plotted as a function of the dimensionless spanwise coordinate y/W. The graphs are arranged in two columns. Atop each column, a line has been drawn to indicate the range of y/W that is spanned by the inlet section blockage. Data are plotted for Re = 6000 and 30,000, which are, respectively, the lowest and highest Reynolds numbers investigated. Lines have been faired through the data to provide continuity.

Inspection of Fig. 4 reveals that marked spanwise variations in the heat transfer coefficient are engendered by the maldistributed inlet flow and that residuals of the variations persist even to the downstream end of the duct. At axial stations corresponding to small and intermediate x/D_h,

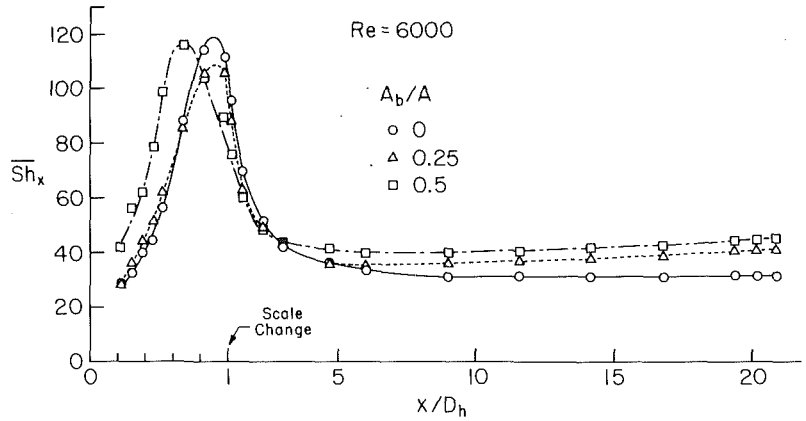

Fig. 6 Axial distributions of the spanwise-average Sherwood number, Re = 6000

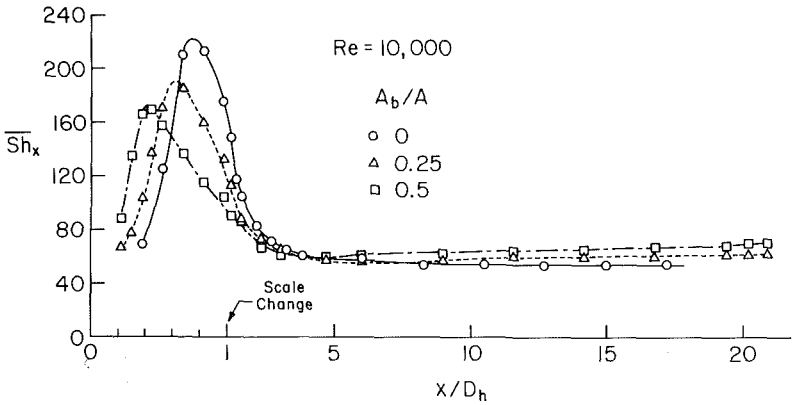

Fig. 7 Axial distributions of the spanwise-average Sherwood number, Re = 10,000

the flow which streams through the unblocked portion of the inlet creates a heat transfer coefficient plateau. The level of the plateau is very much higher than that of the coefficients in the low-velocity region behind the blockage. Indeed, the behind-the-blockage coefficients are a small fraction of the coefficients encountered in any other portion of the duct.

Detectable increases in the level of the low coefficients begin to appear at $x/D_h \sim 2$, and these increases continue at larger x/D_h as the mainflow tends to occupy more and more of the duct width and as the more vigorous part of the recirculation eddy is encountered (see Fig. 3). Meanwhile, in this same range of x/D_h, the level of the high plateau decreases slowly in response to the spreading of the mainflow.

At the last measuring station ($x/D_h = 20.91$), although the flow is in the forward direction at all points in the cross section (Fig. 3), velocity and temperature profile nonuniformities persist and yield a nonuniform distribution of the heat transfer coefficient. This is especially true for the higher Reynolds number (Re = 30,000), where the ratio of the highest to the lowest of the plotted transfer coefficients is almost 1.4.

A detailed examination of the results for small x/D_h reveals two special characteristics, both of which are more marked for Re = 6000 than for Re = 30,000. First, the level of the plateau created by the stream which passes through the open part of the inlet tends, at first, to rise with increasing x/D_h and, after the attainment of a maximum, decreases. This behavior is due to the flow separation and reattachment induced by the sharp-edged inlet, whereby the maximum occurs when the flow reattaches.

The second special feature is the peak in the spanwise distributions that is in evidence at the initial measurement stations. This peak is believed to be a manisfestation of the eddies that are shed from the sharp edge of the blockage plate [8].

A presentation similar to Fig. 4, but for the ½-blockage case, is made in Fig. 5. Inspection of Fig. 5 reveals an overall behavior that is similar to that which was identified and discussed in the preceding paragraphs. There are, however, certain differences in detail. In particular, significant differences in the levels of the high- and low-coefficient zones persist to greater downstream distances when the ½ blockage is in place. Thus, at the last measurement station ($x/D_h = 20.91$), the ratio between the highest and lowest coefficients is about a factor of two in Fig. 5 compared with about 1.4 in Fig. 4. This significant spanwise variation of the heat transfer coefficient reflects the nonuniformity in the fluid flow pattern that is in evidence in the right-hand diagram of Fig. 3. Also, at certain axial stations, in the low portion of the spanwise distribution, there is a tendency for the coefficients to tip up near the side wall. This behavior may be attributed to the existence of higher recirculation velocities adjacent to the side wall than in the eye of the recirculation eddy.

The highly nonuniform local heat transfer coefficients displayed in Figs. 4 and 5 suggest that hot or cold spots will exist for certain types of heating conditions (e.g., uniform heat flux) due to the maldistributed entering flow.

Spanwise-Average Sherwood Number Results. Axial distributions of the spanwise-average Sherwood number are presented in Figs. 6–9, respectively, for Re = 6000, 10,000, 21,000 and 30,000 and for mass transfer at both principal walls. In each figure, $\overline{Sh}_x$ is plotted as a function of the dimensionless axial coordinate x/D_h. To provide better

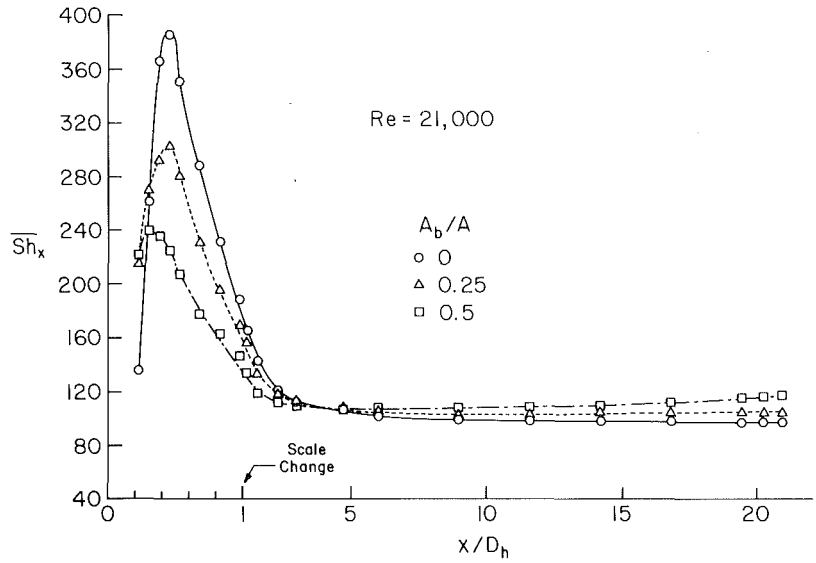

Fig. 8 Axial distributions of the spanwise-average Sherwood number, Re = 21,000

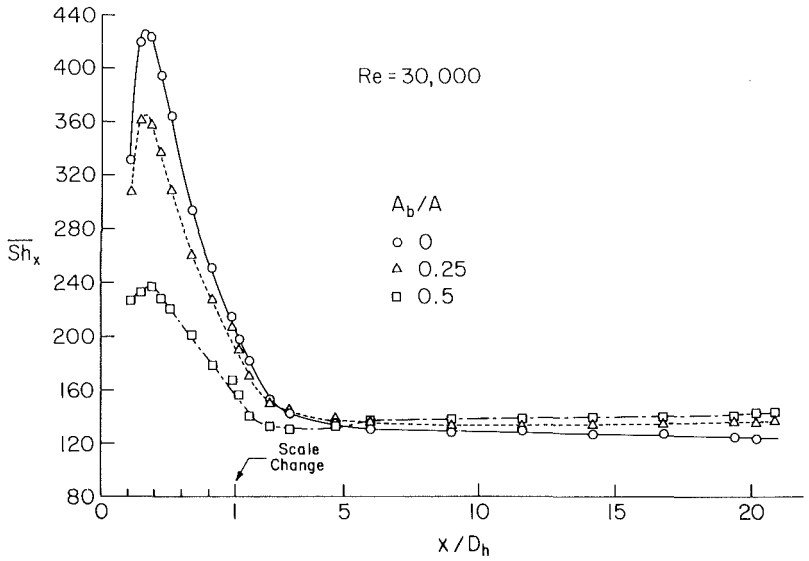

Fig. 9 Axial distributions of the spanwise-average Sherwood number, Re = 30,000

resolution in the region just downstream of the inlet, the abscissa scale has been enlarged in the region $0 \leq x/D_h < 1$. Three sets of data are plotted in each figure corresponding to the blockage ratios 0 (no blockage), ¼, and ½. Curves have been faired through the data for continuity.

In comparing the results for the three cases that are presented in each figure, it should be noted that a fixed Reynolds number implies a fixed mass flow of air, $\dot{w}$, regardless of the blockage. This can be seen from equation (13), from which $\dot{w} = (\mu P/4)\mathrm{Re}$ and, since the perimeter, P, is the same for ducts with or without blockage, $\dot{w} \sim \mathrm{Re}$. Thus, in any given figure, the results are compared for a fixed $\dot{w}$.

All of the axial distributions of the Sherwood number presented in Figs. 6–9 share a common shape. Starting at the first measurement station, the transfer coefficients rise sharply to a maximum and then drop off, rapidly at first, and then more and more gradually. In the far downstream region, the coefficients for the no-blockage case tend to a fully developed value, while those for the blockage cases continue to vary slowly.

As was noted earlier, the rise of the transfer coefficient just downstream of the inlet and the attainment of a maximum is related to the reattachment of the separated entering flow. The subsequent dropoff is the result of the hydrodynamic and thermal development processes operating on the reattached flow. There is an overall tendency for the reattachment point (i.e., the peak of the curve) to move upstream with increasing Reynolds number, with the range of x/D_h at reattachment extending from 0.9 to 0.35. Furthermore, the sensitivity of the reattachment-point location to blockage diminishes with the Reynolds number. At the lower Reynolds numbers, the more highly blocked flow tends to reattach sooner, while for Re = 30,000 the reattachment-point location ($x/D_h \sim 0.35$) is about the same for all of the inlet conditions investigated.

In contrast to the reattachment-point location, the magnitude of the transfer coefficient at the reattachment peak becomes increasingly sensitive to the blockage ratio as the Reynolds number increases, with lower peaks for greater blockages. At the lowest Reynolds number (Re = 6000), the peaks for the three inlet conditions are about at the same

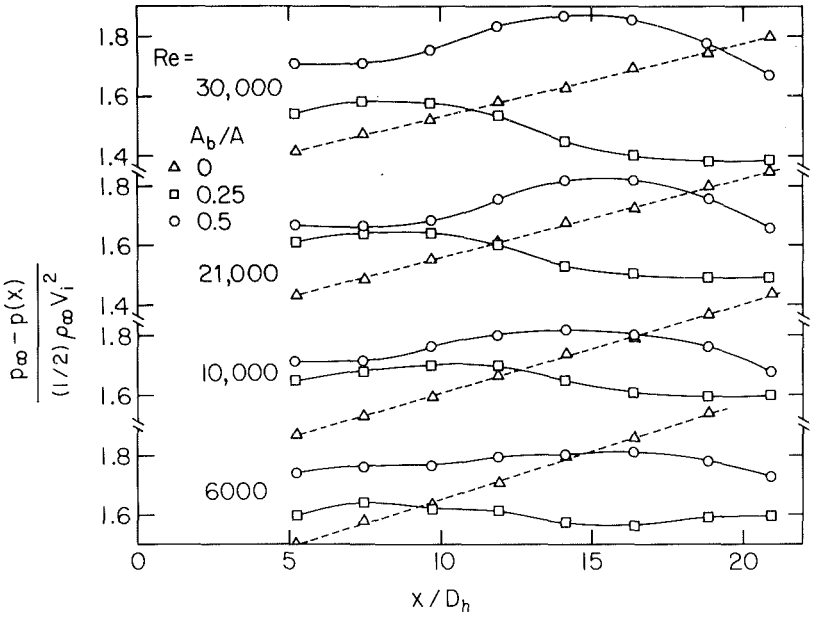

Fig. 10 Pressure distributions corresponding to the 1/4 and 1/2 inlet blockages

level. On the other hand, for Re = 30,000, the peak value for the unblocked case is about 1.8 times the peak for the ½ blockage case.

The aforementioned ordering of the peaks with blockage also holds for the distribution curves proper in the x/D_h range just upstream of reattachment and extending downstream throughout the region of rapid dropoff of the curves. In this range of axial stations, the maldistribution of the inlet flow reduces the heat transfer.

In the downstream region, say, $x/D_h > 5$, a new ordering of the results emerges. Here, the transfer coefficients increase monotonically with increasing blockage ratio. This ordering is reflective of the degree to which the various cases approach the fully developed regime—with the no-blockage case having attained complete development while the ½ blockage case is rather far from being developed. The enhancement in the downstream coefficients due to blockage is greatest at low Reynolds numbers—about 35 percent at $x/D_h = 20$ for Re = 6000 and 15 percent at the same x/D_h for Re = 30,000.

From the standpoint of practice, it is relevant to inquire how the heat (mass) transfer coefficient, averaged over various lengths of duct, is affected by the blockage. Such averages were computed for three lengths: x/D_h between 0.2 and 1, between 0.2 and 5, and between 0.2 and 20. For the highest investigated Reynolds number, Re = 30,000 (Fig. 9), the ratio of the average coefficient for the ½-blockage case to that for the no-blockage case was 0.63, 0.80, and ~ 1, respectively, for each aforementioned length. These results reflect a blockage-related degradation (or, at best, a parity) in the heat transfer. This negative effect of the blockage is compounded by the blockage-related pressure drop penalty.

At the lowest Reynolds number, Re = 6000 (Fig. 6), the situation is somewhat different since the three ratios, corresponding to those of the preceding paragraph, are 1.18, 1.01, and 1.21. Thus, for this Reynolds number, there is a moderate enhancement of the heat transfer, but the pressure drop penalty remains.

The presentation of the mass (heat) transfer results has, thus far, been focused on the case where mass transfer occurs at both principal walls (symmetric heat transfer). The results for the case in which only one of the walls actively participates are essentially coincident (within data scatter) with those already presented for x/D_h values up to about five and, in some instances, beyond. This is as it should be, reflecting the independence of the transfer processes at the two principal walls until the respective boundary layers have met. Thereafter, the coefficients for the unsymmetric-transfer case tend to lie below those for symmetric transfer. In the absence of blockage, the deviations are about 7 percent. For the blockage cases, the deviations are less regular, ranging from 2 to 10 percent, depending on the blockage ratio and Reynolds number. This irregularity is probably reflective of the non fully developed nature of the flow and temperature fields. The results for unsymmetric heat (mass) transfer are avaible in [6].

Pressure Distributions. The axial pressure distributions will be presented in terms of the pressure loss coefficient of equation (12), which is plotted as a function of x/D_h in Fig. 10. The figure consists of four tiers of graphs, one for each of the investigated Reynolds numbers. In interpreting the results, it should be noted that decreasing values of $p(x)$ give rise to increasing values of the loss coefficient, while increasing $p(x)$ (i.e., a pressure recovery) causes the loss coefficient to decrease. It should also be kept in mind that the velocity, V_i, which appears in the denominator of the loss coefficient is based on the actual open area (i.e., the free flow area) at the duct inlet cross section. Thus, for a given Reynolds number, V_i for the ¼ blockage case is 4/3 that for the no-blockage case, while V_i for the ½ blockage case is twice that for no blockage.

As seen in the figure, the pressure distributions for the no-blockage case are linear, indicating the attainment of fully developed flow. As noted earlier, the friction factors which correspond to these pressure distributions are in very good agreement with the literature.

All the pressure distributions for the ¼ blockage share a common pattern, while those for the ½ blockage share a seemingly different common pattern. For the ¼ blockage, a slight friction-related pressure drop in the x/D_h range from five to ten is followed by a pressure recovery which results from the spreading of the mainflow (see Fig. 3). Near the downstream end of the duct, the pressure recovery is com-

pleted and friction-related pressure drop is about to take over.

The pressure distribution for the ½ blockage case is actually a shifted and amplified version of that for the ¼ blockage case. The small initial pressure drop for the ¼ blockage is shifted downstream and enlarged (by inertial losses) for the ½ blockage, and a similar shift occurs for the region of pressure recovery. The duct is not suffiently long to enable the pressure recovery to be completed for the ½ blockage case.

Concluding Remarks

The results presented here have demonstrated that spanwise nonuniformities in the local heat transfer coefficient induced by flow maldistribution at the inlet can persist to far downstream locations. The downstream persistence of the spanwise nonuniformities was found to be greater with a more extreme inlet flow maldistribution. Higher spanwise-average heat transfer coefficients were encountered in the downstream region of the duct due to the flow maldistribution. However, at more upstream locations, where the entering flow reattaches to the duct wall following its separation at the sharp-edged inlet, the spanwise-average coefficients for the maldistributed flows are lower.

Acknowledgment

This research was performed under the auspices of the Power Program of the Office of Naval Research.

References

1 Mills, A. F., "Experimental Investigation of Turbulent Heat Transfer in the Entrance Region of a Circular Conduit," *Journal of Mechanical Engineering Science*, Vol. 4, 1962, pp. 62–70.

2 Koram, K. K., and Sparrow, E. M., "Turbulent Heat Transfer Downstream of an Unsymmetric Blockage in a Tube," JOURNAL OF HEAT TRANSFER, Vol. 100, 1978, pp. 588–594.

3 Sparrow, E. M., and Kemink, R. G., "The Effect of a Mixing Tee on Turbulent Heat Transfer in a Tube," *International Journal of Heat and Mass Transfer*, Vol. 22, 1979, pp. 909–917.

4 Sparrow, E. M., and Cur, N., "Turbulent Heat Transfer in a Symmetrically or Asymmetrically Heated Flat Rectangular Duct with Flow Separation at Inlet," JOURNAL OF HEAT TRANSFER, Vol. 104, 1982, pp. 82–89.

5 Merzkirch, W., *Flow Visualization*, Academic Press, New York, 1974, pp. 53–56.

6 Cur, N., "Local Turbulent Heat Transfer Coefficients in a Symmetrically or Asymmetrically Heated Flat Rectangular Duct with Either Uniform or Nonuniform Inlet Velocity," Ph.D. thesis, Department of Mechanical Engineering, University of Minnesota, Minneapolis, Minn., 1982.

7 Sogin, H. H., "Sublimation from Disks to Air Streams Flowing Normal to their Surfaces," ASME *Transactions*, Vol. 80, 1958, pp. 61–71.

8 Beavers, G. S., and Wilson, T. A., "Vortex Growth in Jets," *Journal of Fluid Mechanics*, Vol. 44, 1970, pp. 97–112.

C. P. Bellmore[1]
Graduate Assistant.
Assoc. Mem. ASME

R. L. Reid[2]
Professor.
Mem. ASME

Mechanical and Aerospace Engineering Department,
The University of Tennessee,
Knoxville, Tenn.

Numerical Prediction of Wall Temperatures for Near-Critical Para-Hydrogen in Turbulent Upflow Inside Vertical Tubes

Presented herein is a method of including density fluctuations in the equations of turbulent transport. Results of a numerical analysis indicate that the method may be used to predict heat transfer for the case of near-critical para-hydrogen in turbulent upflow inside vertical tubes. Wall temperatures, heat transfer coefficients, and velocities obtained by coupling the equations of turbulent momentum and heat transfer with a perturbed equation of state show good agreement with experiments for inlet reduced pressures of 1.28–5.83.

Introduction

With an increase of applications of helium, water, carbon dioxide, neon, hydrogen, and oxygen as coolants, working fluids, and fuels, it is becoming important to have available accurate prediction methods for the heat transfer characteristics of these fluids in the near-critical region. An application of current interest is the mixed-mode, second-generation space shuttle engine where the thrust chambers are regeneratively cooled with liquid oxygen [1]. Design of these systems is extremely difficult for lack of a satisfactory model for fluid flow and heat transfer in the near critical region.

Development of theoretical models has been hindered by uncertainty as to whether flows should be described by single or two-phase models and by the extreme variations of the fluid properties in the near-critical region. Several empirical relations have been advanced, [2, 3], to correlate heat flux-wall temperature experimental data. These correlations give unsatisfactory predictions of wall temperatures and heat transfer coefficients and, as pointed out in [2], the most critical design region is often the most difficult to predict. The available data, theories, and correlations for the near-critical region were surveyed by Hendricks et al. [4] and more recently by Hall [5]. Considerable data for upward flow of hydrogen in vertical tubes is reported by Hendricks et al., [6, 7]. The inability of empirical correlations to describe experimental data has increased interest in numerical predictions of near-critical fluid flow and heat transfer.

Near-critical heat transfer predictions by direct solution of the momentum and energy equations have been encouraging. In particular, the predictions of Schnurr et al. [8, 9, 10] for near-critical helium, carbon dioxide, water, and hydrogen demonstrate the generality of such methods.

While these analyses represent a significant improvement in near-critical heat transfer prediction capability when compared to the results of prior analyses [11–13], there yet remains a large body of experimental data which is not handled by Schnurr's program.

A recent analysis by Hendricks et al. [15] showed that much of the available near-critical heat transfer data could be grouped or correlated using a bulk expansion factor given as

$$F = 1 + \beta(T_w - T_b) \tag{1}$$

The authors noted that while the thermal expansion coefficient was successful in grouping the data, it did not appear in the governing equations except to account for thermogravitational effects. Further analysis showed that the compressible form of the time-averaged turbulent momentum and energy equations required the prescription of a fluctuating density. By using the thermal expansion coefficient to relate the turbulent density fluctuations to energy fluctuations in the flow field, the equations for the turbulent momentum and energy fluxes could be coupled more strongly.

In this study the fluctuating density model proposed by Hendricks et al. was further developed to predict near-critical heat transfer and flow phenomenon.

The Equations of Turbulent Transport

Convective Transport Equations. The equations for steady turbulent compressible axisymmetric boundary layer flow in a circular tube may be written as

Continuity:

$$\frac{\partial}{\partial x}(\bar{\rho}\bar{u} + \overline{\rho' u'}) + \frac{1}{r}\frac{\partial}{\partial r}[r(\bar{\rho}\bar{v} + \overline{\rho' v'}] = 0 \tag{2}$$

Momentum:

$$(\bar{\rho}\bar{u} + \overline{\rho' u'})\frac{\partial u}{\partial x} + (\bar{\rho}\bar{v} + \overline{\rho' v'})\frac{\partial \bar{u}}{\partial r} = -\frac{dP}{dx} + \bar{\rho} g_x + \frac{1}{r}\frac{\partial}{\partial r}(-r\tau^*) \tag{3}$$

Energy:

$$(\bar{\rho}\bar{u} + \overline{\rho' u'})\frac{\partial \bar{H}}{\partial x} + (\bar{\rho}\bar{v} + \overline{\rho' v'})\frac{\partial \bar{H}}{\partial r} = \frac{1}{r}\frac{\partial}{\partial r}[r(u\tau - q^*)] \tag{4}$$

For turbulent boundary layer calculations it is convenient to define a turbulent stream function, ψ, such that the continuity equation, equation (2), is satisfied exactly. Thus

$$\frac{\partial \psi}{\partial r} = r(\bar{\rho}\bar{u} + \overline{\rho' u'}) \tag{5}$$

and

[1] Current address: Sohio Research Center, Cleveland, Ohio.
[2] Current address: Professor and Chairman, Mechanical and Industrial Engineering Department, The University of Texas at El Paso, El Paso, Texas 79968.

Contributed by the Heat Transfer Division and presented at the ASME Winter Annual Meeting, Chicago, Illinois, November 16–21, 1980. Manuscript received by the Heat Transfer Division April 1, 1981. Paper No. 80-WA/HT-52.

$$\frac{\partial \psi}{\partial x} = -r(\bar{\rho}\bar{v} + \overline{\rho' v'}) \tag{6}$$

In terms of the turbulent stream function, equations (3) and (4) become, respectively

$$\frac{\partial \bar{u}}{\partial x} = \frac{\partial}{\partial \psi}[-r\tau^*] - \left(\frac{1}{\bar{\rho}\bar{u} + \overline{\rho' u'}}\right)\left[\frac{dP}{dx} - \bar{\rho} g_x\right] \tag{7}$$

and

$$\frac{\partial \bar{H}}{\partial x} = \frac{\partial}{\partial \psi}[r\bar{u}\tau - rq^*] \tag{8}$$

The Turbulent Momentum and Heat Fluxes. Retaining the fluctuating density terms in the time-averaged compressible turbulent momentum and energy equations, the following forms may be obtained for the turbulent shear stress and heat flux

$$\tau_t = -\bar{\rho}\overline{u'v'} - \bar{v}\overline{\rho' u'} - \overline{\rho' u' v'} \tag{9}$$

$$q_t = \bar{\rho}\overline{v'H'} + \bar{v}\overline{\rho' H'} + \overline{\rho' v' H'} \tag{10}$$

Writing the equation of state as

$$\rho = \rho(h, P) \tag{11}$$

and expanding to the first order in terms of property fluctuations yields

$$\rho' \cong \left(\frac{\partial \rho}{\partial h}\right)_P h' + \left(\frac{\partial \rho}{\partial P}\right)_h P' \tag{12}$$

Considering only variation with enthalpy, the fluctuating density is then given by

$$\rho' = -\bar{\rho}\beta^* h' \tag{13}$$

Using mixing length theory the velocity and enthalpy fluctuations may be expressed as

$$u' = l_m \, \partial u/\partial y \tag{14}$$

$$v' = -l_m \, \partial u/\partial y \tag{15}$$

$$h' = -l_h \, \partial h/\partial y \tag{16}$$

Assuming that $H' = h'$, and substituting equations (13–16) into equations (9) and (10), the turbulent shear stress and heat flux may be written as

$$\tau_t = \bar{\rho} l_m^2 \left(\frac{\partial \bar{u}}{\partial y}\right)^2 \left[1 - \beta^* l_h \frac{\partial \bar{H}}{\partial y} - \left(\beta^* l_h \frac{\partial \bar{H}}{\partial y}\right)^2\right] \tag{17}$$

and

$$q_t = -\bar{\rho} l_m l_h \frac{\partial \bar{u}}{\partial y}\frac{\partial \bar{H}}{\partial y}\left[1 - \beta^* l_h \frac{\partial \bar{H}}{\partial y} - \left(\beta^* l_h \frac{\partial \bar{H}}{\partial y}\right)^2\right] \tag{18}$$

respectively. Employing the Boussinesq relation

$$\tau_t = \mu_t \frac{\partial u}{\partial y} \tag{19}$$

the following expression is obtained for the turbulent viscosity.

$$\mu_t = \bar{\rho} l_m^2 \left|\frac{\partial \bar{u}}{\partial y}\right| \left[1 - \beta^* l_h \frac{\partial \bar{H}}{\partial y} - \left(\beta^* l_h \frac{\partial \bar{H}}{\partial y}\right)^2\right] \tag{20}$$

Similarly, the turbulent heat flux may be expressed as

$$q_t = -k_t \frac{\partial T}{\partial y} \tag{21}$$

Substituting equation (21) into equation (18), the familiar relation $\mathrm{Pr}_t = l_m/l_h$ is obtained.

Thus, the momentum and energy equations may be written as

$$\frac{\partial \bar{u}}{\partial x} = \frac{\partial}{\partial \psi}\left[r(\mu + \mu_t)\frac{\partial \bar{u}}{\partial r}\right] - \frac{1}{(\bar{\rho}\bar{u} + \overline{\rho' u'})}\left[\frac{dP}{dx} - \bar{\rho} g_x\right] \tag{23}$$

and

$$\frac{\partial \bar{H}}{\partial x} = \frac{\partial}{\partial \psi}\left\{r\left[\left(\frac{\mu}{\mathrm{Pr}} + \frac{\mu_t}{\mathrm{Pr}_t}\right)\frac{\partial \bar{H}}{\partial r} - \left(\frac{\mu}{\mathrm{Pr}} + \frac{\mu_t}{\mathrm{Pr}_t}\right)\frac{\partial (u^2/2)}{\partial r} + \mu \frac{\partial (u^2/2)}{\partial r}\right]\right\} \tag{24}$$

Prescription of Mixing Length. For turbulent boundary

Nomenclature

A^+ = 26.0, a constant
B^+ = 33.8, a constant
C_p = specific heat at constant pressure
D = tube diameter
D_1 = $1 - \beta^* l_h (\partial h/\partial y) - (\beta^* l_h (\partial h/\partial y))^2$
D_2 = $\beta^* l_h (\partial h/\partial y)$
F = bulk expansion factor of [15]
$f\delta$ = step size multiplier
g_x = acceleration of gravity, positive in positive x-direction
G = mass flux
h = fluid static enthalpy
H = total (stagnation) enthalpy
k_t = $\mu_t C_p/\mathrm{Pr}_t$, turbulent conductivity
l = a length scale
L/D = length to diameter ratio
$\dot{m}$ = mass flow rate
P = pressure
Pr = Prandtl number
q = heat flux
r = radius
R = wall radius
s = seconds
T = temperature
T^* = transposed-critical temperature: c_p is a maximum for a given pressure
u = axial velocity component
v = radial velocity component
w = 1-exp $(-y^+/A^+)$, Van Driest damping function
w_h = 1-exp $(-y^+/B^+)$, damping function for enthalpy mixing length
x = axial coordinate
y = distance from wall
y^+ = $\int_0^y \sqrt{\tau_w/\rho}\,\frac{\rho}{\mu}\,dy$
β^* = $-\left(\frac{\partial \ln \rho}{\partial h}\right)_P$
δ = 0.09, a constant
κ = 0.4, a constant
κ_h = 0.43, a constant
κ^* = $-\left(\frac{\partial \ln \rho}{\partial P}\right)_h$
μ = dynamic viscosity
ρ = fluid density
τ = shear stress
ψ = turbulent stream function

Subscripts

b = bulk reference
c = critical point reference
h = enthalpy reference
m = momentum reference or mean quantity
t = turbulence reference
w = wall reference
x = corresponding to the x-coordinate

Superscripts

$(')$ = quantity fluctuates with time
$(-)$ = time average quantity
$(*)$ = quantity represents total of laminar and turbulent contributions

layer flows the mixing length may be obtained from the following empirical relations

$$l_m = k\, y\, w,\ 0 \le y/R \le \delta/\kappa \tag{25}$$

$$l_m = \delta R,\ \delta/\kappa < y/R \le 1 \tag{26}$$

While these equations were developed primarily for constant property flows with zero pressure gradient and are based more on phenomenological arguments than on a detailed analysis of turbulence length scales, they have enjoyed wide usage. The equations are not, however, wholly independent of property variations. The damping function, w, becomes property dependent when the nondimensional distance from the wall, y^+, is computed following an analysis of variable property flows by Goldman [12].

The mixing length for enthalpy, l_h, may be determined from the relation

$$l_h = k_h\, y\, w_h \tag{27}$$

This form is essentially that of Meier and Rotta [16] and seems to give good results for the conditions being considered. Equation (27) for l_h, together with equation (25) and (26), gave turbulent Prandtl numbers ranging from about 1.3 near the wall to 0.9 near the tube center.

When the velocity profile exhibits a "M" shape, enthalpy length scales given by equation (27) may cause the turbulent viscosity (see equation (20)) to be negative. When this occurs, equation (27) is abandoned and l_h is set to a value calculated to give maximum mixing. The conditions under which this behavior will occur may be derived from equation (20), rewritten here as

$$\mu_t = \bar{\rho} l_m{}^2 \left| \frac{\partial u}{\partial y} \right| D_1 \tag{28}$$

Note that D_1 is a maximum at $D_2 = -0.5$ and that for fixed β^* and l_h, D_2 represents the magnitude of the enthalpy gradient, $(\partial h/\partial y)$. If

$$\left| \frac{\partial h}{\partial y} \right| \ge \left| \frac{-.5}{\beta^* l_h} \right| \tag{29}$$

the character of D_1 is such that heat transfer would be impaired. Computer analysis of this behavior showed that D_2 became less than -0.5 only when the velocity gradient went through a zero, the case of the "M" shaped velocity profiles. Further analysis showed that the onset of a velocity gradient minima caused the turbulent viscosity to go to zero, implying zero turbulent momentum and heat transfer near this region. Very large cross-stream enthalpy gradients occur as a result of this effective heat transfer barrier.

The following procedure is suggested in order that "M" shaped velocity profiles may be treated. If $D_2 < -.5$, then $D_2 = -.5$ and

$$l_h = \frac{-.5}{\beta^* \dfrac{\partial h}{\partial y}} \tag{30}$$

Thus, D_1 attains its maximum value and l_h is reduced. The overall effect of the procedure is that μ_t is increased but $\tau_t \propto (\partial u/\partial y)^2$ and $(\partial u/\partial y) \cong 0$, so that momentum transport is relatively unaffected. Similarly, the increase in μ_t is partially offset by the increase in Pr_t, resulting from a decrease in l_h. But when $\partial h/\partial y$ is large and $\partial u/\partial y \neq 0$, this method allows for appreciable turbulent heat transfer.

The Calculation Procedure

A finite difference code based on the Patankar-Spalding method [17, 18] was developed to predict near-critical fluid flows with heat transfer in straight tubes. The basic Patankar-Spalding method has been used by researchers to solve many different types of flows, it is well documented and provides an easily modified solution procedure for boundary layer type equations.

Boundary conditions were taken to be: no-slip at the tube wall, symmetry about the tube centerline, and prescribed heat flux at the tube wall. The initial condition for the momentum solution was a 1/7th power law profile. A profile generator fit the power law profile to the tube radius, and a prescribed number of radial nodes were defined such that the percentage change in mass flow rate between adjacent nodes was a constant for all nodes and the boundary of the last radial fluid node coincided with the inside of the tube wall. This scheme provided a concentration of nodes in the near-wall region and a progressively wider node spacing away from the tube wall. To assure internally consistent initial velocity profiles, the momentum equation was solved iteratively before the downstream march with heat transfer began. The initial condition for the energy equation was a uniform inlet enthalpy.

The large momentum pressure drops associated with evaporative two-phase flows are also characteristic of near-critical fluid flows. For this analysis, the pressure gradient was determined by an iterative scheme whereby the pressure gradient was adjusted by amounts proportional to the mean velocity and the difference between the actual tube radius and the predicted outer radius of the flow field. This rather simple approach usually converged quickly.

Due in part to the iterations required for pressure gradient determination, the solutions obtained were found to be very stable although little effort was expended to determine actual stability limits. Results showed some dependency on the mesh spacing used to set up the runs. The number of cross-stream nodes varied from 28 to 30 for the cases considered in this paper. The variance is due to the capability given the grid generator routine to change the number of nodes used to define the initial velocity profile.

The initial downstream step size was somewhat arbitrarily defined as

$$\Delta x = \left| \frac{\dot{m}}{\pi q R} \right| (.1) f\delta \tag{31}$$

where $f\delta$ is an input parameter. As the solution marched up the tube, $f\delta$ increased by 0.1 percent at each step unless and until $f\delta$ became greater than 2. This capability proved useful in cases with very high wall heat fluxes where axial fluid property gradients could be severe near the tube inlet.

Fluid properties were obtained by including the property routine of [18] directly into the finite difference code, thereby eliminating any additional uncertainty attributable to interpolating tabulated property data.

Results

Selected cases representing a range of inlet fluid conditions, heat and mass fluxes, and tube diameters from the experimental results of [6, 7] for near-critical para-hydrogen in vertical tubes were run to test the proposed model. The conditions considered are listed in Table 1. Results presented here were obtained using a downstream step size factor of 2.

Figures 1–4 show the axial wall and bulk temperature profiles for each of the cases listed in Table 1. The agreement is generally quite good with respect to both trend and magnitude. The original experiment for Run 28-681 (see Fig. 2) was performed using a stainless steel test section. Measurements show an axial heat flux distribution which varies by up to 20 percent as shown in Fig. 5. Reducing the step size factor for this case from 2.0 to 1.25 gave wall temperature predictions within 2 K of the experimental values for L/D ratios less than 32. Excessive computing time

Table 1 Description of test cases for para-hydrogen

	Run			
	77	28-681	8-1044	23-1165
$T_{b,\,in}$(K)	31.1	25.1	32.0	59.8
$T_{b,\,out}$(K)	43.9	34.2	35.8	121.2
P_{in}(MPa)	7.54	1.65	1.85	2.81
D(cm)	.800	.851	.559	1.288
G(Kg/m^{2}s)	1987	1401	1665	283
q(KW/m^2)	1668	1230	1241	1437
T_{in}/T_c	.94	.76	.97	1.81
T_{out}/T_c	1.33	1.04	1.08	3.68
P_{in}/P_c	5.83	1.28	1.43	2.18
Reference	[7]	[6]	[6]	[6]

$T_c = 32.98$ K
$P_c = 1.29$ MPa

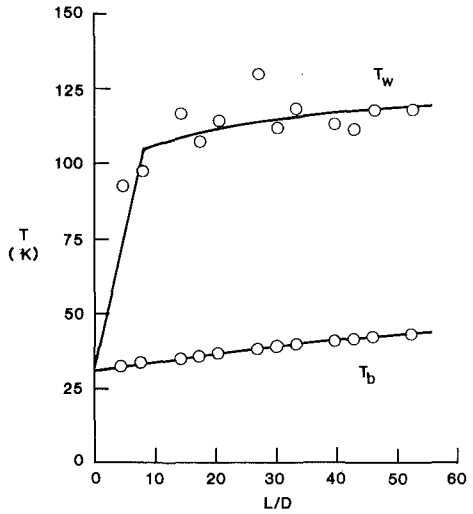

Fig. 1 *Comparison of numerical results to experimental data of [7]:* **axial wall and bulk temperature profiles for Run 77**

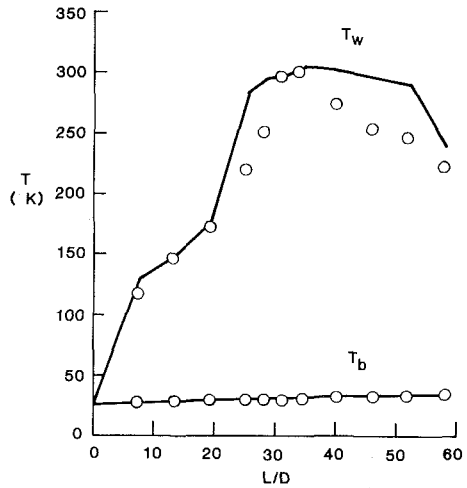

Fig. 2 Comparison of numerical results to experimental data of [6]: axial wall and bulk temperature profiles for Run 28-681

prohibited a full run using this step size. As should be expected, cases with significant axial variation in wall boundary conditions require a smaller step size. Results shown in Figs. 2 and 6 indicate that good results can be obtained with a large step size specification.

Schnurr et al, were successful in predicting heat transfer coefficients for Run 28-681 using a constant wall heat flux and a special analysis of the laminar sublayer [9]. The results shown here were obtained without special treatment of the sublayer but with an emphasis on the rates of turbulent transport to and from the wall region. Figures 6–9 show the

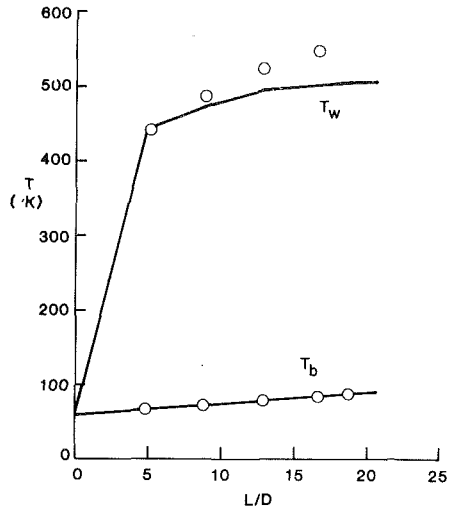

Fig. 3 Comparison of numerical results to experimental data of [6]: axial wall and bulk temperature profiles for Run 23-1165

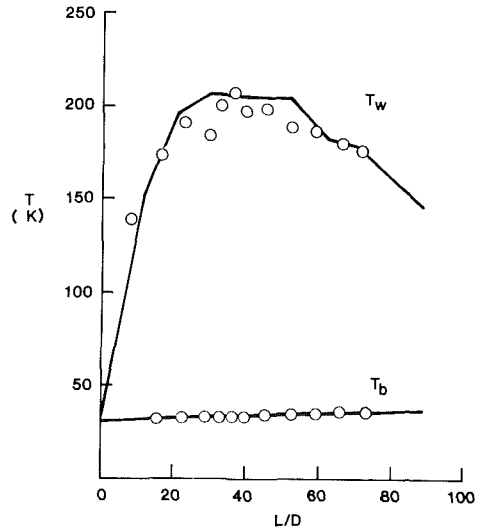

Fig. 4 Comparison of numerical results to experimental data of [6]: axial wall and bulk temperature profiles for Run 8-1044

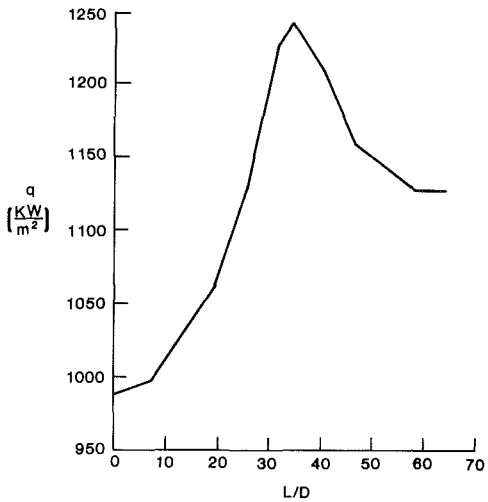

Fig. 5 Axial measured heat flux distribution for Run 26-681

variation of heat transfer coefficients with axial distance. Agreement between predicted values and experiment is again quite good. Figure 7, for Run 77, shows some scatter of the experimental data which is not shown in the predictions. The

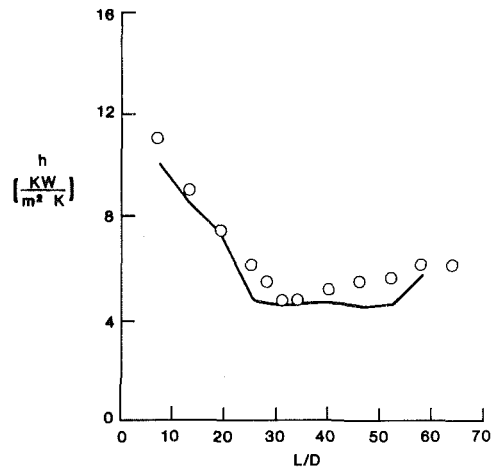

Fig. 6 Comparison of numerical results to experimental data of [6]: axial heat transfer coefficient distribution for Run 28-681

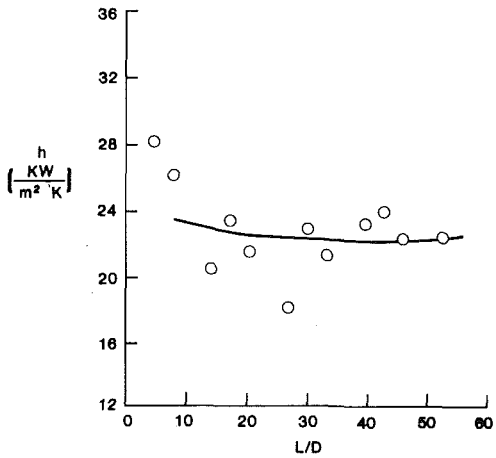

Fig. 7 Comparison of numerical results to experimental data of [6]: axial heat transfer coefficient distribution for Run 77

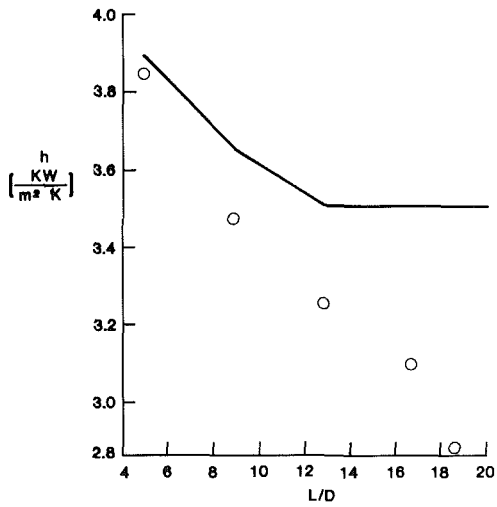

Fig. 8 Comparison of numerical results to experimental data of [6]: axial heat transfer coefficient distribution for Run 23-1165

numerical results give a "best fit" type curve which follows the trend of the experimental values.

The predicted mean velocities agree very well with the experimental values. Typical agreement is shown in Fig. 10. Axial pressure profiles (not shown) exhibit similar agreement. In all, the predicted mean and bulk quantities show excellent agreement. Previous investigation of convection to near-

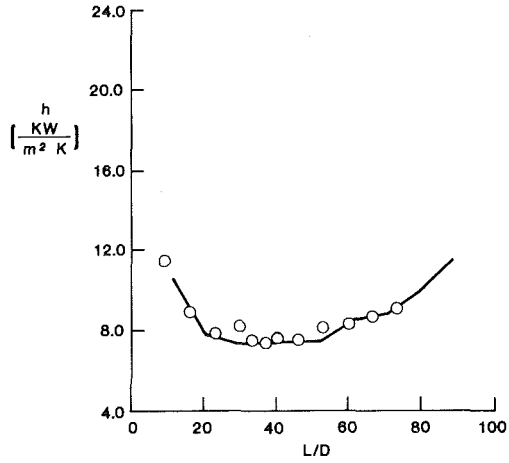

Fig. 9 Comparison of numerical results to experimental data of [6]: axial heat transfer coefficient distribution for Run 8-1044

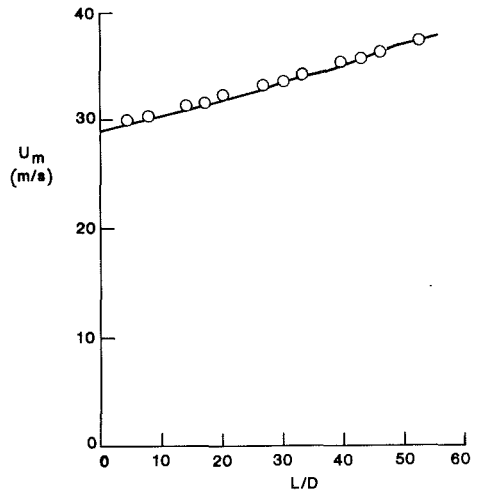

Fig. 10 Comparison of numerical results to experimental data of [6]: mean velocity profile for Run 28-681

critical fluids have shown some success in predicting wall temperatures or heat transfer coefficients by using special treatment of the near-wall region at the expense of poor bulk flow predictions, or have predicted the bulk flow well at the expense of poor heat transfer agreement. The success of the current model in predicting bulk flow parameters and wall temperature indicates that the density fluctuation turbulence model can be used to account for variable property influences on transport rates.

The heat transfer enhancement characteristics of near-critical fluids that make these fluids attractive coolants in special applications are shown in case 28-681, which also exhibits a region of heat transfer degradation, and in case 8-1044. The wall temperatures for case 8-1044 rise steadily to the point where the velocity gradient goes to zero in the region near the wall. From $L/D = 30$ to the end if the tube wall temperatures tend to remain constant or decrease slightly. This behavior is opposite to that seen in case 28-861 where the onset of the "M" shaped velocity profile causes wall temperatures to rise considerably to a peak and then fall off. The "M" shaped profile starts at $L/D = 20$ for this case and persists over the rest of the tube. Wall temperatures peak at $L/D = 34$, where the predictions show that the velocity maxima first exceeds the velocity at the tube centerline.

The factors which determine whether heat transfer enhancement or degradation will occur require further study. The "M" shaped velocity profile and the characteristic velocity maxima away from the tube centerline are seen to

influence the heat transfer in high heat flux cases. If there are regions with equal or nearly equal momentum on either side of the velocity maxima then turbulent eddy motion produces little or no net momentum transport between the regions. However, intense eddy motion in this region will cause large amounts of heat to be transferred from the hot side of the maxima to the cooler side. This reasoning does not address heat transfer degradation. From Table 1, note that cases 8-1044 and 28-681 do not differ much in heat flux, mass flux or inlet fluid condition. The difference in tube diameters may then be an important factor for identifying enhancement or degradation effects, indicating, as suggested by Hall [5] and others, that bouyancy effects may be significant for heat transfer processes in near critical fluids.

Conclusion

A model has been developed for predicting heat transfer to near-critical para-hydrogen in turbulent upflow inside vertical tubes. Agreement with experimental results is good over a range of mass flux, heat flux, and inlet fluid conditions.

The effects of near-critical property variation have been shown to include "M" shaped velocity profiles and sharply diminished heat transfer rates. Wall temperature excursions observed in experiments have been predicted with sufficient accuracy to enable a detailed analysis of the phenomenon. Radial fluid density variations were shown to have a significant effect on turbulent transport mechanisms in near-critical fluid flows with heat transfer.

Acknowledgments

The authors would like to acknowledge Robert C. Hendricks, Lewis Research Center, National Aeronautics and Space Administration, for making the details of his work on density fluctuation modeling available prior to their publication. His enthusiastic support of this project is greatly appreciated.

This work was sponsored in part by National Aeronautics and Space Administration, Lewis Research Center, grant NSG-3173.

References

1 Beichel, R., "Propulsion Systems for Single-Stage Shuttles," *Astronautics and Aeronautics*, Vol. 12, No. 11, Nov. 1974, pp. 32–39.

2 Rousar, D., and Miller, F., "Cooling with Supercritical Oxygen," AIAA Paper No. 75-1248, presented at the AIAA/SAE 11th Propulsion Conference, Anaheim, Calif., Sept. 29 – Oct. 1, 1975.

3 Sleicher, C. A., and Rouse, M. W., "A Convenient Correlation for Heat Transfer to Constant and Variable Property Fluids in Turbulent Pipe Flow," *International Journal of Heat Mass Transfer*, Vol. 18, 1975, pp. 677–683.

4 Hendricks, R. C., Simoneau, R. J., and Smith, R. V., "Survey of Heat Transfer to Near-Critical Fluids," NASA TN D-5886, 1970.

5 Hall, W. B., and Jackson, J. D., "Heat Transfer Near the Critical Point," *Keynote Papers, Heat Transfer 1978*, Vol. 6, Toronto, Canada, pp. 377–39.

6 Hendricks, R. C., Graham, R. W., Hsu, Y. Y., and Freidman, R., "Experimental Heat-Transfer Results for Cryogenic Hydrogen Flowing in Tubes at Subcritical and Supercritical Pressures to 800 Pounds per Square Inch Absolute," NASA TN D-3095, 1966.

7 Hendricks, R. C., Simoneau, R. J., and Friedman, R., "Heat Transfer Characteristics of Cryogenic Hydrogen From 1000 to 2500 PSIA Flowing Upward in Uniformly Heated Straight Tubes," NASA TN D-2977, Sept. 1965.

8 Sastry, V. S., and Schnurr, N. M., "An Analytical Investigation of Forced Convection Heat Transfer to Fluids Near the Thermodynamic Critical Point," ASME Paper No. 74-WA/HE-29, 1974.

9 Schnurr, N. M., Sastry, V. S., and Shapiro, A. B., "A Numerical Analysis of Heat Transfer to Fluids Near the Thermodynamic Critical Point Including the Thermal Entrance Region," ASME JOURNAL OF HEAT TRANSFER, Vol. 98, Nov. 1976, pp. 609–615.

10 Schnurr, N. M., "Numerical Predictions of Heat Transfer to Supercritical Helium in Turbulent Flow Through Circular Tubes," ASME Paper 77-HT-6, 1977.

11 Hess, H. L., and Kunz, H. R., "A Study of Forced Convection Heat Transfer to Supercritical Hydrogen," ASME JOURNAL OF HEAT TRANSFER, Vol. 87, No. 1, Feb. 1965, pp. 41–48.

12 Goldman, K., "Heat Transfer to Supercritical Water and Other Fluids with Temperature Dependent Properties," *Chemical Engineering Progress Symposium Ser.*, Vol. 50, No. 11, 1954, pp. 105–113.

13 Hsu, Y. Y., and Smith, J. M., "The Effects of Density Variation on Heat Transfer in the Critical Region," ASME JOURNAL OF HEAT TRANSFER, Vol. 83, No. 2, May 1961, pp. 176–182.

14 Hendricks, R. C., Yeroshenko, V. M., Yaskin, L. A., and Starostin, A. D., "Bulk Expansion Factors and Density Fluctuations in Heat and Mass Transfer," Paper B/119, XV International Congress of Refrigeration, Venice, Italy, Sept. 1979.

15 Meier, H. U., and Rotta, J. C., "Temperature Distributions in Supersonic Turbulent Boundary Layers," *AIAA Journal*, Vol. 9, 1971, pp. 2149–2155.

16 Patankar, S. V., and Spalding, D. B., *Heat and Mass Transfer in Boundary Layers*, CRC Press, Cleveland, Ohio, 1968.

17 Patankar, S. V., and Spalding, D. B., *Heat and Mass Transfer in Boundary Layers*, 2d ed., International Text Book, London, 1970.

18 Hendricks, R. C., Baron, A. K., and Peller, I. C., "GASP-A Computer Code for Calculating the Thermodynamic and Transport Properties for Ten Fluids: Parahydrogen, Helium, Neon, Methane, Nitrogen, Carbon Monoxide, Oxygen, Flouring, Argon, and Cargon Dioxide," NASA TN D-7808, Apr. 1975.

Heat Transfer of Power Law Fluid at Low Peclet Number Flow

Vi-Duong Dang
Associate Professor.
Department of Chemical Engineering
And Materials Science,
The Catholic University of America,
Washington, D.C. 20064

An exact solution is presented for the temperature distribution and local Nusselt number of power law fluid in conduit at low Peclet number flow by considering axial conduction in both the upstream and the downstream regions while keeping the wall at constant temperature. Solutions are also reported for the parallel plate geometry for the aforementioned heat transfer condition and for constant wall heat flux boundary condition. The order of importance of axial conduction is established for different geometries and different boundary conditions. The effect of axial conduction is more significant when power law model index, s, increases for constant wall heat flux case, but the effect changes with Peclet number for constant wall temperature case.

Introduction

The relative importance of axial conduction in heat transfer depends on the magnitude of Peclet number. For example, the effect of axial conduction is relatively small compared to axial convection when Peclet number is greater than 100. However, Peclet number of liquid metal can be less than 100 and axial conduction becomes significant. In considering the effect of axial conduction, it is often necessary to investigate this effect in two semi-infinite regions of the tube or parallel plates; i.e., in the upstream ($-\infty < x \le 0$) and the downstream ($0 \le x < \infty$) regions. Heat transfer at high Peclet number flow of Newtonain and non-Newtonian fluid has been reported by investigators in tubes [1–12, 24] and between parallel plates [2, 14]. Heat transfer of Newtonian fluid at low Peclet number flow in conduits have been published in [15–21]. However, in some practical problems, such as: (*i*) heat transfer of polymer flow in circular or rectangular die with viscous dissipation, and (*ii*) liquid metal heat transfer with heat generation, there is practically no work reported on heat transfer in the two semi-infinite regions of power law fluid flowing inside conduit or between parallel plates at low Peclet number with the effect of viscous dissipation and heat generation considered. There would thus appear to be a need for a thorough analysis of the general problems of these types. The objectives of the present paper are to present exact analysis of low Peclet number power law fluid in conduit and between parallel plates with constant wall temperature and constant wall heat flux boundary conditions

Analysis

Let's consider a power law fluid of constant physical properties flowing in a tube of the domain $-\infty < x < \infty$. The fluid enters at $x = -\infty$ with inlet temperature T_0. The effect of viscous dissipation and heat generation on heat transfer is considered in the downstream region ($0 \le x < \infty$) but is neglected in the upstream region. Figure 1 illustrates the geometry and the coordinates of the system. The dimensionless energy equations in the upstream and the downstream regions are (the dimensionless quantities are defined in the Nomenclature): where Br is the

$$\left(1-\eta^{\frac{s+1}{s}}\right)\frac{\partial\theta_1}{\partial\xi}=\frac{1}{\eta}\frac{\partial}{\partial\eta}\left(\eta\frac{\partial\theta_1}{\partial\eta}\right)+\frac{1}{\mathrm{Pe}^2}\frac{\partial^2\theta_1}{\partial\xi^2}\quad -\infty<\xi\le 0 \tag{1}$$

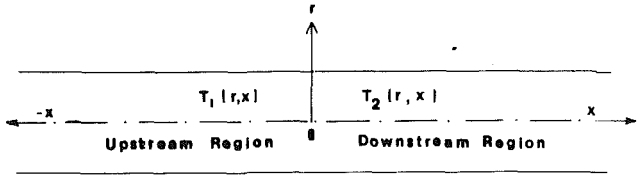

Fig. 1 Geometry and coordinate of the system

$$\left(1-\eta^{\frac{s+1}{s}}\right)\frac{\partial\theta_2}{\partial\xi}=\frac{1}{\eta}\frac{\partial}{\partial\eta}\left(\eta\frac{\partial\theta_2}{\partial\eta}\right)+\frac{1}{\mathrm{Pe}^2}\frac{\partial^2\theta_2}{\partial\xi^2}+\mathrm{Br}\left(\frac{s+1}{s}\right)^{s+1}\eta^{\frac{s+1}{s}}+\delta\quad 0\le\xi<\infty \tag{2}$$

Brinkman number, and δ is the heat generation term. Two kinds of boundary conditions, constant wall temperature (UWT) and constant wall heat flux (UHF) conditions are investigated. For constant wall heat flux conditions, the upstream region is kept insulated while the downstream region is maintained at a constant heat flux value. For constant wall temperature condition, the temperature of the wall in the upstream and the downstream regions is maintained at two different values. In summary, one has the following boundary conditions

		UWT	UHF	
$\xi = -\infty$		$\theta_1 = 1$	$\theta_1 = 0$	(3)
$\eta = 0$		$\frac{\partial\theta_1}{\partial\eta}=\frac{\partial\theta_2}{\partial\eta}=0$		(4)
$\eta = 1, \xi<0$	$\theta_1 = 1$		$\frac{\partial\theta_1}{\partial\eta} = 0$	(5)
$\eta = 1, \xi\ge 0$	$\theta_2 = 0$		$\frac{\partial\theta_2}{\partial\eta} = -1$	(6)
$\xi = 0$	$\theta_1(0,\eta) = \theta_2(0,\eta)$			(7)
	$\frac{\partial\theta_1}{\partial\xi}(0,\eta) = \frac{\partial\theta_2}{\partial\xi}(0,\eta)$			(8)

In the following, the solution of the constant wall temperature case will be presented. The solutions of equations (1-6) for the upstream and the downstream regions are

$$\theta_1(\xi,\eta)=1+\sum_{n=1}^{\infty}A_n Y_{1n}(\eta)\ \exp\ (\alpha^2{}_{1n}\xi) \tag{9}$$

$$\theta_2(\xi,\eta)=g(\eta)+\sum_{n=1}^{\infty}B_n Y_{2n}(\eta)\ \exp\ (-\alpha^2{}_{2n}\xi) \tag{10}$$

Contributed by the Heat Transfer Division for publication in the JOURNAL OF HEAT TRANSFER. Manuscript received by the Heat Transfer Division June 23, 1982.

where $g(\eta)$ is the far downstream solution which can be obtained from the solution of the inhomogeneous terms of equation (2) and is given by

$$g(\eta) = \mathrm{Br}\left(\frac{s+1}{s}\right)^{s+1} \frac{s^2}{(3s+1)^2}\left(1-\eta^{\frac{3s+1}{s}}\right) + \frac{\delta}{4}(1-\eta^2) \quad (11)$$

The series summation terms become significant in the region close to $x = 0$ and are determined by the following set of ordinary differential equations.

$$\frac{1}{\eta}\frac{d}{d\eta}\left(\eta\frac{dY_{in}}{d\eta}\right) + (-1)^i\alpha^2{}_{in}\left\{1-\eta^{\frac{s+1}{s}} + (-1)^i\frac{\alpha_{in}^2}{\mathrm{Pe}^2}\right\}Y_{in} = 0 \quad i = 1,2 \quad (12)$$

$$\frac{dY_{in}}{d\eta}(0) = 0 \quad (13)$$

$$Y_{in}(1) = 0 \quad (14)$$

Equations (12–14) are not Sturm-Liouville type equations, so the coefficients A_n, B_n in equations (9) and (10) cannot be determined by the regular orthogonal expansion technique. Instead another method is applied to determine A_n and B_n. One first generates a set of orthonormal functions ψ_j and ϕ_j in terms of the functions Y_{1n} and Y_{2n}, respectively, as

$$\psi_j = \sum_{n=1}^{j} a_{jn} Y_{1n}(\eta) \quad j = 1,2 \ldots . \quad (15)$$

$$\phi_j = \sum_{n=1}^{j} b_{jn} Y_{2n}(\eta) \quad j = 1,2 \ldots . \quad (16)$$

Once ψ_j and ϕ_j are known [16, 23], one can now expand Y_{1j} and Y_{2j} in terms of a set of orthonormal functions ψ_j and ϕ_j, respectively.

$$Y_{1j} = \sum_{n=1}^{j} C_{jn}\psi_n \quad (17)$$

$$Y_{2j} = \sum_{n=1}^{j} d_{jn}\phi_n \quad (18)$$

where the coefficients C_{jn} and d_{jn} can be determined by inversion of the matrix consisting of the elements of a_{jn} and b_{jn}, respectively. Now one can substitute equations (9–10) together with equations (17–18) in equations (7–8) to determine the coefficients A_n and B_n

$$1 + \sum_{n=1}^{\infty}\sum_{j=n}^{\infty} A_j d_{jn}\phi_n = \frac{\mathrm{Br}\left(\frac{s+1}{s}\right)^{s+1} s^2}{(3s+1)^2}\left(1-\eta^{\frac{3s+1}{s}}\right) + \frac{\delta}{4}(1-\eta^2) + \sum_{n=1}^{\infty}\sum_{j=n}^{\infty} B_j C_{jn}\psi_n \quad (19)$$

$$\sum_{n=1}^{\infty}\sum_{j=n}^{\infty} A_j\alpha^2{}_j d_{jn}\phi_n + \sum_{n=1}^{\infty}\sum_{n=j}^{\infty} B_j\beta_j^2 C_{jn}\psi_n = 0 \quad (20)$$

Equations (19) and (20) are in terms of the orthonormal functions ψ_n and ϕ_n so one can determine A_n and B_n by means of the orthogonal property of the orthonormal functions ψ_n and ϕ_n. Multiply equation (19) by ψ_m and equation (20) by ϕ_m and integrate with respect to η from 0 to 1, one gets

$$\sum_{n=m}^{\infty} B_n C_{nm} - \sum_{n=1}^{\infty} A_n\left(\sum_{j=1}^{n} d_{nj}\int_0^1 \phi_j\psi_m d\eta\right) = \int_0^1\left[1 - \frac{\mathrm{Br}\left(\frac{s+1}{s}\right)^{s+1} s^2}{(3s+1)^2}\left(1-\eta^{\frac{3s+1}{s}}\right) - \frac{\delta}{4}(1-\eta^2)\right]\psi_m d\eta \quad (21)$$

$$\sum_{n=1}^{\infty} B_n\alpha_{2n}^2\left(\sum_{j=1}^{n} C_{nj}\int_0^1 \psi_j\phi_m d\eta\right) + \sum_{n=m}^{\infty} A_n\alpha^2{}_{1n}{}^d{}_{nm} = 0 \quad (22)$$

Equations (21) and (22) are simultaneous algebraic equations for A_n and B_n which can be solved by truncating the infinite

Nomenclature

a = radius of tube or half-thickness between parallel plates
a_{jn} = coefficients defined in equation (15)
A_n = coefficients of series expansion coefficients in equation (9)
b_{jn} = coefficients defined in equation (16)
B_n = coefficients of series expansion coefficients in equation (10)
Br = Brinkman number $\dfrac{mu_{\max}^{s+1}\, a^{1-s}}{k(T_0 - T_w)}$
C_0 = parameter defined in equations (B4) and (B10)
C_2 = parameter defined in equations (B5) and (B11)
C_{jn} = coefficients defined in equation (17)
C_p = heat capacity of fluid
d_{jn} = coefficients defined in equation (18)
h = heat transfer coefficient
k = thermal conductivity of fluid
m = power law model parameter
Nu = Nusselt number, defined in equations (25), (All), (B8), and (B14)
Pe = Peclet number, $\dfrac{\rho C_p a u_{\max}}{k}$ for tube, $\dfrac{2\rho C_p a u_{\max}}{3k}$ for parallel plates
q = heat generation term
q_w = constant heat transfer rate from the wall
r = transverse coordinate from center of tube or parallel plates
R_n = eigenfunctions
s = power law model index
T_1 = temperature of fluid in the upstream region
T_2 = temperature of fluid in the downstream region
T_0 = inlet temperature of fluid
T_w = temperature of solid wall
$u_{\max}$ = maximum velocity of fluid
u_x = axial velocity of fluid
x = axial coordinate of tube or parallel plates
Y_{1n} = eigenfunctions of upstream region
Y_{2n} = eigenfunctions of downstream region

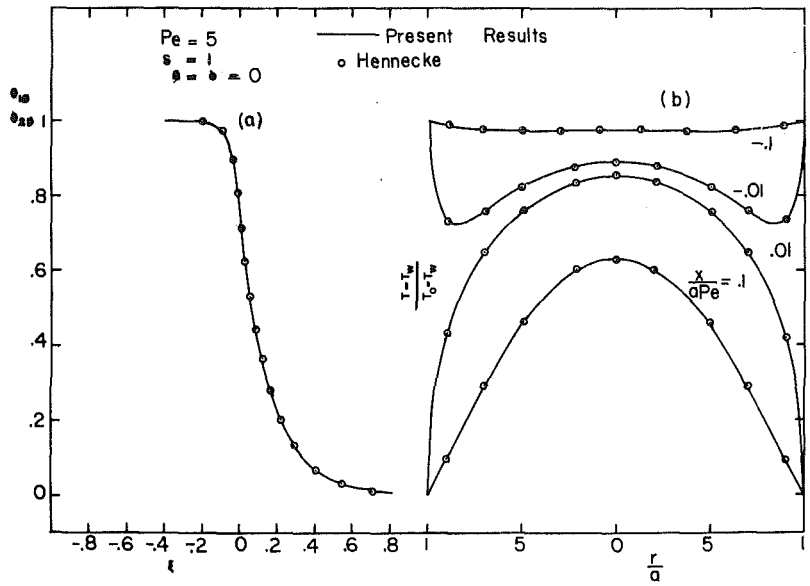

Fig. 2 Comparison of dimensionless average temperature (a) and radial temperature (b) between present results and those of Hennecke for constant wall temperature tubular flow

series to finite terms. In the present work 20 terms are used for A_n and B_n respectively.

The dimensionless average temperatue in the upstream and the downstream region is then

$$\theta_{1B}(\xi) = \frac{\int_0^a u_x \theta_1 r dr}{\int_0^a u_x r dr}$$

$$= 1 + \frac{2(3s+1)}{s+1} \sum_{n=1}^{\infty} \frac{A_n e^{\alpha_{1n}^2 \xi}}{\alpha_{1n}^2} \left[Y'_{1n}(1) + \frac{\alpha_{1n}^4}{\mathrm{Pe}^2} \int_0^1 \eta Y_{1n} d\eta \right] \quad (23)$$

$$\theta_{2B}(\xi) = \frac{\mathrm{Br}\left(\frac{s+1}{s}\right)^{s+1} s^2(4s+1)}{(3s+1)^2(5s+1)} + \frac{\delta(7s+1)}{8(5s+1)} - \frac{2(3s+1)}{s+1}$$

$$\sum_{n=1}^{\infty} \frac{B_n e^{-\alpha_{2n}^2 \xi}}{\alpha_{2n}^2} \left[Y'_{2n}(1) + \frac{\alpha_{2n}^4}{\mathrm{Pe}^2} \int_0^1 Y_{2n} d\eta \right] \quad (24)$$

and the downstream Nusselt number can be determined as

$$\mathrm{Nu} = \frac{2ha}{k} = \frac{-2\frac{\partial \theta_2}{\theta \eta}\Big|_{\eta=1}}{\theta_{2B}(\xi)}$$

$$\mathrm{Nu} = \frac{2}{\theta_{2B}(\xi)} \left[\frac{\mathrm{Br}\left(\frac{s+1}{s}\right)^{s+1} s}{3s+1} + \frac{\delta}{2} - \sum_{n=1}^{\infty} B_n \frac{dY_{2n}(1)}{d\eta} e^{-\alpha_{2n}^2 \xi} \right] \quad (25)$$

Nomenclature (cont.)

Greek Symbols

α_{1n} = eigenvalues in equations (9)

α_{2n} = eigenvalues in equations (10)

$\gamma = \dfrac{m u_{\max}^{s+1} a^{-s}}{q_w}$

$\delta = \dfrac{qa^2}{k(T_0 - T_w)}$ for constant wall temperature problem, $\dfrac{qa}{q_w}$ for constant wall heat flux problem

$\eta = \dfrac{r}{a}$

$\xi = \dfrac{kx}{\rho C_p a^2 u_{\max}}$

ψ_j = functions defined in equation (15)

ϕ_j = functions defined in equation (16)

$\theta_1 = \dfrac{T_1 - T_w}{T_0 - T_w}$ for constant wall temperature problem, $\dfrac{T_1 - T_0}{aq_w/k}$ for constant wall heat flux problem

$\theta_2 = \dfrac{T_2 - T_w}{T_0 - T_w}$ for constant wall temperature problem, $\dfrac{T_2 - T_0}{aq_w/k}$ for constant wall heat flux problem

θ_{ss} = defined in equations (B3) and (B9)

θ_{1b} = defined in equations (23), (A9), (B6), and (B12)

θ_{2b} = defined in equations (24), (A10), (B7), and (B13)

ξ^+_{dT} = dimensionless distance required for 5 percent deviation from its final steady-state dimensionless temperature in the downstream region

ξ^-_{dT} = dimensionless distance required for 5 percent deviation from the dimensionless initial temperature in the upstream region

$\xi_{d\mathrm{Nu}}$ = dimensionless distance required for 5 percent deviation from its final steady state Nusselt number in the upstream region

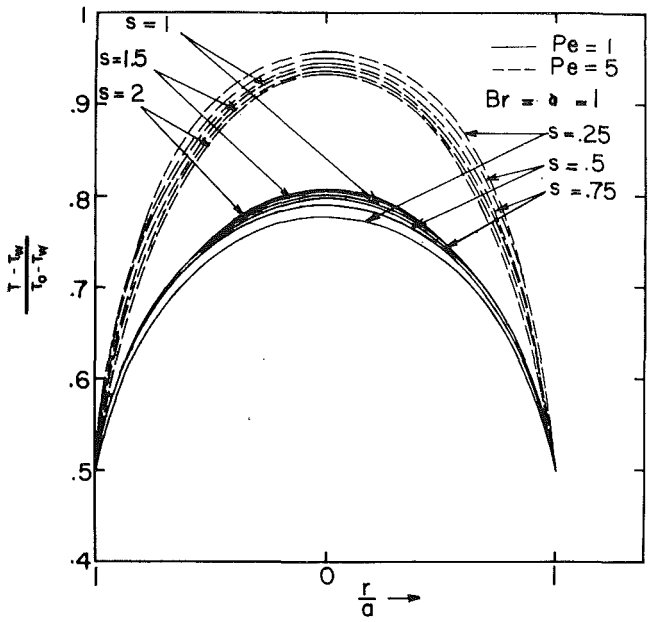

Fig. 3 Temperature profile at the entrance ($x = 0$) of tube flow with constant wall temperature: Pe = 1, 5; Br = δ = 1; s = 0.25, 0.5, 0.75, 1, 1.5, and 2

Table 1 Dimensionless average temperature and the development length (5 percent deviation from its steady-state value) for Br = δ = 1 heat transfer in tubular flow with constant wall temperature

Pe	s	$\theta_b(0)$	ξ_{dT}^+	ξ_{dNu}	$\xi_{d\bar{T}}$
1	.25	.697	1.834	1.446	.564
	.5	.714	1.719	1.151	.579
	.75	.721	1.653	1.046	.588
	1.	.724	1.613	.993	.595
	1.5	.728	1.565	.930	.604
	2.	.729	1.538	.892	.609
5	.25	.843	.694	.584	.039
	.5	.841	.611	.496	.045
	.75	.838	.574	.453	.049
	1.	.835	.532	.423	.052
	1.5	.831	.510	.382	.057
	2.	.828	.496	.377	.059
10	.25	.910	.623	.528	.007
	.5	.904	.548	.447	.009
	.75	.900	.501	.401	.010
	1.	.896	.478	.378	.012
	1.5	.892	.444	.347	.014
	2.	.888	.420	.327	.015

The same method can be applied to parallel plate geometry and the results are shown in Appendix A. One can also apply the present method to constant wall heat flux case and the results are given in Appendix B [25].

Results and Discussions

In the present work, twenty eigenvalues and eigenfunctions each are obtained for the upstream and the downstream region. Equations (12–14) are solved by the Runge-Kutta method and equations (21–22) are solved by the Gauss-Seidel method.

Several simplified problems can be obtained from the present results. When Peclet number is large and the flow is non-Newtonian, the asymptotic downstream Nusselt number reduces to those values reported previously [3, 7, 22]. For Newtonian fluid (s = 1) at low Peclet number, comparison of the present results with those of Hennecke [15] is shown in Fig. 2. It is seen that exact agreement is obtained between the present results and those of Hennecke [15].

The dimensionless radial temperature distribution at the plane x = 0 is shown in Fig. 3. The dimensionless wall

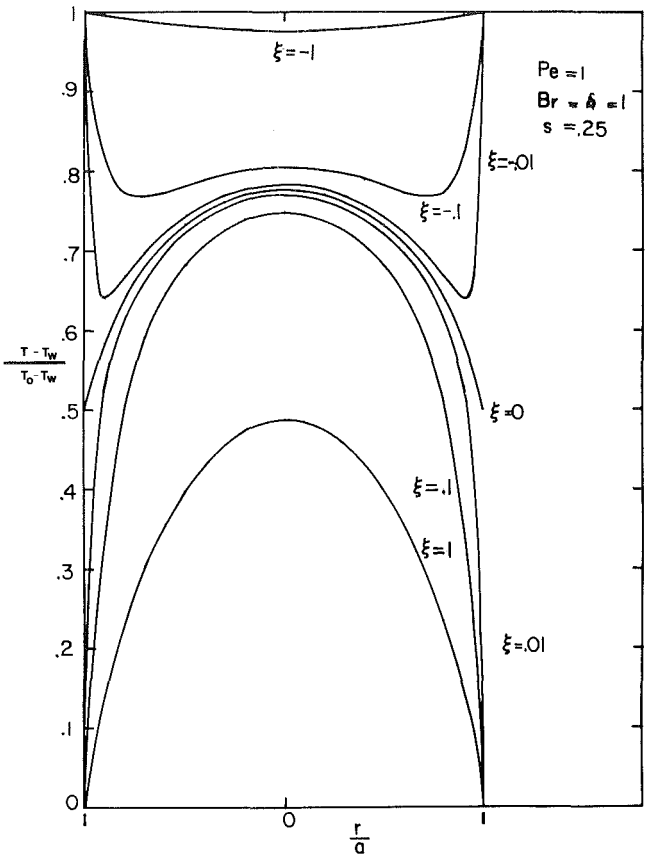

Fig. 4 Radial temperature profile at different axial distance of the tube with constant wall temperature: Pe = 1; Br = δ = 1; s = 0.25

temperature in Fig. 3 is the arithmetic average value determined from the upstream and the downstream regions. The dimensionless temperature is not uniform radially. Indeed, it varies significantly with Peclet number and the power law model index, s. When the value of Peclet number decreases, deviation of the dimensionless temperature at x = 0 from the upstream inlet temperature is more drastic. An opposite effect of power law model index, s, on the temperature field is found for Pe = 1 and 5 for tubular flow due to crossover of the temperature curves when power law model index, s, changes. Results from constant wall heat flux boundary condition case have also been obtained for tubular and parallel plate systems, and they indicate that the effect of the axial conduction is less significant for the parallel plate geometry than for the tubular geometry.

Figure 4 shows the dimensionless radial temperature at different axial distance for tubular geometry with constant wall temperature boundary condition. Heat transfer to the fluid in the vicinity of the wall in the upstream region close to the plane x = 0 from the downstream wall causes a minimum temperature close to the wall and a maximum temperature in the center in the upstream region. For constant wall heat flux boundary conditions, the maximum temperature is found close to the wall and the minimum temperature is at the center.

Figure 5 is the dimensionless average temperature along the axial distance of the tube for different power law model index s and Pe = 1. Due to the effect of axial conduction, the dimensionless temperature at x = 0 is lower than the dimensionless inlet temperature upstream. The dimensionless penetration depth required in the upstream region in order to reach 5 percent of its dimensionless inlet temperature is tabulated in Table 1. Also tabulated in Table 1 is the dimensionless distance ξ_{dT}^+ required in the downstream region in order to reach 5 percent of its steady-state temperature.

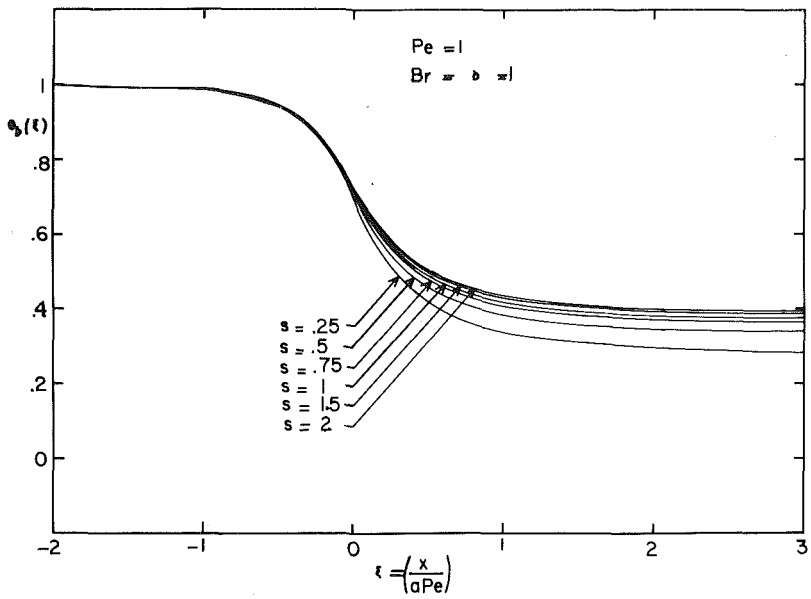

Fig. 5 Dimensionless average temperature versus axial distance for different values of power law model index for Pe = 1, Br = δ = 1 in a tube with constant wall temperature

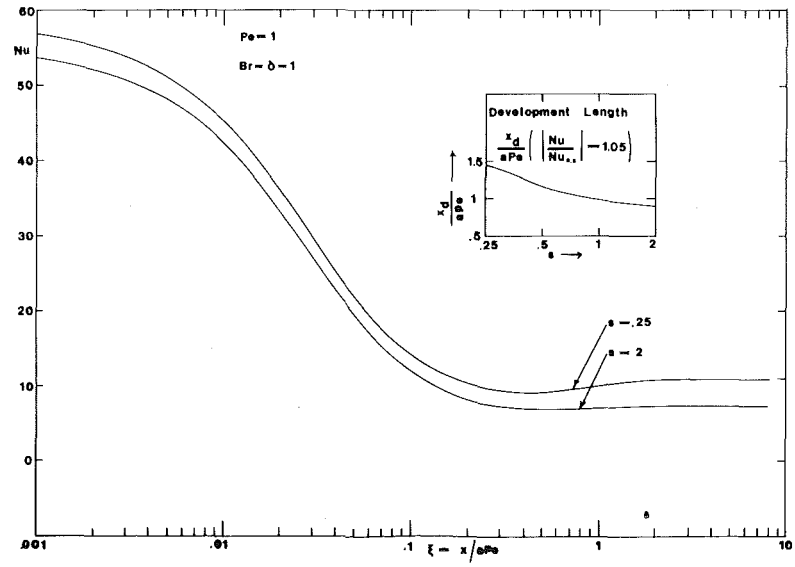

Fig. 6 Nusselt number versus axial distance for different values of power law model index for Pe = 1, Br = δ = 1 in a tube with constant wall temperature

Local Nusselt number in the downstream region of the tube is shown in Fig. 6. The downstream steady-state Nusselt number decreases when the power law model index, s, increases. When Br = δ = 1, the downstream steady-state Nusselt number is mainly due to the effect of viscous dissipation and heat generation, and the effect of convective heat transfer is less important. The development length required for the Nusselt number to reach 5 percent of its downstream steady-state value for different values of the power law model index, s, is also shown in Fig. 6. Figure 7 shows the Nusselt number along the axial distance of a tube with constant wall heat flux boundary condition. Figure 8 and 9 show the Nusselt number for parallel plate geometry with constant wall temperature and constant wall heat flux boundary condition respectively. Negative Nusselt number is found in the thermal entrance region in Fig. 9 because the average temperature of the fluid is lower than the temperature of the wall. These phenomena are first reported here. At higher Peclet numbers, say Pe = 5, 10, the Nusselt number is not negative. Downstream steady-state Nusselt numbers for flow between parallel plates and inside the tube with constant wall temperature and constant wall heat flux boundary conditions are also reported in Table 2.

Conclusions

Several conclusions can be obtained from the present work:

(*i*) The significant effect of axial conduction on heat transfer is found in the following descending order: (*a*) constant wall heat flux tubular flow; (*b*) constant wall heat flux flowing between parallel plates; (*c*) constant wall temperature tubular flow; (*d*) constant wall temperature flowing between parallel plates.

(*ii*) The error of assuming the temperature at the plane $x = 0$ to be the same as T_0 at $x = -\infty$ lies between 5 percent for flow between parallel plates with constant wall boundary conditions at Pe ≥ 5 and 500 percent for tubular flow with constant wall heat flux condition at Pe = 1 and s = 2.

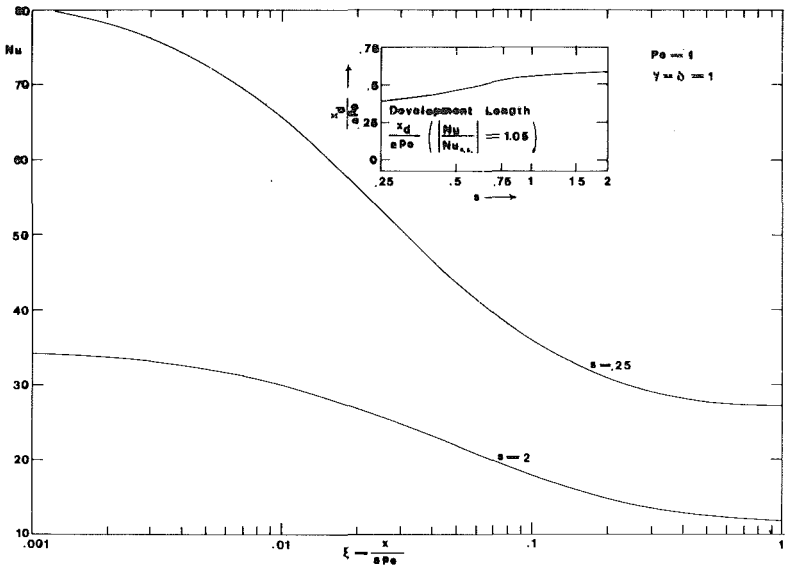

Fig. 7 Nusselt number versus axial distance for different values of power law model index for Pe = 1, $\gamma = \delta = 1$ in a tube with constant wall heat flux

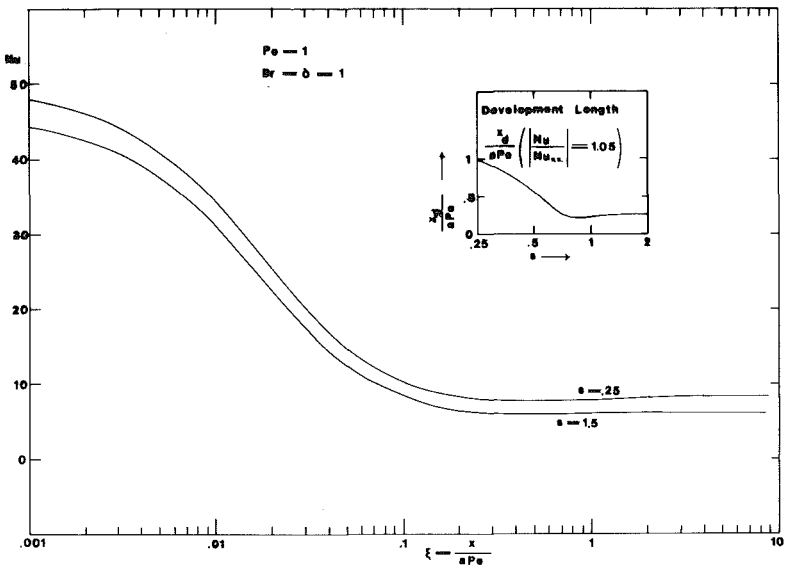

Fig. 8 Nusselt number versus axial distance for different values of power law model index for Pe = 1, Br = δ = 1 between parallel plates with constant wall temperature

(*iii*) For the constant wall temperature case, the effect of axial conduction is less significant at Pe = 1 but is more significant at Pe = 5 and 10, when the power law model index, *s*, increases.

(*iv*) The effect of axial conduction is more significant when the power law model index, *s*, increases for the constant wall hear flux case.

References

1 Sellars, J. R., Tribus, M., and Klein, J. S., "Heat Transfer Laminar Flow in a Round Tube or Flat Conduit—The Graetz Problem Extended," ASME *Trans.*, Vol. 78, 1956, pp. 441–448.

2 Siegel, R., Sparrow, E. M., and Hallman, T. M., "Steady Laminar Heat Transfer in a Circular Tube With Prescribed Wall Heat Flux," *Appl. Sci. Res.*, A7, 1958, pp. 386–392.

3 Whiteman, I. R., and Drake, W. B., "Heat Transfer to Flow in a Round Tube With Arbitrary Velocity Distribution," ASME *Trans.*, Vol. 80, 1958, pp. 728–732.

4 Toor, H. L., "Heat Transfer in Forced Convection With Internal Heat Generation," *AIChE Journal*, Vol. 4, 1958, pp. 319–323.

5 Metzner, A. B., and Gluck, D. F., "Heat Transfer to Non-Newtonian Fluids Under Laminar-Flow Conditions," *Chem. Eng. Sci.*, Vol. 12, 1960, pp. 185–190.

6 Gill, W. N., "Heat Transfer in Laminar Power Law Flows With Energy Sources," *AIChE Journal*, Vol. 8, 1962, pp. 137–138.

7 McKillop, A. A., "Heat Transfer for Laminar Flow of Non-Newtonian Fluids in Entrance Region of a Tube," *International Journal of Heat and Mass Transfer*, Vol. 7, 1964, pp. 853–862.

8 Ziegenhagen, A. J., "Approximate Eigenvalues for Heat Transfer to Laminar or Turbulent Flow in an Annulus," *International Journal of Heat and Mass Transfer*, Vol. 8, 1965, pp. 499–505.

9 Griskey, R. G., and Wiehe, I. A., "Heat Transfer to Molten Flowing Polymers," *AIChE Journal*, Vol. 12, 1966, pp. 308–312.

10 Cox, H. W., and Macosko, C. W., "Viscous Dissipation in Die Flows," *AIChE Journal*, Vol. 20, 1974, pp. 785–795.

11 Winter, H. H., "Viscous Dissipation in Shear Flows of Molten Polymers," *Advances In Heat Transfer*, Vol. 13, 1977, pp. 205–267.

12 Bird, R. B., Armstrong, R. C., and Hassager, O., "Dynamics of Polymeric Liquids," *Fluid Mechanics*, Vol. 1, J. Wiley & Sons, 1977, pp. 233–265.

13 Vlachopoulos, J., and Keung, C. K. Jr., "Heat Transfer to a Power Law Fluid Flowing Between Parallel Plates," *AIChE Journal*, Vol. 18, 1972, pp. 1272–1274.

14 Ybarra, R., and Eckert, R. E., "Viscous Heat Generation In Slit Flow," *AIChE Journal*, Vol. 26, 1980, pp. 751–762.

15 Hennecke, D. K., "Heat Transfer by Hagen-Poiseuille Flow in the Thermal Development Region With Axial Conduction," *Warme Und Stofubertragung*, Bd 1, 1968, pp. 177–184.

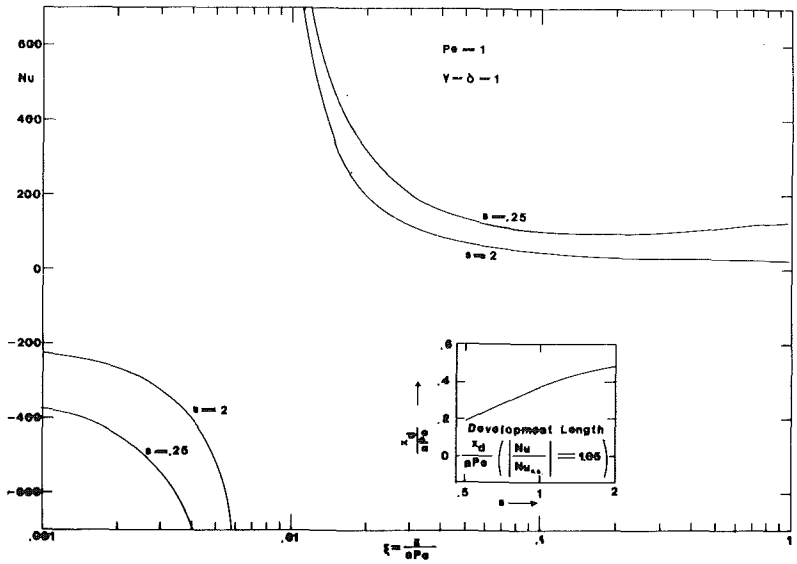

Fig. 9 Nusselt number versus axial distance for different values of power law model index for Pe = 1, $\gamma = \delta = 1$ between parallel plates with constant wall heat flux

Table 2 Downstream steady-state Nusselt number for flow between parallel plates and inside the tube with constant wall temperature and constant wall heat flux boundary conditions for Pe = 1, Br = $\delta = \gamma = 1$

Flow in a tube with constant wall temperature

s	$\overline{Nu}$
0.25	10.874134
0.50	9.084541
0.75	8.378244
1.00	8.000000
1.50	7.603381
2.00	7.397774

Flow in a tube with constant wall heat flux

s	$\overline{Nu}$
0.25	26.938468
0.50	17.917784
0.75	15.094660
1.00	13.714286
1.50	12.352496
2.00	11.677725

Flow between parallel plates with constant wall temperature

s	$\overline{Nu}$
0.25	8.276866
0.50	7.304894
0.75	6.869048
1.00	6.621622
1.50	6.350728
2.00	6.205379

Flow between parallel plates with constant wall heat flux

s	$\overline{Nu}$
0.25	128.690500
0.50	55.457385
0.75	41.076691
1.00	35.000000
1.50	29.532130
2.00	27.000000

16 Hsu, C. J., "An Exact Analysis of Low Peclet Number Thermal Entry Region Heat Transfer in Transversely Nonuniform Velocity Fields," *AIChE Journal*, Vol. 17, 1971, pp. 732-740.

17 Jones, A. S., "Extensions To The Solution of The Graetz Problem," *International Journal of Heat and Mass Transfer*, Vol. 14, 1971, pp. 619-623.

18 Sorensen, J. P., and Stewart, W. E., "Computation of Forced Convection in Slow Flow Through Ducts and Packed Beds—I: Extensions Of The Graetz Problem," *Chem. Eng. Sci.*, Vol. 29, 1974, pp. 811-817.

19 Michelsen, M. L. and Villadsen, J., "The Graetz Problem With Axial Heat Conduction," *International Journal of Heat and Mass Transfer*, Vol. 17, 1974, pp. 1399-1402.

20 Papoutsakis, E., Ramkrishna, D., and Lim, H. C., "The Extended Graetz Problem With Dirichlet Wall Boundary Conditions," *Appl. Sci. Res.*, Vol. 36, 1980, pp. 13-33.

21 Papoutsakis, E., Ramkrishna, D., and Lim, H. C., "The Extended Graetz Problem With Prescribed Wall Flux," *AIChE Journal*, Vol. 26, 1980, pp. 779-787.

22 Lynche, B. C., and Bird, R. B., "The Graetz-Nusselt Problem For Power-Law Non-Newtonian Fluid," *Chem. Eng. Sci.*, Vol. 6, 1956, pp. 35-41.

23 Dang, V. D., "Mass Transfer With Axial Diffusion and Chemical Reaction," *Chem. Eng. Sci.*, Vol. 33, 1978, pp. 1179-1190.

24 Chow, Y. I., and Hartnett, J. P., "Non-Newtonian Fluids in Circular Pipe Flow," in *Advances in Heat Transfer*, edited by J. P., Hartnett and T. F., Irvine, Jr., *Academic Press*, Vol. 15, 1982, pp. 59-141.

25 Dang, V. D., "Axial Conduction Heat Transfer of Power Law Fluid Between Parallel Plates," 21st National Heat Transfer Conference, Seattle, Wash., July 1983, (also in press in AIChE Symposium Session).

APPENDIX A

Solution for Parallel Plate Geometry With Constant Wall Temperature

The dimensionless temperature for the upstream and downstream regions is

$$\theta_1(\xi,\eta) = 1 + \sum_{n=1}^{\infty} A_n Y_{1n}(\eta)\exp(\alpha^2{}_{1n}\xi) \tag{A1}$$

$$\theta_2(\xi,\eta) = g(\eta) + \sum_{n=1}^{\infty} B_n Y_{2n}(\eta)\exp(-\alpha^2{}_{2n}\xi) \tag{A2}$$

where

$$g(\eta) = \mathrm{Br}\left(\frac{s+1}{s}\right)^{s+1} \frac{s^2}{(2s+1)(3s+1)}\left(1-\eta^{\frac{3s+1}{s}}\right) + \frac{\delta}{2}(1-\eta^2) \tag{A3}$$

The differential systems for Y_{in} $(i = 1, 2)$

$$\frac{d^2 Y_{in}}{d\eta^2} + (-1)^i \alpha^2{}_{in}\left[1-\eta^{\frac{s+1}{s}} + (-1)^i \frac{4}{9\mathrm{Pe}^2}\alpha^2{}_{in}\right] Y_{in} = 0 \tag{A4}$$

$$Y'_{in}(0) = 0 \tag{A5}$$

$$Y_{in}(1) = 1 \tag{A6}$$

The coefficients A_n and B_n are determined by the following equations

$$\sum_{n=m}^{\infty} B_n C_{nm} - \sum_{n=1}^{\infty} A_n \left(\sum_{j=1}^{n} d_{nj} \int_0^1 \phi_j \psi_m d\eta \right) =$$

$$\int_0^1 \left[1 - \frac{\mathrm{Br}\left(\frac{s+1}{s}\right)^{s+1} s^2}{(2s+1)(3s+1)} \left(1 - \eta^{\frac{3s+1}{s}}\right) - \frac{\delta}{2}(1-\eta^2) \right] \psi_m d_\eta \quad \text{(A7)}$$

$$\sum_{n=1}^{\infty} B_n \alpha_{2n}^2 \left(\sum_{j=1}^{n} C_{nj} \int_0^1 \psi_j \phi_m d\eta \right) + \sum_{n=m}^{\infty} A_n \alpha^2{}_{1n} d_{nm} = 0 \quad \text{(A8)}$$

The dimensionless average temperature and Nusselt number are

$$\theta_{1B}(\xi) = 1 + \frac{2s+1}{s+1} \sum_{n=1}^{\infty} \frac{A_n e^{\alpha_{1n}^2 \xi}}{\alpha^2{}_{1n}} \left[\frac{dY_{1n}(1)}{d\eta} + \frac{4\alpha_{1n}^4}{9\mathrm{Pe}^2} \int_0^1 Y_{1n} d\eta \right] \quad \text{(A9)}$$

$$\theta_{2B}(\xi) = \mathrm{Br}\left(\frac{s+1}{s}\right)^{s+1} \frac{2s^2(3s+1)}{(4s+1)(2s+1)(5s+2)} + \frac{\delta(5s+1)}{3(4s+1)}$$

$$- \frac{2s+1}{s+1} \sum_{n=1}^{\infty} \frac{B_n e^{-\alpha_{2n}^2 \xi}}{\alpha_{2n}^2} \left[Y'_{2n}(1) + \frac{4\alpha_{2n}^4}{9\mathrm{Pe}^2} \int_0^1 Y_{2n} d\eta \right] \quad \text{(A10)}$$

$$\mathrm{Nu} = \frac{2hb}{k} = \frac{-2}{\theta_{2B}(\xi)} \frac{\partial \theta_2}{\partial \eta}\bigg|_{\eta=1}$$

$$= \frac{2}{\theta_{2B}(\xi)} \left[\mathrm{Br}\left(\frac{s+1}{s}\right)^{s+1} \frac{s}{2s+1} + \delta - \sum_{n=1}^{\infty} B_n \frac{dY_{2n}(1)}{d\eta} e^{-\alpha_{2n}^2 \xi} \right] \quad \text{(A11)}$$

APPENDIX B

Solution For Constant Wall Heat Flux Care. The dimensionless temperature in the upstream and the downstream region is

$$\theta_1(\xi,\eta) = \sum_{n=1}^{\infty} A_n Y_{1n}(\eta) \exp(\alpha^2{}_{1n} \xi) \quad \text{(B1)}$$

$$\theta_2(\xi,\eta) = \theta_{ss}(\xi,\eta) + \sum_{n=1}^{\infty} B_n Y_{2n}(\eta) \exp(-\alpha^2{}_{2n} \xi) \quad \text{(B2)}$$

1 For Tubular Geometry.

$$\theta_{ss}(\xi,\eta) = C_0 \xi + C_0 \left[\frac{\eta^2}{4} - \left(\frac{s}{3s+1}\right)^2 \eta^{\frac{3s+1}{s}} \right] - \gamma \left(\frac{s+1}{s}\right)^{s+1} \left(\frac{s}{3s+1}\right)^2 \eta^{\frac{3s+1}{s}} - \frac{\delta\eta^2}{4} + C_2 \quad \text{(B3)}$$

where

$$C_0 = \frac{2(3s+1)}{s+1} \left[\gamma \left(\frac{s+1}{s}\right)^{s+1} \frac{s}{3s+1} + \frac{\delta}{2} - 1 \right] \quad \text{(B4)}$$

$$C_2 = \frac{(3s+1)C_0}{(s+1)\mathrm{Pe}^2} - \frac{\gamma}{4} \left(\frac{s+1}{s}\right)^{s+1} \frac{s}{3s+1} - \frac{s\delta}{4(3s+1)} + \frac{19s^2+8s+1}{4(3s+1)(5s+1)} \quad \text{(B5)}$$

The dimensionless average temperature an Nusselt number are

$$\theta_{1B}(\xi) = \frac{2(3s+1)}{s+1} \sum_{n+1}^{\infty} A_n e^{\alpha_{1n}^2 \xi} \frac{\alpha_{1n}^2}{\mathrm{Pe}^2} \int_0^1 \eta Y_{2n} d\eta \quad \text{(B6)}$$

$$\theta_{2B}(\xi) = C_0 \xi + \frac{(19s^3+27s^2+9s+1)C_0 - 8\gamma\left(\frac{s+1}{s}\right)^{s+1} s^3}{8(3s+1)^2(5s+1)} - \frac{(3s+1)\delta}{8(5s+1)} + C_2 - \frac{2(3s+1)}{s+1} \sum_{n=1}^{\infty} B_n e^{-\alpha_{2n}^2 \xi} \frac{\alpha_{2n}^2}{\mathrm{Pe}^2} \int_0^1 \eta Y_{2n} d\eta \quad \text{(B7)}$$

$$\mathrm{Nu} = \frac{2ha}{k} = \frac{2aqw}{k[T_{2b}(\xi) - T_2(\xi,1)]}$$

$$\mathrm{Nu} = 2/\left\{ \frac{-(s+1)(31s^2+12s+1)C_0}{8(3s+1)^2(5s+1)} + \gamma\left(\frac{s+1}{s}\right)^{s+1} \left(\frac{s}{3s+1}\right)^2 \left(\frac{4s+1}{5s+1}\right) + \frac{\delta}{8}\left(\frac{7s+1}{5s+1}\right) - \sum_{n+1}^{\infty} B_n e^{-\alpha_{2n}^2 \xi} \left[\frac{2(3s+1)\alpha_{2n}^2}{(s+1)\mathrm{Pe}^2} \int_0^1 \eta Y_{2n} d\eta + Y_{2n}(1) \right] \right\} \quad \text{(B8)}$$

2 For Parallel Plate Geometry.

$$\theta_{ss}(\xi,\eta) = C_0 \xi + C_0 \left(\frac{\eta^2}{2} - \frac{s^2}{(2s+1)(3s+1)} \eta^{\frac{3s+1}{s}} \right) - \gamma \left(\frac{s+1}{s}\right)^{s+1} \frac{s^2}{(2s+1)(3s+1)} \eta^{\frac{3s+1}{s}} - \frac{\delta\eta^2}{2} + C_2 \quad \text{(B9)}$$

where

$$C_0 = \left(\frac{2s+1}{s+1}\right) \left[\gamma \left(\frac{s+1}{s}\right)^{s+1} \left(\frac{s}{2s+1}\right) + \delta - 1 \right] \quad \text{(B10)}$$

$$C_2 = \left(\frac{2s+1}{s+1}\right) \left\{ \frac{4C_0}{9\mathrm{Pe}^2} - \gamma \left(\frac{s+1}{s}\right)^{s+1} \frac{s(9s^2+11s+2)}{6(3s+1)(4s+1)(5s+2)} + \frac{6s^2 - s(3s+1)(5s+2)}{6(3s+1)(4s+1)(5s+2)} \delta + \frac{(2s+1)(3s+1)(5s+2) - 6s^3}{6(3s+1)(4s+1)(5s+2)} \right\} \quad \text{(B11)}$$

The dimensionless average temperature and Nusselt number are

$$\theta_{1B}(\xi) = \frac{2s+1}{s+1} \sum_{n=1}^{\infty} A_n e^{\alpha_{1n}^2 \xi} \frac{4\alpha^2{}_{1n}}{9\mathrm{Pe}^2} \int_0^1 Y_{1n} d\eta \quad \text{(B12)}$$

$$\theta_{2B}(\xi) = C_0 \xi + \frac{C_0(24s^3+37s^2+15s+2)}{6(3s+1)(4s+1)(5s+2)} - \gamma \left(\frac{s+1}{s}\right)^{s+1} \frac{s^3}{(3s+1)(4s+1)(5s+2)} - \frac{\delta(2s+1)}{6(4s+1)} + C_2 - \frac{2s+1}{s+1} \sum_{n=1}^{\infty} B_n e^{-\alpha_{2n}^2 \xi} \frac{4\alpha^2{}_{2n}}{9\mathrm{Pe}^2} \int_0^1 Y_{2n} d\eta \quad \text{(B13)}$$

$$\mathrm{Nu} = 2/\left\{ \frac{-C_0(s+1)(32s^2+17s+2) + 6\gamma\left(\frac{s+1}{s}\right)^{s+1} s^2(3s+1)}{3(2s+1)(4s+1)(5s+2)} + \frac{(5s+1)\delta}{3(4s+1)} - \sum_{n=1}^{\infty} B_n e^{-\alpha_{2n}^2 \xi} \left[Y_{2n}(1) + \left(\frac{2s+1}{s+1}\right) \frac{4\alpha^2{}_{2n}}{9\mathrm{Pe}^2} \int_0^1 Y_{2n} d\eta \right] \right\} \quad \text{(B14)}$$

Measurement of Fusion Boundary Energy Transport During Arc Welding

C. S. Landram
Lawrence Livermore National Laboratory,
Livermore, Calif. 94550
Mem. ASME

An experimental technique is presented to identify fusion boundary (liquid/solid interface) energy transport mechanisms during welding procedures. The gas-tungsten-arc spot-welding procedure, using a low melting point specimen material (lead), was chosen to demonstrate the methods. Vaporization energy losses were found to be important during the growth of the fusion boundary. Significant thermal convection was absent within the weld pool for applied currents less than about 100 A, and for such cases the location of the fusion boundary was found to be governed primarily by heat conduction. At the current levels of almost 300 A, significant weld pool convection was found to exist, especially at the (inner) stagnation point, causing a deeper penetration of the fusion boundary there.

Introduction

Energy transport during welding procedures is important for determining the ultimate integrity of the weld. Location of the liquid-solid interface (fusion boundary), and its associated interfacial heat fluxes are requisites for metallurgical and structural studies. Computational [1, 2] methods used for predicting such results require specification of the heat source strength as a boundary condition and generally assume a diffusive transfer mechanism between the source and the fusion boundary. The purpose of this work is to present an experimental technique which can be used to improve existing modeling capabilities. Though several welding processes could be treated here, the application is confined to the inert gas-tungsten-arc (GTA) process. Two transfer mechanisms are identified through measurements: vaporization from the weld pool surface, and convection within the pool. Their effect on fusion boundary location and heat transfer is presented.

Existing GTA heat source correlations of the calorimetric type [3, 4] have been obtained from steady or quasi-steady measurements which mask energy transport during the growth of the liquid-solid interface. Correlations obtained through the quasi-steady, moving source method [5] not only lose the same temporal identity, but also assume a purely diffusive transfer in the weld pool.

Weld pool fluid dynamics, relative to the GTA process, have been analyzed in a series of papers [6, 7, 8, 9, 10], beginning with the pioneering work of [11] and all presume the Lorentz body force to drive the fluid motion. Flow visualization experiments [12, 13, 14] qualitatively confirm the analytical results in terms of the existence of a stagnation point type flow within the weld pool directly under the arc in conjunction with an axisymmetric recirculating flow. The effect of such a flow field has not been assessed in terms of heat transfer, and its effect on promoting both overall pool growths and local pool distortions from that predicted by diffusional transport alone.

Experimental results for fusion boundary propagation, total fusion zone power, and liquid-solid interfacial heat flux are presented based on data obtained from an axisymmetric apparatus having stationary anode and cathode (spot-welding). Overall and local interfacial conductance and heat flux are reported as a function of the current applied. The experimental approach is novel in that the resulting data do not depend on postulation of the source physics, the energy losses off the specimen surface or the transport phenomena within the weld pool. Because the techniques become more elaborate with accommodation of specimen property variation with temperature and also since spatial resolution is important, only a low melting point material (lead) was considered as a test specimen. Applied current levels were as high as 290 A.

Apparatus

The apparatus is shown in Fig. 1, and except for preliminary steady-state verification experiments, was operated in absence of the cooling gas shown. The selection of materials and sizes was based on a compromise between the following: good spatial resolution of measurement, small

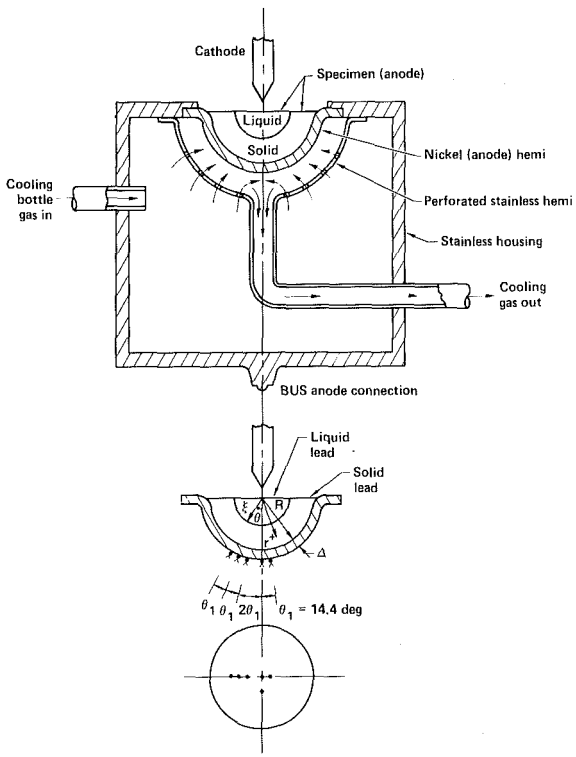

Fig. 1 Experimental apparatus and thermocouple locations

Contributed by the Heat Transfer Division for publication in the JOURNAL OF HEAT TRANSFER. Manuscript received by the Heat Transfer Division February 15, 1982.

effective area for electron flux heating in comparison to specimen surface area, pure specimen material (lead) of low melting point (and having been previously analyzed by calorimetry [3]), anode cup (nickel) electrical conductivity large compared to that of specimen (so as to have nearly radial current density lines within the specimen). Chromel-Alumel thermocouples were resistance-welded to the outer convex surface of the nickel hemi of Fig. 1, and their locations are shown in the inset. The experimental methods used require azimuthal symmetry; thus, some necessary duplicity of measurement is noted by thermocouple orientation. Adjacent thermocouples were also welded on the inner concave surface, separating the lead and nickel, with insulated leads penetrating small drilled holes within the nickel hemi. The adjacent thermocouples separated by the hemi-wall are connected differentially (eventually to be used for steady-state measurements) and separately to a recorder. In all cases presented here, the instantaneous temperature differential across the hemi (but not its thermal capacitance) could be neglected.

The cathode was 1 percent thoriated tungsten having a conical 25 deg tip and had argon as the shielding gas. The welding machine was operated at constant current level, and its power was terminated at given positions of the liquid-solid interface. The tests were conducted at atmospheric pressure. In a preliminary series of steady-state experiments a soldering iron with its power monitored was substituted for the arc in Fig. 1, and its tip contacted a very low melting point (75° C) bismuth alloy used for the specimen. The only important mechanism for heat transfer within the melted specimen pool for this case is conduction (the Prandtl and Rayleigh numbers are small and the Lorentz forces are absent; the Maragoni effects [15] are negligible). Also, no noticeable spatial variation in temperature around the outer shell was observed for these preliminary experiments. Therefore, the melt boundary was very nearly spherical, as was confirmed by sectioning the alloy. The calculated diffusional melt radius agreed with that observed geometrically over a range of input powers and necessary steady-state cooling rates.

Experimental Method

The specimen material in $0 < r^+ < R$ is a solid for $\xi(\theta, t) < r^+ < R$, where $\xi(\theta, t)$ is the location of the liquid solid interface (Fig. 1). The surrounding nickel shell, adiabatic on its convex surface and of thickness $\Delta << R$, has a thermal capacitance $(\rho c \Delta)_s$. The boundary conditions, both at $r^+ = R$, are then given by

$$T(R,\theta,t) = T_w(\theta,t)$$

$$\frac{\partial T}{\partial r^+}(R,\theta,t) = -\frac{(\rho c\Delta)_s}{k_A}\frac{\partial T_w}{\partial t}(\theta,t)$$

where $T_w(\theta,t)$ is the measured hemi-wall temperature at any position, θ.

Having two unique boundary conditions along the same surface of the solid constitutes a description of the inverse heat conduction problem [16] and the solution for any point within the solid can then be found if the solid specimen properties can be considered constant. In this particular application, separate numerical calculations demonstrated that radial temperature gradients dominate polar gradients in the solid. Hence, to a good approximation, polar conduction in the solid may be ignored and the inverse solution with the above boundary conditions gives

$$T(r,\theta,t) = T_w(\theta,r) + \tau\sum_{n=1}^{\infty} A_n(r)\frac{d^n T_w}{dt^n}\ (\theta,t) \tag{1}$$

where

$$A_n(r) = \frac{6^n}{(2n+1)!}\tau^{(n-1)}\left[(2n+r)(1-r) + \frac{(2n+1)!}{(2n-1)!}\epsilon\right]\frac{(1-r)}{r}^{(2n-1)}$$

At the melt surface $r = x = \xi/R$. With T_M the melt temperature, equation (1) gives the melt surface location $x(\theta,t)$ implicitly as

$$\sum_{n=1}^{\infty} A_n(x)\frac{d^n T_w}{dt^n}(\theta,t) = \frac{T_M - T_w(\theta,t)}{\tau} \tag{2}$$

Equation (2) can be differentiated with respect to time to give the rate of melt surface propagation as

$$\frac{1}{R}\frac{d\xi}{dt} = \frac{dx}{dt} = -\frac{\frac{1}{\tau}\frac{dT_w}{dt} + \sum_{n=1}^{\infty} A_n\frac{d^{n+1}T_w}{dt^{n+1}}}{\sum_{n=1}^{\infty}\frac{dA_n}{dx}\frac{d^n T_w}{dt^n}} \tag{3}$$

The instantaneous heat flux conducted into the solid at the melt surface is obtained from equation (1) as

$$q_c(x,\theta,t) = -k_A\frac{\partial T}{\partial r^+}(x,\theta,t)$$

$$= -\frac{k_A\tau}{R}\sum_{n=1}^{\infty}\frac{dA_n}{dr}(x,\theta,t)\frac{d^n T_w}{dt^n}(t) \tag{4}$$

and the latent heat flux at the same location is given by

$$q_{\text{lat}}(x,\theta,t) = \rho_A RL\frac{dx}{dt}(\theta,t) \tag{5}$$

where dx/dt is available from equation (3). The total energy flux to the interface is the sum of equations (4) and (5).

Each measured wall temperature history, T_w, in excess of the initial temperature, T_o, was observed to behave in a common temporal fashion. For times after arc initiation of less than about a second, very little temporal variation in

Nomenclature

- c = specific heat capacity
- k = thermal conductivity
- L = latent heat of fusion (5.5 cal/g for lead)
- q = heat flux, W/m^2
- Q_o = source strength, W
- r = dimensionless radial coordinate (r^+/R)
- r^+ = radial coordinate
- R = lead specimen radius (1.9 cm)
- t = time
- T = temperature
- x = dimensionless melt boundary location (ξ/R)
- ρ = density
- Δ = thickness of hemispherical cup (.076 cm)
- α = thermal diffusivity
- θ = polar angle measured from symmetry line, deg
- ξ = melt boundary location
- τ = $R^2/(6\alpha)$, s
- ϵ = $(\rho c\Delta)_s/(\rho cR)_A$

Subscripts

- A = lead specimen properties
- B = bulk or mixed mean
- M = melt isotherm (327.4° C for lead)
- w = conditions at hemispherical cup $(r = 1)$
- s = properties of hemispherical cup
- c = transport by conduction
- lat = transport by latent heat
- o = ambient
- ML = at fusion boundary

$T_w - T_o$ was noticeable, and this "dead time" is characteristic of the arrival time of the initial thermal disturbance propagating as a wave in a semi-infinite medium [17]. In subsequent times, a short period occurred when $T_w - T_o \sim t^2$, followed by a long period (comprising most of the growth of the melt-time) when $T_w - T_o \sim t$. In this latter period, no departure from this linearity was discernible (though any departure could be accommodated) over the range of arc power applied. Following the dead time, each measured history was well fitted by the following curve

$$T_w(t) - T_o = a_1 t^2 \epsilon^{-b_1 t} + (-y_o + a_2 t)(1 - e^{-b_2 t}) + y_o b_2 t \quad (6)$$

with the constant coefficients a_1, a_2, b_1, b_2, and y_o depending on polar location and current applied.

In later times, when only the first term in the series of equation (2) applied, the melt line history could be obtained explicitly from a cubic equation. For early times, when $T_w - T_o \sim t^2$, the series can be truncated after $n = 2$. In applying equation (6) for intermediate times, the series could be truncated after $n = 2$, making an error in the melt line displacement of less than 0.5 percent. Retention of higher ordered terms beyond $n = 3$ would not be consistent with minor inadequacies of the data representation (6).

After equation (6) is applied to equations (2) through (5), local angular results are used to obtain the total power to the fusion surface

$$Q_{ML} = 2\pi R^2 \int_o^{\pi/2} (q_c + q_{\text{lat}})\, x^2 \sin\theta\, d\theta \quad (7)$$

As will be subseqently shown, $(q_c + q_{\text{lat}})x^2$ varies with θ most significantly near $\theta = 0$, when $\sin\theta$ is small. Thus, equation (7) was confidently evaluated despite having only discrete values for the integrand.

It should be stated that the above experimental method produces results which do not depend on either the heat source specification nor the calculation of energy transfer between heat source and fusion boundary. To assess the effects of weld pool convection, the experimental results which are consequences of all modes of transfer within the weld pool, were compared to those obtained assuming only diffusional transport within the pool.

Heat Conduction Solution

The direct heat conduction solution in $0 < r < 1$ is now considered (absence of pool convection). In this formulation, the small hemi thermal capacitance and the latent heat of the specimen can be ignored. If the arc produces a point source of strength $Q_o(t)$ at $r = 0$, then the (constant properties) diffusional temperature field $T(r,t)$ is prescribed by

$$\frac{\partial T}{\partial t} = \frac{\alpha_A}{R^2}\frac{1}{r^2}\frac{\partial}{\partial r}\left(r^2\frac{\partial T}{\partial r}\right), \quad 0<r<1 \quad (8)$$

with

$$r^2\frac{\partial T}{\partial r} = -\frac{Q_o}{2\pi k_A R}, \quad r=0, \quad t>0$$

$$\frac{\partial T}{\partial r} = 0, \quad r=1$$

$$T - T_o = 0, \quad t=0$$

The solution for a step in Q_o at time zero is found by standard methods [18] as

$$\frac{T(r,t) - T_o}{\dfrac{Q_o(t)}{2\pi k_A R}} = f(r,t) = \frac{3\alpha_A t}{R^2} + \frac{1}{r} + \frac{r^2}{2} - \frac{9}{5} - \frac{2}{r}\sum_{n=1}^{\infty}\frac{(1+\beta_n{}^2)}{\beta_n{}^3}\sin(\beta_n r)\, e^{\frac{-\alpha_A \beta_n^2 t}{R^2}} \quad (9)$$

where the eigenvalues are the nonzero roots of

$$\beta_n \cot\beta_n - 1 = 0$$

An instantaneous bulk energy balance on the control volume represented by the molten pool revealed not only that the bulk pool sensible energy could be ignored (negligibly small pool thermal capacitance), but that the source strength, Q_o, is identically then the fusion boundary power measured, Q_{ML}, in equation (7). The form of the results for $Q_{ML}(t)$, i.e., small step in Q_{ML} at time zero, followed by a continuous function thereafter, allows the final conduction solution to be written from Duhamel's theorem [18] as

$$T(r,t) - T_o = \int_o^t f(r,t-\lambda)\frac{d}{d\lambda}\left[\frac{Q_{ML}(\lambda)}{2\pi k R_A}\right]d\lambda + \frac{Q_{ML}(0)}{2\pi k R_A} f(r,t) \quad (10)$$

where $f(r,t)$ is equation (9). Once equation (10) is evaluated, the radial conductive melt radius, x_c, (at isotherm $T = T_M$) can be found along with the corresponding heat flux

$$q(x_c,t) = -k_A/R\ \partial T/\partial r\ (x_c,t) \quad (11)$$

Additionally, the diffusive bulk temperature in $0 < r < x_c$ is given by

$$T_B(t) - T_o = \frac{3}{x_c{}^3}\int_o^{x_c}[T(r,t) - T_o]r^2\, dr \quad (12)$$

and so the diffusive heat transfer coefficient (latent heat effects are ignored here) is then defined by

$$h_c \equiv \frac{q(x_c,t)}{T_B(t) - T_M}$$

An overall increase in the size of the weld pool is expected if convection is present. If $t_c - t$ is the time lag for the diffusive (spherical) melt surface to possess the same melt surface area, A_s, as in the measured case, the spatially overall increase in conductance on the fusion boundary is interpreted as

$$\frac{\bar{h}(t)}{h_c} = 1 + \frac{Q_{ML}(t_c) - Q_{ML}(t)}{A_s\, q(x_c,t)}, \quad (13)$$

where all parameters have been previously defined.

Result and Discussion

Results for three applied currents of 50, 100, and 290 A are presented in Figs. 2, 3, and 4, respectively. Note is made that the results shown have not been extended to the very early times when confidence of the methods used would be lost (see the previous section). Omission of the early-time results is not of particular consequence here except in the evaluation of equation (10), which proved to be insensitive to early time extrapolation of Q_{ML} (equation (7)).

Previous calorimetric results [3] denoted by anode power have been corrected for heat losses to the housing of the apparatus at the waist of the nickel hemispherical shell. In all the cases presented, the measured fusion boundary power from equation (7) is observed to rise to a level below the anode power at arc termination, and the difference between the two powers is an increasing function of current level. The difference between anode power and equation (7) is the vaporization energy transferred from the top of the pool, and this conclusion is supported by the fact that the measured loss in lead specimen mass following a given run corresponded to the temporally integrated difference in the two powers during

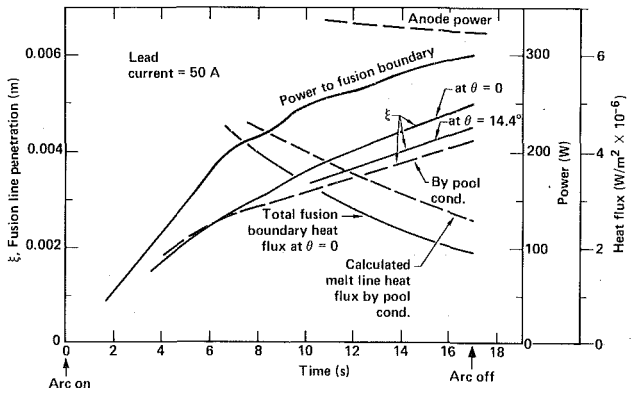

Fig. 2 Results for 50 A. Measurements of fusion zone power, heat flux, and penetration are shown by solid curves. Anode power [3] is corrected for structural heat losses.

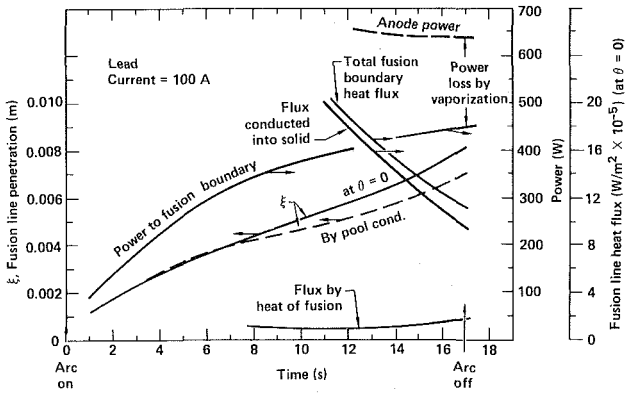

Fig. 3 Results for 100 A (otherwise the same as caption of Fig. 2.)

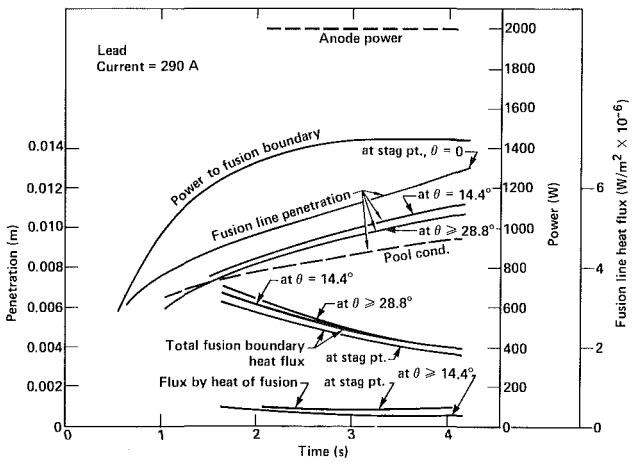

Fig. 4 Results for 290 A (otherwise the same as caption of Fig. 2.)

the heating divided by the heat of varporization (203 cal/g for lead).

In Figs. 3 and 4, the latent heat flux is shown to be much smaller than the heat conducted into the solid at the melt surface. Thus, the treatment of constant properties in the conduction solution (equation (10)) is valid. A comparison between the measured melt line penetration and that calculated in absence of weld pool convection (pool diffusive transport only) is shown in Figs. 2–4 in the range of applied currents. These results are summarized in Fig. 5(*a*), where the increase in penetration above diffusional transport is pronounced at the higher current levels but relatively

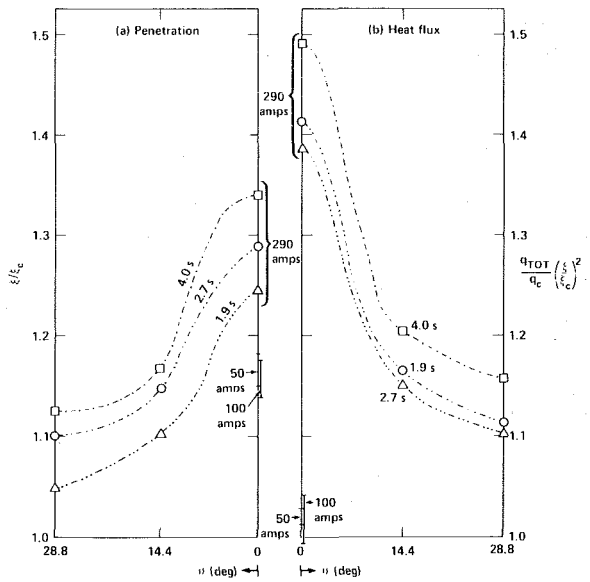

Fig. 5 Angular variation of fusion surface penetration and heat flux normalized to conduction solution

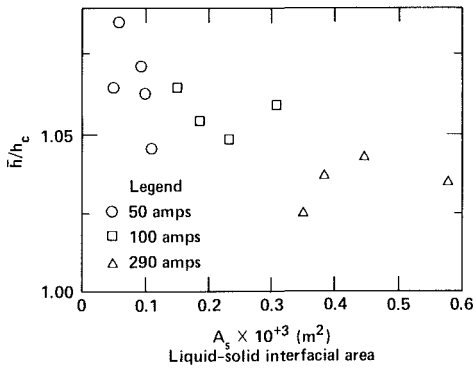

Fig. 6 Overall enhancement of thermal conductance at melt surface (equation (13))

unimportant for currents less than about 100 A. Following each run, the largest diameter of the melt contour on the top surface of the specimen was distinguishable and corresponded very closely to the melt-line location sensed via equation (2) at power termination for locations far from the symmetry line ($\theta = 0$). Similar comparison for interior points within the sample was not possible since sectioning and etching procedures for the lead specimens did not reveal a discernible maximum interior melt surface propagation.

The heat flux at the melt surface is compared to the diffusional heat flux evaluated at the diffusional melt isotherm (equations (4), (5), and (11), respectively) in Fig. 2. This comparison is complicated by the fact that the melt surface has propagated further than the diffusional melt isotherm (i.e., $x > x_c$) at the same instant of time. A more meaningful heat flux comparison is plotted in Fig. 5(*b*), whose ordinate necessarily collapses to unity in the diffusional limit. Consequences of a stagnation point type flow as revealed by Fig. 5(*b*) for the larger current levels are consistent with observations from flow visualization experiments [12]. The results of Fig. 5(*b*) (and 5(*a*)) are also in accord with selective results of prior analytical models aproximating the coupled electromagnetic and fluid flow fields [10].

Evaluation of equation (13) allowed an assessment of the effect of current level in increasing the overall fusion zone size through an increase in overall fusion boundary conductance. The results of Fig. 6 demonstate that of the two correlating

parameters, arc current and pool size, the ratio $\bar{h}/h_c$ best correlates with the latter.

Conclusions

The experimental technique presented provides a method of investigating work-piece heat tranfer processes without the need to prescribe the physics of the heating source used. Therefore, other more complex welding procedures, whose heating source characteristics are not predictable, could also be investigated.

For the material and conditions investigated, vaporization energy losses are more important than weld pool convection in determining heat transfer to the fusion zone in a GTA welding procedure. The Lorentz forces for the material studied tend to promote a fusion boundary penetration in the vicinity of the stagnation point but do not enlarge the entire fusion zone. Other fluid phenomenon such as surface tension gradients [15] may be responsible for the enhancement of overall fusion zone heat conductance in the smaller weld pools. Not until a more complete data base is available, comprising several (more important) materials, will better analytical modeling techniques be forthcoming.

Acknowledgments

The author is very appreciative of the laboratory assistance of Mr. James G. Moore. This work was performed with discretionary research funds from the Mechanical Engineering Department, Lawrence Livermore National Laboratory, for U.S. Department of Energy under Contract No. W-7405-Eng-48.

References

1 Rosenthal, D., "The Theory of Moving Sources of Heat and Its Application to Metal Treatments," *ASME Transactions*, Vol. 68, 1946, pp. 849–866.

2 Andrews, J. G., and Atthey, D. R., "The Response of a Weld Pool to Perturbations in Power," *International Journal of Heat and Mass Transfer*, Vol. 22, 1979, pp. 1533–1537.

3 Apps, R. L., and Milner, D. E., "Heat Flow in Argon-Arc Welding," *British Welding Journal*, Vol. 2, 1955, pp. 475–485.

4 Wilkinson, J. B., and Milner, D. R., "Heat Transfer from Arcs," *British Welding Journal*, Vol. 7, 1960, pp. 115–128.

5 Niles, R. W., and Jackson, C. E., "Weld Thermal Efficiency of the GTAW Process," *Welding Journal*, Vol. 54, 1975, pp. 25S–32S.

6 Sozou, C., "On Fluid Motions Induced by an Electric Current Source," *Journal of Fluid Mechanics*, Vol. 46, 1971, pp. 25–32.

7 Sozou, C., and English, H., "Fluid Motions Induced by an Electric Current Discharge," *Procedure Royal Society London A*, Vol. 329, 1972, pp. 71–82.

8 Sozou, C., and Pickering, W. M., "The Development of Magnetohydrodynamic Flow Due to an Electric Current Discharge," *Journal of Fluid Mechanics*, Vol. 70, 1975, pp. 509–517.

9 Sozou, C., and Pickering, W. M., "Magnetohydrodynamic Flow Due to the Discharge of an Electric Current in a Hemispherical Container," *Journal of Fluid Mechanics*, Vol. 73, 1976, pp. 641–650.

10 Andrews, J. C., and Craine, R. E., "Fluid Flow in a Hemisphere Induced by a Distributed Source of Current," *Journal of Fluid Mechanics*, Vol. 84, 1978, pp. 284–290.

11 Shercliff, J. A., "Fluid Motions Due to an Electric Current Source," *Journal of Fluid Mechanics*, Vol. 40, pp. 241–250.

12 Woods, R. A., and Milner, D. R., "Motion in the Weld Pool in Welding," *Welding Journal*, Vol. 50, 1971, pp. 163S–173S.

13 Lawson, W. H. S., and Kerr, H. W., "Fluid Motion in GTA Weld Pools, Part I: Flow Patterns," *Welding Research International*, Vol. 6, 1976, pp. 63–77.

14 Lawson, W. H. S., and Kerr, H. W., "Fluid Motion in GTA Weld Pools, Part II: Weld Pool Shapes," Vol. 6, 1976, pp. 1–17.

15 Brimacombe, J. K., and Weinberg, F., "Observations of Surface Movements of Liquid Copper and Tin," *Metallurgical Transactions*, Vol. 3, 1972, pp. 2298–2299.

16 Burggraf, O. R., "An Exact Solution of the Inverse Problem in Heat Conduction Theory and Applications," ASME, JOURNAL OF HEAT TRANSFER, Vol. 86, 1964, pp. 373–382.

17 Goodman, T. R., "The Heat-Balance Integral and Its Application to Problems Involving a Change of Phase," ASME *Transactions*, Vol. 80, 1958, pp. 335–342.

18 Carslaw, H. S., and Jaeger, J. C., *Conduction of Heat in Solids*, 2d ed., Oxford University Press, 1959.

A Stochastic Approach to Thermal Modeling Applied to Electro-Discharge Machining

S. M. Pandit
Professor.
Mem. ASME

K. P. Rajurkar
Assistant Professor.
Assoc. Mem. ASME

Mechanical Engineering-Engineering Mechanics Department,
Michigan Technological University,
Houghton, Mich. 49931

The usual method of making some simplifying assumptions and formulating thermal models that yield results confirmed by experiments does not work in many cases where the problem is complex and random. Electro-Discharge Machining (EDM) is such a process that is not only complicated and random but also physically little understood. The paper illustrates thermal modeling of this process with the help of a recently developed stochastic methodology called Data Dependent Systems (DDS). An equation to the melting iosthermal curve is defined from the DDS (stochastic empirical) model obtained from readily measurable surface profiles of actual machined surfaces created by the random superposition of electrical discharges. This equation of the melting isothermal curve is then combined with the heat conduction equation, under rather realistic and intuitively obvious assumptions, to develop a transient temperature distribution. The form of this (hybrid) thermal model is mathematically much simpler and yet its predictions are much closer to the experimental results, compared to the complicated models proposed in the literature.

Introduction

Electro-Discharge Machining (EDM) is a process of removing material in a closely controlled manner from an electrically conductive material immersed in a liquid dielectric with a series of randomly distributed discrete electric sparks or discharges. The advance in tool electrode's vertical position is controlled by the servo-mechanism which maintains a constant gap (between tool and work electrodes) needed for an electric discharge. Extensive investigations have been conducted in elucidating the basic characteristics of a single electric discharge and the resulting expulsion of electrode material [1-4]. A systematic study of the phenomenon of the electrical discharge in a liquid dielectric has proven to be very difficult due to its complexity and also the difficulty in its scientific observation. Therefore, a comprehensive quantitative theory concerning the mechanism of material removal by spark-erosion is yet to be formulated [5]. The erosion by an electric discharge involves phenomena such as heat conduction, melting, evaporation, ionization, formation, and collapse of gas bubbles and energy distribution in the discharge channel. These complicated phenomena coupled with surface irregularities of electrodes, interactions between two successive discharges, and the presence of debris particles make the process random in time as well as space [6], and therefore, deterministically derived thermal models [7-11] yield results that do not match favorably with the experimental evidence.

Such complications and difficulties arise in many other situations requiring realistic thermal modeling of actual processes. As the conventional approach of making some simplified assumptions about the idealized situations and formulating the model to fit experimental results does not work in the case of a highly random process of this kind, it is necessary to obtain the corresponding models directly from observed (experimental or actual) data. A systematic methodology, called Data Dependent Systems (DDS), for accomplishing this objective has been recently developed and is being extensively applied in various fields [12-17]. This paper illustrates an application of DDS to thermal modeling by developing a transient temperature distribution for the EDM process as an example. A similar approach can be employed in many other situations involving such random and complicated phenomena.

Data Dependent Systems (DDS) methodology is briefly introduced in section 1. The representation of the random nature of the EDM process by a first-order DDS model and its physical interpretation are also discussed. Section 2 outlines the procedure of obtaining the temperature distribution from the DDS model in conjunction with the heat conduction equation. The experimental verification of erosion rates obtained from this thermal model is presented in section 3, along with the discussion. The conclusions of this study are summarized in section 4.

1 Data Dependent Systems (DDS) Model for Electro-Discharge Machining (EDM)

DDS Methodology. Data Dependent System (DDS) methodology provides accurate mathematical model for the complex and stochastic systems, directly from the experimental data without requiring any other knowledge of the system. The experimental digitized data are modeled using specially developed computer routines to obtain the DDS model representing the underlying system in differential/difference equation form. The DDS modeling approach uses least-squares techniques to fit a series of differential/difference equations to the experimental data until statistically adequate approximation is reached.

The difference equation form of the DDS model can be used for prediction and control of the system, whereas the differential equation form is more suitable for system analysis and interpretation, characterization, basic mechanism, stability, improved design, etc. From the properly selected and recorded data, the DDS provides a true mathematical representation of the system and therefore can be used for the purposes of system analysis in much the same way as the conventional methods.

First-Order DDS Model (Empirical) for EDM. In-process measurement of an output parameter (e.g., metal removal rate) is extremely difficult in the case of EDM. However, the

Contributed by the Heat Transfer Division and presented at the ASME Winter Annual Meeting, Washington, D.C., November 15-21, 1981. Manuscript received by the Heat Transfer Division January 27, 1981. Paper No. 81-WA/HT-3.

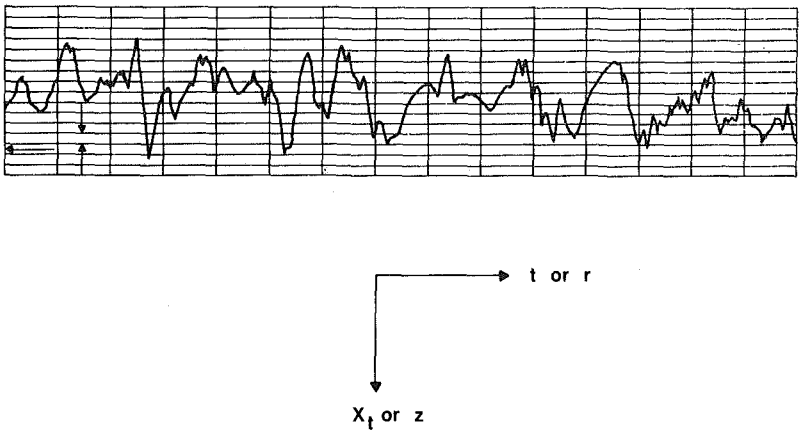

Fig. 1 A typical EDMed surface profile

electro-discharge machined surface seems to be a suitable source of data that "truly" reflects the mechanism of the process. The machined surface is generated by the discrete random attack of pulses of electrical energy with randomly varying intensity and spatial distribution. Each discharge creates a crater and the machined surface can be considered as a superposition of overlapping craters of randomly varying depths and positions. Thus the stochastic characteristics of the multiple erosion mechanism are preserved by the machined surface and the digitized surface profile data should very closely represent the process mechanism.

A typical surface profile of the electro-discharge machined surfaces obtained using a stylus type of profilometer is shown in Fig. 1. The amplified undulations of the stylus movement along the surface are recorded on a strip chart and a magnetic tape for further processing. The relevant cylindrical coordinate system used in the thermal analysis is also shown in Fig. 1.

The analog surface profile data recorded on a magnetic tape is conveyed through a digital analyzer (Norland 3001) to UNIVAC-1110 computer, where it is modeled by the standard DDS modeling procedure. The resulting Data Dependent Systems (DDS) model in the form of a stochastic difference and differential equation is given by [16]

$$X_t - \phi X_{t-1} = a_t \tag{1}$$

and

$$\frac{dX(t)}{dt} + \alpha_0 \mathrm{X(t)} = \mathrm{Z(t)} \tag{2}$$

where, for these discrete and continuous representations, respectively, X_t and $X(t)$ are the height of the surface profile at a distance t, ϕ, and α_0 are autoregressive parameters, and a_t and $Z(t)$ denote the white noise or uncorrelated random disturbances, with the following properties

$$E(a_t) = 0 \text{ and } E[Z(t)] = 0,$$

$$E[a_t a_{t-k}] = \delta_k \sigma^2{}_a \text{ and } E[Z(t)\,Z(t-u)] = \sigma^2{}_z \delta(u)$$

δ_k and $\delta(u)$ are Kronecker and Dirac delta functions, respectively; $\sigma^2{}_a$ represents the variance of a_t, whereas $Z(t)$ has a convariance function in the form of an impulse of strength $\sigma^2{}_z$. The estimation procedure for obtaining the

Nomenclature

a = heat source radius
a_t = uncorrelated random disturbances (discrete white noise)
A_i = constants in exponential approximation
c = specific heat
$erfc$ = complimentary error function
$ierfc$ = first integral of complimentary error function
J_0 = Bessel function of first kind, order zero
J_1 = Bessel function of first kind, order one
k = thermal conductivity
K = nondimensional constant for a given material and set of machining parameters
p_i = slopes (for $i = 1,2,3, \ldots$)
q = heat flux per unit area per unit time
Q = heat supply
r = radial coordinate
$\bar{r}$ = nondimensional radial coordinate, equal to r/a
$\bar{r}_m$ = nondimensional melting radius at the surface of the electrode
$\bar{r}'_m$ = first derivative of $\bar{r}_m$ with respect to nondimensional time
t = distance reference
T = temperature
T_m = melting temperature
T_∞ = ambient temperature
x = space coordinate
X_t = height of the surface profile at any distance, t (a discrete representation)
$X(t)$ = height of the surface profile at any distance, t (a continuous representation)
z = distance under electrode surface
$\bar{z}$ = nondimensional distance under electrode surface, equal to z/a
$\bar{z}_m$ = nondimensional melt depth
$Z(t)$ = white noise process (continuous)
α = thermal diffusivity
α_0 = autoregressive parameter of the continuous first-order DDS model
ψ = polar coordinate
ϕ = autoregressive parameter of the discrete first-order DDS model
λ = eigenvalue
ν = nondimensional time $= \dfrac{2\sqrt{\alpha\tau}}{a}$
ρ = density
θ = nondimensional temperature $\dfrac{T - T_\infty}{T_m - T_\infty}$
σ_a^2 = variance of a_t in the discrete model
σ_z^2 = strength of the impulse in the covariance function of white noise $Z(t)$
τ = time
δ_k = Kronecker delta
$\delta(u)$ = Dirac delta

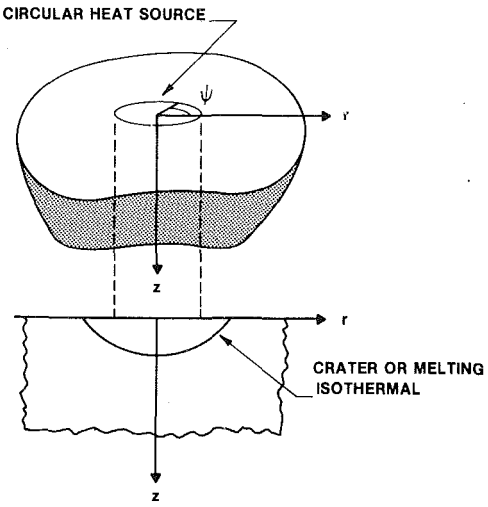

Fig. 2 Circular heat source on a semi-infinite solid and melting isothermal

values of parameters ϕ, $\sigma^2{}_a$, α_0, and σ_z^2 is given in [16, 18]. Although statistically a higher-order DDS model is adequate for EDM surface profile data, the mathematically simple first-order model has been found to provide sufficiently good approximation for the physical analysis of the process.

An important physical interpretation of the first-order stochastic differential equation is given by the corresponding impulse response or Green's function. The Green's function for this first-order model is given by [12]

$$G(t)=e^{-\alpha_0 t}$$

and the following particular integral then alternatively represents the first-order model

$$X(t)=\int_0^\infty G(u)Z(t-u)\,du=\int_0^\infty e^{-\alpha_0 u}Z(t-u)\,du$$

Therefore, the profile $X(t)$ is a convolution of $G(t)$ with $Z(t)$, i.e., the surface profile shown in Fig. 1 can be considered to be the result of the superposition of exponential impulse responses of random heights. The generation of such a profile is illustrated in [19].

The characterization of the first-order DDS model (empirical) by the impulse response function, or Green's function, is physically meaningful as the EDM surface is indeed generated by a series of impulses in the form of erosive discharges. Therefore, the exponential shape of the Green's function can be considered to be representing a half-section of a "characteristic crater" in two dimensions. The three-dimensional crater shape can be obtained by rotating the exponential around a suitable vertical axis, as the EDM surface is known to be isotropic. The EDM surface can be considered as a superposition of such occasionally overlapping craters with randomly varying depths and spatial distributions. Following the assumption that the crater shape is given by the melting isothermal [7-11], it can be assumed that the characteristic error crater defines the melting isothermal curve.

2 Development of Transient Temperature Distribution

The simplest temperature distribution in the case of single discharge EDM can be assumed to be the result of the heat conduction in a semi-infinite solid [9]. Therefore the present attempt of developing a temperature distribution from crater shape is concentrated on this type of heat transfer. The results in [7, 9] clearly indicate that melting isothermals are not hemispherical as has been assumed previously [5, 8, 10].

To check whether the isothermals obtained for theoretically derived thermal models reported in [7, 9] can be approximated by a sum of exponentials, an iterative technique of exponential fitting using integral equations [20, 21] was employed. It was found that the isothermal curves obtained for the thermal models for a circular heat source, on (*i*) a semi-infinite solid, (*ii*) a semi-infinite cylinder, and (*iii*) on a finite cylinder [9, 22], can be appproximated by an exponential function

$$y=A_1e^{p_1x}+A_2e^{p_2x}+A_3e^{p_3x}+\ \ldots \tag{3}$$

where $A_1, A_2, \ldots$ are constants, and $p_1, p_2, \ldots$ are the corresponding slopes. The constants $A_2, A_3 \ldots$ were found to be very small compared to A_1 and therefore these isothermals can be represented by

$$y=A_1e^{p_1x} \tag{4}$$

The error introduced in the volume of a single discharge crater by such an approximation varied between 2.6 to 5.8 percent. This error is negligible compared to the large differences between experimental and theoretical results found in the literature and considering the difficulties and computer time spent in either inverting the thermal distribution expression to get the isothermal curve equation or the iterations to get the isothermal values. As the thermal modeling for a regular EDM (i.e., multiple discharge phenomena) has not been reported in the literature (and seems to be almost impossible with the conventional approach because of the complexity of the phenomena), the comparison has been made with the isothermals obtained for a single discharge phenomena, as a first approximation. The present development of a physically meaningful thermal model is centered around the integration of the characteristic crater shape with the existing physico-mathematical analysis of the EDM process.

A realistc temperature distribution for multiple discharge EDM should result in a melting isothermal curve defined by an equation of the characteristic crater curve, and should satisfy the most realistic boundary conditions. It is to be noted that in the present case, a geometrical impression (characteristic crater shape) is known, and machining parameters and material properties have to be introduced in such a way that the development closely adheres to the physics and mathematics without losing the practical usefulness of the outcome. Instead of guessing a form of the thermal distribution, the well-known solution by Oosterkamp [23] for a circular heat source on a semi-infinite solid is used as a starting point. Of the thermal models developed for EDM process, the simplest temperature distribution for a single discharge can be obtained considering the heat transfer due to a circular heat source on a semi-infinite medium (Fig. 2).

It is important to note the correspondence between Figs. 1 and 2. The melting isothermal in Fig. 2 represents the boundary and shape of a single melting crater under ideal conditions of conduction, whereas a series of such craters superimposed randomly after ejection and resolidification of molten metal eventually yield the profile shown in Fig. 1. Therefore, the vertical coordinate, X_t, of Fig. 1 used in the DDS modeling is the same as z-coordinate of Fig. 2. The space coordinate, t, of Fig. 1 in DDS modeling corresponds to the space coordinate (radial), r, in Fig. 2.

For the heat supply at the rate, q, per unit time per unit area for $\tau > 0$ over the circle of radius, a, at $z = 0$, the temperature at the point (r, ψ, z) has been obtained by Oosterkamp, using the heat conduction equation

$$\frac{\partial^2 T}{\partial z^2}+\frac{1}{r}\frac{\partial}{\partial r}\left(r\frac{\partial T}{\partial r}\right)=\frac{1}{\alpha}\frac{\partial T}{\partial \tau} \tag{5a}$$

with initial and boundary conditions as

$$T(r,z,0)=0 \tag{5b}$$

and

$$T(0,z,\tau)=\text{Finite} \tag{5c}$$

$$T(\infty,z,\tau)=0 \tag{5d}$$

$$T(r,\infty,\tau)=0 \tag{5e}$$

$$k\frac{\partial T(r,0,\tau)}{\partial z}=0 \text{ for } r>a$$

$$=-q \text{ for } r\le a \tag{5f}$$

The temperature distribution for the problem described by equations (5a-5e) is given by

$$T(r,z,\tau)=\frac{aq}{2k}\int_0^\infty J_0(\lambda r)\,J_1(\lambda a)\left\{e^{-\lambda z}\,erfc\left[\frac{z}{2\sqrt{\alpha\tau}}-\lambda\sqrt{\alpha\tau}\right]-e^{\lambda z}\,erfc\left[\frac{z}{2\sqrt{\alpha\tau}}+\lambda\sqrt{\alpha\tau}\right]\right\}\frac{d\lambda}{\lambda} \tag{6}$$

However, the boundary condition (5f) is too restrictive for the actual EDM process. The extent of the plasma channel (heat source) is not completely known, but still this temperature distribution can be assumed to be practically valid near $r = 0$, which is away from the boundary of the plasma channel.

The transient temperature distribution along $r = 0$ axis in the median plane is given by

$$T(0,z,\tau)=\frac{2q\sqrt{\alpha\tau}}{k}\left\{ierfc\,\frac{z}{2\sqrt{\alpha\tau}}-ierfc\,\frac{\sqrt{z^2+a^2}}{2\sqrt{\alpha\tau}}\right\} \tag{7}$$

which, in the nondimensionalized form, can be written as

$$\theta(0,\bar{z},\nu)=\frac{4Q}{\theta_m\,\pi c\rho a^3}\,\frac{1}{\nu}\left[ierfc\left(\frac{\bar{z}}{\nu}\right)-ierfc\left(\frac{\sqrt{\bar{z}^2+1}}{\nu}\right)\right] \tag{8}$$

The nondimensional parameters in the above equation are

$$\bar{z}=z/a,\ \bar{r}=r/z,\ \nu=\frac{2\sqrt{\alpha\tau}}{a} \text{ and } \theta=\frac{T-T_\infty}{T_m-T_\infty}$$

where a is the heat source radius, α is the thermal diffusivity, T_m and T_∞ are melting and ambient temperatures. Similarly θ_m and Q are given by

$$\theta_m=T_m-T_\infty,$$

$$Q=(q)\,(\pi a^2)(\tau)$$

where q is the supply of heat per unit time per unit area. The repeated integral of the complimentary error function is denoted by *ierfc*.

Similarly, the nondimensionalized form of the characteristic crater shape which represents the melting isothermal (Appendix) is

$$\bar{z}=\bar{z}_m[1-e^{-4.5(1-\bar{r}/\bar{r}_m)}] \tag{9}$$

where $\bar{z}_m = z_m/a$, z_m, being the depth at $r=0$ on a melting isothermal, and $\bar{r}_m = r_m/a$, r_m, being the radius of the crater along the melting isothermal on the surface, $z=0$.

The machining parameters, material properties, and time dimension can be added to equation (9) by substituting $\bar{z}_m$, the melt depth, from equation (8). However equation (8) cannot be explicitly solved for $\bar{z}_m$. Hence, using the power series expansion of $ierfc(u)$, equation (8) can be approximated [24] as

$$\theta(0,\bar{z},\nu)=\frac{4Q}{\pi c\rho a^3\theta_m}\,\frac{1}{\nu}\left[\left(\frac{1}{\nu}-\frac{1}{\nu^2\sqrt{\pi}}+\frac{1}{6\nu^4\sqrt{\pi}}\right)-\frac{\bar{z}}{\nu}\right] \tag{10}$$

neglecting higher-order terms such as $(\bar{z}/\nu)^2$, $(\bar{z}/\nu)^4$, and $1/\nu^6$, $1/\nu^8$, etc.

The error introduced by such an approximation lies between 4 to 10 percent melting temperature for various values of $\bar{z}$ (<1) and ν (≥ 1). The approximation seems to be valid, at least practically, even when ν is less than 1, but not for ν less than 0.5.

The approximate expression given by equation (10) is practically valid since $\bar{z}$ is usually less than 1 for the practical domain of EDM, and in case of rough machining, ν is greater than 1. Also the variation of θ with $\bar{z}$ is almost linear in various thermal models proposed for EDM.

The above expression can be rewritten as

$$\theta(0,\bar{z},\nu)=\frac{K}{\nu^2}\left[\left(1-\frac{1}{\nu\sqrt{\pi}}+\frac{1}{6\nu^3\sqrt{\pi}}\right)-\bar{z}\right] \tag{11}$$

where

$$K=\frac{4Q}{\pi c\rho a^3\,\theta_m}=\frac{4q\tau}{c\rho a\theta_m}$$

Now, for $T = T_m$, $\theta = 1$ and $\bar{z} = \bar{z}_m$, equation (11) becomes

$$1=\frac{K}{\nu^2}\left[\left(1-\frac{1}{\nu\sqrt{\pi}}+\frac{1}{6\nu^3\sqrt{\pi}}\right)-\bar{z}_m\right]$$

which gives

$$\bar{z}_m=\left(1-\frac{1}{\nu\sqrt{\pi}}+\frac{1}{6\nu^3\sqrt{\pi}}\right)-\frac{\nu^2}{K} \tag{12}$$

Substituting $\bar{z}_m$ from (12) in (9)

$$\bar{z}=\left[\left(1-\frac{1}{\nu\sqrt{\pi}}+\frac{1}{6\nu^3\sqrt{\pi}}\right)-\frac{\nu^2}{K}\right][1-e^{-4.5(1-\bar{r}/\bar{r}_m)}] \tag{13}$$

Now, if the temperature distribution can be expressed as the product of two solutions in the following manner

$$\theta(\bar{r},\bar{z},\nu)=F(\bar{z},\nu)\;G(\bar{r},\nu)$$

where

$$F(\bar{z},\nu)=\left[\left(1-\frac{1}{\nu\sqrt{\pi}}+\frac{1}{6\nu^3\sqrt{\pi}}\right)-\bar{z}\right]\frac{K}{\nu^2}$$

then

$$\bar{z}=\left(-\frac{1}{\nu\sqrt{\pi}}+\frac{1}{6\nu^3\sqrt{\pi}}\right)-\frac{\nu^2}{K}\,\frac{\theta(\bar{r},\bar{z},\nu)}{G(\bar{r},\nu)}$$

Along the melting isothermal, then

$$\bar{z}=\left(1-\frac{1}{\nu\sqrt{\pi}}+\frac{1}{6\nu^3\sqrt{\pi}}\right)-\frac{\nu^2}{K}[G(\bar{r},\nu)]^{-1} \tag{14}$$

Equating (13) and (14) gives

$$\left(1-\frac{1}{\nu\sqrt{\pi}}+\frac{1}{6\nu^3\sqrt{\pi}}\right)-\frac{\nu^2}{K}G(\bar{r},\nu)^{-1}$$

$$=\left[\left(1-\frac{1}{\nu\sqrt{\pi}}+\frac{1}{6\nu^3\sqrt{\pi}}\right)-\frac{\nu^2}{K}\right][1-e^{-4.5(1-\bar{r}/\bar{r}_m)}]$$

Rearranging yields

$$G(\bar{r},\nu)=1\Big/\left[1+\left\{\left(1-\frac{1}{\nu\sqrt{\pi}}+\frac{1}{6\nu^3\sqrt{\pi}}\right)\frac{K}{\nu^2}-1\right\}e^{-4.5(1-\bar{r}/\bar{r}_m)}\right] \tag{15}$$

Although equation (15) has been obtained along the melting isothermal, it will be assumed that it is valid in the region of melting, and therefore can be used in the product form of temperature distribution. It is evident from the isothermal curves of various EDM thermal models [9, 22], that the shape of isothermals in the region of melting temperature is similar to that of melting isothermal. The shapes of isothermal curve near the heat source and far away from the melting region are certainly different. But we are mainly concerned with the region of melting that is the practical domain of EDM. Moreover, the metallographic studies of EMDed surface

clearly indicate that the recast layer (or solidified layer) has a contour similar to that of the melting front.

Therefore, the temperature distribution can be written as

$$\theta(\bar{r},\bar{z},\nu) = \frac{\frac{K}{\nu^2}\left[\left(1-\frac{1}{\nu\sqrt{\pi}}+\frac{1}{6\nu^3\sqrt{\pi}}-\bar{z}\right]\right.}{\left[1+\left\{\left(1-\frac{1}{\nu\sqrt{\pi}}+\frac{1}{6\nu^3\sqrt{\pi}}\right)\frac{K}{\nu^2}-1\right\}e^{-4.5(1-\bar{r}/\bar{r}_m)}\right]}$$

or

$$\theta(\bar{r},\bar{r},\nu) = \frac{\frac{K}{\nu^2}\left[\frac{\nu^2}{K\beta}-\bar{z}\right]}{\left[1+\left(\frac{1}{\beta}-1\right)e^{-4.5(1-\bar{r}/\bar{r}_m)}\right]} \tag{16}$$

where

$$\beta = \frac{\nu^2}{K\left(1-\frac{1}{\nu\sqrt{\pi}}+\frac{1}{6\nu^3\sqrt{\pi}}\right)} = \frac{\nu^5}{K\left(\nu^3-\frac{\nu^2}{\sqrt{\pi}}+\frac{1}{6\sqrt{\pi}}\right)}$$

Now, as the two non-dimensionalized parameters ν and K cover all the possible input variables (i.e., material properties and machining parameters), the most general form of the radius, $\bar{r}_m$, at the surface for melting isothermal can be given by a function of ν and K. It is to be noted that $\bar{r}_m$ in equation (9) is implicitly assumed to be a function of ν and K, as the characteristic crater has been obtained for a given material and machining parameters.

Assuming that the thermal distribution of equation (16) is valid in the region of melting point, an expression for $\bar{r}_m$ can be obtained by substituting proper derivatives of equation (16) in equation (17) which is the nondimenionalized form of heat equation (5)

$$\frac{\partial^2\theta}{\partial z^2}+\frac{1}{\bar{r}}\frac{\partial}{\partial\bar{r}}\left(\bar{r}\frac{\partial\theta}{\partial r}\right)=\frac{2}{\nu}\frac{\partial\theta}{\partial\nu} \tag{17}$$

Therefore

$$\frac{\frac{K}{\nu^2}\left(\frac{\nu^2}{K\beta}-1\right)\left(1-\frac{1}{\beta}\right)\left(\frac{4.5}{\bar{r}_m(\nu,K)}\right)}{\left[1+\left(\frac{1}{\beta}-1\right)e^{-4.5\left(1-\frac{r}{\bar{r}_m(\nu,K)}\right)}\right]^2}\left\{\frac{4.5}{\bar{r}_m(\nu,K)}e^{-4.5\left(1-\frac{\bar{r}}{\bar{r}_m(\nu,K)}\right)}+\frac{(4.5)}{r_m(\nu,K)}\frac{(-2)\left(\frac{1}{\beta}-1\right)e^{-4.5\left(1-\frac{r}{\bar{r}_m(\nu,K)}\right)}}{\left[1+\left(\frac{1}{\beta}-1\right)e^{-4.5\left(1-\frac{\bar{r}}{\bar{r}_m(\nu,K)}\right)}\right]}\right\}$$

$$+\frac{\frac{4.5K}{\bar{r}_m(\nu,K)\bar{r}\nu^2}\left(\frac{\nu^2}{K\beta}-\bar{z}\right)(-1)\left(\frac{1}{\beta}-1\right)e^{-4.5\left(1-\frac{r}{\bar{r}_m(\nu,K)}\right)}}{\left[1+\left(\frac{1}{\beta}-1\right)e^{-4.5\left(1-\frac{r}{\bar{r}_m(\nu,K)}\right)}\right]^2}=\frac{\frac{2K}{\nu}\left(\frac{-\beta'}{K\beta^2}+\frac{2\bar{z}}{\nu^3}\right.}{\left[1+\left(\frac{1}{\beta}-1\right)e^{-4.5\left(1-\frac{r}{\bar{r}_m(\nu,K)}\right)}\right]}$$

$$+\frac{\frac{2K}{\nu}\left(\frac{1}{\beta K}-\frac{z}{\nu^2}\right)(-1)\left[\left(\frac{1}{\beta}-1\right)4.5\bar{r}\left\{\frac{-\bar{r}'_m(\nu,K)}{\bar{r}_m{}^2(\nu,K)}\right\}+\left(\frac{-\beta'}{\beta^2}\right)e^{-4.5\left(1-\frac{r}{\bar{r}_m(\nu,K)}\right)}\right]}{\left[1+\left(\frac{1}{\beta}-1\right)e^{-4.5\left(1-\frac{\bar{r}}{\bar{r}_m(\nu,K)}\right)}\right]^2} \tag{18}$$

were β' and $\bar{r}'_m(\nu,K)$ are the first derivatives with respect to ν of β and $\bar{r}_m(\nu,K)$, respectively. Along the melting isothermal on the surface, i.e., at $z = 0$, $r = \bar{r}_m$; therefore, equation (18) reduces to

$$\frac{4.5}{\bar{r}_m{}^2}(\beta-1)+\frac{20.25}{\bar{r}_m{}^2}(\beta-1)(2\beta-1)=\frac{9}{\nu}\frac{\bar{r}'_m}{\bar{r}_m}(1-\beta)$$

or

$$\bar{r}_m\bar{r}'_m+(4.5\beta-1.75)\nu=0 \tag{19}$$

Equation (19) is a nonlinear differential equation of the form of Bernoulli equation, which can be solved by the substitution procedure. However, the following direct approach yields $\bar{r}_m$ as a function of ν.

Equation (19) can be written as

$$\frac{1}{2}\frac{d}{d\nu}(\bar{r}^2{}_m)=1.75\nu-4.5\beta\nu \tag{20}$$

Integrating (20) with respect to ν

$$\frac{1}{2}\bar{r}_m{}^2=1.75\int_0^\nu\nu d\nu-4.5\int_0^\nu\beta\nu d\nu$$

or

$$\bar{r}_m{}^2=1.75\nu^2-9\int_0^\nu\beta\nu d\nu \tag{21}$$

$$\bar{r}_m{}^2=1.75\nu^2-\frac{9}{K}\int_0^\nu\frac{\nu^6}{\left(\nu^3-\frac{\nu^2}{\sqrt{\pi}}+\frac{1}{6\sqrt{\pi}}\right)}d\nu \tag{22}$$

Equation (22) satisfies the initial condition that $\bar{r}_m$ at $\nu = 0$ is zero, since the integrand approaches zero as $\nu\to 0$. Equation (22) can be solved by numerical integration. However, for a closed form solution, an approximation (for $\nu>1$) can be made by writing the integrand as

$$\left[\nu^3+c_1\nu^2+c_1{}^2\nu+(c_1^3-c_2)+\left(\frac{c_1^4-2c_1c_2}{\nu}\right)+\left(\frac{c_1^5-3c_1c_2}{\nu^2}\right)\right.$$
$$\left.+\left(\frac{c_1^6-3c_1^2c_2+c_2^2-3c_1^3c_2}{\nu^3}\right)+\ldots+\ldots\right]$$

where $c_1=\frac{1}{\sqrt{\pi}}$ and $c_2=\frac{1}{6\sqrt{\pi}}$

Therefore, equation (22) becomes

$$\bar{r}_m{}^2=1.75\nu^2-\frac{9}{K}\left[\frac{\nu^4}{4}+c_1\frac{\nu^3}{3}+c_1^2\frac{\nu^2}{2}+(c_1^3-c_2)\nu\right.$$

Table 1 Predicted and experimentally measured crater volume

Material	Pulse duration μs	Melted volume per discharge $\times 10^6 \mu m^3$	Eroded volume per discharge $\times 10^6 \mu m^3$ Predicted	Eroded volume per discharge $\times 10^6 \mu m^3$ Measured	Diameter to depth ratio
AISI 1020	200	0.338	0.203	0.218	5.3
	500	1.045	0.627	0.628	6.8
	1000	2.238	1.343	0.935	8.5
	1200	2.845	1.707	1.954	9.2
	1500	3.662	2.197	1.872	10.1
AISI 1045	100	0.121	0.072	0.073	4.2
	200	0.283	0.170	0.189	5.1
	500	0.882	0.529	0.312	6.5
	1000	1.984	1.190	1.085	8.2

Table 2 Physical and thermal properties of materials investigated

Material	Specific gravity ρ Kg/m^3	Specific heat C J/Kg°C	Thermal conductivity K J/m°Cs	Diffusivity α 10^{-6}m^2/s	Melting point °C
AISI 1020	7870	874.87	28.46	4.132	1510
AISI 1045	7860	950.22	26.75	3.58	1510

$$-c_1^4-2c_1c_2)ln\nu-\left(\frac{c_1^5-3c_1c_2}{\nu}\right)$$

$$-\frac{1}{2}\left(\frac{c_1^6+c_2^2-3c_1^2c_2-3c_1^3c_2}{\nu^2}\right)+\ldots\Bigg] \tag{23}$$

for values of $\nu>1$, i.e., rough machining conditions in the EDM.

For small values of ν, i.e., $\nu<1$, (i.e., for finish machining conditions), Taylor series expansion can be used to get

$$\bar{r}_m=\sqrt{1.75\nu}-\frac{(108)(120)}{7!}\sqrt{\frac{\pi}{1.75}}\frac{\nu^6}{K}-\frac{(972)(2400)}{9!}\sqrt{\frac{\pi}{1.75}}\frac{\nu^8}{K}$$

$$+\frac{(189)(720)}{10!}\sqrt{\frac{\pi}{1.75}}\frac{\nu^9}{K}-\ldots\ldots \tag{24}$$

Equation (24) clearly satisfies the initial condition $\bar{r}_m(0)=0$. Equations (16), (23), and (24) specify the desired temperature distribution.

It should be noted that the expressions for temperature distribution, melt depth, and melt radius have been developed under much less restrictive assumptions. Basically the assumptions can be summarized as:

1 The heat conduction equation is approximately satisfied at $r=0$ to give linear variation of θ with z.

2 The melting isothermal is given by equation (9).

3 The heat conduction partial differential equation is satisfied at the surface along melting isothermal, i.e., for $z=0, r=r_m$.

3 Experimental Verification and Discussion

To verify the theoretical results of metal removal rate, experiments were carried out using an Electro-Discharge Machine (Cincinnati Milacron's Little Scotsman) having a solid-state power supply (80–300 V, 40 A). The specimens of AISI 1020 and AISI 1045 were machined using a cylindrical tool electrode (25 mm dia) of electrolytic copper. The pressure fed dielectric flow was maintained at 100 × 10^3 pascal through the tool centerhole of 4.5 mm. Pulse durations in the range of 50 to 1000 s were used with a duty factor of 50 percent for the power settings of 60–80 V and 10 A. After machining, the workpieces were ultrasonically cleaned and using a stylus instrument "Surfcom-3B" of DEM Equipment Co., the surface profiles were recorded on the paper as well as on an FM tape recorder. The signal from the tape recorder was transferred to a digital analyzer Norland 3001 where it was digitized. This digitized data was then conveyed to UNIVAC-1110 computer for modeling by the standard Data Dependent Systems modeling program. The metal removal rate values were calculated by determining the weight loss of specimens using an analytical scale 'Mettler H80'.

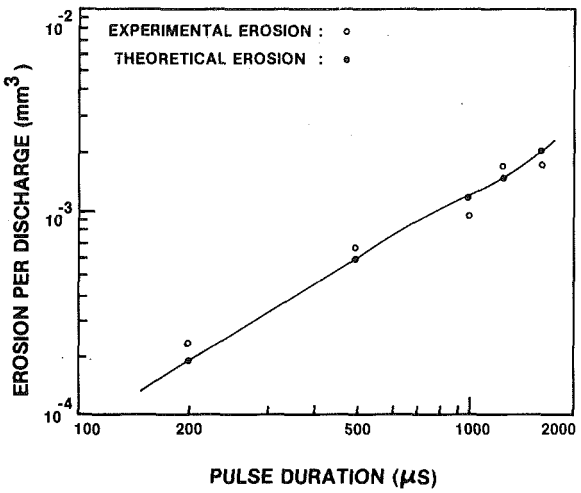

Fig. 3 Comparison between theoretical and experimental results (AISI 1020)

The values of the theoretically calculated melted volume, the experimentally measured erosion volume, and the theoretical diameter to depth ratio of the melting crater are given in Table 1. To account for the phase change in the calculations, thermophysical properties were modified. These modified properties are given in Table 2. The heat source radius is assumed to be 50 μm [22].

As can be seen from Table 1, the agreement between calculated melted volume and experimental erosion values is fairly good. The difference between calculated and experimental values ranges from 1.5 to 2.4 times as compared to about 20 times under similar conditions reported in [8, 22].

It is well known that material removed in a single discharge is more than the removal obtained from the actual machining or multiple discharge measurements [5, 8]. The reasons for such a difference are said to be numerous factors which individually and in combination contribute to make actual machining a random phenomenon. The random physical conditions of the working zone impose irregularity on the electrical parameters of the erosive impulses. Hence, all the erosive discharges do not remove the same amount of metal as removed by a single discharge under a configuration with smooth electrode surfaces and uniform dielectric fluid. However, the present estimation which takes into account this randomness via the characteristic crater, results in a close agreement.

Even for a single discharge, the difference between melted volume and the actually removed volume is attributed to metal ejection and resolidification mechanism occurring after the completion of the discharge. It is believed that the forces of various origin including electrostatic, electromagnetic, and hydrodynamic, are involved in the metal ejection process, and a thorough study is yet to be conducted to identify and evaluate the effect of these forces. The results of a single discharge experiment with Fe in [25] indicate that the measured volume is approximately 60 percent of the melted

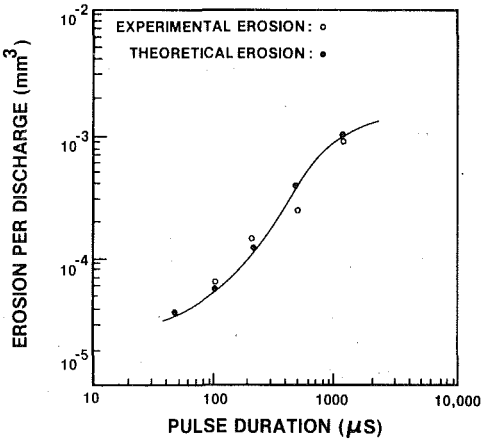

Fig. 4 Comparison between theoretical and experimental results (AISI 1045)

volume, and this ratio has been shown to be fairly constant over the practical domain of EDM. This ratio of the eroded volume to the melted volume has been defined as the net metal removal efficiency. Taking the net metal removal efficiency of 60 percent for Fe, the predicted volume is, therefore, calculated and is given in Table 1, along with the measured volume. These values are also plotted in Figs. 3 and 4. It can be seen that the predicted erosion volume agrees very well with the measured volume for AISI 1020 and AISI 1045.

The agreement between experimental and theoretical values can be improved if the precise nature and magnitude of ejection forces is known. Moreover for a complete thermal analysis of EDM, evaporation, and radiation modes of heat transfer should also be taken into consideration. The treatment presented here has the potential of incorporating the influence of other EDM parameters, such as dielectric flowrate, tool geometry, gap voltage, etc. These factors will mainly affect the values of the parameters of the DDS (empirical) model.

However, in spite of the uncertainties associated with the lack of full understanding of the physics of the process, the present (hybrid) model estimates values quite close to actual machining results. The merits of this model can be summarized as follows:

1 The first thermal model takes into account the randomness involved in the actual machining process.

2 It is based on relatively simple mathematics encountered in heat transfer problems.

3 It is in a closed form which can be handled with a greater amount of mathematical ease than other models which usually involve series functions (complimentary error function and Bessel function and their products) or equations which need to be solved by finite difference approach.

4 It is easier to use in determining thermal stresses and residual stresses.

5 It predicts more accurate results for actual machining conditions.

4 Conclusions

The approach presented in this paper, i.e., developing a meaningful physical representation of a complex and random process by the integration of Data Dependent Systems model with the laws of physics, can be applied to many other similar engineering and scientific situations. The plasma heat transfer in reentry problem, arc technology, transient heat conduction involving random initial and boundary conditions, cathode spots, and traditional and nontraditional machining processes (such as grinding and electro-chemical machining) are some of the areas for the application of the present approach.

To conclude, the Data Dependent Systems (DDS) approach in capturing the randomness involved in Electro-Discharge Machining (EDM) is outlined along with the development of a transient temperature distribution (a hybrid model) based on the DDS model (empirical). The main features of the development are:

1 Electro-Discharge Machined surface profiles obtained under actual machining conditions are modeled by Data Dependent Systems methodology in the form of a first-order stochastic differential equation. The impulse response function of such a model (empirical) gives the shape and geometry of a characteristic crater which is identified with the melting isothermal.

2 Using the assumptions of a circular heat source on a surface of a semi-infinite solid with constant heat flux and constant thermal properties, a mathematically simple transient temperature distribution has been developed. The temperature distribution development takes into account the exponential shape of melting isothermal, i.e., that of the characteristic crater.

3 It is shown that the calculated values of various technological parameters such as metal removal per discharge from such a model (hybrid) correspond well with those obtained from experiments conducted under actual machining conditions.

4 The possibility of the application of DDS approach in other fields of engineering as well as science is discussed.

Acknowledgment

Reviewers' help in substantially improving the manuscript is gratefully acknowledged. This research was supported by the National Science Foundation under Grant No. DAR-7917999.

References

1 Franklin, R. N., *Plasma Phenomena in Gas Discharges*, Clarendon, 1976.

2 Chadband, W. G , Coelho, R., and Debeau, J., "Electrical Discharges in Liquid Dielectrics," *Journal of Physics D: Applied Physics*, Vol. 4, 1971, pp. 539-540.

3 Llewellyn, J. P.., "Electro Erosion by Spark Discharges," *British Journal of Applied Physics*, Vol. 1, No. 3, 1950, pp. 60-65.

4 Hockenberry, T. O., and Williams, E. M., "Dynamic Evolution of Events Accompanying the Low-Voltage Discharges Employed in EDM," *IEEE Transactions on Industry and General Applications*, Vol. IGA-3, No. 4, 1967, pp. 302-309.

5 Mironoff, N., *Introduction to the Study of Spark Erosion*, Microtechnic-Scriptar, 1970, pp. 19-33.

6 Cooke, R. F., and Crookall, J. R., "An Investigation of Some Statistical Aspects of Electro-Discharge Machining," *International Journal of Machine Tool Design Research*, Vol. 13, 1973, pp. 271-286.

7 Snoeys, R., and Van Dijck, F., "Physico-Mathematical Analysis of the EDM Process," *Proceedings of the North American Metal Working Research Conference*, Vol. I, 1973, pp. 181-200.

8 König, W., Wertheim, R., Zvirin, Y., and Toren, M., "Material Removal and Energy Distribution in Electrical Discharge Machining," *Annals of the CIRP*, Vol. 24/1, 1975, pp. 95-100.

9 Marty, C. C., "Investigation of Surface Temperature in Electro-Discharge Machining," ASME *Journal of Engineering for Industry*, Vol. 99B, 1977, pp. 682-684.

10 Toren, M., Zvirin, Y., and Winograd, Y., "'Melting and Evaporation Phenomena During Electrical Erosion," ASME JOURNAL OF HEAT TRANSFER, Vol. 97, 1975, pp. 576-581.

11 Richardson, P. D., Gurland, J., and Chen, C. H., "Heat and Mass Transfer in Spark Machining," *Proceedings of the 6th International Heat Transfer Conference*, Toronto, Vol. 4, 1978, pp. 73-78.

12 Pandit, S. M., "Stochastic Linearization by Data Dependent Systems," ASME *Journal of Dynamic Systems, Measurement and Control*, Vol. 99G, 1977, pp. 221-226.

13 Pandit, S. M., "Analysis of Vibration Records by Data Dependent Systems," *Shock and Vibration Bulletin*, No. 47, pt. 4, 1977, pp. 161-174.

14 Pandit, S. M., and Revach, S., "A Data Dependent Systems Approach to Dynamics of Surface Generation in Turning," ASME *Journal of Engineering for Industry*, Vol. 103B, 1977, pp. 437-445.

15 Pandit, S. M., Suzuki, H., and Kahng, C. H., "Application of Data Dependent Systems to Diagnostic Vibration Analysis," ASME *Journal of Mechanical Design*, Vol. 102, 1980, pp. 233-241.

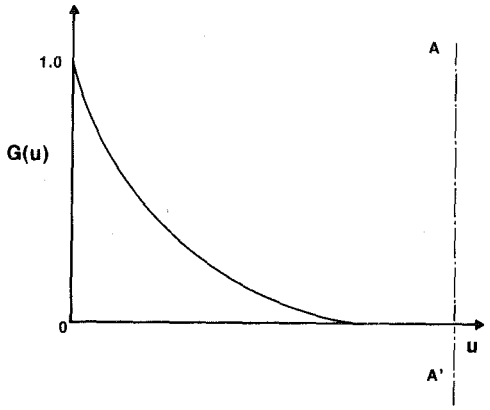

Fig. 5 Green's function

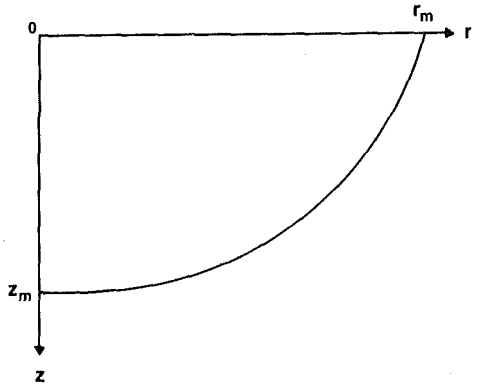

Fig. 6 A portion of the characteristic crater

16 Pandit, S. M., and Rajurkar, K. P., "Crater Geometry and Volume from Electro-Discharge Machined Surface Profiles by Data Dependent Systems," ASME *Journal of Engineering for Industry*, Vol. 102B, 1980, pp. 289-295.

17 Pandit, S. M., and Rajurkar, K. P., "Data Dependent Systems Approach to Solar Energy Simulation Inputs," *Proceedings of the ASME/SSEA Conference: Solar Engineering—1981*, pp. 389-398.

18 Pandit, S. M., and Rajurkar, K. P., "A Mathematical Model for Electro-Discharge Machined Surface Roughness," *Proceedings of the North American Metal Working Research Conference*, Vol. VI, 1978, pp. 339-345.

19 Pandit, S. M., and Rajurkar, K. P., "Data Dependent Systems Approach to EDM Process Modeling from Surface Roughness Profiles," *Annals of the CIRP*, Vol. 29, 1980, pp. 107-112.

20 Moore, E., "Exponential Fitting Using Integral Equations," *International Journal for Numerical Methods in Engineering*, Vol. 8, 1974, pp. 271-276.

21 Lal, M., and Moore, E., "An Iterative Technique for Fitting Exponentials," *International Journal for Numerical Methods in Engineering*, Vol. 10, 1976, pp. 979-990.

22 Van Dijck, F., "Physico-Mathematical Analysis of the Electro-Discharge Machining Process," Ph.D. thesis, Catholic University of Leuven, 1973.

23 Carslaw, H. S., and Jager, J. C., *Conduction of Heat in Solids*, 2d ed., Oxford, 1959.

24 *Handbook of Mathematical Functions*, ed. M. Abramowitz, and I. A. Stegun, Dover Publications, 1972, pp. 295-329.

25 Guerrero-Alavarez, J. L., "Experimental and Theoretical Study of Electro-Erosion of Metals," Ph.D. thesis, University of Illinois, Urbana, 1972.

APPENDIX

Nondimensionalized Characteristic Crater Equation

The impulse response function or the Green's function for first-order DDS model (empirical), is given by

$$G(u) = e^{-\alpha_0 u}$$

Since the exponential does not mathematically become zero until infinity, it is necessary to select some finite large value of its argument to represent the bottom of the crater. Usually, four time constants are taken for dropping the response to 2 percent of its initial value. By selecting 4.5 time constants, the response reduces to 1 percent its initial value (actually $e^{-4.5} = 0.0111089$). Moreover, the cut off at $4.5/\alpha_0$ not only leads to better predictions of erosion volume, but also has been shown to approximate more closely with the commonly assumed spherical shape of a crater [16]. Therefore, the rotation of this exponential about the axis AA′ in Fig. 5 gives the three-dimensional crater shape. The depth of this crater is nearly 1 and the diameter at the top is $9/\alpha_0$.

The parameter σ_z^2 of the DDS model (empirical), representing the intensity of white noise as a measure of random discharge phenomenon in an actual EDM process, has been taken as the depth of the characteristic crater. Usually the depth of the crater has been taken as the measure of the discharge energy [5]. This hypothesis was tested with experimental work of other investigators under similar conditions and was found to give fairly good agreement [16, 18].

The equation of the characteristic crater curve of unit depth shown in Fig. 6 can be obtained as

$$1 - z = e^{\alpha_0\left(r - \frac{4.5}{\alpha_0}\right)}$$

Following the assumption made in [7-9] that the crater shape is the same as that of the melting isothermal, the melting depth corresponding to any r along the melting isothermal is given by

$$z = \sigma_z^2\left\{1 - e^{\alpha_0\left(\frac{r}{\sigma_z^2} - \frac{4.5}{\alpha_0}\right)}\right\} \tag{A1}$$

but as $z_m = \sigma_z^2 = \dfrac{r_m \alpha_0}{4.5}$ equation (A1) becomes

$$z = z_m\left\{1 - e^{-4.5\left(1 - \frac{r}{r_m}\right)}\right\} \tag{A2}$$

which in the nondimensionalized form can be written as

$$\bar{z} = \bar{z}_m\left\{1 - e^{-4.5(1 - \bar{r}/\bar{r}_m)}\right\} \tag{A3}$$

Transient Response of Gas-to-Gas Crossflow Heat Exchangers With Neither Gas Mixed

F. E. Romie
Palos Verdes Estates,
Calif. 90274

The transient mixed mean temperatures of the two gases leaving a crossflow heat exchanger are found for a unit step increase in the entrance temperature of either gas. The temperature responses are given in graphical form for the range of parameters: Ntu from 1 to 8, capacity rate ratio from 0.6 to 1.67, and conductance ratio from 0.5 to 2.0. The solutions are found using the Laplace transform method and apply to single-pass crossflow exchangers with neither gas mixed.

Introduction

Knowledge of the transient behavior of the temperatures of fluids leaving heat exchangers is required for process control applications. The purpose of this paper is to present, for the gas-to-gas crossflow heat exchanger, the mixed mean exit gas temperatures that are obtained in response to a unit step change in the entrance temperatures of either gas. The solutions given are for the neither-fluid-mixed condition typical of such exchangers and are found using the Laplace transform method.

Dusinberre [1] describes a general finite difference method for computing transients in a crossflow heat exchanger and illustrates the method for a gas-to-gas heat exchanger with neither fluid mixed. Myers, Mitchell, and Norman [2] use an approximate integral technique to compute temperature responses of the fluids leaving a crossflow heat exchanger with one fluid mixed. The excitation is a unit step change of the inlet temperature of the mixed fluid. Their solution is applicable under the condition that the thermal capacity of the exchanger core is very large compared to the thermal capacities of the fluids contained in the exchanger. This condition is generally satisfied if both fluids are gases.

Yamashita, Izumi, and Yamaguchi [3] use finite difference methods to calculate the exit fluid temperature responses for crossflow heat exchangers with neither fluid mixed. The excitation is a step change in inlet temperature. They illustrate the effects of the governing parameters by varying each one with the others fixed at the same constant values. Their work is not limited to the large wall capacitance condition and the consequent large number of independent parameters serves to limit the data presented for the gas-to-gas crossflow exchanger. This paper gives the gas temperature responses for all values of the governing parameters and presents the responses in graphical form for a range of the parameters believed to cover the majority of applications.

The Differential Equations

The crossflow exchanger analyzed is described by the following idealizations:

1 No lateral mixing occurs for either fluid and no heat is transferred from one flow passage to the next containing the same fluid: neither fluid is mixed.

2 The thermal conductances, $(hA)_a$ and $(hA)_b$, are uniform and constant as are the fluid capacity rates, $(wc)_a$ and $(wc)_b$, and the thermal capacity, WC, of the exchanger core.

3 The thermal capacities of the masses of the two fluids contained (at any instant) in the exchanger are negligibly small relative to the thermal capacity, WC, of the exchanger core. (The ratios, V_a and V_b, of the contained-fluid thermal capacities to the core thermal capacity will be equated to zero.)

4 Heat is conducted in the core material only in the direction mutually perpendicular to the two fluid flow directions. The material offers no thermal resistance to conduction in this direction.

5 The exchanger shell or shroud is adiabatic and influences neither the steady state nor transient behavior of the fluid temperatures.

Three differential equations are required to describe the behavior of the exchanger. An energy balance on an element, $dydx$, of the exchanger core gives the first equation.

$$WC\frac{\partial T}{\partial t} = (hA)_a(\tau_a - T) + (hA)_b(\tau_b - T) \tag{1}$$

The remaining two equations relate the heat flow from the exchanger core element to the change in temperature of the two fluids.

$$(hA)_a(T-\tau_a) = (LA_x\rho c)_a\frac{\partial \tau_a}{\partial t} + L_a(wc)_a\frac{\partial \tau_a}{\partial x} \tag{2}$$

$$(hA)_b(T-\tau_b) = (LA_x\rho c)_b\frac{\partial \tau_b}{\partial t} + L_b(wc)_b\frac{\partial \tau_b}{\partial y} \tag{3}$$

These three equations will be written using the following dimensionless variables and parameters.

$$\theta = \frac{(hA)_a t}{WC},\quad X = N_a x/L_a,\quad Y = N_b y/L_b$$

$$R = (hA)_b/(hA)_a, V_a = \frac{(LA_x\rho c)_a}{WC}, V_b = \frac{(LA_x\rho c)_b}{WC}$$

Using these definitions permits writing the equations in the following form.

$$\frac{\partial T}{\partial \theta} + (1+R)T = \tau_a + R\tau_b \tag{4}$$

$$T - \tau_a = \frac{\partial \tau_a}{\partial x} + V_a\frac{\partial \tau_a}{\partial \theta} \tag{5}$$

$$T - \tau_b = \frac{\partial \tau_b}{\partial y} + \frac{V_b}{R}\frac{\partial \tau_b}{\partial \theta} \tag{6}$$

The capacity ratios, V_a and V_b, will be equated to zero in accordance with idealization (3). The ratios are, typically, very small if the fluids are gases, and the solutions to be obtained are therefore, in effect, restricted to gases. The smallness of the capacity ratios means, necessarily, that the gas transit or dwell times, L_a/u_a and L_b/u_b, are small compared to the duration of the transient, and in the limit,

Contributed by the Heat Transfer Division for publication in the JOURNAL OF HEAT TRANSFER. Manuscript received by the Heat Transfer Division July 18, 1972.

with $V_a = V_b = 0$, are zero. For a symmetric crossflow exchanger ($(hA)_a = (hA)_b$, $(wc)_a = (wc)_b$, $V_a = V_b$) Yamashita et al. [3] show, for Ntu = 1, that the general solution ($V \neq 0$) and the solution with $V = 0$ are in good agreement provided that $V \lesssim 0.05$.

Equations (4), (5), and (6) will be solved with the conditions that for $\theta < 0$: $T = \tau_a = \tau_b = 0$ and for $\theta > 0$: $\tau_a = 1$ at $x = 0$ and $\tau_b = 0$ at $y = 0$. The temperatures T, τ_a, and τ_b are thus the responses to a unit step change in the entrance temperature of gas "a". (The subscripts a and b always refer, respectively, to the stepped and unstepped gases.) The equations are linear, and the requirement that the responses are initially zero implies nothing about the operating conditions of the exchanger at the time of the transient.

The major steps of the solution are given in the following sections. The functions H_n, K_n, and M_o used in the equations and the relations required to proceed from one step to the next are given in the Appendix and in Table 1.

Solution of the Equations

The Laplace transforms of equations (4), (5), and (6) (with $V_a = V_b = 0$) are taken with respect to θ using s as the Laplace transform parameter. The Laplace transform of the resultant equations is then taken with respect to X using p as the Laplace parameter and the equations so-obtained are solved for the double Laplace transforms, τ_{asp} and τ_{bsp}, of τ_a and τ_b.

$$\tau_{asp} = \frac{1}{(1+p)}\left(\frac{1}{s+\frac{p}{1+p}} + \frac{1}{s\left(s+\frac{p}{1+p}\right)}\right)$$

Pg. 564

$$- \frac{e^{-Y\left(\frac{\frac{s}{R}+\frac{p}{R(1+p)}}{\frac{s}{R}+1+\frac{p}{R(1+p)}}\right)}}{R^2(1+p)^2\,\frac{s}{R}\left(\frac{s}{R}+\frac{p}{R(1+p)}\right)\left(\frac{s}{R}+1+\frac{p}{R(1+p)}\right)} \tag{7}$$

$$\tau_{bsp} = \frac{1}{(1+p)R^2\,\frac{s}{R}\left(\frac{s}{R}+\frac{p}{R(1+p)}\right)\left(1-e^{-Y\left(\frac{\frac{s}{R}+\frac{p}{R(1+p)}}{\frac{s}{R}+1+\frac{p}{R(1+p)}}\right)}\right)} \tag{8}$$

The inverse transforms with respect to s are found using standard Laplace transform tables and entries 1, 6, and 8 of Table 1.

$$\tau_{ap} = \frac{1}{p} - \frac{e^{-\frac{\theta p}{1+p}}}{p(1+p)}\,[1 - M_o(Y, R\theta)] - \frac{R(1+R)}{q(R+q)}\,e^{-\frac{Y}{(1+R)}\,\frac{q}{(R+q)}}\,M_o\left(\frac{RY}{(1+R)Q}, \theta(1+R)Q\right) \tag{9}$$

$$\tau_{bp} = \frac{1}{p} - \frac{e^{-\frac{\theta p}{1+p}}}{p}\,[1 - K_o(Y, R\theta)] - \frac{(1+R)}{q}\,e^{-\frac{Y}{(1+R)}\,\frac{q}{(R+q)}}\,K_o\left(\frac{RY}{(1+R)Q}, \theta(1+R)Q\right) \tag{10}$$

For brevity of notation $q = (1+R)p$ and $Q = (R+q)/(1+R+q)$.

Steady-State Solutions

The steady-state responses are obtained as θ increases without limit. The functions $H_n(u,v)$, $K_n(u,v)$, and $M_o(u,v)$ vary between zero and unity and approach unity as v becomes large compared to u. Therefore, the Laplace transforms, $\tau_{ap\infty}$ and $\tau_{bp\infty}$, of the steady-state responses $\tau_{a\infty}$ and $\tau_{b\infty}$ are obtainable from equations (9) and (10).

$$\tau_{ap\infty} = \frac{1}{p} - \frac{R(1+R)}{q(R+q)}\,e^{-\frac{Y}{1+R}\,\frac{q}{R+q}} \tag{11}$$

Nomenclature

A = heat transfer area, m^2
A_x = cross-sectional area for fluid flow, m^2
c = unit heat capacity of fluid, $W \cdot s/C \cdot$ kg
C = unit heat capacity of core material, $W \cdot s/C \cdot$ kg
E = $(wc)_b/(wc)_a$, capacity rate ratio, dimensionless
h = thermal conductance per unit heat transfer area, $W/C \cdot m^2$
H_n = function, equation (A6)
K_n = function, equation (A7)
L = fluid flow length of exchanger, m
M_o = function, equation (A5)
N = hA/wc, dimensionless
Ntu = number of transfer units, defined equation (19), dimensionless
p = Laplace parameter
R = $(hA)_b/(hA)_a$, conductance ratio, dimensionless
s = Laplace parameter
t = Time, s
T = core temperature, °C
u = fluid velocity, m/s (also argument of function)
v = argument of function
V = $\rho c A_x L/WC$, ratio of contained-fluid thermal capacity to core thermal capacity, dimensionless
w = mass flow rate of fluid, kg/s
wc = lesser of $(wc)_a$ and $(wc)_b$, W/C
W = mass of exchanger core, kg
x = distance from fluid "a" entrance, m
X = $(hA/wc)_a\,x/L_a = N_a\,x/L_a$, dimensionless
y = distance from fluid "b" entrance, m
Y = $(hA/wc)_b\,y/L_b = N_b\,y/L_b$, dimensionless
θ = $(hA)_a\,t/WC$, dimensionless
ρ = fluid density, kg/m^3
τ = fluid temperature, °C
$\bar{\tau}$ = mixed-mean exit temperature, °C
ϕ = defined in equation (26), dimensionless

Subscripts

a = refers to stepped fluid
b = refers to unstepped fluid
p = denotes Laplace transform w/r to X
s = denotes Laplace transform w/r to θ
∞ = refers to steady-state response

Table 1 Some Laplace transform pairs

	$F(s)$	$f(v)$
1	$F\left(\frac{s}{a}\right)$	$af(av)$
2	$\frac{e^{-u\frac{s}{1+s}}}{s}$	$H_o(u,v)$
3	$\frac{e^{-\frac{us}{1+s}}}{s^2}$	$vH_1(u,v)$
4	$\frac{e^{-u\frac{s}{1+s}}}{s(1+s)}$	$K_o(u,v)$
5	$\frac{e^{-\frac{us}{1+s}}}{s^2(1+s)}$	$vK_1(u,v)=vH_1(u,v)-K_o(u,v)$
6	$\frac{e^{-\frac{u(s+a)}{s+1+a}}}{s(s+a)}$	$\frac{e}{a}^{-\frac{au}{1+a}}K_o\left(\frac{u}{1+a},v(1+a)\right)-\frac{e^{-av}}{a}K_o(u,v)$
7	$\frac{e^{-\frac{u(s+a)}{s+1+a}}}{s(s+1+a)}$	$\frac{e^{-\frac{au}{1+a}}}{1+a}K_o\left(\frac{u}{1+a},v(1+a)\right)$
8	$\frac{e^{-\frac{u(s+a)}{s+1+a}}}{s(s+a)(s+1+a)}$	$\frac{e^{-\frac{au}{1+a}}}{a(1+a)}M_o\left(\frac{u}{1+a},v(1+a)\right)-\frac{e^{-av}}{a}M_o(u,v)$
9	$\frac{e^{-\frac{u(s+a)}{s+1+a}}}{s^2(s+a)^n}$	$P_n(u,v)=\frac{e}{a^n}^{-\frac{au}{1+a}}\left(vH_1\left(\frac{u}{1+a},v(1+a)\right)-\frac{n}{a}K_o\left(\frac{u}{1+a},v(1+a)\right)\right)$ $+\frac{e^{-av}}{a^{n+1}}\left(-n\frac{\partial K_o}{\partial v}(u,v)+\sum_{j=0}^{n}(n-j)a^j\frac{v^j}{j!}H_j(u,v)\right)$

$$\tau_{bp\infty}=\frac{1}{p}-\frac{(1+R)}{q}e^{-\frac{Y}{1+R}\frac{q}{R+q}} \tag{12}$$

The inverse transforms of these two equations are found from entries 1, 2 and 4 of Table 1 (also see equation (A4)).

$$\tau_{a\infty}=1-K_o\left(\frac{Y}{1+R},\frac{RX}{1+R}\right)=H_o\left(\frac{RX}{1+R},\frac{Y}{1+R}\right) \tag{13}$$

$$\tau_{b\infty}=1-H_o\left(\frac{Y}{1+R},\frac{RX}{1+R}\right)=K_o\left(\frac{RX}{1+R},\frac{Y}{1+R}\right) \tag{14}$$

The mixed-mean temperatures, $\bar{\tau}_a$ and $\bar{\tau}_b$, of the gases leaving the exchanger are the temperatures of greatest applicability and are defined as follows.

$$\bar{\tau}_a=\frac{1}{N_b}\int_0^{N_b}\tau_a(\theta,N_a,Y)dY \tag{15}$$

$$\bar{\tau}_b=\frac{1}{N_a}\int_0^{N_a}\tau_b(\theta,X,N_b)dX \tag{16}$$

The steady-state responses of the mixed mean temperatures are found using equations (13) and (14) as integrands in these two equations and equations (A15) and (A16) to evaluate the integrals (also see equation (A8)).

$$\bar{\tau}_{a\infty}=1-E[1-H_1\left(\frac{N_b}{1+R},\frac{N_aR}{1+R}\right)]=H_1\left(\frac{N_aR}{1+R},\frac{N_b}{1+R}\right) \tag{17}$$

$$\bar{\tau}_{b\infty}=1-H_1\left(\frac{N_b}{1+R},\frac{N_aR}{1+R}\right) \tag{18}$$

The constant E equals N_aR/N_b that, from the definitions of N_a, R, and N_b, equals $(wc)_b/(wc)_a$. Equations (17) and (18) satisfy a simple energy balance which equates, in the steady

state, the heat rate transferred from fluid "a" to the heat rate transferred to fluid "b": $(wc)_a(1-\bar{\tau}_{a\infty}) = (wc)_b\,\bar{\tau}_{b\infty}$

The number of transfer units, Ntu, of the exchanger is defined by

$$\frac{1}{\text{Ntu}} = wc\left(\frac{1}{(hA)_a} + \frac{1}{(hA)_b}\right) \tag{19}$$

For this definition wc is the lesser of $(wc)_a$ and $(wc)_b$. Thus, using the definitions of N_a, N_b, R, E, and Ntu, if $E>1$ then $N_a = \text{Ntu}(1+R)/R$ and $N_b = \text{Ntu}(1+R)/E$ and if $E<1$ then $N_a = \text{Ntu}\,E\,(1+R)/R$ and $N_b = \text{Ntu}(1+R)$. When $E \gtrless 1$, equation (18) gives the thermal effectiveness, ϵ, of the exchanger [4, 5, 6].

$$\epsilon = \bar{\tau}_{b\infty} = 1 - H_1(\text{Ntu}, E\text{Ntu}), (E \gtrless 1) \tag{20}$$

The function, H_1, is easily computed using equation (A12), and equation (20) therefore represents a very simple expression for the thermal effectiveness of the single-pass crossflow heat exchanger with neither fluid mixed. (The steady-state responses are not restricted to gas-to-gas exchangers: in the steady state, the time derivatives are zero and hence the values of V_a and V_b do not influence the steady-state relations.)

Transient Exit Temperatures

The Laplace transform, $\bar{\tau}_{ap}$, of the mixed-mean exit temperature, $\bar{\tau}_a$, is obtained from equations (9) and (15) using equations (A17) and (A18) to carry out the required integrations.

$$\bar{\tau}_{ap} = \frac{1}{p} + \frac{e^{-\frac{\theta p}{1+p}}}{p(1+p)}\left[\frac{e^{-R\theta}}{N_b} - H_1(R\theta,N_b) - \frac{H_o(R\theta,N_b)}{N_b} + \frac{(1+R)K_o(R\theta,N_b)}{N_b}\right] + \frac{Re^{-\frac{\theta p}{1+p}}}{N_b p^2(1+p)}K_o(R\theta,N_b)$$

$$- \frac{(1+R)^2 R}{N_b q^2}\left(1 - e^{\frac{N_b}{(1+R)}\,\frac{q}{(R+q)}}\right)$$

$$- \frac{(1+R)^2 e^{-\frac{\theta(1+R)(R+q)}{1+R+q}}}{N_b q(1+R+q)}$$

$$+ \frac{(1+R)^2 e^{-\frac{N_b}{(1+R)}\,\frac{q}{(R+q)}}}{N_b q(R+q)} QH_o\left(\theta(1+R)Q, \frac{N_b R}{(1+R)Q}\right)$$

$$- \frac{(1+R)^3}{N_b}\,\frac{e^{-\frac{N_b}{(1+R)}\,\frac{q}{(R+q)}}}{q^2} QK_o\left(\theta(1+R)Q, \frac{N_b R}{(1+R)Q}\right) \tag{21}$$

The Laplace transform, $\bar{\tau}_{bp}$, of $\bar{\tau}_b$ is obtained from equations (10) and (16) and is found by dividing the right side of equation (10) by p Na and setting $Y = N_b$.

$$\bar{\tau}_{bp} = \frac{1}{N_a p^2}\left[1 - e^{\frac{\theta p}{1+p}} H_o(R\theta,N_b)\right]$$

$$- \frac{(1+R)^2}{N_a}\,\frac{e^{-\frac{N_b}{(1+R)}\,\frac{q}{(R+q)}}}{q^2} + \frac{(1+R)^2}{N_a}\,\frac{e^{-\frac{N_b}{(1+R)}\,\frac{q}{(R+q)}}}{q^2}$$

$$H_0\left(\theta(1+R)Q, \frac{N_b R}{(1+R)Q}\right) \tag{22}$$

The inverse transforms of the terms in equation (21) are found using equation (A21) and entries 3, 4, 5, 7, and 9 of Table 1. The inverse transform of equation (22) is found using equation (A22) and entries 3 and 9 of Table 1.

$$\bar{\tau}_a = \bar{\tau}_{a\infty} - K_o(\theta,N_a)H_1(R\theta,N_b) + EG \tag{23}$$

$$\bar{\tau}_b = \bar{\tau}_{b\infty} - G \tag{24}$$

with

$$G = H_1(\theta,N_a)H_o(R\theta,N_b) - \frac{(1+R)}{N_b}e^{-\frac{N_b}{1+R}}e^{+\theta(1+R)} \sum_{n=0}^{\infty}\left(\frac{N_b R}{1+R}\right)^n \frac{1}{n!}H_n\left(\theta(1+R), \frac{N_b R}{1+R}\right) P_n\left(\theta(1+R), \frac{N_a}{1+R}\right) \tag{25}$$

The functions, H_n, are given by equations (A11) to (A13) and P_n by entry 9 of Table 1.

Equations (23) and (24) have been programmed. Computer-generated data are presented in the next section.

Results of Calculation

The three parameters and the time variable used in the analysis to express the mixed-mean exit temperatures are N_a, N_b, R, and θ. ($E = N_a R/N_b$.) The three parameters and the time variable used to express the results of calculation are Ntu, E, R, and ϕ.

$$\phi = \frac{wct}{WC} \tag{26}$$

For the definition of ϕ, as for the definition of Ntu, wc is the lesser of $(wc)_a$ and $(wc)_b$. Either set of four numbers can be translated into the other.

The mixed-mean exit temperatures are normalized by dividing them by their final values to give $\bar{\tau}_a/\bar{\tau}_{a\infty}$ and $\bar{\tau}_b/\bar{\tau}_{b\infty}$ which approach unity as ϕ increases. The complements of these quotients are presented in Figs. 1(*a*) to 1(*i*) that, with interpolation, give the normalized exit temperature histories for Ntu = 1 to 8, E = 0.6 to 1.67, and R = 0.5 to 2.0. The steady-state responses are given in Table 2 for the discrete values of Ntu and E used in the figures.

Curves giving $\bar{\tau}_b/\bar{\tau}_{b\infty}$ are in the lower halves of Figs. 1(*a*), 1(*b*), and 1(*c*). Two phenomena make the presentation of data for $\bar{\tau}_b/\bar{\tau}_{b\infty}$ particularly simple. The first, shown by the numerical work, is that

$$\frac{\bar{\tau}_b}{\bar{\tau}_{b\infty}}(\phi,\text{Ntu},E,R) = \frac{\bar{\tau}_b}{\bar{\tau}_{b\infty}}(\phi,\text{Ntu},1/E,1/R) \tag{27a}$$

The second is that $\bar{\tau}_b$ is almost independent of R. For the range of parameter values used in the figures the largest absolute difference between values of $\bar{\tau}_b/\bar{\tau}_{b\infty}$ for R = 1 and R = ½ or 2 occurred with E = 0.6 and Ntu = 1 and was only 0.032. Thus, although the data for $\bar{\tau}_b/\bar{\tau}_{b\infty}$ were calculated using R = 1, the curves are indicated to be applicable for R = 0.5 to 2.0.

Equation (27*a*) shows that the normalized exit temperature history of the unstepped gas will be the same no matter which gas of the exchanger is subjected to a unit step change in inlet temperature. Unreported work by the writer using finite-difference methods show that equation (27*a*) is also true for

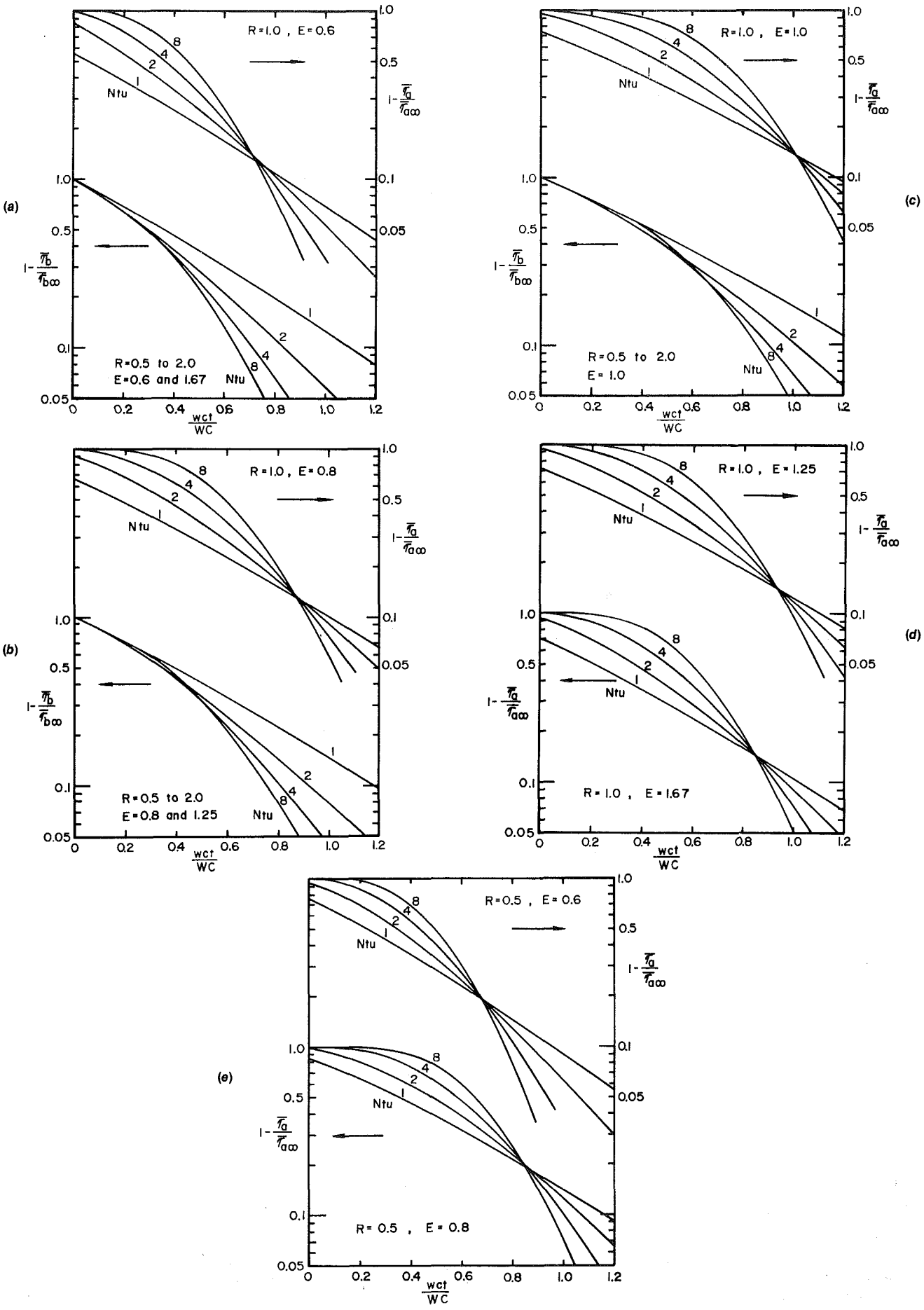

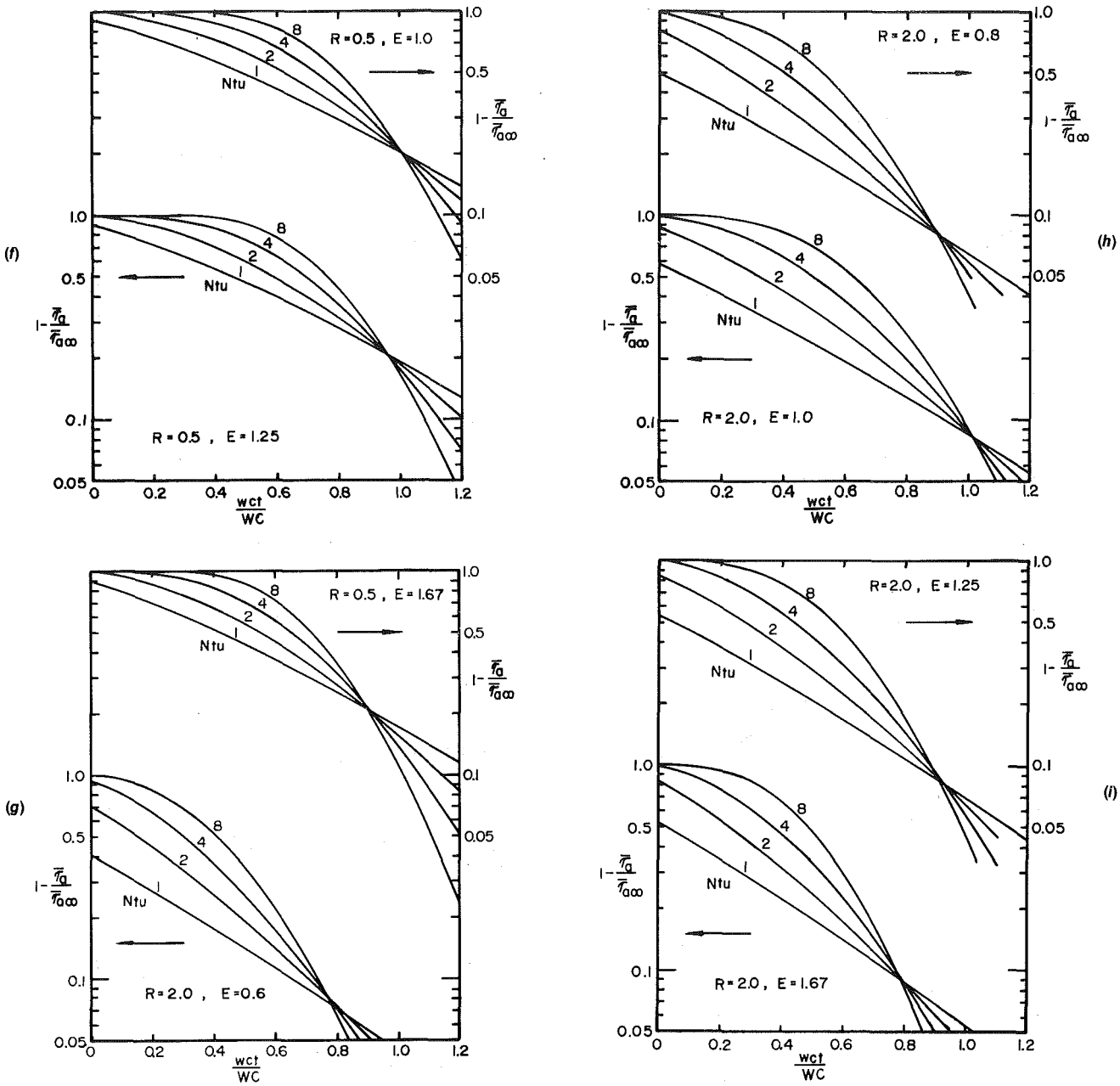

Fig. 1 Exit gas temperature responses

the gas-to-gas counterflow heat exchanger. The general applicability of equation (27*a*) to all configurations of gas-to-gas heat exchangers therefore seems evident.

Inspection of Figs. 1(*a*) to 1(*i*) shows that $\bar{\tau}_a/\bar{\tau}_{a\infty}$ is not always zero at time zero. This observation indicates a step change in $\bar{\tau}_a$ at initiation of the transient since the value of $\bar{\tau}_a$ before the excitation is zero. The magnitude of the step change in $\bar{\tau}_a$ at time zero is exp $(-N_a)$, which can be derived by noting that all gas "*a*" lamina entering at unity temperature at time zero see the core at zero temperature during their travel through the exchanger. (The transient time of the lamina is zero when $V_a = 0$.)

The computed results of this analysis agree with the results of Yamashita et al. [3] to the accuracy with which their curves for $V = 0$ can be read.

Two solutions given by Myers, Mitchell, and Lindeman [10] can be treated as special cases of the analysis given. For both solutions, which correspond to $E = 0$ and $E = \infty$, the configuration (counterflow, parallelflow, crossflow, etc.) of the heat exchanger is immaterial. When E increases, the temperature change of gas "*b*" (the unstepped gas) decreases, and in the limit with $E = \infty$, the temperature of gas "*b*" becomes constant and uiniform. For this case, the solution for $\bar{\tau}_a$ (equation (23) with $E = \infty$) describes the temperature history of gas "*a*", leaving a heat exchanger which has a constant and uniform temperature fluid on the "*b*" side. The excitation is a unit step increase of the inlet temperature of gas "*a*".

$$\bar{\tau}_a = e^{-\mathrm{Ntu}} H_o\left(\frac{\mathrm{Ntu}}{R}, \phi(1+R)^2\frac{\mathrm{Ntu}}{R}\right), (E=\infty) \qquad (27b)$$

When E decreases, the axial temperature change of gas "*a*" decreases, and in the limit with $E = 0$, the temperature of gas "*a*" becomes uniform. For this case, a step change in the inlet temperature of gas "*a*" corresponds to a step change in the uniform temperature of gas "*a*" (fluid "*a*"), and $\bar{\tau}_b$ (equation (24) with $E = 0$) describes the response of the "*b*" gas to the step change of the temperature of the uniform temperature fluid. An example is an exchanger with a condensing or

Table 2 $\bar{\tau}_{a\infty}$ and $\bar{\tau}_{b\infty}$ ($\bar{\tau}_{b\infty}$ is the lower entry of a pair)

	Ntu			
E	1	2	4	8
0.6	.681	.576	.495	.443
	.532	.707	.841	.928
0.8	.597	.473	.374	.304
	.503	.659	.782	.870
1.0	.524	.386	.278	.198
	.476	.614	.722	.802
1.25	.497	.341	.218	.130
	.403	.528	.626	.696
1.67	.468	.293	.159	.072
	.319	.424	.505	.557

$\bar{\tau}_{a\infty}(\text{Ntu},E) + \bar{\tau}_{b\infty}(\text{Ntu},1/E) = 1$
$\bar{\tau}_{b\infty}(\text{Ntu},E) = \bar{\tau}_{b\infty}(\text{Ntu},1/E)/E$

evaporating fluid on the "a" side and gas on the "b" side. The excitation corresponds to an abrupt pressure change of the evaporating or condensing fluid.

$$\bar{\tau}_b = 1 - e^{-\text{Ntu}} + e^{-\text{Ntu}} H_o\left(\phi(1+R)^2 \frac{\text{Ntu}}{R}, R\text{Ntu}\right)$$

$$- e^{-\phi(1+R)\frac{\text{Ntu}}{R}} H_o(\phi(1+R)\text{Ntu},(1+R)\text{Ntu}),(E=0) \qquad (27c)$$

Concluding Remarks

The mixed-mean temperature histories of the two gases leaving a crossflow heat exchanger have been found for a unit step increase in the inlet temperature of either gas. The work permits the transient temperature responses to be calculated for arbitrary variations of the inlet temperature by applying the usual methods of linear analysis. It has been found that the normalized exit temperature history of the unstepped gas is the same irrespective of which gas of a heat exchanger is subjected to a unit step increase in inlet temperature.

The computation time is believed to be short compared to the computation time that would be required using a finite difference method of solution.

The infinite series of equation (25) was evaluated for $n = 0$ to N.

$$N = \text{INT}\,(3 + 2.05\,\text{Ntu}^{0.85})$$

This value of N gave the computed temperature ratios to an accuracy of $\pm$ 0.00005. (INT = integer of)

References

1 Dusinberre, G. M., "Calculation of Transients in a Crossflow Heat Exchanger," ASME JOURNAL OF HEAT TRANSFER, Vol. 81, 1959, pp. 61-67.

2 Myers, G. E., Mitchell, J. W., and Norman, R. F., "The Transient Response of Crossflow Heat Exchangers, Evaporators, and Condensers," ASME, JOURNAL OF HEAT TRANSFER, Vol. 89, 1967, pp. 75-80.

3 Yamashita, H., Izumi, R., and Yamaguchi, S., "Analysis of the Dynamic Characteristics of Crossflow Heat Exchangers With Both Fluids Unmixed," *JSME Bulletin*, Vol. 21, 1978, pp. 479-485.

4 Nusselt, W., "Eine neue Formel für den Wärmedurchgang in Kreuzstrom," *Technische Mechanik und Thermodynamik*, Vol. 1, 1930, pp. 417-422.

5 Mason, J. L., "Heat Transfer in Crossflow," *Proceedings of the Second U.S. National Congress of Applied Mechanics*, ASME, New York, N.Y., 1955, pp. 801-803.

6 Baclic, B. S., "A Simplified Formula for Crossflow Heat Exchanger Effectiveness," ASME JOURNAL OF HEAT TRANSFER, Vol. 100, 1978, pp. 746-747.

7 Anzelius, A., "Über Erwärmung Vermittels durchströmeder Medien," *Zeitschrift fur Angewandte Mathematik and Mechanik*, Vol. 6, 1926, pp. 291-294.

8 Schumann, T. E. W., "Heat Transfer: A Liquid Flowing Through a Porous Prism," *Franklin Institute Journal*, Vol. 208, 1929, pp. 405-416.

9 Klinkenberg, A., "Heat Transfer in Crossflow Heat Exchangers and Packed Beds," *Industrial and Engineering Chemistry*, Vol. 46, 1954, pp. 2285-2289.

10 Myers, G. E., Mitchell, J. W., and Lindeman, C. F., "The Transient Response of Heat Exchangers Having an Infinite Capacitance Rate Fluid," ASME JOURNAL OF HEAT TRANSFER, Vol. 92, 1970, pp. 269-275.

11 Romie, F. E., "Periodic Thermal Storage: The Regenerator," ASME JOURNAL OF HEAT TRANSFER, Vol. 101, 1979, pp. 726-731.

APPENDIX A

The functions, $H_o(u,v)$ and $K_o(u,v)$, are solutions [7-9] of two differential equations,

$$-\frac{\partial H_o}{\partial u} = H_o - K_o = \frac{\partial K_o}{\partial v} \qquad (A1)$$

with conditions that $H_o(0,v) = 1$ and $K_o(u,0) = 0$. The functions are expressible in the form

$$K_o(u,v) = \int_0^v e^{-(u+\eta)} I_o(2\sqrt{u\eta})\,d\eta \qquad (A2)$$

$$H_o(u,v) - K_o(u,v) = e^{-(u+v)} I_o(2\sqrt{uv}) \qquad (A3)$$

I_o is the modified Bessel function of the first kind, zero order. A useful relation is

$$H_o(u,v) + K_o(v,u) = 1 \qquad (A4)$$

The related function $M_o(u,v)$ is defined by

$$\frac{\partial K_o}{\partial u} = M_o - K_o = -\frac{\partial M_o}{\partial v} \qquad (A5)$$

The functions $H_n(u,v)$ and $K_n(u,v)$ have been used in the analysis [11] of the regenerative heat exchanger. By definition

$$\frac{v^{n+1} H_{n+1}(u,v)}{n+1} = \int_0^v \eta^n H_n(u,\eta)\,d\eta \qquad (A6)$$

and

$$K_n(u,v) = H_n(u,v) + \frac{\partial H_n}{\partial u}(u,v) \qquad (A7)$$

Useful relations are

$$v[1 - H_1(u,v)] = u[1 - H_1(v,u)] \qquad (A8)$$

$$\frac{v}{1+n}[H_{n+1}(u,v) - K_{n+1}(u,v)] = K_n(u,v) \qquad (A9)$$

Numerical values of the functions, H_n, can be found from their series expressions [11]. Let $B(u,v) = H_o(u,v) - K_o(u,v)$ (cf., equations (A1) and (A3)).

$$B(u,v) = e^{-(u+v)}\left\{1 + \frac{vu}{1!1!} + \frac{v^2u^2}{2!2!} + \frac{v^3u^3}{3!3!} + - - -\right\} \qquad (A10)$$

$$H_o(u,v) = e^{-(u+v)}0!\left\{\frac{1}{0!} + \frac{v}{1!}(1+u) + \frac{v^2}{2!}\left(1+u+\frac{u^2}{2!}\right) + - - -\right\} \qquad (A11)$$

$$H_1(u,v) = e^{-(u+v)}1!\left\{\frac{1}{1!} + \frac{v}{2!}(2+u) + \frac{v^2}{3!}\left(3+2u+\frac{u^2}{2!}\right) + - - -\right\} \qquad (A12)$$

$$H_2(u,v) = e^{-(u+v)}2!\left\{\frac{1}{2!} + \frac{v}{3!}(3+u) + \frac{v^2}{4!}\left(6+3u+\frac{u^2}{2!}\right) + - - -\right\} \qquad (A13)$$

Series expressions of H_n for larger values of the index, n, can be found by extension on noting that if $b_{n,p}$ is the polynomial in u multiplying the pth power of v in the expression for H_n then

$$b_{n,p} = b_{n-1,p} + b_{n,p-1} \tag{A14}$$

Namely, a polynomial term is the sum of the polynomial above it (in H_{n-1}) and to the left of it.

The following integrals are used in the analysis and can be derived from the preceding equations.

$$\int_0^u K_0(\eta,v)d\eta = v[1 - H_1(u,v)] \tag{A15}$$

$$\int_0^v H_0(u,\eta)d\eta = vH_1(u,v) \tag{A16}$$

$$\int_0^u M_o(\eta,v)\,d\eta = u + e^{-v} - uH_1(v,u) - H_0(v,u) \tag{A17}$$

$$\int_0^u e^{-a\eta} M_0(\eta,v)\,d\eta = \frac{1}{a}(1 - e^{-au}) + e^{-v} - e^{-au}H_o(v,u) + \frac{1+a}{a}\left[e^{-au}K_o(v,u) - e^{-\frac{av}{1+a}}K_o\left(\frac{v}{1+a},(1+a)u\right)\right] \tag{A18}$$

The last terms of equations (21) and (22) contain the function $H_o(AQ, B/Q)$ in which, for brevity, $A = \theta(1+R)$, $B = RN_b/(1+R)$ and Q, defined following equation (10), is $(R+q)/(1+R+q)$ with $q = (1+R)p$. This function can be expressed in a form amenable to inversion by expanding it in series form and collecting terms having common factors of $1/(R+q)^n$.

$$H_o(AQ,B/Q) \doteq e^{-(AQ+B/Q)}e^{+(A+B)}\sum_{n=0}^{\infty}\frac{1}{(R+q)^n}\frac{B^n}{n!}H_m(A,B) \tag{A19}$$

The function $K_o(AQ, B/Q)$ can also be expressed in a form amenable to inversion using equation (A3).

$$K_o(AQ,B/Q) = H_o(AQ,B/Q) - e^{-(AQ+B/Q)}I_o(2\sqrt{AB}) = H_o(AQ,B/Q) - e^{-(AQ+B/Q)}e^{+(R\theta+N_b)}[H_o(R\theta,N_b) - K_o(R\theta,N_b)] \tag{A20}$$

The last two terms, denoted by W, of equation (21) can be expressed using equations (A19) and (A20).

$$W = -\frac{R(1+R)^2}{N_b}e^{-\frac{N_b}{1+R}}e^{+\theta(1+R)}\sum_{n=0}^{\infty}\frac{e^{-\frac{\theta(1+R)(R+q)}{1+R+q}}}{q^2(R+q)^n}\left(\frac{RN_b}{1+R}\right)^n\frac{1}{n!}H_n\left(\theta(1+R),\frac{N_bR}{1+R}\right) + [H_o(R\theta,N_b) - K_o(R\theta,N_b)]\frac{e^{-\frac{\theta p}{1+p}}}{N_b}\left(\frac{1}{p(1+p)} + \frac{R}{p^2}\right) \tag{A21}$$

The inverse transform is found from entries 1, 4, 5, and 9 of Table 1.

Similarly, let Z denote the last term of equation (22) and use equation (A19) to find the form amenable to inversion.

$$Z = \frac{(1+R)^2}{N_a}e^{-\frac{N_b}{1+R}}e^{+\theta(1+R)}\sum_{n=0}^{\infty}\frac{e^{-\frac{\theta(1+R)(R+q)}{1+R+q}}}{q^2(R+q)^n}\left(\frac{N_bR}{1+R}\right)^n\frac{1}{n!}H_n\left(\theta(1+R),\frac{N_bR}{1+R}\right) \tag{A22}$$

The inverse transform is found from entries 1 and 9 of Table 1.

Entry 1 of Table 1 is a standard Laplace transform pair. Entries 2 through 5 are obtained directly from equations (A1-A8). Entries 6 through 9 are obtained using the convolution integral. Entry 9 required repeated use of the integral ($n = 0, 1, 2\ldots$) until the general form for P_n became apparent.

Experiments on a Crossflow Heat Exchanger With Tubes of Lenticular Shape

E. K. Ruth[1]
California Institute of Technology,
Pasadena, Calif.

Measurements of pressure losses and heat transfer rates were made for an unconventional crossflow heat exchanger with tubes of lenticular cross section so spaced to reduce variation in the velocity of the fluid outside the tubes, thus reducing separation and drag. The results of these experiments are reported for various tube spacing and demonstrate that the performance of the lenticular tube heat exchanger is superior to that of conventional circular tubes by 20 percent at Reynolds numbers of 20,000 to 50,000.

Introduction

One of the major objectives in the design of heat exchangers is the reduction of pressure drop for a given amount of heat transferred. In some applications, for example, the natural draft dry cooling tower, the overall performance is critically dependent on pressure drop. This paper gives the results of an investigation of a method of reducing the pressure drop.

Crossflow tubular heat exchangers have been studied by many investigators, with most of the experiments performed on exchangers made up of tubes of circular cross section in regular arrays. Pierson, Huge, and Grimison [1-3] undertook extensive measurements in 1926 for the Babcock and Wilcox Company on both staggered and inline arrangements with various ratios of pitch to diameter. Correlations of these data with the work of others have been done for heat transfer by Fishenden and Saunders [4] and for pressure loss by Jakob [5]. More recently, Zhukauskas [6] performed many heat transfer experiments with single tubes and banks of cylinders. The effect of the number of rows has been investigated by Kays [7-8].

Tubes of circular cross section cause severe separation and large wakes in turbulent flow normal to the tubes. Such separated flow increases pressure drop more than heat transfer when compared with turbulent flow inside a smooth tube of constant cross section. In the experiments described here, heat exchanger tubes of lenticular cross section were arranged to reduce the area variations presented to the crossflow. In this fashion, the severity of the separation is reduced and the pressure loss decreased.

Performance Criteria

The cross section of a lenticular tube heat exchanger is depicted in Fig. 1. The cross section of these tubes is formed from two circular arcs joined together. The geometrical arrangement is defined by the chord, C, the half thickness, h, the spacings, s_1, s_2, and the number of rows, N.

By arranging the lenticular tubes with the spacing s_1 equal to s_2, the flow area through the heat exchanger is more nearly constant than is possible with tubes of circular cross section. This gives an advantage in that flow through the nearly constant area will have lower accelerations and pressure gradients, and thus, there should be smaller wakes and lower form drag for the lenticular tubes.

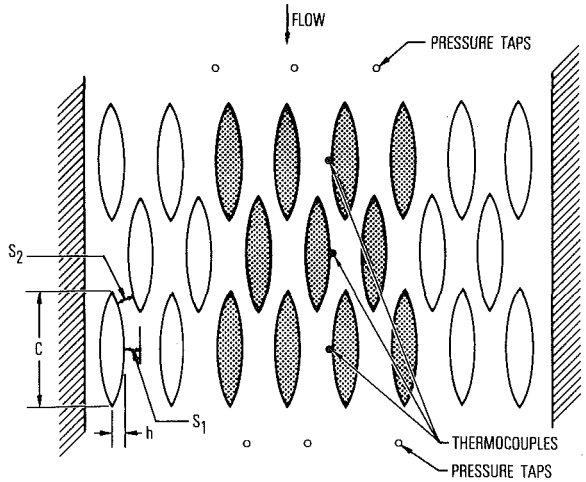

Fig. 1 Schematic diagram of top view of bundle with heated tubes shown in solid

The drag on the outside of a crossflow heat exchanger can be expressed as

$$A\Delta P = \rho\, U_{\max}^2 S C_f/2$$

The drag is equal to the product of the frontal area of the heat exchanger, A, and the pressure difference across it, ΔP. C_f is a dimensionless drag coefficient, which is the usual skin friction coefficient if there is no separation. Here ρ is the density of the fluid, $U_{\max}$ the reference velocity based on the velocity through the minimum flow area, and S the wetted surface area.

The heat transfer rate, $\dot{Q}$, can be expressed as

$$\dot{Q} = \rho C_p \Delta T_w S C_h U_{\max}$$

where C_p is the specific heat at constant pressure for the fluid and ΔT_w is the temperature difference between the fluid and the wall of the heat exchanger. The parameter, C_h, is the Stanton number. The pumping power, $\dot{W}$, required to drive the fluid across the heat exchanger is given by the product of the drag and the velocity

$$\dot{W} = A\ \Delta P\ U_{\max}$$

Thus the ratio of pumping power to heat transfer rate is

$$\dot{W}/\dot{Q} = U_{\max}^2/(C_p \Delta T_w)\cdot(C_f/2C_h)$$

For a forced draft application with a prescribed velocity and temperature difference and a given heat transfer rate, the minimum required pumping power will occur at the minimum value of $C_f/2C_h$.

A natural draft heat exchanger at the base of a cooling

[1] Graduate Research Assistant, California Institute of Technology, now Member of the Technical Staff, The Aerospace Corporation, El Segundo, Calif. 90009

Contributed by the Heat Transfer Division for publication in the JOURNAL OF HEAT TRANSFER. Manuscript received by the Heat Transfer Division March 1, 1982.

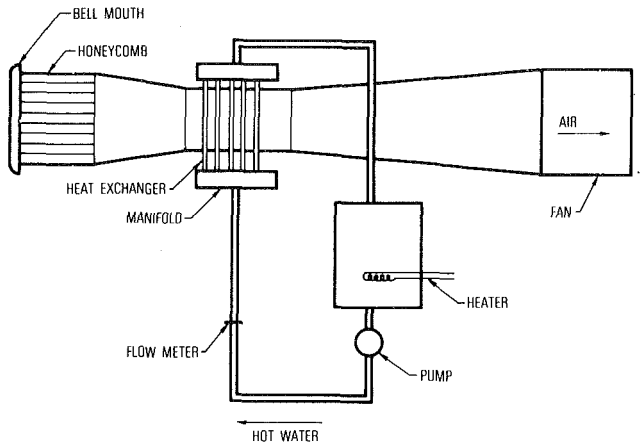

Fig. 2 Wind tunnel layout

tower is slightly more complicated, but it can be shown [9] that for the optimum value of S/A

$$\dot{Q}/A = 0.5690[\gamma/(\gamma-1)](gH)^{1/2}(\Delta T_w/T_o)^{3/2}P_o(C_f/2C_h)^{-2}$$

where g is the acceleration due to gravity, H is the height of the tower, T_o and P_o are ambient absolute temperature and pressure, and γ is the ratio of specific heats of air. For given values of these parameters with this configuration, the heat transfer per unit frontal area is a maximum for the minimum value of $C_f/2C_h$.

In general, the ratio of the coefficients $C_f/2C_h$ is a function of geometry, Prandtl number, and Reynolds number. For turbulent flow of a gas inside a smooth tube, Reynolds analogy leads to $C_f/2C_h \cong 1$. Wall roughness or any other geometry that causes flow separation increases drag more than heat transfer giving $C_f/2C_h > 1$.

The choice of design of a heat exchanger is strongly dependent on the system of which it is a part. Here, the parameter $C_f/2C_h$ will be used to compare heat exchangers of different geometries, a measure of both pumping requirements and heat transfer.

Experimental Apparatus

A small wind tunnel, as shown in Fig. 2, was built to carry out these experiments. The tunnel was made of plywood and was about 6.1 m in length. It was an open-circuit tunnel with air drawn through it by a 5.6 kW fan. A deep aluminum honeycomb at the entrance smoothed the flow and reduced or eliminated temperature fluctuations with time constant less than about 4.5 s. The working section measured 0.23-m high by 0.41-m wide. The maximum velocity through the empty tunnel was about 25 m/s.

Water was heated to temperatures of 70 to 90°C in a 55-gal stainless steel drum by a 5-kW electric resistance heater and was thoroughly stirred before being pumped upward into a manifold which distributed the hot water through flexible hoses to the heat exchanger tubes. After passing through the working section,, the water was collected by an upper manifold and returned to the heater tank to be recycled. The water mass flow rate was determined by an orifice flow meter located upstream of the first manifold. Iron-constantan thermocouples of small diameter, inserted into both manifolds and referenced against each other, measured the temperature drop in the water as it flowed through the manifolds, connecting plastic tubes, and heat exchanger tubes.

Similar thermocouples were laid into shallow grooves cut along the half-chord and running the length of the heat exchanger tubes with their junctions at the midpoint and referenced to a total temperature probe upstream of the tube bank. These gave the difference between the tube wall temperature and the temperature of the undisturbed air.

The static pressure drop across the heat exchanger was found by the averaged differential between three upstream static pressure taps in the floor of the tunnel and three downstream static pressure taps. There were also provisions for inserting a total temperature probe and a pitot probe into the tunnel at a number of locations upstream and downstream of the heat exchanger to make surveys across the width of the tunnel.

The lenticular tubes were constructed of segments cut from a brass pipe of circular cross section. The outside chord was 51 mm, the outside half-thickness was 6.4 mm, and the wall 3.2-mm thick. Since these tubes were expensive to manufacture, and since there was a limited capacity of heated water for a large number of tubes, only the middle tubes were "active" with hot water flowing through them. The rest were unheated, "passive" tubes made of wood as shown in Fig. 1. This was felt to be an acceptable procedure as long as the temperature profile had a steep gradient downstream of the boundary between active and passive tubes, as was confirmed in the experiments. The wetted surface of all the tubes was used for the calculation of $C_f/2$; the surface area of the heated tubes was used for C_h.

Estimates of experimental uncertainty indicated that the temperature measurements were accurate to ±0.24 K. The accuracy of the pressure drop across the heat exchanger was ±24.0 Pa. The velocity through the tunnel was known to ±0.4 m/s. A check on the heat transfer rate was done by making velocity and temperature surveys across the tunnel

Nomenclature

A = frontal area, m²
A_{min} = minimum free area, m²
C = chord of lenticular tube, m
$C_f/2$ = drag coefficient, dimensionless
C_h = Stanton number (the Colburn factor = $C_h\,Pr^{2/3}$), dimensionless
C_p = specific heat at constant pressure, J/kg K
h = half-thickness of lenticular tube, m
N = number of rows of heat exchanger
Pr = Prantdl number, dimensionless
ΔP = pressure drop across heat exchanger, Pa
$\dot{Q}$ = heat transfer rate, W
Re = Reynolds number = $2s_1 U_{max}/\nu$, dimensionless
S = wetted surface area, m²
s_l = longitudinal tube spacing, m
s_t = transverse tube spacing, m
s_1 = distance from side of lenticular tube to centerline of adjacent tube in next row, m
s_2 = minimum distance between lenticular tube and adjacent tube in next row, m
ΔT = temperature difference between fluid and wall, K
U_{max} = nominal maximum velocity calculated from minimum area, m/s
$\dot{W}$ = pumping power, W
γ = ratio of specific heats, dimensionless
ν = kinematic viscosity, m²/s
ρ = fluid density, kg/m³

[2] Relationship between nomenclature of this paper and Kays and London [10]:

Ruth	Kays-London
$C_f/2$	$f/2\sigma$
C_h	N_{St}
Re	$N_R 2s_1/(4\,r_h)$

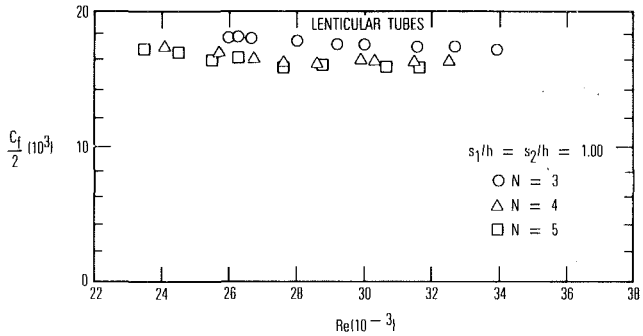

Fig. 3 C_f versus Re for $s_1 = s_2 = h$

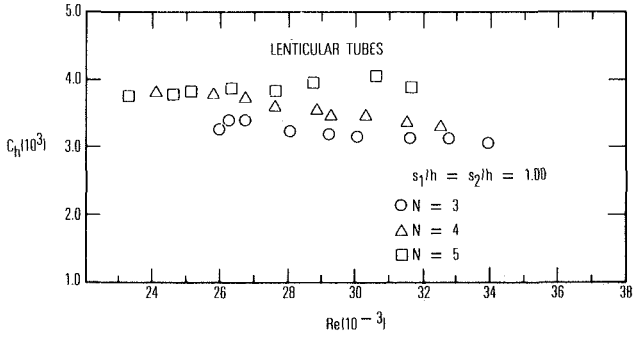

Fig. 4 C_h versus Re for $s_1 = s_2 = h$

midplane both up and downstream of the heat exchanger and numerically integrating the results. The difference in the integrated energy flux calculated from these surveys should equal the heat transfer rate of the exchanger. However, since these surveys did not include the boundary layers on the upper and lower tunnel surfaces, some discrepancies occurred. Vertical surveys showed that the temperature difference across the heat exchanger was higher in the boundary layer than in the midplane. Generally, the mass flow rate was 10 percent higher and the heat transfer rate 5 percent lower for the integrated measurements than for the direct measurements. Given that the survey results did not take the boundary layers into account, this was considered a good check on the heat transfer measurements.

Results and Discussion

Three spacings of lenticular tubes were investigated: $s_1/h = s_2/h = 1.00$ ($s_t/h = 2, s_l/h = 5.89$), $s_1/h = s_2/h = 3.50$ ($s_t/h = 4.50, s_l/h = 6.30$), and the geometric mean of the two: $s_1/h = s_2/h = 1.91$ ($s_t/h = 2.91, s_l/h = 6.05$).[3] These spacings were selected to give a range of tube packing from densely packed to a more open spacing. Tests were run with 3, 4, and 5 rows for each spacing.

The results of the experiments are plotted with the parameters C_h, $C_f/2$, and $C_f/2C_h$ as functions of Reynolds number, Re. The reference velocity U_{max} is based on the nominal maximum velocity calculated from the minimum area. The Reynolds number is based upon U_{max} and the minimum spacing between the tubes.

$$\mathrm{Re} = U_{max} 2s_1/\nu$$

where ν the kinematic viscosity for air.

The first set of experiments was carried out for the configuration with $s_1 = s_2 = h$. In Fig. 3, $C_f/2$ is plotted against Re. As can be seen, there is a slight decrease in $C_f/2$ with increasing number of rows. The plot of C_h versus Re in Fig. 4 shows some increase with the addition of more rows. Thus, the ratio of $C_f/2C_h$ in Fig. 5 shows an improvement in performance with the addition of more rows. The improvement from 4 to 5 rows is somewhat less than the improvement from 3 to 4 rows.

In comparison, the data for circular tubes [7-8] show that $C_f/2$ is nearly independent of the number of rows and that C_h increases with each additional row until a constant value is reached for 10 or more rows. At similar Reynolds numbers, heat exchangers made up of inline arrangements of circular cylinders have values of $C_f/2C_h$ of 12 or less, depending on the number of rows and spacing of the tubes. This will be discussed more fully in the section following.

Tufts placed on the roof and floor of the test section just downstream of the last row of lenticular tubes revealed the existence of a region of recirculating flow at the center of the tunnel. Velocity surveys showed this region to be a "bubble" of separated flow 10- to 15-cm wide and 1- to 2-cm high just after the last row but apparently not extending upstream into the tube bank (Fig. 6).

[3] The ratio of minimum free flow area to frontal area for the three test geometries was 0.50, 0.78, and 0.66.

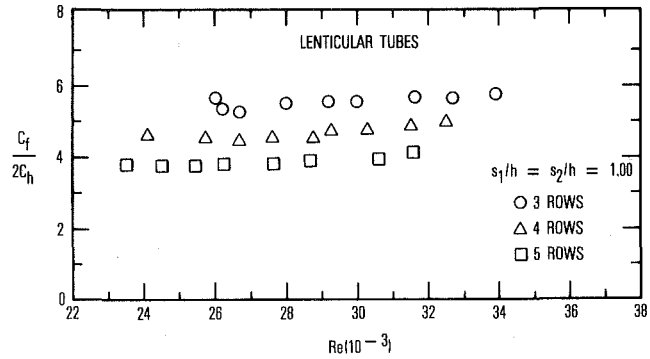

Fig. 5 $C_f/2C_h$ versus Re for $s_1 = s_2 = h$

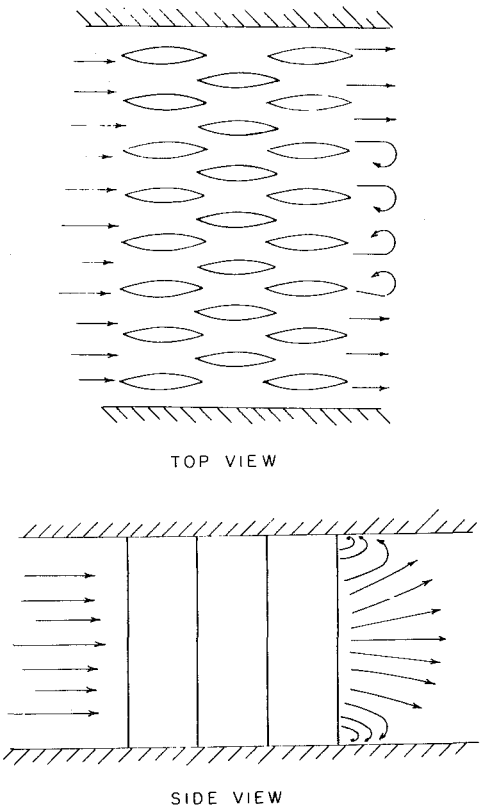

Fig. 6 Separation bubble

An explanation of this phenomenon is that the cross-sectional area of the channels between the tubes diverges rapidly after the midpoint of the last row. The consequent deceleration, if large enough, tends to cause separation of the boundary layer in the corners of the tube surfaces and tunnel walls. In effect, this last row of tubes forms an array of diffusers. Separation occurs for the closer spacings, since these have the greater diffuser angles. As to why the separation occurs only in the middle of the tunnel, an analogy might be made with the case of a stalled three-dimensional wing or of rotating stall in a compressor. There separation occurs in patches, relieving conditions along the rest of the wing or blades where the flow remains attached.

The most closely spaced arrangement, $s_1 = s_2 = h$, had a separation bubble for all numbers of rows tested; whereas, the wide spacing $s_1 = s_2 = 3.5\,h$ did not have a separated region for any case. For the intermediate spacing, $s_1 = s_2 = 1.91h$, there was no separation for 3 and 4 rows, but for 5 rows the separation bubble appeared. Best performance was for this last case, i.e., $s_1 = s_2 = 1.91h$ and 5 rows. In all cases, $C_f/2C_h$ decreased with increasing number of rows. These results are presented in detail in Table 1 and discussed in [9].

Some experiments were made at low Reynolds numbers using the configuration that gave the best performance at higher Reynolds numbers, $s_1 = s_2 = 1.91h$ and 5 rows. To achieve low Reynolds numbers, an orifice plate was installed at the diffuser exit to reduce the flow through the fan. By changing the size of the hole in the orifice plate in combination with the normal velocity control, a range of Reynolds number was explored.

Figure 7 is a plot of $C_f/2$ as a function of Re. A simple power relationship is drawn through the points. The plot of C_h versus Re is shown in Fig. 8 again with a simple power curve fit. Both $C_f/2$ and C_h are rapidly decreasing functions with increasing Reynolds number near the origin. Figure 9 shows that $C_f/2C_h$ is an increasing function of the Reynolds number.

Comparison of Heat Exchanger Configuration

The characteristics desired in a heat exchanger depend strongly on the particular application. In this investigation, the ratio $C_f/2C_h$ has been used as a figure of merit to compare heat exchangers of the same type. However, this ratio is dependent on the geometry and Reynolds number, which in turn depend on the application. Hence, it is not possible in general to find a single criterion for comparing different types of heat exchangers and pronounce one superior to the other. Here no attempt will be made to select one type of heat ex-

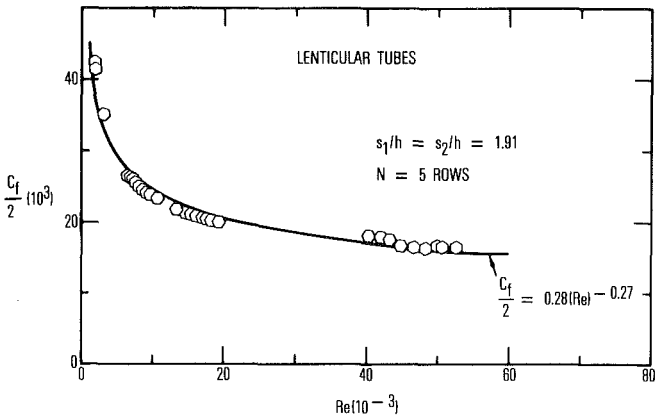

Fig. 7 $C_f/2$ versus Re extended Reynolds number for $s_1 = s_2 = 1.91\,h$, $N = 5$

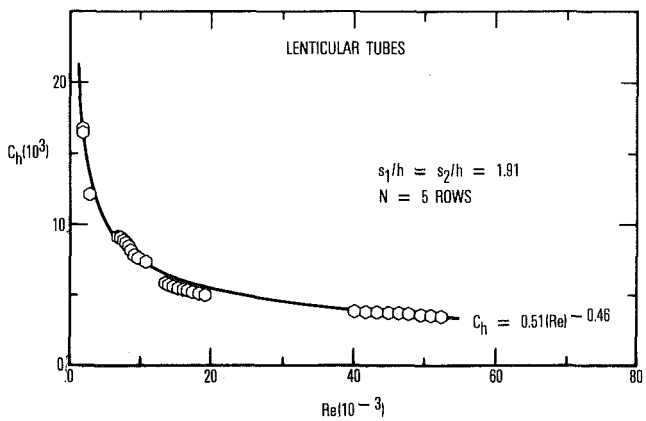

Fig. 8 C_h versus Re extended Reynolds number for $s_1 = s_2 = 1.91\,h$, $N = 5$

Table 1 Experimental data for lenticular heat exchanger

	$s_1 = s_2 = h$			$s_1 = s_2 = 1.91\,h$			$s_1 = s_2 = 3.5\,h$		
	Re(10^{-3})	$C_f/2(10^3)$	$C_h(10^3)$	Re(10^{-3})	$C_f/2(10^3)$	$C_h(10^3)$	Re(10^{-3})	$C_f/2(10^3)$	$C_h(10^3)$
	25.9	18.0	3.30	42.3	19.2	4.06	67.0	36.8	3.75
	26.2	18.2	3.42	43.6	19.0	4.00	71.0	36.5	3.75
	26.6	18.0	3.45	45.1	19.3	3.90	75.0	36.2	3.75
	27.9	17.9	3.26	46.3	20.0	3.89	80.0	35.3	3.65
$N=3$ rows	29.1	17.5	3.23	47.7	19.7	3.80	85.0	35.5	3.60
	29.9	17.5	3.20	49.2	19.5	3.74			
	31.6	17.4	3.20	50.6	19.5	3.60			
	32.7	17.2	3.17	52.5	19.3	3.51			
	33.8	17.0	3.10	54.3	18.9	3.45			
	24.0	17.3	3.85	41.3	18.4	4.00	66.5	31.5	4.25
	25.7	16.9	3.82	42.5	18.3	3.96	70.6	31.2	4.06
	26.6	16.4	3.75	44.1	18.0	3.95	75.0	30.6	4.05
	27.6	16.3	3.61	45.8	17.5	3.86	79.5	30.9	3.94
$N=4$ rows	28.7	16.1	3.56	47.5	17.5	3.85	84.6	30.0	3.92
	29.1	16.4	3.50	49.8	17.5	3.80			
	30.2	16.3	3.48	50.5	17.5	3.80			
	31.5	16.2	3.40	52.1	17.3	3.75			
	32.5	16.2	3.34	53.7	17.2	3.67			
	23.0	17.1	3.80	40.0	17.8	4.00	65.8	26.2	4.18
	24.5	16.8	3.81	41.5	17.6	3.87	70.2	25.7	4.00
	25.4	16.4	3.86	42.9	17.3	3.89	74.9	25.6	3.97
$N=5$ rows	26.2	16.5	3.90	44.6	17.0	3.82	77.3	25.5	3.89
	27.6	15.8	3.88	46.2	16.7	3.76	79.6	25.1	3.87
	28.6	16.0	4.00	47.6	16.7	3.72	84.6	24.6	3.81
	30.6	15.9	4.10	49.2	16.5	3.78			
	31.5	15.7	3.94	50.7	16.4	3.69			

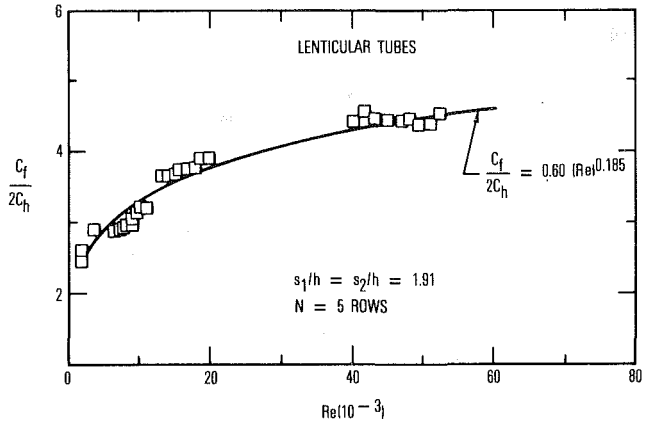

Fig. 9 $C_f/2C_h$ versus Re extended Reynolds number for $S_1 = s_2 = 1.91\ h$, $N = 5$

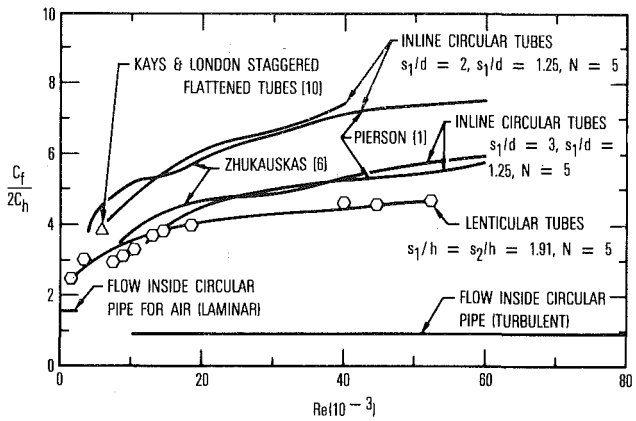

Fig. 10 Comparison of different types of heat exchangers

changer over another, but, information on the arrangements investigated will be compared with the available data for more conventional types of similar size.

Calculations based on the data [1, 6] for circular cylinders in staggered and inline arrangements show that staggered layouts have high Stanton numbers, but also very high pressure loss coefficients, so that the ratio of $C_f/2C_h$ turns out to be lower for inline arrangements, although the latter have lower values of C_h. For this reason, the inline arrangement was used as a standard for comparison with the lenticular shaped tubes.

Figure 10 is a comparison of these data with the results for lenticular tube heat exchanger. The hexagons represent the experiment described previously for $s_1 = s_2 = 1.91\ h$ and 5 rows. This was the arrangement with the lowest values of $C_f/2C_h$. The ratio of frontal area to minimum free area, $A/A_{\min}$, was 1.52 and the value of S/A was 14.3

For comparison an inline bank of circular tubes with a transverse spacing of $s_t/d = 3$, a longitudinal spacing $s_l/d = 1.25$, and corrected for 5 rows was picked since it has the lowest values of $C_f/2C_h$ appearing in Pierson's data. For this configuration, $S/A = 5.24$, $A/A_{\min} = 1.50$.

At the higher Reynolds numbers, the lenticular tubes are about 20 percent better than the circular tubes. The lenticular tubes have higher surface area/frontal area and are much more compact.

Besides the inline tube data of Pierson and Zhukauskas, Fig. 10 includes data from Kays and London [10] for a staggered arrangement of oval tubes made of flattened circular cylinders.[4] This arrangement is similar to the lenticular tube heat exchanger but has larger variations of nominal velocity in the tube bank. Information is available only for one spacing with $A/A_{\min} = 2.59$ and a surface area per unit volume of 354 m^2/m^3. The tubes were 8-mm long, 3.2-mm thick and had a transverse spacing of 5.6 mm and longitudinal spacing of 8.7 mm.

For reference, the plot for turbulent flow of air inside a circular pipe is shown. This plot is simply the result of Reynolds analogy using the mean velocity as a reference of $C_f/2C_h = \mathrm{Pr} = 0.7$ for air.

Conclusion

The purpose of these experiments was to investigate the performance of an unconventional crossflow heat exchanger configuration to determine if it might lead to a decrease in the pressure loss of the flow through the heat exchanger for a given heat transfer rate. As stated earlier, it is difficult to compare different types of heat exchangers without considering their intended applications. In this investigation, the ratio of friction coefficient to heat transfer coefficient in the form $C_f/2C_h$ was chosen as a figure of merit to be used in comparing different geometries of both forced and natural draft heat exchangers, since it takes into account both pressure loss and heat transfer rate.

The experiments considered lenticular shaped tubes spaced so that the flow area between them was nearly constant through the tube bank and gave lower values of $C_f/2C_h$ than conventional heat exchangers with tubes of circular cross section, especially for Re = 20,000 to 50,000. The better performance of the lenticular tubes compared with circular tubes must be balanced against the disadvantage of a shape that may be more difficult to manufacture and to install in a device (i.e., it is more difficult to design headers for odd shaped tubes). Also, the lenticular shape is not as good a pressure vessel as a circular tube.

[4] All the data of Pierson [1], Zhukauskas [6], and Kays and London [10] have been recomputed based on $2s_1$, (the minimum spacing between tubes) as the characteristic length to conform with the lenticular tube data.

Acknowledgment

This investigation was supported by the U.S. Department of Energy under Contract EX 76-G-OJ-1305 with the California Institute of Technology. The author wishes to express his thanks for this support and to Professor W. D. Rannie, who suggested the investigation and gave advice during its execution.

References

1 Pierson, O., "Experimental Investigation of Influence of Tube Arrangement on Convection Heat Transfer and Flow Resistance in Crossflow of Gases Over Tube Banks," ASME *Transactions*, Vol. 59, 1937, pp. 563-572.

2 Huge, E., "Experimental Investigation of Effects of Equipment Size of Convection Heat Transfer and Flow Resistance in Crossflow of Gases Over Tube Banks," ASME *Transactions*, Vol. 59, 1937, pp. 573-582.

3 Grimison, E., "Correlation and Utilization of New Data on Flow Resistance and Heat Transfer for Crossflow of Gases Over Tube Banks," ASME *Transactions*, Vol. 59, 1937, pp. 583-594.

4 Fishenden, M., and Saunders, O., *An Introduction to Heat Transfer*, Clarendon Press, Oxford, 1950, pp. 132-145.

5 Jakob, M., "Heat Transfer and Flow Resistance in Crossflow of Gases Over Tube Banks," ASME *Transactions*, Vol. 60, 1938, pp. 384-380.

6 Zhukauskas, A., *Heat Transfer in Banks of Tubes in Crossflow of Fluid*, Mintis, Vilnius, Lithuania, 1968.

7 Kays, W., and Lo, R., "Basic Heat Transfer and Flow Friction Design Data for Gas Flow Normal to Banks of Staggered Tubes—Use of a Transient Technique," TR No. 15, Mechanical Engineering Department, Stanford University, 1952.

8 Kays, W., "Basic Heat Transfer and Flow Friction Design Data for Gas Flow Normal to Banks of In-line Circular Tubes—Use of a Transient Technique," TR No. 21, Mechanical Engineering Department, Stanford University, 1954.

9 Ruth, E., "Experiments With Unconventional Crossflow Heat Exchangers," PhD thesis, California Institute of Technology, 1981.

10 Kays, W., and London, A., *Compact Heat Exchangers*, McGraw-Hill Book Company, New York, 1964, p. 165.

Analysis of Mechanical-Draught Counterflow Air/Water Cooling Towers

J. W. Sutherland
Experimental Officer,
Agricultural Engineering Group,
Commonwealth Scientific and
Industrial Research Organization,
Highett, Victoria, Australia 3190

This paper compares an accurate analysis of mechanical draught counterflow cooling towers, including water loss by evaporation, with the approximate common method based on enthalpy driving force developed by Merkel in 1925. Computer programs were developed for both the accurate analysis (TOWER A) and the approximate analysis (TOWER B). Substantial underestimates of tower volume of from 5 to 15 percent are obtained when the approximate analysis is used, indicating the possibility of quite serious consequences as far as cooling tower design is concerned. Computer predictions of cooling tower integral are shown to compare well with published values.

1 Introduction

The function of the cooling tower is to reduce the temperature of circulating water so that it may be reused in condensers and other heat exchange equipment. Mechanical draught counterflow cooling towers are found principally in air conditioning applications. Air can be either blown upward through the tower with the fan at the bottom (forced draught), or drawn upwards through the tower with the fan at the top (induced draught). Most towers contain a fill of some type which retards the rate of water fall and increases the water surface exposed to the air. Eliminator plates are generally placed at the air outlet to minimize drift or carryover of liquid water in the exhaust air.

The basic theory of cooling tower operation was first proposed in 1923 by Walker et al. [1]. However, the first practical use of the differential equations was developed by Merkel in 1925 [2]. He combined the equations for heat and water vapor transfer and used enthalpy as the driving force to allow for both sensible and latent heat transfer. Heat is removed from the water by a transfer of sensible heat due to a difference in temperature levels and by the latent heat equivalent of the mass transfer resulting from the evaporation of a portion of the circulating water. Merkel combined these into a single process based on enthalpy difference as the driving force.

The theory used by Merkel requires two main assumptions, namely, that the water loss by evaporation is neglected and that the Lewis number for air/water vapor systems is unity. The theory states that all of the heat transfer taking place at any position in the tower is proportional to the difference between the enthalpy of air saturated at the temperature of the water at that point in the tower and the enthalpy of the air at that point in the tower. Quantitative treatment of cooling tower performance by dealing with heat and mass transfer separately is very laborious. Therefore the simplifying approximation of Merkel's enthalpy theory has been almost universally adopted for the calculation of tower performance.

Merkel's differential equation for the cooling tower was redeveloped by Nottage [3] and converted to a graphical method of solution by Lichtenstein [4]. Another graphical procedure, for determining the air process line in a cooling tower, was suggested by Mickley [5]. Simpson and Sherwood [6] carried out experimental studies on several small-scale cooling towers, and examined the dependence of the mass transfer coefficient on the various air and water properties. Carey and Williamson [7] extended Merkel's theory to be applicable to gas cooling and humidification, and proposed the Stevens diagram (devised by W. L. Stevens) for the solution of the cooling tower integral necessary for determining the required volume of a tower. Baker and Shryock [8] reviewed Merkel's work and examined the effects of some of the approximations. Further theoretical work on cooling towers has been carried out by Berman [9], Hsu et al. [10], Threlkeld [11], Yadigaroglu and Pastor [12], and Whillier [13]. Extensive sets of curves for cooling tower design, based on Merkel's theory, have been prepared by the American Society of Heating, Refrigerating and Air Conditioning Engineers [14].

As far as the author is aware, however, no detailed computer study has been made of the underestimation of cooling tower volume introduced if Merkel's approximate analysis is used, and this is the main aim of this paper. Digital computer analysis also makes easy determination of the effects of variation of operating parameters—e.g., atmospheric pressure—on cooling tower design and performance.

2 Theory

2.1 Accurate Analysis. Consider the direct contact of moist air and water in counter flow over the differential volume element, dV, (control volume HCDG) as shown in Fig. 1. It is assumed that water loss by drift and heat transfer through the walls of the tower are negligible, and that steady-flows conditions apply.

A mass balance for water over the element dV gives rise to the following two relationships

$$dm_w = m_a dw \tag{1}$$

and

$$m_w = m_{w1} - m_a(w_2 - w) + m_a dw \tag{2}$$

A heat balance over dV gives

$$m_a dh = [m_{w1} - m_a(w_2 - w)]dh_{fw} + m_a h_{fw} dw \tag{3}$$

Consider now the rate equations for mass and heat transfer. Firstly, the rate of evaporation of water in the element dV can be expressed as

$$m_a dw = h_d A_v dV(w_{sw} - w) \tag{4}$$

Yadigaroglu and Pastor [12] use water vapor density difference as the driving force for mass transfer citing Rohsenow and Choi [15]. However, Rohsenow and Choi suggest that if the mixture density is not uniform then it is preferable to use mass fraction. This is confirmed by Spalding

Contributed by the Heat Transfer Division for publication in the JOURNAL OF HEAT TRANSFER. Manuscript received by the Heat Transfer Division January 12, 1982.

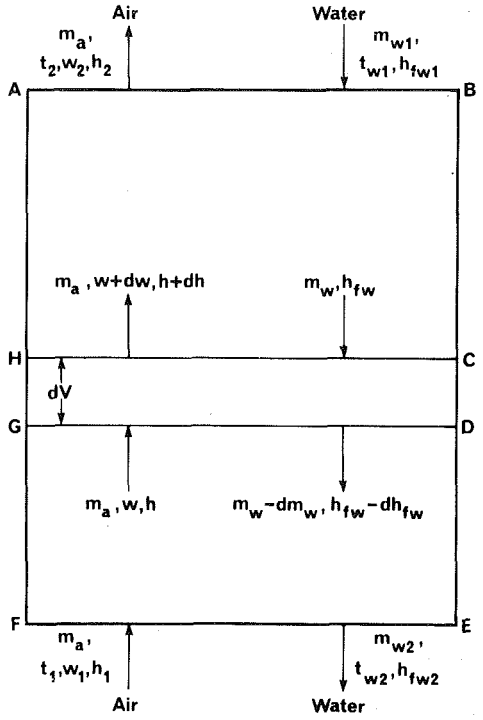

Fig. 1 Schematic diagram of a counterflow cooling tower

[16] who derives an expression for mass transfer which can be shown to be equivalent to equation (4), noting that mass fraction is equal to $w/(1 + w)$. Equation (4) is the same formulation as used by Baker and Shryock [8], Threlkeld [11] and Maclaine-cross and Banks [17], and experimental values of the mass transfer coefficient, $h_d A_v$, [kg water/(m^{3}s) (kg water/kg dry air)] for cooling towers are available in the literature e.g., [11, 26].

Integration of equation (4) between the bottom and the top of the tower gives the required tower volume as follows

$$V = \frac{m_a}{h_d A_v} \int_{w_1}^{w_2} \frac{dw}{w_{sw} - w} \tag{5}$$

Secondly, heat is lost by the water by convection and evaporation, leading to the equation

$$m_a dh = h_c A_v dV (t_w - t) + h_d A_v dV (w_{sw} - w) h_{gw} \tag{6}$$

Equation(6), as used by Maclaine-cross and Banks [17], employs the enthalpy of water vapor at the water temperature, t_w (h_{gw}), instead of the latent heat of vaporization of water at temperature, t_w (h_{fgw}), to allow for the sensible heat of the water above a datum level of 0°C ($h_{fw} = c_w t_w$), noting that $h_{gw} = h_{fw} + h_{fgw}$.

Using the Lewis relation $\mathrm{Le}_c = h_c / h_d c_{ma}$ (ASHRAE [18], Close and Banks [19]) and dividing equation (6) by equation (4), it can be shown that

$$\frac{dh}{dw} = \frac{\mathrm{Le}_c c_{ma} (t_w - t)}{w_{sw} - w} + h_{gw} \tag{7}$$

Defining the enthalpy of moist air, h, as $c_{ma} t + h_{go} w$ (see section 3), it can be shown that

$$c_{ma} (t_w - t) = (h_{sw} - h) - h_{gw} (w_{sw} - w) \tag{8}$$

noting that c_{ma} is not taken as a constant.

Substitution from equation (8) into equation (7) then gives

$$\frac{dh}{dw} = \mathrm{Le}_c \left(\frac{h_{sw} - h}{w_{sw} - w} \right) + h_{gw} (1 - \mathrm{Le}_c) \tag{9}$$

Now by dividing both sides of equation (3) by $m_a dw$, and using $dh_{fw}/dw = c_w dt_w/dw$, it can be shown that

$$\frac{dt_w}{dw} = \frac{\dfrac{dh}{dw} - h_{fw}}{c_w \left[\dfrac{m_{w1}}{m_a} - (w_2 - w) \right]} \tag{10}$$

2.2 Approximate Analysis. In the analysis developed by Merkel in 1925 [2] and still used largely today, the water loss by evaporation is neglected and the Lewis number is taken as unity.

Performing a similar derivation as in section 2.1, and taking m_w as constant and Le_c equal to 1, leads to the following relationships

$$\frac{dh}{dt_w} = \frac{m_w c_w}{m_a} \tag{11}$$

$$m_a dh = h_d A_v dV (h_{sw} - h) \tag{12}$$

from which tower volume is given by

$$V = \frac{m_w c_w}{h_d A_v} \int_{t_{w2}}^{t_{w1}} \frac{dt_w}{h_{sw} - h} \tag{13}$$

and

$$\frac{dh}{dt} = \frac{h_{sw} - h}{t_w - t} \tag{14}$$

Nomenclature

A = approach ($t_{w2} - t_1^*$), K
A_v = surface area of water droplets per unit volume of tower, m^2/m^3
c_a = specific heat of dry air at constant pressure, J/(kg K)
c_{ma} = specific heat of moist air at constant pressure ($c_a + c_v w$), J/(kg dry air) (K)
c_v = specific heat of water vapor, J/(kg K)
c_w = specific heat of liquid water, J/(kg K)
E = error in tower volume if the approximate analysis is used [$100(1 - V_b/V_a)$], %
h = enthalpy of moist air, J/kg dry air
h_c = convective heat transfer coefficient, W/(m^{2}K)
h_d = convective mass transfer coefficient, kg water/(m^{2}s) (kg water/kg dry air)
h_{fgw} = latent heat of vaporization of water at the water temperature t_w, J/kg
h_{fw} = enthalpy of liquid water at the water temperature t_w, J/kg
h_{go} = enthalpy of water vapor at 0°C, J/kg
h_{gw} = enthalpy of water vapor at the water temperature t_w, J/kg
h_{sw} = enthalpy of saturated moist air at the water temperature t_w, J/kg dry air
Int_a = accurate tower integral $\left(\int_{w_1}^{w_2} \dfrac{dw}{w_{sw} - w} \right)$, dimensionless
Int_b = approximate tower integral $\left(\int_{t_{w2}}^{t_{w1}} \dfrac{dt_w}{h_{sw} - h} \right)$, K/(J/kg dry air)
Le_c = convective Lewis number for moist air ($h_c / h_d c_{ma}$), dimensionless
m_a = mass flow rate of dry air, kg/s
m_w = mass flow rate of water, kg/s
M_a = molecular weight of dry air, kg/mole
M_w = molecular weight of water vapor, kg/mole

Yadigaroglu and Pastor [12] make four other assumptions (in addition to $dm_w = 0$ and $\mathrm{Le}_c = 1$) to arrive at Merkel's formulation; all of these are unnecessary in the present analysis.

The process lines and operating states in the cooling tower for this case are shown by an enthalpy temperature diagram (Fig. 2). The operating lines for air and water are shown respectively by AB and CD. The enthalpy difference $h_{sw} - h$ at a typical point in the tower where the water temperature is t_w is given by EF. The air and corresponding saturated air enthalpies at both ends of the tower are also shown. The slope of the air operating line is found from equation (11), and the limiting value of m_w/m_a is seen to occur when $h \geq h_{sw}$. Similarly, w_{sw} must be greater than w in the accurate analysis.

3 Properties of Moist Air

In order to carry out the cooling tower analysis, mathematical expressions for the properties of the dry air/water vapor mixture are required, and these are established using ideal gas relationships as described by Sutherland [20].

The saturation vapor pressure of water is calculated by the empirical equation of Keenan and Keyes [21] as follows

$$p_s = a/\exp\left[\frac{bX(c+dX+eX^3)}{(f-X)(1+gX)}\right] \tag{15}$$

where $X = 673.4 - 1.8\,t$, and the values of the constants a to g are given in the Nomenclature.[1]

The actual pressure of water vapor is given by the following ideal gas relationship [22]

$$p = \frac{p_t w}{(M_w/M_a) + w} \tag{16}$$

The enthalpy of moist air, with the datum level for dry air and for liquid water at 0°C, is given with sufficient accuracy over the range of interest [23] by

$$h = c_a t + (c_v t + h_{go})\,w \tag{17}$$

where the values of c_a, c_v, and h_{go} are given in the Nomenclature.

The relationship between temperature and mositure content along a constant thermodynamic wet-bulb temperature or adiabatic saturation line [22] is as follows

$$w = w_s^* - \frac{(c_a + c_v w_s^*)(t - t^*)}{c_v t + h_{go} - c_w t^*} \tag{18}$$

4 Method of Solution

4.1 Accurate Analysis. In order to determine the air and water conditions throughout the cooling tower, equations (9) and (10) must be solved.

Thus

$$\frac{dh}{dw} = \mathrm{Le}_c\left(\frac{h_{sw}-h}{w_{sw}-w}\right) + h_{gw}(1-\mathrm{Le}_c) = f_1(w,h,t_w) \tag{19}$$

and

$$\frac{dt_w}{dw} = \frac{\mathrm{Le}_c\left(\frac{h_{sw}-h}{w_{sw}-w}\right) + h_{gw}(1-\mathrm{Le}_c) - h_{fw}}{c_w\left[\frac{m_{w1}}{m_a} - (w_2 - w)\right]} = f_2(w,h,t_w) \tag{20}$$

These two linear simultaneous differential equations can be solved by a fourth-order Runge-Kutta method [24]. The initial values at the bottom of the tower are w_1, h_1, and t_{w2} (Fig. 1). Thus, the value of the air moisture content, w, is increased in small steps, and the corresponding values of h and t_w are calculated.

Now the value of w_2 is needed in order to solve equation (20), and this value is not known until the top of the cooling tower is reached (Fig. 1). So an iteration technique is used whereby two sensible initial values of w_2 (both greater than w_1) are selected, the air and water process lines are generated ending at the top of the tower at the correct inlet water temperature, and two values of error between the set value of w_2 and the calculated value (for the process line) are obtained. A new value of w_2 is then calculated from these two error values (using linear extrapolation), and the process is continued until sufficient accuracy (within 0.00001 kg water/kg dry air) is obtained for w_2.

To calculate the cooling tower volume from equation (5), the integral is solved by a four-point Gaussian Quadrature technique [25].

4.2 Approximate Analysis. To determine the air and water process lines in this case, it is necessary to solve equations (11) and (14).

Thus

Nomenclature (cont.)

Ntu_a = number of transfer units for accurate analysis (Int_a), dimensionless
Ntu_b = number of transfer units for approximate analysis ($c_w \mathrm{Int}_b$), dimensionless
p = pressure of water vapor, Pa
p_s = saturation pressure of water vapor at the air dry-bulb temperature t, Pa
p_t = total pressure of the dry air/water vapor mixture, Pa
R = range ($t_{w1} - t_{w2}$), K
t = dry-bulb temperature of moist air, °C
t^* = thermodynamic wet-bulb temperature of moist air, °C
t_w = temperature of water, °C
V = volume of cooling tower, m³; V_a for accurate analysis (equation (5)), V_b for approximate analysis (equation (13))
w = moisture content of moist air, kg water/kg dry air
w_s^* = moisture content of saturated moist air at the air thermodynamic wet-bulb temperature t^*, kg water/kg dry air
w_{sw} = moisture content of saturated moist air at the water temperature t_w, kg water/kg dry air

Subscripts[2]

1 = inlet states (bottom of tower, air; top of tower, water)
2 = outlet states (top of tower, air; bottom of tower, water)

[1] Constants: equation (15): $a = 2.210584 \times 10^7$, $b = 2.302585$, $c = 3.2437814$, $d = 3.26014 \times 10^{-3}$, $e = 2.00658 \times 10^{-9}$, $f = 1.16509 \times 10^3$, $g = 1.21547 \times 10^{-3}$. Equation (16): $M_w/M_a = 0.622$. Equations (17) and (18): $c_a = 1.0048 \times 10^3$ J/(kg K), $c_v = 1.8003 \times 10^3$ J/(kg K), $c_w = 4.1868 \times 10^3$ J/(kg K), $h_{go} = 2.50268 \times 10^6$ J/kg.

[2] See Fig. 1.

$$\frac{dt}{dh} = \frac{t_w - t}{h_{sw} - h}$$
$$= f_1(h, t, t_w) \tag{21}$$

and

$$\frac{dt_w}{dh} = \frac{m_a}{m_w c_w}$$
$$= f_2 \text{ (constant)} \tag{22}$$

Equations (21) and (22) are also solved by a fourth-order Runge-Kutta method with initial values h_1, t_1, and t_{w2}. In this case, the value of the air enthalpy, h, is incremented and the corresponding values of t and t_w are calculated.

The integral in equation (13) is also solved by four-point Gaussian Quadrature. Since t_w varies linearly with h (equation (22)), the tower volume can be calculated without determining the air process line and so is not affected by the Runge-Kutta routine.

5 Extension to Chilled Spray Dehumidifiers

In the case of the cooling tower, the aim of the process is to cool the inlet water to the tower so that it may be reused. This means that the inlet water temperature at the top of the tower t_{w1} is always higher than the outlet water temperature at the bottom of the tower t_{w2}. However, it is also possible to cool and dehumidify moist air by direct contact with cold water in such a tower, and in this case t_{w1} is lower than t_{w2}. Cool air leaving the chamber can be circulated to areas which are to be conditioned. The practical application for this type of process, however, is not great in comparison to heat exchangers using extended surfaces. The analysis and solution for the spray dehumidifier are exactly the same as for the cooling tower.

6 Results and Discussions

It is now necessary to compare the values of the cooling tower integral calculated by both the accurate analysis (computer program TOWER A) and the approximate analysis (computer program TOWER B). Initially, to cover a wide range of operating conditions in broad steps, the values given in Table 1 were used [14]. These twelve combinations were used with four values of m_{w1}/m_a, namely, 0.5, 1.0, 1.5, and 2.0, keeping m_a at 10 kg/s throughout. The value of atmospheric pressure, p_t, was taken as the standard value of 101 325 Pa. The convective Lewis number, Le_c, was set at a value of 0.9 for program TOWER A [11, 18]. The cooling tower integral is independent of the value of the mass transfer coefficient, h_d, (see equations (5) and (13)). However, in order to compare the integrals directly between programs TOWER A and TOWER B, a typical value of 0.5 kg/(m^{3}s) was taken for $h_d A_v$ [11, 26], and the values of tower volumes V_a and V_b compared.

A study of the sensitivity of program TOWER A was carried out, and it was found that values of step size in air moisture content of 0.0001 and 0.00001 kg water/kg dry air gave values of the cooling tower integral Int_a within 1 part in 5000 over the range of conditions considered in this paper. A step size of 0.0001 kg water/kg dry air was thus sufficiently small, being changed to 0.00001 kg water/kg dry air only when t_w was within 0.1°C of t_{w1}, to enable finer resolution at the top of the tower. For program TOWER B (Merkel's method), the value of Int_b is unaffected by the Runge-Kutta routine, as explained in section 4.2. The step size in air enthalpy for program TOWER B was set at 100 J/kg dry air, and changed to 10 J/kg dry air when t_w was within 0.1°C of t_{w1}.

The effect of variation of the inlet air dry-bulb temperature, t_1, on the cooling tower integral based on the accurate analysis (Int_a) can be established from the runs in Table 1 for a value of t_1^* of 20°C (Runs 2, 3, 4, 8, 9 and 10), and the results are given in Table 2. The effect of t_1 is thus seen to be fairly small, being a maximum of 1.3 percent for the range of conditions tried, and decreasing with increasing value of m_{w1}/m_a. Also, the smaller the wet-bulb depression $(t_1 - t_1^*)$ the larger the value of Int_a, and for design purposes the lower value of $t_1 - t_1^*$ is therefore preferable to achieve a margin of safety. For the remainder of this work, a wet-bulb depression of 5 K is used.

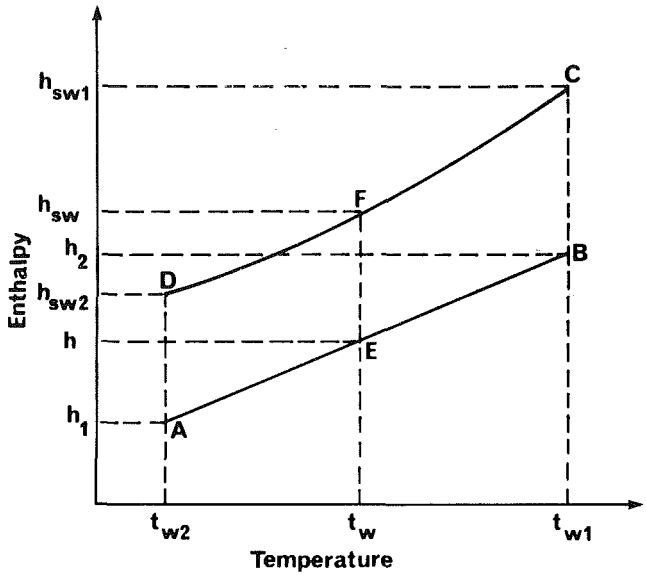

Fig. 2 Approximate analysis of a counterflow cooling tower depicted on an enthalpy temperature diagram

Table 1 Initial operating conditions for runs of computer programs TOWER A and TOWER B

Run	t_1^* °C	t_1 °C	t_{w1} °C	t_{w2} °C	A $(t_{w2} - t_1^*)$ K	R $(t_{w1} - t_{w2})$ K
1	30	35	50	40	10	10
2	20	25	50	40	20	10
3	20	25	40	30	10	10
4	20	25	50	30	10	20
5	10	15	50	40	30	10
6	10	15	40	30	20	10
7	10	15	50	30	20	20
8	20	35	50	40	20	10
9	20	35	40	30	10	10
10	20	35	50	30	10	20
11	30	35	60	50	20	10
12	30	35	60	40	10	20

The results for the first seven sets of conditions in Table 1 are shown in Figs. 3 and 4. As the ratio m_{w1}/m_a increases at a fixed value of m_a and fixed air and water states, the same quantity of air is required to cool more water. Thus the tower volumes increase (Fig. 4), and the percentage error, E, (i.e., the underestimation of tower volume if the approximate analysis is used) also increases (Fig. 3). This means that the effect of water loss by evaporation is more important the higher the water flow rate. It should be remembered that the value of m_w/m_a reduces from the top to the bottom of the tower for program TOWER A (Fig. 1), whereas it is a constant for program TOWER B. The value of V_a is obtained from Int_a by multiplying by m_a and dividing by $h_d A_v$ (equation (5)), i.e., multiplying Int_a by 20 in this particular case. Values of V_a can of course be calculated from Int_a for any other values of m_a and $h_d A_v$.

From Fig. 3, it can be seen that for a value of m_{w1}/m_a of

0.5 the range of errors in tower volume experienced is from 5.4 to 7.2 percent (average 6.4 percent); for 1.0 from 6.4 to 7.6 percent (average 7.0 percent); for 1.5 from 7.5 to 8.4 percent (average 8.0 percent); and for m_{w1}/m_a equal to 2.0 the range of values of E is from 8.4 to 14.2 percent (average 10.3 percent). The overall average error for the four values of m_{w1}/m_a is 7.9 percent. There is no special significance in the crossing over of some of the error curves in Fig. 3. It can be explained by the behaviour of the difference $w_{sw} - w$ in the accurate analysis in relation to that of $h_{sw} - h$ in the approximate analysis, and the effects on the respective integrals Int_a (equation (5)) and Int_b (equation (13)).

Runs 11 and 12 in Table 1 were carried out to check the effect on tower volume of a high inlet water temperature 60°C. For values of m_{w1}/m_a of 0.5, 1.0, 1.5, and 2.0, the volume errors ranged from 8.3 to 9.3 percent for Run 11 and from 6.5 to 9.3 percent for Run 12, thus giving a similar average error to the other runs.

A number of conclusions regarding cooling tower behaviour at a fixed value of m_{w1}/m_a can be drawn from Fig. 4 as follows:

1 For the same range and approach, the higher the wet-bulb temperature the smaller the tower: i.e., Int_a (1) < Int_a (3) and Int_a 2 < Int_a (6). (The numbers in parenthesis refer to the appropriate set of conditions in Table 1.)

2 For the same wet-bulb temperature and range, the larger

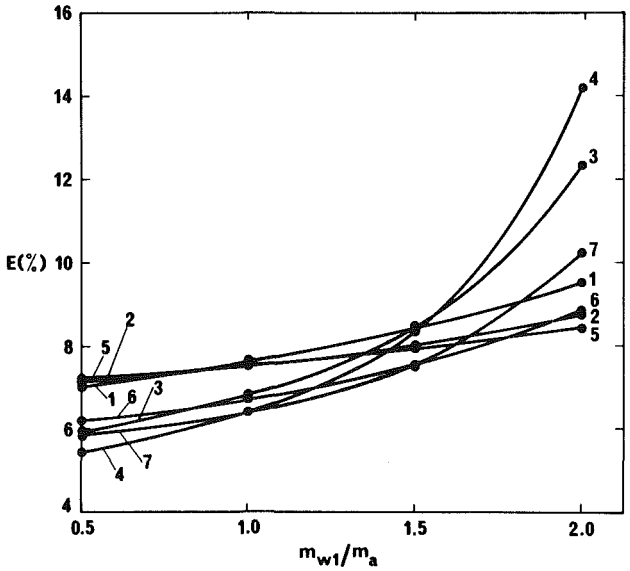

Fig. 3 Variation of tower volume error with water to air mass flow rate ratio for initial cooling tower runs. The number of each curve refers to the run number in Table 1

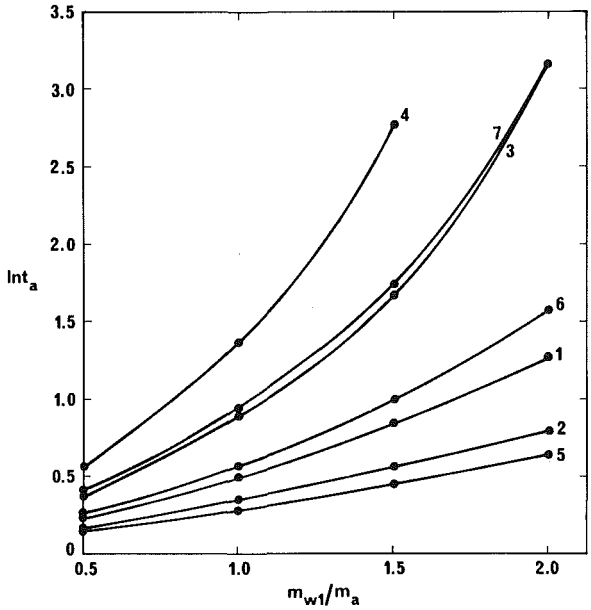

Fig. 4 Variation of accurate tower integral with water to air mass flow rate ratio for initial cooling tower runs. The number of each curve refers to the run number in Table 1

Table 2 Effect of inlet air dry-bulb temperature on cooling tower integral

m_a kg/s	m_{w1} kg/s	t_{w1} °C	t_{w2} °C	t_1 °C	t_1^* °C	Int_a	Difference[a] %
10	5	50	40	35	20	0.1564	
				25		0.1571	0.45
	10			35		0.3349	
				25		0.3364	0.45
	15			35		0.5421	
				25		0.5445	0.44
	20			35		0.7884	
				25		0.7917	0.42
10	5	50	30	35	20	0.5457	
				25		0.5517	1.09
	10			35		1.3509	
				25		1.3632	0.90
	15			35		2.7478	
				25		2.7657	0.65
	20			35		6.3363	
				25		6.3594	0.36
10	5	40	30	35	20	0.3671	
				25		0.3720	1.32
	10			35		0.8683	
				25		0.8789	1.21
	15			35		1.6353	
				25		1.6513	0.97
	20			35		3.1366	
				25		3.1525	0.50

[a]The percentage difference is based on the value of t_1 of 25°C.

the approach the smaller the tower: i.e., Int_a (2) < Int_a (3) and Int_a (5) < Int_a (6).

3 For the same wet-bulb temperature and approach, the larger the range the larger the tower: i.e., Int_a (3) < Int_a (4) and Int_a (6) < Int_a (7).

4 For the same initial and final water temperatures, the lower the inlet air wet-bulb temperature the smaller the tower: i.e., Int_a (5) < Int_a (2) < Int_a (1), Int_a (6) < Int_a (3) and Int_a (7) < Int_a (4).

The results in Fig. 4 which are not obvious, e.g., cooling water from 50 to 40°C with an inlet air wet-bulb temperature of 30°C (1) requiring a smaller tower than for cooling water from 40 to 30°C at 10°C wet-bulb temperature (6), and also cooling water from 40 to 30°C at 20°C wet-bulb temperature (3) requiring a smaller tower than for cooling water from 50 to 30°C at 10°C wet-bulb temperature (7), can be explained by the behaviour of the difference $w_{sw} - w$ and its effect on Int_a. The explanation is more readily understandable in terms of the enthalpy driving force $h_{sw} - h$ and thus Int_b, which are encountered in the approximate analysis (Fig. 2).

A series of computer runs was then carried out which relate more typically to Australian air conditioning applications of cooling towers, and operating conditions for these are given in Table 3. The design ambient air states were taken from the Australian Department of Housing and Construction air conditioning systems design manual [27]. Perth has approximately the same design wet-bulb temperature as Brisbane and Sydney but has a design dry-bulb temperature of 35°C instead of 30°C [27]. As shown previously, it is safer to use the lower value of $t_1 - t_1^*$ for design purposes. Similarly, Melbourne and Adelaide have about the same design t_1^* as Hobart but a design t_1 of 35°C instead of 25°C [27].

The five sets of conditions given in Table 3 were used with five values of m_{w1}/m_a, namely 0.5, 1.0, 1.5, 2.0, and 2.5. As before m_a, p_t, Le_c, and $h_d A_v$ were set at 10 kg/s, 101 325 Pa, 0.9 and 0.5 kg/(m^{3}s), respectively. The results are shown in Figs. 5 and 6, where it is seen as before that the cooling tower integral, and thus the tower volume, and also the percentage volume error all increase as the value of m_{w1}/m_a is increased. The values of E range from 5.8 to 15.2 percent with an average of 8.3 percent. For Runs 1, 2, and 5 which give values of Int_a at the five values of m_{w1}/m_a, the average errors are 6.3, 6.8, 7.7, 9.1, and 11.8 percent, respectively. The four conclusions referred to earlier regarding cooling tower behaviour can be seen to apply again.

The behaviour of tower outlet air relative humidity with variation of m_{w1}/m_a was examined for Runs 3 and 5 in Table 3, which both cooled water from 35 to 30°C. For Run 3, the inlet air relative humidity was 67.0 percent, and the outlet air relative humidities were 78.4, 88.0, 95.4, and 99.7 percent, for values of m_{w1}/m_a of 0.5, 1.0, 1.5, and 2.0, respectively. For Run 5, the inlet air relative humidity was 63.5 percent, and the outlet air relative humidities were 75.4, 84.8, 91.9, 96.9, and 99.9 percent, for values of m_{w1}/m_a of 0.5, 1.0, 1.5, 2.0, and 2.5, respectively. The corresponding outlet air dry-bulb temperatures are 30.67, 31.45, 32.39, and 33.61°C for Run 3 (t_1 = 30°C), and 26.37, 27.77, 29.21, 30.69, and 32.24°C for Run 5 (t_1 = 25°C).

The effect of variation in atmospheric pressure, p_t (from 91.4 to 105.0 kPa, i.e. from 27 to 31 inches of mercury) on cooling tower performance was examined for the case of cooling water from 35 to 30°C with air of wet-bulb temperature 25°C and dry-bulb temperature 30°C (Run 3 in Table 3). The results are given in Table 4 where it can be seen that the values of Int_a increase with increasing value of p_t. As p_t increases, the value of $w_{sw} - w$ decreases and thus the value of Int_a increases (see equation (5)). The underestimation of tower volume provided by the approximate analysis again increases with increasing value of m_{w1}/m_a, but increasing p_t at each value of m_{w1}/m_a only slightly increases the value of E. The recommended procedure for design purposes should therefore be to use the largest value of p_t likely to be encountered in practice, so that the cooling tower would give slightly better performance (i.e., lower final water temperature) for lower values of p_t (e.g., at higher altitudes).

As a check on the accuracy of the computer predictions, some comparisons were made with published values of cooling tower integrals, as shown in Table 5. Firstly, values of Ntu_b given by Baker and Shryock [8] are in excellent agreement with those calculated by computer program TOWER B. Secondly, values of Ntu_a calculated by two methods for worked example 11.2 in Threlkeld [11] are within approximately 2 percent of the value determined by program TOWER A. The latter value would be expected to be more accurate because of the much greater precision involved in the computer solution, and also because of some approximations made in the analysis by Threlkeld even though Lewis number and evaporation of water effects were included.

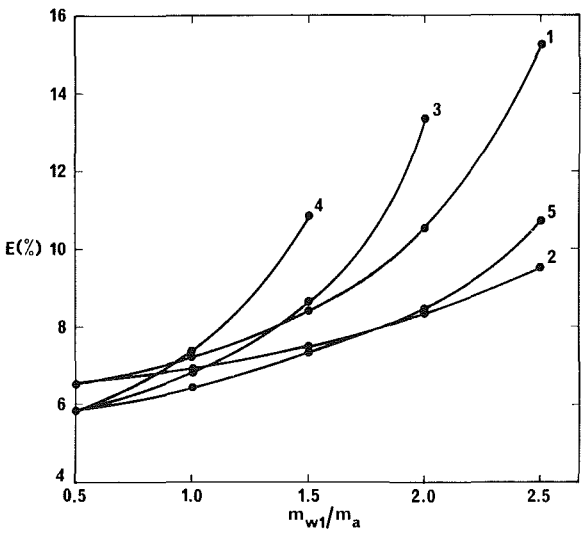

Fig. 5 Variation of tower volume error with water to air mass flow rate ratio for Australian air conditioning cooling tower runs. The number on each curve refers to the run number in Table 3

Table 3 Runs of programs TOWER A and TOWER B for Australian air conditioning applications

Location	Run	t_1^* °C	t_1 °C	t_{w1} °C	t_{w2} °C	$\frac{A}{(t_{w2}-t_1^*)}$ K	$\frac{R}{(t_{w1}-t_{w2})}$ K
Darwin	1	30	35	40	35	5	5
Brisbane	2	25	30	40	35	10	5
Sydney	3	25	30	35	30	5	5
	4	25	30	40	30	5	10
Hobart	5	20	25	35	30	10	5

7 Conclusions

It has been shown in this work that counterflow cooling towers can be significantly undersized if the approximate analysis, which was developed by Merkel in 1925 and which is still used today, is employed. For an extensive series of runs of computer programs TOWER A (accurate analysis) and TOWER B (approximate analysis) errors in tower volume of up to 15 percent were obtained with the average value being approximately 8 percent. Real errors in practice are probably not as great as this, because the mass transfer coefficient is generally determined experimentally from small-scale tests and use of the approximate analysis. Consequently, this coefficient will be somewhat low, thus increasing subsequent estimates of tower volume. It is suggested, however, that previous and future experimental results could be analysed using program TOWER A, thus eliminating the errors involved in Merkel's theory.

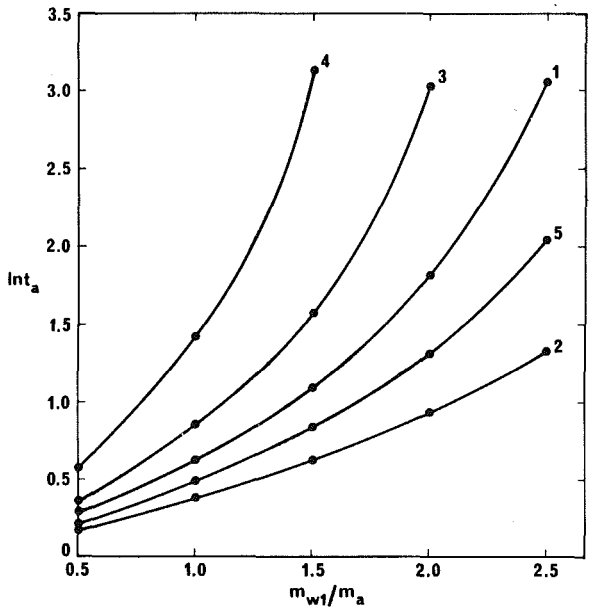

Fig. 6 Variation of accurate tower integral with water to air mass flow rate ratio for Australian air conditioning cooling tower runs. The number on each curve refers to the run number in Table 3

The results presented in this paper cover a wide range of air conditioning applications of cooling towers and should be of real value for design purposes. The accurate thermodynamic predictions apply generally and not to one particular tower and packing. The thermodynamic model can then be combined with air flow rate determination and prediction of pressure drop through various types of tower packing to provide a complete design procedure. The two computer programs are available from the author and have sufficient documentation to be run easily by other users. The programs can be easily modified to accommodate any changes desired in the model equations.

Acknowledgments

This work was undertaken as part of the requirement for a M.Eng.Sc. degree at Monash University. The author wishes to express his appreciation to his supervisor, Mr. C. W. Ambrose, for many constructive suggestions. Dr. J. G. van Leersum of CSIRO Division of Energy Technology is also thanked for his valuable comments during the work.

References

1 Walker, W. H., Lewis, W. K., and McAdams, W. H., *Principles of Chemical Engineering*, McGraw-Hill, New York, 1923.

Table 4 Effect of atmospheric pressure on cooling tower performance

m_a	m_{w1}	t_{w1}	t_{w2}	t_1	t_1^*	p_t	Int$_a$	E	Difference in Int$_a$ from value at standard p_t
kg/s	kg/s	°C	°C	°C	°C	Pa		%	%
10	5	35	30	30	25	91 400	0.3176	5.6	−9.8
						98 200	0.3416	5.8	−3.0
						101 325	0.3521	5.8	0.0
						105 000	0.3646	5.8	3.6
	10					91 400	0.7363	6.6	−11.5
						98 200	0.8007	6.7	−3.7
						101 325	0.8318	6.8	0.0
						105 000	0.8671	6.8	4.2
	15					91 400	1.3367	8.0	−14.5
						98 200	1.4897	8.4	−4.7
						101 325	1.5635	8.6	0.0
						105 000	1.6551	8.9	5.9
	20					91 400	2.3607	11.0	−22.0
						98 200	2.7889	12.4	−7.9
						101 325	3.0266	13.3	0.0
						105 000	3.3483	14.5	10.6

Note: A decrease in p_t of 10,000 Pa corresponds to an increase in altitude of approximately 850 m.

Table 5 Comparison of results from programs TOWER A and TOWER B with literature

m_{w1}/m_a	t_{w1}	t_{w2}	t_1	t_1^*	Ntu$_a$ (= Int$_a$) Threlkeld [11]	TOWER A	Ntu$_b$ (= c_wInt$_b$) Baker and Shryock [8]	TOWER B
	°C	°C	°C	°C				
1.2	32.22	26.67	26.67	21.11	26.67		1.053	1.054
1.2	48.89	26.67	26.67	21.11	26.67		2.878	2.886
1.0	37.78	29.44	35.00	23.89	1.162[a]	1.188		
					1.173[b]			

[a] Graphical integration
[b] Stevens diagram

2 Merkel, F., "Verdunstungskühlung," *VDI Forschungsarbeiten*, No. 275, Berlin, 1925.

3 Nottage, H. B., "Merkel's Cooling Diagram as a Performance Correlation for Air-Water Evaporative Cooling Systems," *ASHVE Transactions*, Vol. 47, 1941, pp. 429–448.

4 Lichtenstein, J., "Performance and Selection of Mechanical-Draft Cooling Towers," *ASME Transactions*, Vol. 65, No. 7, 1943, pp. 779–787.

5 Mickley, H. S., "Design of Forced Draft Air Conditioning Equipment," *Chemical Engineering Progress*, Vol. 45, No. 12, 1949, pp. 739–745.

6 Simpson, W. M., and Sherwood, T. K., "Performance of Small Mechanical Draft Cooling Towers," *Refrigerating Engineering*, Vol. 52, No. 6, 1946, pp. 535–543, 574–576.

7 Carey, W. F., and Williamson, G. J., "Gas Cooling and Humidification: Design of Packed Towers from Small-Scale Tests," *Proceedings of the Institution of Mechanical Engineers*, Vol. 163, 1950, pp. 41–53.

8 Baker, D. R., and Shryock, H. A., "A Comprehensive Approach to the Analysis of Cooling Tower Performance," ASME JOURNAL OF HEAT TRANSFER, Vol. 83, No. 3, 1961, pp. 339–350.

9 Berman, L. D., *Evaporative Cooling of Circulating Water*, ch. 2, Pergamon, Oxford, 1961.

10 Hsu, H. L., Davis, G. de Vahl, and Sapsford, C. M., "An Investigation of the Tie Line Method of Cooling Tower Analysis," *ASHRAE Transactions*, Vol. 72, pt. II, 1966, pp. 3.1–3.10.

11 Threlkeld, J. L., *Thermal Environmental Engineering*, Prentice-Hall, Inc., ch. 11, New Jersey, 1970.

12 Yadigaroglu, G., and Pastor, E. J., "An Investigation of the Accuracy of the Merkel Equation for Evaporative Cooling Tower Calculations," ASME Paper No. 74-HT-59, *Proceedings of the AIAA/ASME Thermophysics and Heat Transfer Conference*, Boston, 1974.

13 Whillier, A., "A Fresh Look at the Calculation of Performance of Cooling Towers," *ASHRAE Transactions*, Vol. 82, pt. I, 1976, pp. 269–282.

14 American Society of Heating, Refrigerating and Air Conditioning Engineers, *ASHRAE Handbook and Product Directory—Equipment*, ch. 21, 1975.

15 Rohsenow, W. M., and Choi, H. Y., *Heat, Mass, and Momentum Transfer*, ch. 14, Prentice-Hall, Inc., New Jersey, 1961.

16 Spalding, D. B., *Convective Mass Transfer*, ch. 2, Edward Arnold Ltd, London, 1963.

17 Maclaine-cross, I. L., and Banks, P. J., "A General Theory of Wet Surface Heat Exchangers and its Application to Regenerative Evaporative Cooling," ASME JOURNAL OF HEAT TRANSFER, Vol. 103, No. 3, 1981, pp. 579–585.

18 American Society of Heating, Refrigerating and Air Conditioning Engineers, *ASHRAE Handbook of Fundamentals*, ch. 3, 1972.

19 Close, D. J., and Banks, P. J., "Coupled Heat and Mass Transfer in a Packed Bed with the Lewis Relation not Satisfied," *Chemical Engineering Science*, Vol. 29, No. 5, 1974, pp. 1147–1155.

20 Sutherland, J. W., "The Solution of Psychrometric Problems Using a Digital Computer," *Australian Refrigeration Air Conditioning and Heating*, Vol. 25, No. 4, 1971, pp. 43–49.

21 Keenan, J. H., and Keyes, F. G., *Thermodynamic Properties of Steam*, Wiley, New York, 1936.

22 Wexler, A., and Wildhack, W. A., eds., *Humidity and Moisture—Measurement and Control in Science and Industry*, Vol. 3, *Fundamentals and Standards*, National Bureau of Standards, Reinhold, New York, 1965.

23 Dunkle, R. V., and Norris, D. J., "General Analysis of Regenerative Evaporative Cooling Systems," *Proceedings of the XIIth International Congress of Refrigeration*, Madrid, Vol. IV, 1967, pp. 103–112.

24 Grove, W. E., *Brief Numerical Methods*, Prentice-Hall, Inc., New Jersey, 1966.

25 Lowan, A. N., Davids, N., and Levenson, A., "Table of the Zeros of the Legendre Polynomials of Order 1-16 and the Weight Coefficients for Gauss' Mechanical Quadrature Formula," *Bulletin of the American Mathematical Society*, Vol. 48, 1942, pp. 739–743.

26 Kern, D. Q., *Process Heat Transfer*, ch. 17, McGraw-Hill, New York, 1950.

27 Australian Department of Housing and Construction—Mechanical Engineering Services, *Air Conditioning Systems Design Manual*, ch. 2, Australian Government Publishing Service, Canberra, 1974.

A. Pignotti

G. O. Cordero

Techint S. A.
1001 Buenos Aires,
Argentina

Mean Temperature Difference in Multipass Crossflow

A procedure is developed to obtain analytical expressions for the mean temperature difference in crossflow heat exchangers with arbitrary number of passes and rows per pass. The influence of air mixing, along with different flow arrangements for the tube fluid between passes, is analyzed, both in co- and counter-crossflow.

1 Introduction

Variables in a heat exchanger are usually related through the expressions

$$Q = FUA\Delta T_{lm} = WC(T_I - T_F) = wc(t_F - t_I) \tag{1}$$

where F is a correction factor which accounts for deviations from counterflow. Introducing the dimensionless variables P, R, and N_{tu} defined in the nomenclature, it follows from (1) that

$$F = \chi(R,P)/N_{tu} \tag{2}$$

where

$$\chi(R,P) = (t_F - t_I)/\Delta T_{lm} = \begin{cases} \dfrac{1}{R-1} ln\left(\dfrac{1-P}{1-RP}\right), R \neq 1 \\ P/(1-P), \qquad R = 1 \end{cases} \tag{3}$$

These relations hold for all possible flow arrangements. In addition, for any particular configuration, a functional relation arises between P, R, and N_{tu}, thus allowing F to be expressed only in terms of two independent variables. Assuming some simplifying hypothesis (such as constant heat transfer coefficient and heat capacities, no change of phase, and uniform velocity distribution) many cases have been solved in the literature [1-5].

The present work concentrates on crossflow aircoolers, where the air stream runs perpendicular to successive rows of tubes carrying the hot fluid. The results obtained are, however, also applicable to other crossflow exchangers, in which the tube fluid is the cold one, such as in gas heat recovery applications. Because the equations are not symmetric under the exchange of the temperatures T and t, when dealing with such special cases care should be taken to interpret T always as the tube fluid temperature, and t as the temperature of the fluid outside the tubes. The latter is called "air" in the text, but could be a different gas or any other fluid.

The tubes are arranged in N_P series-connected passes, each consisting of N_R parallel-connected rows (see sketches of Fig. 1). For each type of flow pattern, P is obtained as an explicit function of R and N_{tu}, which, along with equations (1-3), constitutes a complete explicit solution to the heat transfer problem. A simple "regula falsi" iteration technique is used to express the results in terms of other sets of independent variables.

The following mixing assumptions are used. The tube fluid mixes within each tube cross section and has a temperature $T_{(p,q)}(x)$ that is a continuous function of the row coordinate, x, and a discrete function of the pass and row indices, p and q. The extreme cases of the tube fluid completely mixed or unmixed within each pass are found as limiting cases of the solutions obtained here when the number of rows per pass is set equal to one or infinity, respectively. Between passes, three different assumptions are dealt for the tube fluid: completely mixed; unmixed with identical order of the rows; and un-

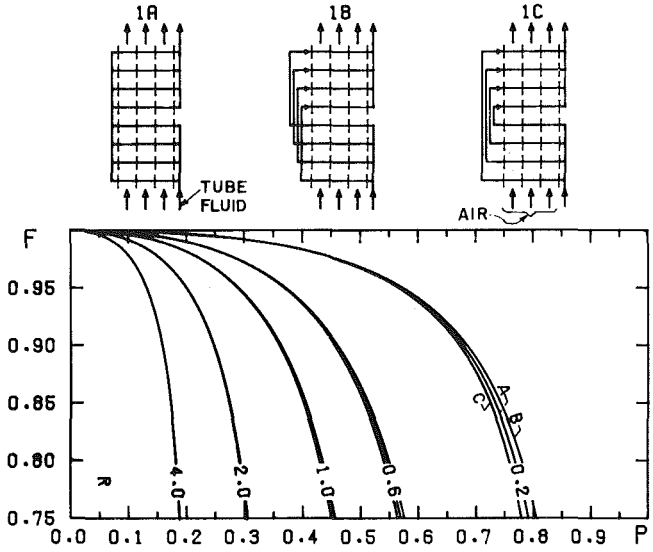

Fig. 1 Correction factor for $N_P = 2$ passes, $N_R = 4$ rows per pass, cocrossflow, air mixing between rows, with three different cases for tube fluid mixing between passes: Case (1A), completely mixed; Case (1B), unmixed with identical order; Case (1C), unmixed with inverted order

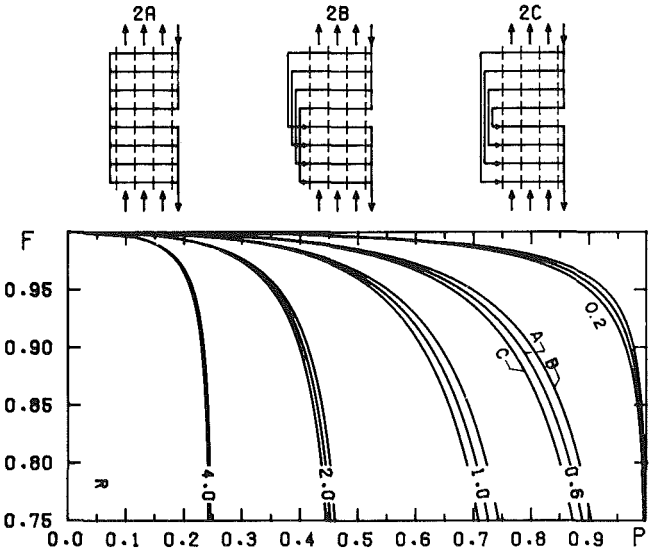

Fig. 2 Correction factor for 2 passes, 4 rows per pass, countercrossflow, air mixing between rows, with three different cases for tube fluid mixing between passes (cases (2A), (2B), and (2C))

Contributed by the Heat Transfer Division for publication in the JOURNAL OF HEAT TRANSFER. Manuscript received by the Heat Transfer Division February 17, 1982.

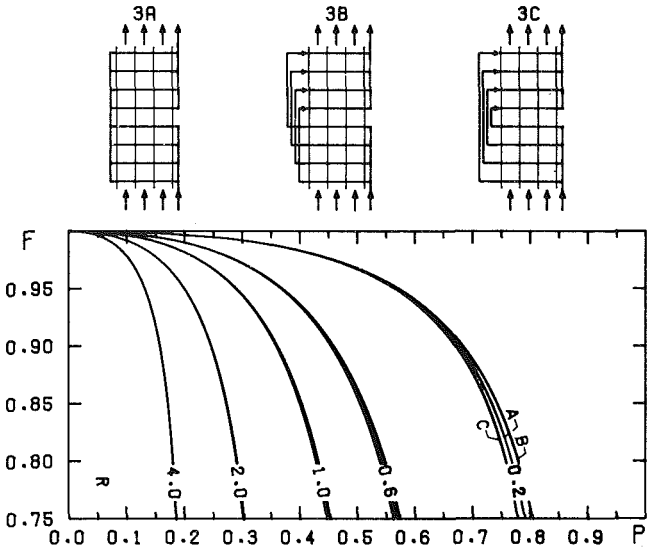

Fig. 3 Correction factor for 2 passes, 4 rows per pass, co-crossflow, no air mixing with three different cases for tube fluid mixing between passes (cases (3A), (3B), and (3C))

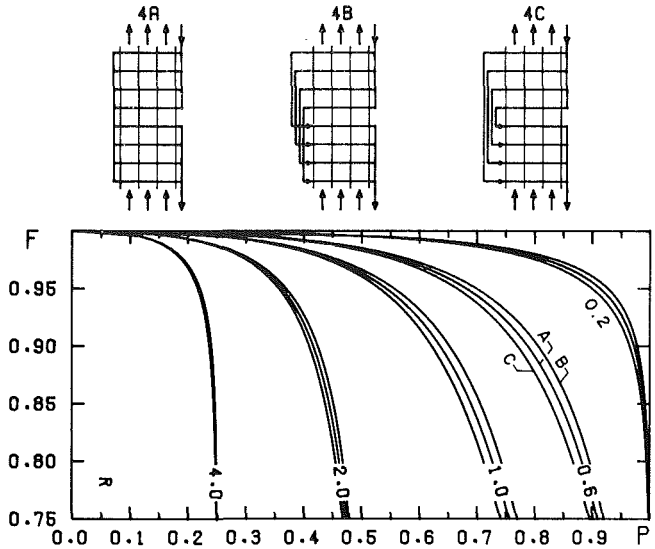

Fig. 4 Correction factor for 2 passes, 4 rows per pass, counter-crossflow, no air mixing with three different cases for tube fluid mixing between passes (cases (4A), (4B), and (4C))

mixed with inverted order of the rows (see cases A, B, and C, respectively, in Figs. 1 to 4). With regard to the air mixing, two alternatives are considered, in both of which the air is assumed not to mix as it proceeds past a row of tubes: in the first one, the air mixes completely between consecutive rows; in the second one, it does not mix at all. In addition, when more than one pass is involved, both the co-crossflow and counter-crossflow cases are treated, yielding a total of 12 possible flow patterns for each pair of values of N_P and N_R.

2 Single-Row Analysis

The following usual idealizations are made for the analysis: constant heat transfer coefficient, constant heat capacities, no change of phase, uniform air velocity distribution, constant temperature at any given tube cross section, and negligible heat losses. The temperature variation of an air streamline which crosses N_P passes of tubes of N_R rows each, can be obtained for every single row from the heat transfer equation

$$\frac{wc}{LN_T}\frac{\partial t(x,\omega)}{\partial \omega} = UD[T(x) - t(x,\omega)],\ 0 \le \omega \le \pi \tag{4}$$

At any fixed value of x, equation (4) can be integrated in the ω variable yielding

$$t_F(x) = \rho t_I(x) + (1-\rho)T(x) \tag{5}$$

where

$$\left.\begin{aligned} t_F(x) &= t(x,\pi) \\ t_I(x) &= t(x,0) \\ \rho &= e^{-N_{tu}/N} \end{aligned}\right\} \tag{6}$$

The temperature variation of the tube fluid is obtained from the relation

$$-(WC/N_R)\,dT = wc[t_F(x) - t_I(x)]dx = \\ = (1-\rho)[T(x) - t_I(x)]wcdx \tag{7}$$

Nomenclature

A = heat transfer surface area, m^2
a_k, a_k', a_k'' = coefficients in the initial air temperature profile, equations (48) and (76)
b_k, b_k', b_k'' = coefficients in the tube fluid temperature profile, equations (49) and (77)
c_k, c_k', c_k'' = coefficients in the final air temperature profile, equations (50) and (78)
C = specific heat of tube fluid, J/kg°C
c = specific heat of air, J/kg°C
C_{ij} = coefficients in the set of linear equations (91)
D = tube diameter used to calculate U, m
F = log-mean temperature difference correction factor, dimensionless
f = function of R and N_{tu} defined by equation (85)
$g_{(p)}$ = functions of R and N_{tu} defined for each pass by equation (86)
L = length of each tube, m
N = total number of tube rows
$N_a, N_b, N_c, N_\alpha, N_\beta, N_\gamma$ = upper limits for the summations in equations (48–50), defined by equations (51) and (52)
N_P = number of tube passes
N_R = number of tube rows per pass
N_T = number of tubes per row
N_{tu} = UA/wc, number of heat transfer units, dimensionless
$P = \dfrac{t_F - t_I}{T_I - t_I}$, air temperature effectiveness, dimensionless
$\underset{\sim}{P} = \dfrac{T_I - T_F}{T_I - t_I}$, tube fluid temperature effectiveness, dimensionless
Q = heat flow rate, W
$R = \dfrac{T_I - T_F}{t_F - t_I} = \dfrac{wc}{WC}$, heat capacity rates ratio, dimensionless
T = tube fluid temperature, °C
t = air temperature, °C
U = overall coefficient of heat transfer, W/m^2°C

which gives

$$\frac{dT}{dx} = -\lambda[T(x) - t_I(x)] \tag{8}$$

with

$$\lambda = RN_R(1-\rho) = R_R(1-\rho) \tag{9}$$

In terms of the inlet air temperature profile, $t_I(x)$, and the initial tube fluid temperature, $T(0)$, the particular solution of the first-order, linear differential equation (8) is

$$T(x) = e^{-\lambda x}\left[T(0) + \lambda\int_0^x e^{\lambda y} t_I(y)\,dy\right] \tag{10}$$

Equations (5) and (10) completely define the air and process fluid temperature variations for the row. Using for convenience dimensionless variables θ and τ, the working equations are

$$\theta_F(x) = \rho\theta_I(x) + (1-\rho)\tau(x) \tag{11}$$

$$\tau(x) = e^{-\lambda x}\left[\tau(0) + \lambda\int_0^x e^{\lambda y}\theta_I(y)\,dy\right] \tag{12}$$

The application of equations (11) and (12) to successive rows allows the solution of any flow arrangement. This method has already been used to solve several particular cases [3, 6, 7].

3 Air Mixing Between Rows

Since the assumption of the air mixing between rows implies flat inlet air temperature profiles, equation (10) reduces to

$$T_{(p,q)}(x) = (T_{(p,q)}(0) - t_{I(p,q)})e^{-\lambda x} + t_{I(p,q)} \tag{13}$$

From equations (5) and (13), the outlet air temperature is

$$t_{F(p,q)} = \int_0^1 t_{F(p,q)}(x)\,dx = t_{I(p,q)} + \frac{1-e^{-\lambda}}{R_R}(T_{I(p,q)} - t_{I(p,q)}) \tag{14}$$

It follows that the single-row air effectiveness can be expressed explicitly in terms of R and N_{tu}, and therefore is the same for all rows

$$P_R = (t_{F(p,q)} - t_{I(p,q)})/(T_{I(p,q)} - t_{I(p,q)}) = (1-e^{-\lambda})/R_R = P_R(R, N_{tu}) \tag{15}$$

The single-row tube fluid effectiveness $\tilde{P}_R = P_R R_R = P_R RN_R = 1 - e^{-\lambda}$ is also independent of the row.

The number of heat transfer units follows explicitly from equations (6), (9), and (15).

$$N_{tu} = -N\ ln\left[1 + \frac{1}{R_R} ln(1 - P_R R_R)\right] = N\varphi(R_R, P_R) \tag{16}$$

Hence, the correction factor for any N-row configuration with N_P passes and N_R rows per pass, can be written as

$$F = \chi(R,P)/[N\varphi(R_R, P_R)] \tag{17}$$

where $N = N_R N_P$.

In some special configurations, R_R and P_R can be written explicitly in terms of R and P which, using equation (17), provides a simple way for the calculation of F. In all cases, P can be calculated as a function of R and N_{tu} and F can be evaluated with equation (2) in terms of the latter variables.

Before considering more complex arrangements, the case of one pass with N_R parallel rows is solved. Since the initial tube fluid temperature is the same for every row of the given pass ($T_{(p,q)}(0) = T_{I(p)}$) and $t_{I(p,q+1)} = t_{F(p,q)}$, the pass air effectiveness P_P is related to P_R through the expression

$$\prod_{q=1}^{N_R} \frac{T_{I(p)} - t_{F(p,q)}}{T_{I(p)} - t_{I(p,q)}} = (1-P_R)^{N_R} = \frac{T_{I(p)} - t_{F(p,N_R)}}{T_{I(p)} - t_{I(p,1)}} = 1 - P_P \tag{18}$$

Hence

$$P_P = 1 - (1-P_R)^{N_R} \tag{19}$$

and

$$P_R = 1 - (1-P_P)^{1/N_R} \tag{20}$$

For a single pass ($P = P_P$), F is obtained from R and N_{tu} through equations (15), (19), and (2).

Nomenclature (cont.)

W = mass flow rate of tube fluid, kg/s
w = air mass flow rate, kg/s
x = dimensionless axial coordinate of tubes, increasing from 0 to 1 in the direction of the hot fluid flow
α_k = coefficients in the initial air temperature profile, equation (48)
β_k = coefficients in the tube fluid temperature profile, equation (49)
γ_k = coefficients in the final air temperature profile, equation (50)
ΔT_{lm} = log-mean temperature difference, °C
ΔT_m = $F\Delta T_{lm}$, true-mean temperature difference, °C
θ = $(t - t_0)/\Delta T_0$, dimensionless air temperature (t_0 and ΔT_0 are reference values suitably chosen for each case)
λ = function of R, N_{tu}, N_R, and N, defined by equation (9)
ρ = function of N_{tu} and N defined by equation (6)
τ = $(T - t_0)/\Delta T_0$, dimensionless tube fluid temperature (t_0 and ΔT_0 are reference values suitably chosen for each case)
φ = function of R_R and P_R defined by equation (16)
χ = function of R and P defined by equation (3)
ψ = $\Delta T_m/(T_I - t_I)$, dimensionless true-mean temperature difference
ω = tube central angle, radians

Subscripts

F = final
I = initial
P = corresponding to one pass
R = corresponding to one row

Subscripts Within Parentheses

(p) = belonging to pass p (passes are numbered from 1 to N_P in the direction of air flow)
(q) = belonging to row q (within each pass, rows are numbered from 1 to N_R in the direction of air flow)

Alternatively, F is obtained from R and P through equations (20) and (17).

Six possible connections of such passes are discussed below. They correspond to either co-crossflow (cases 1 and 3) or counter-crossflow (cases 2 and 4), each one with three different assumptions of tube fluid mixing between passes: A for tube fluid mixed, B for tube fluid unmixed, keeping identical order of the rows, and C for tube fluid unmixed, with inverted order of the rows. The meaning of "identical order" and "inverted order" is most easily understood by inspection of the flow sketches labeled (1B) and (1C), respectively, in Fig. 1.

Case 1: Co-Crossflow With Air Mixing.

(1A). Tube fluid mixed between passes:

Since

$$t_{I(p+1)} = t_{F(p)},\ T_{I(p+1)} = T_{F(p)}$$

it follows that

$$\prod_{p=1}^{N_p} \frac{T_{F(p)} - t_{F(p)}}{T_{I(p)} - t_{I(p)}} = [1 - P_P(1+R_P)]^{N_P} =$$

$$= (T_F - t_F)/(T_I - t_I) = 1 - P(1+R) \tag{21}$$

Hence

$$P = \{1 - [1 - P_P(1+R)]^{N_P}\}/(1+R) \tag{22}$$

and

$$P_P = \{1 - [1 - P(1+R)]^{1/N_P}\}/(1+R) \tag{23}$$

F is obtained from R and N_{tu} through equations (15), (19), (22), and (2). Alternatively, F is obtained from R and P through equations (23), (20), and (17).

(1B). Tube fluid unmixed between passes with identical order of the rows:

Choosing the following dimensionless variables, which provide known initial values

$$\theta_{I(p,q)} = (t_{I(p,q)} - t_I)/(T_I - t_I),$$
$$\theta_{F(p,q)} = (t_{F(p,q)} - t_I)/(T_I - t_I) \tag{24}$$

$$\tau_{I(p,q)} = (T_{I(p,q)} - t_I)/(T_I - t_I),$$
$$\tau_{F(p,q)} = (T_{F(p,q)} - t_I)/(T_I - t_I) \tag{25}$$

from equation (13) it follows

$$\tau_{F(p,q)} = \underset{\sim}{P}_R \theta_{I(p,q)} + (1 - \underset{\sim}{P}_R)\tau_{I(p,q)} \tag{26}$$

and from equation (14)

$$\theta_{F(p,q)} = (1 - P_R)\theta_{I(p,q)} + P_R \tau_{I(p,q)} \tag{27}$$

Air temperatures are related by

$$\theta_{I(p,q+1)} = \theta_{F(p,q)} \tag{28}$$

$$\theta_{I(p+1,1)} = \theta_{F(p,N_R)} \tag{29}$$

and tube fluid temperatures by

$$\tau_{I(p+1,q)} = \tau_{F(p,q)} \tag{30}$$

with the initial values

$$\theta_{I(1,1)} = 0, \quad \tau_{I(1,q)} = 1 \tag{31}$$

Successive application of equations (26), (27), and (28) within each pass, and equations (29) and (30) to obtain the initial values for the following pass, gives $\theta_{F(N_P,N_R)}$ as a function of R and N_{tu}. From equation (24)

$$P = \theta_{F(N_P,N_R)} \tag{32}$$

Subsequently, F can be calculated from equation (2).

(1C). Tube fluid unmixed between passes, with inverted order of the rows:

The same procedure of case (1B) is applied, with the only exception that equation (30) is replaced by

$$\tau_{I(p+1,q)} = \tau_{F(p,N_R+1-q)} \tag{33}$$

Case 2. Counter-Crossflow With Air Mixing.

(2A). Tube fluid mixed between passes:

Since

$$t_{I(p+1)} = t_{F(p)} \quad \text{and} \quad T_{F(p+1)} = T_{I(p)}$$

it follows that

$$\prod_{p=1}^{N_P} \frac{T_{I(p)} - t_{F(p)}}{T_{F(p)} - t_{I(p)}} = \left(\frac{1-P_P}{1-RP_P}\right)^{N_P} =$$

$$= (T_I - t_F)/(T_F - t_I) = (1-P)/(1-RP) \tag{34}$$

Hence

$$P = \begin{cases} \dfrac{1 - [(1-P_P)/(1-RP_P)]^{N_P}}{1 - R[(1-P_P)/(1-RP_P)]^{N_P}}, & R \neq 1 \\ P_P/[P_P + (1-P_P)/N_P], & R = 1, \end{cases} \tag{35}$$

which is a known result [8].

The inverse relations are

$$P_P = \begin{cases} \dfrac{1 - [(1-P)/(1-RP)]^{1/N_P}}{1 - R[(1-P)/(1-RP)]^{1/N_P}}, & R \neq 1 \\ P/[P + N_P(1-P)], & R = 1 \end{cases} \tag{36}$$

F is obtained from R and N_{tu} through equations (15), (19), (35), and (2). Alternatively, F is obtained from R and P through equations (36), (20), and (17).

(2B). Tube fluid unmixed between passes, with identical order of the rows:

In this case the following dimensionless variables are used, since they provide known initial values:

$$\theta_{I(p,q)} = (t_{I(p,q)} - t_F)/(T_I - t_F),$$
$$\theta_{F(p,q)} = (t_{F(p,q)} - t_F)/(T_I - t_F) \tag{37}$$

and

$$\tau_{I(p,q)} = (T_{I(p,q)} - t_F)/(T_I - t_F),$$
$$\tau_{F(p,q)} = (T_{F(p,q)} - t_F)/(T_I - t_F) \tag{38}$$

In addition, it is convenient to rearrange equations (26) to (29) in the following way

$$\theta_{I(p,q)} = \theta_{F(p,q)}/(1-P_R) - \tau_{I(p,q)} P_R/(1-P_R) \tag{39}$$

$$\tau_{F(p,q)} = \underset{\sim}{P}_R \theta_{I(p,q)} + (1 - \underset{\sim}{P}_R)\tau_{I(p,q)} \tag{40}$$

$$\theta_{F(p,q-1)} = \theta_{I(p,q)} \tag{41}$$

$$\theta_{F(p-1,N_R)} = \theta_{I(p,1)} \tag{42}$$

Equation (30) is replaced by the following one

$$\tau_{I(p-1,q)} = \tau_{F(p,q)} \tag{43}$$

and the initial values for the last pass which follow from equations (37) and (38) are

$$\theta_{F(N_P,N_R)} = 0, \quad \tau_{I(N_P,q)} = 1 \tag{44}$$

Successive application of equations (39) to (41) within each pass, and of equations (42) and (43) to find the initial values for consecutive passes, gives $\theta_{I(1,1)}$ as a function of R and N_{tu}. From equation (37)

$$\theta_{I(1,1)} = P/(P-1) \tag{45}$$

Hence

$$P = \theta_{I(1,1)}/(\theta_{I(1,1)} - 1) \tag{46}$$

Consequently, F follows from equation (2) as an explicit function of R and N_{tu}.

(2C). Tube fluid unmixed between passes, with inverted order of the rows:

The same procedure of case (2B) is applied, with the only exception that equation (43) is replaced by

$$\tau_{I(p-1,q)} = \tau_{F(p,N_R+1-q)} \tag{47}$$

4 No Air Mixing Between Rows

Equations (11) and (12), derived from the single-row analysis, with a vanishing value for the inlet air temperature $\theta_{I(1,1)}$, give rise to temperature profiles that are products of polynomials in x times the exponentials $\exp(\pm\lambda x)$, namely,

$$\theta_{I(p,q)}(x) = e^{-\lambda x}\sum_{k=0}^{N_a} a_{k(p,q)}x^k + e^{\lambda x}\sum_{k=0}^{N_\alpha}\alpha_{k(p,q)}x^k \tag{48}$$

$$\tau_{(p,q)}(x) = e^{-\lambda x}\sum_{k=0}^{N_b} b_{k(p,q)}x^k + e^{\lambda x}\sum_{k=0}^{N_\beta}\beta_{k(p,q)}x^k \tag{49}$$

$$\theta_{F(p,q)}(x) = e^{-\lambda x}\sum_{k=0}^{N_c} c_{k(p,q)}x^k + e^{\lambda x}\sum_{k=0}^{N_\gamma}\gamma_{k(p,q)}x^k \tag{50}$$

The upper limits for the summations are obtained as follows. For odd numbered passes ($p=2i-1$)

$$N_a+1 = N_b = N_c = (i-1)N_R - 1 + q,$$
$$N_\alpha = N_\beta = N_\gamma = (i-1)N_R - 1 \tag{51}$$

For even numbered passes ($p=2i$)

$$N_a+1 = N_b = N_c = (i-1)N_R - 1 + q,$$
$$N_\alpha = N_\beta = N_\gamma = iN_R - 1 \tag{52}$$

In the above expressions, a negative value for the upper limit indicates that the corresponding summation reduces to zero.

It is easy to establish recurrence formulas for calculating the coefficients in equations (48) to (50). Within the same pass, the relation

$$\theta_{I(p,q+1)}(x) = \theta_{F(p,q)}(x) \tag{53}$$

implies

$$a_{k(p,q+1)} = c_{k(p,q)} \tag{54}$$

$$\alpha_{k(p,q+1)} = \gamma_{k(p,q)} \tag{55}$$

From equations (11), (12) and (48) to (50)

$$\beta_{k(p,q)} = \frac{1}{2k!}\sum_{j=k}^{N_\beta}\alpha_{j(p,q)}j!\left(-\frac{1}{2\lambda}\right)^{j-k} \tag{56}$$

$$\gamma_{k(p,q)} = \rho\alpha_{k(p,q)} + (1-\rho)\beta_{k(p,q)} \tag{57}$$

$$b_{0(p,q)} = \tau_{(p,q)}(0) - \beta_{0(p,q)} \tag{58}$$

$$b_{k(p,q)} = \lambda a_{k-1(p,q)}/k, \quad k \geq 1 \tag{59}$$

$$c_{k(p,q)} = \rho a_{k(p,q)} + (1-\rho)b_{k(p,q)} \tag{60}$$

Since x is defined to increase in the direction of tube fluid flow, when a change of pass is made

$$\theta_{I(p+1,1)}(x) = \theta_{F(p,N_R)}(1-x) \tag{61}$$

Hence

$$a_{k(p+1,1)} = (-1)^k\frac{e^\lambda}{k!}\sum_{j=k}^{N_a}\gamma_{j(p,N_R)}j!/(j-k)!, \tag{62}$$

$$\alpha_{k(p+1,1)} = (-1)^k\frac{e^{-\lambda}}{k!}\sum_{j=k}^{N_\alpha}c_{j(p,N_R)}j!/(j-k)!. \tag{63}$$

Dimensionless variables are always defined so that $\theta_{I(1,1)}=0$ which gives

$$a_{k(1,1)} = \alpha_{k(1,1)} = 0 \tag{64}$$

Additional relations depend on each type of flow pattern, and are discussed below.

Case 3: Co-Crossflow With No Air Mixing.

(3A). Tube fluid mixed between passes:

Choosing the following dimensionless variables

$$\tau_{(p,q)}(x) = (T_{(p,q)}(x) - t_I)/(T_I - t_I)$$
$$\theta_{I(p,q)}(x) = (t_{I(p,q)}(x) - t_I)/(T_I - t_I) \tag{65}$$
$$\theta_{F(p,q)}(x) = (t_{F(p,q)}(x) - t_I)/(T_I - t_I)$$

the initial values for the first pass are

$$\tau_{(1,q)}(0) = 1 \tag{66}$$

For all other passes

$$\tau_{(p+1,q)}(0) = \tau_{F(p)} \tag{67}$$

where the final pass temperature $\tau_{F(p)}$ is obtained as the average of the temperature of the rows belonging to that pass at $x=1$,

$$\tau_{F(p)} = \frac{1}{N_R}\sum_{q=1}^{N_R}\tau_{(p,q)}(1) =$$
$$= \frac{1}{N_R}\sum_{q=1}^{N_R}\left[e^{-\lambda}\sum_{k=0}^{N_b}b_{k(p,q)} + e^{\lambda}\sum_{k=0}^{N_\beta}\beta_{k(p,q)}\right] \tag{68}$$

The coefficients can then be calculated in this order: equations (54–60) provide all coefficients for each pass, given the initial conditions; equations (64) and (66) provide initial conditions for the first pass; and equations (62), (63), and (67) provide initial conditions for all other passes.

The outlet tube fluid temperature is obtained using equation (68) for the last pass, i.e., for $p=N_P$. Therefore,

$$\tau_F = \tau_{F(N_P)} = 1 - PR \tag{69}$$

whence

$$P = (1 - \tau_{F(N_P)})/R \tag{70}$$

F is then obtained from equation (2), as an explicit function of R and N_{tu}.

(3B). Tube fluid unmixed between passes, with identical order of the rows:

The procedure is the same as in case (3A), with the only exception that equation (67) is replaced by

$$\tau_{(p+1,q)}(0) = \tau_{(p,q)}(1) \tag{71}$$

(3C) Tube fluid unmixed between passes with inverted order of the rows:

Again the same procedure as in case (3A) is used, with the only exception that equation (67) is replaced by

$$\tau_{(p+1,q)}(0) = \tau_{(p,N_R+1-q)}(1) \tag{72}$$

Case 4. Counter-Crossflow With no Air Mixing.

(4A). Tube fluid mixed between passes:

Choosing the following dimensionless variables

$$\theta_{I(p,q)}(x) = (t_{I(p,q)}(x) - t_I)/(T_F - t_I),$$
$$\theta_{F(p,q)}(x) = (t_{F(p,q)}(x) - t_I)/(T_F - t_I) \tag{73}$$

and

$$\tau_{(p,q)}(x) = (T_{(p,q)}(x) - t_I)/(T_F - t_I) \tag{74}$$

a known value results for τ_F

$$\tau_F = \tau_{F(1)} = \frac{1}{N_R}\sum_{q=1}^{N_R}\tau_{(1,q)}(1) = 1 \tag{75}$$

Since the initial values $\tau_{(p)}(0)$ are not known beforehand, it is necessary to split the coefficients, a, b, and c, as follows

$$a_{k(p,q)} = a'_{k(p,q)}\ \tau_{(p)}(0) + a''_{k(p,q)} \tag{76}$$

$$b_{k(p,q)} = b'_{k(p,q)}\ \tau_{(p)}(0) + b''_{k(p,q)} \tag{77}$$

$$c_{k(p,q)} = c'_{k(p,q)}\ \tau_{(p)}(0) + c''_{k(p,q)} \tag{78}$$

The new coefficients, a', a'', b', b'', c', and c'' satisfy equations (54), (59), and (60), while equation (58) is replaced by

$$b'_{0(p,q)} = 1 \tag{79}$$

$$b''_{0(p,q)} = -\beta_{0(p,q)} \tag{80}$$

Initial values for each pass are

$$a'_{k(p,1)} = 0 \tag{81}$$

$$a''_{k(p,1)} = a_{k(p,1)} \tag{82}$$

From equations (79) and (81) and the recurrence formulas (54), (59), and (60), it is easily seen that the coefficients $a'_{k(p,q)}$, $b'_{k(p,q)}$, $c'_{k(p,q)}$ are the same for every pass, so that the pass index can be dropped: $a'_{k(p,q)} = a'_{k(q)}$, $b'_{k(p,q)} = b'_{k(q)}$, $c'_{k(p,q)} = c'_{k(q)}$.

The condition of tube fluid mixing between passes implies that

$$\tau_{F(p)} = \frac{1}{N_R}\sum_{q=1}^{N_R} \tau_{(p,q)}(1) \tag{83}$$

Hence

$$\tau_{F(p)} = f\tau_{(p)}(0) + g_{(p)} \tag{84}$$

where

$$f(R,N_{tu}) = \frac{e^{-\lambda}}{N_R}\sum_{q=1}^{N_R}\sum_{k=0}^{q-1} b'_{k(q)} \tag{85}$$

and

$$g_{(p)}(R,N_{tu}) = \frac{1}{N_R}\sum_{q=1}^{N_R}\left[e^{-\lambda}\sum_{k=0}^{N_b} b''_{k(p,q)} + e^{\lambda}\sum_{k=0}^{N_\beta}\beta_{k(p,q)}\right]. \tag{86}$$

Because within the first pass the coefficients β and b'' vanish, the function $g_{(1)}$ is zero.

Calculations are performed in this order: using equations (54–57), (59), (60), (79), and (80) and the initial values given by equations (81), (82), and (62–64), all the coefficients are calculated for each pass. Next, the initial tube fluid temperature for each pass is obtained from equation (84) as

$$\tau_{(p)}(0) = (\tau_{F(p)} - g_{(p)})/f \tag{87}$$

Since $\tau_{F(1)} = 1$, and

$$\tau_{F(p+1)} = \tau_{(p)}(0) \tag{88}$$

successive application of equation (87) provides $\tau_{(N_P)}(0)$, which, through the relation

$$\tau_{(N_P)}(0) = 1/(1 - PR) \tag{89}$$

can be used to solve for P as follows

$$P = (\tau_{(N_P)}(0) - 1)/(R\tau_{(N_P)}(0)) \tag{90}$$

F is obtained from equation (2) as an explicit function of R and N_{tu}.

(4B). Tube fluid unmixed between passes, with identical order of the rows:

It is convenient to adopt the dimensionless variables of equation (65), in order to have known values for $\tau_{(N_P,q)}(0)$. In this case there are N_R unknowns $\tau_{(1,q)}(0)$ for the first pass, which cannot be solved until the boundary values for the last pass $\tau_{(N_P,q)}(0) = 1$ provide a set of N_R linear equations of the form

$$\sum_{j=1}^{N_R} C_{ij}\tau_{(1,j)}(0) = 1, \quad i = 1, \ldots, N_R \tag{91}$$

In order to calculate the coefficients C_{ij}, the following procedure is used:

(*i*) Assuming

$$\tau_{(1,j)}(0) = 1,\ \tau_{(1,q)}(0) = 0 \text{ for } q \neq j \tag{92}$$

equations (54–60), and the initial values from equation (64) provide the coefficients for the first pass.

(*ii*) The initial values for the next pass follow from equations (62), (63) and the condition

$$\tau_{(p+1,q)}(1) = \tau_{(p,q)}(0) \tag{93}$$

which allows the calculation of $\tau_{(p+1,q)}(0)$ as

$$\tau_{(p+1,q)}(0) = e^{\lambda}\tau_{(p,q)}(0) - e^{2\lambda}\sum_{k=0}^{N_\beta}\beta_{k(p+1,q)} + \beta_{0(p+1,q)} - \sum_{k=1}^{N_b} b_{k(p+1,q)} \tag{94}$$

(*iii*) Again equations (54–60) provide all the coefficients needed for the expansion of $\theta_I(x)$, $\tau(x)$, and $\theta_F(x)$ for the pass.

(*iv*) When arriving to the last pass, since $\tau_{(N_P,q)}(0) = 1$, the second member of equation (94) gives the required C_{ij}, for $i = 1, \ldots, N_R$ as

$$C_{ij} = e^{\lambda}\tau_{(N_P-1,i)}(0) - e^{2\lambda}\sum_{k=0}^{N_\beta}\beta_{k(N_P,i)} + \beta_{0(N_P,i)} - \sum_{k=1}^{N_b} b_{k(N_P,i)}. \tag{95}$$

(*v*) Steps (*i–iv*) are repeated for every j between 1 and N_R.

(*vi*) The linear system of equations (91) provides the unknowns $\tau_{(1,q)}(0)$, which allow the calculation of the coefficients for the first pass. The tube fluid outlet temperature can then be found from

$$\tau_F = \frac{1}{N_R}\sum_{q=1}^{N_R}\tau_{(1,q)}(1) = \frac{1}{N_R}\sum_{q=1}^{N_R} e^{-\lambda}\sum_{k=0}^{q-1} b_{k(1,q)} \tag{96}$$

Since

$$\tau_F = 1 - PR \tag{69}$$

it follows that

$$P = (1 - \tau_F)/R \tag{97}$$

F is obtained from equation (2) as an explicit function of R and N_{tu}.

(4C). Tube fluid unmixed between passes, with inverted order of the rows: The same procedure of case (4B) is applied, with the only exception that equation (93) is replaced by

$$\tau_{(p+1,q)}(1) = \tau_{(p,N_{R+1-q})}(0) \tag{98}$$

5 Comparative Analysis

Figures 1–4 show plots of the correction factor as a function of P, with R as a parameter, for the twelve cases considered (1A–4C) and a configuration of two passes, four rows per pass. The first obvious comment from inspection of these figures is that counter-crossflow (Figs. 2 and 4) is far superior to co-crossflow (Figs. 1 and 3), which comes as no surprise. Another straightforward conclusion is that the tube fluid unmixed in the header gives rise to higher correction factors with the identical order of the rows, (curves labeled B), and lower ones when the order is inverted (curves C), whereas intermediate results are obtained for the tube fluid mixed between passes (curves A). This is so because case B has more evenly distributed temperature differences between the hot and cold fluids, which is the same reason why counter-crossflow is superior to co-crossflow. In the example and range of variables shown, however, the difference in the

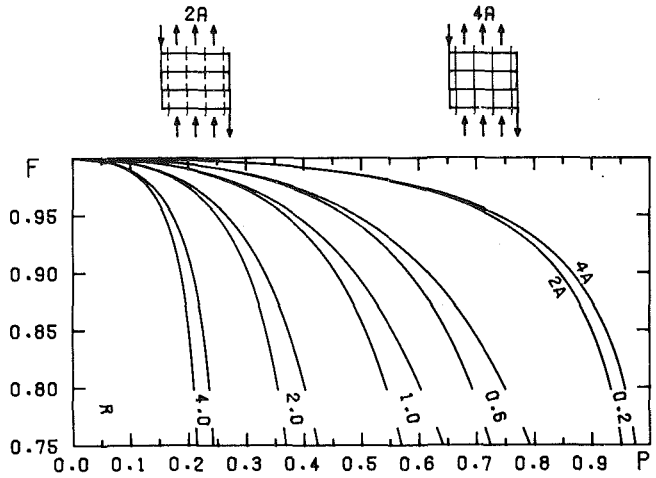

Fig. 5 Correction factor for 1 pass, 4 rows, for air mixing between rows (case (2A), and no air mixing (case (4A))

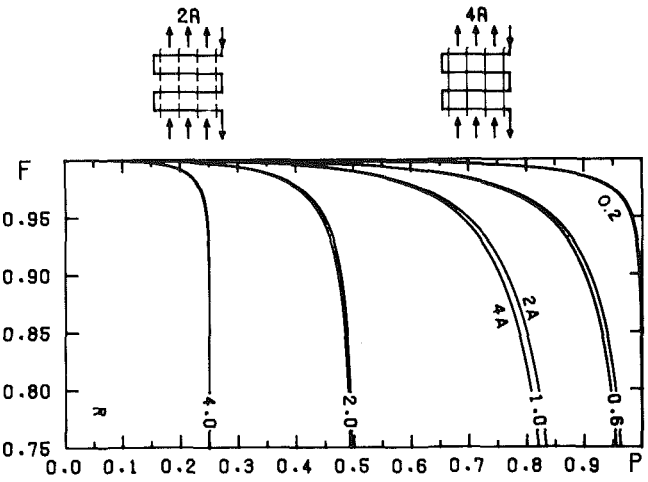

Fig. 6 Correction factor for 4 passes, 1 row per pass, counter-crossflow, for both air mixing between rows (case (2A)), and no air mixing (case (4A))

correction factor between tube fluid mixed and unmixed (cases A, and B or C) does not exceed 4 percent.

An interesting comparison can be drawn between the curves corresponding to the assumption of air mixing between rows (Figs. 1 and 2) and no air mixing (Figs. 3 and 4). In the example shown, no air mixing gives rise to higher values of F, but this is not a general rule, and, furthermore, in the co-crossflow case (Figs. 1 and 3) the difference is practically nonexistent. In order to analyze in more detail the effect of the air mixing hypothesis, the correction factors for two different geometries are compared in Figs. 5 and 6, for counter-crossflow and tube fluid mixed between passes. Figure 5 corresponds to one pass, four rows, and shows a substantial difference in favor of no air mixing: for example, for case (2A), with $R=1.0$ and $P=0.57$, the correction factor is $F=0.749$, whereas for case (4A) the corresponding value of F for the same values of the parameters R and P is $F=0.834$. Figure 6 shows, however, that in the case of four passes, one row per pass, higher values of F are associated with the assumption of air mixing between rows (case (2A). Why this is so can be understood by an inspection of Figs. 7 and 8, which show the dimensionless air temperature profiles with no air mixing for the simpler cases of $N_P=1$, $N_R=2$, and $N_P=2$, $N_R=1$, respectively. It is clear that if, in the first case, the air is mixed between rows 1 and 2, the effect is to cool the air at the warmer end of the second row, and increase its temperature at the cooler end. The resulting temperature differences depart even more from the ideal distribution of

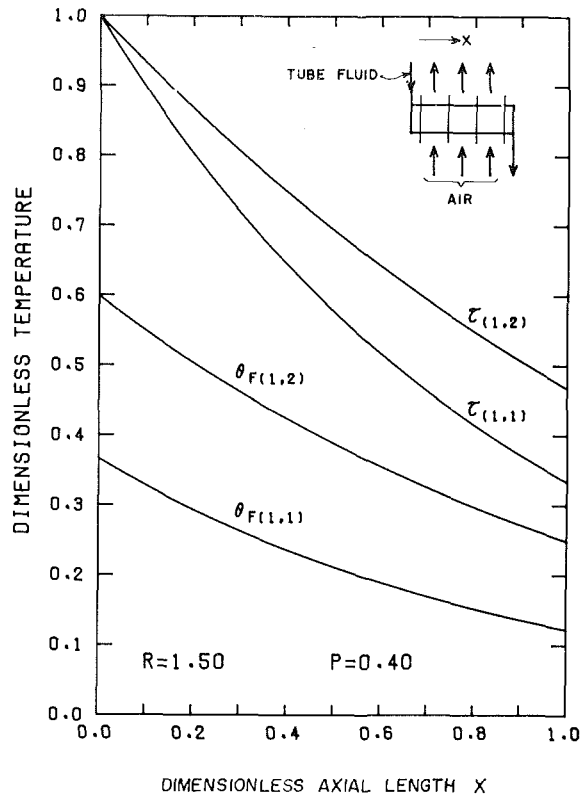

Fig. 7 Dimensionless temperature profiles for 1 pass, 2 rows, no air mixing (case (4A))

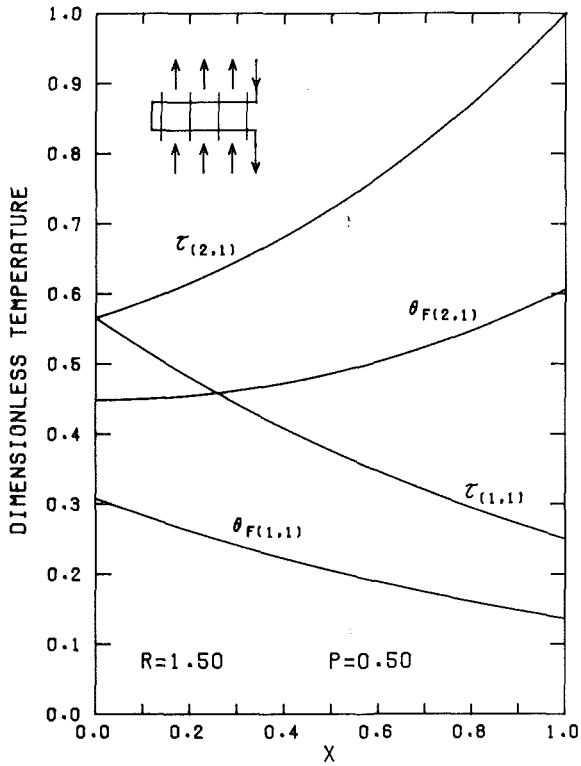

Fig. 8 Dimensionless temperature profiles for 2 passes, 1 row per pass, counter-crossflow, no air mixing (case (4A))

temperature differences of the countercurrent case, and correspondingly, yield lower correction factors. If additional rows are present within the same pass, such as in the case of Fig. 5, the effect is enhanced. Conversely, in the case of two one-row passes shown in Fig. 8, because of the reversal of the direction of the hot fluid flow in the second pass, warmer air

is at the cool end of the tube, so that air mixing helps to achieve a better distribution of temperature differences, and, therefore, increases the correction factor. The effect remains if more one-row passes are added, as shown in Fig. 6, but because successive passes slant the air temperature distribution in alternating directions, the effect is not as significant as the cumulative one verified in Fig. 5.

There are two cases in which the difference between the two air mixing assumptions tends to disappear in the region selected as of practical interest ($F \geq 0.8$). One is for several two-row passes, where both the effects previously discussed are present with such strengths that they practically cancel out. The other one is in co-crossflow configurations. In this case, the condition $F \geq 0.8$ forces sizable temperature gaps between the hot and cold fluids, and when this occurs the impact of changes in temperature profiles which leave the average temperature constant is very small. For this reason, Figs. 1 and 3 are practically indistinguishable.

6 Conclusions

(*i*) The procedure in sections 3 and 4 makes it possible to obtain P as an analytic function of R and N_{tu} for any of the twelve flow arrangements analyzed, given the numbers of passes and rows. For instance, for a co-crossflow air cooler with two passes and two rows per pass with no air mixing and hot fluid mixed between passes (case (3A)), the effectiveness is found to be

$$P = (3+\rho^2)(1+\rho)(1-e^{-2\lambda})/(8R) - [(1+\rho)^2 + \rho(1-\rho)\lambda](1-\rho)\lambda e^{-2\lambda}/(4R) \quad (99)$$

Analogous expressions have been published for several other cases [2, 3, 6, 7].

(*ii*) In addition to providing a systematic way to obtain analytical expressions such as equation (99), the recursion relations presented here are easily programmable in a computer. Thus, the numerical result for the effectiveness can be obtained for arbitrary values of N_P and N_R without having to derive the corresponding analytical expressions. This is particularly useful when several rows are present, because such a derivation becomes more and more complicated as the total number of rows increases.

(*iii*) When solving the rating problem for a given exchanger, the available data are N_{tu} and R. In such case, P is obtained directly through the calculation of only two exponentials and a finite number of elementary operations. It is therefore unnecessary, for the air cooler arrangements analyzed, to resort to modeling through approximate polynomial expressions, which have proved useful in the case of more complex compound exchangers [9].

(*iv*) When solving the sizing problem for given process conditions, the available data are either R and P or, for the specific case of air coolers, N_{tu} and P, as pointed out in [10]. In both cases, the same procedure of section 3 and 4 may be used in an iterative way in order to determine N_{tu} or P, respectively. This method has actually been implemented by the authors in a computer program for the design of air coolers. Another option is to develop approximate polynomial expressions for the direct solution of each specific case, as proposed in [10].

(*v*) After P, R, and N_{tu} are known from either the analytical expressions discussed in (*i*) or the calculations described in (*iii*) and (*iv*), the correction factor follows from equation (2). The dimensionless mean temperature difference is also easily derived from equation (1) as

$$\psi = \Delta T_m/(T_1 - t_1) = P/N_{tu} \quad (100)$$

(*vi*) In two of the twelve arrangements analyzed, N_{tu} can be easily obtained as an explicit function of R and P. These are cases (1A) and (2A), where equations (23) or (36), (20), and (16) give the analytical expression for N_{tu} for arbitrary values of N_P and N_R. Precisely these cases, which involve simple couplings of single-row exchangers, can also be handled by the method used by Domingos for the calculation of assemblies of heat exchangers [11].

(*vii*) The effects of fluid mixing can be summarized as this: When the tube fluid is not mixed between passes, F is higher than in the mixed case, if connected with identical order of the rows, and lower if connected with inverted order. When the air is not mixed between rows, which is the usual case for air coolers, two opposite effects arise. The distribution of temperature differences becomes more favourable between rows belonging to the same pass, where the tube fluid in each row meets the air streamlines in identical order. On the contrary, the distribution becomes more uneven when the air streamlines leaving one pass are met in inverted order by the fluid inside the first row of the next pass. F may result higher or lower than in the case of mixed air, depending on which effect prevails.

References

1 Bowman, R. A., Mueller, A. C., and Nagle, W. M., "Mean Temperature Difference in Design," ASME *Transactions*, Vol. 62, 1940, pp. 283–294.

2 Stevens, R. A., Fernandez, J., and Woolf, J. R., "Mean Temperature Difference in One, Two, and Three-Pass Crossflow Heat Exchangers," ASME *Transactions*, Vol. 79, 1957, pp. 287–297.

3 Nicole, F. J. L., "Mean Temperature Difference in Cross-Flow Heat Exchange, Applied to Multipass Air-Cooled Fin-Tube Units with a Finite Number of Rows," M.Sc. thesis, University of Pretoria, CSIR Special Report CHEM 223, Nov. 1972.

4 Worsøe-Schmidt, P., "On the Effectiveness of a Class of Compound Heat Exchangers," Refrig. Lab. Dth. Rept., The Technical University of Denmark, Mar. 1976.

5 Baclic, B. S., and Gvozdenac, D. D., "ϵ-N_{tu}—ω Relationships for Inverted Order Flow Arrangements of Two-Pass Crossflow Heat Exchangers," *Regenerative and Recuperative Heat Exchangers*, edited by R. K. Shah and D. E. Metzger, HTD-Vol. 21, ASME, New York, 1981, pp. 27–41.

6 Schedwill, H., "Thermische Auslegung von Kreuzstrom-warmeaustauschern," *Fortschritt-Ber.* VDI-Z, Reihe 6, Nr. 19, 1968.

7 Braun, B., "Wärmeübergang und Temperaturverlauf in Querstrom—Rohrbündeln bei beliebiger Schaltung der Rohrreihen," *Forsch.Ing.-Wes.*, 41, Nr.6, 1975, pp. 181–191.

8 Kays, W. M., and London, A. L., *Compact Heat Exchangers*, 2d. ed. McGraw Hill, New York, 1964, p. 20.

9 Worsøe-Schmidt, P., and Hogaard Knudsen, H. J., "Thermal Modeling of Heat Exchangers for Simulation Purposes," *Proceedings of the 1976 Heat Transfer and Fluid Mechanics Institute*, Stanford University Press, pp. 495–511.

10 Roetzel, W., and Neubert, J., "Calculation of Mean Temperature Difference in Air-Cooled Crossflow Heat Exchangers," ASME JOURNAL OF HEAT TRANSFER, Vol. 101, 1979, pp. 511–513.

11 Domingos, J. D., "Analysis of Complex Assemblies of Heat Exchangers," *International Journal of Heat and Mass Transfer*, Vol. 12, Pergamon Press, 1969, pp. 537–548.

A. Pignotti

G. O. Cordero

Techint S.A.,
1001 Buenos Aires,
Argentina

Mean Temperature Difference Charts for Air Coolers

Computer generated graphs are presented for the mean temperature difference in typical air cooler configurations, covering the combinations of numbers of passes and rows per pass of industrial interest. Two sets of independent variables are included in the graphs: the conventional one (heat capacity water ratio and cold fluid effectiveness), and the one required in an optimization technique of widespread use (hot fluid effectiveness and the number of heat transfer units). Flow arrangements with side-by-side and over-and-under passes, frequently found in actual practice, are discussed through examples.

1 Introduction

Multipass air coolers can be arranged with the hot fluid passes (*i*) over-and-under each other, as shown in Fig. 1, (*ii*) side-by-side, as shown in Fig. 2, and (*iii*) in combined configurations as presented in section 5 of this paper. A complete description of the flow arrangement may be done through the picture of only one header. However, since the visualization becomes difficult for the complex configurations often found in actual practice, both headers, with a clear indication of the inlet and outlet area for each pass, are included in the figures. Solid lines represent baffles existing in the headers; dotted lines represent an immaterial separation between passes, imposed only by the pressure gradient.

The mean temperature difference in case (*i*), for arbitrary numbers of passes and rows per pass, can be obtained analytically or numerically through the procedure developed in a previous article [1], under the usual idealizations of constant heat transfer coefficient, constant heat capacities, no change of phase, and uniform air velocity distribution. Two sets of charts, presenting the results of these calculations for most cases of practical interest, are discussed in sections 2 and 3.

Case (*ii*) can usually be reduced to the single-pass exchanger, as shown in section 4. Case (*iii*) is discussed through examples in section 5.

2 *F-P-R* Charts

The log-mean temperature difference correction factor, F, is represented in Figs. 3(*a*)-3(*j*) as a function of the effectiveness, P, and the heat capacity rates ratio, R. Since F compares the true mean temperature difference of a given exchanger, with that of reference counterflow equipment, these charts provide a well-suited means of finding out the best of several possible flow arrangements. The one with the higher F will require the lower N_{tu}, i.e., the lower area if U remains constant, operating with the same R and P. An illustration of this method is given in section 5.

The selection of the charts presented is based on the following criteria: no geometries with less than four rows are considered, because they are generally not economical. The maximum number of rows considered is eight, because additional rows are not common, and because many cases with more than eight rows can be safely assimilated to cases for which curves are given. Only counter-crossflow is included because it is by far the most efficient alternative. Only very special geometrical or physical restrictions (such as the possibility of freezing) may justify the use of co-crossflow. The hot fluid is assumed to mix between passes because the possible increase in performance with the rows connected in identical order [1] is usually not worth the corresponding cost increase of the headers. The no air mixing assumption is used, because it is the most realistic one.

The general pattern of the results shown in Fig. 3 is the following:

(*i*) The curves are most sensitive to the value of the number of passes, N_P, and less so to the number of rows per pass, N_R.

(*ii*) As N_P grows, the limit of pure counterflow is approached. Correspondingly, F grows with N_P and approaches the step function

$$F = \begin{cases} 1 \text{ for } P < 1/R \quad \text{and} \quad P < 1 \\ 0 \text{ otherwise} \end{cases}$$

Whereas for $N_P = 8$, F is close to the step function for $R = 8.0$ and for $R = 0.2$, it is not so close for the intermediate case $R = 1.0$ (see Fig. 3(*j*).

(*iii*) For fixed values of N_P, F grows with N_R under the hypothesis and restrictions stated above for this set of charts. The limit for large values of N_R, which corresponds to the case of N_P passes with both fluids totally unmixed, is approached fairly quickly, and more so the higher is the value of N_P. Figure 3(*b*) shows that the curves for $N_P = 1$, $N_R = 6$, are within 2 percent of the corresponding ones for $N_P = 1$, $N_R = \infty$, given by the formula of Nusselt [2], which are included in the same figure for the sake of comparison.

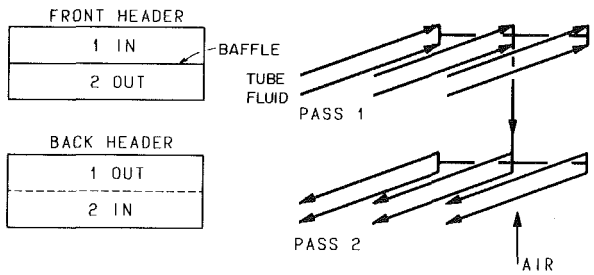

Fig. 1 Flow arrangement with two passes over-and-under

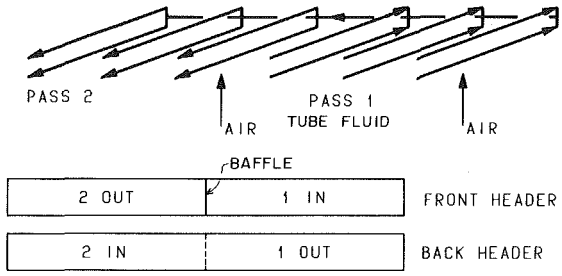

Fig. 2 Flow arrangement with two passes side-by-side

Contributed by the Heat Transfer Division for publication in the JOURNAL OF HEAT TRANSFER. Manuscript received by the Heat Transfer Division February 17, 1982.

3 ψ-$\underset{\sim}{P}$-N_{tu} Charts

In the air coolers design process, the air outlet temperature and air flow rate are usually unspecified. The number of transfer units, N_{tu}, on the other hand, is approximately known for a given type of fin-tube bundle through an optimization analysis for the air face velocity [3]. With N_{tu} and the hot fluid effectiveness, $\underset{\sim}{P}$, as the available data, an iterative procedure is required [1, 4] to find ψ, R, or P, and then the area of the heat transfer surface. This has been pointed out by Roetzel and Neubert [5], who presented a set of approximate equations giving ψ as an explicit function of N_{tu} and $\underset{\sim}{P}$ for several flow arrangements.

A direct graphical solution for this sizing problem cannot be obtained from any of the current F-P-R, P-N_{tu}-R, or ψ-$\underset{\sim}{P}$-$\underset{\sim}{N}_{tu}$ -R charts[1]. This difficulty is removed in Figs. 4(*a*)–4(*e*), through the inclusion of a family of constant N_{tu} curves in the Mueller charts [6], widely used for other design and rating problems. These additional curves are drawn within the following ranges of values: $0 \le \underset{\sim}{P} \le 0.99$, $0 \le R \le 8$, and $F \ge 0.5$. The constraints $R \le 8$ and $F \ge 0.5$ account for interruption of the curves corresponding to low and high values of N_{tu}, respectively, at values of $\underset{\sim}{P}$ smaller than 0.99. In addition, in these graphs the constant $\underset{\sim}{N}_{tu}$ lines are straight lines through the origin, and the corresponding endings and values of the parameter $\underset{\sim}{N}_{tu}$ are drawn in Fig. 4. The precision with which the mean temperature difference can be read from these curves is not as high as that of the plots of F in Figs. 3(*a*)–3(*j*). For this reason and because the minimum number of rows considered is 4, only one chart is given for each number of passes. The same chart can safely be used for a number of rows larger than the one for which it is presented.

4 Side-by-Side Arrangements

Side-by-side arrangements[2], such as shown in Fig. 2, can be handled through the results obtained for a single pass with N_R rows. The general case of n bundles of N_R rows each presents two main alternatives:

(*i*) If headers are built so that the hot fluid from different rows is not allowed to mix, the boundary conditions coincide with those of a single bundle with tubes n times longer. Figures 3 and 4 for $N_P = 1$ provide a direct solution for the MTD, and it is obvious that increasing the numbers of side-by-side passes has no effect on the true-mean temperature difference for the same heat transfer area.

(*ii*) If the hot fluid mixes in the headers such as in the case of Fig. 2, the correction factor decreases with the number of side-by-side passes, tending to that of a single pass with a single row. Domingo's method [7] for exchangers in parallel in one of the streams readily gives

$$P_P = [1-(1-PR)^{1/n}]/R_P \tag{1}$$

Since the air flow rate for each pass is the nth part of the total, $R_P = R/n$ and the number of transfer units for the complete exchanger coincides with that for each pass. From the known relation,

$$F = \chi(R,P)/N_{tu} \tag{2}$$

it follows

$$F = F(R_P,P_P)\,\frac{\chi(R,P)}{\chi(R_P,P_P)} \tag{3}$$

where $F\,(R_P, P_P)$ can be obtained from Fig. 3 for $N_P = 1$.

5 Combined Configurations

Configurations combining passes both over-and-under and side-by-side are frequently used in industrial applications. An accurate solution of these complex arrangements is beyond the scope of the present article, and requires the step-by-step methods [8] also used to handle variations in the process parameters. For the purpose of manual calculations, however, a reasonable estimate of F within upper and lower bounds can easily be established, considering the influence of the different variables discussed in section 2. Such a procedure is illustrated by the following examples.

Example 1. When the total number of rows, N, is larger than the number of passes, N_P, but not a multiple of it, the usual configuration is that of Fig. 5, where each air streamline meets tubes from every pass, and baffles with irregular shapes are required in the headers to generate the desired flow pattern. In this case, lower and upper bounds can be obtained for F, assuming N_{R1} equal to the integer part of N/N_P, and $N_{R2} = N_{R1} + 1$, respectively. For instance, if $N = 6$ and $N_P = 4$, Figs. 3(*f*) and 3(*g*) provide the required bounds for F.

Example 2. Figure 6 shows an arrangement with two passes side-by-side, and two passes over-and-under, where $N_R = 2$ is assumed. If hot fluid of different rows were not allowed to

[1] Here N_{tu} and $\underset{\sim}{N}_{tu}$ designate the number of heat transfer units based on the *cold* and *hot* side heat capacity rates, respectively.

[2] In the literature, side-by-side pass arrangements are also referred to as multipass exchangers with one stream in series and other stream in parallel.

Nomenclature

A = heat transfer surface area, m^2
C = specific heat of hot fluid, J/kg °C
c = specific heat of cold fluid, J/kg °C
F = log-mean temperature difference correction factor, dimensionless
N = total number of tube rows
n = number of side-by-side passes
N_P = number of over-and-under tube passes
N_R = number of tube rows per pass
N_{tu} = number of heat transfer units referred to the cold fluid, dimensionless, UA/wc
$\underset{\sim}{N}_{tu}$ = number of heat transfer units referred to the hot fluid, dimensionless, UA/WC
P = cold fluid temperature effectiveness, dimensionless, $(t_F - t_I)/(T_I - t_I)$
$\underset{\sim}{P}$ = hot fluid temperature effectiveness, dimensionless, $(T_I - T_F)/(T_I - t_I)$
R = wc/WC = heat capacity rates ratio, dimensionless, $(T_I - T_F)/(t_F - t_I)$
T = hot fluid temperature, °C
t = cold fluid temperature, °C
U = overall coefficient of heat transfer, W/m^2 °C
W = mass flow rate of hot fluid, kg/s
w = mass flow rate of cold fluid, kg/s
ΔT_{lm} = log-mean temperature difference, °C
ΔT_m = true-mean temperature difference, °C

$$\chi(R,P) = (t_F - t_I)/\Delta T_{lm} = \begin{cases} \dfrac{1}{R-1}\,ln\,\dfrac{(1-P)}{(1-RP)}, & R \neq 1 \\ \dfrac{P}{1-P}, & R = 1 \end{cases}$$

ψ = $\Delta T_m/(T_I - t_I)$ = dimensionless true-mean temperature difference

Subscripts

F = final
I = initial
P = corresponding to one pass

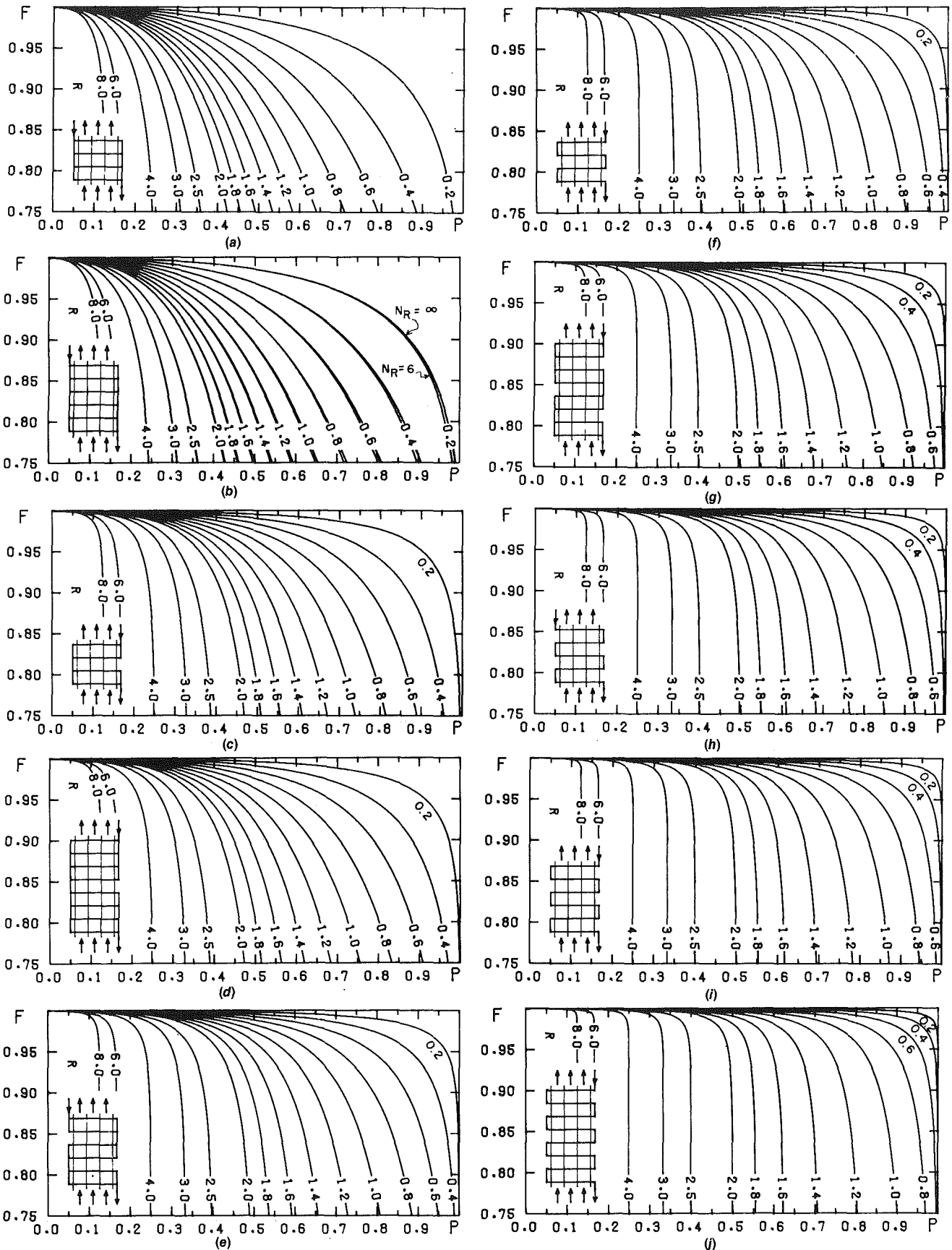

Fig. 3 *F-P-R* charts: (*a*) one pass, four rows; (*b*) one pass, six rows (lower curves) and infinite rows (upper curves); (*c*) two passes, two rows per pass; (*d*) two passes, four rows per pass; (*e*) three passes, two rows per pass; (*f*) four passes, one row per pass; (*g*) four passes, two rows per pass; (*h*) five passes, one row per pass; (*i*) six passes, one row per pass; (*j*) eight passes, one row per pass

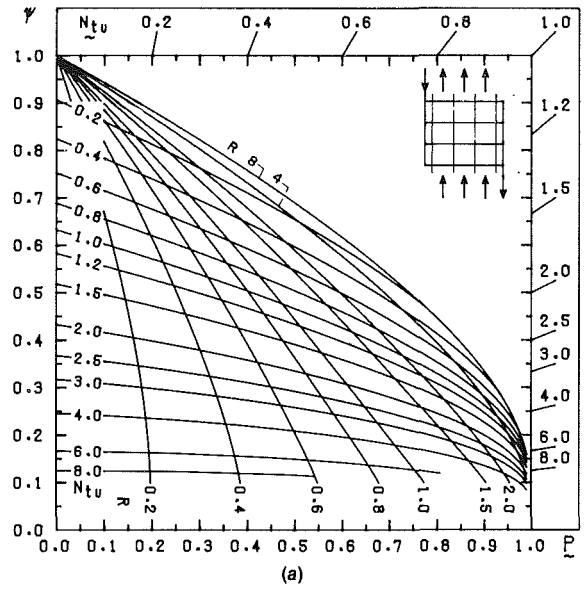

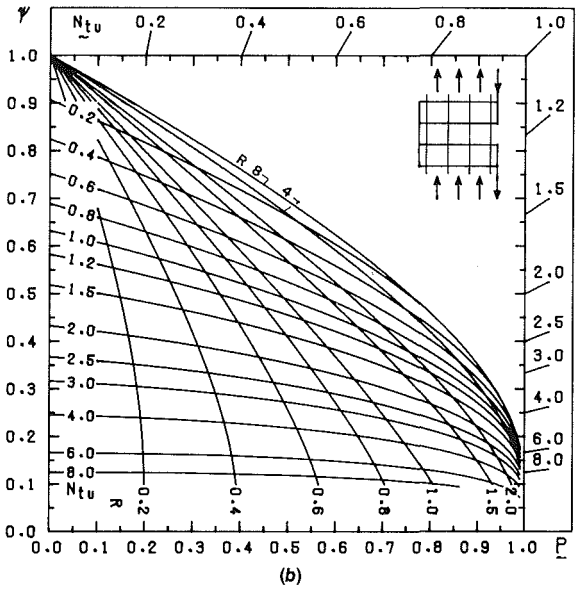

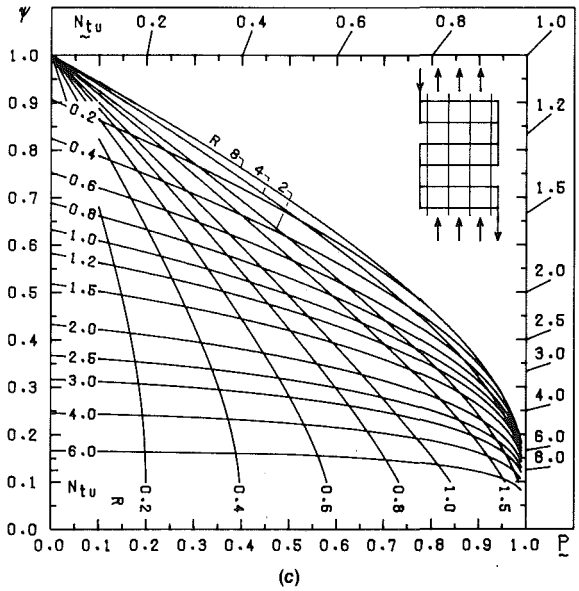

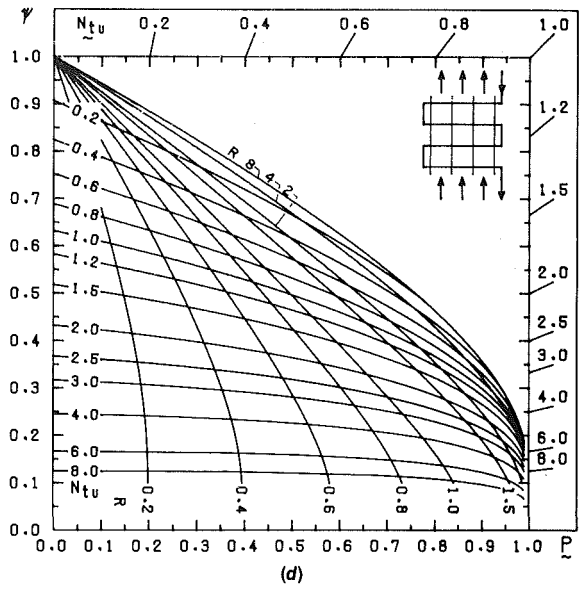

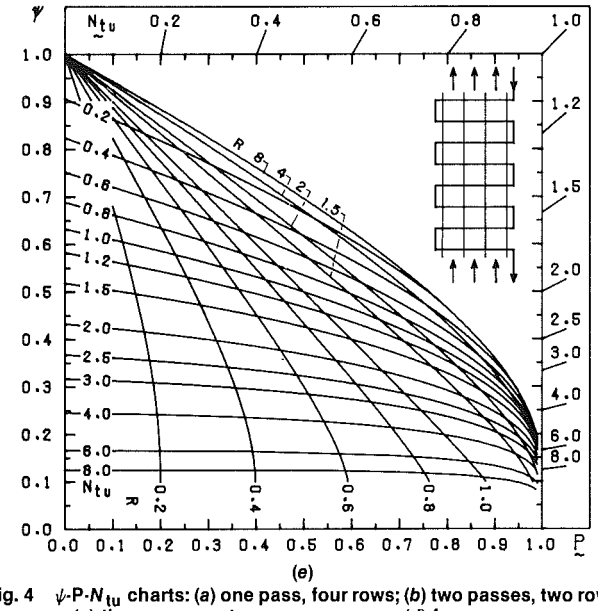

Fig. 4 ψ-P-N_{tu} charts: (*a*) one pass, four rows; (*b*) two passes, two rows per pass; (*c*) three passes, two rows per pass; (*d*) four passes, one row per pass, (*e*) eight passes, one row per pass

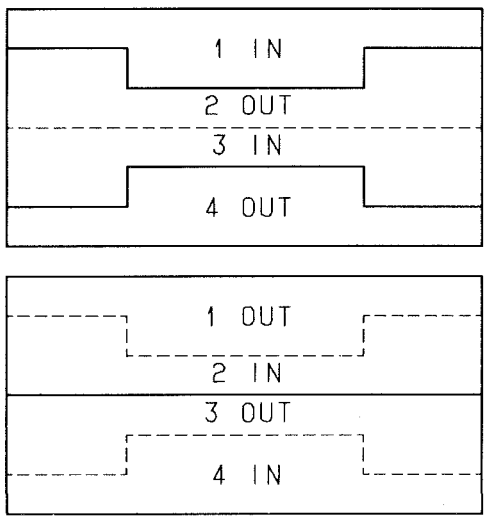

Fig. 5 Flow arrangement in the headers, for example 1.

mix between passes 1 and 2, and between passes 3 and 4, the same conditions of a two-pass exchanger with tubes two times longer would apply. Figure 3(*c*) gives then the upper bound for F. On the other hand, a lower bound is provided by case of two passes, one row per pass, which would correspond to allowing the fluids of the two rows within each pass to mix throughout. This is a known case and F can be obtained, for instance, from Fig. 15 in [6].

Example 3. Figure 7 presents the same case as before, but with passes 3 and 4 in inverted position. A pipe is required in the front header to connect passes 2 and 3 but with this arrangement the hotter air from pass 3 meets the hotter fluid of pass 1 giving a more uniform temperature difference and consequently a higher F. This effect was early recognized in the design of trombone coolers and Bowman et al. [9] published the correction factor. Figure 13 in [9] corresponds to $N_R = 1$ and gives a lower bound for F in the present case. The true value of F for $N_R = 2$ can be obtained analytically or numerically with a procedure similar to that developed in [1].

Example 4. A typical case of an exchanger with the number of passes greater than the number of rows is presented in [10]: a kerosene air-fin cooler made up of standard sections with four rows and two tube passes side-by-side per section is analyzed. Three sections, also connected side-by-side, are needed to provide the required heat transfer surface. Four different arrangements of the headers are analyzed next, to show that differences up to 15 percent in F, and consequently in the required area, arise according to the solution adopted.

Case (a): Hot Fluid Mixed Between Side-by-Side Passes (Fig. 8(a)). In the example quoted, $P = 0.33$, $R = 2.14$. Since there are six side-by-side passes, $R_p = R/6 = 0.357$ and from equation (1), $P_P = 0.518$. The correction factor for each pass, obtained from Fig. 3(*a*) with $R_P = 0.357$ and $P_P = 0.518$ is $F = 0.959$. Then from equation (3), the correction factor for the whole exchanger is $F = 0.858$.

Case (b): Hot Fluid of Different Rows, Unmixed Between Passes (Fig. 8(b)). This case is equivalent to a single pass of four rows, so that from Fig. 3(*a*), with $R = 2.14$ and $P = 0.33$, the correction factor is $F = 0.886$. A 3 percent decrease in the area required for the given process conditions would be thus obtained, but with more expensive headers.

Case (c): Two Passes Over-and-Under in Each of the Three Sections, Which Are Connected Side-by-Side (Fig.

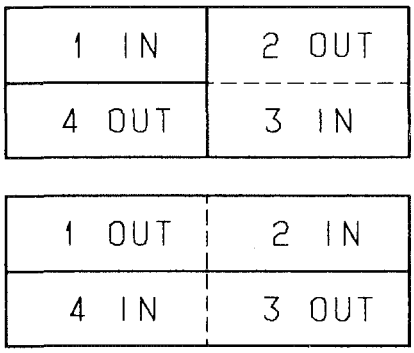

Fig. 6 Flow arrangement in the headers, for example 2.

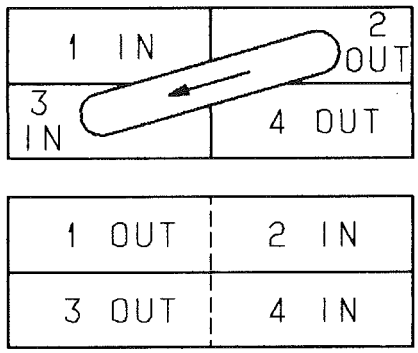

Fig. 7 Flow arrangement in the headers, for example 3.

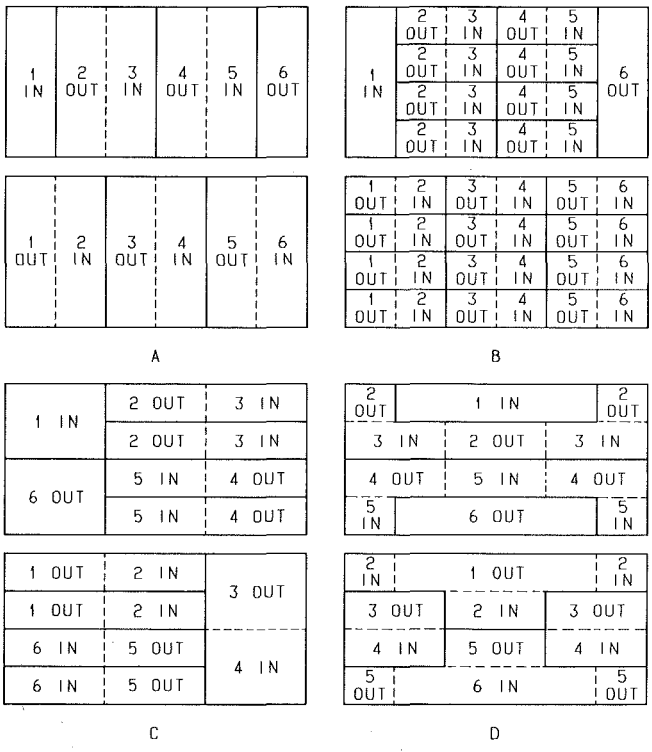

Fig. 8 Flow arrangement in the headers, for example 4.

8(c)). This configuration is equivalent to an exchanger with two passes over-and-under and tubes three times longer. Consequently, from Fig. 3(c) with $R = 2.14$ and $P = 0.33$, $F = 0.958$. An 11 percent decrease in the required area is obtained in comparison with case (a).

Case (d): Complex Arrangement, Shown in Fig. 8(d), Typical of Air Coolers Built With Specially Designed Headers. An obvious upper bound for this geometry is set by the conventional configuration with six passes over-and-under and one row per pass, for which $F = 0.995$, from Fig. 3(i) with $R = 2.14$ and $P = 0.33$. A lower bound can be obtained considering a three-row geometry, in which the six passes are arranged setting three over-and-under and duplicating each side-by-side. This is equivalent to the case $N_P = 3$, $N_R = 1$, for which $F = 0.980$. Rearrangement of the tubes in an adequate four-row configuration, such as shown in Fig. 8(d), is expected to increase the correction factor to the vicinity of the value $F = 0.988$, which corresponds to $N_P = 4$, $N_R = 1$. This last arrangement provides then a 15 percent increase in F, if compared with the first one.

6 Conclusions

(i) An accurate comparison between the mean temperature difference obtained in different configurations, operating under the same process conditions, is provided through Figs. 3(a)-3(j).

(ii) A direct graphical solution for the mean temperature difference, when N_{tu} and the hot fluid effectiveness are the available data, is made possible through modified Mueller charts (Figs. 4(a-e)), which are also useful for other design and rating problems.

(iii) Lower and upper bounds can be established for the mean temperature differences in complex arrangements with passes over-and-under and side-by-side, through the methods described in sections 4 and 5. A better flow arrangement, associated with a higher number of passes over-and-under, can thus be explored without resorting to lengthy step-by-step calculations, which may be reserved only for the final check.

References

1 Pignotti, A., and Cordero, G. O., "Mean Temperature Difference in Multipass Crossflow," ASME JOURNAL OF HEAT TRANSFER, Vol. 105, 1983.

2 Nusselt, W., "Eine neue Formel für den Wärmedurchgang im Kreuzstrom," *Technische Mechanik und Thermodynamik*, Vol. 1, 1930, pp. 417-422.

3 Smith, E. C., "Air Cooled Heat Exchangers," *Chem. Eng.*, Vol. 65, Nov. 17, 1958, pp. 145-150.

4 Ludwig, E. E., *Applied Process Design for Chemical and Petrochemical Plants*, Gulf, Houston, 1964, p. 156.

5 Roetzel, N., and Neubert, J., "Calculation of Mean Temperature Difference in Air-Cooled Crossflow Heat Exchangers," ASME JOURNAL OF HEAT TRANSFER, Vol. 101, 1979, pp. 511-513.

6 Mueller, A. C., "Heat Exchangers," ch. 18, *Handbook of Heat Transfer*, edited by W. M. Rohsenow and J. P. Hartnett, 1973, pp. 18-31.

7 Domingos, J. D., "Analysis of Complex Assemblies of Heat Exchangers," *International Journal of Heat and Mass Transfer*, Vol. 12, 1969, pp. 537-548.

8 Urbicain, M. J., and Paloschi, J., "Simulation of Air Cooled Heat Exchangers," *Computers and Chemical Engineering*, Vol. 5, 1981, pp. 75-81.

9 Bowman, R. A., Mueller, A. C., and Nagle, W. M., "Mean Temperature Difference in Design," ASME *Transactions*, Vol. 62, 1940, pp. 283-294.

10 Kern, D. Q., and Kraus, A. D., *Extended Surface Heat Transfer*, McGraw-Hill, New York, 1972, pp. 571-576.

S. Mochizuki[1]
Wen-Jei Yang
Mem. ASME

Department of Mechanical Engineering
and Applied Mechanics,
The University of Michigan,
Ann Arbor, Mich. 48109

Y. Yagi
M. Ueno

Department of Mechanical Engineering,
Tokyo University of Agriculture
and Technology,
Koganei, Tokyo, Japan

Heat Transfer Mechanisms and Performance in Multiple Parallel Disk Assemblies

Heat transfer and frictional loss performance in radial flow through multiple parallel disk assemblies are experimentally studied by a modified single-blow transient test method. The mechanisms of heat transfer enhancement are determined in the four flow regimes which are characterized by different combinations of flow patterns: pure laminar, laminar-oscillating-laminar, laminar-oscillating-turbulent-laminar, and laminar-oscillating-turbulent type convection. The fifth convective regime is predicted. The results of a condensation-heated disk core are incorporated for discussion and performance comparison. The effects of the disk spacing and size and influx disturbance on the transfer performance are investigated. It is concluded that the disk device has the performance characteristics comparable to high-performance plate-fin type surfaces that are commonly employed in compact heat exchangers.

Introduction

The study concerns transport phenonmena in radial flow between parallel annular disks, with the flow supplied without swirl through the center of one side of the disks, as shown in Fig. 1. The results can be applied to the design of hydrostatic air bearings, centrifugal compressor diffusers, and radial flow type heat exchangers. The problem is of some intrinsic interest. For creeping flow, the radial pressure distribution decreases logarithmically downstream, whereas for ideal flow it increases radially. In practice, pressure gradients are usually negative near the entrance, changing to positive gradients downstream. Above a certain critical volume flow, the adverse pressure gradient combined with the presence of wall friction leads to the occurrence of separation, reverse flow, and subsequent reattachment. A reverse transition from turbulent to laminar flow may take place.

A recent theoretical and experimental study [1] on radial flow through two parallel disks with steady influx disclosed the following: (*i*) when the Reynolds number Re is low, the slug flow at the inlet develops into a laminar profile toward the exit; (*ii*) as Re reaches a critical value, Re_c, vortices separate alternately from both walls of the radial channel and stretch a distance downstream. Self-sustained flow oscillations are thus induced which diminish downstream and a laminar profile is restored before the flow exits the channel; and (*iii*) when the volume flow is further increased to Re_t, the oscillating flow is grossly amplified and changed into a turbulent flow. However, due to continuous enlargement of the flow cross-sectional area in the radial direction, a reverse transition from turbulent to laminar flow takes place. Contrary to the steady-state formation of "annular separation bubbles" as claimed in the previous studies [for example 2 and 3], the separation phenomena were found to be unsteady in nature.

In contrast to numerous studies on the momentum transfer problems in radial flow through parallel disks, only a few studies have been reported to deal with heat transfer problems in the flow system: Kreith [4] studied heat transfer in a fully developed flow and found the Nusselt number as a function of $\mathrm{Gz}\, D_H/d_m$

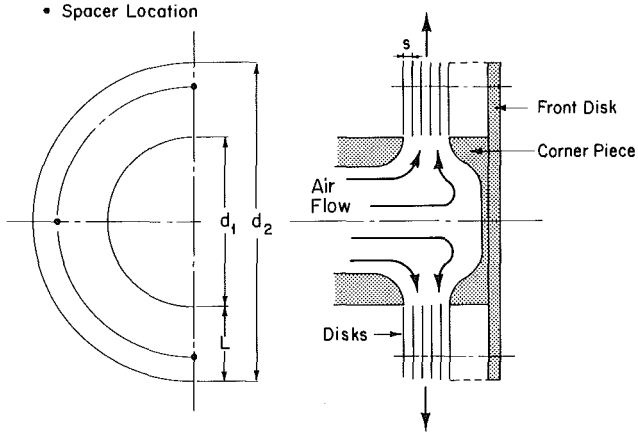

Fig. 1 Test core for single-blow method

$$\mathrm{Nu} = f(Gz\, D_H/d_m) \tag{1}$$

under constant surface temperature conditions. Here, Nu denotes the Nusselt number; Gz, Graetz number; and D_H, hydraulic diameter.

Using the steady test method by condensing steam inside hollow disks, Mochizuki and Yang [5] investigated the same system including the entrance effects. The heat transfer and friction factors, j and f, respectively, at zero rotating speed were determined as

$$j = 1.15\ \mathrm{Re}^{-2/3} \text{ and } f = 1.40\ \mathrm{Re}^{-0.222} \tag{2}$$

The heat transfer performance was comparable to those of high-performance compact plate-fin surfaces of plain, louvered, and strip type, while the f factor was substantially higher than those of the compact surface. High friction losses may be attributed to three main causes: (*i*) the inlet air flow was not rectified (streamlined) due to improper design of the inlet vane; (*ii*) the leading edge of each disk at the inlet was substantially thick relative to the opening (low inlet porosity) and sharp, triggering flow disturbance; and (*iii*) the installation of spacers between disks for structure rigidity further disturbed the radial air flow. The number of spacers has been reduced from 24 in the previous study to 4 in the present case. Obstacle (*i*) was removed by rounding the inlet vane to produce a slug flow profile at the inlet to the disk assembly, while obstacle (*ii*) was minimized by reducing the

[1] On leave from Department of Mechanical Engineering, Tokyo University of Agriculture and Technology, Koganei, Tokyo, Japan.

Contributed by the Heat Transfer Division for publication in the JOURNAL OF HEAT TRANSFER. Manuscript received by the Heat Transfer Division March 19, 1982.

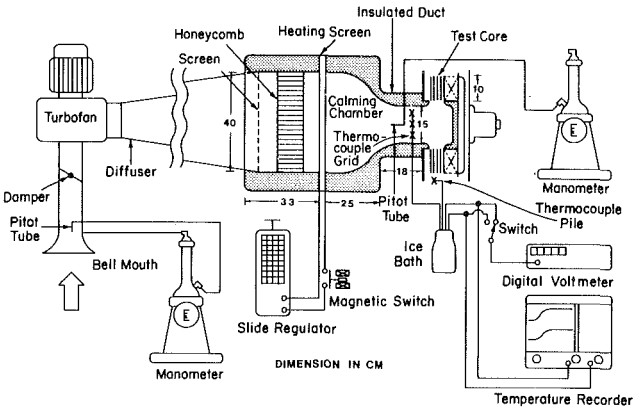

Fig. 2 A schematic of test apparatus for single-blow method

thickness of each heat transfer surface in the disk assembly from 1.8 mm (2 disks of 0.5-mm thickness enclosing a condensation space of 0.8-mm thickness) to 0.5 mm (each disk of 0.5-mm thickness by air heating), thus substantially enlarging the core free-flow to frontal area ratio. It results in a drastic reduction in f.

A modified single-blow (sometime referred to as transient test) technique is employed in the present study to determine the heat transfer and friction loss performance in radial flow through multiple parallel annular disks. Twelve disk assemblies of different geometric dimensions are tested by the single-blow method, while only one disk assembly is studied by the steady-state method. Heat transfer mechanisms are determined by correlating the Nusselt number and Colburn factor versus the Reynolds number. Comparison of tansport performance is made between the disk assemblies and some representative high-performance compact surfaces, as shown in Fig. 5.

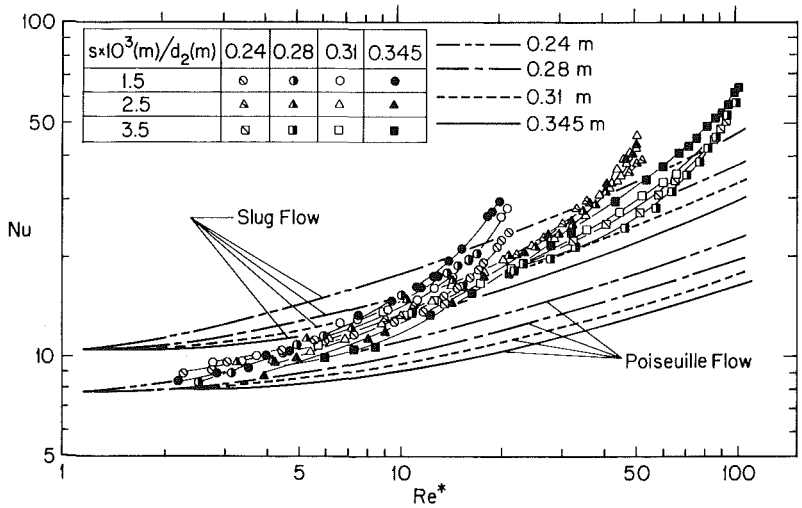

Fig. 3 Nu versus Re* correlation of test results obtained by single-blow method

Nomenclature

a, b, c, d, e = exponents
C_a = specific heat of air at constant pressure, J/(kg•K)
D_H = hydraulic diameter, m
d = disk diameter: d_1, inner; d_2, outer; d_m, mean $= (d_1 + d_2)/2$, m
E_{STD} = flow friction power as defined by equation (9), kW/m^2
f = Fanning friction factor as defined by equation (5)
Gz = Greatz number, $=$ Re Pr D_H/L
h = heat transfer coefficient, W/(m^2•K)
h_{STD} = heat transfer power as defined by equation (8), W/(m^{2}K)
j = Colburn heat transfer factor as defined by equation (7)
K = pressure loss coefficient; K_c, at inlet; K_e, at exit, dimensionless
k = thermal conductivity, W/(m•K)
L = disk length, $= (d_2 - d_1)/2$, m
N = number of disks in a test core
Nu = Nusselt number, $= h D_H/k$
ΔP = total pressure drop: ΔP_f, within test core; ΔP_t, between inlet and exit, Pa
Pr = Prandtl number, $= C_a\mu/k$
Re = Reynolds number as defined by equation (3): Re_c, onset of oscillating flow; Re_t, onset of turbulent flow; Re_e, turbulent flow prevailing to exit; Re_i, turbulent flow commencing at inlet
Re* = Reynolds number as defined by equation (4); Re_c^*, onset of oscillating flow; Re_t^*, onset of turbulent flow; Re_e^*, turbulent flow prevailing to exit; Re_i^*, turbulent flow commencing at inlet
r = radial distance, m
r_1, r_2 = inner and outer disk radii, respectively, m
s = disk spacing, m
u = radial velocity: u_1, at inlet; u_2, at exit; u_m, at midpoint, m/s

Greek Letters

δ = disk thickness, m
μ = dynamic viscosity, Pa•s
ρ = fluid density, kg/m^3
σ = frontal core porosity as defined by equation (12), dimensionless

Table 1 Geometric properties of test core, Re_c^* and Re_t^*

		1	2	3	4	5	6	7	8	9	10	11	12
Disk thickness	$\delta \times 10^3$,m	0.5											
Inside diameter	d_1,m	0.16											
Outside diameter	d_2,m	0.24				0.28			0.31			0.345	
Flow length	$L \times 10^2$,m	4.00				6.00			7.50			9.25	
Mean diameter	d_m,m	0.20				0.22			0.235			0.253	
Disk spacing	$s \times 10^3$,m	1.5	2.5	3.5	1.5	2.5	3.5	1.5	2.5	3.5	1.5	2.5	3.5
Hydraulic diameter	$D_H \times 10^3$,m	3	5	7	3	5	7	3	5	7	3	5	7
	d_m/D_H	66.7	40.0	28.6	73.3	44.0	31.4	78.3	47.0	33.6	84.3	50.6	36.1
	L/D_H	13.3	8.00	5.71	20.0	12.0	8.57	25.0	15.0	10.7	30.8	18.5	13.2
Number of disks	N	9	6	4	9	6	4	9	6	4	9	6	4
	Re_c^*	7.2	12	31	4.5	6.0	—	3.8	4.5	7.6	3.1	3.8	6.5
	Re_t^*	23	45	70	17	32	60	13	29	55	11	27	50

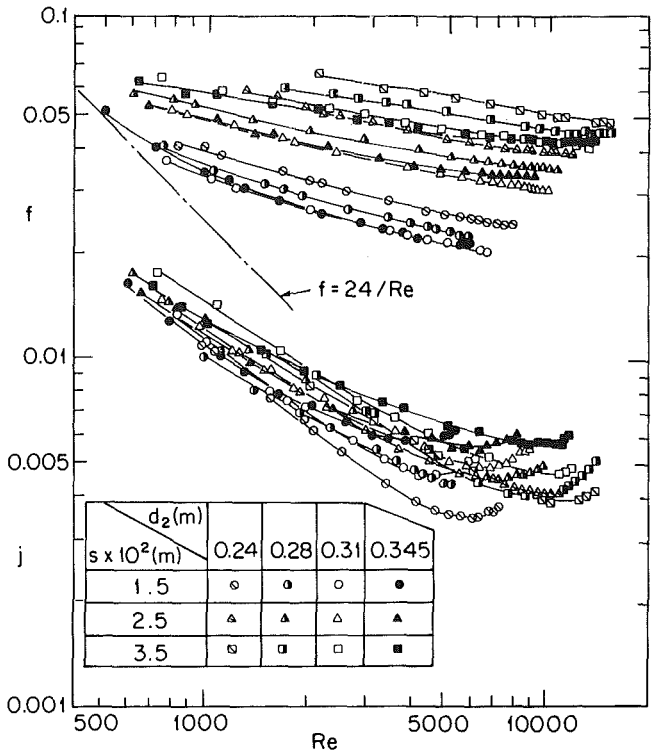

Fig. 4 *j* and *f* versus Re correlation of test results by single-blow method

Experimental Apparatus and Procedure

Th heat transfer system consisted of multiple disks with openings in the center, as shown in Fig. 1. Each disk was made of aluminum 0.5 mm in thickness with 160-mm i.d. (d_1) and variable o.d. (d_2). The corner piece smoothly changed the flow direction, thus eliminating the creation of a stagnant region at the center of the front disk. The corner piece was shaped to produce a slug flow profile at the inlet to the disk assembly. Both the corner piece and the front disk were made of urethane foam and bakelite, respectively, for heat insulation. The disk spacing, s, was varied by varying the number of bakelite washers of fixed thickness. Three values of s of 1.5, 2.5, and 3.5 mm were combined with four variations in d_2, namely 240, 280, 310, and 345 mm. The number of disks, N, was altered depending on the disk spacing. Table 1 depicts twelve combinations of geometric dimensions of the test cores.

The entire experimental setup is schematically illustrated in Fig. 2. Air was supplied to the test core from the turbofan through a calming chamber with the inside surface being covered by a layer of urethane foam. The damper was installed upstream from the turbofan to regulate the rate of air entering the bellmouth. The air flow rate was monitored by the Pitot tube and calculated from the reading of the manometer. After passing through the diffuser, screen, and honeycomb in sequence, the air was heated by the nichrome-wire heating screen located in the calming chamber. The electrical voltage supplied to the heating screen was regulated by the slide regulator with a step change in power input produced by the closing of the magnetic switch. Through the insulated duct, the heated air finally entered the test core. Air temperatures were measured by means of 0.025-mm-dia Alumel, Chromel thermocouples. A thermocouple grid consisting of eight thermocouples joined in series was placed in the duct. It was used to record the average air temperatures at the inlet of the test core. Eight thermocouples were placed at equal circumferential distances around the core exit. Each

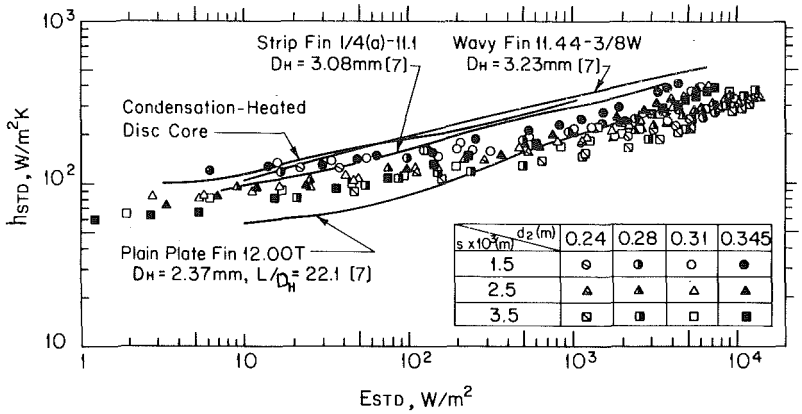

Fig. 5 h_{STD} versus E_{STD} correlation of test results obtained by single-blow method

thermocouple was placed at the midplane between two disks on a circumference at 0.5 mm from the disk edge. They were joined in series to form the thermocouple pile to monitor the mean outlet air temperature around the test core. The ice bath was used for the reference junction of the thermocouples. Steady-state temperatures were measured by means of the digital voltmeter through the switch. Transient temperature measurements were recorded with the Watanabe pen-type recorder. The static pressure drop across the test core was measured by the Pitot tube located 150 mm upstream from the core through the manometer. The Pitot tube and thermocouples were carefully calibrated.

For testing, the desired air flow through the test core was set by means of adjusting the damper. Both pressure measurements and the air temperatures upstream and downstream of the test core were taken. A step power input from the power source, enough to raise the temperature of the incoming air by 15 K in about 15 s, was suddenly applied to the heating screen by closing the electromagnetic switch. The transient temperatures of the air entering and leaving the test core were continuously recorded on the recorder. The air temperatures were recorded again after they had attained a final steady value. The same procedure was repeated for other flow rates.

Test Results

The heat transfer performance was expressed in terms of the Nusselt number Nu and the Colburn factor, j. The former was convenient in determining heat transfer mechanisms. The friction loss characteristics were presented in terms of the friction factor, f. For heat transfer calculation, all physical properties of air were evaluated at the arithmatic mean of the final steady temperature of the air at the core inlet and exit.

The Reynolds number is defined on the basis of the hydraulic diameter of the flow channels in the core as

$$\mathrm{Re} = \frac{\rho U_m D_H}{\mu} \tag{3}$$

where ρ denotes the fluid density; $D_H = 2s$ for the system; u_m, air velocity at the midpoint $(d_1 + d_2)/4$ of the test core; and μ, dynamic viscosity. Another Reynolds number convenient to the radial flow system Re* is also employed, which is defined as

$$\mathrm{Re}^* = \frac{\rho u_1 d_1}{2\mu}\left(\frac{s}{d_1}\right)^2 = \frac{(d_1+d_2)s}{8\,d_1{}^2}\mathrm{Re} \tag{4}$$

where u_1 represents the velocity at the core inlet. Re* signifies the Graetz number for a gas with Pr = 1 and a disk geometry of d_1 and d_2: $1/32\,[(d_2/d_1)^2 - 1]\,\mathrm{Re}\,D_H/L$.

The Fanning friction factor, f, is defined from the total pressure drop within the test core ΔP_f as

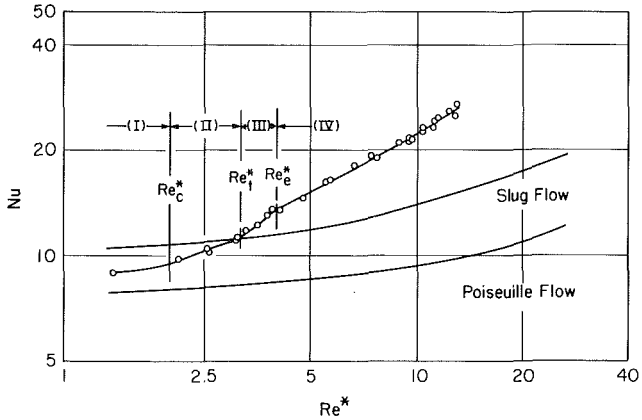

Fig. 6 Nu versus Re* for condensation-heated test core

$$f = \frac{\Delta P_f D_H}{2\rho u_m{}^2 L} \tag{5}$$

Here, L signifies length of the test core in the radial direction, $L = (d_2 - d_1)/2$; and

$$\Delta P_f = \Delta P_t - \frac{\rho}{2}\left(K_c u_1{}^2 + K_e u_2{}^2\right) \tag{6}$$

ΔP_t is the total pressure loss between the core inlet and exit; K_c and K_e, inlet and exit loss coefficients obtained from [7], p. 94 for parallel-plates entrance; and u_1 and u_2, inlet and exit mean velocities.

The heat transfer factor, j, is defined as

$$j = \frac{\mathrm{Nu}}{\mathrm{Re}\,\mathrm{Pr}^{1/3}} \tag{7}$$

wherein Pr denotes the Prandtl number of air. The heat transfer coefficent was determined by the modified single-blow transient test technique described in [6].

Twelve test cores were fabricated and tested in an effort to determine (*i*) heat transfer characteristics in various flow regimes and (*ii*) the effects of the governing physical parameters L/D_H, d_m/D_H and Re on f and j. The test results were also presented in terms of the heat transfer power h_{STD} and the flow friction power E_{STD}, which are defined as

$$h_{STD} = \left(\frac{C_a\,\mu}{\mathrm{Pr}^{2/3}}\right)_{STD}\frac{j\,\mathrm{Re}}{D_H} \tag{8}$$

$$E_{STD} = \frac{f}{2}\left(\frac{\mu^3}{\rho^2}\right)_{STD}\left(\frac{\mathrm{Re}}{D_H}\right)^3 \tag{9}$$

The subscript STD stands for standard conditions of dry air at 533 K and 1 atm.

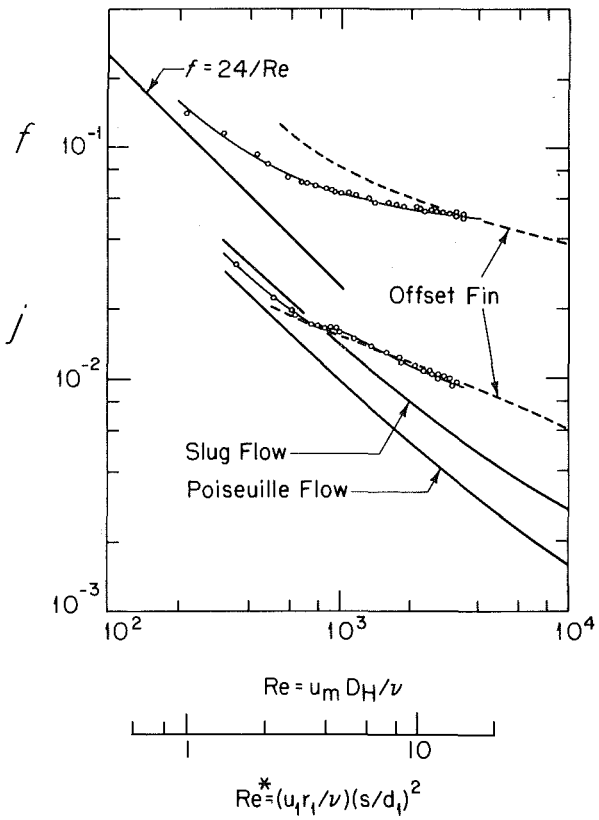

Fig. 7 *j* and *f* versus Re and Re* correlations for condensation-heated test core

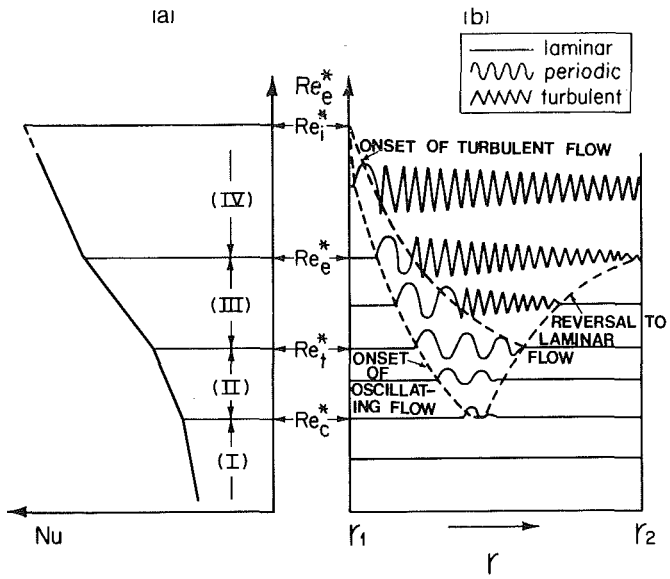

Fig. 8 Flow map (right) and the corresponding heat transfer performance (left) for radial flow between two parallel annular disks

The test results are presented in terms of Nu versus Re* in Fig. 3, *f* and *j* versus Re in Fig. 4, and h_{STD} versus E_{STD} in Fig. 5.

Figures 6 and 7 show the performance of a multiple parallel disk assembly heated by condensing steam inside the core. The test apparatus and procedure used in obtaining Figs. 6 and 7 were identical with those described in [5]. This unit had the geometric dimensions of $d_1 = 160$ mm, $d_2 = 310$ mm, disk thickness $\delta = 2$ mm, $s = 2$ mm and $N = 31$. Each disk consisted of two 0.5-mm-thick, ring-shaped plates with a 1-mm-thick spacer being sandwiched in between. The inner part of the spacer was cut to form the condensation spaces and steam passages. Spacers of 2 mm thickness were sandwiched between two disks, forming radial flow passages for the cooling air. The same test setup and procedure as in [5] were employed. No corner piece was placed to guide the influx to the test core. Different boundary geometries upstream from the entrance produced various degrees of disturbance in the entering stream, resulting in a significant disparity in the development stages of heat transfer performance between those cores tested by the transient method and the condensation-heated core, as will be discussed later in the following section.

Discussion

Both Figs. 3 and 6 demonstrate the effect of Re* on Nu. Under the thermal boundary condition of constant surface temperature, theoretical results for heat transfer performance were obtained for two special velocity patterns, uniform profile (slug flow) and parabolic profile (Poiseuille flow). The velocity profiles were assumed to prevail throughout the entire radial flow field (no entrance length was considered) and the heat transfer coefficient based on the logarithmic mean temperature difference between the core entrance and exit was employed. The results were superimposed in Figs. 3 and 6. Similarly, the *f* lines in Figs. 4 and 7 represented theoretical prediction of the friction factor for fully developed laminar flow throughout the test core. One interesting observation in Fig. 3 is that all theoretical lines for each extreme converge as Re* diminishes.

Based on the flow study in [1] and the present performance study, the variation of flow patterns with the Reynolds number, Re*, can be summarized in the flow map, the Re* versus *r* plot, in Fig. 8(*a*). Four flow regimes have been confirmed: In regime I, for Re* less than the critical value Re_c^*, the flow in the radial passage is laminar from the entrance to the exit. When the flow velocity reaches Re_c^*, boundary layer separation occurs at a location in the radial channel depending on r_1. It marks the onset of Regime II which ends at Re_t^*, the transition Reynolds number from laminar into turbulent flow. Regime III covers the flow between Re_t^* and Re_e^*. The flow pattern undergoes a sequential change, consisting of a transition from laminar through oscillating to turbulent flow followed by a reverse transition from turbulent to laminar flow. Re_e^* corresponds to the Reynolds number for which turbulent flow persists to the exit from the channel. In Regime IV, both the laminar and oscillating flow districts continue to diminish with Re*, while the turbulent flow section propagates upstream. The first two broken lines indicate the radial locations for initiation of the oscillating and turbulent flows, respectively, while the third broken line shows where the flows reverse to laminar flow. An extrapolation of the first two lines suggests that both the laminar and oscillating flow districts disappear at Re_i^* beyond which turbulent flow commences at the entrance and prevails over the entire channel. An experimental confirmation of the existence of Re_i^* was not realized due to limitation in the blower capacity. For the sake of identifying the heat transfer performance of each flow regime, the heat transfer performance curves of two representative cores No. 7 and 8 in Fig. 3 and the condensation-heated core in Fig. 6 are reproduced in Fig. 9. These three cores have identical d_1 and d_2. An examination of Fig. 9 leads to the classification of heat transfer performance according to the flow regimes shown in Fig. 8(*b*).

Heat Transfer Performance in Various Flow Regimes.

Regime I, Re < Re_c^*.* It is seen in Fig. 3 that as Re* decreases, each experimental curve asymptotically approaches an appropriate "Poiseuille Flow" line for all test cores. This

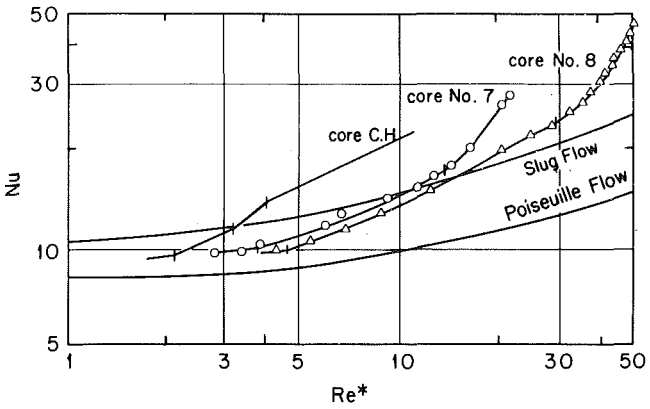

Fig. 9 Classification of heat transfer performance in different flow regimes in condensation-heated test core and single-blow test cores No. 7 and 8

is caused by the effect of fluid viscosity which predominates at low Reynolds number flow. However, as the volume flow is increased, the inertia effects become progressively important, resulting in a gradual shift of the performance curve toward the "Slug Flow" line. The condensation heated test core follows suit in Fig. 6. As seen in Fig. 9, the heat transfer enhancement with flow increase is rather minor in this pure laminar flow regime.

Regime II, $Re_c^* \le Re^* < Re_t^*$. When the volume flow reaches a critical value, Re_c^*, the performance curve changes its slope and becomes steeper with an increase in Re* (see Fig. 3). The values of Re_c* and Re_t* are listed in Table 1 for each core tested by the single blow method.

The nucleation, growth, migration and decay of vortices occur alternately on both sides of the channel walls, forming vortex streets in part of the radial channel [1]. These vortex streets induce self-sustained flow oscillations and enhance the local heat transfer performance. The nucleation sites move upstream while the region of fluctuating flow or enhanced heat transfer extends both ways toward the inlet and the exit as Re* is increased. The latter effect is reflected in an upturn of the Nu curve in the flow regime. Re_c^* decreases with an increase in L/D_H or a decrease in s. In Fig. 6, $Re_c^* \cong 2.0$ is a deflection point where a change in the slopes of the performance curve may be observed. Table 1 lists the values of Re_c^* for the transient-heating cores. For both Regimes I and II, the j and f versus Re correlations, Figs. 4 and 7, can be approximated by [5]

$$j \propto \mathrm{Re}^a (D_H/d_m)^b (D_H/L)^g \tag{10}$$

$$f \propto \mathrm{Re}_f^c (D_H/L)^d (D_H/d_m)^e \tag{11}$$

In Fig. 4, for the transient-testing cores, the exponent, a, varies from $-1/2$ to $-3/4$, while c changes from -0.2 to -0.3. The exponents b,g,d, and e for the units studied here are found to be approximately 0.69, 0, 0.44, and 0.81, respectively. In Fig. 7, for the condensation-heated core, the j-curve shifts toward the "Slug Flow" line, while the f-curve moves away from the laminar line as Re is increased. The exponents a and c are -0.767 and -0.607, respectively. The c value is different from that for the transient-testing cores because of higher influx disturbance in the condensation core as will be discussed later in section 4. The exponents b, g, d, and c for the condensation-heating case are not determined since only one core was fabricated and tested.

Regime III, $Re_t^* \le Re^* < Re_e^*$. With increasing volume flow to Re_t^*, the vortex-induced oscillating flow becomes grossly amplified, resulting in a flow transition into a turbulent manner. If the radial-flow length, L, is sufficiently large, the phenomenon of flow relaminarization takes place before the flow reaches the disk edge. A further increase in Re* causes the regions of the fluctuating flow, and its subsequent turbulent stream to extend both upstream and downstream. As a consequence, the Nusselt number increases significantly. Figure 6 exhibits a deflection point at $Re_t^* \cong 3.2$ beyond which the slope of the performance curve increases appreciably. The values of Re_t^* in Fig. 3 for the transient-heating cores are listed in Table 1.

Regime IV, $Re^* \ge Re_e^*$. For the flow volume beyond Re_e^*, an enlargement in the turbulent flow area at outer disk region ceases, and thus a rate of enhancement in the heat transfer performance becomes less than that in the third regime. The regime commences at $Re_e^* \cong 4.0$ in Fig. 6 where the slope of the performance curve is approximately 0.53. Figure 7 exhibits $Re_e \cong 900$ beyond which the j and f have the slopes of -0.454 (the exponent a in equation (10)), and -0.262 (the exponent c in equation (11)), respectively. It is of interest to point out that while the heat transfer performance is comparable to that of a compact high-performance, offset-finned plate heat exchanger [7], the core experiences less friction loss.

No tests in Figs. 3 and 4 had high enough volume flow to reach the regime IV. It is important to note that while Re is most commonly used in correlating the system performance, Re* is useful in identifying the structure of radial flow through parallel disks.

Effect of Disk Spacing. For a fixed values of d_1 and d_2, a reduction in the disk spacing implies an increase in L/D_H, which promotes the occurrence of separation at lower Re_c^*. The appearance of vortex streets augments flow mixing resulting in heat transfer enhancement. Hence, the Nu curves for small values of s are steeper than those of large values of s. This can be seen in Figs. 3 and 9 by comparing the symbols of different geometrical shapes having the same content (for example • versus ■).

Effect of d_m. With s and d_1 fixed, a large d_m means large values of d_2 and d_m/D_H. The higher is d_m/D_H, the steeper is the Nu curve, as observed in Fig. 3 by comparing the symbols of the same geometrical shape but different contents. The reason is simple: a large d_m/D_H is synonymous with a large L/D_H.

Effect of Influx Disturbance. The frontal core porosity of a multiple parallel disk assembly can be defined as

$$\sigma = \frac{(N+1)s}{(N+1)s + N\delta} \tag{12}$$

The porosity and upstream turbulence constitute two major sources of influx disturbance to the test core. Due to sharpness of the disk edges and abrupt turning of flow from the upstream duct into the core, flow disturbances are induced at the leading edges of the disks. Since the flow is rectified through the honeycomb section and the calming chamber and is smoothly guided by a corner piece into the cores, upstream turbulence is relatively low in the cores tested by the single-blow method. The condensation-heated disk assembly suffered from higher influx disturbance than the transient heating cores, due to higher δ (which was 2 mm compared to 0.5 mm in the cores tested by the single-blow method) and in the absence of a honeycomb section and a corner piece. The higher influx disturbance promoted higher f and j, advanced the occurrence of vortex streets and a transition from laminar to turbulent flow, and lowered the values of both Re_c^* and Re^*_t, as seen in Fig. 9. More study is needed to quantify the effect of influx disturbance for future use in design.

Performance Comparison With Compact Surfaces. Performance comparison of the multiple parallel disk assembly with respect to the high-performance, plate-fin surfaces of plain, wavy, and strip type [7] was presented in the form of h_{STD} versus E_{STD} in Fig. 5. They have approximately the same

hydraulic diameter. It can be observed that the disk assemblies are either comparable to or even superior to the compact surfaces when operated at low values of E_{STD}, while the opposite is true at higher E_{STD} range. The condensation-heated disk core has a better performance than the strip surface at any E_{STD}.

Error Analysis of Data. An error analysis was carried out to determine the uncertainties in the test data using the method described in [8]. The factors taken into account included the uncertainties in the physical properties, geometric measurements of the test core, temperature and pressure measurements. The uncertainties in f and j were estimated to be about 3 percent and 6 percent, respectively.

Conclusions

The mechanisms of heat transfer enhancement in the multiple parallel disk assembly are determined in the four flow regimes. The Nu versus Re* correlations is instrumental in the determination of heat transfer mechanisms, while the j versus Re plot is suitable for empirical correlations, i.e., the derivation of empirical correlation expressions. Except for the region III, heat transfer and friction loss performance of the disk cores can be correlated in the form of equations (10) and (11), respectively. Their dependence on the disk spacing, disk size, and influx disturbance is discussed. The transport performance of a condensation-heated disk core is also included for comparison. It is concluded that the disk device has the performance characteristics comparable to high-performance, plate-fin compact surfaces that are commonly employed in vehicular power plants.

Acknowledgment

The authors wish to express their gratitude to Messrs. A. Fujimoto and S. Kuroda for their effort in carrying out the experiments. The study was partially supported by the N. Iwatani Foundation and by the U.S. National Science Foundation under the Grant Number ME 80-18031.

References

1 Mochizuki, S., and Yang, Wen-Jei, "Self-Sustained Radial Oscillating Flows Between Parallel Discs," submitted to the *Journal of Fluid Mechanics*, 1983.

2 Moller, P. S., "Radial Flow Without Swirl Between Parallel Discs," *Aeronautical Quarterly*, Vol. 14, 1963, pp. 163–186.

3 Raal, J. D., "Radial Source Flow Between Parallel Discs," *Journal of Fluid Mechanics*, Vol. 85, 1978, pp. 401–416.

4 Kreith, F., "Transfert de Chaleur et de Masse dans un Ecoulement Radial entre Deux Desques Paralleles Fixes, ou Tourant a la meme Vitesse," *International Journal of Heat Mass Transfer*, Vol. 9, 1966, pp. 265–282.

5 Mochizuki, S., and Yang, Wen-Jei, "Heat Transfer and Friction Loss in Laminar Radial Flows Through Rotating Annular Disks," ASME JOURNAL OF HEAT TRANSFER, Vol. 103, 1981, pp. 212–217.

6 Liang, C. Y., and Yang, Wen-Jei, "Modified Single-Blow Technique for Performance Evaluation on Heat Transfer Surfaces," ASME JOURNAL OF HEAT TRANSFER, Vol. 97, 1975, pp. 16–21.

7 Kays, W. M., and London, A. L., *Compact Heat Exchangers*, 2d ed., McGraw-Hill, New York, 1964.

8 Kline, S. J., and McClintock, F. A., "Describing Uncertainty in Single Sample Experiments," *Mechanical Engineering*, Vol. 75, 1953, pp. 3–8.

Boiling Heat Transfer With Freon 11 (R11) in Brazed Aluminum, Plate-Fin Heat Exchangers

J. M. Robertson

P. C. Lovegrove

General Heat Transfer Group,
Engineering Sciences Division,
AERE, Harwell,
Oxfordshire, OX11 ORA England

The results of laboratory experiments with Freon 11 (R11) flowing in an electrically heated, serrated-fin test section to measure local boiling coefficients over a wide range of vapor quality, with mass fluxes up to 150 kg/m² s, heat fluxes to 4 kW/m², and pressure from 3–7 bar, are reported. These low mass and heat fluxes reflect the industrial process application of these heat exchangers where exceedingly small temperature differences may exist between streams. Results are compared with the very similar boiling characteristics previously reported elsewhere for the same test section, with liquid nitrogen as a test fluid under comparable flow conditions. A simple method using the Reynolds number of the total flow regarded as a liquid has been used to correlate boiling heat transfer coefficients with quality for both fluids. The use of a liquid-film flow model to produce a nondimensional correlation connecting the Nusselt, Reynolds, and Prandtl numbers of the film is discussed.

1 Introduction

Plate-fin heat exchangers are widely used in the chemical process industries, for example, to liquefy gases of industrial importance often at very low temperatures. Boiling and condensing of single and multicomponent fluids take place in these exchangers, which may contain several streams, and design procedures for these heat transfer processes in plate-fin exchangers have been developed by firms involved in their manufacture.

For these procedures to be tested, developed, and extended, it is necessary that relevant data are available from laboratory experiments utilizing appropriate test sections and test fluids.

Information about the single-phase heat transfer and pressure drop characteristics of the various forms of finned passages used in these exchangers, together with details of their industrial application is generally available, see, for example, [1–5]. However, the characteristics of boiling and condensing heat transfer within plate-fin heat exchangers have not been widely studied by experimenters, and few papers have been produced on this topic [6, 7, 8, 15].

The conditions of flow within these exchangers are also very dissimilar to those in other forms employing, for example, round tubes. In this respect, flow passages are very small rectangular finned channels with walls spaced approximately a millimetre or so apart, mass fluxes are about 100 kg/m² s, and heat fluxes about 3 kW/m². Since operation of these exchangers is usually associated with cryogenic plants, temperature differences between adajacent stream can be as low as fractions of 1 degree Kelvin in order to reduce the energy consumption of a compressor. These features indicate that thermal design correlations based on the results of experimental work using large-bore round tubes, usually at higher mass and heat fluxes, would not necessarily be applicable to relevant design procedures. Moreover, the characteristics of boiling and condensing in these small channels, where most of the area for heat transfer is present on fins or secondary surfaces, may have unusual aspects.

With these requirements, the Heat Transfer and Fluid Flow Service of the Harwell and National Engineering Laboratories in the UK has set out to determine the boiling and condensing characteristics of these plate-fin passages in a systematic manner. Results of tests using liquid nitrogen in the HTFS Boiling Cryogenic Rig on a serrated-fin test section have already been published [10]. This electrically heated, 3.4-m long test section is representative of a portion of one channel of a plate-fin heat exchanger (assuming uniform flow distribution), and the flow conditions of the testwork and fluids are representative of those occurring in many industrial applications. The results from tests carried out with this test section with liquid nitrogen at a system pressure of 3 bar illustrated:

(*a*) The high wall-superheat associated with the inception of the first bubble at the onset of evaporation in this form of passage

(*b*) The magnitude of the boiling heat transfer coefficients over a wide range of vapor qualities and the effects of mass flux on this coefficient

(*c*) The predominance of forced convective boiling over nucleate boiling under the test conditions

In this paper, some of the results of experiments with Freon 11[1] on the same serrated-fin test section placed in an HTFS Boiling Refrigerant Rig are now presented. Boiling heat transfer coefficients are reported from tests with mass fluxes up to 150 kg/m² s, heat fluxes up to 4 kW/m², and pressures from 3–7 bar. Results are compared with those from the same test section using liquid nitrogen as the test fluid already reported in [10].

2 Experimental Equipment

A flow diagram of the experimental apparatus used for this experimentation is shown in Fig. 1. The test rig was designed specifically for use with refrigerants similar to Freon 11 and consisted of a main circulation loop, a pressurizing system, a dump tank circuit, and water cooling circuits. The test rig is fully described elsewhere [13]. Referring to the flow diagram given in Fig. 1, it can be seen that the circulating pump propels fluid through a rotameter, previously calibrated with water and with Freon 11, vertically up through the test section and then through a water-cooled condenser which adequately subcools the condensate before it returns to the pump to complete the circuit.

Contributed by the Heat Transfer Division for publication in the JOURNAL OF HEAT TRANSFER. Manuscript received by the Heat Transfer Division December 14, 1981. Paper No. 80-HT-58.

[1] Freon 11 is manufactured by Du Pont.

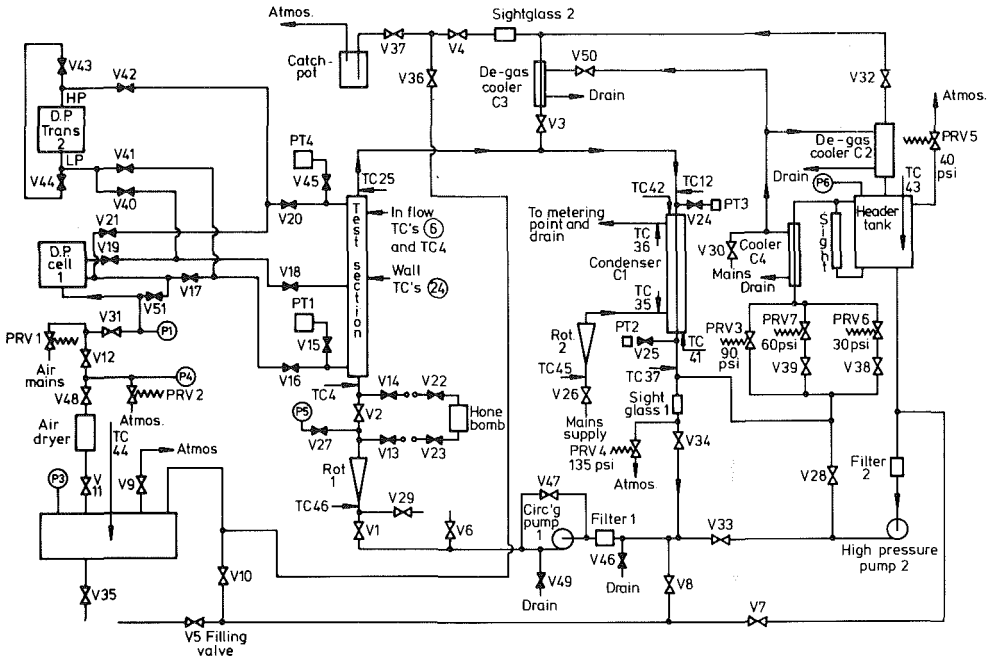

Fig. 1 Diagram of the apparatus

The system pressure is controlled by a separate circuit consisting of a high-pressure pump connected to the main flow circuit at the inlet to the main circulation pump. Liquid is drawn from a separate header tank by the high-pressure pump and excess liquid is returned through a set of relief valves and coolers to this header tank. With this equipment, it was possible to maintain the required system pressure within acceptable limits. This method of pressure control had the advantage that it was unnecessary to utilize an incondensible gas as a pressurizing medium with the possibility that the main circulating Freon would contain dissolved gas.

Static pressure was measured at the inlet and outlet of the test-section and the condenser with strain gauge transducers to a limit of approximately ± 140 Pa (approximately one-thousandth of an atmosphere). Flows to the test section were measured with a calibrated rotameter capable of resolving to approximately ± 0.1 g/s at a full-scale reading of 60 g/s (i.e., better than 1 percent).

Full details of the serrated-fin test section are given in the report describing the tests with liquid nitrogen [10]. It is 3.4-m long and consists of a rectangular duct with internal dimensions of 6.35 mm × 76.2 mm (Fig. 2).

The serrated finning is formed from 0.2-mm-thick aluminum sheet with 591 corrugations per meter (0.25-in. high × 15 fins per inch × 0.008-in. thick) with serrations at 3.18-mm intervals. The finning is sandwiched between two aluminum outer plates 6.35-mm thick and dip-brazed to them to form a strong mechanical and thermal bond. The test

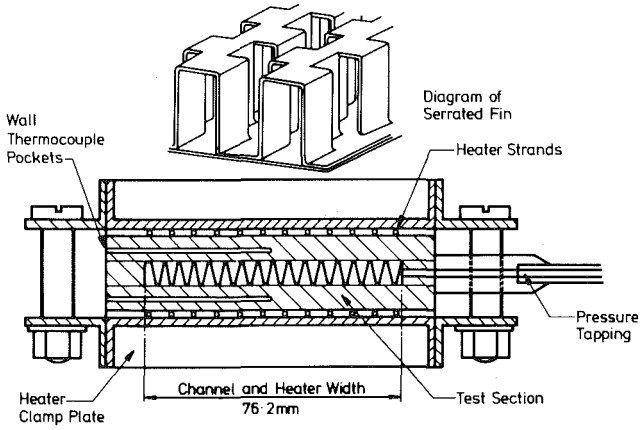

Fig. 2 Diagram of cross section of serrated fin test section

Nomenclature

a = channel height, m
A_p = primary surface of a plate-fin subchannel, m^2
A_s = secondary surface of a plate-fin subchannel, m^2
D_e = equivalent diameter of a subchannel, m
g = gravitational acceleration, m/s^2
G = mass flux based on channel flow area and total flow, kg/m^2 s
h_η = heat transfer coefficient based on fin efficiency, W/m^2K
J = Colburn factor, $(St.Pr^{0.66})$
j_g = volumetric flux of vapor over total channel flow area, m/s
k_L = thermal conductivity of liquid, W/mK
k_f = thermal conductivity of fin, W/mK
Pr = Prandtl number = $C_p\mu_L/k_L$
Q_T = total heat input to test section, W
Re_L = Reynolds number, $D_e\,G/\mu_L$
Re_{LF} = liquid film Reynolds number, $D_eG(1-x)/\mu_L$
St = Stanton number $h_\eta/C_p\,G$
t = fin thickness, m
T_{sat} = saturation temperature, local, K
T_{pw} = wall temperature of primary surface, K
x = thermodynamic vapor mass quality
z = distance up test section, measured from beginning of the heated length, m

Greek

η = fin efficiency
μ_L = liquid viscosity Pa s
ρ_L = liquid density, kg/m^3
ρ_g = vapor density, kg/m^3

section is heated by electrical heaters clamped along the entire 3.4-m length to each of the large faces. The heaters consist of 12 strands of 3.175-mm-dia, stainless-steel clad, Pyrotenax heater cable placed across the full channel width of each face of the test section. The aluminum side plates of the test section were sufficiently thick to produce a reasonably uniform heat flux on their inner faces in contact with the test fluid. The test section and associated pipework were completely encased in glass fibre insulation approximately 0.1-m thick.

Wall and bulk temperatures at many positions along the test section were measured using 1-mm-dia, stainless-steel-sheathed, chromel-alumel thermocouples. The thermocouples were connected through a data-logger to a digital voltmeter capable of resolving to ± 2 microvolts. All the thermocouples used were individually calibrated, before assembly in the test section, against a platinum resistance thermometer over the working temperature range of the experiments. Taking into account the response of the chromel-alumel thermocouples of approximately 30 microvolts per degree K, it was estimated that the thermocouples and the recording system would be accurate to better than ± 0.1 K.

3 Experimental Procedure

All the heat transfer tests were carried out with subcooled liquid Freon 11 at the entry to the test section. In those tests used for investigating the single-phase heat transfer characteristics, the Freon 11 remained subcooled over the whole length of the test section; in other tests, boiling commenced within the heated length of the test section.

An experimental run was conducted as follows. The required flow rate and the system pressure at the inlet to the test section were obtained by adjustment of the appropriate flow control valves on the main circuit and the relief valves on the pressurizing circuit. The electrical heater power was then applied and, by continual adjustment of all three parameters, the required experimental conditions were attained at thermal equilibrium. A full set of test readings was then taken and other sets were taken at short intervals until the variation with time on all the thermocouples within the test section was about ± 2 microvolts.

A heat balance was carried out by comparing the measured gradient of the bulk temperature of the single-phase liquid at a chosen position along the test section, with the calculated value using measured mass flow, heat input, and the appropriate fluid thermal properties. The difference between estimated and experimental values of this gradient was attributed mainly to heat leaks from the test section and the value found for each run (approximately 5 percent) was taken into account in the analysis of the experimental data. It was also possible to determine any systematic error associated with a thermocouple position by comparing the output of all thermocouples during unheated runs at various system temperatures. Systematic errors in this category were, in most cases, less than ± 0.2 K.

For the boiling heat transfer experiments, the onset of boiling was arranged to occur a short distance after the inlet to the test section by controlling the inlet temperature of the test fluid. This produced a length in which only liquid was heated and proved to be useful in determining the heat balance and a correction factor for each boiling run.

An axial profile of wall and bulk temperatures along the test section, as shown in Fig. 3, was drawn for each boiling run and studied for detail; the distance, z, is measured from the beginning of the heated length. In this example, for Run 133, boiling commenced approximately 1 m from the inlet to the test section and was associated with a sharp change in the slope of the bulk temperature of the liquid at that point. Before boiling occurs, the well temperature profile, as may be expected, is very nearly parallel to the subcooled liquid temperature. It then displays an overshoot of *wall* temperature (superheating) near the onset of boiling, characteristic of the test conditions of heat flux, pressure, and flow rate. The temperature difference in the liquid zone between wall and bulk is much greater (by approximately 3 times) than that of the temperature difference at the beginning of the boiling region and after the superheating peak. Included on the plot of bulk temperature on Fig. 3 is the local thermodynamic mixture quality, x, calculated from the net heat input, mass flux, and appropriate latent heat. For the purpose of analysis, the quality was taken to be zero at the point of intersection of the profiles of the bulk temperatures in the boiling and in the subcooleed liquid zones.

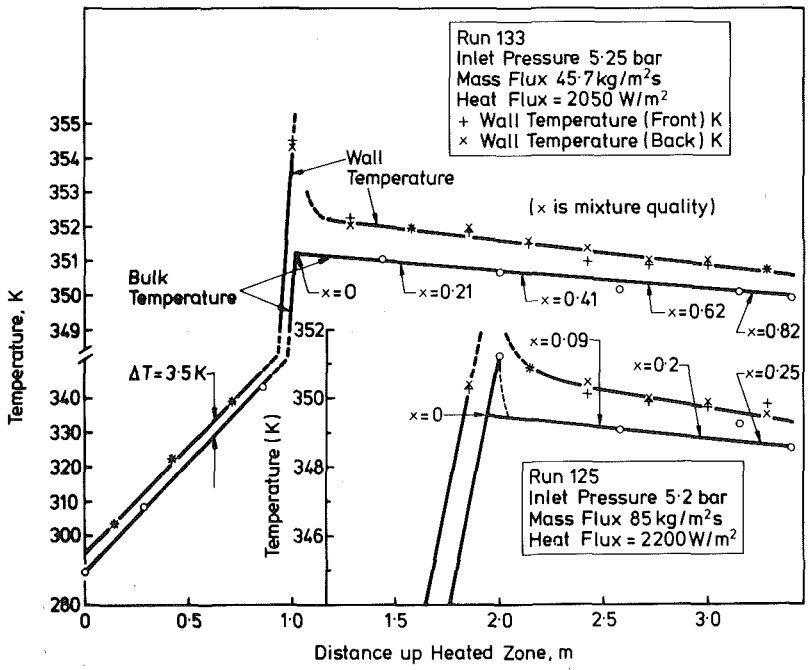

Fig. 3 Typical temperature profiles along serrated-fin test section, showing wall superheating and bulk superheating (inset)

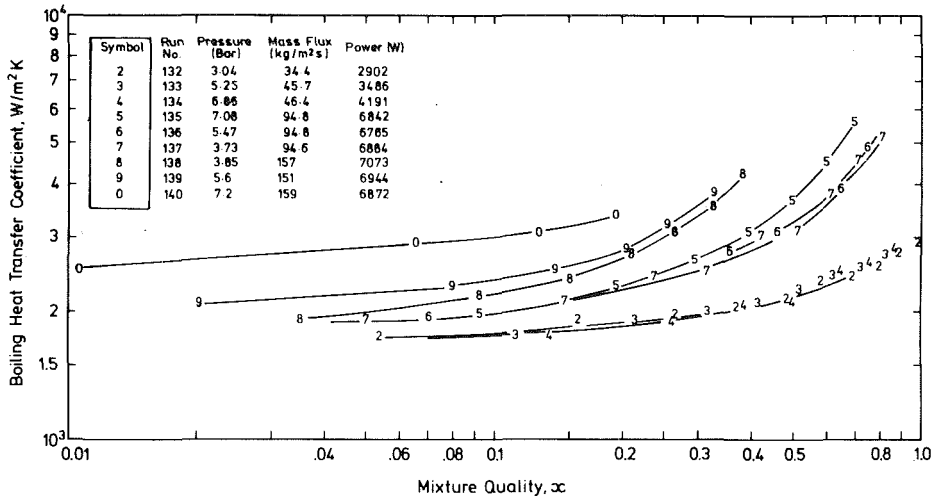

Fig. 4 Plot of boiling heat transfer coefficient against mixture quality for Freon 11 (R11) in serrated fin test section

The diagram inset on Fig. 3 (for Run 125) gives an example of the large overshoot in the *bulk* temperature at the beginning of the boiling region which is caused by superheating of the liquid. The test procedure only allowed the wall and bulk liquid superheating peaks to be seen in detail when they happened to coincide with the local thermocouples.

4 Results

4.1 Method of Analysis. Since the local bulk temperature was not measured in the test section precisely at the wall thermocouple position, results from each test were first analyzed in the following manner.

The test results were plotted on a graph of wall and bulk temperatures along the length of the test section as illustrated in Fig. 3, and the best lines through the bulk temperatures in the subcooled and in the boiling zones were drawn. With these plots, it was then possible to estimate the bulk temperature at the location of the wall thermocouples and thereby to derive the temperature difference between wall and bulk. The temperature drop from the wall thermocouple location in the aluminum plate to the wetted surface of the channel was then taken into account in determining the temperature of the wall on the primary heat transfer surface.

4.2 Single-Phase Heat Transfer. Results from the heated runs carried out with only liquid along the test section were used to determine the single-phase heat transfer coefficient which were assumed to be uniform around the perimeter of the small channels. This coefficient was determined using the fin efficiency term in the equation

$$Q_T = h_\eta (A_P + \eta A_s)(T_{pw} - T_{\text{sat}})$$

where η, the fin efficiency, is given by

$$\eta = \frac{\tanh(s)}{s}; \quad s = \frac{a}{2}\sqrt{\frac{2h_g}{k_L t}}$$

These results have already been reported [10].

4.3 Initiation of Wall Nucleation. The high wall superheat associated with the initiation of bubble nucleation at the wall had alrady been observed in the tests in this test section with liquid nitrogen. From the few experimental runs in which this feature happened to coincide with the fixed pattern of thermocouples, it was possible to deduce that the peaks were similar with both fluids.

From the estimates of the peak wall temperature, the Davis and Anderson correlation [14] had been used to estimate that the effective size of the nucleation sites on the aluminum surface in the presence of liquid nitrogen was approximately 0.25 micron. With Freon 11, this effective size appeared to be slightly greater, probably as a result of the higher surface tension of the Freon 11 reducing its wetting abilities in comparison with nitrogen.

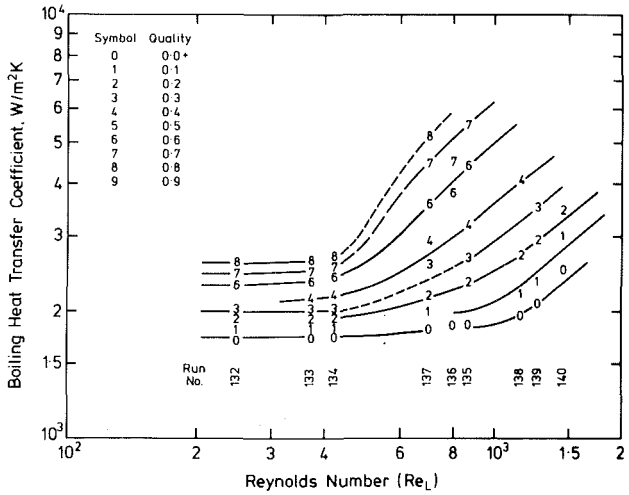

Fig. 5 Plot of boiling heat transfer coefficient against Reynolds number of total flow as liquid. (Cross-plot from curves on Fig. 4, with quality as parameter)

4.4 Boiling Heat Transfer Coefficients. During the tests with liquid nitrogen [10], heat flux had been systematically altered in order to determine the effect of this parameter on the boiling heat transfer coefficients. It had been shown that, for the range of pressure and mass flux in these tests, boiling heat transfer coefficients were independent of the level of heat flux.

In the tests with Freon 11, it was not possible to vary heat flux systematically. However, it was argued that if nucleate boiling had been present the heat fluxes would require to have been very much higher in order to approach those in pool boiling tests with Freon 11 as reported by Seki et al. [12]. The results from the Freon 11 tests were, therefore, regarded as if convective boiling were the dominant mechanism.

Using the concept of fin efficiency (as previously described) for the boiling heat transfer test results and making the assumption of a uniform boiling heat transfer coefficient round the wetted perimeter of the subchannel, boiling

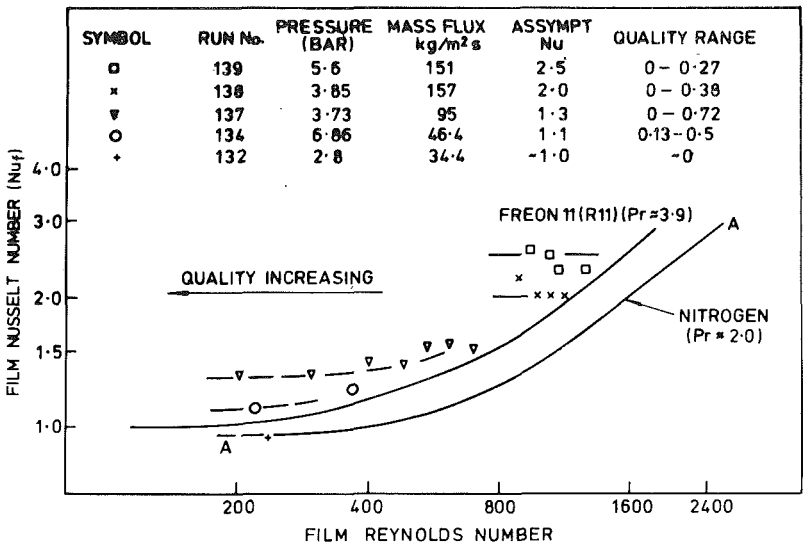

Fig. 6 Plot of film Nusselt number (Nu_f) against film Reynolds number (Re_{LF}) for convective boiling of Freon 11 (R11) in serrated-fin channels

coefficients (h_μ) were computed at each wall thermocouple location along the test section. In some tests, Runs 132 and 134, superheated vapor conditions occurred at or near the exit of the test section and dry-out was not observed up to a quality of approximately 95 percent. The thermocouple arrangement on the test section make it difficult to resolve the onset of dry-out with any greater degree of certainty than this general limit.

A plot of the boiling heat transfer coefficients against mass quality, with mass flux as a parameter, is presented in Fig. 4 for nine tests. Three ranges of mass flux were used over the pressure range from 3–7 bar and, at the highest power of 7 kW used on the test section, the heat fluxes on the primary surface were approximately 4 kW/m^2. In Fig. 4, it can be seen that boiling heat transfer coefficients tend to a constant value as mixture quality approaches zero; the coefficients increase considerably at higher qualitites and with mass flux.

Another pattern of the boiling characteristics of the serrated fin, with Freon 11 as a test fluid, is given in Fig. 5. This is a cross-plot of the *curves* through the experimental data presented in Fig. 4; the boiling heat transfer coefficient is plotted against Reynolds number with vapor quality as a parameter. (The numerals on this plot refer to the values of vapor quality at which boiling coefficients have been extracted from Fig. 4.)

The Reynolds number, Re_L, is calculated using the total mass flux and the liquid viscosity and was chosen as a correlating parameter, instead of mass flux (as in [10]), in order to take into account the change of liquid viscosity over the pressure range used in the tests. In Fig. 5, the main features which were apparent with boiling liquid nitrogen are also present with Freon 11: above a critical Reynolds number the boiling heat transfer coefficients, as in turbulent single-phase channel flow, are dependent on mass flux to the power of approximately 0.8; below that critical value the heat transfer coefficients appear to be almost independent of mass flux.

The critical liquid Reynolds number at which this change occurs, for mass qualities close to zero, is about 1100, and the transition region exists between 800–1600. These values are practically identical with those obtained with liquid nitrogen for 3 bar. This observation supports the argument already advanced [10] that the most prevalent two-phase flow pattern within these interrupted passages consists of a thin film of liquid flowing along each fin from leading to trailing edge where it is disrupted, at high vapor velocities, into the form of a spray and then reformed on the following fin. This film can be expected to be turbulent or laminar and it will not necessarily exhibit the same heat transfer characteristics of single-phase flow in a serrated-fin passage where no clear division between the laminar or turbulent region is identifiable on the Colburn J versus Reynolds number plots. If heat transfer is dominated by the evaporation of a thin liquid film then it can be expected that the liquid film Reynolds number, Re_{LF}, which has the same value as if the liquid occupied the whole flow cross-section area, will be an important correlating parameter. At low quality, Re_{LF}, approaches the value of the liquid Reynolds number.

At higher vapor qualities, for the same mass flux, the film Reynolds number will decrease and eventually the film will become laminar. There is evidence, particularly from the liquid nitrogen results, that the dependence of the boiling heat transfer coefficient on Reynolds number to the power 0.8 holds for values of film Reynolds number as low as 150. This may be a result of the interrupted film flow in this form of finning.

At low qualities it is to be expected that a form of slug flow may occur. This two-phase flow pattern is more likely to occur at very low fluxes over much of the quality range. For example, the value of j_g^*, which is a possible criterion for the existence of slug flow, is lower than 1.0 at the lowest Reynolds numbers for several runs on Fig. 5. By definition

$$j_g^* = j_g \rho_g^{1/2} [g D_e (\rho_L - \rho_g)]^{-1/2}$$

4.5 Correlation of Boiling Heat Transfer Coefficients. Results from these tests with Freon 11 and with nitrogen have also been correlated using a film-flow model of the evaporation or convective boiling process in these small, narrow, interrupted channels. This work, reported elsewhere [16], explores the value of this form of boiling model to correlate convective boiling coefficients in terms of the Nusselt, Reynolds (Re_{TL}), and Prandtl numbers of the liquid film. This approach has already been used for correlating the results of convective boiling in vertical and horizontal round tubes by others, for example, [17, 18] and by Yung et al. [15] for laminar films in a serrated-fin passage. It makes use of a chosen velocity profile in the liquid film and requires the development of a relationship between shear stress in the film and film thickness. For this, it is necessary to know or to be

able to predict the total pressure gradient of the two-phase flow. The velocity profile in the film takes into account the laminar, buffer, and turbulent layers that may be present, and this will be reflected in the thermal resistance of the film that is given in terms of its Nusselt number; a Nusselt number of unity indicates that the film is a laminar. The effect of altering the composition of the fluid is taken into account by the Prandtl number of the liquid.

Some of the results of the tests with Freon 11 are plotted in terms of this model on Fig. 6, taken from [16]. It can be seen that the liquid film remains laminar below a critical value of the Reynolds number of the film of about 200–300. It can also be seen that the results from tests with nitrogen at a lower Prandtl number also have similar characteristics. It is apparent that the Nusselt number of the film during convective boiling has a relatively modest value. This reflects the thickness of the film which has a calculated value, typically of less than 100 microns. It is also apparent from Fig. 6 that a simple model of convective boiling of a smooth, evaporating, liquid film requires to take into account the highly interrupted nature of the serrated fin. This in in accordance with the model, just discussed, of the film being totally entrained in the vapor core at the trailing edge of each serration.

5 Conclusions

Single-phase and boiling heat transfer tests have been carried out with Freon 11 in an electrically heated, serrated-fin test section simulating part of a plate-fin heat exchanger. The range of pressure, mass flux, heat flux, and vapor quality during the tests reflects the conditions of industrial operation of these exchangers. These tests complement others carried out on the same test section, under similar test conditions, at very much lower temperatures with liquid nitrogen [10].

The various features of boiling in the very small channels characteristic of these exchangers were observed with both test fluids: for example, the high wall and bulk liquid superheating peaks at the commencement of boiling. The magnitude of the boiling coefficients, making use of the fin efficiency concept, has been given as a function of test conditions and also of a simple correlating parameter, Re_L.

The use of a film flow model of the evaporating process, reported in [16], to correlate the results from the same test section with nitrogen and Freon 11 has been discussed. This nondimensional method for correlating boiling heat transfer coefficients in these complex passages of plate-fin heat exchangers appears to be promising.

6 Acknowledgment

The funding of part of this study by the Chemical and Minerals Requirements Board of the Department of Industry, UK, is gratefully acknowledged.

References

1 Lenfesty, A. G., "Low Temperature Heat Exchangers," *Progress in Cryogenics*, Heywood & Co., London, 1961, pp. 25–47.

2 Crawford, D. B., and Eschenbrenner, G. P., "Heat Transfer and Heat Exchanger Applications for LNG," *Chemical Engineering World*, Vol. VIII, No. 5, May 1973, pp. 77–94.

3 Stebbing, R., and O'Brien, J. O., "An Up-Dated Report on the PRICO Process for LNG Plants," Gastech 75, Paper 15; International LNG/LPG Congress, Paris, 1975.

4 Kays, W. M., and London, A. L., "*Compact Heat Exchangers*," 2d ed., McGraw-Hill, 1964.

5 Mochizuka, S., and Yagi, Y ., "Heat Transfer and Friction Characteristics of Strip Fins," *Heat Transfer Japan Research*, Vol. 6, No. 3, 1977, pp. 36–59.

6 Galezha, V. B., Usyukin, I. P., and Kan, K. D., "Boiling Heat Transfer with Freons in Finned-Plate Heat Exchangers," *Heat Transfer - Soviet Research*, Vol. 8, No. 3, May 1976, pp. 103–110.

7 Panitsidis, H., Gresham, R. D., and Westwater, J. W., "Boiling of Liquids in a Compact Plate-Fin Heat Exchanger," *International Journal of Heat and Mass Transfer*, Vol. 18, 1975, p. 37–42.

8 Shorin, C. N., Sukhov, V. I., Shevyakova, S. A., and Orlov, V. K., "Experimental Investigation of Heat Transfer With the Boiling of Oxygen in Vertical Channels during Condensation Heating," *International Chemical Engineering*, Vol. 14, No. 3, July 1974, pp. 517–521.

9 Clark, J. A., and Thorogood, R. M., "*Cryogenic Fundamentals*" edited by G. G. Haselden, Academic Press, 1971, p. 164.

10 Robertson, J. M., "Boiling Heat Transfer with Liquid Nitrogen in Brazed-Aluminum Plate-Fin Heat Exchangers," *AIChE Symposium Series*, No. 189, Vol. 75, 1979, pp. 151–164.

11 Bland, M. E., Bailey, C. A., and Davey, G., "Boiling from Metal Surfaces Immersed in Liquid Nitrogen and Liquid Hydrogen," *Cryogenics*, Vol. 13, No. 11, 1973, pp. 651–657.

12 Seki, N., Fukusako, S., and Torikoshi, K., "Experimental Study on the Effect of Orientation of Heating Circular Plate on Film Boiling Heat Transfer for Fluorocarbon Refrigerant R-11," ASME JOURNAL OF HEAT TRANSFER, Vol. 100, No. 4, 1978, pp. 624–826.

13 Lovegrove, P. C., "An Experimental Apparatus for the Study of the Boiling Heat Transfer to Noninflammable Organic Liquids, AERE-M2790, 1976.

14 Davis, E. J., and Anderson, G. H., "The Incipience of Nucleate Boiling in Forced Convection Flow," *AIChE Journal*, Vol. 12, No. 4, 1966, pp. 774–780.

15 Yung, D., Lorentz, J. J., and Panchal, C., "Convective Vaporization and Condensation in Serrated-Fin Channels," ASME HTD-Vol. 12, 1980, pp. 29–37.

16 Robertson, J. M., "The Correlation of Boiling Coefficients in Plate-Fin Heat Exchanger Passages with a Film-Flow Model," *Proceedings 7th International Heat Transfer Conference*, Vol. 6, Munich, 1982.

17 Hewitt, G. F., and Hall-Taylor, N. S., *Annular Two-Phase Flow*, Pergammon Press, 1970.

18 Butterworth, D., "An Analysis of Film Flow and its Application to Condensation in a Horizontal Tube, *Int. J. Multiphase Flow*, Vol. 1, Pergammon Press, 1974, pp. 671–682.

A Numerical Finite Difference Method for Performance Evaluation of a Periodic-Flow Heat Exchanger

Chung-Hsiung Li
Engineering Technologies Department,
C-E Air Preheater Company
Wellsville, N.Y. 14895

A numerical finite difference method is presented for calculating the fluid and metal temperature distributions for the periodic-flow type heat exchanger, accounting for the effect of heat conduction in the wall in the direction of fluid flow. Unlike previous solution techniques that use the Gauss-Seidel method based on a single element calculation, the method presented here uses a column of elements to compute the fluids and metal temperature distributions, and it allows variable or constant thermal properties (specific heats, densities, heat transfer coefficients, and thermal conductivities). Nonuniform mass flow rates and a nonuniform grid spacing may be employed. The present method reduces the computational time required for convergence and improves the numerical stability while allowing an arbitrary metal temperature distribution as a starting case. After qualifying the numerical method, illustrative results are presented for counterflow and parallel flow rotary regenerators with three different surfaces in the flow direction and variable fluid and material properties.

1 Introduction

The advantages of the rotary periodic-flow heat exchanger for industrial waste heat recovery systems and vehicular gas turbine-regenerator applications have been known for many years. Storage and release of thermal energy is the unique feature of the regenerative heat exchanger. The basic rotary type air preheater regenerative principle is very simple, as shown in Fig. 1. The cylindrical rotor containing the heat transfer surface rotates at 1 to 3 rpm inside a housing and is divided into two or three sectors. Waste heat is absorbed from the fuel gas and transferred to incoming cold air by means of the continuously rotating heat transfer surfaces formed from metal plates (matrix). As the heat transfer surfaces pass through the counterflowing or parallel-flowing exhaust gas and incoming air streams, heat is absorbed uniformly and released to the combustion air. Unlike recuperative type air preheaters, heat need not pass through tube or plate walls. Instead, the heat is simply absorbed by and released from the same heat transfer surfaces of the entire mass as it rotates. This storage type heat exchanger is generally referred to as a rotary regenerator. Its three major advantages relative to the recuperative air preheaters are: (*i*) a much more compact heat transfer surface can be employed; (*ii*) the heat transfer surface is substantially less expensive per unit of transfer area, and (*iii*) because of the periodic flow reversals, the surface tends to be self-cleaning.

In the analysis of the performance of periodic-flow heat exchangers, the differential equations and boundary conditions which result when considering the most general case are sufficiently complex to preclude a general analytical closed-form solution [1–4]. A number of approximate solutions have been obtained by researchers by employing different mathematical techniques. One of the more complete solutions has been obtained by Lamberston [5], Bahnke and Howard [6], and Mondt [7] by employing a finite difference method. They considered two coupled crossflow heat exchangers with fluid unmixed as shown in Fig. 2. In this figure, for the heat exchanger of the left, one fluid stream is the hot gas and the other fluid stream is the matrix material "stream." For the heat exchanger on the right, the cold gas

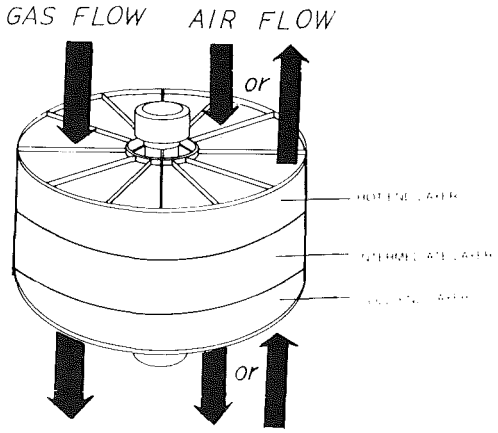

Fig. 1 Periodic-flow heat exchanger schematic

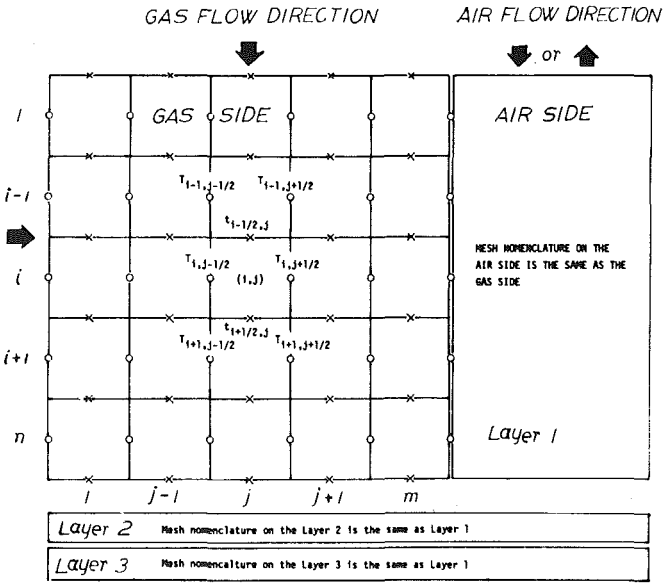

Fig. 2 A staggered mesh representing the periodic-flow heat exchanger schematic

Contributed by the Heat Transfer Division for publication in the JOURNAL OF HEAT TRANSFER. Manuscript received by the Heat Transfer Division September 17, 1982.

and the matrix material are the two "streams." Lamberston [5] and Bahnke and Howard [6] use a calculation procedure in which a matrix temperature distribution is assumed on the left edge, and with this initial estimate of all element temperatures, the Gauss-Seidel point-by-point marching procedure is applied starting with the upper left-hand corner element. Since its introduction, this method has been a typical standard numerical calculation procedure for the rotary periodic-flow heat exchanger. Holmberg [8, 9] and Van Leersum and Ambrose [10] applied the Gauss-Seidel method to compute heat and mass transfer in a regenerator with nonhygroscopic and hygroscopic materials, and nonsorbing matrices.

Recently, Razelos and Benjamin [11] also developed a new computer model based on the Gauss-Seidel method to calculate the thermal performance of a blast furnace stove regenerator without the effect of conduction in the wall along the flow direction. The important differences in their solution as compared to previous work are variable flow-rate and variable thermal properties of the walls and the fluids. Their excellent analysis is one of the current industry standards for performance predictions of blast furnace stove regenerators.

A major disadvantage of the otherwise attractive Gauss-Seidel method is that its convergence is slow, especially when a large number of grid points are involved. The reason for slowness is easy to understand: the method transmits the boundary condition information at a rate of one grid interval per iteration.

The purpose of this investigation is to study an effective calculation method for the rotary periodic-flow regenerator. A numerical finite difference method of calculating the temperature distributions of both fluids and the matrix for the periodic-flow heat exchanger accounting for the effect of heat conduction in the wall along the direction of fluid flow, which is important in high effectiveness rotary type regenerators [1], is presented. These distributions are required for primary seal matching and core and thermal stress calculations. The case of zero heat conduction in the wall along the flow direction is a special case of the method presented here. The calculation procedure allows for the use of variable thermal properties such as the specific heat and thermal conductivity of the metal, and the specific heats, densities, and convection heat transfer coefficients of the fluids. The present method is not only applicable to counterflow in bisectors, but can also be applied to counterflow or parallel-flow with multiple layers and multiple sector regenerators.

2 Theoretical Analysis

The idealizations and boundary conditions assumed in the derivation of the governing finite difference equations for the periodic-flow heat exchanger are as follows:

1 The thermal conductivity of the heat exchanger matrix is zero in the direction of "metal flow" (peripheral direction), finite in the direction of fluid flow, and infinite in the direction which is normal to both the fluid and metal flow (radial direction).

2 Thermal properties of the two fluids and the matrix vary with temperature.

3 No mixing of the fluids occurs either as a result of direct leakage or carryover (entrainment).

4 The convective heat transfer coefficients and thus the convective conductances between the fluids and matrix vary with temperatures and Reynolds number.

5 The fluids pass in either counterflow or parallel-flow directions.

6 Entering fluid temperatures are constant with time but can be nonuniform over the inlet cross section.

7 There is no convective heat exchange at the fluid entering or exit cross section.

Nomenclature

A = cross-section area of the regenerator, m^2
A_s = cross-section area of a sector, m^2
A_s^* = conduction area ratio
a = dummy constant defined in equation (14*a*)
a' = dummy constant defined in equation (1*c*) for Colburn factor
b = dummy constant defined in equation (14*b*)
b' = dummy constant defined in equation (1*d*) for Colburn factor
C = specific heat of matrix metal, J/(kg K)
C_{min}/C_{max} = capacity rate ratio of fluid streams
C_R/C_{min} = capacity rate ratio of matrix to minimum fluid capacity rate
c = dummy constant defined in equation (14*c*)
c_p = specific heat of gas or air, J/(kg K)
d = dummy constant defined in equation (14*d*)
e = dummy constant defined in equation (14*e*)
f = row fraction or column fraction in finite difference scheme (index i for row, index j for column)
H = matrix height of a layer, m
h = heat transfer coefficient, $W/(m^2 K)$
$(hA)^*$ = conductance ratio
j_H = Colburn factor, $StPr^{2/3}$, dimensionless
k = conductivity of matrix, W/(m K)
$\dot{M}$ = matrix flow rate, kg/s
m = column number of a section
$\dot{m}_g$ = gas or air flow rate, kg/s
N = layer number
Ntu_0 = overall number of transfer units
n = row number of a layer
P = dummy constant defined in equation (15)
Pr = Prandtl number, $\mu c_p/k$, dimensionless
Q = dummy constant defined in equation (15)
Re = Reynolds number, DG_h/μ, dimensionless
S = convective heat transfer area in a sector of a layer, m^2
T = matrix temperature, °C
t = gas or air temperature, °C
α = dummy constant defined in equation (5)
β = dummy constant defined in equation (6)
γ = heat transfer surface area density, m^2/m^3
σ = porosity, dimensionless
ϵ = heat exchanger effectiveness
$\Delta\epsilon/\epsilon$ = conduction effect
λ = dummy constant defined in equations (7) and (8)
λ_c = total conduction parameter
ρ = metal density of matrix, kg/m^3
Ω = revolutions per minute, rpm

Subscripts

Dev = deviation
i = row number
j = column number
l = layer number

Superscripts

c = cold side
h = hot side
$'$ = dummy
$''$ = dummy

8 Regular periodic conditions are established for all matrix elements, i.e., steady-state operation.

If the elements are considered to be fixed in space, then each element can be regarded as a crossflow heat exchanger with a gas stream and a metal stream. For an element on the gas side, the heat transfer rate by convection is equal to the rate of change in enthalpy of the fluid across the element.

$$\dot{m}_g f_j c_{p,i,j}(t_{i-1/2,j}-t_{i+1/2,j}) = h_{i,j}Sf_if_j\left(\frac{t_{i-1/2,j}+t_{i+1/2,j}}{2} - \frac{T_{i,j-1/2}+T_{i,j+1/2}}{2}\right) \quad (1a)$$

Where S is the total heat transfer area in a sector of a layer, which can be computed from

$$S=\gamma A_s H \quad (1b)$$

$h_{i,j}$ is the heat transfer coefficient which can be written as

$$h_{i,j}=\frac{j_{H,i,j}c_{p,i,j}\dot{m}_g}{\mathrm{Pr}_{i,j}^{2/3}A_s\sigma} \quad (1c)$$

where $j_{H,i,j}$ is Colburn factor at finite difference element (i, j) and

$$j_{H,i,j}=a'\,\mathrm{Re}_{i,j}^{-b'} \quad (1d)$$

The a' and b' in equation (1d) are the empirical constants obtained either experimentally or theoretically for the given matrix surface for either rotary or fixed-matrix regenerator. The fluid and matrix temperatures are subscripted to indicate the average temperatures across the inlet and outlet of the element for simple unmixed cross-flow.

Considering the energy balance for an element, the energy transferred to or from the element by convection plus energy transferred to and from the element by conduction must equal the energy storage or loss in the element

$$\dot{m}_g f_j c_{p,i,j}(t_{i-1/2,j}-t_{i+1/2,j}) + k_{i-1/2,j}A_s(1-\sigma)f_j\frac{2}{(f_{i-1}+f_i)H}\left(\frac{T_{i-1,j-1/2}+T_{i-1,j+1/2}}{2} - \frac{T_{i,j-1/2}+T_{i,j+1/2}}{2}\right) - k_{i+1/2,j}A_s(1-\sigma)f_j\frac{2}{(f_i+f_{i+1})H}\left(\frac{T_{i,j-1/2}+T_{i,j+1/2}}{2} - \frac{T_{i+1,j-1/2}+T_{i+1,j+1/2}}{2}\right) = f_i\dot{M}C_{i,j}(T_{i,j+1/2}-T_{i,j-1/2}) \quad (2a)$$

where $\dot{M}$ is the metal flow rate which can be computed from

$$\dot{M}=AH(1-\sigma)\rho\Omega/60 \quad (2b)$$

The row fraction f_i $(i=1,2,3,\ldots,n)$ and the column fraction f_j $(j=1,2,3,\ldots,m)$ are not necessarily equal. From the equations (1a), (1b), (1c), (1d), (2a) and (2b), one can obtain the following simplified equations

$$T_{i,j+1/2} = -T_{i,j-1/2} + \left(1-\frac{1}{\alpha_{i,j}}\right)t_{i-1/2,j} + \left(1+\frac{1}{\alpha_{i,j}}\right)t_{i+1/2,j} \quad (3)$$

where

$$i=1,2,3,\ldots,n$$

and

$$\lambda'_{i+1/2,j}\left(1-\frac{1}{\alpha_{i-1,j}}\right)t_{i-3/2,j} + \left[1+\lambda'_{i+1/2,j}\left(\frac{1}{\alpha_{i-1,j}}+\frac{1}{\alpha_{i,j}}\right) - (\beta_{i,j}+\lambda''_{i+1/2,j})\left(1-\frac{1}{\alpha_{i,j}}\right)\right]t_{i-1/2,j} - \left[1+\lambda''_{i+1/2,j}\left(\frac{1}{\alpha_{i,j}}+\frac{1}{\alpha_{i+1,j}}\right)+(\beta_{i,j}+\lambda'_{i+1/2,j})\times\left(1+\frac{1}{\alpha_{i,j}}\right)\right]t_{i+1/2,j} + \lambda''_{i+1/2,j}\left(1+\frac{1}{\alpha_{i+1,j}}\right)t_{i+3/2,j} = -2\beta_{i,j}T_{i,j-1/2} \quad (4)$$

where

$$\alpha_{i,j}=\frac{\gamma Hf_i j_{H,i,j}}{2\sigma\mathrm{Pr}_{i,j}^{2/3}}, \quad (5)$$

$$\beta_{i,j}=\frac{AH\rho(1-\sigma)\Omega f_i C_{i,j}}{60\dot{m}_g c_{p,i,j}f_j}, \quad (6)$$

$$\lambda'_{i+1/2,j}=\frac{k_{i-1/2,j}A_s(1-\sigma)}{\dot{m}_g c_{p,i,j}H(f_{i-1}+f_i)}, \quad (7)$$

$$\lambda''_{i+1/2,j}=\frac{k_{i+1/2,j}A_s(1-\sigma)}{\dot{m}_g c_{p,i,j}H(f_i+f_{i+1})} \quad (8)$$

and

$$i=2,\ 3,\ 4,\ \ldots,n-1,$$
$$j=1,\ 2,\ 3,\ \ldots,m.$$

Since the longitudinal heat conduction is zero at the ends, the energy balance equation modified from equations (3) and (4) for elements of the first and last row can be stated as

$$\left[1-(\beta_{1,j}+\lambda''_{3/2,j})\left(1-\frac{1}{\alpha_{1,j}}\right)\right]t_{1/2,j} - \left[1+\lambda''_{3/2,j}\left(\frac{1}{\alpha_{1,j}}+\frac{1}{\alpha_{2,j}}\right)+\beta_{1,j}\left(1+\frac{1}{\alpha_{1,j}}\right)\right]t_{3/2,j} + \lambda''_{3/2,j}\left(1+\frac{1}{\alpha_{2,j}}\right)t_{5/2,j} = -2\beta_{1,j}T_{1,j-1/2} \quad (9)$$

and

$$\lambda'_{n+1/2,j}\left(1-\frac{1}{\alpha_{n,j}}\right)t_{n-3/2,j} + \left[1+\lambda'_{n+1/2,j}\left(\frac{1}{\alpha_{n-1,j}}+\frac{1}{\alpha_{n,j}}\right)-\beta_{n,j}\left(1-\frac{1}{\alpha_{n,j}}\right)\right]t_{n-1/2,j} - \left[1+(\beta_{n,j}+\lambda'_{n+1/2,j})\left(1+\frac{1}{\alpha_{n,j}}\right)\right]t_{n+1/2,j} = -2\beta_{n,j}T_{n,j-1/2} \quad (10)$$

where $t_{1/2,j}$ in equation (9) is the fluid inlet temperature.

One can solve for the n unknowns $t_{i+1/2,j}$ $(i=1,2,3,\ldots,n)$ from the n simultaneous equations (4), (9), and (10) to obtain the fluid temperature distribution in the matrix. Using these fluid temperatures, one can then obtain the metal temperature distribution $T_{i,j+1/2}$ $(i=1,\ 2,\ 3,\ \ldots,n)$ by using equation (3). This procedure is followed for all the columns from $j=1$ to $j=m$.

The matrix outlet temperatures for elements of the last column of the gas sector are physically the same as the inlet temperatures of the corresponding elements of the air sector. The same calculation procedure is then applied to the airside sector. The boundary conditions for the first column of the next sector are:

1 For counterflow:

$$T^{c}_{i,1/2} = T^{h}_{n-i+1,m+1/2} \tag{11}$$

2 For parallel-flow:

$$T^{c}_{i,1/2} = T^{h}_{i,m+1/2} \tag{12}$$

where $i = 1, 2, 3, \ldots, n$.

3 Numerical Method

The solution of the simultaneous equations (4), (9), and (10) can be obtained by using any number of standard techniques. These standard techniques usually require a large storage space and lengthy computer time for the matrix elimination to solve the simultaneous equations, especially when the number of grid points is large.

Because of the particularly simply form of the simultaneous equations (4), (9), and (10), a convenient algorithm for the solution of this system of equations can be obtained by the standard Gaussian elimination method. Unlike general matrix methods, this algorithm requires computer storage and computer time proportional only to n, rather than to n^2.

For convenience in presenting the algorithm, the equations (4), (9), and (10) are restated as

$$a_i t_{i+1/2,j} = b_i t_{i+3/2,j} + c_i t_{i-1/2,j} + d_i t_{i-3/2,j} + e_i, \tag{13}$$

where

$$a_i = \begin{cases} 1 + \lambda''_{1/2,j}\left(\dfrac{1}{\alpha_{1,j}} + \dfrac{1}{\alpha_{2,j}}\right) + \beta_{1,j}\left(1 + \dfrac{1}{\alpha_{1,j}}\right) & \text{for } i = 1 \\ 1 + \lambda''_{i+1/2,j}\left(\dfrac{1}{\alpha_{i,j}} + \dfrac{1}{\alpha_{i+1,j}}\right) + (\beta_{i,j} + \lambda'_{i+1/2,j}) & \\ \quad \times \left(1 + \dfrac{1}{\alpha_{i,j}}\right) & \text{for } i = 2,3, \ldots, n-1, \\ 1 + (\beta_{n,j} + \lambda'_{n+1/2,j})\left(1 + \dfrac{1}{\alpha_{n,j}}\right) & \text{for } i = n. \end{cases} \tag{14a}$$

$$b_i = \begin{cases} \lambda''_{i+1/2,j}\left(1 + \dfrac{1}{\alpha_{i+1,j}}\right) & \text{for } i = 1,2, \ldots, n-1, \\ 0 & \text{for } i = n. \end{cases} \tag{14b}$$

$$c_i = \begin{cases} 1 - (\beta_{1,j} + \lambda''_{3/2,j})\left(1 - \dfrac{1}{\alpha_{1,j}}\right) & \text{for } i = 1, \\ 1 + \lambda'_{i+1/2,j}\left(\dfrac{1}{\alpha_{i-1,j}} + \dfrac{1}{\alpha_{i,j}}\right) - (\beta_{i,j} + \lambda''_{i+1/2,j}) & \\ \quad \times \left(1 - \dfrac{1}{\alpha_{i,j}}\right) & \text{for } i = 2,3, \ldots, n-1, \\ 1 + \lambda'_{n+1/2,j}\left(\dfrac{1}{\alpha_{n-1,j}} + \dfrac{1}{\alpha_{n,j}}\right) & \\ \quad -\beta_{n,j}\left(1 - \dfrac{1}{\alpha_{n,j}}\right) & \text{for } i = n. \end{cases} \tag{14c}$$

$$d_i = \begin{cases} 0 & \text{for } i = 1, \\ \lambda'_{i+1/2,j}\left(1 - \dfrac{1}{\alpha_{i-1,j}}\right) & \text{for } i = 2,3, \ldots, n. \end{cases} \tag{14d}$$

$$e_i = 2\beta_{i,j} T_{i,j-1/2}, \qquad \text{for } i = 1,2,3, \ldots, n. \tag{14e}$$

Suppose, in the forward-substitution process, we seek a relation

$$t_{i+1/2,j} = P_i t_{i+3/2,j} + Q_i \tag{15}$$

after we have just obtained

$$t_{i-1/2,j} = P_{i-1} t_{i+1/2,j} + Q_{i-1} \tag{16}$$

and

$$t_{i-3/2,j} = P_{i-2} t_{i-1/2,j} + Q_{i-2} \tag{17}$$

Substitution of equations (16) and (17) into equation (13) leads to

$$a_i t_{i+1/2,j} = b_i t_{i+3/2,j} + c_i (P_{i-1} t_{i+1/2,j} + Q_{i-1}) + d_i (P_{i-2} P_{i-1} t_{i+1/2,j} + P_{i-2} Q_{i-1} + Q_{i-2}) + e_i \tag{18}$$

which can be rearranged to look like equation (15). In other words, the coefficients P_i and Q_i then stand for

$$P_i = \frac{b_i}{a_i - c_i P_{i-1} - d_i P_{i-1} P_{i-2}} \tag{19a}$$

$$Q_i = \frac{c_i Q_{i-1} + d_i P_{i-2} Q_{i-1} + d_i Q_{i-2} + e_i}{a_i - c_i P_{i-1} - d_i P_{i-1} P_{i-2}} \tag{19b}$$

where $i = 1, 2, 3, \ldots, n$.

These are recurrence relations, since they give P_i and Q_i in terms of P_{i-1}, Q_{i-1}, P_{i-2}, and Q_{i-2}. To start the recurrent process, P_1 and Q_1 are obtained by comparing equations (13) and (15) for $i = 1$

$$P_1 = \frac{b_1}{a_1} \quad \text{and} \quad Q_1 = \frac{c_1 t_{1/2,j} + e_1}{a_1} \tag{20}$$

It is interesting to note that these expressions also follow from equations (19*a*) and (19*b*) by setting P_{-1}, P_0, Q_{-1} to zero and $Q_0 = t_{1/2,j}$. Using the recurrence relations (19*a*) and (19*b*), one can obtain P_i and Q_i for $i = 2, 3, 4, \ldots, n$.

At the other end of the P_i, Q_i sequence, we note that $b_n = 0$. This leads to $P_n = 0$, and hence from equation (15) we obtain

$$t_{n+1/2,j} = Q_n \tag{21}$$

Now we are in a position to start the back substitution via equation (16) to obtain $t_{n-1/2,j}, t_{n-3/2,j}, \ldots, t_{5/2,j}, t_{3/2,j}$.

It is well known that iterative procedures do not always converge. From the Scarborough stability criterion for the Gauss-Seidel method [12], we can state a sufficient condition of convergence criterion for this presented method as

$$|b_i| + |c_i| + |d_i| \begin{cases} \le |a_i| \text{ for all equations} \\ < |a_i| \text{ for at least one equation,} \end{cases} \tag{22}$$

where a_i, b_i, c_i, and d_i are stated in equations (14*a*), (14*b*), (14*c*), and (14*d*).

4 Calculation Procedure

The calculation procedure is iterative. A matrix temperature distribution is assumed on the left edge and equation (4) is used to compute the fluid temperature distribution of the next column. From the obtained fluid temperature distribution, one can calculate the matrix temperature distribution of the next edge by equation (3). Working down the column, the remaining temperatures of each element can be calculated in the order indicated by the column number by repetitive use of equation (4) then equation (3). If the tem-

perature distribution assumed on the left edge was correct then, it would be duplicated on the right. If, however, this is not the case, then the resulting temperature distribution on the right and the temperature distribution on the left can be used to compute a new starting temperature distribution with the relaxation method. To avoid divergence in the iterative solution, one can speed up or slow down the changes, from iteration to iteration, with a changing relaxation factor. The procedure is repeated until the reversal condition and heat balance error are satisfied to a specified accuracy.

It is impossible to exactly match the matrix temperature distribution of the first column of the gas side and the last column of the air side by the match procedure. The temperature deviation of the match procedure is

$$T_{\text{Dev}} = \sqrt{\frac{\sum_{l=1}^{N}\sum_{i=1}^{n_l}(T_{i,1/2} - T'_{i,m+1/2})^2}{\sum_{l=1}^{N} n_l}} \tag{23}$$

where $T_{i,1/2}$ represents the first column matrix temperature distribution in the gas sector and $T'_{i,m+1/2}$ represents the last column matrix temperature distribution in the air sector. n_l is the row number in layer l and N is the layer number.

The heat balance error is determined from the difference in enthalpy change for the fluid on the hot gas side to the cold air side compared to the enthalpy change on the hot gas side

$$\text{error} = \left| 1 - \frac{\sum_{l=1}^{N}\sum_{i=1}^{N_l}\sum_{j=1}^{m} \dot{m}_g f_j c_{p,i,j}(t_{i-1/2,j} - t_{i+1/2,j})]_{\text{Cold}}}{\sum_{l=1}^{N}\sum_{i=1}^{N_l}\sum_{j=1}^{m} \dot{m}_g f_j c_{p,i,j}(t_{i-1/2,j} - t_{i+1/2,j})]_{\text{Hot}}} \right| \tag{24}$$

An alternative way of solving for the error is to calculate the heat transfer between the gas and matrix in each sector. The values of the error found by these two ways are in agreement.

5 Qualification of the Numerical Method

In order to verify solutions by the method here with the methods presented in [5, 6], two computer programs were written with constant thermal properties. One computer program was based on the method of this study, and the other was based on the method of [5, 6]. Equations (23) and (24) are used to determine the point at which the iterations cease. The maximum errors of temperature deviation and the energy balance are 10^{-4}.

Case A: Comparing the solutions with the method of [5]

$C_{\min}/C_{\max} = 0.90$, $Ntu_0 = 6$, $C_R/C_{\min} = (hA)^* = 1.0$

No. subdivisions	This study	Method of [5]
	ϵ/CP(s)	ϵ/CP(s)
8	0.781607/0.037	0.781569/0.060
16	0.780037/0.099	0.780040/0.217
32	0.779649/0.348	0.779617/0.884

where CP is the central processing execution time on CDC 7600 system.

Case B Comparing the solutions with the method of [6]

Case/λ_2	This study 0.0	This study 0.16		Method of [6] 0.0	Method of [6] 0.16	
	ϵ/CP(s)	ϵ/CP(s)	$\Delta\epsilon/\epsilon$	ϵ/CP(s)	ϵ/CP(s)	$\Delta\epsilon/\epsilon$
1	81.1806/0.152	71.3258/0.144	12.14	81.1767/0.443	71.3220/0.900	12.14
2	94.8459/1.544	83.5903/0.728	11.87	94.8380/11.38	83.5596/13.482	11.89

where Case 1: $C_{\min}/C_{\max} = 1.0$, $Ntu_0 = 10$, $C_R/C_{\min} = (hA)^* = As^* = 1.0$, number of subdivisions = 20,
Case 2: $C_{\min}/C_{\max} = 1.0$, $\text{Ntu}_0 = 20$, $C_R/C_{\min} = 5.0$, $(hA)^* = As^* = 1.0$, number of subdivisions = 40.

Both comparisons show that both methods give virtually identical solutions. But when Ntu_0 or $C_R/C_{\min}$ is increased, the differences in computer time also increase. For Case 2 with $\lambda_c = 0.16$, the calculation of this study is 18 times faster than the method of [6]. It was found that the present method is not only faster but also inherently more stable in arriving at a solution, especially when the Ntu_0 (overall number of transfer units) is large. It was also found that the differences in computer execution time between the present method and the methods of [5, 6] increased when the rotation speed of the matrix increased or Ntu_0 increased.

Another unique qualification of the present method is the ease with which one can start the calculation, since it is not necessary to assume an initial temperature distribution for the regenerator as in [6]. The presented method also rules out unstable solutions, since the stability condition, equation (9) of [5], does not apply to this study.

6 Illustrative Results and Discussion

In order to demonstrate the heat transfer phenomena in a bisector regenerator with multiple layers as well as variable thermal properties of fluid and matrix, a numerical example for counterflow and parallel-flow through the rotary heat exchanger is computed using the following data.

Table 1 Operating conditions for the example

	Gas side	Air side
Inlet temperature	350°C	20°C
Mass flow rate	125 kg/s	97.2 kg/s
Gas composition (mole %)	$N_2 = 73.06$, $O_2 = 2.59$, $H_2O = 11.85$, $CO_2 = 12.5$	$N_2 = 79$, $O_2 = 21$
Sector angle	165 deg (5.5 subsectors)	165 deg (5.5 subsectors)
Column fraction for finite difference	0.1*10	0.1*10

Equation (1c) is used to compute the heat transfer coefficient. All thermal properties, i.e., specific heat, viscosity, and density are functions of temperature and fluid type.

Table 2 Information on the layered regenerator used for the example

	Layer 1	Layer 2	Layer 3
Depth of layer	1m	0.6m	0.4m
Density of metal	7850 kg/m^3	7850 kg/m^3	7850 kg/m^3
Heat transfer surface area density	400 m^2/m^3	400 m^2/m^3	325 m^2/m^3
Conductivity		see table 3	
Specific heat		see table 3	
Row fraction for finite difference	0.1*10	0.166667*6	0.125*8

Rotor speed is 1.56 rpm
Rotor free area per subsector is 3.9 m^2

Table 3 Conductivity and specific heat of steel matrix

T,°C	0	200	400	600
k,W/(m K)	53.9995	45.9996	36.9997	30.099
C,J/(kg K)	453.4304	548.4708	643.9298	739.3889

All thermal properties of air and gas in this sample calculation, i.e., specific heat, viscosity, conductivity, and density, are based on [13]. All thermal properties are evaluated at a pressure of 1 atmosphere and are functions of temperature.

For the counterflow heat exchanger, the gas flow and the air flow are in different directions. For the parallel-flow heat exchanger, the gas flow and the air flow are in the same direction. Both cases are computed in the numerical example. Figures 3–6 are the solution of counterflow through a rotary heat exchanger, and Figs. 7–10 are the solution of parallel-flow through a rotary heat exchanger. The abscissa (flow length) of Figs. 3–10 is based on the gas-flow direction. For counterflow, the entering point of the gas is at flow length = 0, but the entering point of the air is at flow length = 2 m. For parallel-flow, the entering point of both gas and air is at flow length = 0. Figures 3 and 7 show the gas temperature distribution along the flow length at the different circumferential locations. Figures 4 and 8 show the air temperature distribution along the flow length at the different circumferential locations. Figures 5 and 9 show the gas-side matrix temperature distribution along the flow length at the different circumferential locations. Figures 6 and 10 show the air-side matrix temperature distribution along the flow length at the different circumferential locations.

From Figs. 3–10, the temperature distribution has a discontinuity at a flow length of 1.6 m. This is due to the change in matrix materials and a void space between the two different layers at the flow length of 1.6 m. There are three layers in the regenerator of this example. The boundaries between these three layers occur at flow lengths of 1.0 m and 1.6 m. Layers 1 and 2 are the same matrix, but layer 3 is different. The main purpose of layer 3 is to prevent matrix corrosion. The heat transfer surface area density and hydraulic diameter of layer 3 are different from layers 1 and 2, hence the convection heat transfer coefficients are also different. In the actual regenerator design, there is a void space between the layers; hence, there is no heat conduction between matrix layers 2 and 3, which results in a discontinuity at the flow length of 1.6 m.

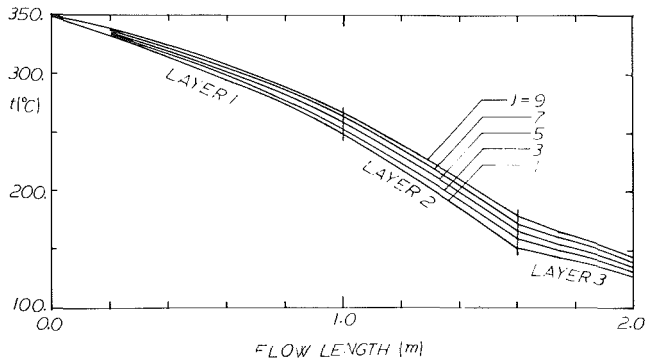

Fig. 3 The gas temperature distribution along flow length in the different circumferential locations for the counterflow regenerative heat exchanger

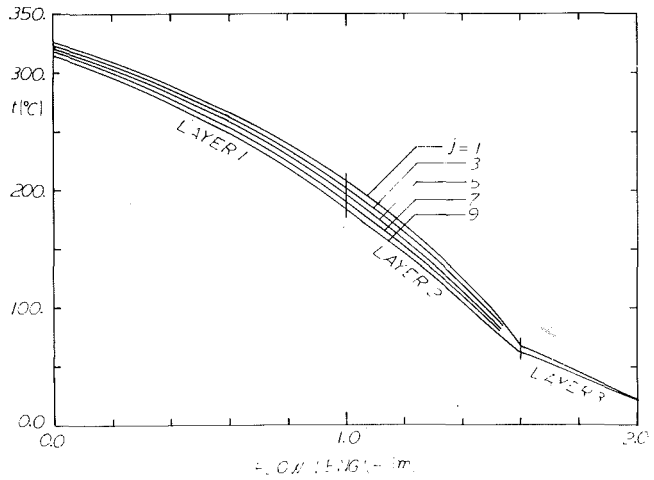

Fig. 4 The air temperature distribution along flow length in the different circumferential locations for the counterflow regenerative heat exchanger

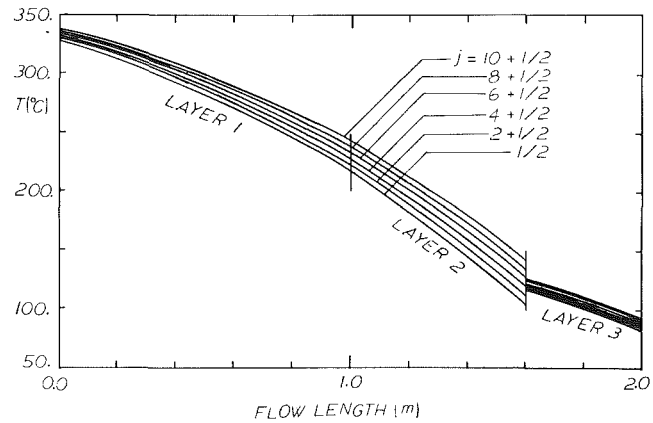

Fig. 5 The gas-side matrix temperature distribution along the flow length in the different circumferential locations for the counterflow regenerative heat exchanger

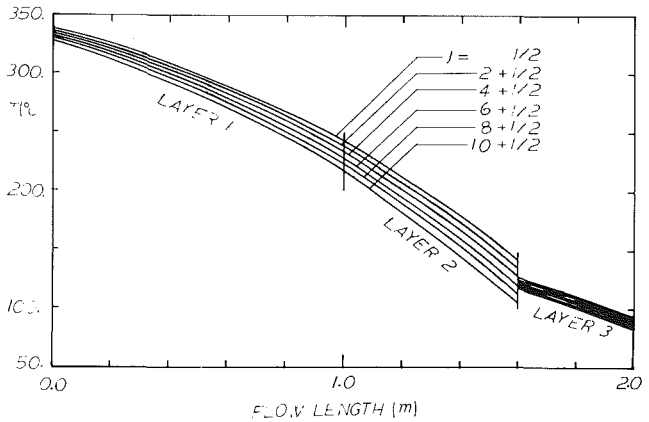

Fig. 6 The air-side matrix temperature distribution along the flow length in the different circumferential locations for the counterflow regenerative heat exchanger

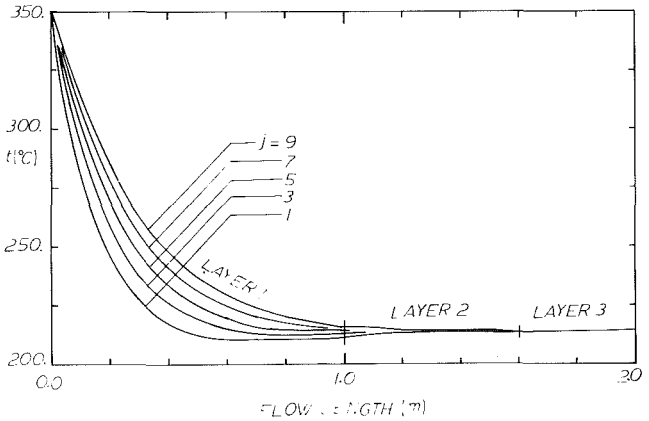

Fig. 7 The gas temperature distribution along flow length in the different circumferential locations for the parallel-flow regenerative heat exchanger

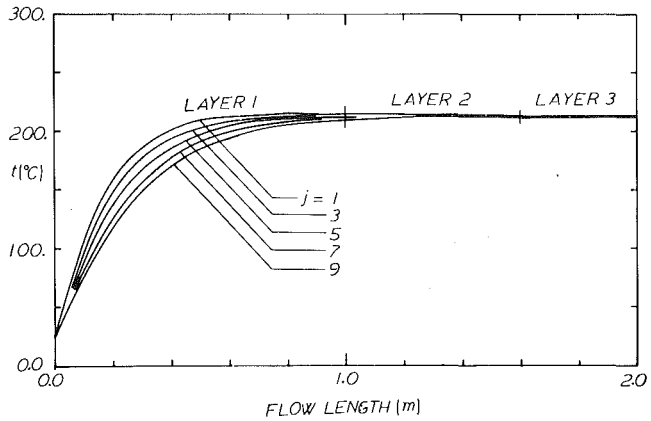

Fig. 8 The air temperature distribution along flow length in the different circumferential locations for the parallel-flow regenerative heat exchanger

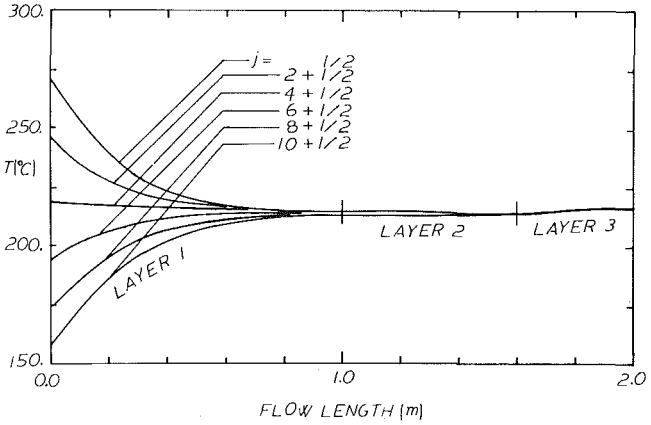

Fig. 9 The gas-side matrix temperature distribution along the flow length in the different circumferential locations for the parallel-flow regenerative heat exchanger

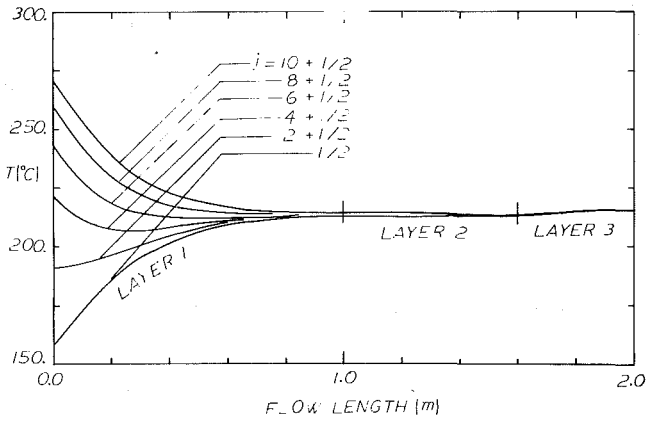

Fig. 10 The air-side matrix temperature distribution along the flow length in the different circumferential locations for the parallel-flow regenerative heat exchanger

From Figs. 3–6, one can see that temperature distributions in the circumferential direction are quite uniform for counterflow. It is interesting to note that the matrix temperature distributions within the gas sector (Fig. 5) and the air sector (Fig. 6) are almost symmetric about the boundary between the gas and air sectors. The maximum temperature difference between the two distributions is less than 3°C. The gas and air temperature distributions (Figs. 3 and 4) also decrease along the flow length as expected for a counterflow rotary regenerator. The parallel-flow matrix temperature distribution for the gas side (Fig. 9) and the air side (Fig. 10) do not have similar shapes as they do for counterflow. Figures 9 and 10 show the maximum matrix temperature distribution decreasing and the minimum matrix temperature distribution increasing along the flow length to approach an asymptotic value as expected for a parallel-flow regenerator. Figures 7 and 8 show that the points of minimum gas temperature and maximum air temperature in a parallel-flow rotary heat exchanger are not necessarily at the exit plane as in the recuperative type of heat exchanger. Figures 7 and 8 also show that the maximum gas and air temperature distribution and the minimum gas and air temperature distribution along the flow length approaches the same asymptotic value as the matrix temperature distributions.

8 Conclusions

A numerical finite-difference method for obtaining the fluid and metal temperature distributions for a rotary regenerator, accounting for the effects of longitudinal heat conduction in the wall in the direction of fluid flow is presented. The present method can reduce the computational time required for convergence and improves the numerical stability of the iteration process. This method can also be applied to compute the fluid and metal temperature distributions for multiple sectors and multiple layers for any kind of flow combination and for any kind of flow nonuniformity. The solution is general and is applicable to any type of regenerator. The case of zero longitudinal heat conduction is a special case of the method presented here, and the solution can be obtained by setting λ' and λ'' equal to zero in equation (4).

References

1 Kays, W. M., and London, A. L., *Compact Heat Exchangers*, McGraw-Hill, New York, 1964.

2 Jakob, M., *Heat Transfer*, Vol. II, Wiley, New York, 1957, pp. 261–341.

3 Coppage, J. E., and London, A. L., "The Periodic Flow Regenerator," ASME *Transactions*, Vol. 75, 1953, pp. 779–787.

4 Shah, R. K., "Thermal Design Theory for Regenerators," *Heat Exchangers: Thermal-Hydraulic Fundamentals and Design*, Edited by S. Kakac, A. E. Bergles, and F. Mayinger, Hemisphere Publishing Corp., Washington, D.C., 1981, pp. 721–763.

5 Lamberston, T. J., "Performance Factors of Periodic-Flow Heat Exchanger," ASME *Transactions*, Vol. 80, 1958, pp. 586–592.

6 Bahnke, G. D., and Howard, C. P., "The Effect of Longitudinal Heat Conduction on Periodic-Flow Heat Exchanger Performance," ASME *Journal of Engineering for Power*, Vol. 86A, 1964, pp. 105–120.

7 Mondt, J. R., "Vehicular Gas Turbine Period-Flow Heat Exchanger Solid and Fluid Temperature Distributions," ASME *Journal of Engineering for Power*, Vol. 86A, 1964, pp. 121–126.

8 Holmberg, R. B., "Heat and Mass Transfer in Rotary Heat Exchangers with Non-hygroscopic Materials," ASME JOURNAL OF HEAT TRANSFER, Vol. 99, 1977, pp. 196–202.

9 Holmberg, R. B., "Combined Heat and Mass Transfer in Regenerators with Hygroscopic Materials," ASME JOURNAL OF HEAT TRANSFER, Vol. 101, 1979, pp. 205–210.

10 Van Leersum, J. G., and Ambrose, C. W., "Comparisons Between Experiments and a Theoretical Model of Heat and Mass Transfer in Rotary Regenerators With Nonsorbing Matrices," ASME JOURNAL OF HEAT TRANSFER, Vol. 103, 1981, pp. 189–195.

11 Razelos, P., and Benjamin, M. K., "Computer Model of Thermal Regenerators With Variable Mass Flow Rates," *International Journal of Heat and Mass Transfer*, Vol. 21, 1978, pp. 735–743.

12 Scarborough, D. B., *Numerical Mathematical Analysis*, 4th ed., Johns Hopkins Press, Baltimore, 1958.

13 Hilsenrath, J., et al., *Tables of Thermal Properties of Gases*, N.B.S. Circular 564, National Bureau of Standards, Gaithersburg, 1955.

Surface Microfouling During the Induction Period

R. E. Baier
A. E. Meyer
V. A. DePalma
R. W. King
M. S. Fornalik

Advanced Technology Center,
Calspan Corporation,
Buffalo, N. Y. 14225

The time during which newly installed or cleaned heat transfer surfaces remain free of fouling deposits thick enough to diminish heat transfer coefficients or energy efficiency is often called the "induction period," a term disguising lack of knowledge of the microfouling events actually occurring. Using novel flow cells to conduct water of fresh, brackish, and oceanic quality, natural and treated with antifouling chemicals, over test surfaces of different clean and coated metals, it has been observed that the initial pattern of fouling deposits is remarkably similar in all circumstances. Rapid adsorption of protein-dominated films is followed by attachment of rodlike bacteria, bacterial exudation, colonization by a second wave of prosthecate microorganisms, additional secretion, and growth of debris-trapping filamentous appendages. Although inappropriate to extrapolate the noted rates of these processes to in-plant heat exchangers at present, this sequence of microfouling events seems universal enough to characterize the induction period of all water-side biofouling phenomena.

Introduction

Considerable attention has been given recently to the important relationships of biofouling films to hydraulic performance, heat transfer deterioration, and energy losses in water conduits (1–4). This previously published work, and many unpublished observations as well, indicates that there usually is an "induction period" of up to 30 days or more during which measurable changes do not occur in the frictional losses of the conduits nor in heat transfer resistance. When such changes are noted, they often suggest improved—though temporarily so—heat exchange, and the possible association of this phenomenon with "microfouling" events well within the laminar boundary layer has been cited [5].

While working with novel heat exhange test cells [6] and isothermal units of similar design for the purpose of examining events occuring during the induction period [7], we have noted a recurrent pattern of microfouling steps that seems remarkably independent of test surface compositions, water types, treatment conditions, temperature gradients, and flow rates over broad ranges. Obviously, some influence of toxic materials and/or toxic water treatments (e.g., chlorination) is seen, but it is surprising how small this influence is at the microfouling level. This preliminary report presents examples of the microfouling pattern discovered, and—on the basis of its general reproducibility in diverse circumstances—suggests that it may be a universal feature of the induction period events on all heat transfer equipment using natural cooling waters.

Methods

Description of the Flow Cells Utilized. Figure 1 shows photos of typical fully assembled and disassembled flow cells. The flow region in such cells is rectangular in cross section, as defined by two test plates separated by two spacers positioned between the plates. The actual cells are contained within split Plexiglas cylinders (item #1) used to apply uniform pressure via hose clamps (item #2) to the plate holders. View B of Fig. 1 shows one-half of a flow cell with a test plate (item #3) in place.

With further reference to Fig. 1, the Teflon inlets/outlets (item #4) are shown inserted in the plate holders (item #5). View B shows a spacer (item #6) that was removed from the test plate shown in the cell. Note the "stained" flow region of the test plate resulting from microfouling film deposition in the area defined by the spacers. View C in Fig. 1 schematically shows the cross section of the flow region.

Two test plates, typically measuring 2 × 5 × 0.08 to 0.16 cm and separated by two 0.3-cm wide by 0.152-cm thick spacers, are placed within each flow cell.

The flow cell plate holders (item #5) and spacers (item #6) are molded from Sylgard 184 (Dow Corning Trademark)—an extremely inert silicone polymer. The inlet and outlet ends of the plate holders are molded so that a smooth transition exists between the Teflon inserts and the flow region. The choice of inert materials in the apparatus assures freedom from contamination of the test surfaces by sources other than those of interest.

Inert materials are also used to connect the flow cells to the various piping systems under test. Polycarbonate male adaptors are used to connect the main piping to PVC stand pipes. Thick-walled amber latex tubing is used to connect the stand pipe water supply to the Telfon inserts within each flow cell. For field studies described here, typically 15 flow cells were connected to each of three separate pipe circuits within an experimental test van located at the oceanic test site.

Operating Conditions. The test units have been operated with fluid flow rates as low as one milliliter per minute and as high as 1000 milliliters per minute, producing fluid shear stresses at the wall from near zero values to the region in excess of 3 N/m^2 where most heat exchangers operate. Although highly polished test surfaces were most often selected to allow greater analytical sensitivity with some of the inspection techniques, test materials having surface textures identical to those of installed heat transfer pipes and plates were also utilized [8]. Waters tested have ranged from fresh conditions of the Great Lakes (Niagara River) to brackish (Hudson River) to open ocean (Gulf of Mexico), coastal ocean (Key West, Florida) and synthetic (aquarium) seawaters. Water treatments have ranged from none to simple gross filtration to deliberate treatment with electrolytic devices or chlorination. The pattern of microfouling events noted has been remarkably similar, and reproduces that seen even in trickling sand filtration of tertiary-treated sewage effluent [9].

For experimental results described here, the flow within each cell was controlled to maintain a fluid shear rate near

Contributed by the Heat Transfer Division for publication in the JOURNAL OF HEAT TRANSFER. Manuscript received by the Heat Transfer Division December 14, 1981.

Table 1 Coatings tested

NAME	MOLECULAR STRUCTURE	CHARACTERISTICS ON GERMANIUM				
		γ_c* (dynes/cm)	γ_d (dynes/cm)	γ_p (dynes/cm)	CONTACT POTENTIAL (millivolts)	THICKNESS (Angstroms)
CHLOROPROPYLTRICHLOROSILANE	$ClCH_2CH_2CH_2SiCl_3$	32.0	33.0	5.5	+30	110
n-2-AMINOETHYL-3-AMINO-PROPYLTRIMETHOXYSILANE	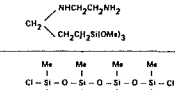	22.0	23.5	5.3	+500	1300
OCTAMETHYLDICHLOROSILANE	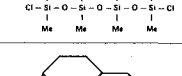	20.6	21.8	1.2	+40	340
β(3,4-EPOXYCYCLOHEXYL)-ETHYLTRIMETHOXYSILANE	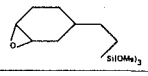	20.5	20.6	2.0	+230	60
DIMETHYLDICHLOROSILANE		21.5	22.4	3.6	+70	160
(HEPTAFLUOROISOPROPOXY)-PROPYLMETHYDICHLOROSILANE	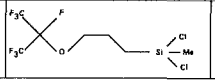	16.0	18.6	3.0	-360	15

*γ_c: CRITICAL SURFACE TENSION
γ_d: DISPERSIVE COMPONENT
γ_p: POLAR COMPONENT

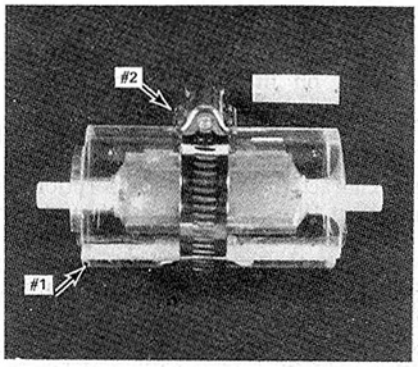

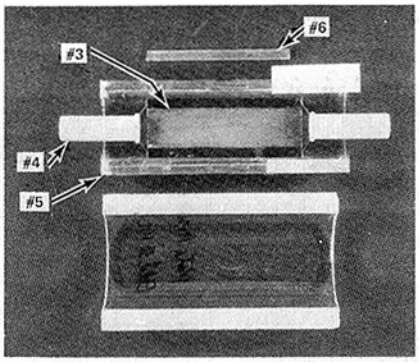

VIEW B: ONE HALF OF FLOW CELL

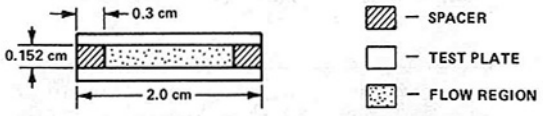

VIEW C: DIMENSIONS OF RECTANGULAR FLOW REGION OF FLOW CELLS (CROSS-SECTIONAL VIEW)

Fig. 1 Photos of flow cell

1000 s^{-1} or a shear stress of 10 dynes/cm^2. This shear stress was chosen after preliminary field trials in the Gulf of Mexico proved this shear rate to be suitable in accessing valuable information on the natural primary fouling films. The desired shear rate of 1000 s^{-1} required a fluid flow rate of 323 ml/min which with constant fluid flow at the stand pipes, was maintained with an accuracy of ±50 ml/min ($v = 1000 \pm 155$ s^{-1}).

Preparation of Test Plates. Most test plates used in these experiments had reflecting surfaces suitable for all the analytical techniques [5]. Germanium test plates were purchased from Harrick Scientific Corporation, Ossining, New York, meeting dimensional requirements ensuring low breakage when assembled in the flow cells.

Titanium and copper-nickel alloy (CA-715)[1] were obtained in rough form from David Taylor Naval Ship Research Development Center, Annapolis, Maryland. Plates were machined to size and then polished on one flat surface. A smooth specular surface was obtained by grinding each plate on 220A wet and dry abrasive paper and then lapping the plates (affixed with sealing wax to solid brass cylinders) on a lapping board charged with "400" lapping compound. The plates were lapped until their surfaces were uniform in appearance. Next, the plates—still mounted on the brass cylinders—were cleaned of any residual grit and placed in an oscillating polisher charged with 0.3 μm α-alumina polishing compound. The titanium plates were polished in light machine oil whereas the copper-nickel alloy plates were polished in distilled water. After several hours of polishing, specular surfaces were achieved on all test plates. At this point, the plates were demounted from the brass cylinders and cleaned in hexane, removing any residual wax. Before use, the plates were given a final cleaning, involving washing with Sparkleen laboratory detergent. This combination of surface treatments served to remove any contamination from the surfaces of the plates. Specific analytical measurements made on the plates at this point documented their freedom from initial contamination, according to previously published criteria [5], and showed textures to be in the range utilized for navy heat transfer pipes under test at the same time [8].

To access the low surface energy range not accessible with clean metals and their alloys, six different silane-based coatings were covalently coupled to germanium prisms that were radio frequency glow discharge cleaned in air for 3 min just prior to coating. The plates were immersed in the individual coating liquids within 30 s after RF glow discharge cleaning, obtaining optimal coating-to-substrate coupling [10].

The molecular structure for each coating compound is given in Table 1, together with the critical surface tension, contact potential, and thickness for each coating (on germanium) as determined by methods published earlier [11].

[1] CA-715 contains 30.8 percent Ni, 0.52 percent Fe, 0.41 percent Mn, 0.10 percent Zn, 0.005 percent Pb, 0.01 percent P, remainder Cu.

Exposure Conditions. A series of preliminary experiments was carried out with subsurface water of the Gulf of Mexico, piped to a battery of flow cells housed within experimental laboratories of the "Stage I" platform operated by the Naval Coastal Systems Center, 12 miles off Panama City, Florida. Most of the data reported here, however, were obtained from exposures of test surfaces from August 3, 1980 to August 15, 1980 at a remote ocean site at Boca Chica, Florida. This test site is part of the Naval Air Development Center, Key West, Florida.

Clean, unmodified ocean water, as well as that same water treated by two potential antifouling systems, was tested for its microfouling level. One of these antifouling systems was the Cathelco sacrificial anode system (which was operated continuously with 1/2 amp on Al and 1 amp on Cu) and the other was a chlorination system (which was cyclically on for one hour and off for three hours to generate 1/2 ppm free available chlorine).

The sequence of microfouling events noted was similar to, but more rapid than, that found in an artificial seawater tank system established and equilibrated to allow initial exposure experiments to be carried out. Live brine shrimp were added to two 50-gal tanks containing thriving fouling organisms every other day, in order to keep the macrofouling barnacles, tubeworms, bryozoa and hydroids in these tanks active. The temperature, specific gravity, and salinity for each tank were monitored almost daily. Salinity changes due to water evaporation were prevented by the addition of aerated tap water to the tanks. Salinity changes due to salt loss by bubble ejection were prevented by the addition of artificial seawater, as required.

Excess algae were removed from an integral scrubber tank in the system every 2 weeks. The schedule for the tank lighting regimen, involving variation of the photoperiod, was a simulation of the solar illumination in the Atlantic coastal region at approximately 30°N (Smithsonian Meteorological Tables, Sixth Revised Edition).

Analytical Methodology. Prior to their exposure to ambient river water, artifical or natural ocean water, plates from each group were analyzed by a battery of surface chemical techniques to assess their initial states [11]. After exposure, the inlet tube to each flow cell was clamped so that the flow region remained filled with water. Then the tubing below the clamp was cut and the cell flushed with 50 ml of a 4 percent glutaraldehyde solution so that flushing took place from bottom to top within one to two min. This procedure was adopted to fix and preserve the morphology of formed elements (e.g., bacteria, algae) that had attached to the plates. This process did not significantly alter the primary film or number of attached organisms, as documented by infrared spectroscopy and scanning electron microscopy.

After this step, the flow cells were taken apart and the plates removed. Any salts adhering to the backs of the plates were removed by gentle rinsing with distilled water. The plates were then placed in a vertical position for air drying before packaging for return to the laboratory.

Once within the surface science laboratory, selected examinations of the plates were made before and after they were given a 2-min distilled water "leach." The "leach" step involved placing about a milliliter of triply distilled water on each test plate surface while it was held in a horizontal plane. The water was then flicked from the plate and the plate allowed to air dry. This practice was followed to remove residual salts and loosely held organic material from the flow region of the plate. The spectroscopic results showed that some loose organic material was removed (i.e., it was not strongly bound to the surface), but selected area scanning electron microscopy proved that organisms attached to the flow region were not removed by this step.

The test plates were examined in a scanning electron microscope having a documented resolution of 100 Å. The surfaces in the flow regions of the plates were typically examined unmetallized and at electron beam voltages of both 5 keV and 20 keV with the specimens inclined at an angle of 45 deg to the electron beam. Images of organic material, such as bacteria, on metal plates are enhanced when observed without extraneous coatings on intrinsically conducting substrata. This is particularly true if the plates do not acquire an insulating oxide film as a result of the water exposure.

In the analysis of each sample in the SEM, several areas in the flow region, chosen at random, were examined. For documentation of the numbers of bacteria on the surfaces, three areas located 0.5, 1.0, and 1.5 cm from the inlet end of each flow cell were photographed at 500 and 2000×. Then, the numbers of bacteria of all types in the field of view at 2000× (an area of 2.01×10^{-5} cm^2) were counted and a number density of bacteria (#/cm^2) calculated. The criteria used in counting the bacteria was to count all organic particles with a length-to-width ratio of at least 3.

Results

The choice of pure polycrystalline germanium plates as test materials included in all our laboratory and field trials was obviously based on their utility for multiple, extremely sensitive and nondestructive analyses of thin surface films attached to them, as described in detail earlier [11, 12]. Of greatest importance among the many analyses allowed is the recording of characteristic infrared absorption spectra for the earliest adsorbed films by directing electromagnetic energy through the plates in the multiple attenuated internal reflection mode [13]. In every case, even with aquarium water, fresh Niagara River water, brackish Hudson River water, or natural ocean water exposures of only a day, these diagnostic infrared spectra revealed the test plate surfaces to have been coated with coherent films of humic- or protein-dominated matter. Only after the acquisition of such "conditioning" films were bacteria noted to begin colonizing

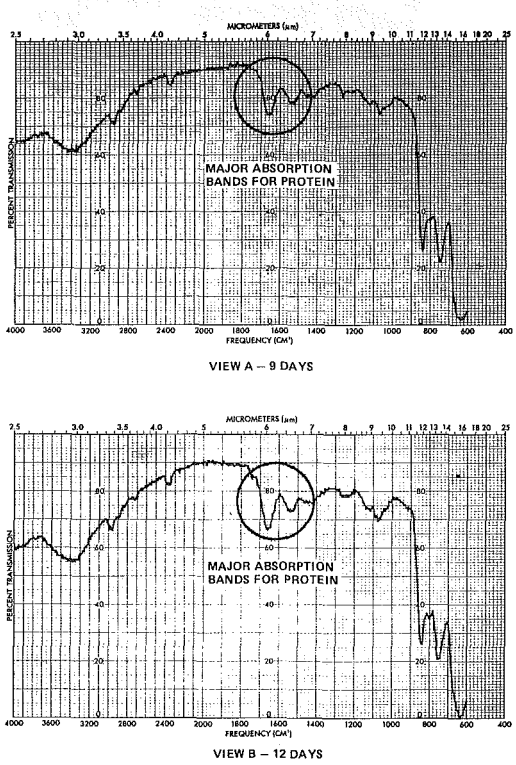

Fig. 2 Internal reflection infrared spectra for germanium test plates exposed to untreated ocean water

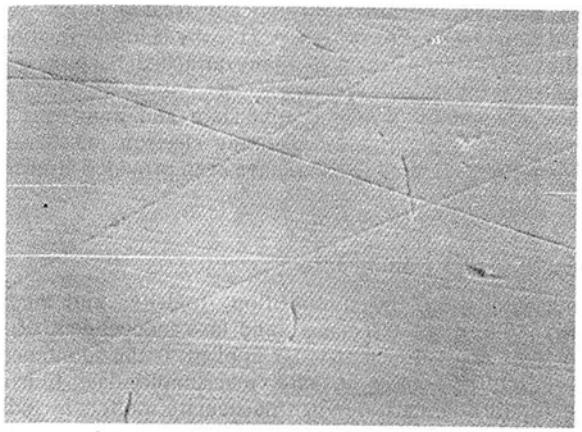

A-1 Day
Test plate coated with only a thin proteinaceous film adsorbed from flowing seawater

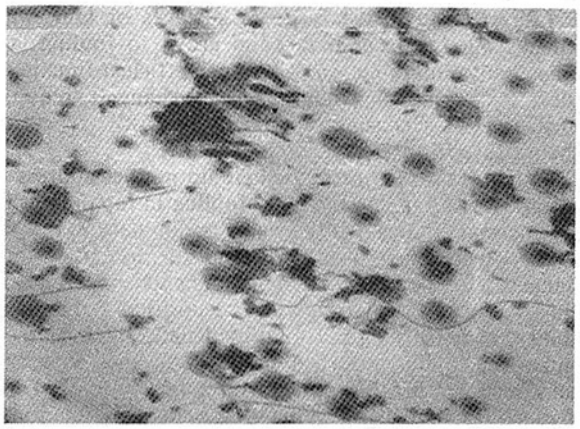

B-9 Days
Darkest areas are rod-shaped and filamentous bacteria. Medium-gray zones surrounding some organisms are bacterial exudates. Light gray background is thickened proteinaceous "conditioning" film accumulated prior to first bacterial attachment.

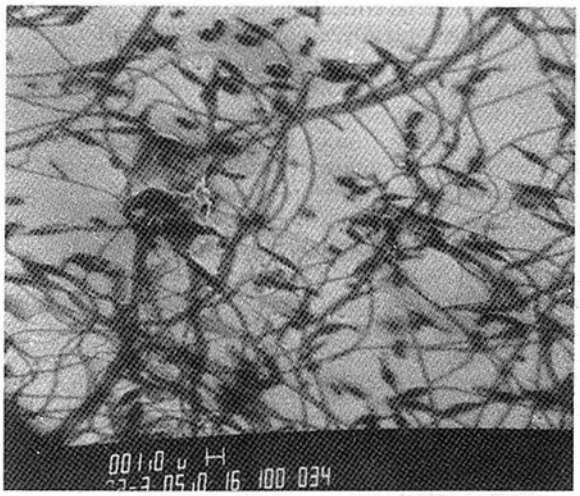

C-12 Days
Filamentous growth of bacterial appendages rapidly converts surface to a state that entraps further organic and particulate matter.

Fig. 3 Scanning electron microscope views of germanium test plates exposed to untreated ocean water for 1, 9, and 12 days (all photos at 2000 ×, specimen tilt 45 deg, unmetallized)

the plate surfaces by attachment to these nutrient layers. Figure 2 provides typical internal reflection infrared spectra of the microfouling films, comprising both preadsorbed proteinaceous layers and attached bacteria, after 9 and 12 days of exposure to flowing, untreated ocean water from the Key West test site.

For the opaque titanium and copper-nickel test plates, similar data were acquired by the method of external specular reflection spectroscopy [13], although with less sensitivity and spectral contrast. Ancillary, nondestructive surface film characterization by the methods of ellipsometry and contact potential analysis [11, 12] revealed that in every case—for clean and precoated surfaces—similar humic acidlike "conditioning" layers were deposited before bacteria began to colonize the test surfaces. Contact potential values always increased as these events occurred, and ellipsometric data indicated film thickness increases of from 200 to 800 Å on the various materials by the time (usually 3 days) significant bacterial deposition was noted.

When the flowing water was intermittently chlorinated, the initial film deposition process was unaffected, as was the initial colonization of the acquired microfouling film by pioneer (first, rod-shaped; next, prosthecate [with long "tail-like" appendages of their surface membranes]) microorganisms. Further bacterial growth, proliferation of filamentous forms, and rapid thickening of the fouling layer was inhibited by chlorination, however, and the originally deposited film was degraded significantly so that it became subject to fragmentation and spalling or reentrainment into the flowing stream.

In contrast, electrolytic treatment of the flowing water by the proprietary Cathelco process led to more rapid fouling-film build-up, greater numbers of attached pioneer organisms, and increased corrosion of some of the test plates (especially copper-nickel alloy CA 715). Nevertheless, this electrolytic treatment process did suppress growth of long filamentous organisms on all test plate surfaces. Even without application of water treatment schemes, the copper-nickel alloy test plates remained substantially free of the filamentous fouling forms, but this was associated with significant corrosion of the material during just 12 days of field testing.

Figures 3, 4, and 5, provide typical scanning electron micrographs documenting the bacterial forms and sequences of succession on the various materials exposed to differing treatment conditions. Clean, uncoated metal surfaces presented essentially the same initial findings in both the aquarium and oceanic trials. Figure 3 illustrates the progression of events with untreated ocean water from the Key West site, especially including the proliferation of long surface-bound filamentous forms. Figure 4 illustrates, with the same nontoxic substratum (results with germanium and titanium were similar), the efficacy of chlorination in suppressing growth of filament formers as well as the apparent "embrittlement" of the microfouling film. Figure 5 reveals that, with water treated by the Cathelco electrolytic process, microfouling continued unabated but only by the hardy rod-shaped pioneer species.

Figure 6 plots the numerical density of all attached microorganisms with length-to-width ratios exceeding 3, for all test plates exposed under different water-treatment conditions at the Key West site. Figure 6 illustrates, confirming the spectroscopic and thickness data acquired for these same fouling films, that, regardless of the test surface, substantially more microfouling took place for the electrolytically treated water exposure compared with the untreated case. The least microfouling took place with the chlorinated-water exposures. After 12 days of exposure of clean germanium plates to chlorine treatment, only one-half as many bacteria were attached compared to the untreated water case, and only one-quarter as many bacteria attached compared to the electrolytically treated water case. With similar chlorination, titanium plates acquired only one-half as many bacteria as from untreated water and only a fifth as

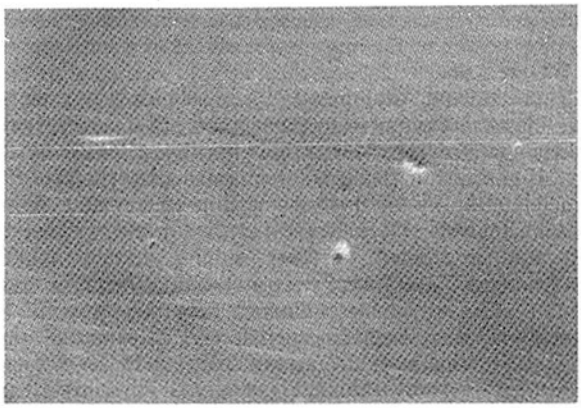

A-1 Day
Test plate coated with only a thin film of spontaneously adsorbed, protein-dominated material from seawater.

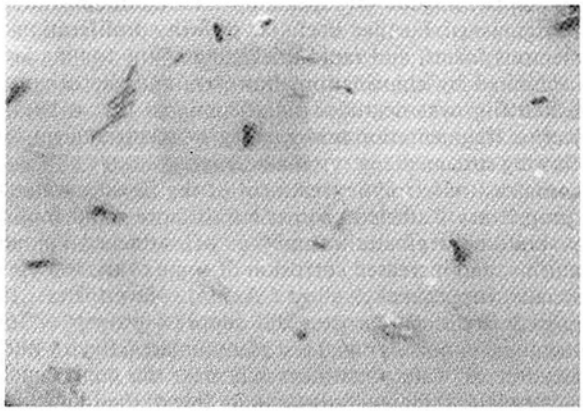

B-9 Days
Dark rod-shaped objects are pioneer attaching bacterial forms. Little exudation is noted at this stage.

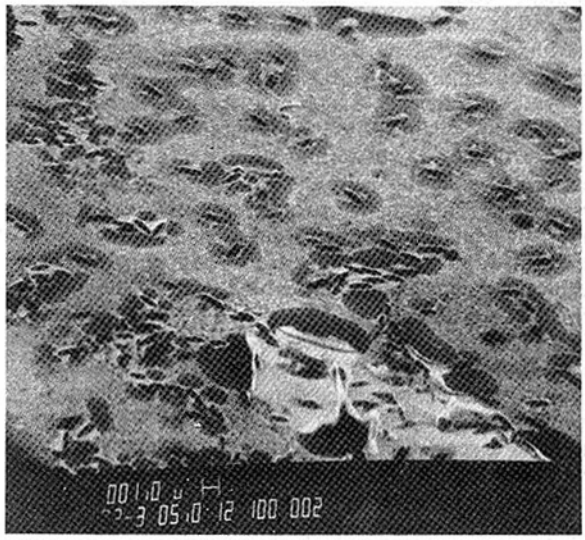

C-12 Days
Dark rod-shaped bacteria are surrounded by their pools of exudate and embedded in an oxidized film of protein-dominated materials.

Note - film cracking and peeling in lower right section of this view, as a probable result of chlorine "embrittlement."

Fig. 4 Scanning electron microscope views of germanium test plates exposed to chlorine treated ocean water for 1, 9, and 12 days (all photos at 2000 ×, specimen tilt 45 deg, unmetallized)

many bacteria as from electrolytically treated water. With regard to copper-nickel alloy CA 715, the chlorine treatment resulted in only one-third as many attached bacteria compared to the untreated water case.

Extensive tables of quantitative data and numerous additional supporting figures (scanning electron micrographs and analytical infrared spectra) have been provided elsewhere [8].

Discussion and Conclusions

Independent of the composition, toxicity, and surface energy state of the test plates, and also independent of the water type or treatment strategy applied, is the spontaneous adsorption of organic, usually macromolecular, films at solid/liquid boundaries. When particulate matter, including viable microorganisms, remains in the flow stream, specific and nonspecific adhesion of such formed elements usually occurs next. Such attachments are potentiated by the presence of the first layers of adherent matter. Living adherent matter, unless directly attenuated by toxic surfaces or bulk water treatment, quickly accumulates and grows to fouling layer thicknesses incompatibile with continued efficient function of the devices affected. Biofouling of heat exhangers, requiring expensive initial oversizing of capacity or costly, repetitious mechanical scouring, is an obvious example.

Although the studies reported here do not yet address the important factors of surface microfouling in the presence of strong thermal gradients at the walls, preliminary indications from work with dairy product fouling of pasteurizing heat exchangers are that high thermal gradients exacerbate the fouling problem by triggering deposition of inverse solubility, scale-forming salts and by denaturing and surface coagulating initially adsorbed proteins. Studies in natural ocean, fresh, or brackish waters have not proceeded long enough with enough different material/water combinations to guarantee that control of surface energy of heat exchange materials is a viable alternative to use of poisons, but it remains our working hypothesis that the same minimization of biological adhesiveness that has been achieved with blood-contacting biomedial devices will be effected in natural waters by control of material critical surface tension [5].

The experimental results reported here are most valuable in their demonstration of the following important conclusions. Conditions that have been historically associated with reduced biological fouling of heat transfer surfaces, including use of copper-rich materials, use of chlorination, and use of electrolytic water treatment, are all associated with suppression of the growth of highly filamentous surface films. These conditions are not effective in eliminating the first deposition of microfouling films of originally dissolved or suspended organic matter, nor in eliminating surface colonization and continued accumulation of the pioneering, rod-shaped microorganisms. Residual active chlorine in the flowing streams seems to oxidize and embrittle the initial fouling film deposits, however, allowing easier sloughing of the surface-bound mass into the flowing stream. Active residual chlorine hastens the corrosion of copper alloys, unfortunately. In the absence of toxicants, the established sequence of bacterial colonization of inert flow surfaces in contact with natural waters is (*i*) deposition of the spontaneously adsorbed conditioning film, (*ii*) attachment of rod-shaped, unflagellated bacteria and their modest secretion of exudates, (*iii*) attachment and active exogenous polymer deposition by prosthecate of other periphytic microorganisms, (*iv*) proliferation of long dense filamentous forms. The surface mat of filaments can easily entrap silt, diatoms, and other suspended debris to completely obscure the original heat transfer interface. Up to step (*iii*) in this sequence, the events of fouling in natural waters can be reasonably well simulated

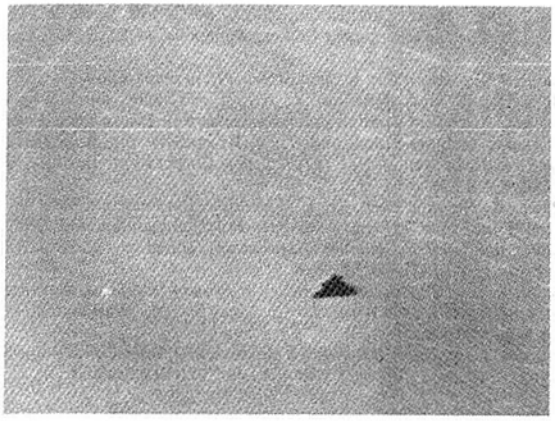

A-1 Day
Test plate coated with only a thin protein-dominated "conditioning" film adsorbed from flowing seawater.

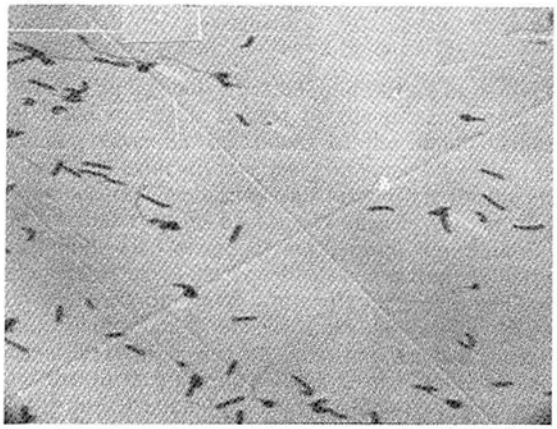

B-9 Days
Dark rod-shaped particles are the pioneer bacteria, attaching to the upper surface of the proteinaceous "conditioning" film. No apparent bacterial exudation is observed.

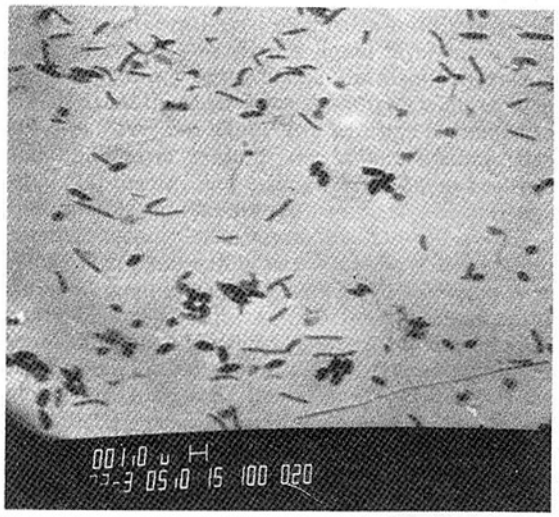

C-12 Days
Dark rods and ellipsoidal particles are bacterial forms, continuously increased in abundance by both new arrivals and "in place" multiplication. Bacterial exudation is not observed, but the film continues to thicken by spontaneous adsorption of seawater-borne macromolecules.

Fig. 5 Scanning electron microscope views of germanium test plates exposed to cathelco-treated ocean water for 1, 9, and 12 days (all photos at 2000 ×, specimen tilt 45 deg, unmetallized)

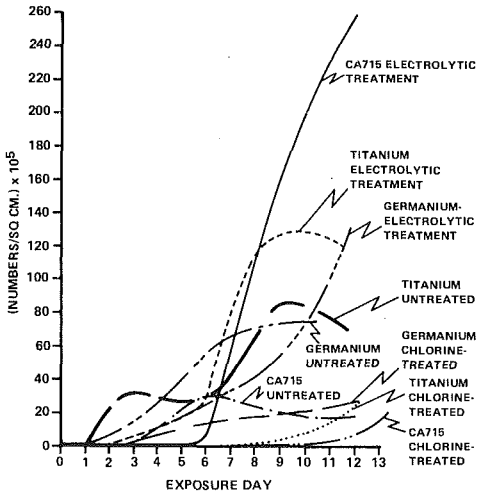

Fig. 6 Density of bacteria on materials exposed to variously treated ocean water

by using water in tanks harboring transplanted communities of fouling organisms, but at a rate significantly less than that noted in once-through natural systems.

Although the pattern of microfouling events described here has been reproduced often enough and in diverse enough conditions to encourage extrapolation to "induction period" phenomena in most water-side biofouling circumstances, extrapolation of the rate data from this study to heat exchangers would be inappropriate at this time. It is probable that radial temperature gradients could significantly change these rates, even though the fouling community might remain the same. Further, it should be recognized that the microfouling events reported here all occur well within the common laminar boundary layer (20 to 40 micrometers thick) [1–4], so that extremes of surface roughness or shear stress that modify these quiescent near-boundary conditions might also interrupt the pattern of deposition observed.

The flow cells utilized to obtain these data have a very short "approach" length from the supply duct entrance to the test surfaces, so that the flow conditions are still being established spatially when the fluid first contacts the test surfaces. Often, an enhanced deposition rate is noted at the entering end of the test plates, and probably results from this feature of the units. Work now in progress is attempting experimental definition of hydrodynamic conditions at the test surfaces so that point-to-point variations of shear stress can be accounted for. It will not be until these conditions are met that rate data can be transferred with confidence from these simple flow cells to engineering equipment operating under in-plant constraints.

Acknowledgments

This work has been supported by Office of Naval Research Contract N00014-81-C-0671, Department of Energy Contract DE-AC02-80ER10766, David W. Taylor Naval Ship Research Development Center Contract N00167-80-C-0178, and internal research/development funds of Calspan Corporation. We are grateful to our colleagues E. Gasiecki, M. Wilkinson, and J. Fisher for assistance with experimental aspects of the program. Mrs. B. J. Spahr and Mr. D. Kogut prepared the manuscript and illustrations.

References

1 Picologlou, B. F., Zelver, N., and Characklis, W. G., "Biofilm Growth and Hydraulic Performance," ASCE, *Journal of the Hydraulics Division*, Vol. 106, No. HY5, Proc. Paper 15421, May 1980, pp. 733–746.

2 Characklis, W. G., Zelver, N., Turakhia, M., and Roe, F. L., "Energy Losses in Water Conduits: Monitoring and Diagnosis," in *Proceedings of the*

42nd International Water Conference, Pittsburgh, Pa., Oct. 26–28, 1981.

3 Characklis, W. G., Nimmons, and Picologlou, B. F., "Influence of Fouling Biofilms on Heat Transfer," *Heat Transfer Engineering*, Vol. 3, No. 1, July-Sept. 1981, pp. 23–37.

4 Characklis, W. G., "Fouling Biofilm Development: A Process Analysis," *Biotechnology and Bioengineering*, Vol. 23, 1981, pp. 1923–1960.

5 DePalma, V. A., and Baier, R. E., "Microfouling of Metallic and Coated Metallic Flow Surfaces in Model Heat Exchange Cells," *Proceedings of the Ocean Thermal Energy Conversion (OTEC) Biofouling and Corrosion Symposium*, United States Department of Energy, Division of Solar Energy, Washington, D.C. 20545, 1978, pp. 89–106.

6 King, R. W., Meyer, A. E., Ziegler, R. C., and Baier, R. E., "New Flow Cell Technology for Assessing Primary Biofouling in Oceanic Heat Exchangers," *Proceedings of the Eighth Ocean Energy Conference*, U. S. Department of Energy, Washington, D. C., 20545, 1982.

7 DePalma, V. A., and Baier, R. E., U.S. Patent No. 4,175,233.

8 DePalma, V. A., King, R. W., Fornalik, M. S., Meyer, A. E., and Baier, R. E., "Analysis of Primary Films Accumlated During Marine Fouling Program," Final Report, Contract No. N00167-80-C-0178, David W. Taylor Naval Ship Research Development Center, Annapolis, M.D., 21402, Oct. 1, 1981.

9 Baier, R. E., Bainbridge, K., and Brown, N., in preparation.

10 Baier, R. E., and DePalma, V. A., "Electrodeless Glow Discharge Cleaning and Activation of High-Energy Substrates to Insure Their Freedom From Organic Contamination and Their Receptivity for Adhesives and Coatings," Calspan Report No. 167, Calspan Corporation, Buffalo, N.Y., Aug. 1970.

11 Baier, R. E., and Loeb, G. I., "Multiple Parameters Characterizing Interfacial Films of a Protein Analogue, Polymethylglutamate," *Polymer Characterization: Interdisciplinary Approaches*, edited by C. D. Craver, Plenum Press, N.Y., 1971, pp. 79–96.

12 Baier, R. E., ed., *Applied Chemistry at Protein Interfaces*, Advances in Chemistry Series, No. 145, American Chemical Society, Washington, D.C., 1975, pp. 1–25.

13 Harrick, N. J., *Internal Reflection Spectroscopy*, Interscience Publishers, N.Y., 1967.

Experimental Observations of the Microlayer in Vapor Bubble Growth on a Heated Solid

L. D. Koffman[1]
Mem. ASME

M. S. Plesset
Fellow ASME

Division of Engineering
and Applied Science,
Department of Engineering Science,
California Institute of Technology,
Pasadena, Calif. 91125

Experimental measurements of microlayer formation and of the time history of microlayer thickness change have been obtained for nucleate boiling of water and ethanol. These detailed measurements were obtained using laser interferometry combined with high-speed cinematography. The measurement technique is discussed in detail with emphasis on the difficulties encountered in interpretation of the fringe patterns. The measurements for water can be reasonably applied to the data of Gunther and Kreith, in which case it is concluded that microlayer evaporation alone cannot account for the increased heat transfer rates observed in highly subcooled nucleate boiling. It appears that microconvection must play at least an equal role.

Introduction

When a liquid cools a heated solid surface by convection the heat transfer rate is limited by the presence of a thermal boundary layer in the liquid at the solid surface. This limitation is evidently overcome in some way when nucleate boiling occurs. The mechanisms responsible for the increased heat transfer rates in nucleate boiling have been sought for some time. Two proposed mechanisms which have gained some acceptance as the most likely competing mechanisms are microconvection and microlayer evaporation. In microconvection a bubble is thought to simply disrupt the thermal layer in such a way that hot liquid is pushed away from the surface during bubble growth while cooler liquid returns during bubble collapse (or lift-off). Thus, additional mixing of the liquid is achieved near the surface to yield a turbulencelike convective effect. This mechanism gained early acceptance [1] but alone did not seem to be an entirely satisfactory explanation. Latent heat transport was also considered in early work but was dismissed as negligible when computed based on observed vapor volume [2]. Latent heat transport was reconsidered by Snyder and Edwards [3], who postulated that a thin viscous liquid layer must be formed beneath a growing vapor bubble on a solid surface. It was postulated that this microlayer evaporates while condensation could occur over the bubble cap which is presumed to be in cooler liquid over most of the bubble lifetime. Based on Plesset's [4] theory, they estimated that latent heat transport due to microlayer evaporation can be significant, especially for highly subcooled nucleate boiling.

While microconvection and microlayer evaporation are understood qualitatively, the relative contribution of each in nucleate boiling is still not well understood. Considerable experimental effort [5–10] has established the existence of the microlayer and some measurements of microlayer thickness are available. It appears from these studies and from more recent direct measurements [11, 12] that microlayer evaporation plays a considerable role in nucleate boiling at low subcooling. For the important case of highly subcooled nucleate boiling it would seem from Snyder and Edwards' proposed mechanism that microlayer evaporation would be even more important and perhaps dominant. Gunther and Kreith [2] reported that latent heat transport based on observed vapor volume could account for only 1–2 percent of the heat transfer in their measurements of highly subcooled nucleate boiling. For this same experimental data, Bankoff and Mikesell [13] suggested that latent heat transport was at least an order of magnitude greater due to turbulent transfer at the (condensing) bubble surface. Measurements of Bankoff and Mason [14] demonstrated that extremely high condensation rates were possible between a steam bubble and subcooled flowing water which further reinforced the latent heat transport model [15]. Snyder and Robin [16–18] proposed a model in which nearly all of the heat transfer is attributed to latent heat transport. Recently, however, Plesset and Prosperetti [19] have analyzed microlayer evaporation using the bubble growth measurements of Gunther and Kreith for highly subcooled nucleate boiling and came to the surprising conclusion that microlayer evaporation is relatively unimportant, accounting for only 10–20 percent of the heat transfer. Furthermore, they found that the importance of latent heat transport decreases with increasing subcooling in seeming contradiction to the proposed latent heat transport models. These conclusions depend upon and are sensitive to the assumed initial microlayer thickness for which Plesset and Prosperetti relied upon in an order of magnitude estimate since discrepancies existed in the literature for measured values for water. The need for an accurate value of microlayer thickness for water prompted the present experimental investigation.

The goal of the present study was to develop a measurement technique suitable for the small, short-lived bubbles characteristic of highly subcooled nucleate boiling and to obtain microlayer thickness measurements for water. This was accomplished by using laser interferometry combined with high-speed cinematography. An important aspect of this paper is a careful discussion of the interpretation of the interference fringe patterns for measurements of the microlayer.

Previous Measurements

Primarily two methods have been used to measure microlayer thickness. One method utilizes surface temperature measurements beneath bubbles from which microlayer thickness can be estimated by an energy balance of the microlayer evaporation. Moore and Mesler [5] first detected the microlayer in this way by using a flush-mounted thermocouple. They estimated that microlayer thickness was of the order of 2 μm for boiling of saturated water at at-

[1] Present address: Assistant Professor, School of Mechanical Engineering, Georgia Institute of Technology, Atlanta, Ga. 30332

Contributed by the Heat Transfer Division for publication in the JOURNAL OF HEAT TRANSFER. Manuscript received by the Heat Transfer Division April 26, 1982.

mospheric pressure. Hendricks and Sharp [6] also used a surface thermocouple while simultaneously taking high-speed movies of bubble growth in order to correlate the temperature data with the presence of the bubble. They observed a very rapid temperature drop as the perimeter of the bubble base passed over the thermocouple, a large heat flux beneath the bubble during growth, and an appreciable decrease in heat flux during lift-off. For water boiling at reduced pressures they estimated that the order of magnitude of the microlayer thickness was greater than 0.8 μm. The most complete study of this kind is due to Cooper and Lloyd [7]. They formed precisely located microthermometers such that a bubble grew out over four thermometers. High-speed movies were also taken and their observations were comparable to those of Hendricks and Sharp. By having four thermometer locations, they were able to determine that the microlayer profiles were wedgelike. Their measurement of a profile is significant since initial microlayer thickness changes with bubble size and with the bubble dynamics. Cooper and Lloyd used an approximate boundary layer analysis to estimate the initial microlayer thickness profile $\delta(r)$ as

$$\delta(r) = C(\nu t_g)^{1/2}$$

where ν is kinematic viscosity and t_g is the growth time for the bubble base to reach radius, r. The empirical constant, C, was in the range 0.5–1.0 for data on toluene and isopropyl alcohol at reduced pressures. We note that these detailed profiles were obtained for large bubbles (20–40 mm dia) with long lifetimes (30–60 ms). For small bubbles (1-mm dia) with short lifetimes (1–5 ms) the surface temperature technique may not be as useful for obtaining detailed profiles, since placement of more than one thermal sensor beneath a bubble would be difficult. The major advantage of this technique is that surface temperature is recorded directly so that interpretation of the data into surface heat flux and hence microlayer thickness evaporation is straightforward. We note that the initial microlayer thickness is taken to be the thickness evaporated, a result which depends on the assumption of no radial flow in the microlayer. This assumption was justified by Cooper and Lloyd [7] and will be discussed briefly later in this paper.

The other measurement technique which has been used is interferometry combined with high-speed cinematography. Sharp [8] introduced this technique which in principle can give time histories of detailed microlayer profiles from which thicknesses and possibly evaporation rates can be determined. Sharp found wedgelike microlayer profiles for water with a thickness of 0.4 μm at a radius of 0.94 mm. We note that this value is significantly less than the estimates for water obtained from the surface temperature technique. Hence a discrepancy exists for the measured values of microlayer thickness for water. In Sharp's experiment, the reflections from the microlayer were imaged through a window at the top of the bubble which constrained the bubble growth. Jawurek [9] followed Sharp's interferometric approach but obtained boiling on a glass surface by resistance heating of a thin transparent SnO_2 film on the glass surface. The reflections from the microlayer could then be imaged through the glass plate so that the bubble growth was not constrained. For boiling of methanol and ethanol at reduced pressures, microlayer profiles were reported to be wedgelike with thicknesses of 0.2-0.8 μm at the outer edge (apparently at a radius of several millimeters). We note that these values are an order of magnitude less than Cooper and Lloyd's measurements for somewhat similar conditions. Sharp and Jawurek both used a mercury arc lamp with a collimating lens and spectral line filters. Voutsinos and Judd [10] suggest that poor coherence in the light sources used by Sharp and Jawurek may have led to incorrect determination of the fringe order thus explaining the discrepancies with the surface temperature technique. Voutsinos and Judd used a He-Ne laser as a light source while adopting the boiling technique of Jawurek. For boiling of methylene chloride at reduced pressure they report wedgelike profiles with a thickness of 5 μm at a radius of 0.75 mm. These measurements appear to be in line with those of Cooper and Lloyd.

The advantage of the interferometric approach is that time histories of detailed microlayer profiles can be obtained. Such detailed information is necessary for further understanding of microlayer formation and evaporation. Because of the detail potentially available, we have adopted the interferometric approach in the present study. This approach is the most promising for study of small, short-lived bubbles. The disadvantage of the interferometric approach is that interpretation of the fringe patterns is not a trivial matter. Possible errors in the interpretation of the fringe patterns have not been properly discussed in the literature and, in fact, several points appear to have been overlooked by previous investigators. We address this problem in some detail.

Experimental Apparatus and Procedure

We adopted Jawurek's method of boiling on glass by d-c resistance heating of a thin SnO_2 film on the surface. Commercially available Pyrex Infrared Reflecting (IRR) Glass No. 7740 has a thin SnO_2 film coating. On plates of dimension 3.2 mm × 51 mm × 63 mm, the SnO_2 film was chemically removed [20, 21] to leave a 12.7 mm × 38 mm rectangular area in the center. Two clean copper strips were bonded to the edges of the rectangular film with the circuit board conducting paint Silver Print. The resulting resistance between the copper strips was typically 10–30 Ω. Fourteen gauge copper electrical cord was soldered to the copper strips and connected to a 40 vd-c power supply controlled by a Variac. The glass plate formed the bottom of the boiling cell.

The fluids used in the present investigation were water and ethanol. Distilled water was degassed by applying a vacuum on a bell jar in which the water was stirred with a magnetic stirrer. The degassed water was heated and then siphoned into the boiling cell. There was no need to degas the ethanol.

Jawurek was not able to boil water because the SnO_2 film was destroyed, apparently by electrolytic action. We experienced similar difficulty but were able to obtain boiling of water at low heat flux. By coating the copper strips with RTV silicon adhesive, the electrolysis was inhibited. This coating also provided adhesive strength to keep the copper strips attached to the plate. Being industrial glass, the Pyrex IRR glass surface had many pits ranging in size up to 100 μm. While being a nuisance optically, these pits facilitated boiling by serving as nucleation sites. In fact, when glass with a surface free from such pits was used, boiling could not be obtained before film breakdown occurred. Even with the pitted glass, film breakdown occurred when heat flux was increased so that we were constrained to low heat flux.

Nomenclature

C = constant of proportionality
d = distance between two interfaces
E = electric field of a plane wave
I = intensity
k = wavenumber ($2\pi/\lambda$)
m = fringe order number
n = index of refraction
r = radius of bubble base
t_g = time for growth of bubble base to a specific radius
u = radial velocity
δ = initial microlayer thickness
λ = wavelength of light
ν = kinematic viscosity

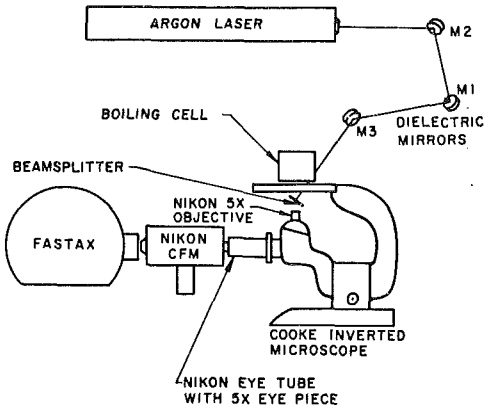

Fig. 1 Schematic of the laser interferometric high-speed camera system

An average heat flux was determined by measuring the dissipated power and the film surface area. We note that more boiling vapor bubbles were observed near the copper strips at the edge of the RTV coating than in the center region of the boiling area. The temperature of the bulk fluid was measured with a mercury-in-glass thermometer. No attempt was made to measure the wall superheat.

A diagram of the laser interferometric high-speed camera system is shown in Fig. 1. A 2-W Coherent Radiation Laboratories 52 G argon ion laser provided the highly collimated, coherent, monochromatic light suitable for interferometry. The high intensity of the laser is necessary since the exposure times in high-speed photography are small and the losses in the optical system were estimated to be a factor of one thousand. The green 514.5-nm wavelength beam was directed by a series of mirrors onto a beamsplitter positioned between the microscope objective and the bottom of the boiling cell. The beam was reflected from the beamsplitter onto the bottom of the bubble with normal incidence. The beams reflected from the microlayer pass through the beamsplitter and into the microscope assembly. The objective used was a Nikon Strain Free Achromat PM 5X (n.a. 0.10, working distance 15.0 mm). The long working distance is necessary in order to allow space for the beamsplitter to be placed between the objective and the glass surface. The Nikon eye tube with a 5X eyepiece was coupled to a Nikon CFM with a 1/4X projection lens. The CFM contains a 15/85 beamsplitter which allows visual observation without viewing through the camera. The total magnification at the film plane was approximately 9X. A Nikon stage micrometer with 10-μm divisions served as a reference scale for measurements taken from data films.

Movies were taken at a maximum framing rate of 15,000 frames/s with a 16-mm Fastax high-speed movie camera with a half-frame prism. For the system described above, the actual field of view recorded on the film is 0.27 mm $\times$ 1.0 mm. To establish an accurate time base, an LED timing light was designed and built which put timing marks on the edge of the film at 1 ms intervals. Light measurements necessary for correct film exposure were obtained with a United Detector Technology (UDT) 40X Optometer.

The following procedure can be expected to result in a film with analyzable fringe patterns resulting from microlayer formation and evaporation (further details are given in [21]). The laser beam is aligned with respect to the beamsplitter and the boiling cell such that a fairly uniform bright intensity results over the film plane. This alignment is crucial since thickness variations in these glass plates give rise to null bands which must be aligned out of the field of view as much as possible. The power density at the film plane is set using the UDT light meter. Typically a power density of 80 μW/cm^2

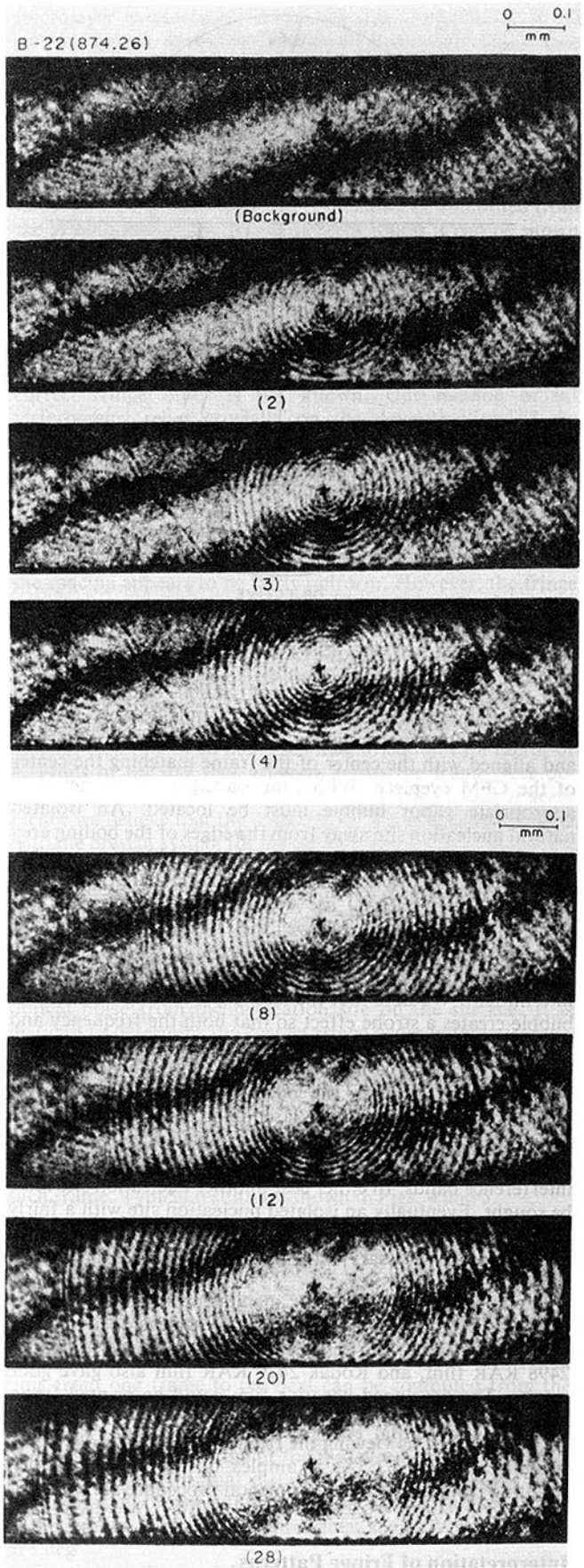

Fig. 2 Fringe patterns for bubble growth sequence in ethanol at atmospheric pressure with a mean heat flux of 26.5 kW/m^2 and a subcooling of 5.7°C. The frames shown are numbered from the first frame in which the bubble appears; the framing rate is 14.87 frames/ms.

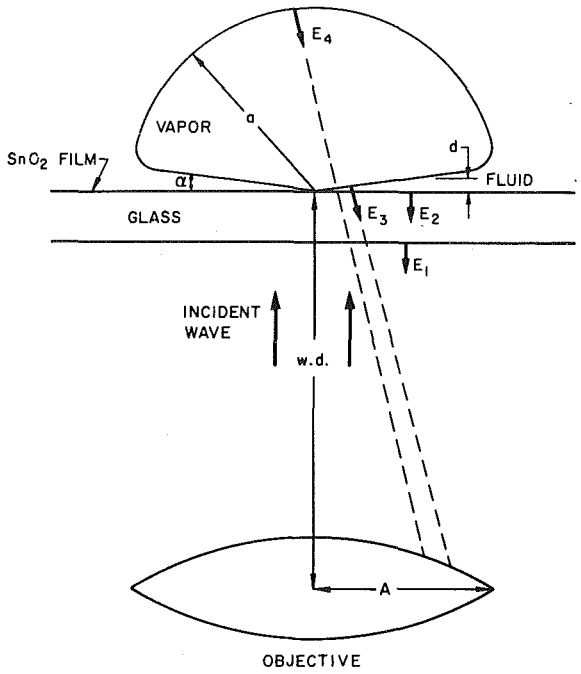

Fig. 3 Idealized model of a vapor bubble on a glass plate

was used with a framing rate of 13,000–15,000 frames/s (exposure time is approximately 1/5 of time between frames) and a film with exposure index of 400. The camera is focused and aligned with the center of the frame matching the center of the CFM eyepiece. With film loaded in the camera, an appropriate vapor bubble must be located. An isolated natural nucleation site away from the edges of the boiling area is sought; the interaction with other bubbles is avoided. Several types of bubble growth were noted. High frequency bubbles (100 bubbles/s) are usually small (1-mm dia) and form bubble streams above the nucleation site. Low frequency bubbles (10 bubbles/s) grow to larger sizes and bubble streams are not evident. Other nucleation sites were intermittent. We note that the laser light shining through the bubble creates a strobe effect so that both the frequency and size of the bubbles can be estimated visually. This same effect helps in centering a nucleation site. Once an appropriate bubble type is located, the nucleation site is judged with optical considerations under laser light. The nucleation site may be a pit which creates spurious interference patterns, or the nucleation site may be at a null point of the background interference bands. In either case another nucleation site must be sought. Eventually an isolated nucleation site with a fairly clean background interference can be located. The film is then taken and all necessary information is recorded on a data sheet.

Facilities were available for manual processing of 30.5-m lengths of 16-mm movie film. Kodak D-19 developer was used to give a high contrast. Best results were obtained with Kodak 2498 RAR film, and Kodak 2479 RAR film also gave good results. The developed negative film could be printed frame by frame with a maximum enlargement of 17.3X. Most of the data were taken by viewing the fringes on a film reader with a magnification of 37.5X. Examples of the fringe patterns resulting from the above experimental procedure are shown in Fig. 2.

Interpretation of Fringe Patterns

The fringe patterns, such as those shown in Fig. 2, must be interpreted into microlayer thickness profiles. The interpretation at first appears to be straightforward but is in fact not a trivial matter, and several points appear to have been overlooked by previous investigators. The basic idea can be seen by referring to Fig. 3 where we see that an incident monochromatic plane wave is reflected from the two sides of the microlayer to form rays E_2 and E_3. For a microlayer of thickness, d, and index of refraction, n, the two rays differ in phase by the optical path length, $2nd$, so that the intensity of the reflected field for unit intensites of E_2 and E_3 is given by [22]

$$I = 2 + 2\cos(2knd) \tag{1}$$

Since the thickness, d, varies with radius, the intensity also varies with radius giving rise to a fringe pattern. The maximum intensity occurs at the points $d = m\lambda/2n$, and the minimum intensity occurs at the points $d = (m + 1/2)\lambda/2n$, where the integer, m, is the fringe order which must be determined from the zero reference, $d = 0$. If the fringe order, fringe spacing, and index of refraction are known, then the thickness profile can be determined. We note that the changes in index of refraction due to temperature variation introduce an error of only a few percent when the thickness, d, is of the order of a few wavelengths of light.

Since laser light has a long coherence length (for the laser used, several centimeters), the reflections from all four surfaces in Fig. 3 can interfere to produce fringe patterns. Reflections E_2 and E_3 interfere to give the microlayer fringe patterns whereas E_1 and E_2 interfere to give the broad bands, shown in Fig. 2, due to the thickness variation of the glass. These broad bands can be considered to be optical background noise and do not present a serious problem, although they can be a nuisance. One problem which was anticipated was difficulty with fringe contrast. From the Fresnel equations for normal incidence [22] the reflected intensity as a percentage of the incident intensity was calculated to be 4 percent for E_1 and 2 percent for E_3, while E_2 (including the effect of the SnO_2 film) was measured to be 10–20 percent. Since E_3 is relatively small compared to E_1 and E_2, we would expect fringes with a small intensity variation to be superimposed on a large d-c intensity, resulting in poor fringe contrast. However, photographic film is sensitive over a relatively narrow range of intensity compared to the d-c level necessary for good exposure. Apparently the fringe intensity variation is large enough compared to the film sensitivity range to record fringes of reasonable contrast, as is evident in Fig. 2.

The reflection E_4 from the top of the bubble should interfere with E_2 to produce dynamic, concentric, circular fringes much like those from the microlayer. Hence, three questions must be addressed:

- How do we know that the circular fringes in Fig. 2 are not totally due to the top of the bubble (i.e., no microlayer)?
- If both these fringes and the microlayer fringes are present, then how can we distinguish one from the other?
- If we feel that the fringes in Fig. 2 are totally due to the microlayer, then how can we dismiss the fringes from the top of the bubble?

In order to characterize the fringes from the top of a bubble, quasi-static CO_2 bubbles in soda water were studied. These bubbles grew very slowly due to diffusion of dissolved CO_2. Two observations led us to believe that the fringes in Fig. 2 are due to the microlayer:

- The fringe spacing due to the top of the bubble decreases with increasing radial position while the opposite is true in Fig. 2.
- The fringes from the top of the bubble were observed only in a region 10–20 percent of the bubble diameter whereas those in Fig. 2 cover a much larger area.

The reason that the fringes from the top of the bubble do not appear on the data films was understood when it was observed

that considerable motion of these fringes occurred with the very slow diffusional growth of the CO_2 bubbles. The argument is similar to that used in the mathematical method of stationary phase. The difference in optical path length between E_4 and E_2 in Fig. 3 is of the order of the bubble diameter 2a. The sinusoidal interference term in (1) thus varies with the bubble growth rate. If the interference term is rapidly varying with respect to the exposure time of the film, then the fringes will cancel one another, leaving a uniform intensity on the film. Even though the exposure time is only about 13 μs, the slowest bubble growth rates observed for the data films change the optical path length by nine fringe orders in this time. Thus the fringes from the top of the bubble will not appear on the data films. However, we must be aware that these fringes could appear if, for example, the growth rate is extremely slow or if an extremely short exposure time is used.

Calibration tests were performed to determine the spatial resolution of the system as well as to check the interpretation of fringe patterns resulting from known thickness profiles. Wedges of known slope were formed with microscope cover slips on top of a glass plate. The resulting equally spaced fringes could be interpreted as slope of the wedge and the calculated values thus obtained were within a few percent of the known slope. As the wedge slope is increased, the fringes become spaced more closely so that the spatial resolution limit could be estimated. The maximum detectable slope measured in this way is 0.063, corresponding to a maximum detectable wedge angle of 3.6 deg and a minimum detectable fringe spacing of 4 μm.

A second calibration was conducted with a 20.6-mm dia steel ball sitting on a glass plate in order to check a thickness profile with curvature. The resulting concentric circular fringe pattern, known as Newton's rings, can be used to determine the diameter [23]. The diameter could be determined within 2 percent if great care was taken and within 10 percent if not done so carefully. This corresponds to determining fringe position within 1 percent and 5 percent, respectively. Thus, a thickness profile with curvature can be measured accurately to within 5 percent with the interferometric system. We note that the ball and glass plate study was also useful in clarifying the effect of focus error. Because laser light is so well collimated, the reflection from a point on a smooth surface is actually a single ray of light. Furthermore, the fringe pattern at the film plane is the result of interference between several rays with only one coming from each point of each surface in the optical path. Hence, if the distance of an object from the objective is changed, the fringe pattern is only shifted in a geometrical way, and we cannot perceive whether the optical system is "in focus." For accurate measurements the focus must be set under white light since focus cannot be determined from the fringe patterns on the film. Similarly, the usual notion of depth of field has little meaning when using laser light since the coherence length determines the distance range over which interference can take place.

As already mentioned the spatial resolution limit of the optical system represents a maximum detectable wedge slope. For the static case, we measured a fringe resolution of 4 μm; for the dynamic case, we estimate from the films that the fringe resolution is about 5 μm. This corresponds to a maximum slope of 0.0385 or a maximum wedge angle of 2.2 deg. The detectable slope is also limited by the light collection of the optics, which is related to the numerical aperture of the objective. In Fig. 3, we see that the ray E_3 must hit the objective to be imaged. If the slope of the upper surface of the microlayer is too great, then the reflected ray will not be imaged. From simple geometrical considerations, this constraint can be estimated to correspond to a maximum wedge angle of 2.9–3.8 deg for our system. The fringe resolution appears to be the limiting consideration.

The greatest limitation of the interferometric approach for microlayer measurement is that the spatial resolution of the optical system limits the maximum detectable slope. Two points must be carefully considered. First, the outer edge of the fringe patterns in Fig. 2 does not necessarily correspond to the edge of the bubble, since in Fig. 3 we can imagine that there could be a significant region of the microlayer near the edge of the bubble with slope greater than 0.0385. Thus, an outer portion of the microlayer may not be detected. Of more importance, the bubble growth rate cannot be computed from the growth rate of the fringe patterns unless it can be shown that the two rates are the same or that they can be related.

The second point to consider carries the most serious consequences and is the most difficult problem to resolve. The contact angle of the microlayer with the glass is not necessarily less than 2.2 deg. If the contact angle is greater than 2.2 deg, then some fringes cannot be resolved so that the correct fringe order is not known. Our method of interferometry relies crucially on the determination of the correct fringe order from a zero reference. A major effort of the present investigation was attempting to resolve this question of contact angle. If the contact angle is greater than 2.2 deg, then we should see the fringes becoming very closely spaced near the edge of the dry spot. In Fig. 2 the fringes do not appear to become much closer near the dry spot; rather, the spacing appears to be fairly uniform. However, the fringe contrast combined with the optical background noise makes the determination of the first fringe difficult so that the above argument is not conclusive. In order to strengthen this argument, data films of ethanol were taken with a higher power objective in order to magnify the fringes near the dry spot. A Leitz 32/0.30 objective was used with the same system, resulting in an increased magnification by a factor of 4. Films of the dry spot growing across the frame were obtained and no evidence of closer fringe spacing could be seen. Hence we believe that the fringe order is correctly determined with the present system for the data obtained.

With confidence in our interferometric system we could turn to data reduction of the films. The circular symmetry of the fringes is evident in Fig. 2 so that measurement of the diameter of the fringes was sufficient to determine the radial position. In the first several frames before the dry spot has grown much, the fringes near the center are obscured by the optical noise from the nucleation site on the surface. It is difficult to determine the correct fringe order in these frames. The fringe order can be clearly determined in a frame with a large dry spot. The fringes can then be tracked in a reasonable way to the preceding frame and so on to the first frame. The number of fringes obscured by the surface pit can thus be determined. With the fringe order and the radial position of each fringe determined, we can plot the microlayer profile for each frame. Typical results are shown in Figs. 4 and 5.

Results and Discussion

In each of Figs. 4 and 5 a series of microlayer profiles are shown. Each profile corresponds to a different instant of time as designated by the frame number which is counted from the first frame in which bubble growth is observed. The actual time from one frame to the next can be computed from the framing rate given in each figure heading; the framing rate varied by only 1/2 percent over the bubble lifetime. The thickness is given in terms of the measured fringe order, and the corresponding actual distance scale is also shown. The thickness is plotted as a function of the radius from the center of the bubble. We note that the contact angles shown are close to 1 deg.

For the conditions of a fluid at low subcooling and atmospheric pressure boiling at low heat flux, the typical bubble growth sequence is as follows. A very rapid initial growth occurs after a waiting period following the previous bubble.

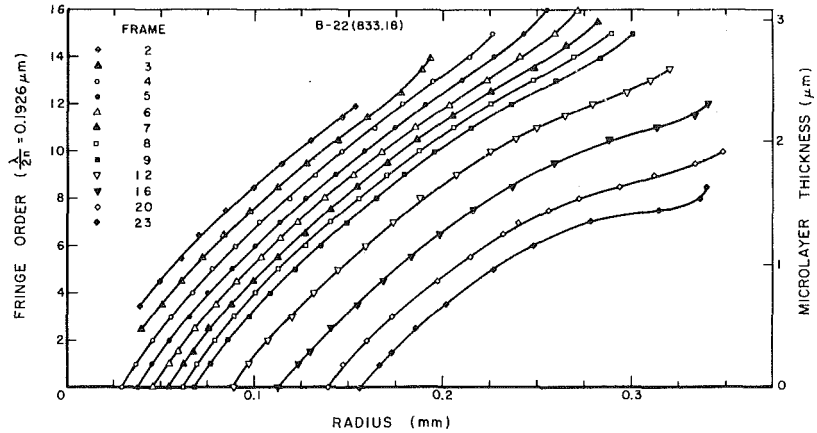

Fig. 4 Microlayer profiles for an ethanol vapor bubble at atmospheric pressure with a mean heat flux of 26.5 kW/m^2 and a subcooling of 5.7°C. The frames shown are numbered from the first frame in which the bubble appears; the framing rate is 13.99 frames/ms.

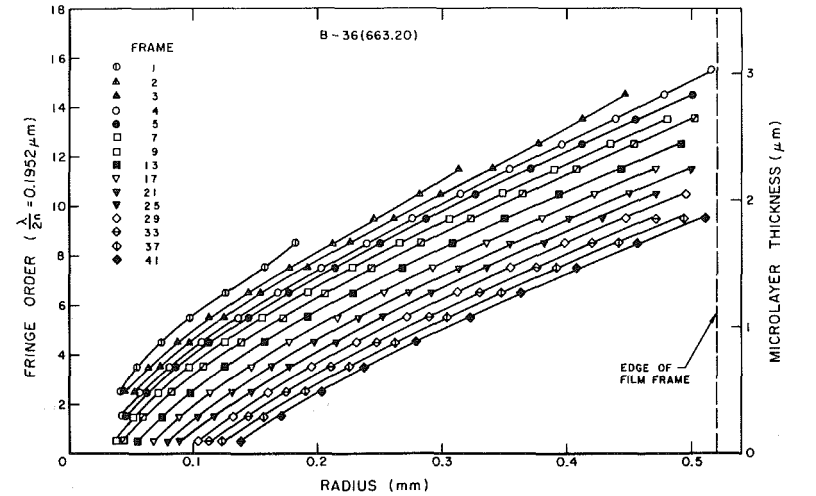

Fig. 5 Microlayer profiles for a water vapor bubble at atmospheric pressure with a mean heat flux of 204 kW/m^2 and a subcooling of 21.7°C. The frames shown are numbered from the first frame in which the bubble appears; the framing rate is 15.25 frames/ms

The rapid initial growth lasts for just a small fraction of a millisecond and a much slower growth continues. The microlayer is formed beneath the bubble during bubble growth, and evaporation of the microlayer continues throughout the bubble lifetime as evidenced by the growth of the dry spot. The dry spot grows all the way to the visible edge of the microlayer in a typical time of a few milliseconds. The dry spot then contracts (rewetting) as the bubble lifts off the surface, typically in a time of a couple of milliseconds. We note that the last profile shown in Figs. 4 and 5 is not at the end of the bubble lifetime. Only a sufficient number of profiles have been plotted to indicate the magnitude of the microlayer evaporation.

We have suggested that the microlayer profiles change with time due to evaporation of the microlayer, but the profiles could also change as a result of radial fluid motion in the microlayer. This consideration is also relevant to microlayer thickness measurement by the surface temperature technique, and Cooper and Lloyd [7] have argued that radial motion in the microlayer can be neglected. As a bubble grows at a solid surface, a boundary layer flow occurs in the region near the bubble interface due to the radial bubble growth. Once the interface has passed, a thin microlayer remains with an initial velocity profile which may be assumed to be similar to that in the boundary layer. However the microlayer is so thin that the inertia forces are negligible compared to viscous forces and, being nearly plane, the governing equation for the radial velocity may be taken to be the diffusion equation

$$\frac{\partial u}{\partial t} = \nu \frac{\partial^2 u}{\partial z^2}$$

With the boundary conditions of no-slip at the wall and zero shear stress at the interface, Cooper and Lloyd show that the radial velocity decays rapidly in a time of the order δ^2/ν, which is of the order of microseconds. Hence radial motion within the microlayer may be neglected after a very short time. For an isothermal simulation there is some experimental evidence to support this conclusion [24]. For the case of microlayer evaporation, which is not isothermal, the assumption of zero shear stress at the interface supposes that surface tension gradients are small which seems to be reasonable. Thus we assume that thickness change of the microlayer is due solely to evaporation. It should be emphasized that the interferometric technique measures thickness directly while the surface temperature technique measures surface heat flux (and hence microlayer evaporation) directly. Reasonable agreement has been obtained between the present measurement for water compared to previous measurements by the surface temperature technique. Also there is reasonable agreement between the

results of Cooper and Lloyd [7] and those of Voutsinos and Judd [10] for somewhat similar conditions. The agreement in these cases provides indirect evidence that the assumption of no radial motion is justified. While it must be admitted that no direct measurement has confirmed this assumption, the evidence to date suggests that radial motion in the microlayer may be neglected. With the assumption of no radial motion, the rate of evaporation from the microlayer can be determined from the measured thickness change in Figs. 4 and 5.

The ethanol data presented in Fig. 4 are taken from a data film which contains a total of 11 bubbles originating from the same nucleation site. The pool boiling occurred at atmospheric pressure with a mean heat flux of 26.5 kW/m^2 and a bulk fluid temperature of 72.8°C (5.7°C subcooling). The bubble growth observed in this film is very regular, with bubble nucleation frequencies of 16.6 bubbles/s which vary only ±10 percent and maximum bubble diameters (based on the edge of the fringe pattern) between 0.7 mm and 1.16 mm. The bubble lifetimes at the surface consist of 2.5–5.5 ms of microlayer evaporation with another 2–4 ms in which the dry spot contracts as the bubble lifts off the surface. The waiting period between departure of a bubble and nucleation of the next bubble is thus 50–60 ms. The microlayer formation and evaporation as shown in Fig. 4 is very reproducible for the bubbles on this data film. The initial microlayer profile is wedgelike with a thickness of 3 μm at a radius of 0.25 mm. We note that Jawurek's [9] measurements for ethanol were an order of magnitude lower than the present measurement. Although the conditions were different in the two experiments, this order of magnitude difference is an indication that Jawurek may not have determined the correct fringe order. Our thickness measurements are similar to those of Voutsinos and Judd [10] and Cooper and Lloyd [7], although the fluids and conditions are different. A very striking feature of the results in Fig. 4 is that the evaporation rate from the microlayer appears to be fairly uniform, giving similar profiles as evaporation proceeds. Actually the evaporation rate is greater near the contact point by 15–30 percent compared to the outer edge of the microlayer. The approximate thickness evaporation rate is initially 2.2 μm/ms and decreases to 1.25 μm/ms after about 1.4 ms. These evaporation rates correspond to heat fluxes of 1385 kW/m^2 and 787 kW/m^2, respectively. Although extremely large, these heat fluxes occur only over short periods of time and over a small area, and the overall effect of microlayer evaporation may or may not be significant depending on the bubble nucleation frequency and the nucleation site number density.

The data for water presented in Fig. 5 are taken from a data film which contains a total of nine bubbles originating from the same site. The pool boiling occurred at atmospheric pressure with a mean heat flux of 204 kW/m^2 and a bulk fluid temperature of 78.3°C (21.7°C subcooling). The bubble nucleation is intermittent with times between bubbles as short as 34 ms and as long as 200 ms; the data presented are for a bubble which occurred 72 ms after the preceding bubble. The bubble fringe patterns grew beyond the field of view of the camera frame and the edge of the film frame is noted on Fig. 5. The microlayer evaporation lasted for 3.8 ms. The initial microlayer profile for water is wedgelike with a thickness of 1.85 μm at a radius of 0.25 mm. We have noted previously that a discrepancy exists in the literature regarding the order of magnitude of the microlayer thickness for water. Our data resolve this discrepancy and indicate that the data obtained by the surface temperature approach are correct. The data of Sharp [8] are possibly in error due to incorrect determination of fringe order. The approximate thickness evaporation rate for water is initially 1.04 μm/ms and decreases to 0.35 μm/ms after about 2 ms. These evaporation rates correspond to heat fluxes of 2256 kW/m^2 and 757 kW/m^2, respectively.

We have noted that the growth rate of the edge of the fringe pattern may not be the same as the growth rate of the bubble. We were not able to obtain simultaneous movies of the fringe patterns and the bubble growth for comparison. However, immediately after the interference data film was taken, the camera was reloaded and a movie of the same nucleation site was taken with white light from above so that a silhouette of the bubble edge is obtained. The growth is very rapid so that the edge appears in only two or three frames but the growth rate can be estimated. The results indicate that the growth rate of the edge of the fringe pattern is lower than the bubble growth rate by 15–35 percent. The microlayer formation equation of Cooper and Lloyd [7], $\delta = C(\nu t_g)^{1/2}$, can be checked against our data. Based on the growth rate of the edge of the fringe pattern, we estimate that C is in the range 0.3–0.4; if these growth rates are corrected by 15–35 percent then C is in the range 0.33–0.5. Our estimate of C is significantly lower than the value of 0.8 suggested by Cooper and Lloyd.

Implications Concerning Mechanisms

We have discussed the mechanisms of microconvection and microlayer evaporation (latent heat transport). For the case of low subcooling, microlayer evaporation has been shown to be significant [11, 12]. For the case of high subcooling it has generally been thought that microlayer evaporation would be of more importance [13–18]. Contrary to this expectation, Plesset and Prosperetti [19] recently concluded that the contribution of microlayer evaporation as a heat transfer mechanism is relatively small for the highly subcooled water data of Gunther and Kreith [2]. With the assumption of no radial motion, they modeled the microlayer evaporation as a one-dimensional moving boundary heat diffusion problem. The evaporative mass flux is determined by an expression from kinetic theory and depends upon the interfacial temperature and the bubble internal pressure [4, 25]. The bubble internal pressure is calculated from the bubble growth measurements of Gunther and Kreith. The only unknown was the initial microlayer thickness, δ, which was treated as a parameter so that the contribution of microlayer evaporation was plotted as a function of δ. These plots show that the contribution of microlayer evaporation is very sensitive to the assumed initial microlayer thickness with strong peaks occurring around $\delta = 2$–4 μm. Plesset and Prosperetti assumed that the initial microlayer thickness was given by $\delta = (\nu t_g)^{1/2}$ which corresponds to $\delta = 6$–9 μm, and hence they concluded that microlayer evaporation could account for only 10–20 percent of the heat transfer. The growth times for the water bubbles in the present study are similar to those of Gunther and Kreith. Hence, if we assume that the proportionality $\delta \propto C(\nu t_g)^{1/2}$ correctly describes microlayer formation, then we might assume that our measured microlayer thickness would be a reasonable estimate for the Gunther and Kreith data. Our data lies close to the values of initial microlayer thickness where the peaks occur in the plots of Plesset and Prosperetti. Hence the contribution of microlayer evaporation may be of more significance than they concluded.

Alternatively, we can use our measurements to estimate directly an upper bound on the contribution of microlayer evaporation for the Gunther and Kreith data. We assume that our measured microlayer profiles for water may be applied to the Gunther and Kreith data based upon the similar bubble growth rates. The latent heat required to evaporate the total mass of the microlayer represents an upper bound on the energy which can be extracted from the microlayer. Hence, for the same bubbles considered by Plesset and Prosperetti, we find that microlayer evaporation can account for a maximum of about 50 percent of the total energy per bubble. Thus, while microlayer evaporation may be significant, we

conclude that microlayer evaporation alone cannot account for the increased heat transfer rates observed in highly subcooled nucleate boiling. It appears that microconvection must play at least an equal role.

Conclusions

A technique has been developed for measurement of microlayer thickness profiles beneath small, short-lived bubbles. The technique uses laser interferometry combined with high-speed cinematography. The difficulties encountered in interpretation of the fringe patterns are discussed in detail. The problems considered are fringe contrast and optical background noise, spurious interference patterns such as from the top of the bubble, spatial resolution of the fringes and the subsequent maximum detectable slope, and the need for a zero reference for determination of the correct fringe order. For the interferometric system reported here, these problems have been satisfactorily resolved.

The results of the experimental measurements for water and ethanol are given by graphs of the time histories of the microlayer profiles. The initial microlayer thickness for water is wedgelike with a thickness of 1.85 μm at a radius of 0.25 mm; the thickness for ethanol is approximately 1.6 times that for water. If the radial motion in the microlayer is assumed to be negligible, as is generally accepted, then the measured thickness change with time is due solely to evaporation. In this case the corresponding evaporation rates of the microlayer require heat fluxes of the order of 1000 kW/m^2 for both water and ethanol.

If, based upon similar bubble growth rates, our measurement of microlayer thickness may be used for the highly subcooled data of Gunther and Kreith, then we can conclude that microlayer evaporation can account for no more than 50 percent of the heat transfer rate for this data.

Acknowledgments

The study was supported by the National Science Foundation under Grant No. ENG 75-22676.

References

1 Jakob, M., *Heat Transfer*, Vol. 1, John Wiley and Sons, New York, 1949, pp. 633–634.

2 Gunther, F. C., and Kreith, F., "Photographic Study of Bubble Formation in Heat Transfer to Subcooled Water," Jet Propulsion Laboratory, Progress Report No. 4-120, Mar. 1950.

3 Snyder, N. W., and Edwards, D. K., "Summary of Conference of Bubble Dynamics and Boiling Heat Transfer Held at the Jet Propulsion Laboratory," JPL Memo No. 20-137, 1956.

4 Plesset, M. S., "Note on the Flow of Vapor Between Liquid Surfaces," *Journal of Chemical Physics*, Vol. 20, No. 5, May 1952, pp. 790–793.

5 Moore, F. D., and Mesler, R. B., "The Measurement of Rapid Surface Temperature Fluctuations During Nucleate Boiling of Water," *AIChE Journal*, Vol. 7, No. 4, Dec. 1961, pp. 620–624.

6 Hendricks, R. C., and Sharp, R. R., "Initiation of Cooling due to Bubble Growth on a Heating Surface," NASA TN D-2290, 1964.

7 Cooper, M. G., and Lloyd, A. J. P., "The Microlayer in Nucleate Pool Boiling," *International Journal of Heat and Mass Transfer*, Vol. 12, 1969, pp. 895–913.

8 Sharp, R. R., "The Nature of Liquid Film Evaporation During Nucleate Boiling," NASA TN D-1997, 1964.

9 Jawurek, H. H., "Simultaneous Determination of Microlayer Geometry and Bubble Growth in Nucleate Boiling," *International Journal of Heat and Mass Transfer*, Vol. 12, 1969, pp. 843–848.

10 Voutsinos, C. M., and Judd, R. L., "Laser Interferometric Investigation of the Microlayer Evaporation Phenomenon," ASME JOURNAL OF HEAT TRANSFER, Vol. 97, No. 1, Feb. 1975, pp. 88–92.

11 Judd, R. L., and Hwang, K. S., "A Comprehensive Model for Nucleate Pool Boiling Heat Transfer Including Microlayer Evaporation," ASME JOURNAL OF HEAT TRANSFER, Vol. 98, No. 4, Nov. 1976, pp. 623–629.

12 Fath, H. S., and Judd, R. L., "Influence of System Pressure on Microlayer Evaporation Heat Transfer," ASME JOURNAL OF HEAT TRANSFER, Vol. 100, No. 1, Feb. 1978, pp. 49–55.

13 Bankoff, S. G., and Mikesell, R. D., "Bubble Growth Rates in Highly Subcooled Nucleate Boiling," *Chemical Engineering Progress Symposium Series*, Vol. 55, No. 29, 1959, pp. 95–102.

14 Bankoff, S. G., and Mason, J. P., "Heat Transfer From the Surface of a Steam Bubble in a Turbulent Subcooled Liquid Stream, *AIChE Journal*, Vol. 8, No. 1, Mar. 1962, pp. 30–33.

15 Bankoff, S. G., "A Note on Latent Heat Transport in Nucleate Boiling," *AIChE Journal*, Vol. 8, No. 1, Mar. 1962, pp. 63–65.

16 Snyder, N. W., and Robin, T. T., "Mass Transfer Model in Subcooled Nucleate Boiling," JOURNAL OF HEAT TRANSFER, Vol. 91, No. 3, Aug. 1969, pp. 404–412.

17 Robin, T. T., and Snyder, N. W., "Theoretical Analysis of Bubble Dynamics for an Artificially Produced Vapor Bubble in a Turbulent Stream," *International Journal of Heat and Mass Transfer*, Vol. 13, 1970, pp. 523–536.

18 Robin, T. T., and Snyder, N. W., "Bubble Dynamics in Subcooled Nucleate Boiling Based on the Mass Transfer Mechanism," *International Journal of Heat and Mass Transfer*, Vol. 13, 1970, pp. 305–318.

19 Plesset, M. S., and Prosperetti, A., "The Contribution of Latent Heat Transport in Subcooled Nucleate Boiling," *International Journal of Heat and Mass Transfer*, Vol. 21, 1978, pp. 725–734.

20 Tarnopol, M. S., "Treatment of Films with Liquid," U.S. Patent No. 2, 606, 566, 1952.

21 Koffman, L. D., "Experimental Observations of the Microlayer in Vapor Bubble Growth on a Heated Solid," Ph.D thesis, pt. 1., California Institute of Technology, 1979, 74 pages.

22 Hecht, E., and Zajac, A., *Optics*, Addison-Wesley, Reading, Mass., 1974, pp. 278 and 74.

23 Palmer, C. H., *Optics: Experiments and Demonstrations*, The Johns Hopkins University Press, 1962.

24 Katto, Y., and Shoji, M., "Principal Mechanism of Micro-Liquid-Layer Formation on a Solid Surface with a Growing Bubble in Nucleate Boiling," *International Journal of Heat and Mass Transfer*, Vol. 13, 1970, pp. 1299–1311.

25 Plesset, M. S., and Prosperetti, A., "Flow of Vapor in a Liquid Enclosure," *Journal of Fluid Mechanics*, Vol. 78, pt. 3, 1977, pp. 433–444.

I. Tanasawa
Professor,
Institute of Industrial Science,
University of Tokyo,
Minato-ku, Tokyo,
Japan 106
Mem. ASME

Y. Utaka
Assistant,
Department of Mechanical Engineering,
Tokyo Institute of Technology,
Meguro-ku, Tokyo,
Japan 152

Measurement of Condensation Curves for Dropwise Condensation of Steam at Atmospheric Pressure

Condensation curves for dropwise condensation of steam at atmospheric pressure were measured for the range of surface subcooling between 0.5 and 180 K using a heat transfer block having a concave spherical condensing surface. The heat transfer coefficient remained constant with the increase of surface subcooling up to about 10 K, and then it decreased. The maximum heat fluxes were found to be between 9.3 and 12.2 MW/m^2. Dropwise condensation could be observed at a surface subcooling larger than the one corresponding to the peak heat flux, but shortly the mode of condensation shifted to pseudo-film or on-ice condensation.

Introduction

The object of this study is to observe the possible change of the mode of dropwise condensation of steam which may occur when the degree of surface subcooling (i.e., the difference between the saturation temperature of vapor and the temperature of condensing surface) of a hydrophobic surface is increased.

In the case of boiling it has been well known that the mode of heat transfer undergoes successive changes from convection to nucleate boiling, then to transition boiling, and finally to film boiling, along with the increase of surface superheat. The heat flux also varies with the degree of superheat. The curve which indicates such a change of heat flux with the surface superheat is called the boiling curve and was first measured by Nukiyama [1].

In dropwise condensation, a similar curve, which is to be called the "condensation curve," must be obtained. However, no measurement on the condensation curve was made until recently, for it is difficult to attain large surface subcooling by the usual means because of the very high heat transfer rate.

The first measurement of condensation curve for water vapor was carried out by Takeyama and Shimizu [2]. For organic vapors (aniline, ethanediol, and nitrobenzene), a report was published by Wilmshurst and Rose [3]. Takeyama and Shimizu [2] devised a heat transfer block of the shape of a truncated cone and observed the change of the mode of condensation. According to their observation, the heat flux first increased with the increase of surface subcooling and reached a maximum. Further increase of subcooling brought about a transition from the dropwise mode to pseudo-film mode, and finally an ice layer was formed on the surface. But as Ochiai et al. [4] have pointed out, the accuracy of their measurement is in doubt.

In the present study, a great deal of care has been taken in the method of measurement to ensure sufficient accuracy. The condensation curves of steam at atmospheric pressure have been obtained taking as the parameter the mean final maximum drop diameter, which is the most significant factor affecting the heat transfer by dropwise condensation.

Apparatuses and Method of Experiment

The heat transfer block designed to ensure sufficient accuracy of measurement and to attain large surface subcooling is shown in Fig. 1. It is a copper block of the shape of a right cone with 90 deg vertical angle truncated by two concentric spherical surfaces, the inner surface being the condensing surface and the outer surface being the cooling surface. The ratio of the areas of these two surfaces is $(60.0/4.52)^2 = 176$. To insert thermocouple wires, this block was first split into two. Constantan wires of 80-μm dia for the thermoelectric thermometry were embedded in four concentric square grooves of 0.5 mm depth machined on the sectional plane of one of the half-split blocks. The tip of the each constantan wire was soldered to the bottom of the groove just at the middle to form a thermocouple junction. Before these two half-split blocks were put together, the location of each thermocouple junction was accurately measured with a traveling microscope.

The heat flux and the temperature of the condensing surface were obtained by extrapolating the four temperatures in the block to the surface, assuming one-dimensional, steady heat conduction inside a sphere, i.e., assuming the temperature to be inversely proportional to r, where r is the radial distance from the virtual apex of the cone. Since the thermocouple wires were placed in the concentric grooves which coincided with the isothermal lines, the error due to heat conduction through the wires was minimized. In addition, since the degree of sphericity of the condensing surface was fairly well achieved (deviation being within ± 1 percent), the assumption of one-dimensional conduction was considered to be well established.

To eliminate the dividing line, a thin layer of copper approximately 10-μm thick was electroplated onto the vapor-side surface.

Before every measurement, the condensing surface was polished with fine alumina powder and then oleic acid was applied as the dropwise condensation promoter.

The heat transfer block was fitted to an insulator block made of bakelite and then settled in the condensing chamber as shown in Fig. 2.

The steam from a boiler was forced to flow closely along the concave, spherical, condensing surface. This was for two reasons: first, to remove noncondensable gas; second, to

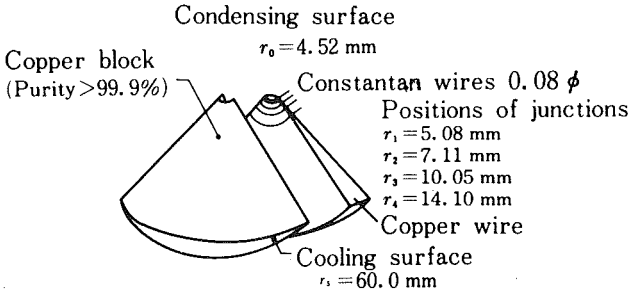

Fig. 1 Heat transfer block and location of thermocouples

Contributed by the Heat Transfer Division for publication in the JOURNAL OF HEAT TRANSFER. Manuscript received by the Heat Transfer Division June 21, 1982.

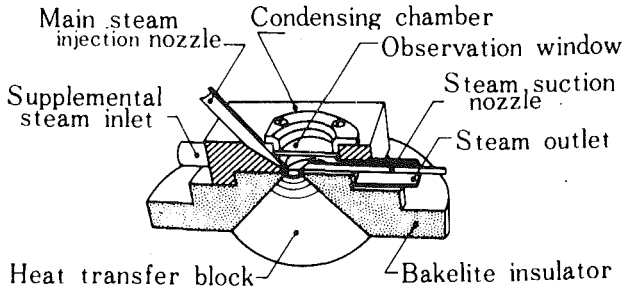

Fig. 2 Condensing chamber

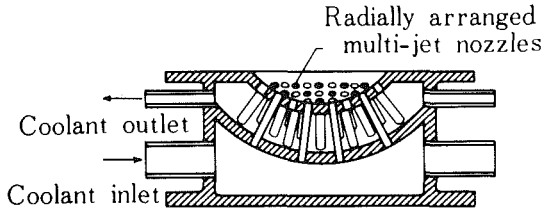

Fig. 3 Cooling chamber (for water and alcohol)

make the maximum drop size small enough to reduce the effect of radius of curvature of the condensing surface. A certain device was needed to cause the steam to flow closely along the concave surface having a large radius of curvature. For this purpose the steam was introduced into the condensing chamber from an inlet nozzle with a flat section, tangentially to the upper stream edge of the condensing surface. In addition, in order to prevent possible decrease of the steam velocity downstream, the steam was sucked off with another nozzle at the outlet. Furthermore, the excess steam was supplied to the chamber from another supplemental inlet nozzle so that the chamber might be always filled with the sufficient amount of steam.

The outlet-to-inlet steam velocity ratio was determined by hot-wire anemometry so that the mean inlet velocity might coincide with the velocity at the center of the condensing surface. Probes made of thin platinum wires with diameters 5 and 20 μm were prepared, and the mean velocities at the inlet and outlet and the local velocity at a distance 0.4 mm above the center of the condensing surface were measured. Detailed description on the determination of the appropriate relationship between these velocities will not be presented here.

Water, alcohol-dry ice mixture, and liquefied nitrogen were used as coolants. The cooling chamber used for water and alcohol-dry ice mixture is shown in Fig. 3. The cooling surface of the condensing block was placed on the upper spherical wall. The coolant passed through multijet nozzles, impinged upon the cooling surface, and returned to the space between two spherical walls. Care was taken so that the surface could be cooled uniformly.

Water was used for the measurement in the low heat flux region (0.58 ~ 4.65 MW/m^2). The heat flux was adjusted by controlling the water temperature in the reservoir. At a higher heat flux (7.3 MW/m^2), ethyl alcohol was used as the coolant. Its temperaure was lowered by adding pieces of dry ice into it.

To obtain much higher surface subcooling, nucleate boiling of liquefied nitrogen on the cooling surface was utilized. The schematic diagram of the apparatus is shown in Fig. 4. Liquefied nitrogen was supplied to the cooling chamber from a Dewar bottle by means of a pressurizing pump. The level of liquid nitrogen in the cooling chamber was regulated with a float-magnetic valve system. Silicone resin containing a filler was applied uniformly to the cooling surface to give an appropriate thermal resistance. Since the fine adjustment of heat flux was difficult with such a method of cooling, only one

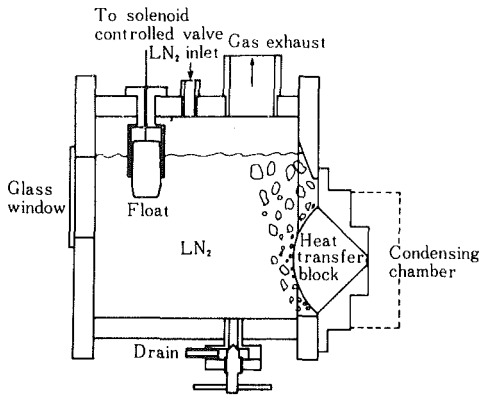

Fig. 4 Cooling chamber (for liquefied nitrogen)

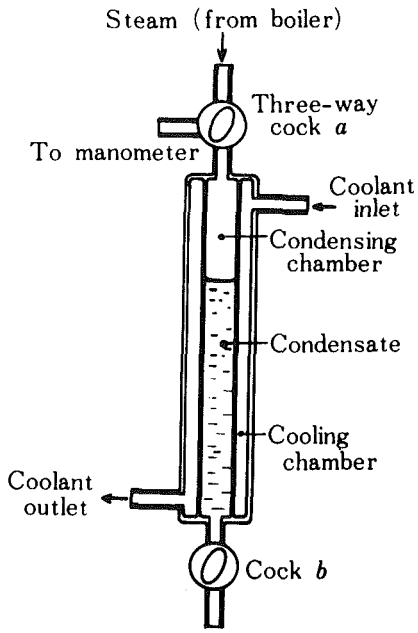

Fig. 5 Apparatus for measuring the amount of noncondensable gas

thickness of the silicone layer was chosen for the steady measurement. Data were obtained within the range of heat flux between 8.7 and 10.2 MW/m^2.

At much higher degree of subcooling, measurement in steady state was almost impossible because of the unstable nature of the heat transfer (that is, the heat flux decreased inspite of increase in the surface subcooling). In such an occasion, a quasi-steady measurement was made in which the temperatures of the condensing surface and those inside the block were varied very slowly by attaching a spherical shell made of a thermally resistant material to the cooling surface. The procedure was as follows: dropwise condensation was first started by exposing the cooling surface to the room air, and then the cooling chamber was rapidly filled with the liquid nitrogen. All the emf's from thermocouples were recorded with a pen-recorder. Very slow but continuous variations of the heat flux and the subcooling were obtained. The one-dimensional temperature distribution was examined during every measurement.

Noncondensable gas has significant effect in condensation heat transfer. The effect is especially remarkable when the rate of condensation is large as is the case with the present experiment. To make clear the effect of noncondensable gas quantitatively, an apparatus as shown in Fig. 5 was made to measure the amount of noncondensable gas contained in the steam.

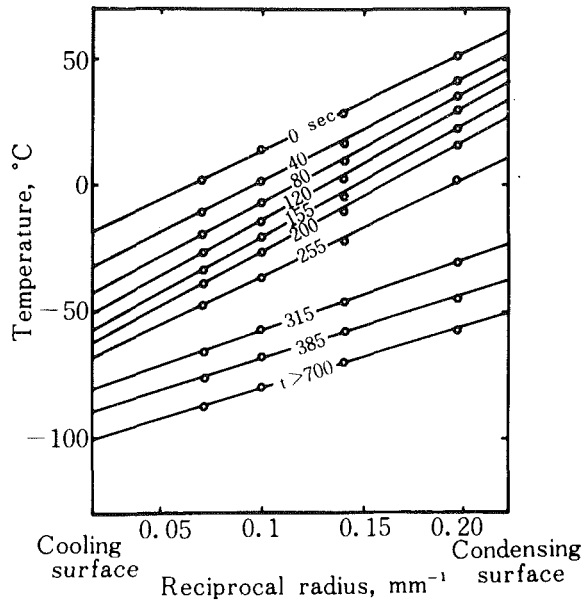

Fig. 6 Quasi-steady temperature distribution inside the heat transfer block

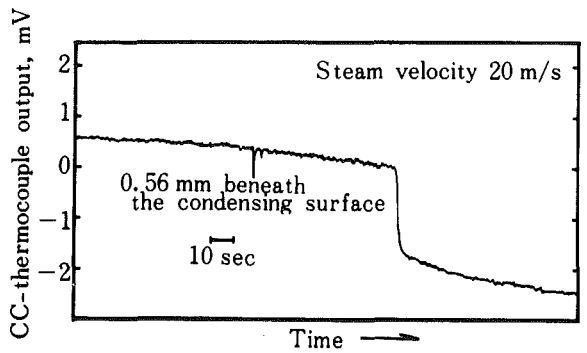

Fig. 7 Timewise change of output from surface thermocouple

The apparatus, which was made of glass, was an annular cylinder; the inner cylinder being the condensing chamber for steam-gas mixture and the outer annular space being the passage of cooling water. The steam which might contain a small fraction of noncondensable gas was supplied to the inner cylinder and was cooled. The condensate and the noncondensable gas were accumulated in the chamber. The concentration of noncondensable gas was obtained by measuring the amount of condensate and the pressure and temperature in the chamber.

Furthermore, the heat transfer measurement was made by injecting an additional amount of nitrogen gas into the steam. Dependence of the heat transfer rate upon the noncondensable gas content was obtained.

Results

Temperature Distribution Inside the Heat Transfer Block. The accuracy of the present experiment is largely dependent upon whether or not the steady, one-dimensional distribution of temperature is precisely established inside the block both in the case of steady measurement and in the quasi-steady measurement. An example of temperature distribution for the quasi-steady measurement is shown in Fig. 6. Figures written in Fig. 6 represent the elapsed times. The temperature hardly changed after 700 s. It is seen that the temperatures plotted against the reciprocal radius show very good linearity, indicating that, even in the quasi-steady experiment, almost steady temperature distribution was established at every instant due to the relatively slow change in the temperature.

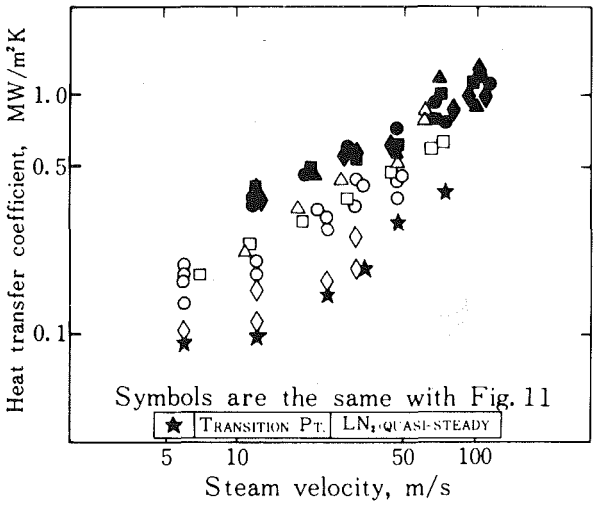

Fig. 8 Dependence of heat transfer coefficient on steam velocity

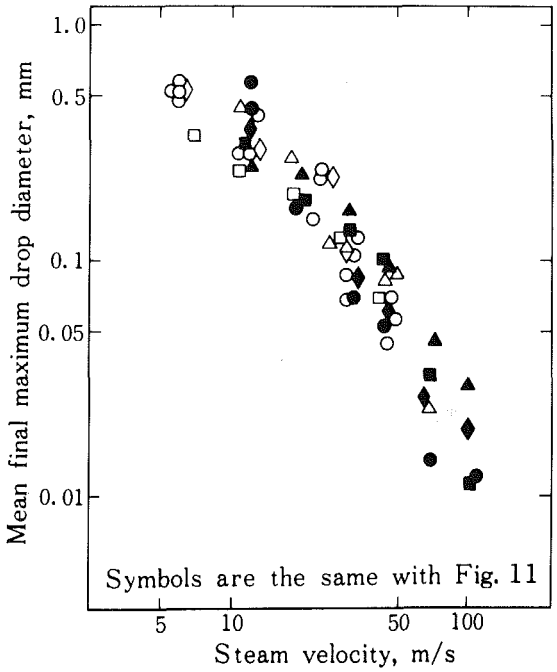

Fig. 9 Dependence of mean final maximum drop diameter on steam velocity

Shown in Fig. 7 is an example of the record of timewise change of emf from the thermocouple located nearest to (0.56 mm beneath) the surface. The temperature decreases gradually for the first period, and then suddenly falls as the result of the transition from dropwise to pseudo-film or on-ice condensation which will be mentioned later.

Effect of Steam Velocity. The heat transfer coefficient and the mean final maximum drop diameter are plotted against the steam velocity in Figs. 8 and 9, respectively. Here the steam velocity means the mean velocity at the inlet nozzle. The heat flux is taken as the parameter. The mean final maximum drop diameter, which is determined by taking 16-mm cinefilms, is the mean diameter of the group of maximum drops residing at the central part of the surface just before being absorbed by a departing drop. In the case when more than two groups of maximum drops belonging to different generations can be distinguished between the residing drops,

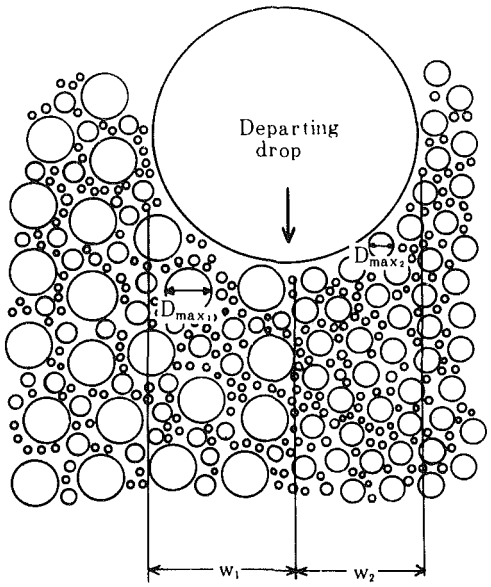

Fig. 10 Way of calculating mean final maximum drop diameter

the mean final maximum diameter is calculated as an average weighted by the width of previously swept area corresponding to the each group (see Fig. 10).

When water or alcohol-dry ice mixture was used as the coolant, the steady experiment was carried out keeping the heat flux constant. The values of heat fluxes were 0.59, 1.13, 2.4, and 4.7 MW/m^2 in the case of water, and 7.3 MW/m^2 in the case of alcohol-dry ice mixture. The steady-state experiment using liquefied nitrogen was performed in the range of heat flux between 8.7 and 10.2 MW/m^2. Data in the higher heat flux region were obtained by the quasi-steady measurement.

Figure 8 shows that, when the heat flux exceeds a certain value, the heat transfer coefficient decreases more rapidly with the decrease of the steam velocity as the heat flux becomes higher. On the other hand, the maximum drop diameter is almost independent of the heat flux, as is seen in Fig. 9.

Effect of Maximum Drop Diameter. Figures 8 and 9 can be redrawn to show the dependence of heat transfer coefficient upon the mean final maximum drop diameter, as shown in Fig. 11. A similar result has been obtained by taking as the abscissa the departing drop diameter, which is defined as the diameter of the drop just before it starts to depart. It can be measured on cinefilms by the method described elsewhere [5]. However, the results on the departing drop diameter are ommitted in this paper because of the limited space. In the figure ΔT and q_{max} denote the degree of surface subcooling and the maximum heat flux, respectively. It is found that, in the range of heat flux between 0.59 and 4.7 MW/m^2, the heat transfer coefficient varies linearly (on logarithmic paper) with the drop size. An expression as follows is obtained by the least squares' calculation

$$h = 0.293 \bar{D}_{max}{}^{-0.290} \quad (1)$$

where h is the heat transfer coefficient in MW/(m^{2}K), $\bar{D}_{max}$ is the mean final maximum drop diameter in mm, respectively.

The dependence of heat transfer coefficient upon the characteristic drop diameter [equation (1)] is quite similar to the one obtained previously by the authors [5] at a heat flux of about 0.6 MW/m^2. At larger heat fluxes, the heat transfer coefficient becomes lower than the one expressed by equation

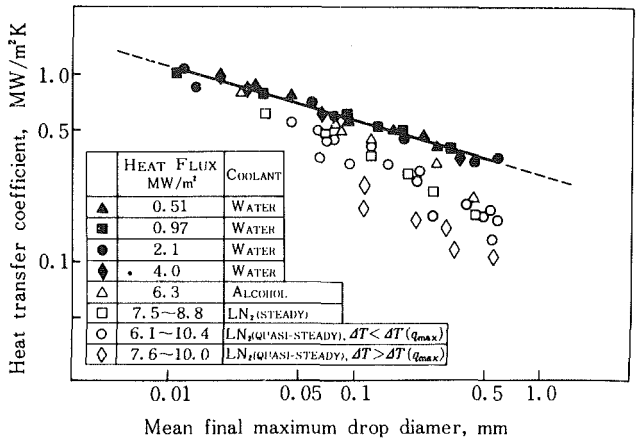

Fig. 11 Dependence of heat transfer coefficient on mean final maximum drop diameter

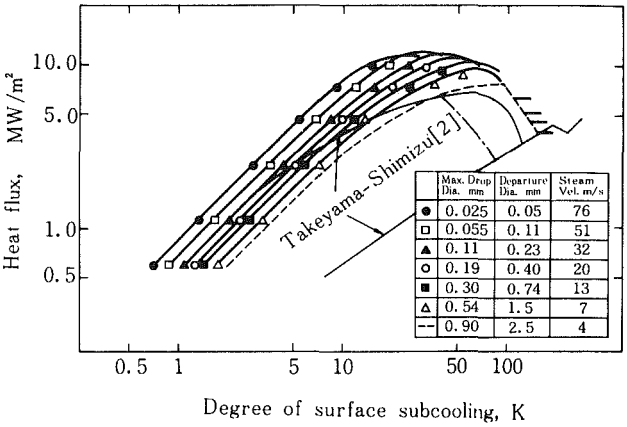

Fig. 12 Dependence of heat flux on surface subcooling (condensation curves)

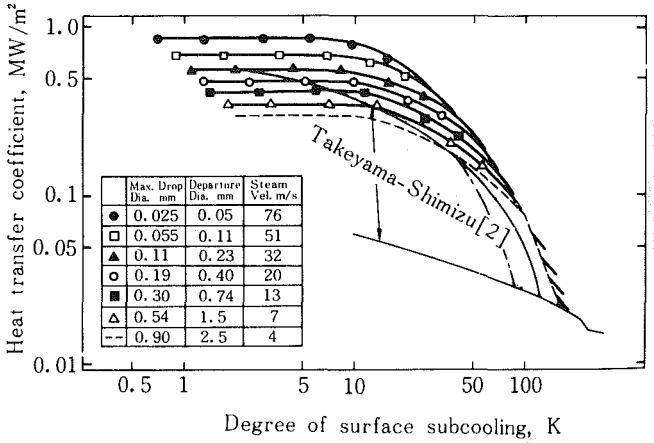

Fig. 13 Dependence of heat transfer coefficient on surface subcooling

(1). The tendency is more remarkable when the drop size is larger.

Effect of Surface Subcooling (Condensation Curves). Figure 12 shows the condensation curves. The change of heat flux against the surface subcooling is shown on a logarithmic graph by taking the mean final maximum drop diameter as the parameter. The numerical values of the parameters are listed in the table in the figure. As the maximum drop diameter becomes smaller, the condensation curve moves to the left. Just similar to the boiling curve, a peak value exists for every one of the curves. The value ranges between 9.3 and 12.2 MW/m^2. For every condensation curve, the original data

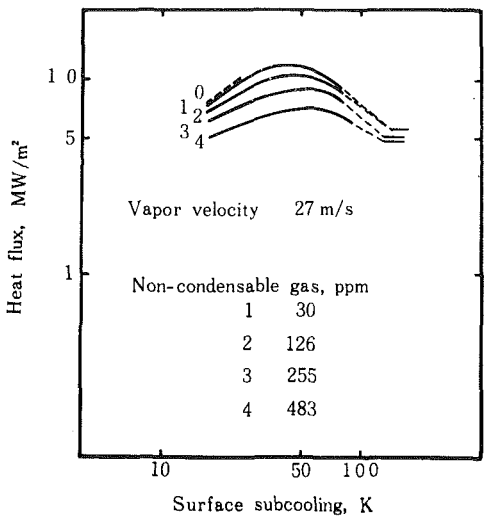

Fig. 14 Effect of noncondensable gas on heat flux – surface subcooling relationship

up to about 9.3 MW/m^2 were obtained by steady measurement. The plotted symbols in Fig. 12 are the secondary data derived from the original by the procedure as follows: In the first place, the data by water cooled and alcohol-dry ice cooled measurements ($q \leqq 4.7$ MW/m^2) were obtained under constant heat flux condition. Since the dependence of the heat transfer coefficient upon the mean final maximum drop diameter for these cases had been obtained as a solid line in Fig. 11 or as equation (1), the relationship between q and ΔT was derived from it. In the case of $q = 7.3$ MW/m^2 and alcohol cooling, equation (1) does no longer hold, as is obvious from Fig. 11. In this case, the dependence of h upon $\bar{D}_{max}$ was obtained using the higher-order, least-squares method (though the fitted curve is not drawn in Fig. 11). The relationship between h and ΔT could be obtained as in the case of $q \leqq 4.7$ MW/m^2. In the steady measurement using liquid nitrogen as the coolant, the data were obtained under the condition of constant thermal resistance, because of the difficulty in obtaining data at constant q. In this case, the $q - \Delta T$ relationship was obtained from the $\bar{D}_{max} - \Delta T$ relationship (which is not shown in the figure) derived from the data. The quasi-steady measurement using liquid nitrogen was carried out for the heat flux exceeding 7 MW/m^2. A continuous $q - \Delta T$ relation was obtained for a single measurement. The solid lines in Fig. 12 are drawn by connecting the data obtained by the steady measurement with the results from the quasi-steady measurement. Thus, no data points are seen in the figures where the heat flux exceeds 7 MW/m^2. Obviously the lines are smoothly connected where the heat fluxes of the both experiments overlap.

As mentioned, the condensation curves in Fig. 12 are obtained by taking the mean final maximum diameter $\bar{D}_{max}$ as the parameter. The same result can be obtained if we choose the departing drop diameter D_f or the steam velocity v as the parameter, because there is roughly one-to-one correspondence between these quantities, as is seen in Fig. 9. The corresponding values of the other two parameters are listed in the table in Fig. 12.

Four, short horizontal lines are seen in Fig. 12 where $\Delta T \geqq 100$ K. These correspond to on-ice condensation (which will be mentioned later) at vapor velocities 7, 13, 20, and 32 m/s (from the lowest upward). When the steam velocity was higher, pseudo-film condensation (which will also be mentioned later) was observed just before on-ice condensation began. The data are not shown here.

Figure 12 can be redrawn to the heat transfer coefficient

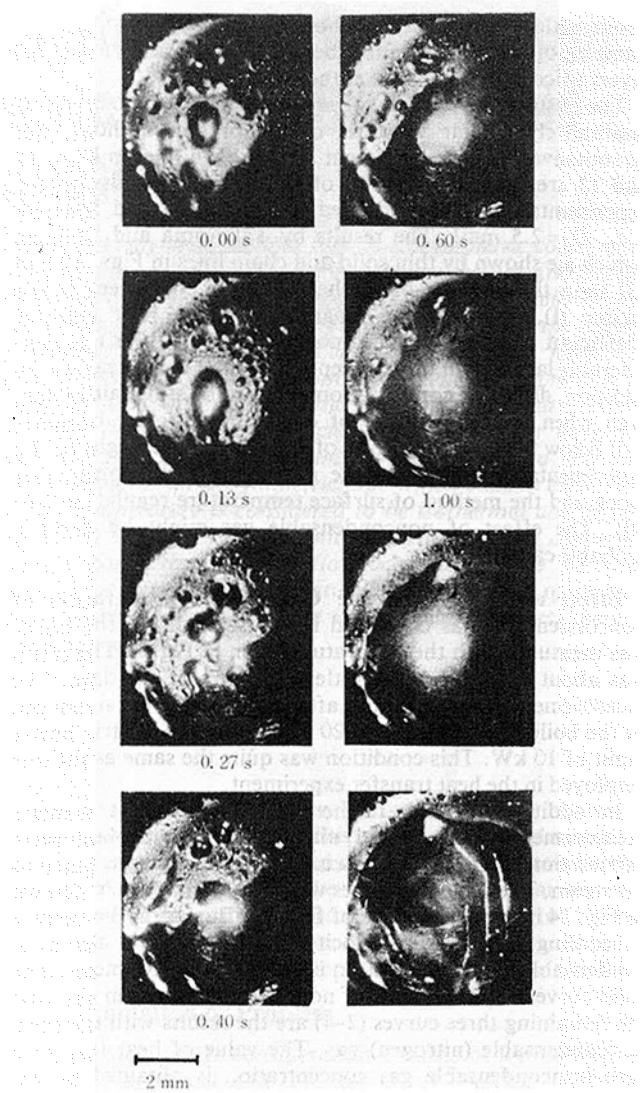

Fig. 15 Transition of mode of condensation

versus surface subcooling relationship as shown in Fig. 13. The heat transfer coefficient in the region of relatively small surface subcooling lies between 350 and 800 kW/(m^{2}K).

From Figs. 12 and 13, the condensation curves in the region of dropwise condensation mode might be divided into the following three regimes. First, the regime (I) where the heat transfer coefficient remains constant (i.e., the heat flux is proportional to the surface subcooling) and is expressed by equation (1). Second, the regime (II) where the heat transfer coefficient decreases but the heat flux still increases (up to the peak flux) with the increase of surface subcooling. Finally, the regime (III) where both the heat transfer coefficient and the heat flux decrease. After the regime (III), the mode of condensation shifts to pseudo-film or on-ice condensation.

Here, pseudo-film condensation indicates a state of apparent film condensation in which the condensing surface, which is essentially nonwettable, is flooded with the condensate, as the result of extremely large rate of condensation. The essential difference between genuine filmwise and pseudo-film condensation has been mentioned elsewhere [6] and will not be repeated here.

On-ice condensation is also a kind of film condensation. When the temperature of condensing surface is well below the freezing point of the condensate, an ice layer is formed on the surface and the vapor condenses onto it as a film. Takeyama and Shimizu [2] referred to this phenomenon as glacial

condensation. The present authors would like to propose the name of on-ice condensation because there are formed two layers of ice and condensate at the same time.

The result obtained by Takeyama and Shimizu [2] is qualitatively similar to those of the present authors, but quantitatively they are different. The broken lines in Figs. 12 and 13 are the extrapolation of the authors' results to the experimental condition adopted by Takeyama and Shimizu (i.e., $D_f = 2.5$ mm). The results by Takeyama and Shimizu (which are shown by thin solid and chain lines in Figs. 12 and 13) show the decrease of the heat transfer coefficient in the regime (I), and that the magnitude of the heat transfer coefficient at small surface subcooling ($\Delta T \leqq 10$ K) is considerably larger than those accepted by many investigators. In addition, dropwise condensation seems to be still maintained, even when the temperature of condensing surface becomes well below 0°C. A main cause of such difference might be the experimental error due to the geometry of the condensing block and the method of surface temperature regulation (see [4]). The effect of noncondensable gas might be another probable cause.

Effect of Noncondensable Gas. The concentration of noncondensable gas contained in the steam from the boiler was measured with the apparatus shown in Fig. 5. The result was about 30 p.p.m. with little dispersion of the data. The measurement was carried out after blowing off the steam out of the boiler for about 15 to 20 min under the electric heater input of 10 kW. This condition was quite the same as the one employed in the heat transfer experiment.

In addition to this, further quasi-steady heat transfer measurements using liquid nitrogen as the coolant were carried out by adding a known amount of nitrogen gas into the steam. The steam velocities were 5, 13, and 27 m/s. Shown in Fig. 14 is the dependence of the heat flux upon the surface subcooling. The steam velocity is 27 m/s, and the noncondensable gas concentration is taken as the parameter. The solid curve 1 is for the case of no additional nitrogen gas, and the remaining three curves (2–4) are the results with the extra noncondensable (nitrogen) gas. The value of heat flux with zero noncondensable gas concentration is obtained by extrapolating the four curves to the 0 p.p.m. condition. The result for lower subcooling region is added to Fig. 14 above the curve 1 as a short broken line numbered 0.

Although the results shown here are only for the steam velocity of 27 m/s, the results obtained for other steam velocities revealed that the effect of noncondensable gas was relatively small in the present measurement; it was 4–5 percent at 5 m/s and 3–4 percent at 13 m/s and 27 m/s. No substantial effect seems to be involved in the condensation curves shown in Fig. 12.

It is interesting to note that a record of the emf from the surface thermocouple, similar to the one shown in Fig. 7, showed much larger fluctuation of the output in this case. This may be because the thickness of the concentration boundary layer of the noncondensable gas on the condensing surface was changed frequently due to the motion of droplets.

Photographs shown in Fig. 15 are reproduced from a 16-mm, highspeed cinefilm taken to observe the transition of the mode of condensation, from dropwise to pseudo-film and on-ice condensation. The steam velocity is 6 m/s. It is seen that a condensate film develops from the downstream part, and the entire surface is covered with it in about 1 s. Considering that departing drops are accumulated to the downstream part, it is natural for the transition to start from the bottom. The lowermost picture on the right-hand column clearly shows cracks formed on the ice layer.

Conclusion

Condensation curves for dropwise condensation of steam were obtained for the range of surface subcooling between 0.5 and 180 K using a specially designed heat transfer block having a concave spherical condensing surface. In drawing the condensation curves, the authors took the mean final maximum drop diameter as the parameter. It was found that the heat transfer coefficient by dropwise condensation remained constant with the increase of surface subcooling up to about 10 K, and then it began to decrease. The maximum heat fluxes were found to be between 9.3 and 12.2 MW/m^2. Dropwise condensation could be observed sometimes at the surface subcooling larger than the one corresponding to the peak heat flux, but shortly the mode of condensation shifted to pseudo-film or on-ice condensation.

As to the effect of noncondensable gas, the concentration of air in the steam was measured. In addition, the heat transfer measurements were made by adding some known amount of nitrogen gas into the steam. It was found that, in the present study, the reduction of heat transfer coefficient due to the noncondensable gas was, at maximum, 4–5 percent.

References

1 Nukiyama, S., "The Maximum and Minimum Values of the Heat Q Transmitted from Metal to Boiling Water under Atmospheric Pressure," *International Journal of Heat and Mass Transfer*, Vol. 9, 1966, pp. 1419–1433; (originally *Journal of the Japan Society of Mechanical Engineers*, Vol. 37, 1934, pp. 367–374).

2 Takeyama, T., and Shimizu, S., "On the Transition of Dropwise-Film Condensation," *Proceedings of the Fifth International Heat Transfer Conference*, Vol. 3, 1974, pp. 274–278.

3 Wilmshurst, R., and Rose, J. W., "Dropwise and Filmwise Condensation of Aniline, Ethanediol and Nitrobenzene," *Proceedings of the Fifth International Heat Transfer Conference*, Vol. 3, 1974, pp. 269–273.

4 Ochiai, J., Tanasawa, I., and Utaka, Y., "On Errors in Heat Transfer Measurements in Dropwise Condensation," *Transactions of the JSME*, Vol. 43, 1977, pp. 2261–2267.

5 Tanasawa, I., Ochiai, J., Utaka, Y., and En-ya, S., "Experimental Study on Dropwise Condensation—Effect of Departing Drop Size," *Transactions of the JSME*, Vol. 42, 1976, pp. 2846–2853.

6 Tanasawa, I., "Discussion on the Paper by Takeyama and Shimizu," *Proceedings of the Fifth International Heat Transfer Conference*, Vol. 7, 1974, p. 92.

Finite Analytic Numerical Solution Axisymmetric Navier-Stokes and Energy Equations

Ching-Jen Chen
Professor.
Mem. ASME

Young Hwan Yoon
Research Assistant.

Division of Energy Engineering and
Iowa Institute of Hydraulic Research,
The University of Iowa,
Iowa City, Iowa 52242

Convective heat transfer for steady-state laminar flow in axisymmetric coordinates is considered. Numerical solutions for flow pattern and temperature distribution are obtained by the finite analytic numerical method applied to the Navier-Stokes equations expressed in terms of vorticity and stream function, and the energy equation. The finite analytic numerical method differs from other numerical methods in that it utilizes a local analytic solution in an element of the problem to construct the total numerical solution. Finite analytic solutions of vorticity, stream function, temperature, and heat transfer coefficients for flow with Reynolds numbers of 5, 100, 1000, and 2000, and Prandtl numbers of 0.1, 1.0, and 10.0 with uniform grid sizes, are reported for an axisymmetric pipe with a sudden expansion and contraction. The wall temperature is considered to be isothermal and differs from the inlet temperature. It is shown that the finite analytic is stable, converges rapidly, and simulates the convection of fluid flow accurately, since the local analytic solution is capable of simulating automatically the influence of skewed convection through the element boundary on the interior nodal values, thereby minimizing the false numerical diffusion.

1 Introduction

This investigation solves flow and heat transfer characteristics for axisymmetric pipe flow with a sudden expansion and contraction by the finite analytic numerical method. Other numerical methods that were previously suggested to solve the Navier-Stokes and energy equations are the finite difference (FD) and the finite element (FE) methods [1,2,3]. While success with the FD method has been reported, some difficulties remain, such as instability of the numerical solution, proper finite difference approximation of the convection terms, and false numerical diffusion at high Reynolds number flow. The FE solution of the Navier-Stokes equations was reported to be stable, but requires a properly selected approximate function within an element. Derivatives of the FE solution are often found to be less accurate and sometimes discontinuous, unless a higher degree approximating function is used. Instability in solving the system of algebraic equations derived from the FE method at high Reynolds number flow also occurs.

The number of studies for solutions of flow in cylindrical coordinates is fewer than the for two-dimensional Cartesian geometries, even though its application is important in engineering design. A numerical solution of the Navier-Stokes equations for flow between infinite concentric cylinders was reported by Strawbridge [4]. Flow through an orifice within a pipe was solved by Mill [5] and Coder [1]. The numerical solution of flow and heat transfer in a cylindrical combustion chamber was examined by Gosman et al. [6]. Results for rotating and recirculating flow in a cylindrical flow in a cylindrical enclosure obtained by a transient-explicit method were presented by Socio [3]. All of these investigations employed the FD method.

Recently, a new numerical scheme, called the Finite Analytic (FA) method, was introduced by Chen and Li [7], and further developed by Chen et al. [8, 9]. The FA method differs from the FD and FE methods in that it invokes an analytic solution of the governing partial differential equations in a small element to construct the numerical solution of the problem. In this study, the FA solutions for stream function, vorticity, and temperature are obtained. The influence of Reynolds number on flow and heat transfer characteristics is examined. Results are also reported for the local heat transfer coefficient or Nusselt number.

2 Formulation of Problem

The system under consideration consists of a pipe with an abrupt enlargement and contraction, as depicted in Fig. 1, where the fluid enters from one end and exists the other end. The geometry considered in the numerical computations is composed of an inlet pipe of radius, R, with a length, $L/4$, followed by an intermediate chamber of radius, R, and length, L, and an outlet pipe of radius, $R/2$, with a downstream length, $3L/4$, where R is equal to L. This simplified system configuration was chosen to simulate several physical systems such as heat exchangers, boilers, and combustion chambers.

The axisymmetric cylindrical flow is assumed to be steady state and laminar. The fluid with constant properties is Newtonian and incompressible. The dimensionless Navier-Stokes equations in vorticity, stream function variables and the energy equation are written in cylindrical coordinates as:

Vorticity transport equation:

$$\left(\mathrm{Re}V_r - \frac{1}{r}\right)\frac{\partial \xi}{\partial r} + \mathrm{Re}V_z\frac{\partial \xi}{\partial z} = \frac{\partial^2 \xi}{\partial r^2} + \frac{\partial^2 \xi}{\partial z^2} + \frac{1}{r}\left(\mathrm{Re}V_r - \frac{1}{r}\right)\xi \tag{1}$$

Definition of stream function:

$$V_z = -\frac{1}{r}\frac{\partial \psi}{\partial r} \quad V_r = \frac{1}{r}\frac{\partial \psi}{\partial z} \tag{2}$$

Vorticity definition equation:

$$\frac{\partial^2 \psi}{\partial z^2} - \frac{1}{r}\frac{\partial \psi}{\partial r} + \frac{\partial^2 \psi}{\partial r^2} = r\xi \tag{3}$$

Contributed by the Heat Transfer Division and presented at the AIAA/ASME Fluids Plasma Thermophysics and Heat Transfer Conference, St. Louis, Mississippi, June 7-11, 1982. Manuscript received by the Heat Transfer Division February 5, 1982. Paper No. 82-HT-42.

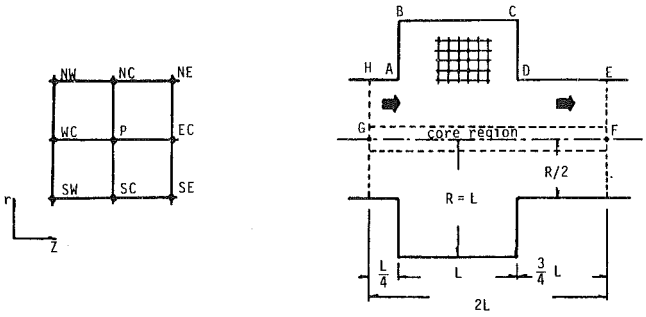

Fig. 1 Finite Analytic Element and Domain for Computation

Energy equation:

$$\left(\mathrm{Pe}V_r - \frac{1}{r}\right)\frac{\partial\theta}{\partial r} + \mathrm{Pe}V_z\frac{\partial\theta}{\partial z} = \frac{\partial^2\theta}{\partial r^2} + \frac{\partial^2\theta}{\partial z^2} \tag{4}$$

where Pe = Pr Re.

All space variables and flow quantities have been nondimensionalized with reference to the radius of the enlarged cylinder chamber, R, and the maximum velocity, $U_{\max}$, at the inlet. The temperature is normalized with the difference between the maximum temperature, $T_{\max}$, at the inlet and the wall temperature, T_o.

$$r=\frac{r^*}{R}, z=\frac{z^*}{R}, V_r=\frac{V_r{}^*}{U_{\max}}, V_z=\frac{V_r{}^*}{U_{\max}},$$

$$\theta=\frac{T-T_o}{T_{\max}-T_o}, \psi=\frac{\psi^*}{U_{\max}R^2}, \mathrm{Re}=\frac{U_{\max}R}{\nu},$$

$$Pr=\frac{\mu C_p}{k}, \xi=\frac{\xi^* R}{U_{\max}}$$

The definition of Reynolds number is based on the chamber radius, R, as the characteristic dimension and the maximum inlet velocity, $U_{\max}$.

The wall boundary conditions are nonslip and impermeable. The temperature boundary conditions for the walls of the inlet and outlet pipes are assumed to be insulated, and that for the chamber wall is isothermal or T_o. The velocity and temperature profiles at the inlet, which is taken to be $L/4$ upstream from the entrance of the enlarged pipe, are parabolic and uniform, respectively. The outlet conditions for velocity and temperature profiles are posed at $3L/4$ downstream from the contraction of the chamber, and these are assumed to be fully developed. Since the profiles are symmetrical about the centerline axis, radial derivatives of axial velocity and temperature at the axis are equal to zero.

The stream function and vorticity boundary conditions at the inlet ($z=0$), outlet ($z=2L$), and centerline axis of the system are determined from the velocity boundary conditions. The vorticity boundary conditions at the walls may be approximately derived by a Taylor series expansion of the stream function about ψ_0 (at the wall) using the nonslip, impermeable wall conditions.

The boundary conditions for the vorticity, stream function, and temperature with the symbols referenced in Fig. 1, are

GH:

$$\xi = 8r\psi_{\max}/r_{\mathrm{in}}{}^4$$
$$\psi=\psi_{\max}[1-2(r/r_{\mathrm{in}})^2+(r/r_{\mathrm{in}})^4]$$
$$\theta=1 \tag{5}$$

EF:

$$\frac{\partial\xi}{\partial z}=\frac{\partial\psi}{\partial z}=\frac{\partial\theta}{\partial z}=0 \tag{6}$$

HA and DE:

$$\xi_0 = (\psi_1-\psi_0)/(r_0\Delta r^2)$$
$$\psi = 0, \quad \frac{\partial\theta}{\partial r}=0 \tag{7}$$

AB, BC and CD:

$$\xi_0 = (\psi_1-\psi_0)/(r_0\Delta_z{}^2) \text{ or } (\psi_1-\psi_0)/(r_0\Delta_r{}^2)$$
$$\psi = 0, \quad \theta=0 \tag{8}$$

FG:

$$\xi = 0, \quad \psi=\psi_{\max}, \quad \frac{\partial\theta}{\partial r}=0 \tag{9}$$

where ψ_1 is the value at an interior nodal point normal to a wall.

3 Finite Analytic Numerical Analysis

In the FA method, like the FD and FE methods, the computational domain is first discretized with a uniform grid, $\Delta z + \Delta r$. However, algebraic equations for numerical calculation are obtained from analytic solutions of locally linearized governing equations in a small element in which an interior node, P, is surrounded by eight boundary nodal points, as shown in Fig. 1.

Nomenclature

C_p = specific heat of fluid, W s/kg K
h = local heat transfer coefficient, W/m K
k = thermal conductivity, W/m K
L = length of cylinder chamber, m
Nu = local Nusselt number, h L/k
$\overline{\mathrm{Nu}}$ = mean Nusselt number
Pe = Paclet number (Re Pr)
r,z = dimensionless radial and axial coordinates
R = radius of cylinder chamber ($R=L$), m
$r_{\mathrm{in}}/r_{\mathrm{out}}$ = dimensionless radius of inlet/outlet pipes ($r_{\mathrm{in}}=r_{\mathrm{out}}=1/2$)
T = temperature, K
$T_{\max}$ = maximum temperature at inlet, K
$U_{\max}$ = maximum velocity at inlet, m/s
V_r, V_z = dimensionless radial and axial velocity
x,y = normalized radial and axial coordinates
$\Delta r, \Delta z$ = radial and axial grid size
ν = kinematic viscosity, m^2/s
ξ = vorticity
θ = dimensionless temperature, $(T-T_o)/(T_{\max}-T_o)$
ρ = density of fluid, kg/m
μ = viscosity, kg/m s
ψ = stream function
$\psi_{\max}$ = maximum stream function at the centerline

Subscripts and Superscripts

in,out = inlet or outlet
i,j = nodal point
N,S,W,E = north, south, west, east
NC,NW,NE = northcenter, northwest, northeast
o = wall
p = center node (i,j)
* = dimensional quantity
[−] = averaged

To obtain an analytic solution for an element, local linearization of the nonlinear terms in equations (1–4) is made by assuming that the axial and radial velocity components, V_z, V_r, respectively, are constant in the small element. The linearized velocity components at node (i, j) are obtained by taking the integral averaged values of the variables in an element of area, A

$$\bar{V}_z = \frac{1}{A}\int_A V_z dA, \quad \bar{V}_r = \frac{1}{A}\int_A V_r dA$$

The $(1/r)$ terms in equations (1) and (4) are also assumed to be constant and given as the averaged distance from the centerline of the system to the element.

A typical element shown in Fig. 1 has four boundaries, i.e., east, west, north, and south sides. Each boundary for dependent variables ξ, ψ, and θ is approximated by a second-degree polynomial using the three nodal values of each side. For example, the east boundary condition of an element for the vorticity ξ can be written as

$$\xi_E = a_E + b_E r + c_E r^2 \tag{10}$$

where

$$a_E = \xi_{EC}, b_E = \frac{1}{2\Delta r}(\xi_{NE} - \xi_{SE}),$$

$$c_E = \frac{1}{2\Delta r^2}(\xi_{NE} - 2\xi_{EC} + \xi_{SE})$$

The other three boundary conditions are also determined in the same manner.

An elliptic partial differential equation with four boundary conditions expressed by second-degree polynomials can be solved analytically in an element by separation of variables. Then the local analytic solution evaluated at the center node, P, of the element gives the FA algebraic equations, relating the central nodal value and its eight neighboring nodal values.

Prior to solving the equations analytically for the (i, j) element located at $r = r_i$, $z = z_i$, equations (1–4) are transformed for convenience of computation through the following relations, $r = r_i + \Delta r \cdot x$ and $z = z_i + \Delta z \cdot y$.

The transformed governing equations and their corresponding FA algebraic solutions for vorticity, stream function, and temperature are as follows.

Vorticity Transport Equations. The linearized and normalized vorticity transport equation (11) is solved by separation of variables with four boundary conditions.

$$2A\gamma^2 \frac{\partial \xi}{\partial x} + 2B\frac{\partial \xi}{\partial y} = \gamma^2 \frac{\partial^2 \xi}{\partial x^2} + \frac{\partial^2 \xi}{\partial y^2} + C\xi \tag{11}$$

where

$$A = \frac{\Delta r}{2}\left(\mathrm{Re}\bar{V}_r - \frac{\bar{1}}{r}\right), B = \frac{\Delta z}{2}\mathrm{Re}\bar{V}_z,$$

$$C = \Delta z^2 \frac{\bar{1}}{r}\left(\mathrm{Re}\bar{V}_r - \frac{\bar{1}}{r}\right)$$

and $\gamma = \dfrac{\Delta z}{\Delta r}$

In this investigation, uniform grid size ($\Delta r = \Delta z$) is considered. When the analytic solution for equation (11) is evaluated at node P, the FA algebraic equation for nodal value ξ_p can be written as

$$\xi_p = \sum_{n=1}^{8} C_n \xi_n = C_{EC}\xi_{EC} + C_{WC}\xi_{WC} + C_{NC}\xi_{NC} + C_{SC}\xi_{SC}$$

$$+ C_{NE}\xi_{NE} + C_{SE}\xi_{SE} + C_{NW}\xi_{NW} + C_{SW}\xi_{SW} \tag{12}$$

The FA coefficients (C_n's) of each nodal value in equation (12) are functions of A, B, C, and ratio of grid size γ. A, B, and C vary from one region to another, since these constants contain the averaged local velocity components. The expressions of the FA coefficients (C_n's) are given in Appendix A.

Stream Function and Velocity Components. In order to solve the stream function equation, the entire region is divided into two parts, namely, outer region and core region, as shown in Fig. 1. In the outer region, the averaged value of $(1/r)$ may be used in approximation of equation (3) for stream function since $(1/r)$ does not vary as rapidly. However, in the core region, the variation of $(1/r)$ is incorporated in the solution.

To compute the stream function, ψ, in the outer region, the normalized vorticity definition equation with the averaged coefficient $(1/r)$ can be written as

$$\frac{\partial^2 \psi}{\partial y^2} - \gamma^2 \Delta r \frac{\bar{1}}{r}\frac{\partial \psi}{\partial x} + \gamma^2 \frac{\partial^2 \psi}{\partial x^2} - \Delta z^2 \cdot r \cdot \xi(x, y) \tag{13}$$

For numerical purposes, the inhomogeneous term in equation (13) may be expressed by a second-degree polynomial of two variables x and y as

$$r\xi(x, y) = a_0 + a_1 x + a_2 y + a_3 x^2 + a_4 y^2 + a_5 xy + a_6 x^2 y + a_7 x y^2 + a_8 x^2 y^2 \tag{14}$$

where the coefficient can be determined by the nine nodal values of vorticity in the element.

The solution of equation (13) is also obtained by separation of variables with four second-degree, polynomial boundary conditions as before. The discretized FA algebraic solution of equation (13) has a form of

$$\psi_p = \sum_{n=1}^{8} C'_n \psi_n + \sum_{n=1}^{9} B_n \xi_n$$

$$= (C'_{EC}\xi_{EC} + C'_{NC} + \xi_{NC} \ldots + C'_{SE}\xi_{SE}) + (B_{EC}\xi_{EC} + \ldots + B_{SE}\xi_{SE} + B_p\xi_p) \tag{15}$$

The first eight terms of equation (15) represent the complementary solution and the latter nine terms represent the particular solution. For a given grid size, the FA coefficients (C_n's and B_n's in equation (15)) are only a function of distance (t) from the axis to the element and are invariant in the axial direction. Therefore, these coefficients are calculated only once for given node coordinates. For the case of $\Delta x = \Delta y$, the expression and typical numerical values of these coefficients are given in [11].

To compute the stream function in the core region, the variation of $1/r$ is kept in the element for equation (3). Since the flow is axisymmetric, the streamline at the centerline must coincide with the axis, and the streamlines near the axis are approximately parallel to the axis. This implies that, in each element near the axis, the value of V_r (or $\partial\psi/\partial z$) is small or

$$\frac{\partial^2 \psi}{\partial z^2} = 0$$

and the variation of vorticity in the axial direction is also small. Under this condition, vorticity may be approximately expressed as

$$\xi(r) = a_0 + a_1 r + a_2 r^2 \tag{16}$$

where a_0, a_1, and a_2 can be determined by nodal values of ξ in the radial direction. Substitution of these assumptions into equation (3) and multiplication by r^2 yields

$$r^2 \frac{d^2 \psi}{dr^2} - r\frac{d\psi}{dr} = r^3(a_0 + a_1 r + a_2 r^2) \tag{17}$$

This approximate equation is an ordinary differential

equation and can be easily solved analytically with north and south boundary conditions of stream function.

Once the stream function is known, velocity components V_r and V_z and be obtained from equation (2).

Temperature. The FA solution for temperature equation (4), in the element can be similarly obtained as for vorticity. If C is taken to be zero in equation (11), and Reynolds number is replaced by Peclet number, the equation for temperature has identical from as equation (11). Therefore, the FA solution of vorticity can be adopted for the FA solution of temperature.

4 Numerical Procedure

For numerical solutions, the velocity field is first solved from the vorticity-stream function equations (1-3), and the temperature field is then solved from equation (4) with the calculated velocity field.

The FA algebraic equations (12) and (15) for ψ, ξ, and θ can be arranged into systems of linear equations in the entire domain with subscripts (i, j) $(i, j+1)$, $(i, j-1)$, etc., instead of subscripts P, EC, WC, etc., for convenience in the numerical calculations. The boundary conditions for the system of equations have been given previously.

To calculate the velocity field, the system of equations for stream function, equation (15), is first solved by a line-by-line implicit interation method with an assumed vorticity field. This iteration procedure is called the inner iteration for stream function. Second, the velocity components, V_r and V_z are obtained from the calculated stream function, and then velocity components are averaged over the element to obtain the linearized convective velocity for computation of vorticity from equation (12). Third, the system of equation (12) for vorticity is solved by the Gauss-Seidel iterative method. This process is called the inner iteration for vorticity. The improved solutions are applied after relaxation (equation (18)) and again used to calculate stream function from equation (15).

$$\xi^{K+1} = \xi^K + \lambda(\bar{\xi}^{K+1} - \xi^K) \tag{18}$$

Here K is Kth iteration of the variable, and $\bar{\xi}^{K+1}$ is the value of vorticity just obtained from the inner iteration. λ is defined as a relaxation parameter.

The iteration between calculations of stream function and vorticity is called the overall interation. Finally, solutions for V_r, V_z, ξ, ψ, and θ are obtained by checking convergence of the overall iteration.

To calculate the temperature field, the averaged velocity components obtained from the former velocity field calculation are used to evaluate the FA coefficients of the temperature equation. The system of equations for temperature is solved by the line-by-line implicit iteration method using the relaxation equation (18) for temperature.

In the computations, the convergence criteria for each iteration are given by comparing differences between the value just evaluated and that of previous iteration such that

$$|\Delta\psi|_{\max} < 10^{-5},\ |\Delta\xi|_{\max} < 10^{-4},\ \text{and}\ |\Delta\theta|_{\max} < 10^{-5}$$

5 Discussion of Results

Profiles of the stress function, vorticity, velocity components, and temperature distributions of the flow field in the r-z-plane ($0 < r < 1$, $0 < z < 2$) are given in Fig. 2-5.

The computations were performed on a PRIME 750 computer system and a computational time between 30-900 CPU s, depending on Reynolds number, was required to obtain a converged solution for the flow or temperature field with uniform grid sizes of 1/20 in both r-and z-directions. However, the total computational time for the temperature equation at high Peclet numbers of 10,000 and 20,000 required approximately 2000.0 CPU s to obtain a converged solution because fine grid sizes of 1/100 were used to capture the thin temperature boundary layer.

Significant rounding errors were found in evaluation of the FA coefficients (Appendix A) in the vorticity and temperature equations when the sum of A and B in equation (11) was approximately greater than 100. Thus, it is required that

$$A + B = \frac{\Delta r}{2}\left(\mathrm{Re}\overline{V_r} - \frac{\bar{1}}{r}\right) + \frac{\Delta z}{2}(\mathrm{Re}\cdot\overline{V_z}) < 100 \tag{19}$$

Hence, for a given Reynolds number or Peclet number, the grid size is kept within the limit of equation (19). The computations of higher Reynolds and Peclet number flows needed

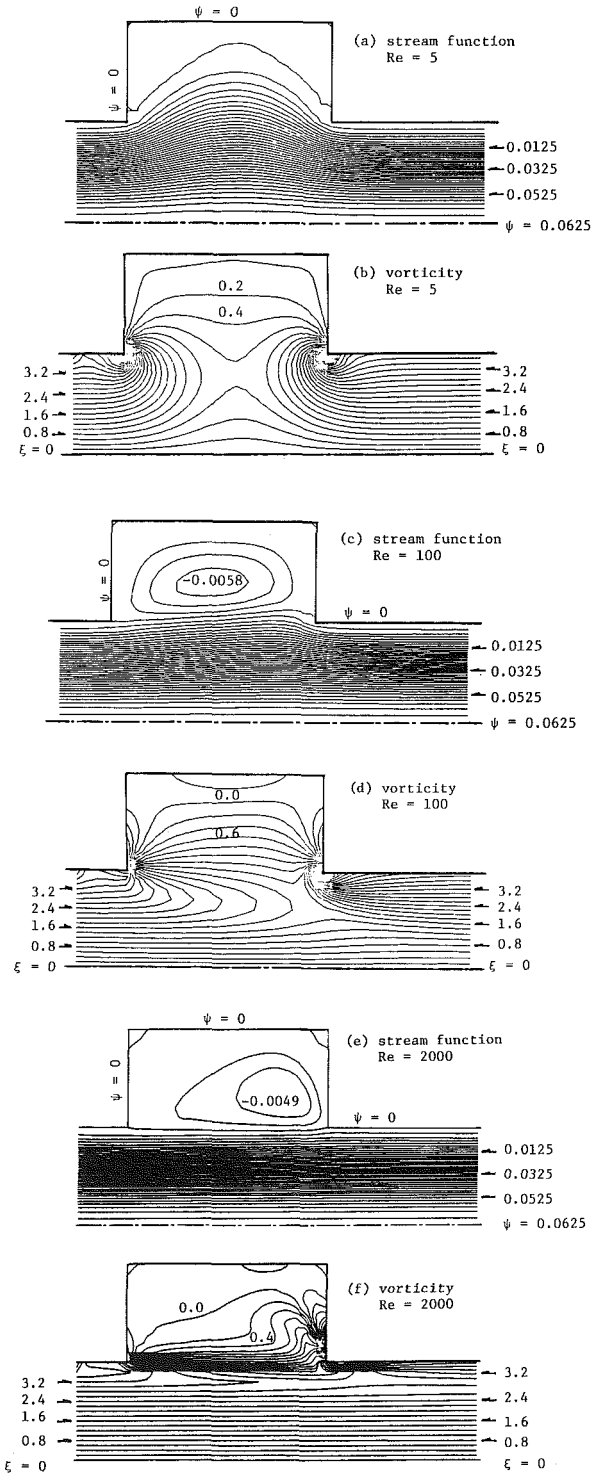

Fig. 2 Distributions of Iso-Streamlines and Iso-Vorticity Lines

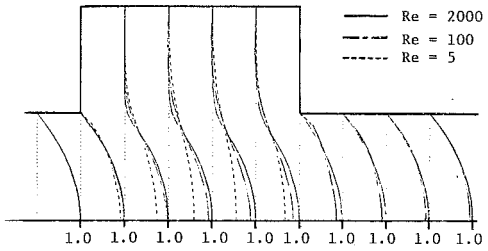

Fig. 3 Axial Velocity Profiles

smaller relaxation parameters: consequently, more computing time was needed for the flow with a higher Reynolds number. Relaxation parameters used during the computations were between 0.5 to 1.0 depending on Reynolds number and Peclet number.

Figure 2 displays distributions of stream function and vorticity for Reynolds number of 5, 100, and 2000. It can be seen that fluid diffuses significantly into the chamber at the low Reynolds number of 5, while a large vortex region is formed in the cavity at high Reynolds numbers of 100 and 2000. The vortex centers in the cavity move downstream from the location (0.5 L, 0.7 R) of enlarged chamber to the location (0.8 L, 0.65 R) as the Reynolds number increases from 100 to 2000.

Results for axial velocity profiles for Reynolds numbers of 5, 100, and 2000 are presented in Fig. 3, where dotted lines indicate locations of axial cross sections for each velocity profile.

The accuracy of the FA solution can be checked from the total circulation and vorticity distribution through Stoke's theorem as follows

$$\oint \mathbf{V}d\mathbf{l} = \int) \nabla x \mathbf{V}) d\mathbf{A} = \int \xi dr dz \qquad (20)$$

The line integration on the left-hand side of equation (20) is taken along ABCDEFGHA as shown in Fig. 1, and the right hand side of equation (20) can be determined from the surface integration in the region which is encircled by the line. In the present computation, the relative errors of the circulation compared with the surface integration of vorticity was found to be between 1.4 and 2.3 percent.

The conservation of mass was checked by numerical integration across each cross section of the system. The largest error occurs at the intersection between the enlarged chamber and the outlet pipe for every Reynolds number. The range of relative errors at that location was between 1.4 and 1.9 percent.

Temperature distributions are given in Fig. 4 for Re = 5, 1000, and 2000, and Pr = 1 and 10. At small Peclet number, thermal diffusion from the cylinder wall penetrates to the center axis, as shown in the figures. However, at high Peclet number of 1000 to 20,000, the temperature of the fluid near the axis is not altered and the thermal diffusion is confined to the cavity and thin thermal boundary layer near the pipe wall.

The conservation of energy was checked by balancing energy influx with the energy efflux and the energy removed from the system wall. Errors are within 5.0 percent for all Peclet numbers. This error is probably due to partial truncation error of the FD approximation used to evaluate the temperature gradient at the boundary wall where the grid size is uniform.

The local and mean Nusselt number may be expressed from the local heat transfer coefficient as

$$\mathrm{Nu} = \frac{hL}{k} = -\left.\frac{\partial\theta}{\partial r}\right|_w \text{(axial wall) or } -\left.\frac{\partial\theta}{\partial z}\right|_w \text{(radial wall)}$$

$$\bar{\mathrm{Nu}} = \frac{1}{A}\int \mathrm{Nu} dA$$

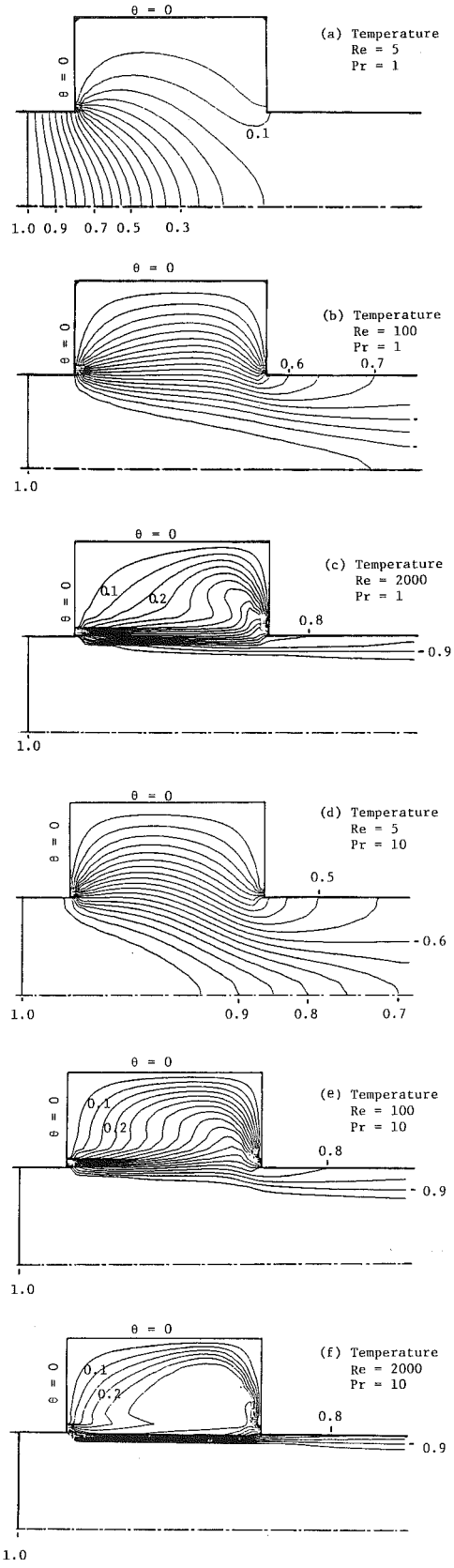

Fig. 4 Distributions of Iso-Temperature Lines

where A is the surface area of the system wall. The local Nusselt numbers for Re = 5 to 2000, and Pr = 0.1 to 10 are shown in Fig. 5. One can see that, at the low Reynolds number of 5, heat transfer between the fluid and wall is almost symmetric about the half plane of the chamber. However,

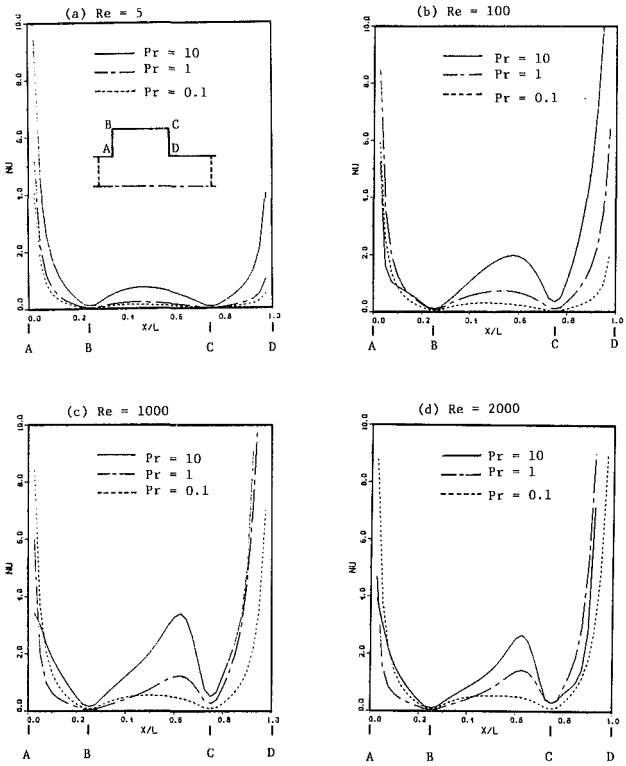

Fig. 5 Local Nusselt Number

when Reynolds number is increased, the heat transfer increases rapidly in the downstream half of the chamber because of strong convection induced by the pipe flow. Heat transfer is particularly strong on the CD surface, and lines of the Nusselt number remain to be minimum at two inner corners (*B*, *C*) for the range of Reynolds numbers considered.

The mean Nusselt number with constant Prandtl number are presented in Fig. 6 as function of the Reynolds number. The mean Nusselt number may be approximately correlated with Reynolds number and Prandtl number for engineering proposes as

$$\bar{\mathrm{Nu}} = 0.4\,\mathrm{Re}^{1/4}\mathrm{Pr}^{1/4}$$

It should be remarked that the mean Nusselt number at the highest Peclet number of 20,000 (Re = 2000 and Pr = 10) slightly decreases as the Reynolds number increases as shown in Fig. 6.

6 Conclusion

Finite analytic solutions are obtained for the axisymmetric cylindrical Navier-Stokes equations in vorticity and stream function form, and for the energy equation. It is found that the FA method is effective in eliminating instability and false numerical diffusion in high Reynolds and Peclet number flows. In this study, stable numerical solutions were obtained from the finite analytic method for steady-state laminar flows with Reynolds numbers from 5 to 2000, and Peclet number from 0.5 to 20,000.

The accuracy of the FA numerical solution is checked by the relation between circulation and integration of vorticity in the flow, conservation of mass, and conservation of energy. Satisfactory results were obtained for every Reynolds number and Peclet number considered.

The mean Nusselt number is approximately proportional to the 1/4 power of both Reynolds number and Prandtl number of the pipe.

In summary, it is demonstrated that the finite analytic numerical method is an effective tool for obtaining steady-state laminar flow and heat transfer problems governed by axisymmetric elliptic partial differential equations.

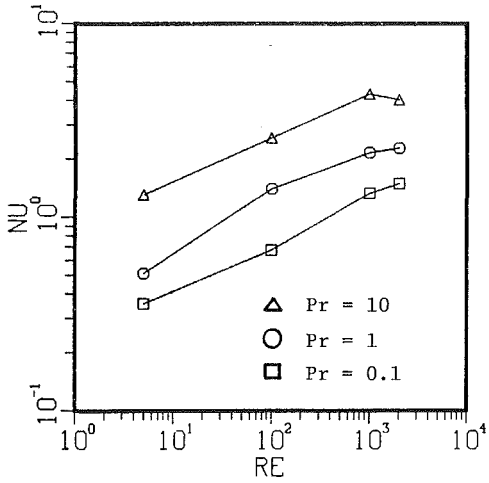

Fig. 6 Mean Nusselt Number

Acknowledgment

This work was in part supported by the U.S. Department of Energy grant De-ACO2-79ER-10515. A000 and NASA grant NSG 3305.

Reference

1 Coder, D. W., and Buckley, F. T., "Implicit Solutions of the Unsteady Navier-Stokes Equation for Laminar Flow Through an Orifice within a Pipe," *Computer and Fluids*, Vol. 2, 1974, p. 295.

2 Olsen, M. D., "Variational-Finite Element Methods for Two Dimensional and Axisymmetric Navier-Stokes Equations," *Finite Elements in Fluid*, Vol. 1, New York, 1975, p. 57.

3 Socio, L. M., Sparrow, E. M., and Eckert, E. R., "The Contrived Transient Explicit Method for Solving Steady-State Flows," *Computer and Fluids*, Vol. 1, 1973, p. 273.

4 Strawbridge, D. R., and Hooper, G. T., "Numerical Solutions of Navier-Stokes Equations for Axisymmetric Flow," *Journal of Mechanical Engineering Science*, Vol. 10, No. 5, Dec. 1968, p. 389.

5 Mills, R. D., "Numerical Solutions of Viscous Flow Through a Pipe Orifice at Low Reynolds Number," *Journal of Mechanical Engineering Science*, Vol. 10, No. 2, 1968, p. 133.

6 Gosman, A. D., Pum, W. M., Runchel, A. K., Spalding, D. B., and Wolfhtein, M., *Heat and Mass Transfer in Recirculating Flows*, Academic Press, 1969.

7 Chen, C. J., and Li, P., "The Finite Analytic Method for Steady-State and Unsteady Heat Transfer Problems," 19th ASME/AIChE U.S. National Heat Transfer Conference, Orlando, Fla. ASME Paper No. 80-HT-86, July 27-30, 1980.

8 Chen, C. J., Naseri-Neshet, H., and Ho, K. S., "Finite Analytic Numerical Solutions of Heat Transfer in Two-Dimensional Cavity Flow," *Journal of Numerical Heat Transfer*, Vol. 4, 1981, p. 179-197.

9 Chen, C. J., and Obasih, K., "Finite Analytic Numerical Solution of Heat Transfer and Flow Past..A Square Channel Cavity," The 7th International Heat Transfer Conference, Munchen Paper No. 82-IHTC-43, September 6-10, 1982.

10 Chen, C. J., and Chen, H. C., "Development of Finite Analytic Numerical Method for Unsteady Two Dimensional Convective Transport Equation," *Proceedings of the First International Symposium on Refined Modeling of Flows*, Vol. 1, International Association for Hydraulic Research Sept. 7-10, 1982, p. 69-79.

11 Yoon, Y. H., "Finite Analytic Numerical Solution of Laminar and Turbulent Convective Heat Transfer in Pipe Flows Past a Cavity," Doctoral Dissertation, Mechanical Engineering, The University of Iowa, Iowa City, Iowa, 1982.

APPENDIX A

The expressions of the FA coefficients C'_n of equation (12) are given as follow

$$C_{NW} = \sum_{n=1}^{21} \left[\frac{e^{-A}(-E_2+E_3)}{4\cosh k_{1n}} \right] + \left[\frac{e^{+B}(F_2+F_3)}{4\cosh k_{2n}} \right] \sin\frac{n\pi}{2}$$

$$C_{NC} = \sum_{n=1}^{21} \frac{e^{-A}(E_1-E_3)}{2\cosh k_{1n}} \cdot \sin\frac{n\pi}{2}$$

$$C_{NE} = \sum_{n=1}^{21} \left[\frac{e^{-A}(E_2+E_3)}{4\cosh k_{1n}} + \frac{e^{-B}(F_2+F_3)}{4\cosh k_{2n}} \right] \sin\frac{n\pi}{2}$$

$$C_{WC} = \sum_{n=1}^{21} \frac{e^{+B}(F_1-F_3)}{2\cosh k_2 n} \cdot \sin\frac{n\pi}{2}$$

$$C_{EC} = \sum_{n=1}^{21} \frac{e^{-B}(F_1-F_3)}{2\cosh k_{2n}} \cdot \sin\frac{n\pi}{2}$$

$$C_{SW} = \sum_{n=1}^{21} \left[\frac{e^{+A}(E_2+E_3)}{4\cosh k_{1n}} + \frac{e^{+B}(-F_2+F_3)}{4\cosh k_{2n}} \right] \cdot \sin\frac{n\pi}{2}$$

$$C_{SC} = \sum_{n=1}^{21} \frac{e^{+A}(E_1-E_2)}{2\cosh k_{1n}} \cdot \sin\frac{n\pi}{2}$$

$$C_{SE} = \sum_{n=1}^{21} \left[\frac{e^{+A}(E_2+E_3)}{4\cosh k_{1n}} + \frac{e^{-B}(-F_2+F_3)}{4\cosh k_{2n}} \right] \sin\frac{n\pi}{2}$$

where

$$k_{1n} = \sqrt{\gamma^2 A^2 + B^2 - C + \left(\frac{n\pi}{2}\right)}$$

$$k_{2n} = \sqrt{\gamma^2 A^2 + B^2 - C + \left(\frac{n\pi\gamma^2}{2}\right)^2}$$

$$E_j = \int_{-1}^{+1} S^{j-1} e^{-BS} \sin\frac{n\pi}{2}(S+1)dS$$

$$F_j = \int_{-1}^{+1} S^{j-1} e^{-AS} \sin\frac{n\pi}{2}(S+1)ds$$

M. Manzoor
Research Fellow,
Department of Applied Mathematical Studies.

D. B. Ingham
Senior Lecturer,
Department of Applied Mathematical Studies.

P. J. Heggs
Senior Lecturer,
Department of Chemical Engineering.

University of Leeds,
Leeds LS2 9JT
England

The One-Dimensional Analysis of Fin Assembly Heat Transfer

The design of finned surfaces is conventionally performed in two stages. First the fin efficiency is determined by simultaneously analyzing the conductive heat flow within the fin, and the convective heat dissipation from the surface of the fin. Then, the effects of the thermal interaction between the supporting interface and the fins and the convective heat exchange at the plain side of the supporting interface are incorporated by employing a technique based on electric circuit theory. In this study, it is shown that this technique in fact has a mathematically rigorous foundation. It is also shown that, for design purposes, there is a far superior alternative to the fin efficiency.

Introduction

The design of finned surfaces is presently based on a method of analysis which originated from the fundamentally innovative work of Harper and Brown [1]. This involves a process of analysis in which the fins and the supporting interface are effectively treated as completely separate entities. The heat flow within the fins is analyzed solely by examining the heat conduction within the fins and the heat convection from the surface of the fins, e.g., [1-7]. The effects of such significant features as the heat conduction within the supporting interface, the proximity of adjacent fins, and the heat exchange from the plain (i.e., unfinned) side of the supporting interface are given no consideration whatsoever in the fin analysis, but are accounted for in a separate analysis. However, this secondary analysis, which is commonly referred to as the sum of resistances method, is not of a mathematically formal nature, but is performed by analogy with electric circuit theory [6].

The principal advantage of examining the fins in isolation from the supporting interface is that this permits a very concise nondimensional representation of the fin heat transfer rate, commonly referred to as the fin efficiency [1-7]. This fin efficiency can usually be parameterized by a relatively small number of bulk parameters instead of the actual fin parameters [1-7]. For example, the fin efficiency of a longitudinal fin of rectangular profile can be parameterized by a single variable comprising a nondimensional combination of the fin length, fin thickness, fin thermal conductivity, and surface heat transfer coefficient, and this enables the fin performance to be characterized by a single curve which accounts for all possible variations in the four fin parameters, e.g. [2]. Consequently, the fin efficiency is widely regarded as the ideal design tool. However, the effects of variations in the individual design parameters on the fin performance cannot easily be deduced from fin efficiency graphs. Furthermore, since the fin efficiency is completely independent of both the heat conduction within the supporting interface, and the heat convection at the plain side of this interface, it gives practically no indication as to the effect of the presence of the fins on the overall heat transfer.

In this study a rigorous theoretical method is devised for analyzing the heat flow within finned surfaces. In contrast to the conventional two-stage method of analysis, this method is formulated by simultaneously examining the heat flow within both the fins and the supporting interface, i.e., by employing a fin assembly representation. The general situation in which the fins and the supporting interface have different thermal conductivities is considered, and the effects of the thermal interaction between the fins and the supporting interface are accounted for in a mathematically formal manner. A salient feature of this method is that it results in exactly the same expression for the overall heat transfer rate as that predicted by the sum of resistance approach, thus indicating that the present work is consistent with the conventional method of analysis. The most significant feature of the present work is the introduction of a superior alternative to the fin efficiency, namely the enhancement factor. This enhancement factor is not as concise as the fin efficiency, in that it requires more charts in order to describe the fin side heat transfer. However, these charts clearly show the effects of variation in the fin dimensions, interfin spacing, fin thermal conductivity and surface heat transfer coefficient. Furthermore, the relationship between the enhancement factor and the overall heat transfer rate is extremely simple, and consequently various aspects of the overall heat transfer rate are readily deduced from the enhancement factor.

Fin Assembly Formulation

Assumptions and Model. Consider a heat exchanger comprised of equally spaced longitudinal rectangular fins

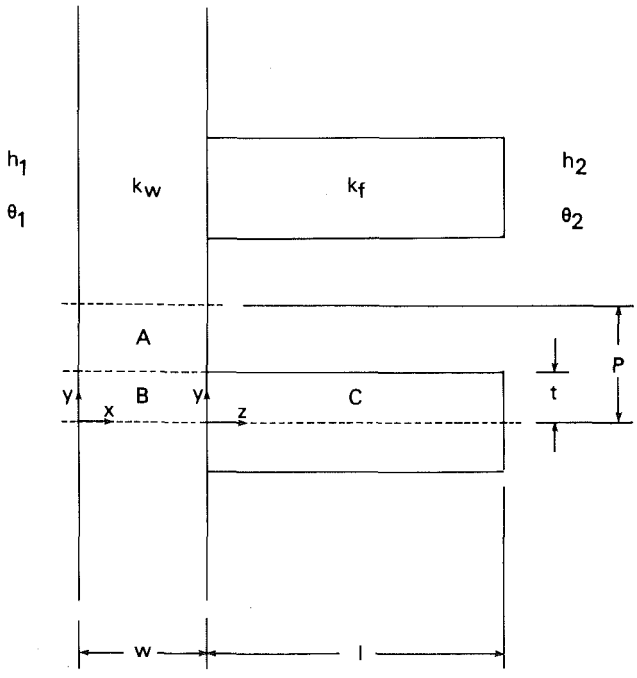

Fig. 1 Schematic representation of a fin assembly

Contributed by the Heat Transfer Division for publication in the JOURNAL OF HEAT TRANSFER. Manuscript received by the Heat Transfer Division May 27, 1982.

attached to a plane wall, as depicted schematically in Fig. 1. In this study a theoretical representation of this device is developed on the basis of the following assumptions:

1 The materials from which the wall and fins are fabricated are isotropic and have constant thermal conductivities
2 There is perfect contact between the wall and fins
3 The convective heat transfer can be described using Newton's Law of Cooling [6]
4 The fin side heat transfer coefficient is constant over the fin surface
5 The heat flow within the fins is one dimensional
6 The heat flow within the wall is one dimensional even in the presence of the fins

These are essentially the classic assumptions inherent in the analysis of conducting-convecting finned surfaces, e.g., see [1-7].

Several investigations [8, 9, 10] have indicated that the fourth assumption is not strictly valid. However, these investigations have failed to establish any generally applicable data regarding the variation of the heat transfer coefficient over the fin surface. Thus, an accurate representation of the convective heat transfer would require a simultaneous analysis of both the heat transfer and the fluid flow around the fins. Unfortunately, the mathematical complexity of such a representation is beyond the scope of the present investigation.

The justification of the fifth assumption is conventionally based on the criterion that the fin length be very much larger than the fin thickness, e.g., see [1-4]. However, several recent investigations [11, 12, 13] have shown that the applicability of the one-dimensional fin approximation is dependent upon the transverse Biot number, Bi, and not the ratio of the fin length to the fin thickness. The inference of both these criteria is that the sum of resistances method for predicting the overall heat transfer rate is applicable provided the heat flow within the fins is effectively one dimensional. However, since the sum of resistances method neglects the two-dimensional effects induced within the wall by the presence of the fins [14, 15, 16], it is apparent that its applicability can only be justified by a direct comparison with the overall heat transfer rates predicted by a completely two-dimensional analysis. Therefore, no attempt is made in this study to qualify the applicability of the one-dimensional approximation. In particular, no approximations which require the fin length to be large in comparison to the fin thickness are introduced.

In order to develop a mathematical representation it is necessary to decide which section of the fin assembly should be examined. The geometrical symmetry of the fin assembly configuration and the thermal symmetry resulting as a consequence of assumptions 2, 5, and 6 indicate that it will suffice to examine the heat flow within the region (A + B + C), Fig. 1. This is the smallest region which includes all the essential features of the complete fin assembly, namely, the wall, fin, and interfin spacing.

It may initially appear superfluous to examine the heat flow within the region A since, by virtue of assumption 6, the temperature distribution within this region will be identical to that within the region B. However, it attention is restricted solely to the region (B + C), then the effects of the interfin spacing will not be accounted for, and, therefore, the model will not be representative of the fin assembly.

Mathematical Analysis. On the basis of the preceeding development, the determination of the temperature distribution within the fin assembly (and hence the heat transfer rate) requires the simultaneous solution of the energy equations [6]

$$\frac{d^2}{dX^2}\phi_w(X) = 0 \tag{1}$$

within the wall (region (A + B), Fig. 1) and

$$\frac{d^2}{dZ^2}\phi_f(Z) - \frac{\mathrm{Bi}}{T^2}\phi_f(Z) = 0 \tag{2}$$

within the fin (region C, Fig. 1.), subject to the boundary conditions,

at $X = 0$

$$\frac{d}{dX}\phi_w(x) = -\mathrm{Bi}_1(1 - \phi_w(X)) \tag{3a}$$

at $X = W (Z = 0)$

$$\phi_w(X) = \phi_f(Z) \tag{3b}$$

and

$$\frac{d}{dX}\phi_w(X) = \kappa T \frac{d}{dZ}\phi_f(Z) - \mathrm{Bi}_2(1 - T)\phi_w(X) \tag{3c}$$

at $Z = L$

$$\frac{d}{dZ}\phi_f(Z) = -\mathrm{Bi}_2\phi_f(Z) \tag{3d}$$

The boundary conditions (3*a*) and (3*d*) describe the convective heat exchange at the plain side of the wall and the tip of the fin, respectively. The boundary conditions (3*b*) and (3*c*) arise as a consequence of the perfect contact assumption, and stipulate continuity of temperature and heat flux across the wall-to-fin interface.

It may appear that the boundary condition (3*c*) can be equivalently re-expressed in the form

at $X = W\ (Z = 0)$

$$\frac{d}{dX}\phi_w(X) = \kappa \frac{d}{dZ}\phi_f(Z), \quad 0 \le Y \le T \tag{4a}$$

Nomenclature

Aug = augmentation factor
Aug_∞ = ideal maximum augmentation factor
Bi = Biot number, $h_2 t/k_f$
Bi_1 = Biot number, $h_1 P/k_w$
Bi_2 = Biot number, $h_2 P/k_w$
h_1, h_2 = heat transfer coefficients, $\mathrm{W/m^2K}$
k_f, k_w = thermal conductivities, W/mK
l = fin length, m
L = aspect ratio, l/P
P = half-fin pitch, m
t = half-fin thickness, m
T = aspect ratio, t/P
w = wall thickness, m
W = aspect ratio, w/P
x = longitudinal displacement in wall, m
X = x/P
y = transverse displacement, m
Y = y/P
z = longitudinal displacement in fin, m
Z = z/P
ϵ = enhancement-factor
η = fin efficiency
κ = k_f/k_w
θ = temperature distribution, K
θ_1, θ_2 = fluid temperatures, K
ϕ = dimensionless temperature distribution, $(\theta - \theta_2)/(\theta_1 - \theta_2)$

Subscripts

1 = plain side
2 = fin side
f = fin
w = wall

Superscript

* = unfinned wall

and

$$\frac{d}{dX}\phi_w(X) = -\mathrm{Bi}_2\phi_w(X), \quad T \le Y \le 1 \tag{4b}$$

However, this results in a solution which, in effect, neglects the thermal interaction of the regions A, B, and C, Fig. 1. The temperature distribution in region A is found to be exactly that as if the fins were not present. Furthermore, the temperature distribution in region B differs from that in region A and is unaffected by variations in the interfin spacing. Thus, it is clearly inappropriate to employ the boundary conditions (4*a*) and (4*b*).

The solution to the problem described by equations (1), (2), and (3) is

$$\phi_w(X) = \frac{-X + W + \epsilon\dfrac{1}{\mathrm{Bi}_2}}{\dfrac{1}{\mathrm{Bi}_1} + W + \epsilon\dfrac{1}{\mathrm{Bi}_2}} \tag{5}$$

and

$$\phi_f(Z) = \frac{\epsilon\dfrac{1}{\mathrm{Bi}_2}}{\dfrac{1}{\mathrm{Bi}_1} + W + \epsilon\dfrac{1}{\mathrm{Bi}_2}} \cdot \left\{ \frac{\cosh(1-Z)\dfrac{L}{T}\mathrm{Bi}^{1/2} + \mathrm{Bi}^{1/2}\sinh(1-Z)\dfrac{L}{T}\mathrm{Bi}^{1/2}}{\cosh\dfrac{L}{T}\mathrm{Bi}^{1/2} + \mathrm{Bi}^{1/2}\sinh\dfrac{L}{T}\mathrm{Bi}^{1/2}} \right\} \tag{6}$$

where

$$\epsilon = \frac{\mathrm{Bi}_2}{\mathrm{Bi}_2(1-T) + \kappa\mathrm{Bi}^{1/2}\left\{ \dfrac{\sinh\dfrac{L}{T}\mathrm{Bi}^{1/2} + \mathrm{Bi}^{1/2}\cosh\dfrac{L}{T}\mathrm{Bi}^{1/2}}{\cosh\dfrac{L}{T}\mathrm{Bi}^{1/2} + \mathrm{Bi}^{1/2}\sinh\dfrac{L}{T}\mathrm{Bi}^{1/2}} \right\}} \tag{7}$$

Fin Assembly Heat Transfer Rate. The heat flow rate through the fin assembly is most conveniently expressed in the form of an augmentation factor, Aug, defined as the ratio of the heat transfer rate of the finned assembly to that of the unfinned wall operating under the same conditions. In order to evaluate the augmentation factor it is first necessary to determine the heat flow rate through the unfinned wall. This requires the solution of the energy equation,

$$\frac{d^2}{dX^2}\phi_w^*(X) = 0 \tag{8}$$

within the wall, subject to the boundary conditions,

at $X = 0$

$$\frac{d}{dX}\phi_w^*(X) = -\mathrm{Bi}_1(1 - \phi_w^*(X)) \tag{9a}$$

at $X = W$

$$\frac{d}{dX}\phi_w^*(X) = -\mathrm{Bi}_2\phi_w^*(X) \tag{9b}$$

where the differential equation (8) is obtained by performing an energy balance on an infinitesimal element of the wall, and the boundary conditions (9*a*) and (9*b*) describe the convective heat exchange from the surfaces of the wall.

The solution to this problem is

$$\phi_w^*(X) = \frac{-X + W + \dfrac{1}{\mathrm{Bi}_2}}{\dfrac{1}{\mathrm{Bi}_1} + W + \dfrac{1}{\mathrm{Bi}_2}} \tag{10}$$

and therefore

$$\mathrm{Aug} = \frac{\dfrac{1}{\mathrm{Bi}_1} + W + \dfrac{1}{\mathrm{Bi}_2}}{\dfrac{1}{\mathrm{Bi}_1} + W + \epsilon\dfrac{1}{\mathrm{Bi}_2}} \tag{11}$$

Discussion of Fin Assembly Formulation

Comparison with Sum of Resistances Method. In the sum of resistances approach the unfinned wall and the fin assembly are considered analogous to electric circuits as shown in Figs. 2(*a*) and 2(*b*), respectively [6]. On the basis of the heat flow (i.e., "electric current") within these circuits, the augmentation factor takes the form

$$\mathrm{Aug} = \frac{R_1 + R_w + R_2}{R_1 + R_w + \dfrac{1}{R_{\mathrm{ifs}} + R_{\mathrm{fin}}}} \tag{12}$$

where R_1 $(= 1/h_1P)$ and R_2 $(= 1/h_2P)$ are the convective resistances of the surfaces of the wall, R_w $(= w/k_wP)$ is the conductive resistance of the wall, R_{ifs} $(= 1/h_2(P-t))$ is the convective resistance of the interfin surface and R_{fin} $(= 1/h_2(l+t)\eta)$ is the total thermal resistance of the fin. The introduction of the appropriate expression for the fin efficiency η (e.g., as given in Kern and Kraus [7, p. 170]) enables the equation (12) to be reexpressed as,

$$\mathrm{Aug} = \frac{R_1 + R_w + R_2}{R_1 + R_w + \epsilon R_2} \equiv \frac{\dfrac{1}{\mathrm{Bi}_1} + W + \dfrac{1}{\mathrm{Bi}_2}}{\dfrac{1}{\mathrm{Bi}_1} + W + \epsilon\dfrac{1}{\mathrm{Bi}_2}} \tag{13}$$

where ϵ is defined by the equation (7). Thus, the sum of resistances method results in exactly the same solution as that given by the mathematically rigorous formulation presented in the preceding section. The principal reason for this, besides the similarity in the underlying assumptions, is the similarity in the way in which the thermal interaction between the wall and fins is represented. In the sum of resistances method, the thermal resistances of the fin (R_{fin}) and the interfin surface of the wall (R_{ifs}) both branch from the same node, Fig. 2(*b*). Thus, by Kirchoff's Law, the total heat flow to that node is

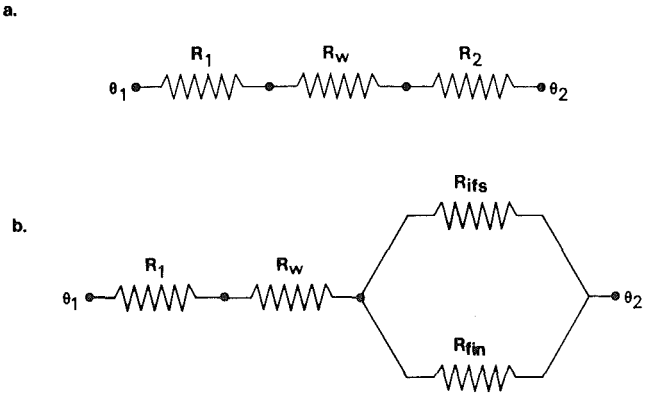

Fig. 2 Thermal curcuit representations for the heat flow within (*a*) the unfinned wall and (*b*) the fin assembly

equal to the sum of the heat flow into the fin and the heat flow across the interfin surface. This is identically equivalent to the boundary condition (3*c*).

Enhancement Factor. From the expression (11) (or (13)) for the augmentation factor, it is apparent that the factor ϵ is the only quantity which involves the fin parameters, namely, the fin length, fin thickness, fin thermal conductivity, and interfin spacing. Thus, the effects of variations in the fin parameters, on the overall heat transfer rate, are indicated solely by this factor ϵ. This is in contrast to the conventional approach in which the fin efficiency η is employed in order to indicate the fin performance, and a separate analysis is performed in order to account for the interfin spacing. Furthermore, because of the relatively simple relationship between this factor ϵ and the augmentation factor, the effect of the fins on the overall heat transfer can easily be deduced from the value of ϵ. In particular, the overall heat transfer rate is enhanced by the addition of fins if, and only if, the fins are arranged in such a manner that the resulting value of ϵ is less than unity; accordingly, ϵ is referred to as the enhancement factor. In addition, this enhancement factor has the property that the smaller its value, the greater is the corresponding augmentation. However, for any given problem, there is an upper limit on the augmentation that can be achieved by the addition of fins. This is denoted by Aug_∞ and corresponds to the ideal case in which $\epsilon = 0$, and the fin heat dissipation is infinite, namely

$$\mathrm{Aug}_\infty = \frac{\dfrac{1}{\mathrm{Bi}_1} + W + \dfrac{1}{\mathrm{Bi}_2}}{\dfrac{1}{\mathrm{Bi}_1} + W} \equiv \frac{R_1 + R_w + R_2}{R_1 + R_w} \qquad (14)$$

It is not practical to design for Aug_∞ because once the fin side resistance ϵR_2, equation (13), is reduced to the value of the sum of the other two resistances, namely R_1 and R_W, any further reductions in ϵR_2 will not yield any significant increase in the heat transfer. Therefore, for sensible utilization of fins the corresponding enhancement factor should be such that the value of ϵR_2 is not less than $R_1 + R_w$, i.e., the augmentation factor should not exceed $\mathrm{Aug}_\infty/2$.

In contrast to the useful design information provided by the enhancement factor, the fin efficiency gives no indication whatsoever regarding the effect of the fins on the overall heat transfer.

Discussion of Results

From the expression (7) it can be deduced that the enhancement factor, ϵ, may be parameterized by the Biot number, Bi_2, the ratio of the thermal conductivities, κ, and the aspect ratios, L and T (since $\mathrm{Bi} = \mathrm{Bi}_2 T/\kappa$). The behaviour of the enhancement factor with variations in these parameters has been extensively examined with a view to understanding the effects of changes in the fin parameters on the overall heat transfer rate. Representative results are given in Figs. 3 and 4. In each of the graphs presented in these figures, the parameters Bi_2 and κ are assigned prescribed values, and then the enhancement factor ϵ is plotted against L for three different values of T. The salient features of these results are discussed below.

The Effects of Variations in the Fin Length. A most prominent feature of the results is the manner in which the enhancement factor inevitably approaches some limiting value as the fin length is increased. This limiting value can in fact be determined analytically by examining the behaviour of ϵ for large values of L.The expression (7) for ϵ can be equivalently expressed as

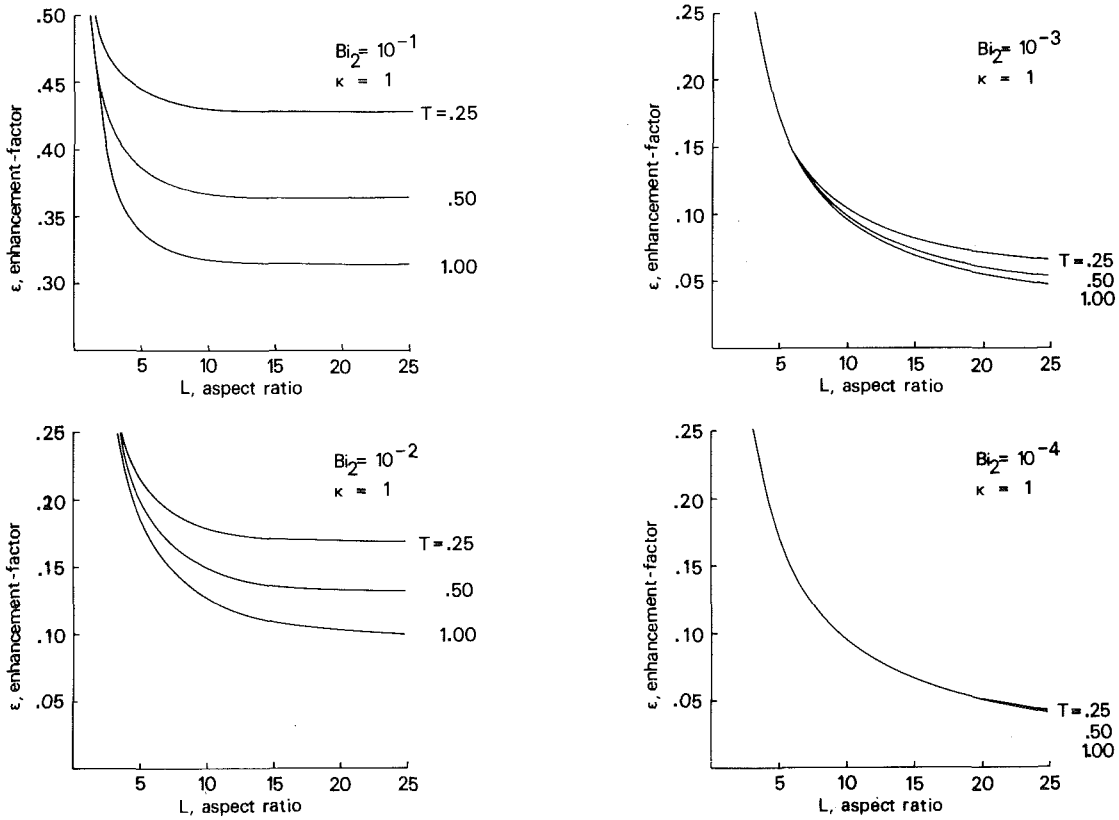

Fig. 3 The effects of variations in Bi_2, L, and T on the enhancement factor, ϵ, for the case $\kappa = 1$

$$\epsilon = \frac{1}{(1-T)+\left(\frac{\kappa T}{\mathrm{Bi}_2}\right)^{1/2}\left\{\frac{\tanh\frac{L}{T}\mathrm{Bi}^{1/2}+\mathrm{Bi}^{1/2}}{1+\mathrm{Bi}^{1/2}\tanh\frac{L}{T}\mathrm{Bi}^{1/2}}\right\}} \quad (15)$$

Therefore, for large values of L

$$\epsilon \sim \frac{1}{(1-T)+\frac{\kappa T}{\mathrm{Bi}_2}^{1/2}} \quad (16)$$

In all cases, the results presented in Figs. 3 and 4 agree with the limiting value predicted by the equation (16).

This tendency of the enhancement factor to approach some limiting value indicates that the overall heat transfer cannot be indefinitely increased by increasing the fin length. It is not immediately apparent why this should be the case. However, an explanation can be formulated from a physical viewpoint. The addition of fins to a plane wall results in an increase in the total heat transfer surface area, but at the same time introduces an additional conductive resistance. Initially, the gain in surface area far outweighs the extra conductive resistance. However, eventually a state is reached such that further increases in the fin length are negated by the respective increases in the conductive resistance.

The Effects of Variation in the Fin Thickness and Fin Pitch. Another prominent aspect of the results presented in Figs. 3 and 4 is the feature that as the Biot number, Bi_2, is reduced, the variation of the enhancement factor with the fin thickness is reduced. In practical terms, reductions in Bi_2 correspond to reductions in the fin pitch, P. A reduction of the fin pitch proportionately reduces the possible variations in the fin thickness and therefore the effect on the enhancement factor is less marked.

A particularly significant deficiency of the one-dimensional analysis is highlighted in the Figs. 3 and 4. The case $T = 1.00$ corresponds to the situation in which the interfin spacing is zero, and, therefore, the fin material effectively increases the wall thickness. This should result in a reduction of the overall heat flow rate and consequently the corresponding value of ϵ should be greater than unity. However, the results show that the corresponding values of ϵ are not only less than unity, but are also less than those for other values of the parameter, T. Thus, the one-dimensional analysis is grossly inappropriate for situations in which the interfin spacing is much less than the fin thickness.

The Effects of Variation in the Fin Thermal Conductivity. The effects of variations in the fin thermal conductivity on the overall heat transfer rate can be deduced by comparing the results for different values of κ. For prescribed fin dimensions, interfin spacing and surface heat transfer coefficient, i.e., for fixed values of L, T, P, and Bi_2, an increase in the fin thermal conductivity, i.e., a higher value of κ, results in a reduction in the value of the enhancement factor (e.g., see Figs. 3 and 4). This reduction can be quite substantial for larger values of Bi_2. Thus, as would be expected, increasing the fin thermal conductivity facilities an increase in the overall heat flow rate.

Conclusions

A mathematically rigorous formulation has been developed for analyzing the heat flow within finned surfaces. The solutions predicted by this formulation are identical to those obtained employing the conventional (mathematically informal) sum of resistances method. However, this new

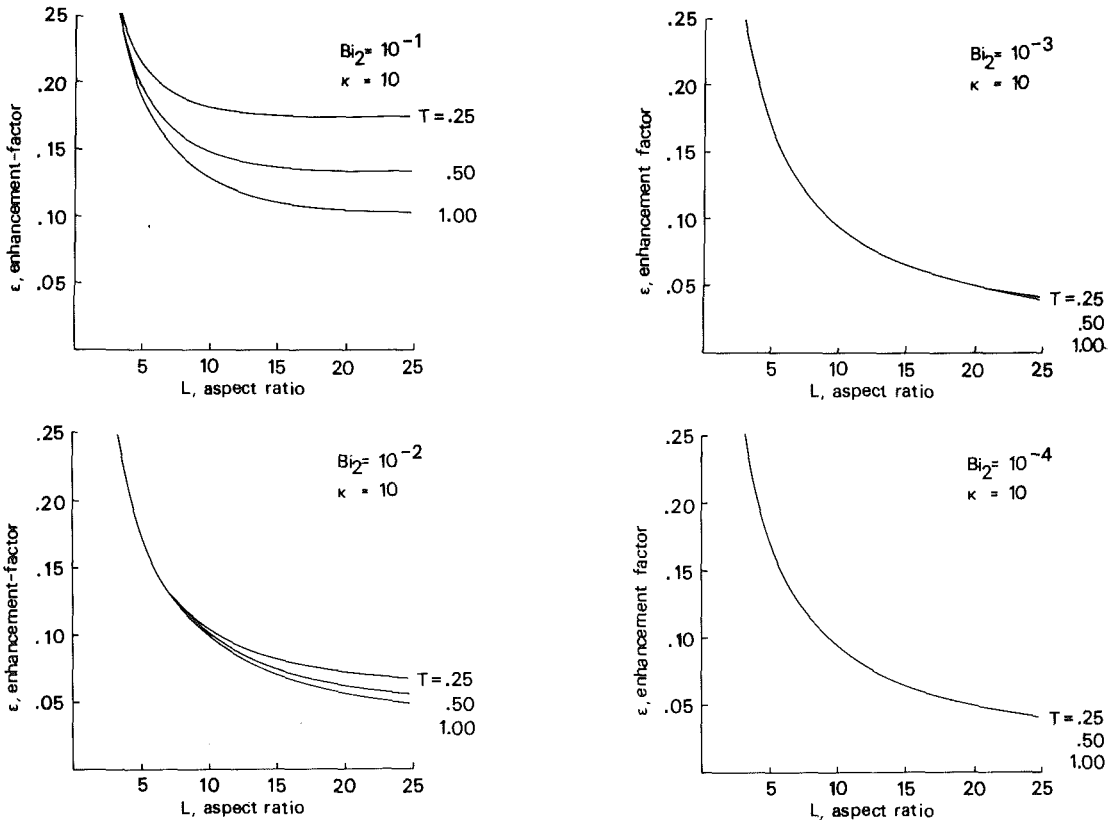

Fig. 4 The effects of variations in Bi_2, L, and T on the enhancement factor, ϵ, for the case $\kappa = 10$

formulation has several advantageous design properties in comparison with the conventional method. In particular, a new factor ϵ is introduced which accounts for the effects of fin dimensions, interfin spacing, and fin thermal conductivity and thereby avoids the need to perform separate design calculations for the various components of the fin assembly, as is necessary with the conventional method.

It must be emphasized that the formulation presented in this paper is equally applicable to other fin profiles and to the annular geometry. In fact, the expressions for the enhancement factor for (*a*) longitudinal rectangular fins attached to a plane wall, (*b*) longitudinal triangular fins attached to a plane wall, (*c*) annular rectangular fins attached to a cylindrical tube, and (*d*) annular triangular fins attached to a cylindrical tube, are tabulated in the Appendix in a form convenient for design purposes, and a complete set of enhancement factor design charts for these four configurations may be obtained from the authors.

References

1 Harper, D. R., and Brown, W. B., "Mathematical Equations for Heat Conduction in the Fins of Air-Cooled Engines," National Advisory Committee for Aeronautics, Report 158, 1922.

2 Gardner, K. A., "Efficiency of Extended Surface," ASME *Transactions*, Vol. 67, 1945, pp. 621–631.

3 Guceri, S., and Maday, C. J., "A Least Weight Circular Cooling Fin," ASME *Journal of Engineering for Industry*, Vol. 97, 1975, pp. 1190–1193.

4 Mikk, I., "Convective Fin of Minimum Mass," *International Journal of Heat and Mass Transfer*, Vol. 23, 1981, pp. 707–711.

5 Heggs, P. J., Ingham, D. B., and Manzoor, M., "The Effects of Nonuniform Heat Transfer From an Annular Fin of Triangular Profile," ASME JOURNAL OF HEAT TRANSFER, Vol. 103, 1981, pp. 184–185.

6 Kreith, F., *Principles of Heat Transfer*, Harper and Row, New York, 1976.

7 Kern, D. Q., and Kraus, A. D., *Extended Surface Heat Transfer*, McGraw-Hill, New York, 1972.

8 Wong, P. W., "Mass and Heat Transfer From Circular Finned Cylinders," *Journal of the Institution of Heating and Ventilating Engineers*, Vol. 23, 1963, pp. 1–23.

9 Stachiewicz, J. W., "Effect of Variation of Local Film Coefficient on Fin Performance," ASME JOURNAL OF HEAT TRANSFER, Vol. 91, 1969, pp. 21–26.

10 Heggs, P. J., and Stones, P. R., "Improved Design Methods for Finned Tube Heat Exchangers," *Transactions of the Institution of Chemical Engineers*, Vol. 58, 1980, pp. 147–154.

11 Irey, R. K., "Errors in the One-Dimensional Fin Solution," ASME JOURNAL OF HEAT TRANSFER, Vol. 90, 1968, pp. 175–176.

12 Levitsky, M., "The Criterion for the Validity of the Fin Approximation," *International Journal of Heat and Mass Transfer*, Vol. 15, 1972, pp. 1960–1963.

13 Lau, W., and Tan, C. W., "Errors in One-Dimensional Heat Transfer Analysis in Straight and Annular Fins," ASME JOURNAL OF HEAT TRANSFER, Vol. 95, 1973, pp. 549–551.

14 Sparrow, E. M., and Lee, L., "Effects of Fin-Base Temperature Depression in a Multifin Array," ASME JOURNAL OF HEAT TRANSFER, Vol. 97, 1975, pp. 463–465.

15 Suryanarayana, N. V., "Two-dimensional Effects on Heat Transfer From an Array of Straight Fins," ASME JOURNAL OF HEAT TRANSFER, Vol. 99, 1977, pp. 129–132.

16 Heggs, P. J., and Stones, P. R., "The Effects of Dimensions on the Heat Flowrate Through Extended Surfaces," ASME JOURNAL OF HEAT TRANSFER, Vol. 102, 1980, pp. 180–182.

APPENDIX

Expressions for the Enhancement Factor ϵ

Longitudinal fins attached to a plane wall

(*a*)	Rectangular profile	$\mathrm{Bi}_2/\left\{\mathrm{Bi}_2(1-T)\text{-}\kappa\mathrm{Bi}^{1/2}\dfrac{(\tanh\xi+\mathrm{Bi}^{1/2})}{(1+\mathrm{Bi}^{1/2}\tanh\xi)}\right\}$, where $\xi=\dfrac{L}{T}\mathrm{Bi}^{1/2}$
(*b*)	Triangular profile	$\mathrm{Bi}_2/\left\{\mathrm{Bi}_2(1-T)+\kappa\dfrac{\mathrm{Bi}}{\cos\alpha}\dfrac{I_1(\xi)}{I_0(\xi)}\right\}$, where $\xi=2\dfrac{L}{T}\dfrac{\mathrm{Bi}}{\cos\alpha}$

Annular fins attached to a cylindrical tube

(*c*)	Rectangular profile[a]	$\mathrm{Bi}_2/\left\{\mathrm{Bi}_2(1-T)+\kappa\mathrm{Bi}^{1/2}\dfrac{(K_1(\xi)I(\eta)-I_1(\xi)K(\eta))}{(K_0(\xi)I(\eta)+I_0(\xi)K(\eta))}\right\}$ where $\xi=\dfrac{R_b}{T}\mathrm{Bi}^{1/2}$, $\eta=\dfrac{R_t}{T}\mathrm{Bi}^{1/2}$, $I(\eta)=I_1(\eta)+\mathrm{Bi}^{1/2}I_0(\eta)$ and $K(\eta)=K_1(\eta)-\mathrm{Bi}^{1/2}K_0(\eta)$
(*d*)	Triangular profile[a]	$\mathrm{Bi}_2/\left\{\mathrm{Bi}_2(1-T)+\kappa\dfrac{T}{L}\left(\sum_{n=1}^{\infty}n\,a_n\Big/\sum_{n=0}^{\infty}a_n\right)\right\}$ where $a_0=1$, $a_1=\xi$, $a_2=(\{n(n+1)+\xi\eta\}a_{n-1}-\xi a_n)/n^2\eta$, $n\geq 2$ with $\xi=\left(\dfrac{L}{T}\right)^2\dfrac{\mathrm{Bi}}{\cos\alpha}$ and $\eta=\dfrac{Rt}{L}$

[a] $R_b=r_b/P$, $R_t=r_t/P$; where r_b is the radius of the fin base and r_t is the radius of the fin tip

Journal of Heat Transfer

Technical Notes

This section contains shorter technical papers. These shorter papers will be subjected to the same review process as that for full papers.

Natural Convection Experiments in a Triangular Enclosure

D. Poulikakos[1] and A. Bejan[2]

Nomenclature

g = gravitational acceleration, ms^{-2}
H = maximum height of the enclosure, m
k = thermal conductivity, $Wm^{-1}K$
L = length of the enclosure, m
Nu = Nusselt number, equation (3)
Q = net heat transfer rate, W, equation (3)
Ra = Rayleigh number based on maximum height, equation (4)
Re = Reynolds number, equation (2)
St = Strouhal number, equation (1)
T_B = bursting period, s, equation (1)
T_c = cold (top) wall temperature, K
T_H = warm (bottom) wall temperature, K
T_m = mean temperature, K, $T_m = (T_H + T_c)/2$
ΔT = temperature difference between warm and cold walls, K
Δt = time interval, s
V = streak velocity to the right, ms^{-1}
W = width of the enclosure, m
x = longitudinal position, m

Greek Symbols

α = thermal diffusivity, $m^2\ s^{-1}$
β = coefficient of volumetric thermal expansion, K^{-1}
δ = boundary layer thickness, m
ν = kinematic viscosity, $m^2\ s^{-1}$

Introduction

The object of this note is to report the results of a study of steady natural convection heat transfer in an attic-shaped (triangular) space. The general subject of natural convection in enclosures has received considerable attention; however, most of this research has been focused on rectangular enclosures [1, 2]. Two recent papers by Flack, Konopnicki, and Rooke [3] and Flack [4] discuss for the first time the phenomenon of natural circulation in air-filled triangular enclosures, in the range $7.5 \times 10^4 < \text{Ra} < 10^6$. This range of Rayleigh numbers characterizes solar collector spaces of triangular shape; however, it is much too low to be relevant to the study of natural convection in building-sized spaces. For example, in an attic the Rayleigh number reaches as high as 10^8–10^9.

The experiment described in this note was designed to shed light on the unknown phenomenon which might occur in a large-scale system, for example, in a life-size attic space or in ocean waters near shores with sloping bottoms. For this reason, the experimental study focused on: (*i*) a high Rayleigh number range not studied before, 10^6–10^9; (*ii*) the flow regime and, especially, those flow features which may prove essential in the future effort of modeling the phenomenon analytically. These objectives were achieved using a relatively large apparatus filled with air or water. The experiment simulated the "night" mode of operation of an attic space, or the "day" mode of a shallow-sloped coastal body of water heated from below by solar radiation. This simulation consisted of cooling the upper wall and heating the bottom wall of the experimental enclosure. The opposite operating regime (warm top, cold bottom) was shown earlier to be dominated by pure conduction [4].

Experimental Apparatus

The main feature of the apparatus is a triangular cavity of length $L = 737$ mm, height $H = 152$ mm, and width $W = 559$ mm. The height to length ratio is therefore, $H/L = 0.207$. The enclosure is shown drawn to scale in Fig. 1. The top and bottom walls were constructed out of massive pieces of aluminum of thickness 19 mm. Along these walls we achieved acceptable isothermal conditions (within 1°C). The side walls were constructed out of plexiglas plate with a thickness of 19 mm. The sloping wall was maintained at constant temperature by means of a jacket filled with chilled alcohol supplied by a constant temperature bath refrigerator. The refrigerator was capable of controlling the coolant temperature within 0.1°C. The base wall was heated with eight electric strip heaters capable of dissipating a maximum power of 1000 W.

The temperature of the aluminum plates was measured using ten Chromel-Alumel thermocouples (five on each plate) equally spaced along the centerline of the apparatus (Fig. 1). The thermocouples were imbedded in the aluminum walls at a distance of 1.6 mm from the surface facing the inside of the enclosure. In order to prevent the direct thermal contact between the top (cold) and bottom (warm) walls, we adopted the "truncated tip" design shown in Fig. 1.

The experiments were performed using distilled water and air in the triangular cavity. A sequence of steady states was achieved by varying the electric heat input to the bottom wall and keeping the top wall at constant temperature. The

[1]Department of Mechanical Engineering, University of Illinois at Chicago, Chicago, Ill. 60680.
[2]Department of Mechanical Engineering, University of Colorado, Boulder, Colo. 80309, Assoc. Mem. ASME
Contributed by the Heat Transfer Division for publication in the JOURNAL OF HEAT TRANSFER. Manuscript received by the Heat Transfer Division, September 20, 1982.

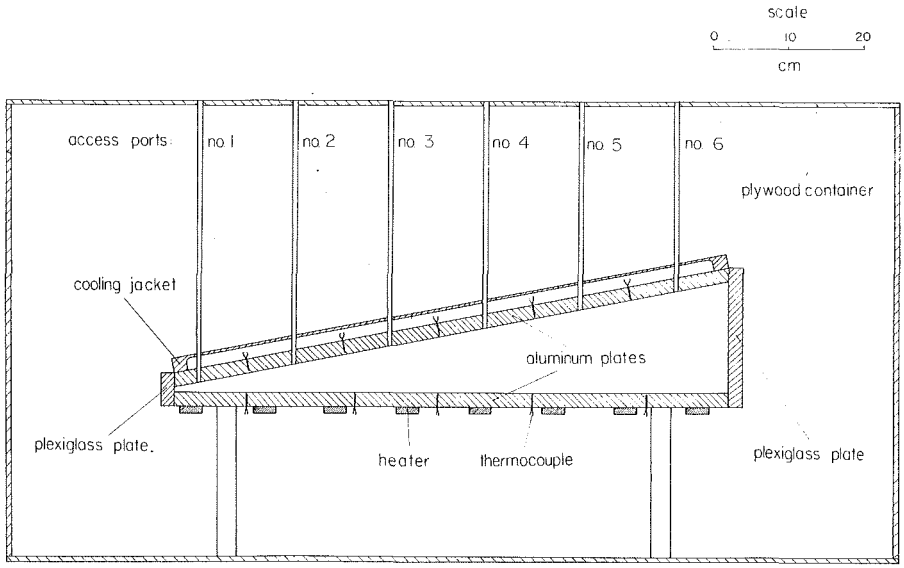

Fig. 1 Schematic of experimental apparatus

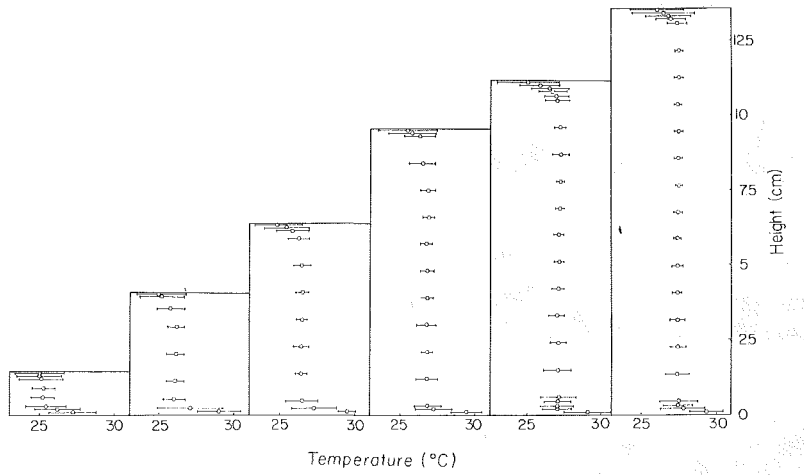

Fig. 2 Average temperature distribution and standard deviation, Ra = 4.7×10^8

fluctuations of the voltage supplied to the electric heaters were successfully reduced by installing a constant-voltage transfomer between the voltage supply and the heaters. The apparatus was insulated on all sides with 200 mm of fiberglass insulation supported by an outer container of 13-mm thick plywood (Fig. 1). During the flow visualization phase of this study, the insulation covering the side windows (the triangular walls) was removed in order to be able to photograph the flow: This operation had no effect on the flow, as it lasted only 1 min, which is "very fast" relative to transient natural convection in a cavity filled with water.

Overall, the experimental apparatus simulates an asymmetic triangualr space of the kind found in an attic whose roof is supported structurally by a vertical wall positioned under the crest. However, since the vertical side wall is insulated and since the flow is driven by the sloped wall, it is felt that the flow and heat transfer picture revealed by the present experiments is also an adequate description of the natural convection phenomenon occurring in a symmetric triangular space (as in an A-shaped attic).

Temperature Measurements

The temperature field inside the triangular enclosure was probed using a variable depth Chromel-Alumel thermocouple of 0.4-mm bead diameter. The thermocouple was mounted at the end of a stiff stainless steel capillary tube which was lowered to any desired depth through six access ports. The thermocouple voltage was measured with a digital voltmeter yielding temperature measurements accurate within 0.05°C.

Extensive temperature measurements were made at one of the highest Rayleigh numbers achieved in the apparatus, Ra $= 4.7 \times 10^8$: this appears to be the highest Rayleigh number studied experimentally in connection with natural convection in triangular enclosures. The flow regime at this high Rayleigh number was found to be turbulent; this finding agrees with Flack's observations of natural convection in an air-filled triangular enclosure, at much lower Rayleigh numbers ($7.5 \times 10^4 < \text{Ra} < 10^6$). The time-averaged temperature at each point was determined after taking measurements at time intervals of 3 s over a period of 5 min. Figure 2 shows the temperature variation under each access port. Both the time-averaged temperature and the standard deviation are reported. The basic feature of the temperature field is the presence of an approximately isothermal core which covers most of the local height. Near the top and the bottom, the temperature distribution departs abruptly from the isothermal pattern present in the core, indicating the presence of thermal boundary layers. The temperature fluctuation range is considerably smaller in the core than near the walls,

showing that the turbulence intensity decreases away from each wall.

Flow Visualization

To visualize the flow we used the thymol blue pH indicator technique developed by Baker [5]. This technique was used successfully in a number of natural convection experiments [6–9]. In the present study, we lowered a vertical stainless steel wire (welding rod, 0.8-mm dia) through each access port. We then applied 6 V between the wire (cathode) and the nearest aluminum plate. As shown in Fig. 3, a dark streak was generated at the exposed (1.8-mm long) tip of the vertical wire. Since the flow was turbulent, we studied the local characteristics of the flow at discrete points, rather than trying to measure complete velocity profiles under each port.

Figure 3 shows the evolution of the dark streak released from the tip of the wire at a distance of 4 mm from the bottom wall, under port no. 5. The photographs were taken at time intervals $\Delta t = 2$s. The evolution of the streak reveals the existence of a turbulent jet moving to the right (away from the tip of the enclosure). The "hill-valley" flow structure shown in Fig. 3 proves the existence of a periodic fluid motion which consists of an "eruption away from the wall followed by inrush towards the wall" [10]. The mechanism responsible for eruptions and inrushes is still open to question; however, it is often suggested that the eruptions are produced by an "instability" of the boundary layer region. The large scale features documented in Fig. 3 are also encountered in the transition to turbulence in boundary layer flow.

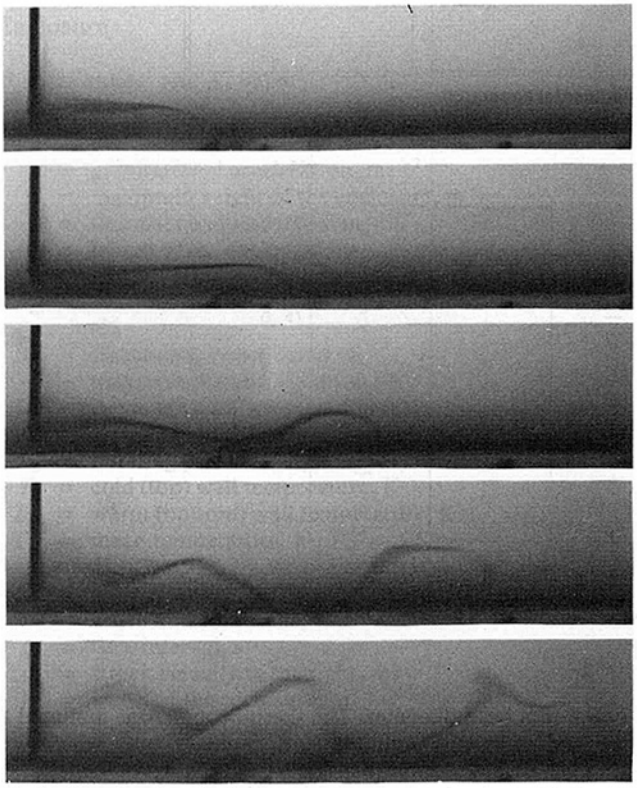

Fig. 3 Streak pattern in the bottom jet at access port no. 5, Ra = 4.7 × 10^8, Δt = 2 s

The bursting period, T_B (time between two consecutive bursts or in-rushes at a fixed point on the wall), can be calculated and cast in a dimensionless form as a Strouhal number

$$\mathrm{St} = \frac{\delta}{T_B V} \tag{1a}$$

where δ, V are the boundary layer thickness and the velocity of the top of the dark streak. From Fig. 3 we found

$$\mathrm{St} = \frac{1}{6.1} \tag{1b}$$

This result matches perfectly the growing volume of measurements on the bursting frequency of turbulent boundary layers, (the experimental measurements are usually reported as $T_B V/\delta \approx 5$, which is predicted by the buckling theory of inviscid flow [10]). The Reynolds number for the boundary layer flow was

$$\mathrm{Re} = \frac{\delta V}{\nu} = 41 \tag{2}$$

The size of the boundary layer thickness, δ, used in equations (1) and (2) was taken as approximately equal to the amplitude of the sinuous fluid motion (Fig. 3). The bursting period, T_B, appearing in equation (1) was estimated as the wavelength of the sinuous streak divided by the speed of the wave (to the right in Fig. 3). It is important to note that the sinuous streak shown here in Fig. 3 is a property of the boundary layer, as a flow region of thickness, δ. It is observed that the sinuous character of the streak does not depend on the specific position of the probe, as long as the distance between the blue-generating tip of the probe and the wall is less than δ.

More flow visualization results have been compiled in [11].

Heat Transfer Results

The heat transfer results are reported in Fig. 4 as a plot of Nusselt number versus Rayleigh number

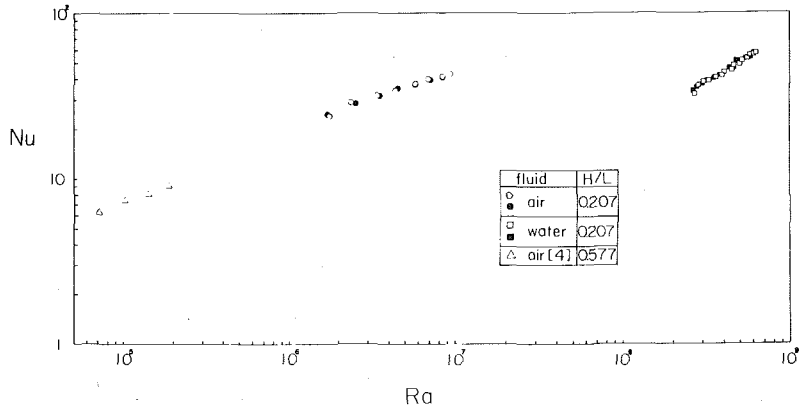

Fig. 4 Summary of heat transfer measurements: Direction of experiments: ○ □ increasing Q; ● ■ decreasing Q

$$\mathrm{Nu} = QH/(kWL\Delta T) \quad (3)$$

$$\mathrm{Ra} = g\beta H^3 \Delta T/(\alpha\nu) \quad (4)$$

For each steady state achieved in the apparatus, we measured the top and bottom plate temperatures using the ten thermocouples (five on each plate) located as shown in Fig. 1. The arithmetic means of the measured local temperatures were used as the top and bottom wall temperatures. The physical properties appearing in the definitions of Nu and Ra were evaluated at the arithmetic mean temperature of the top and bottom walls. The net heat transfer rate, Q, was measured electrically, by recording the voltage across the current through the bottom heaters. Thus, the measured Q value includes the effect of radiation, which is negligible in the temperature range of this experiment.

A separate experiment showed that the heat leak through the insulation is negligible (roughly 1.5 percent); in this experiment there was no coolant in the top wall jacket, so that the electric heat input was balanced by the leakge of heat across the fiberglass insulation surrounding the apparatus.

In order to check the validity of our high Ra measurements, we ran the same heat transfer experiment with air as the working fluid: heat transfer data for an air-filled triangular space have already been reported [4]. In our air experiment the Rayleigh number range was 10^6–10^7, which is still considerably higher than the regime tested in [4] ($7.5 \times 10^4 < \mathrm{Ra} < 2 \times 10^5$). In [4], $H/L = 0.577$ was the aspect ratio closest to the aspect ratio of the present experiment ($H/L = 0.207$). The heat leak for the present air experiment was manageable, of order 25 percent. Figure 4 shows that our results are in good agreement with Flack's [4]. It should be noted that the results of [4] were reported based on the overall temperature difference $\Delta T = T_H - T_m$, where $T_m = (T_H + T_L)/2$ (in other words, Flack's ΔT is half the ΔT used to report Nu and Ra in the present experiments, equation (3, 4)). In the present notation, Flack's data of Fig. 9 are correlated by

$$\mathrm{Nu} = 0.225\ \mathrm{Ra}^{0.3},\ (H/L = 0.577,\ \text{air},\ 7.5\times10^4 < \mathrm{Ra} < 2\times10^5) \quad (5)$$

whereas the present measurements for air follow the curve

$$\mathrm{Nu} = 0.345\ \mathrm{Ra}^{0.3},\ (H/L = 0.207,\ \text{air},\ 10^6 < \mathrm{Ra} < 10^7) \quad (6)$$

The fact that the numerical coefficients in the two Nu correlations (5, 6) are similar indicates that the aspect ratio, H/L, plays only a minor role in the Nu function. Note that Flack [4] found that decreasing H/L increases Nu for a given Ra.

The Nusselt number measurements obtained with the cavity filled with water are correlated within 4 percent by

$$\mathrm{Nu} = 0.00038\mathrm{Ra}^{0.59},\ (H/L = 0.207,\ \text{water},\ 2.5\times10^8 < \mathrm{Ra} < 6.5\times10^8) \quad (7)$$

This Nu result shows a relatively strong dependence on Rayleigh number. Recalling the Prandtl number difference between water and air, equation (7) can only be regarded as an approximate guide for heat transfer calculations concerning attic spaces filled with air. However, since in the air-water range of Pr numbers the Nusselt number is influenced only slightly by Pr, the high-Ra water data represent a better approximation of Nu than the extrapolation of the low-Ra air data.

Finally, we checked the repeatability of our data by running the heat transfer experiments in the reverse direction, i.e., by gradually decreasing the power dissipated in the bottom heaters while keeping the coolant temperature constant. Figure 4 shows that the Nu-Ra measurements do not depend on the direction of the experiment (the history of the apparatus).

Acknowledgment

This research was supported by the National Science Foundation, through grant no. ENG78-20957. The authors thank Prof. Jorg Imberger of the University of Western Australia for his part in defining the present research topic. Messrs Michael Hacker, Karl Rupp, and Richard Cowgill constructed the apparatus and its instrumentation.

References

1 Ostrach, S., "Natural Convection in Enclosures," *Advances in Heat Transfer*, Vol. 8, 1972, p. 161.

2 Catton, I., "Natural Convection in Enclosures," Keynote Paper, *Proceedings of the 6th Internatinal Heat Transfer Conference, Toronto 1978*, Vol. 6, 1979, pp. 13–43.

3 Flack, R. D., Konopnicki, T. T., and Rooke, J. H., "The Measurement of Natural Convective Heat Transfer in Triangular Enclosures," ASME JOURNAL OF HEAT TRANSFER, Vol. 101, No., 4, Nov. 1979, pp. 648–654.

4 Flack, R. D., "The Experimental Measurement of Natural Convection Heat Transfer in Triangular Enclosures Heated or Cooled from Below," ASME JOURNAL OF HEAT TRANSFER, Vol. 102, Nov. 1980, pp. 770–772.

5 Baker, D. J., "A Technique for the Precise Measurement of Small Fluid Velocities," *Journal of Fluid Mechanics*, Vol. 26, 1966, pp. 573–575.

6 Imberger, J., "Natural Convection in a Shallow Cavity With Differentially Heated End Walls, Part 3: Experimental Results," *Journal of Fluid Mechanics*, Vol. 65, 1974, p. 246.

7 Kimura, S., and Bejan, A., "Experimental Study of Natural Convection in a Horizontal Cylinder With Different End Temperatures," *International Journal of Heat and Mass Transfer*, Vol. 23, 1980, pp. 1117–1126.

8 Sparrow, E. M., Husar, R. B., and Goldstein, R. J., "Observations and Other Characteristics of Thermals," *Journal of Fluid Mechanics*, Vol. 41, 1970, pp. 793–800.

9 Vedhanayagam, M. Lienhard, J. H., and Eichhorn, R., "Method for Visualizing High Prandtl Number Heat Convection," *ASME* JOURNAL OF HEAT TRANSFER, Vol. 101, 1979, pp. 571–573.

10 Bejan, A., *Entropy Generation Through Heat and Fluid Flow*, Wiley, New York, 1982, p. 87.

11 Poulikakos, D., "Natural Convection in a Triangular Enclosure Filled With Newtonian Fluid or Fluid-Saturated Porous Medium," Ph.D. thesis, University of Colorado, Boulder, May 1983.

Variable Fluid Property Effects on Transport in Pure Water Around the Density Extremum

R. D. Padlog[1] and J. C. Mollendorf[2]

Nomenclature

b,c = similarity functions, $G/4x$ and G
C_p = fluid specific heat
d = temperature difference, $T_o - T_\infty$
f = nondimensional stream function, $\psi/\nu c$
$f(0)$ = nondimensional streamfunction at the surface
$f(\infty)$ = nondimensional streamfunction far from surface
g = gravitational acceleration
G = modified Grashof number, $4\sqrt[4]{\mathrm{Gr}_x/4}$
Gr_x = local Grashof number, $gx^3\Delta\rho_r/\nu^2$
h_{il} = latent heat of melting (h_{il} = 79.77 cal/gm)

[1]Analytical Engineer, Turbocompressor Division, Joy Machinery Company, Buffalo, N.Y. 14225

[2]Associate Professor, Department of Mechanical and Aerospace Engineering, State University of New York at Buffalo, Amherst, N.Y. 14260. MEM. ASME

Contributed by the Heat Transfer Division for publication in the JOURNAL OF HEAT TRANSFER. Manuscript received by the Heat Transfer Division November 8, 1982.

$$\mathrm{Nu} = QH/(kWL\Delta T) \quad (3)$$

$$\mathrm{Ra} = g\beta H^3 \Delta T/(\alpha\nu) \quad (4)$$

For each steady state achieved in the apparatus, we measured the top and bottom plate temperatures using the ten thermocouples (five on each plate) located as shown in Fig. 1. The arithmetic means of the measured local temperatures were used as the top and bottom wall temperatures. The physical properties appearing in the definitions of Nu and Ra were evaluated at the arithmetic mean temperature of the top and bottom walls. The net heat transfer rate, Q, was measured electrically, by recording the voltage across the current through the bottom heaters. Thus, the measured Q value includes the effect of radiation, which is negligible in the temperature range of this experiment.

A separate experiment showed that the heat leak through the insulation is negligible (roughly 1.5 percent); in this experiment there was no coolant in the top wall jacket, so that the electric heat input was balanced by the leakge of heat across the fiberglass insulation surrounding the apparatus.

In order to check the validity of our high Ra measurements, we ran the same heat transfer experiment with air as the working fluid: heat transfer data for an air-filled triangular space have already been reported [4]. In our air experiment the Rayleigh number range was 10^6–10^7, which is still considerably higher than the regime tested in [4] ($7.5 \times 10^4 < \mathrm{Ra} < 2 \times 10^5$). In [4], $H/L = 0.577$ was the aspect ratio closest to the aspect ratio of the present experiment ($H/L = 0.207$). The heat leak for the present air experiment was manageable, of order 25 percent. Figure 4 shows that our results are in good agreement with Flack's [4]. It should be noted that the results of [4] were reported based on the overall temperature difference $\Delta T = T_H - T_m$, where $T_m = (T_H + T_L)/2$ (in other words, Flack's ΔT is half the ΔT used to report Nu and Ra in the present experiments, equation (3, 4)). In the present notation, Flack's data of Fig. 9 are correlated by

$$\mathrm{Nu} = 0.225\ \mathrm{Ra}^{0.3},\ (H/L = 0.577,\ \text{air},\ 7.5\times10^4 < \mathrm{Ra} < 2\times10^5) \quad (5)$$

whereas the present measurements for air follow the curve

$$\mathrm{Nu} = 0.345\ \mathrm{Ra}^{0.3},\ (H/L = 0.207,\ \text{air},\ 10^6 < \mathrm{Ra} < 10^7) \quad (6)$$

The fact that the numerical coefficients in the two Nu correlations (5, 6) are similar indicates that the aspect ratio, H/L, plays only a minor role in the Nu function. Note that Flack [4] found that decreasing H/L increases Nu for a given Ra.

The Nusselt number measurements obtained with the cavity filled with water are correlated within 4 percent by

$$\mathrm{Nu} = 0.00038\mathrm{Ra}^{0.59},\ (H/L = 0.207,\ \text{water},\ 2.5\times10^8 < \mathrm{Ra} < 6.5\times10^8) \quad (7)$$

This Nu result shows a relatively strong dependence on Rayleigh number. Recalling the Prandtl number difference between water and air, equation (7) can only be regarded as an approximate guide for heat transfer calculations concerning attic spaces filled with air. However, since in the air-water range of Pr numbers the Nusselt number is influenced only slightly by Pr, the high-Ra water data represent a better approximation of Nu than the extrapolation of the low-Ra air data.

Finally, we checked the repeatability of our data by running the heat transfer experiments in the reverse direction, i.e., by gradually decreasing the power dissipated in the bottom heaters while keeping the coolant temperature constant. Figure 4 shows that the Nu-Ra measurements do not depend on the direction of the experiment (the history of the apparatus).

Acknowledgment

This research was supported by the National Science Foundation, through grant no. ENG78-20957. The authors thank Prof. Jorg Imberger of the University of Western Australia for his part in defining the present research topic. Messrs Michael Hacker, Karl Rupp, and Richard Cowgill constructed the apparatus and its instrumentation.

References

1 Ostrach, S., "Natural Convection in Enclosures," *Advances in Heat Transfer*, Vol. 8, 1972, p. 161.

2 Catton, I., "Natural Convection in Enclosures," Keynote Paper, *Proceedings of the 6th Internatinal Heat Transfer Conference, Toronto 1978*, Vol. 6, 1979, pp. 13–43.

3 Flack, R. D., Konopnicki, T. T., and Rooke, J. H., "The Measurement of Natural Convective Heat Transfer in Triangular Enclosures," ASME JOURNAL OF HEAT TRANSFER, Vol. 101, No., 4, Nov. 1979, pp. 648–654.

4 Flack, R. D., "The Experimental Measurement of Natural Convection Heat Transfer in Triangular Enclosures Heated or Cooled from Below," ASME JOURNAL OF HEAT TRANSFER, Vol. 102, Nov. 1980, pp. 770–772.

5 Baker, D. J., "A Technique for the Precise Measurement of Small Fluid Velocities," *Journal of Fluid Mechanics*, Vol. 26, 1966, pp. 573–575.

6 Imberger, J., "Natural Convection in a Shallow Cavity With Differentially Heated End Walls, Part 3: Experimental Results," *Journal of Fluid Mechanics*, Vol. 65, 1974, p. 246.

7 Kimura, S., and Bejan, A., "Experimental Study of Natural Convection in a Horizontal Cylinder With Different End Temperatures," *International Journal of Heat and Mass Transfer*, Vol. 23, 1980, pp. 1117–1126.

8 Sparrow, E. M., Husar, R. B., and Goldstein, R. J., "Observations and Other Characteristics of Thermals," *Journal of Fluid Mechanics*, Vol. 41, 1970, pp. 793–800.

9 Vedhanayagam, M. Lienhard, J. H., and Eichhorn, R., "Method for Visualizing High Prandtl Number Heat Convection," *ASME* JOURNAL OF HEAT TRANSFER, Vol. 101, 1979, pp. 571–573.

10 Bejan, A., *Entropy Generation Through Heat and Fluid Flow*, Wiley, New York, 1982, p. 87.

11 Poulikakos, D., "Natural Convection in a Triangular Enclosure Filled With Newtonian Fluid or Fluid-Saturated Porous Medium," Ph.D. thesis, University of Colorado, Boulder, May 1983.

Variable Fluid Property Effects on Transport in Pure Water Around the Density Extremum

R. D. Padlog[1] and J. C. Mollendorf[2]

Nomenclature

b,c = similarity functions, $G/4x$ and G
C_p = fluid specific heat
d = temperature difference, $T_o - T_\infty$
f = nondimensional stream function, $\psi/\nu c$
$f(0)$ = nondimensional streamfunction at the surface
$f(\infty)$ = nondimensional streamfunction far from surface
g = gravitational acceleration
G = modified Grashof number, $4\sqrt[4]{\mathrm{Gr}_x/4}$
Gr_x = local Grashof number, $gx^3\Delta\rho_r/\nu^2$
h_{il} = latent heat of melting (h_{il} = 79.77 cal/gm)

[1]Analytical Engineer, Turbocompressor Division, Joy Machinery Company, Buffalo, N.Y. 14225

[2]Associate Professor, Department of Mechanical and Aerospace Engineering, State University of New York at Buffalo, Amherst, N.Y. 14260. MEM. ASME

Contributed by the Heat Transfer Division for publication in the JOURNAL OF HEAT TRANSFER. Manuscript received by the Heat Transfer Division November 8, 1982.

I_w = integrated buoyancy force, $\int_0^\infty W d\eta$

I_m = integrated momentum flux, $\int_0^\infty (f')^2 d\eta$

k = fluid thermal conductivity

Pr = fluid Prandtl number, $\mu C_p/k$

q = exponent in density equation ($q = 1.894916$)

R = density extremum parameter, $(T_m - T_\infty)/(T_o - T_\infty)$

T = temperature

u = vertical component of velocity, $(\rho_r/\rho)\frac{\partial \psi}{\partial y}$

v = horizontal component of velocity, $-(\rho_r/\rho)\frac{\partial \psi}{\partial x}$

W = buoyancy force

x = vertical distance measured from leading edge

y = horizontal distance from the surface

α = coefficient in density equation ($\alpha = 9.297173 \times 10^{-6}\,°C^{-q}$)

$\Delta\rho_r$ = scaling density difference for the buoyancy term, $\alpha|T_o - T_m|^q$

η = similarity variable, $y\sqrt{b}$

μ = fluid absolute viscosity

ν = fluid kinematic viscosity

ρ = fluid density

ϕ = temperature excess ratio, $(T - T_\infty)/(T_o - T_\infty)$

$\phi'(0)$ = derivative of temperatures excess ratio at the plate

ψ = streamfunction, νcf

Subscripts

m = extremum condition (e.g., $T_m = 4.029325\,°C$)

o = fluid-solid interface

r = reference value

∞ = ambient medium condition

Introduction

Numerous previous studies of buoyancy induced flows in cold water have been described by Gebhart and Mollendorf [1]. Ice melting experiments were done in pure water by Bendell and Gebhart [2] followed by measurements in pure and saline water by Johnson and Mollendorf [3]. At small temperature differences, the error between experiment and the constant property theory of [1] is very small. However, as the temperature difference increases, the data are seen to be about 15 percent lower than constant property theory at about 20°C.

In an attempt to explain the difference between constant property calculations and previous experiments, this study extends the variable property calculations of Shaukatullah and Gebhart [4] to include the region of convective inversion. Convective boundary layer flow is considered adjacent to an isothermal flat plate, which is in water at atmospheric pressure. Complications due to ice melting are considered, inasmuch as the effect of melted water produced is included in the boundary conditions as blowing and is shown to have an important effect on heat transfer.

Analysis

Using the transformations given in the Nomenclature, the governing equations and boundary conditions used by [4] become

$$\left(\frac{k}{k_r}\frac{\rho}{\rho_r}\phi'\right)' + 3\mathrm{Pr}_r\frac{C_p}{C_{p_r}} f\phi' = 0 \tag{1}$$

$$\left(\frac{\mu}{\mu_r}\frac{\rho}{\rho_r}f''\right)' + 3ff'' - 2f'^2 \pm \frac{(\rho_\infty/\rho - 1)}{\Delta\rho_r} = 0 \tag{2}$$

$$f(0) = f'(0) = \phi(0) - 1 = f'(\infty) = \phi(\infty) = 0 \tag{3}$$

where primes denote differentiation with respect to η, and where μ_r, k_r, ρ_r, C_{p_r} and Pr_r are constant properties taken at some arbitrary reference temperature, in this case $(T_o + T_\infty)/2$.

For pure water, at one atmosphere, the following relations from Kukulka [5] were used to characterize property variation with temperature: k(cal/cm°C s) = $0.001365\,(1 + 0.003T + 1.025 \times 10^{-5}T^2)$, C_p(cal/gm°C) = $1.0099 - 3.2506 \times 10^{-4}T + 3.8013 \times 10^{-6}T^2$, μ(centipose) = $1.79084 - 6.144 \times 10^{-2}T + 1.451\,T^2 - 1.6826 \times 10^{-5}T^3$, $\rho(\mathrm{gm/cm^3}) = \rho_m(1 - \alpha|T - T_m|^q)$. Where temperature is in °C and, within the range $0 \le T \le 20$°C, the property relations used are accurate to 5 percent for μ, C_p, k and 3 parts per million for ρ.

For the case of ice melting, blowing is subsequently shown to be important. The only change is the boundary condition, $f(0) = 0$. Equating the heat transfer to the latent heat absorbed by the melt-water gives the following boundary condition

$$k_o\frac{\partial T}{\partial y} = h_{i1}\rho_o V(0) \tag{4}$$

Or, in similarity form:

$$f(0) = -\frac{\phi'(0)C_p(T_o - T_\infty)}{3\mathrm{Pr}h_{i1}} \tag{5}$$

In the numerical integration, a new value of $f(0)$ was

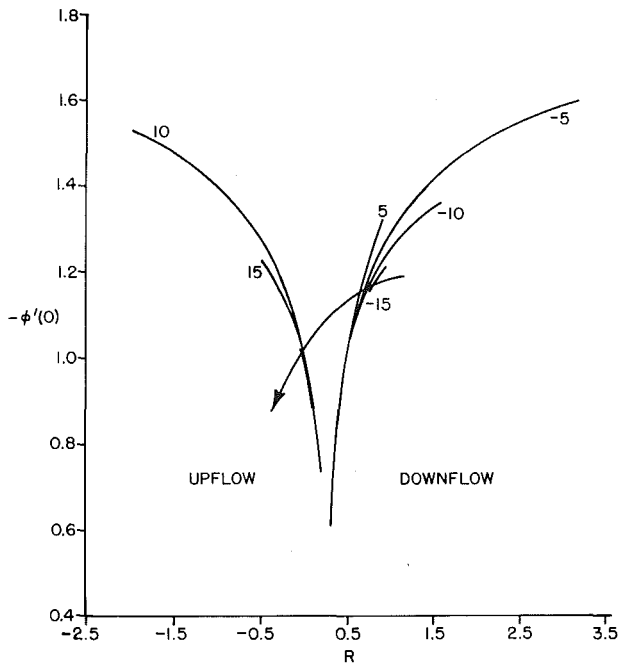

Fig. 1 Variation of heat transfer, $\phi'(0)$, with R. Arrows indicate increasing values of d, as shown.

Table 1 Values of calculated transport quantities at various d and R with blowing

d	R	$\phi'(0)$	$f''(0)$	$f(\infty)$	I_w	I_m
−5.000	3.200	−1.5995	1.3811	.3979	−1.8422	.0743
−5.000	3.000	−1.5869	1.3065	.3887	−1.7408	.0695
−5.000	2.800	−1.5727	1.2309	.3792	−1.6387	.0648
−5.000	2.600	−1.5567	1.1544	.3693	−1.5355	.0602
−5.000	2.400	−1.5386	1.0766	.3592	−1.4312	.0556
−5.000	2.200	−1.5179	0.9976	.3486	−1.3254	.0511
−5.000	2.000	−1.4943	0.9169	.3375	−1.2179	.0466
−5.000	1.800	−1.4668	0.8343	.3259	−1.1081	.0421
−5.000	1.600	−1.4346	0.7492	.3136	−0.9956	.0377
−5.000	1.400	−1.3963	0.6611	.3003	−0.8795	.0332
−5.000	1.200	−1.3496	0.5688	.2859	−0.7585	.0288
−5.000	1.000	−1.2911	0.4705	.2698	−0.6304	.0242
−5.000	0.900	−1.2554	0.4180	.2609	−0.5624	.0219
−5.000	0.800	−1.2135	0.3622	.2512	−0.4906	.0196
−5.000	0.700	−1.1632	0.3026	.2404	−0.4141	.0172
−5.000	0.500	−1.0178	0.1662	.2140	−0.2407	.0120
−5.000	0.400	−0.8967	0.0826	.1963	−0.1358	.0092
−5.000	0.300	−0.6261	−0.0414	.1720	0.0138	.0062
−15.000	0.750	−1.1515	0.2971	.2401	−0.4720	.0187
−15.000	0.800	−1.1691	0.3249	.2416	−0.5130	.0201
−15.000	0.850	−1.1850	0.3522	.2512	−0.5542	.0210
−15.000	0.900	−1.1991	0.3790	.2593	−0.6939	.0231
−15.000	0.950	−1.2117	0.4054	.2648	−0.6330	.0246
−10.000	1.600	−1.3632	0.7374	.3225	−1.0535	.0417
−10.000	1.400	−1.3364	0.6448	.3061	−0.9236	.0360
−10.000	1.200	−1.3018	0.5495	.2887	−0.7902	.0305
−10.000	1.000	−1.2557	0.4501	.2697	−0.6511	.0252
−10.000	0.800	−1.1909	0.3432	.2484	−0.5020	.0199
−10.000	0.600	−1.0905	0.2232	.2234	−0.3360	.0145
5.000	0.900	−1.3191	0.4619	.2669	−0.5305	.0210
5.000	0.800	−1.2620	0.4032	.2594	−0.4677	.0192
5.000	0.700	−1.1970	0.3390	.2506	−0.3990	.0172
5.000	0.600	−1.1203	0.2682	.2392	−0.3230	.0150
5.000	0.500	−1.0247	0.1883	.2269	−0.2371	.0126
5.000	0.400	−1.8912	0.0932	.2096	−0.1354	.0098
5.000	0.300	−0.5960	−0.0544	.1845	0.0168	.0067
5.000	0.100	−0.9025	0.2706	.1530	−0.2747	.0048
5.000	−0.100	−1.0998	0.4141	.2218	−0.4470	.0125
5.000	−0.200	−1.1583	0.4767	.2421	−0.5209	.0156
5.000	−0.400	−1.2455	0.5920	.2667	−0.6571	.0213
5.000	−0.600	−1.3097	0.6986	.2879	−0.7837	.0266
5.000	−0.800	−1.3602	0.7990	.3057	−0.9038	.0317
5.000	−1.000	−1.4012	0.8949	.3213	−1.0194	.0366
5.000	−1.200	−1.4355	0.9871	.3355	−1.1316	.0416
5.000	−1.400	−1.4645	1.0765	.3485	−1.2411	.0465
5.000	−1.600	−1.4896	1.1635	.3607	−1.3485	.0513
5.000	−1.800	−1.5114	1.2486	.3722	−1.4543	.0562
5.000	−2.000	−1.5305	1.3319	.3831	−1.5587	.0612
10.000	0.000	−1.0032	0.3712	.2086	−0.3728	.0100
10.000	−0.100	−1.0740	0.4442	.2348	−0.4570	.0139
10.000	−0.200	−1.1259	0.5119	.2543	−0.5351	.0174
10.000	−0.300	−1.1668	0.5760	.2704	−0.6096	.0208
10.000	−0.400	−1.2002	0.6373	.2844	−0.6814	.0241
10.000	−0.500	−1.2282	0.6965	.2969	−0.7512	.0274
15.000	−0.050	−1.0202	0.4338	.2348	−0.4243	.0131
15.000	0.000	−0.9847	0.3940	.2196	−0.3794	.0109
15.000	0.050	−0.9389	0.3517	.1995	−0.3313	.0085
15.000	0.100	−0.8795	0.3075	.1719	−0.2810	.0058

calculated each time an iteration was performed on $\phi'(0)$. Values of C_p and Pr used in the numerical calculations are those obtained from the property relations given earlier.

Results

Equations (1) and (2) were numerically integrated from $\eta = 0$ to $\eta = 20$, using a predictor-corrector method. A shooting technique was used to satisfy boundary conditions (3) by iterating on $\phi'(0)$ and $f''(0)$. The convergence criterion was when solutions were unchanging to 5 digits at $\eta = 15$ and 20. The solutions were compared with results of [4] at a few points, by using the same property equations as [4]. They agreed to 5 digits. Tabulated results are given in Table 1.

The physical meaning of the effects of R, seen in the present results, have been previously explained in [1]. However, it is important to note that there is very little difference between the d-curves on Fig. 1. Similar effects were seen for the other profiles and parameters plotted in Padlog [6]. Thus the variable, d, could be eliminated by using the results for $d = -5$ or $d = +5$ without incurring much error.

An important application of these calculations is to ice melting in pure water. With $T_o = 0$, only one independent parameter is necessary. Using $d = T_\infty$, instead of R, is preferable because it has more physical meaning. Values of resulting flow parameters ϕ', f'', I_w, I_m, and $f(0)$ are shown in [6].

Of major importance is the blowing produced by melting ice. In Fig. 2, the variation of $\phi'(0)$ for various combinations of blowing and property variations is shown along with the constant property variation of $\phi'(0)$. The blowing becomes more important as T_∞ increases until at $T_\infty = 20°C$ the maximum difference is 7 percent.

In the same manner as blowing, variable property effects become more important as d increases, but only lower the curve an additional 1.7 percent at $T_\infty = 20°C$. The data of [2] and [3] agree with these curves much better than for constant

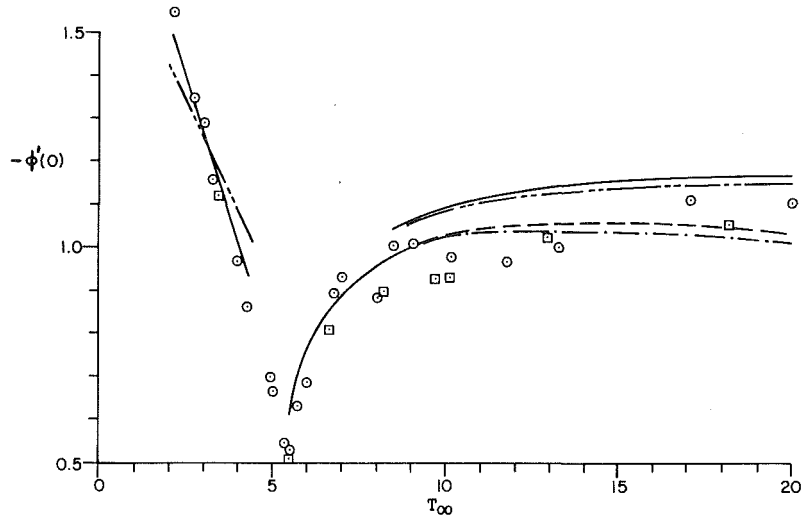

Fig. 2 Variation of calculated heat transfer, $\phi'(0)$, with T_∞. The symbols correspond to the data of: ⊙ Bendell and Gebhart [2]; ⊡ Johnson and Mollendorf [3]. The solid line is no property variation, no blowing; the dashed line is no property variation with blowing; the dashed-dotted line is both property variation and blowing; and the dashed-double-dot line is variable property effects, no blowing.

property analysis without blowing. At lower d's there is little difference between calculated and experimentally determined heat transfer.

Conclusions

In this analysis, all the fluid properties were allowed to vary with temperature during the integration of the natural convection flow equations for a vertical flat surface in cold water. Variable property solutions for pure water require only two independent parameters, namely R and d, which is no more than for constant property results, i.e., Pr and R. However, it should be noted that many dependent parameters are "buried" in the numerical scheme, namely, $\mu(t)$, $\rho(t)$, $C_p(t)$, $k(t)$ and h_{il}. Critical in characterizing heat transfer, flow reversals, and buoyancy force reversals, the variable R has much more effect than the temperature difference, d. The influence of d on heat transfer is small enough so that for any actual $d \leq 20°C$, an approximation of using $d = 5$ or $d = -5$ incurs very little error in using the present results. Also, velocity and temperature profiles at the largest value of d studied here show little effect. The addition of blowing and variable property effects improves agreement with previous ice melting experiments. Blowing is seen to be a major effect causing a maximum decrease in heat transfer of 7 percent at 20°C. Including property variation is seen to result in an additional decrease of only 1.7 percent.

Acknowledgments

The authors gratefully acknowledge support for this research from the National Science Foundation [ENG7727945], and typing by Bonnie Boskat.

References

1 Gebhart, B., and Mollendorf, J. C., "Buoyancy Induced Flows in Water in Which Density Extrema May Arise," *Journal of Fluid Mechanics*, Vol. 89, 1978, pp. 673-707.

2 Bendell, M. S., and Gebhart, B., "Heat Transfer and Ice Melting in Ambient Water Near Its Density Extrema," *International Journal of Heat and Mass Transfer*, Vol. 10, 1976, pp. 1081-1087.

3 Johnson, R. S., and Mollendorf, J. C., "Transport From a Vertical Ice Surface Melting in Saline Water," submitted for publication.

4 Shaukatullah, H., and Gebhart, B., "Laminar Natural Convection Boundary Layer Over a Vertical Isothermal Surface in Water With Variable Properties," *Numer. Heat Transfer*, Vol. 2, 1978, pp. 215-232.

5 Kukulka, D. J., "Thermodynamic and Transport Properties of Pure and Saline Water," M.S. thesis, State University of New York at Buffalo, Amherst, N.Y., June 1981.

6 Padlog, R. D., "Variable Property Effects on Transport in Pure Water Around the Density Extremum," M.S. thesis, State University of New York at Buffalo, Amherst, N.Y., Sept. 1979.

A Heat Transfer Correlation for Natural Convection From a Vertical Surface in Cold Water

V. P. Carey[1]

Nomenclature

g = gravitational acceleration
Gr_L = $gL^3\alpha|t_o - t_\infty|^q/\nu^2$
Gr_x = $gx^3\alpha|t_o - t_\infty|^q/\nu^2$
h_x = local heat transfer coefficient at x
h = mean heat transfer coefficient over surface
k = fluid thermal conductivity
L = surface length
Nu_L = hL/k
Nu_x = $h_x x/k$
Pr = Prandtl number
q = constant from the density correlation (equal to 1.8948)
R = $(t_m - t_\infty)/(t_0 - t_\infty)$
t = local temperature
t_m = temperature at maximum density (equal to 4.029°C)
t_o = surface temperature
t_∞ = ambient temperature
x = coordinate parallel to surface
y = coordinate normal to surface
α = constant from the density

[1] Department of Mechanical Engineering, University of California, Berkeley, Calif. 94720, Mem. ASME

Contributed by the Heat Transfer Division for publication in the JOURNAL OF HEAT TRANSFER. Manuscript received by the Heat Transfer Division September 16, 1982.

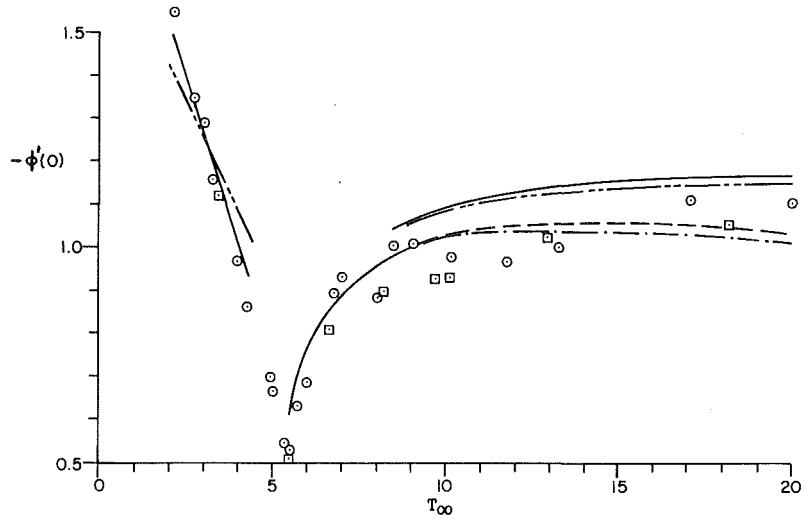

Fig. 2 Variation of calculated heat transfer, $\phi'(0)$, with T_∞. The symbols correspond to the data of: ⊙ Bendell and Gebhart [2]; ⊡ Johnson and Mollendorf [3]. The solid line is no property variation, no blowing; the dashed line is no property variation with blowing; the dashed-dotted line is both property variation and blowing; and the dashed-double-dot line is variable property effects, no blowing.

property analysis without blowing. At lower d's there is little difference between calculated and experimentally determined heat transfer.

Conclusions

In this analysis, all the fluid properties were allowed to vary with temperature during the integration of the natural convection flow equations for a vertical flat surface in cold water. Variable property solutions for pure water require only two independent parameters, namely R and d, which is no more than for constant property results, i.e., Pr and R. However, it should be noted that many dependent parameters are "buried" in the numerical scheme, namely, $\mu(t)$, $\rho(t)$, $C_p(t)$, $k(t)$ and h_{il}. Critical in characterizing heat transfer, flow reversals, and buoyancy force reversals, the variable R has much more effect than the temperature difference, d. The influence of d on heat transfer is small enough so that for any actual $d \leq 20°C$, an approximation of using $d = 5$ or $d = -5$ incurs very little error in using the present results. Also, velocity and temperature profiles at the largest value of d studied here show little effect. The addition of blowing and variable property effects improves agreement with previous ice melting experiments. Blowing is seen to be a major effect causing a maximum decrease in heat transfer of 7 percent at 20°C. Including property variation is seen to result in an additional decrease of only 1.7 percent.

Acknowledgments

The authors gratefully acknowledge support for this research from the National Science Foundation [ENG7727945], and typing by Bonnie Boskat.

References

1 Gebhart, B., and Mollendorf, J. C., "Buoyancy Induced Flows in Water in Which Density Extrema May Arise," *Journal of Fluid Mechanics*, Vol. 89, 1978, pp. 673-707.

2 Bendell, M. S., and Gebhart, B., "Heat Transfer and Ice Melting in Ambient Water Near Its Density Extrema," *International Journal of Heat and Mass Transfer*, Vol. 10, 1976, pp. 1081-1087.

3 Johnson, R. S., and Mollendorf, J. C., "Transport From a Vertical Ice Surface Melting in Saline Water," submitted for publication.

4 Shaukatullah, H., and Gebhart, B., "Laminar Natural Convection Boundary Layer Over a Vertical Isothermal Surface in Water With Variable Properties," *Numer. Heat Transfer*, Vol. 2, 1978, pp. 215-232.

5 Kukulka, D. J., "Thermodynamic and Transport Properties of Pure and Saline Water," M.S. thesis, State University of New York at Buffalo, Amherst, N.Y., June 1981.

6 Padlog, R. D., "Variable Property Effects on Transport in Pure Water Around the Density Extremum," M.S. thesis, State University of New York at Buffalo, Amherst, N.Y., Sept. 1979.

A Heat Transfer Correlation for Natural Convection From a Vertical Surface in Cold Water

V. P. Carey[1]

Nomenclature

g = gravitational acceleration
Gr_L = $gL^3\alpha|t_o - t_\infty|^q/\nu^2$
Gr_x = $gx^3\alpha|t_o - t_\infty|^q/\nu^2$
h_x = local heat transfer coefficient at x
h = mean heat transfer coefficient over surface
k = fluid thermal conductivity
L = surface length
Nu_L = hL/k
Nu_x = $h_x x/k$
Pr = Prandtl number
q = constant from the density correlation (equal to 1.8948)
R = $(t_m - t_\infty)/(t_0 - t_\infty)$
t = local temperature
t_m = temperature at maximum density (equal to 4.029°C)
t_o = surface temperature
t_∞ = ambient temperature
x = coordinate parallel to surface
y = coordinate normal to surface
α = constant from the density

[1] Department of Mechanical Engineering, University of California, Berkeley, Calif. 94720, Mem. ASME

Contributed by the Heat Transfer Division for publication in the JOURNAL OF HEAT TRANSFER. Manuscript received by the Heat Transfer Division September 16, 1982.

correlation (equal to $9.297 \times 10^{-6}\,°C^{q}$)
δ = boundary layer thickness
ν = kinematic viscosity
ρ = local fluid density
ρ_∞ = ambient fluid density
$\phi = (t - t_\infty)/(t_o - t_\infty)$

Introduction

Previous studies of the laminar natural convection flow near a vertical isothermal surface in cold water have produced numerous predictions and measurements of the resulting surface heat transfer. Recent studies [1-6] have focused on the anomalously low heat transfer rates which characterize these flows when the buoyancy effect is bidirectional.

To calculate the surface heat transfer for such circumstances, without solving the full governing equations, one can either interpolate the tabulated results of numerical calculations [2,4,6,7], or use the correlation method proposed by Merk [8] for melting ice in the manner described by Ede [9]. Merk's [8] correlation calculates the Nusselt number as if the flow was Boussinesq and then applies a correction to account for the nonlinear density effect. The correction term is a complicated function of the coefficients in the density relation and the surface and ambient temperatures.

In this note, a new correlation is presented for natural convection heat transfer from a vertical isothermal surface in cold water. The correlation contains only one additional dimensionless parameter beyond the Nusselt, Grashof, and Prandtl numbers. This additional parameter quantifies the nonlinear density effect on transport. A major advantage of this correlation over Merk's [8] is that its simple form makes it easier to observe and interpret trends in the heat transfer as conditions change. As shown in the next section, this simplicity is achieved without significant loss in accuracy.

Results and Discussion

If the boundary layer equations for laminar natural convection flow near a vertical surface are solved using an integral technique with polynomial approximations for the temperature and velocity profiles, a relation of the following form is obtained for the local Nusselt number

$$\mathrm{Nu}_x = \frac{0.669\,\mathrm{Pr}^{1/2}\,\mathrm{Gr}_x^{1/4}\,|I_B|^{1/4}}{[0.952+\mathrm{Pr}]^{1/4}} \tag{1}$$

where I_B is the dimensionless integral of the buoyancy force across the boundary layer.

For pure water at one atmosphere pressure, the density correlation of Gebhart and Mollendorf [10] is used here to evaluate I_B. While the form of the correlation is mathematically simple, its accuracy for temperatures between 0 and 20°C is comparable to more complex correlations containing a large number of terms. At one atmosphere, the correlation agrees with the pure water correlation of Fine and Millero [12] to an rms difference of 3.5 ppm. Use of this correlation thereby permits a simpler formulation of the analysis, without significant loss in accuracy. A detailed discussion of the development of the correlation and its accuracy may be found in [10].

Using the density correlation of Gebhart and Mollendorf [10] for pure water in atmospheric pressure, the definitions of Gr_x and I_B are

$$\mathrm{Gr}_x = \frac{gx^3}{\nu^2}\,\alpha\,|t_o - t_\infty|^q \tag{2}$$

$$I_B = \frac{1}{\delta\alpha\,|t_o - t_\infty|^q}\int_0^\delta \left(\frac{\rho_\infty - \rho}{\rho}\right)dy = \int_0^1 [\,|\phi - R|^q - |R|^q]\,d\eta \tag{3}$$

where

$$\phi = \frac{t - t_\infty}{t_o - t_\infty}, \quad R = \frac{t_m - t_\infty}{t_o - t_\infty}, \quad \eta = y/\delta$$

and α, t_m, and q are constants from the density correlation

$$\begin{aligned} \alpha &= 9.297 \times 10^{-6}(°C)^q \\ t_m &= 4.029°C \\ q &= 1.8948 \end{aligned} \tag{4}$$

It can be seen that the integral, I_B, depends on the parameter, R, which places the surface and ambient temperatures relative to the temperatures of maximum density, t_m. The integral, I_B, was evaluated numerically for various R values with an assumed polynomial temperature profile to determine the form of the function $I_B(R)$ in the correlation. However, the heat transfer obtained in this manner deviated as much as 20 percent from the calculated results of Gebhart and Mollendorf [2].

To obtain an improved correlation, $I_B(R)$ was determined by curve-fitting the calculated results of Gebhart and Mollendorf [2] and Carey, Gebhart, and Mollendorf [4]. The calculated results of Carey et al. [4] for $R = 0.30$ and 0.292 were not used since the experiments of Carey and Gebhart [4] indicate that unidirectional boundary-layer flow does not result for these conditions. The resulting correlation for the local Nusselt number is

$$\mathrm{Nu}_x = \frac{0.543\,|R - 0.26|^{0.242}\,\mathrm{Gr}_x^{1/4}\,\mathrm{Pr}^{1/4}}{[0.952+\mathrm{Pr}]^{1/4}} \tag{5}$$

which is valid for $|R - 0.26| > 0.01$.

A comparison of this correlation with the calculated results of Gebhart and Mollendorf [2] and Carey et al. [4] for $\mathrm{Pr} = 8.6$, 11.6, and 13.6 is shown in Fig. 1. The correlation is seen to fit the calculated results very well. The rms difference for all the calculated points is only 2.3 percent.

Figure 2 shows a comparison of the results predicted by the correlation with the experimental ice melting data of Bendell and Gebhart [1] and Johnson [11]. Note that the correlation equation (5) has been integrated from 0 to L to obtain the mean Nusselt number. Also, shown in Fig. 2 are the measured

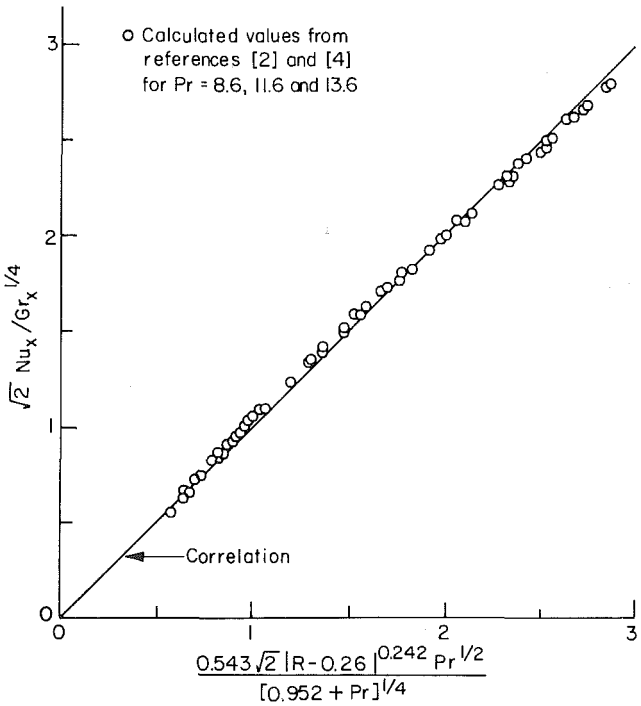

Fig. 1 Comparison of the correlation results with the calculated results of Gebhart and Mollendorf [2] and Carey et al. [4]

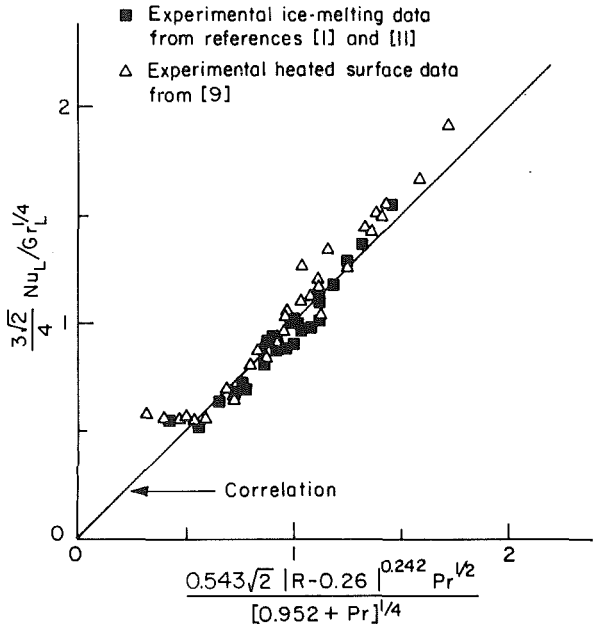

Fig. 2 Comparison of the correlation results with the ice melting data of Bendell and Gebhart [1] and Johnson [11], and the heated surface data of Ede [9]

heat transfer data of Ede [9] for a heated vertical surface in cold water.

At $R=0.26$, the correlation predicts zero heat transfer. While no experimental results are known to exist exactly for $R=0.26$, zero heat transfer is clearly unrealistic. Although convective motion may be very weak for such conditions, conduction into the fluid will still occur.

Failure of the correlation for R very near 0.26 is detectable in Fig. 2. The four left most experimental data points, which are above the correlation line, correspond to R values between 0.25 and 0.27. As R approaches 0.26, the correlation predicts that the heat transfer coefficient decreases to zero, whereas the experimental data suggests that it levels off to a constant value.

For $|R-0.26|>0.01$, however, the experimental data generally agrees well with the correlation. The rms deviation is only 7.9 percent. The uppermost points show some slight deviation from the correlation. However, the t_o-t_∞ values corresponding to the four uppermost points are all less than 3°C, and for the highest point it is only 1.5°C. For the majority of the data, this temperature difference is 5°C or more. Given the difficulty in measuring temperatures to better than ±0.1°C accuracy, the uncertainty in the location of these points is higher than most of the others. Hence, the slight deviation of the upper data points could be due to greater experimental error in the measurements.

As a result of the above considerations, the correlation (5) is recommended for $|R-0.26|>0.01$. For $0.25\le R\le 0.27$, the available experimental data suggest that the Nusselt number is best estimated by assuming that it is constant and equal to the value predicted by the correlation at $R=0.27$.

Acknowledgments

The author wishes to acknowledge support from the Union Oil Foundation during the completion of this work.

References

1 Bendell, M. S., and Gebhart, B., "Heat Transfer and Ice Melting in Ambient Water Near Its Density Extremum," *International Journal of Heat and Mass Transfer*, Vol. 19, 1976, pp. 1081-1087.

2 Gebhart, B., and Mollendorf, J. C., "Buoyancy-Induced Flows in Water Under Conditions in Which Density Extrema May Arise," *Journal of Fluid Mechanics*, Vol. 81, 1978, pp. 673-707.

3 Wilson, N. W., and Vyas, B. D., "Velocity Profiles Near a Vertical Ice Surface Melting into Fresh Water," ASME JOURNAL OF HEAT TRANSFER, Vol. 101, 1979, pp. 313-317.

4 Carey, V. P., Gebhart, B., and Mollendorf, J. C., "Buoyancy Force Reversals in Vertical Natural Convection Flows in Cold Water," *Journal of Fluid Mechanics*, Vol. 97, 1980, pp. 279-297.

5 Carey, V. P., and Gebhart, B., "Visualization of the Flow Adjacent to a Vertical Ice Surface Melting in Cold Pure Water," *Journal of Fluid Mechanics*, Vol. 107, 1981, pp. 37-55.

6 Wilson, N. W., and Lee, J. J., "Melting of a Vertical Ice Wall by Free Convection into Fresh Water," ASME JOURNAL OF HEAT TRANSFER, Vol. 103, 1981, pp. 13-17.

7 Vanier, C. R., and Tien, C., "Effect of Maximum Density and Melting on Natural Convection Heat Transfer from a Vertical Plate," *Chemical Engineering Progress Symposium Series*, Vol. 64, 1968, pp. 240-254.

8 Merk, H. J., "The Influence of Melting and Anomalous Expansion on the Thermal Convection in Laminar Boundary Layers," *Applied Scientific Research*, Vol. 4, 1953, pp. 435-452.

9 Ede, A. J., "The Influence of Anomalous Expansion on Natural Convection in Water," *Applied Scientific Research*, Vol. 5, 1955, pp. 458-460.

10 Gebhart, B., and Mollendorf, J. C., "A New Density Relation for Pure or Saline Water," *Deep Sea Research*, Vol. 24, 1977, pp. 831-848.

11 Johnson, R. S., "Transport from a Melting Vertical Ice Slab in Saline Water," M.S. thesis, State University of New York at Buffalo, 1978.

12 Fine, R. A., and Millero, F. J., "Compressibility of Water as a Function of Temperature and Pressure," *Journal of Chemical Physics*, Vol. 59, 1973, pp. 5529-5536.

Transient and Steady-State Natural Convection in a Porous Medium Between Two Concentric Cylinders

G. N. Facas[1] and B. Farouk[2]

Nomenclature

- c = specific heat
- g = acceleration of gravity
- K = permeability
- r = radial coordinate
- r^* = nondimensional radial coordinate, $\frac{r}{R_i}$
- R_i = radius of inner cylinder
- R_o = radius of outer cylinder
- Ra = Rayleigh number based on inner cylinder radius
- Ra* = Modified Rayleigh number (heat flux boundary condition)
- T = temperature
- T_i = temperature of inner cylinder
- T_o = reference temperature or temperature of outer cylinder
- T^* = nondimensional temperature, $\frac{T-T_o}{T_i-T_o}$
- t = time
- v_r = radial velocity component
- v_r^* = nondimensional radial velocity component
- v_θ = angular velocity component

[1] Graduate Student, Department of Mechanical Engineering and Mechanics, Drexel University, Philadelphia, Pa. 19104

[2] Assistant Professor, Department of Mechanical Engineering and Mechanics, Drexel University, Assoc. Mem. ASME

Contributed by the Heat Transfer Division for publication in the JOURNAL OF HEAT TRANSFER. Manuscript received by the Heat Transfer Division July 15, 1982.

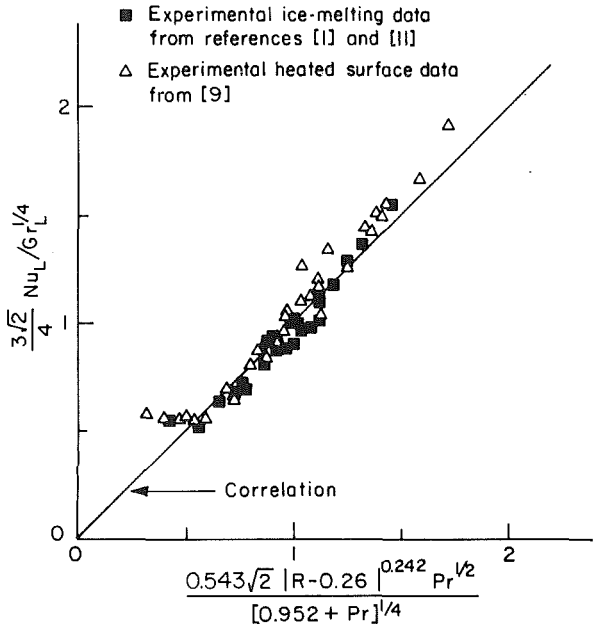

Fig. 2 Comparison of the correlation results with the ice melting data of Bendell and Gebhart [1] and Johnson [11], and the heated surface data of Ede [9]

heat transfer data of Ede [9] for a heated vertical surface in cold water.

At $R=0.26$, the correlation predicts zero heat transfer. While no experimental results are known to exist exactly for $R=0.26$, zero heat transfer is clearly unrealistic. Although convective motion may be very weak for such conditions, conduction into the fluid will still occur.

Failure of the correlation for R very near 0.26 is detectable in Fig. 2. The four left most experimental data points, which are above the correlation line, correspond to R values between 0.25 and 0.27. As R approaches 0.26, the correlation predicts that the heat transfer coefficient decreases to zero, whereas the experimental data suggests that it levels off to a constant value.

For $|R-0.26|>0.01$, however, the experimental data generally agrees well with the correlation. The rms deviation is only 7.9 percent. The uppermost points show some slight deviation from the correlation. However, the t_o-t_∞ values corresponding to the four uppermost points are all less than 3°C, and for the highest point it is only 1.5°C. For the majority of the data, this temperature difference is 5°C or more. Given the difficulty in measuring temperatures to better than ±0.1°C accuracy, the uncertainty in the location of these points is higher than most of the others. Hence, the slight deviation of the upper data points could be due to greater experimental error in the measurements.

As a result of the above considerations, the correlation (5) is recommended for $|R-0.26|>0.01$. For $0.25\le R\le 0.27$, the available experimental data suggest that the Nusselt number is best estimated by assuming that it is constant and equal to the value predicted by the correlation at $R=0.27$.

Acknowledgments

The author wishes to acknowledge support from the Union Oil Foundation during the completion of this work.

References

1 Bendell, M. S., and Gebhart, B., "Heat Transfer and Ice Melting in Ambient Water Near Its Density Extremum," *International Journal of Heat and Mass Transfer*, Vol. 19, 1976, pp. 1081-1087.

2 Gebhart, B., and Mollendorf, J. C., "Buoyancy-Induced Flows in Water Under Conditions in Which Density Extrema May Arise," *Journal of Fluid Mechanics*, Vol. 81, 1978, pp. 673-707.

3 Wilson, N. W., and Vyas, B. D., "Velocity Profiles Near a Vertical Ice Surface Melting into Fresh Water," ASME JOURNAL OF HEAT TRANSFER, Vol. 101, 1979, pp. 313-317.

4 Carey, V. P., Gebhart, B., and Mollendorf, J. C., "Buoyancy Force Reversals in Vertical Natural Convection Flows in Cold Water," *Journal of Fluid Mechanics*, Vol. 97, 1980, pp. 279-297.

5 Carey, V. P., and Gebhart, B., "Visualization of the Flow Adjacent to a Vertical Ice Surface Melting in Cold Pure Water," *Journal of Fluid Mechanics*, Vol. 107, 1981, pp. 37-55.

6 Wilson, N. W., and Lee, J. J., "Melting of a Vertical Ice Wall by Free Convection into Fresh Water," ASME JOURNAL OF HEAT TRANSFER, Vol. 103, 1981, pp. 13-17.

7 Vanier, C. R., and Tien, C., "Effect of Maximum Density and Melting on Natural Convection Heat Transfer from a Vertical Plate," *Chemical Engineering Progress Symposium Series*, Vol. 64, 1968, pp. 240-254.

8 Merk, H. J., "The Influence of Melting and Anomalous Expansion on the Thermal Convection in Laminar Boundary Layers," *Applied Scientific Research*, Vol. 4, 1953, pp. 435-452.

9 Ede, A. J., "The Influence of Anomalous Expansion on Natural Convection in Water," *Applied Scientific Research*, Vol. 5, 1955, pp. 458-460.

10 Gebhart, B., and Mollendorf, J. C., "A New Density Relation for Pure or Saline Water," *Deep Sea Research*, Vol. 24, 1977, pp. 831-848.

11 Johnson, R. S., "Transport from a Melting Vertical Ice Slab in Saline Water," M.S. thesis, State University of New York at Buffalo, 1978.

12 Fine, R. A., and Millero, F. J., "Compressibility of Water as a Function of Temperature and Pressure," *Journal of Chemical Physics*, Vol. 59, 1973, pp. 5529-5536.

Transient and Steady-State Natural Convection in a Porous Medium Between Two Concentric Cylinders

G. N. Facas[1] and B. Farouk[2]

Nomenclature

- c = specific heat
- g = acceleration of gravity
- K = permeability
- r = radial coordinate
- r^* = nondimensional radial coordinate, $\frac{r}{R_i}$
- R_i = radius of inner cylinder
- R_o = radius of outer cylinder
- Ra = Rayleigh number based on inner cylinder radius
- Ra* = Modified Rayleigh number (heat flux boundary condition)
- T = temperature
- T_i = temperature of inner cylinder
- T_o = reference temperature or temperature of outer cylinder
- T^* = nondimensional temperature, $\frac{T-T_o}{T_i-T_o}$
- t = time
- v_r = radial velocity component
- v_r^* = nondimensional radial velocity component
- v_θ = angular velocity component

[1] Graduate Student, Department of Mechanical Engineering and Mechanics, Drexel University, Philadelphia, Pa. 19104

[2] Assistant Professor, Department of Mechanical Engineering and Mechanics, Drexel University, Assoc. Mem. ASME

Contributed by the Heat Transfer Division for publication in the JOURNAL OF HEAT TRANSFER. Manuscript received by the Heat Transfer Division July 15, 1982.

v_θ^* = nondimensional angular velocity component velocity vector
$\bar{v}$ = velocity vector

Greek Letters

α = thermal diffusivity, $\dfrac{\lambda^*}{\rho_f c_f}$
β_f = thermal coefficient of volume expansion of fluid
θ = circumferential (angle) coordinate
λ = thermal conductivity
λ^* = equivalent thermal conductivity of medium
μ = molecular viscosity
ρ = density
ϕ = porosity (void volume fraction)
ψ = stream function, $V_r = \dfrac{1}{\rho_f r}\dfrac{\partial \psi}{\partial \theta}, v_\theta = -\dfrac{1}{\rho_f}\dfrac{\partial \psi}{\partial r}$
ψ^* = nondimensional stream function, $\dfrac{\psi}{\alpha \rho_f}$
τ = nondimensional time $\dfrac{\lambda^*}{(\rho c)^*}\dfrac{t}{R_i^2}$

Subscripts

f = fluid
s = solid
o = reference condition

Introduction

The natural convective fluid flow, heat, and mass transport in porous medium has become a subject of increased recent investigations. This is primarily due to the enhanced use of the ground water systems for industial and agricultural uses, renewed interest in geological and astrophysical problems, as well as problems arising in the storage of highly radioactive nuclear waste materials [1]. Combarnous and Bories [2] have extensively reviewed the state of the art on natural convection in porous media. A number of applications of buoyancy driven flows in fluid-per-meated porous structures are discussed in Cheng's comprehensive review [3] on heat transfer in geothermal systems. Several different analytic and experimental methods have been used to seek solutions of this class of problems [4–6].

There are many problems where transient effects are of primary interest. In some cases, steady-state conditions may not exist. Steady-state results for natural convection in a porous medium bounded by two concentric horizontal cylinders have been reported by Caltagirone [4, 5]. Numerical results were presented for a limited range of Rayleigh numbers (<500) for an outer to inner radius ratio of 2.0. No time varying results were presented in the above references and constant property formulations were used.

In this work, transient, two-dimensional numerical calculations are presented for natural convective flow in a porous concentric annulus heated from inside. Several areas in which the natural convective transport of heat in such a geometry is important include buried pipelines, storage of solar energy in underground containers, and recovery of geothermal energy. Transient and steady-state solutions are obtained over a large range of Rayleigh number ($10^0 - 10^3$) using a finite difference method with central difference expressions.

Problem Statement

The heat conducting porous medium considered is confined between two concentric cylinders. Thermal conductivities and specific heats of both fluid and the matrix are taken as constant, as is thermal expansion coefficient of the fluid. However, the ratio of fluid viscosity to matrix permeability, μ/K, is allowed to vary with the vertical distance, z, from any point to the outer cylinder. It can be readily shown that

$$z = r\mathrm{Cos}\theta + R_o \mathrm{Sin}\left\{\mathrm{Cos}^{-1}\left(\frac{r}{R_o}\,\mathrm{Sin}\,\theta\right)\right\} \tag{1}$$

The governing equations for transient, natural convection are obtained from Boussinesq, Darcy flow, and negligible inertia approximations [6]. Fluid viscosity, μ, and matrix permeability, K, appear only through the ratio μ/K in the governing equations. Following Ribando and Torrance [7], we attribute variations of either μ or K. The ratio is modeled by the exponential form

$$\frac{\mu}{K} = \left(\frac{\mu}{K}\right)_o e^{-z/z_o} \tag{2}$$

where the reference amplitude $(\mu/K)_0$ is evaluated at the uppermost point. A positive value of the e-folding distance, z_o, corresponds to μ/K decreasing with depth; a negative value corresponds to μ/K increasing with depth. Setting $z_o = \pm\infty$ corresponds to a medium with constant viscosity and constant permeability, or to a constant ratio of the two. Introducing the stream function, the governing equations reduce to

$$\frac{1}{r^*}\left[\frac{\partial}{\partial r^*}\left(r^*\left(\frac{\mu}{K}\right)^*\frac{\partial \psi^*}{\partial r^*}\right) + \frac{\partial}{\partial \theta}\left(\frac{1}{r^*}\left(\frac{\mu}{K}\right)^*\frac{\partial \psi^*}{\partial \theta}\right)\right] = -\mathrm{Ra}.\left[\mathrm{Sin}\theta\frac{\partial T^*}{\partial r^*} + \frac{\mathrm{Cos}\theta}{r^*}\frac{\partial T^*}{\partial \theta}\right] \tag{3}$$

where

$$\left(\frac{\mu}{K}\right)^* = \left(\frac{\mu}{K}\right)\Big/\left(\frac{\mu}{K}\right)_o$$

and

$$\nabla^2 T^* - \frac{1}{r^*}\left[\frac{\partial \psi^*}{\partial \theta}\frac{\partial T^*}{\partial r^*} - \frac{\partial \psi^*}{\partial r^*}\frac{\partial T^*}{\partial \theta}\right] = \frac{\partial T^*}{\partial \tau} \tag{4}$$

where the Rayleigh number is given as

$$\mathrm{Ra} = \frac{g\rho_o \beta_f c_f R_i \Delta T.\rho_f}{\lambda^*\left(\frac{\mu}{K}\right)_o}$$

and $\Delta T = (T_i - T_o)$

Symmetry about the vertical axis is assumed and only half of the flow domain is considered for the calculations. The hydrodynamic boundary condition for an impermeable surface (i.e., the inner and outer cylinder) is the Dirichlet condition $\psi^* = 0$.

For the transient calculations, the fluid initially is assumed to be motionless and the medium temperature is the same as that of the outer boundary. It is noted that the governing equations for flow in a porous medium do not permit the additional hydrodynamic constraint of no-slip. Flow or recharge through a permeable outer cylinder may occur when either a standing liquid or a second porous medium (with a much larger permeability) overlies the porous layer of interest. For such cases, the least restrictive boundary condition at the permeable outer surface is one of constant pressure. The constant pressure assumption implies no viscous interaction between an overlying liquid and the porous layer. From the radial momentum balance and the stream function

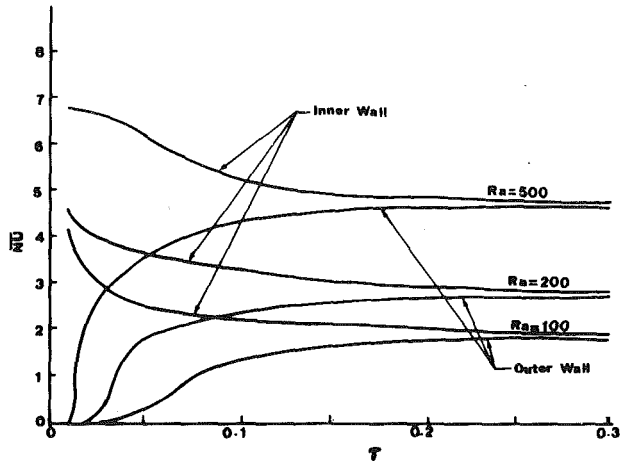

Fig. 1 Mean Nusselt number for both inner and outer boundaries as a function of time

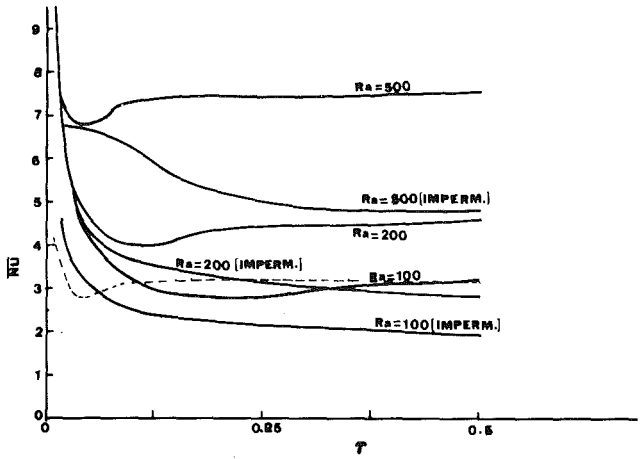

Fig. 2 Average Nusselt number (for inner cylinder) for permeable and impermeable outer boundary

definitions, a constant pressure cylindrical surface is represented by

$$\frac{\partial \psi^*}{\partial r^*} = 0$$

Local Nusselt numbers are defined for the inner and outer cylinder surfaces, respectively, as

$$\mathrm{Nu}_i(\theta) = -\ln(R_o/R_i)\frac{\partial T^*}{\partial r^*}\bigg|_i \tag{5}$$

$$\mathrm{Nu}_o(\theta) = -\frac{R_o}{R_i}\ln(R_o/R_i)\frac{\partial T^*}{\partial r^*}\bigg|_o \tag{6}$$

Numerical Solution

The numerical solution to the transient governing equations is obtained by a finite difference scheme. The parabolic energy equation is solved by an efficient Alternating Direction Implicit (ADI) procedure whereas, the elliptic stream function equation is solved iteratively for every time-step by the method of Successive Over Relaxation (SOR).

Starting from the initial conditions, the temperature distribution is obtained for the first time increment for the entire domain of interest. Using the values of temperature calculated, values for the stream function are obtained by solving equation (3) by an iterative scheme. When $\overline{\mathrm{Nu}_i}$ and $\overline{\mathrm{Nu}_o}$ become nearly equal and the flow field solutions do not change appreciably, steady-state is believed to have been reached.

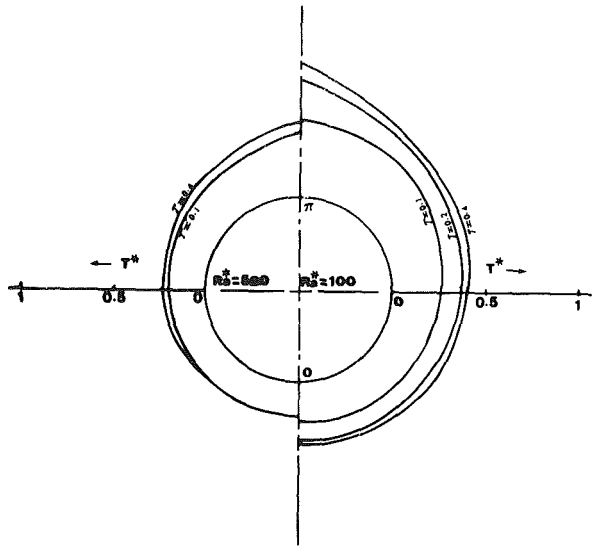

Fig. 3 Transient wall temperature development for Ra* = 100, Ra* = 500

A uniform 25 × 25 ($r \times \theta$) spatial grid appeared sufficient to obtain solutions for the entire range of Rayleigh numbers considered for the transient solutions. No minimum time increment ($\Delta\tau$) value for the solution procedure was found in the literature. For each flow considered, solutions were obtained with gradually decreasing time steps until they become independent of the increment used. For the case of Rayleigh number of 100, a time increment ($\Delta\tau$) of 10^{-3} was found adequate.

Results and Discussion

All results presented are for the R_o/R_i ratio of 2.0. The specific geometry was chosen such that the obtained results could be compared with limited available experimental data in the literature. The steady-state predictions agreed well with those given by Caltagirone [5].

Time dependent solutions were obtained up to the Rayleigh number of 1000. Extremely small time-steps were necessary for any higher Rayleigh number predictions and instabilities arose.

The time variation of the mean Nusselt numbers for the inner and outer cylinders are given in Fig. 1. The time-dependent solutions could not be compared due to the lack of any previously reported results. However, the trends of the result agree qualitatively with the predictions of Holst and Aziz [8], who carried out both computations and experiments in a cubical enclosure filled with a porous medium. It was interesting to find out that the mean inner and outer Nusselt number values reach near steady-state values at about the same τ values, independent of the Rayleigh numbers. Constant (μ/K) ratios and impermeable outer walls are assumed in the above cases. The heat transfer from the inner cylinder is high at the beginning and the variation over the entire surface is uniform. The transient response of the outer cylinder is found to be quite different. The heat transfer increases substantially when the plume forms after a certain amount of time and hits the upper surface. When the outer boundary is changed from a rigid-lid to a constant pressure surface, enhanced convective motion results which in turn gives higher heat transfer for the inner cylinder. The transient heat transfer results for three different Rayleigh numbers, for both permeable and rigid outer walls (outer boundary having zero gradient temperature condition) are displayed in Fig. 2. The

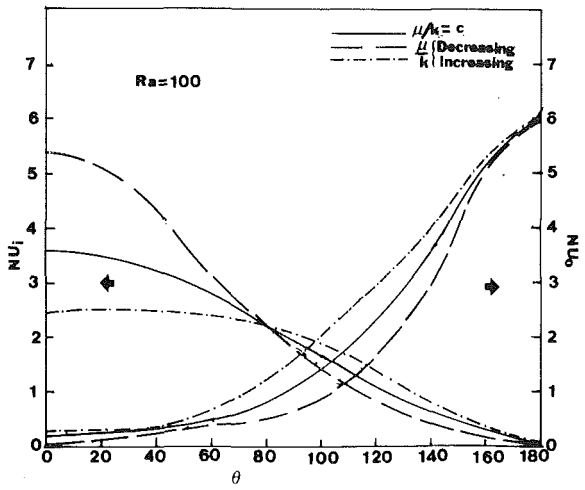

Fig. 4 Distribution of local Nusselt number for constant and variable μ/K ratios, Ra = 100

dashed line on Fig. 2 is for a Rayleigh number of 100, but constant temperature outer wall boundary condition was used for the computations. The transient response to the heat transfer characteristics also changes when the outer wall is changed from impermeable to a permeable surface as shown in Fig. 2.

The convective motion in the case of uniform inner heating is less intense, in terms of both isotherm distortion and maximum value of the stream function compared to the isothermal inner wall case. The nondimensionalized inner wall temperature distribution for cases of Ra* = 100 and Ra* = 500 are shown in Fig. 3 for various values of time. The nondimensionalized wall temperature gets smaller for increasing Rayleigh number and also becomes more uniform as convection dominates conduction at the higher Rayleigh numbers.

The effects of allowing μ/K to vary, using the exponential form given previously, are now presented. The value of z_o was taken to be $\pm 2R_o$ in equation (2). Two cases are considered: μ/K increasing with depth z and μ/K decreasing with depth z. Physically, the first case is interpreted as a decrease in permeability with depth due to compaction of the porous medium by over burden pressure. The second case models a fluid whose viscosity decreased with increasing temperature [7]. The steady-state heat transfer results for variable μ/K ratio are shown on Fig. 4 for Ra = 100. Constant wall temperature boundary conditions along with rigid walls are considered. For the μ/K ratio increasing with depth, i.e., permeability decreasing with depth, the heat transfer from the inner cylinder decreases at the lower region. However, both for the inner and outer cylinders, the heat transfer increases at the top region due to vigorous fluid motion in that area. For the μ/K ratio decreasing with depth, higher heat transfer results are found but this situation is less likely to occur in practical geothermal or other porous media systems. The results demonstrate effectively that such property variations can affect the heat transfer and flow characteristics and should be considered for realistic modeling of such systems.

References

1 Bear, J., *Dynamics of Fluids in Porous Media*, American Elsevier, 1972.

2 Combarnous, M. A., and Bories, S. A., "Hydrothermal Convection in Saturated Porous Medium," *Advances in Hydroscience*, Vol. 10, 1975, pp. 231-307.

3 Cheng, P., "Heat Transfer in Geothermal Systems," *Advances in Heat Transfer*, Vol. 14, 1978, pp. 1-105.

4 Caltagirone, J. P., "Aerothermique-Analyse Numerique de la Convection Naturelle en Milieu Pouex Centre deux Cylinders Concentriques," *C. R., Acad. Sciences*, Vol. 275, Paris, 1972, pp. 274-275.

5 Caltagirone, J. P., "Thermoconvective Instabilities in a Porous Medium Bounded by Two Concentric Horizontal Cylinders," *Journal of Fluid Mechanics*, Vol. 76, pt. 2, 1976, pp. 337-362.

6 Facas, G. N., and Farouk, B., "Transient and Steady-State Natural Convection in a Porous Medium between Two Concentric Cylinders," ASME Winter Annual Meeting, Phoenix, Arizona, HTD-Vol. 22, Nov. 1982, ASME, New York, pp. 19-34.

7 Ribando, R. J., and Torrance, K. E., "Natural Convection in a Porous Medium: Effects of Confinement, Variable Permeability and Thermal Boundary Conditions," ASME JOURNAL OF HEAT TRANSFER, Vol. 97, Feb. 1976, pp. 42-48.

8 Holst, P. H., and Aziz, K., "Transient Three-dimensional Natural Convection in Confined Porous Media," *International Journal of Heat Mass Transfer*, Vol. 15, 1972, pp. 73-90.

Measurements of Turbulent Prandtl Number in a Plane Jet

L. W. B. Browne[1] and R. A. Antonia[2]

Nomenclature

- d = nozzle width
- f = distribution of U in the self-preserving region $f(\eta) = U/U_0$
- h = distribution of T in the self-preserving region $h(\eta) = T/T_0$
- H = nozzle height
- L_u = velocity half-width $L_u = y\,|_{U=U_0/2}$
- L_θ = temperature half-width $L_\theta = y\,|_{T=T_0/2}$
- P = production rate of turbulent energy $P = \overline{uv}\partial U/\partial y$
- Pr_t = turbulent Prandtl number $\mathrm{Pr}_t = \overline{uv}(\partial T/\partial y)/\overline{v\theta}(\partial U/\partial y)$
- t = time
- T = mean temperature relative to ambient
- T_j = temperature of jet at nozzle exit, relative to ambient
- T_0 = local mean temperature relative to ambient on jet centerline
- u = velocity fluctuation in x-direction
- U = mean velocity in x-direction
- U_j = velocity of jet at nozzle exit
- U_0 = local mean velocity in x-direction on jet centerline
- v = velocity fluctuation in y-direction
- V = mean velocity in y-direction
- x = streamwise coordinate measured from jet exit
- y = transverse coordinate measured from jet centerline
- ϵ = dissipation rate of turbulent energy
- η = dimensionless y co-ordinate $\eta = y/L_u$
- θ = temperature fluctuation
- $\overline{(\ )}$ = time-averaged value of ( )

Introduction

Jenkins and Goldschmidt [1] presented data, obtained from several sources, of spreading parameters for turbulent plane and circular jets into still air. Although relatively wide

[1]Senior Lecturer, Department of Mechanical Engineering, University of Newcastle, N.S.W., 2308, Australia

[2]Professor, Department of Mechanical Engineering, University of Newcastle

Contributed by the Heat Transfer Division for publication in the JOURNAL OF HEAT TRANSFER. Manuscript received by the Heat Transfer Division May 3, 1982.

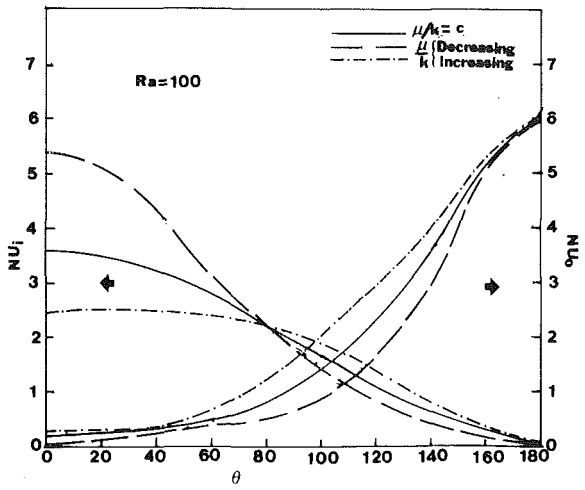

Fig. 4 Distribution of local Nusselt number for constant and variable μ/K ratios, Ra = 100

dashed line on Fig. 2 is for a Rayleigh number of 100, but constant temperature outer wall boundary condition was used for the computations. The transient response to the heat transfer characteristics also changes when the outer wall is changed from impermeable to a permeable surface as shown in Fig. 2.

The convective motion in the case of uniform inner heating is less intense, in terms of both isotherm distortion and maximum value of the stream function compared to the isothermal inner wall case. The nondimensionalized inner wall temperature distribution for cases of Ra* = 100 and Ra* = 500 are shown in Fig. 3 for various values of time. The nondimensionalized wall temperature gets smaller for increasing Rayleigh number and also becomes more uniform as convection dominates conduction at the higher Rayleigh numbers.

The effects of allowing μ/K to vary, using the exponential form given previously, are now presented. The value of z_o was taken to be $\pm 2R_o$ in equation (2). Two cases are considered: μ/K increasing with depth z and μ/K decreasing with depth z. Physically, the first case is interpreted as a decrease in permeability with depth due to compaction of the porous medium by over burden pressure. The second case models a fluid whose viscosity decreased with increasing temperature [7]. The steady-state heat transfer results for variable μ/K ratio are shown on Fig. 4 for Ra = 100. Constant wall temperature boundary conditions along with rigid walls are considered. For the μ/K ratio increasing with depth, i.e., permeability decreasing with depth, the heat transfer from the inner cylinder decreases at the lower region. However, both for the inner and outer cylinders, the heat transfer increases at the top region due to vigorous fluid motion in that area. For the μ/K ratio decreasing with depth, higher heat transfer results are found but this situation is less likely to occur in practical geothermal or other porous media systems. The results demonstrate effectively that such property variations can affect the heat transfer and flow characteristics and should be considered for realistic modeling of such systems.

References

1 Bear, J., *Dynamics of Fluids in Porous Media*, American Elsevier, 1972.

2 Combarnous, M. A., and Bories, S. A., "Hydrothermal Convection in Saturated Porous Medium," *Advances in Hydroscience*, Vol. 10, 1975, pp. 231-307.

3 Cheng, P., "Heat Transfer in Geothermal Systems," *Advances in Heat Transfer*, Vol. 14, 1978, pp. 1-105.

4 Caltagirone, J. P., "Aerothermique-Analyse Numerique de la Convection Naturelle en Milieu Pouex Centre deux Cylinders Concentriques," *C. R., Acad. Sciences*, Vol. 275, Paris, 1972, pp. 274-275.

5 Caltagirone, J. P., "Thermoconvective Instabilities in a Porous Medium Bounded by Two Concentric Horizontal Cylinders," *Journal of Fluid Mechanics*, Vol. 76, pt. 2, 1976, pp. 337-362.

6 Facas, G. N., and Farouk, B., "Transient and Steady-State Natural Convection in a Porous Medium between Two Concentric Cylinders," ASME Winter Annual Meeting, Phoenix, Arizona, HTD-Vol. 22, Nov. 1982, ASME, New York, pp. 19-34.

7 Ribando, R. J., and Torrance, K. E., "Natural Convection in a Porous Medium: Effects of Confinement, Variable Permeability and Thermal Boundary Conditions," ASME JOURNAL OF HEAT TRANSFER, Vol. 97, Feb. 1976, pp. 42-48.

8 Holst, P. H., and Aziz, K., "Transient Three-dimensional Natural Convection in Confined Porous Media," *International Journal of Heat Mass Transfer*, Vol. 15, 1972, pp. 73-90.

Measurements of Turbulent Prandtl Number in a Plane Jet

L. W. B. Browne[1] and R. A. Antonia[2]

Nomenclature

- d = nozzle width
- f = distribution of U in the self-preserving region $f(\eta) = U/U_0$
- h = distribution of T in the self-preserving region $h(\eta) = T/T_0$
- H = nozzle height
- L_u = velocity half-width $L_u = y\,|_{U=U_0/2}$
- L_θ = temperature half-width $L_\theta = y\,|_{T=T_0/2}$
- P = production rate of turbulent energy $P = \overline{uv}\partial U/\partial y$
- Pr_t = turbulent Prandtl number $\mathrm{Pr}_t = \overline{uv}(\partial T/\partial y)/\overline{v\theta}(\partial U/\partial y)$
- t = time
- T = mean temperature relative to ambient
- T_j = temperature of jet at nozzle exit, relative to ambient
- T_0 = local mean temperature relative to ambient on jet centerline
- u = velocity fluctuation in x-direction
- U = mean velocity in x-direction
- U_j = velocity of jet at nozzle exit
- U_0 = local mean velocity in x-direction on jet centerline
- v = velocity fluctuation in y-direction
- V = mean velocity in y-direction
- x = streamwise coordinate measured from jet exit
- y = transverse coordinate measured from jet centerline
- ϵ = dissipation rate of turbulent energy
- η = dimensionless y co-ordinate $\eta = y/L_u$
- θ = temperature fluctuation
- $\overline{(\ )}$ = time-averaged value of ( )

Introduction

Jenkins and Goldschmidt [1] presented data, obtained from several sources, of spreading parameters for turbulent plane and circular jets into still air. Although relatively wide

[1]Senior Lecturer, Department of Mechanical Engineering, University of Newcastle, N.S.W., 2308, Australia

[2]Professor, Department of Mechanical Engineering, University of Newcastle

Contributed by the Heat Transfer Division for publication in the JOURNAL OF HEAT TRANSFER. Manuscript received by the Heat Transfer Division May 3, 1982.

variations were evident in individual spread rates for temperature and velocity fields, the ratio of these spread rates was constant, the constant being slightly larger for the plane jet (1.42) than the circular jet (1.22). There are few measurements of momentum and heat fluxes in both plane and circular jets. In a plane jet, Jenkins and Goldschmidt [2] found that conditional averages, in the turbulent part only of the flow, of turbulent momentum and thermal diffusivities were approximately constant. The ratio of these diffusivities or turbulent Prandtl number Pr_t was also approximately constant (equal to 0.4) in the intermittent region of the jet and showed a tendency to increase towards the centerline. Van der Hegge Zijnen [3] had calculated Pr_t using measured mean velocity and mean temperature profiles in a plane jet. The calculation showed that Pr_t was 0.6 at the centerline, decreased to about 0.4 where the flow became intermittent before increasing through the intermittent region to a value of about 1.0. In this note, we present measured values of Pr_t in the self-preserving region of a slightly heated plane jet and discuss them in the context of previously reported distributions for Pr_t.

Experimental Procedure

Air is supplied to the nozzle ($d = 12.7$ mm, $H = 250$ mm) by a centrifugal squirrel-cage blower via a 25 cm × 25 cm × 2 m duct, screens and a 20: 1 two-dimensional contraction. The jet is heated with 1-kW electrical coil elements distributed across the duct immediately downstream of the blower. Side walls (0.7 × 1.1 m) were installed downstream of the nozzle exit plane. The present measurements were made at a nominal U_j of 9 ms^{-1} and T_j of 25°C. The boundary layers are laminar at the nozzle exit, and the rms longitudinal velocity and temperature, measured at the centreline of the exit plane, are approximately 0.1 percent of U_j and T_j, respectively.

The velocity fluctuations and temperature fluctuation were made with an X-probe/cold wire arrangement. The hot wires (5 μm Pt-10 percent Rh, 0.6-mm length) were mounted in the horizontal x-y-plane with a separation of about 0.5 mm. The 0.63 μm cold wire (of length 0.6 mm) was located about 0.5 mm upstream of the center of the X-probe, orthogonally to the X-probe plane. The hot wires were operated with constant temperature anemometers at an overheat ratio of 1.8 while the cold wire was operated with a constant current (0.1 mA) circuit. Signals from the wires were digitized into a PDP 11/34 computer; the hot wire signals were linearized following removal of temperature contamination. The products $\overline{uv}$, $\overline{v\theta}$ were obtained for digital records of approximately 60 s duration. The mean velocity, U, and temperature, T, were obtained from the X-wire and cold wire voltages, respectively. The X-probe was calibrated for speed and yaw at the nozzle exit plane. The temperature calibration of the cold wire was also obtained at the nozzle exit.

Results and Discussion

Measured distributions of $\overline{uv}$ and $\overline{v\theta}$ are shown at $x/d = 20$ and 40 in Figs. 1 and 2, respectively. Previously measured mean velocity and mean temperature profiles for $x/d \geq 20$ were consistent with self-preservation. Distributions of normal stresses (not shown here) and of the fluxes shown in Figs. 1 and 2 are also consistent with self-preservation.

Also shown in Figs. 1 and 2 are the distributions of $\overline{uv}$ and $\overline{v\theta}$ calculated using the measured mean velocity and mean temperature profiles. The kinematic Reynolds shear stress $\overline{uv}$ and the thermometric heat flux $\overline{v\theta}$ are calculated using

$$U\frac{\partial U}{\partial x} + V\frac{\partial U}{\partial y} = -\frac{\partial \overline{uv}}{\partial y} \tag{1}$$

and

$$U\frac{\partial T}{\partial x} + V\frac{\partial T}{\partial y} = -\frac{\partial \overline{v\theta}}{\partial y} \tag{2}$$

The normal stresses term $\partial(\overline{u^2} - \overline{v^2})/\partial x$ is neglected in (1) and the longitudinal heat flux term $\partial \overline{u\theta}/\partial x$ has been neglected in (2). The y-direction velocity, V, was determined using continuity. Equations (1) and (2) can be rewritten in the form

$$\frac{\overline{uv}}{U_0^2} = -\frac{VU}{U_0^2} + \frac{dL_u}{dx}\eta f^2 - \left(2\frac{L_u}{U_0}\frac{dU_0}{dx} + \frac{dL_u}{dx}\right)\int_0^\eta f^2 d\eta \tag{3}$$

and

$$\frac{\overline{v\theta}}{U_0 T_0} = -\frac{V}{U_0}\frac{T}{T_0} + \frac{dL_u}{dx} fh\eta - \left(\frac{L_u}{T_0}\frac{dT_0}{dx} + \frac{L_u}{U_0}\frac{dU_0}{dx} + \frac{dL_u}{dx}\right)\int_0^\eta fh d\eta \tag{4}$$

The calculated $\overline{uv}$ and $\overline{v\theta}$ distributions are slightly larger than the measured distributions over the range $0 < \eta \lesssim 1.1$. Maxima for the calculated distributions are approximately 13 percent larger than the corresponding maxima for the measured distributions. It should be noted however that the observed scatter in the measurements indicated that the random component of the uncertainty in $\overline{uv}$ and $\overline{v\theta}$ were about ±7 and ±12 percent, respectively. These intervals are

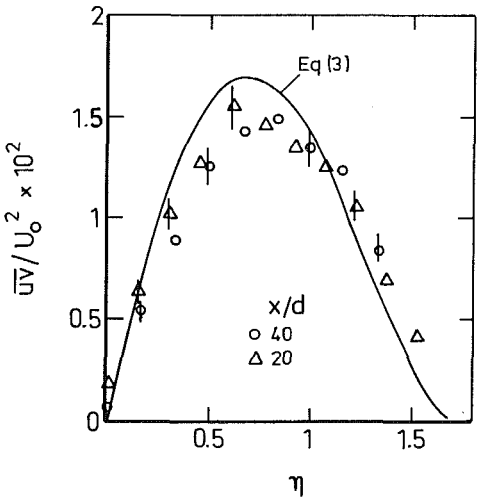

Fig. 1 Reynolds shear stress distributions

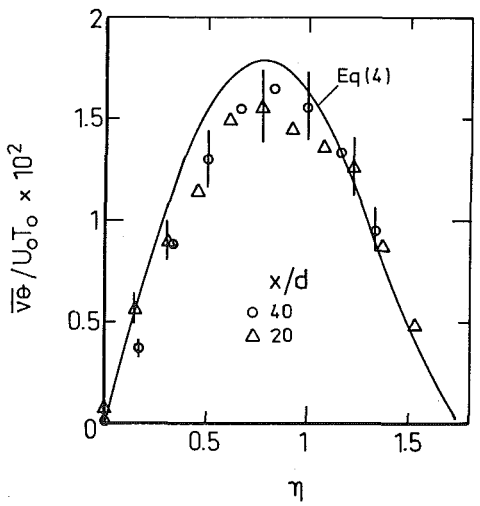

Fig. 2 Heat flux distributions

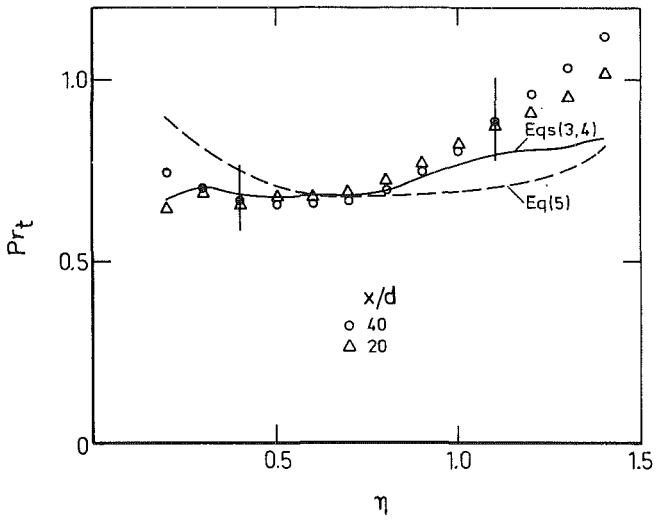

Fig. 3 Turbulent Prandtl number distributions

shown in Figs. 1 and 2 as vertical bars through a few data points. For $\eta > 1.1$, the calculated distributions are smaller than the measurements, especially in the case of $\overline{uv}$. It should be noted, however, that measurements for $\eta > 1$ are most likely in error as a result of flow reversal. Flow reversal, as evidenced by the contamination of the cold wire signal by the thermal wake from the X-probe wires, was first noted at $\eta = 1$. At this position, "spikes" (see for example [4]) are relatively infrequent. The frequency increases with η, and the contamination is significant at $\eta = 1.5$. Moallemi and Goldschmidt [5] attributed flow reversal in a plane jet to large coherent structures, somewhat similar to a vortex street. The observation that profiles of $\overline{uv}/U_0^2$, $\overline{v\theta}/U_0 T_0$ and other appropriately normalized turbulence quantities remain self-preserving in the outer part of the jet seems consistent with the idea that flow reversal is caused by these coherent structures.

Values of Pr_t, obtained from both measured and calculated values of the fluxes, are shown in Fig. 3. On the basis of the previously noted uncertainties in $\overline{uv}$ and $\overline{v\theta}$ and with an uncertainty in $\partial T/\partial U$ of about ± 3 percent, the uncertainty in Pr_t was estimated, using a propagation at constant probability, to be about ± 14 percent. An indication of this interval is given as vertical bars in Fig. 3. Agreement between measured and calculated values is good for η extending up to about 0.9. The rapid increase in the measured values of Pr_t for $\eta > 1$ may be due to the occurrence of flow reversal and/or the intermittent nature of the flow. Also shown in Fig. 3 is the distribution

$$Pr_t = 0.225 \frac{(5.4 + P/\epsilon)}{(1.2 + P/\epsilon)} \tag{5}$$

Equation (5) was proposed by Gibson and Launder [6] using a simplified second-order closure. Measured values of P and ϵ, inferred from $\overline{(\partial u/\partial t)^2}$ using local isotropy and Taylor's hypothesis, were used in (5). Agreement between (5) and the measured or calculated values of Pr_t is good near the region of maxima $\overline{uv}$ and $\overline{v\theta}$. In this region, P/ϵ is nearly unity.

The values of Pr_t in Fig. 3 are larger than those inferred from the conventionally averaged distributions $\overline{uv}$, $\overline{v\theta}$, U, and T of Jenkins and Goldschmidt [2]. No significant difference is expected between conventional averages and conditional (zone or point) averages in this region. Indeed, in the range $0.6 < \eta < 1.4$, Pr_t, as inferred from Jenkins and Goldschmidt's conventional averages, is about 0.43, in agreement with the point averaged values. Since the intermittency factor (obtained on the basis of θ) is 0.95 at $\eta = 1$, the difference between the present values of Pr_t and those of [2] cannot be directly ascribed to intermittency effects in the region $0 < \eta \leq 1$. Strictly, for $\eta > 1$, conditional measurements should be compared but flow reversal and high turbulence intensities in the outer part of the jet seriously impair the accuracy of these measurements. The above difference in Pr_t values for $\eta < 1$ seems nevertheless consistent with the difference in relative spread rates of the velocity and temperature fields in the two experiments. In Jenkins and Goldschmidt's [2] experiment, $dL_\theta/dx \simeq 0.135$ and $dL_u/dx \simeq 0.092$ so that $dL_\theta/dL_u \simeq 1.41$. In the present experiment, $dL_\theta/dL_u \simeq 1.23$ ($dL_\theta/dx \simeq 0.128$, $dL_u/dx \simeq 0.104$). Gibson and Launder's [6] "turbulence" model yielded $dL_\theta/dL_u \simeq 1.23$. It should also be noted that Davies et al. [7] found, for a plane jet, that $dL_\theta/dx \simeq 0.125$, $dL_u/dx \simeq 0.109$ so that $dL_\theta/dL_u \simeq 1.15$.

The magnitudes of $\overline{uv}U_0^2$ and especially $\overline{v\theta}/U_0 T_0$ measured by Jenkins and Goldschmidt [2], see also [8], are larger than the present values. Maximum values of $\overline{uv}/U_0^2$ and $\overline{v\theta}/U_0 T_0$ obtained in [2] are larger than the present maxima by factors of 1.37 and 2.0, respectively. Relatively large differences in Reynolds stresses in the self-preserving region of a plane jet in still air have already been reported in the literature (e.g., [9]). Gutmark and Wygnanski [10] concluded that the differences in reported values of dL_u/dx, dU_0/dx and Reynolds stress distributions can easily be attributed to initial conditions. It is possible that the difference in measured values of Pr_t or dL_θ/dL_u for the plane jet, reflect differences in initial conditions. A possible way to quantify the effect of initial conditions on the turbulence structure would be to consider the dependence of Pr_t on the total strain to which the turbulence was subjected, in the manner outlined by Townsend [11]. His calculation, based on the rapid-distortion assumption, was shown to account, in a qualitative way, for differences in Pr_t between different classes of flows. It should, in principle, be able to account for differences in Pr_t in the same flow.

Acknowledgments

The assistance of Drs A. J. Chambers and S. Rajagopalan with the experiment and data reduction is gratefully acknowledged. The support of the Australian Research Grants Scheme is also gratefully acknowledged.

References

1 Jenkins, P. E., and Goldschmidt, V. W., "Mean Temperature and Velocity in a Plane Turbulent Jet," ASME *Journal of Fluids Engineering*, Vol. 95, 1973, pp. 581–584.

2 Jenkins, P. E., and Goldschmidt, V. W., "A Study of the Intermittent Region of a Heated Two-Dimensional Plane Jet," Report HL74-75, School of Mechanical Engineering, Purdue University, 1974.

3 van der Hegge Zijnen, B., "Measurements of the Distribution of Heat and Matter in a Plane Turbulent Jet of Air," *Applied Scientific Research*, Vol. A7, 1957, pp. 277–292.

4 Antonia, R. A., Chambers, A. J., and Hussain, A. K. M. F., "Errors in Simultaneous Measurements of Temperature and Velocity in the Outer Part of a Heated Jet," *Physics of Fluids*, Vol. 23, 1980, pp. 871–874.

5 Moallemi, M. K., and Goldschmidt, V. W., "Smoke Wire Visualization of the External Region of a Two Dimensional Jet," *Proceedings of Seventh Biennial Symposium on Turbulence*, University of Missouri-Rolla, 1981, pp. 42-1-42-10.

6 Gibson, M. M., and Launder, B. E., "On the Calculation of Horizontal, Turbulent, Free Shear Flows Under Gravitational Influence," ASME JOURNAL OF HEAT TRANSFER, Vol. 98, 1976, pp. 81–87.

7 Davies, A. E., Keffer, J. F., and Baines, W. D., "Spread of a Heated Plane Turbulent Jet," *Physics of Fluids*, Vol. 18, 1975, pp. 770–775.

8 Jenkins, P. E., "Some Measured Temperature Characteristics in a Two-Dimensional Heated Jet of Air," ASME *Journal of Engineering for Power*, Vol. 98, 1976, pp. 501–505.

9 Everitt, K. W., and Robins, A. G., "The Development and Structure of Turbulent Plane Jets," *Journal of Fluid Mechanics*, Vol. 88, 1978, pp. 563–583.

10 Gutmark, E., and Wygnanski, I., "The Planar Turbulent Jet," *Journal of Fluid Mechanics*, Vol. 73, 1976, pp. 465–495.

11 Townsend, A. A., *The Structure of Turbulent Shear Flow*, 2d ed., Cambridge University Press, Cambridge.

Prediction of the Transit Time of a Stably Stratified Flow in a Channel With Inclined Surface

Seung Oh[1] and B. K. H. Sun[2]

Nomenclature

A = channel flow area, $\Delta \cdot b$ in Fig. 1
A_h = cold layer flow area, $h \cdot b$ in Fig. 1
C = constant, as defined in equation (2)
$\bar{C}$ = constant, as defined in equation (7)
D = diameter of cold leg
Fr = Froude number in the channel, as defined in equation (5)
g = acceleration due to gravity
h = height of cold layer, Fig. 1
j = superficial velocity of cold water, $j = Q/A$
Q = volumetric flow rate of cold water
V = cold layer flow velocity
V_w = wave velocity of the stratified layer, as defined in equation (1)
ρ = density of warm water
ρ_c = density of cold water
$\Delta\rho$ = density difference $\Delta\rho = \rho_c - \rho$
Δ = the channel height, Fig. 1

Introduction

Mixing and stratification due to fluid density difference have been an important subject in oceanography, meteorology, environmental engineering [1, 2], and nuclear power technology [3]. The phenomena may occur in the light-water reactors during an overcooling transient where the cold water from the high-pressure injection (HPI) is mixed with the warm water in the cold legs and the downcomer. If the downcomer vessel wall faces a cold water flow in a sustained period of time, the steel vessel can be subjected to severe thermal stress, known as the thermal shock phenomenon [3].

The scenario of possible reactor overcooling transient conditions can lead the loop flow temperature to vary between 120 and 290°C (250–550°F), while the HPI flow temperature is typically around 10 to 20°C (50–70°F). The large temperature difference can create a wide range of mixing and stratification phenomena in the cold legs. Since the downcomer fluid temperature history is a main parameter for reactor thermal shock evaluations, it is of interest to predict the transit time from HPI initiation to the time when the cold flow reaches the downcomer. The transit time prediction can be used to assess the rate of transient temperature decay and the velocity of the cold front that, in turn, is needed for entrainment evaluations.

The experimental data relevant to the phenomena of interest were obtained by Rothe and Marscher [4] from their transparent test facility, which is an approximate 1/5-scale model of a sloped cold leg and a vertical downcomer of typical Babcock and Wilcox nuclear reactors. The tests covered three different HPI geometries, which they termed the "bottom big," the "bottom small," and the "top big." The HPI flow rate was varied between 0.025 and 1.26 L/s (0.4-20 gal/min), while the loop flow was set equal to zero to simulate conditions where the reactor natural circulation breaks down. The density difference was obtained by the temperature difference of about 47°C (85°F) and by using saline solutions (salt water). Photographic studies and numerous thermocouple measurements were made to provide data on flow regimes, temperature distributions, and the transit time.

In this paper, a simple correlation based on mechanistic approaches was developed for the prediction of transit time of a stably stratified flow in a channel with an inclined surface. It is shown that the model is able to correlate all the data of Rothe and Marscher [4] for a wide range of test conditions.

Analysis

When cold water is introduced to a channel such as the one shown in Fig. 1, the cold water front spreads down along the bottom of the channel while warm water stays on top of it due to the buoyancy effect. The transit time is defined as the time for the cold layer to reach the end of the channel from the injection location and is essentially the cold front propagation time. Thus, the phenomenon resembles the spreading of the gravity current. In the study of two-dimensional gravity current by Benjamin [5] and Kao [6], it was concluded that, for the case of gravity current over a horizontal surface, the current velocity is proportional to the wave velocity. Britter and Linden [7] determined experimentally the proportional constant to be about 1.5 for inclined surfaces. By using similar approaches, it is hypothesized that the front velocity of the cold HPI water is proportional to the wave velocity in an inclined channel. The wave velocity of a stratified flow in a rectangular channel is given by [1, 2].

$$V_w = (gh\Delta\rho/\rho_c)^{1/2} \tag{1}$$

Therefore, the cold front velocity becomes

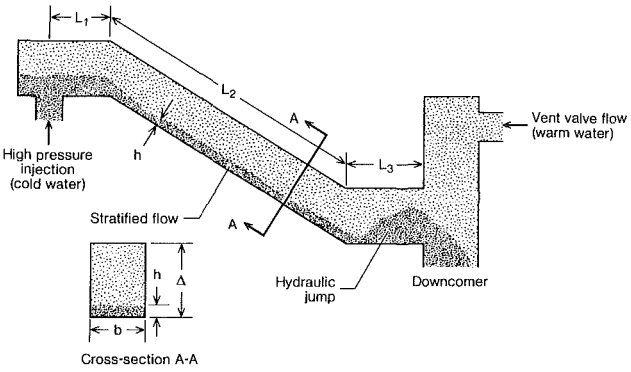

Fig. 1 Sketch of the phenomenon of cold water flowing down an inclined surface in a stratified layer with a hydraulic jump at the bottom horizontal surface

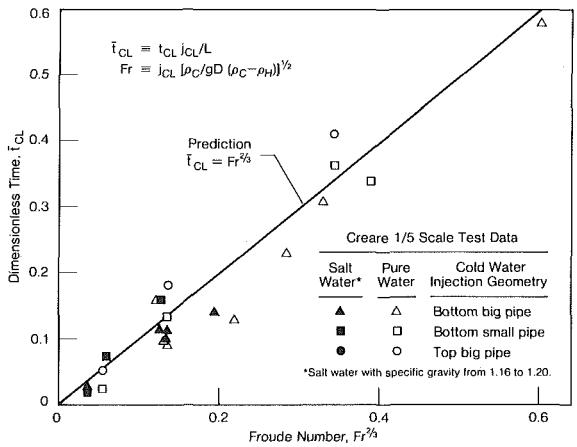

Fig. 2 Comparison of present prediction with test data from the Creare 1/5-scale B&W model (Rothe and Marscher [4])

[1]Staff Scientist, JAYCOR, Inc., San Diego, Calif. 92138
[2]Program Manager, Nuclear Power Division, Electric Power Research Institute, Palo Alto, Calif. 94303, Mem. ASME

Contributd by the Heat Transfer Division for publication in the JOURNAL OF HEAT TRANSFER. Manuscript received by the Heat Transfer Division May 21, 1982.

$$V = CV_w = C(gh\Delta\rho/\rho_c)^{1/2} \quad (2)$$

where h is the height of the stratified layer, and C is an empirical constant.

The local velocity, V, is related to the HPI flow rate through the definition of a superficial velocity, j, and a mass balance consideration. As shown in Fig. 1, this is expressed as

$$Aj_{CL} = A_h V \quad (3)$$

The combination of equations (2) and (3) leads to the following form

$$V = C^{2/3}\mathrm{Fr}^{-2/3} j_{CL} \quad (4)$$

Where Fr, the Froude number corresponding to the HPI superficial velocity, is defined as

$$\mathrm{Fr} = j_{CL}(gD\Delta\rho/\rho_c)^{-1/2} \quad (5)$$

The transit time for the HPI water to flow from the injection location to the end of the cold leg, t_{CL}, can be obtained from equations (4) and (5) as follows

$$t_{CL} = \int_o^L dx/V = \mathrm{Fr}^{2/3}\left(\int_0^L C^{-2/3}dx\right)/j_{CL} = \bar{C}\mathrm{Fr}^{2/3}L/j_{CL} \quad (6)$$

where $\bar{C}$ is defined as

$$\bar{C} = \left(\int_o^L C^{-2/3}dx\right)/L \quad (7)$$

and L is the total length of the channel.

It is shown from equations (6) and (7) that L and j_{CL} are known parameters, and once the constant $\bar{C}$ is known, the transit time can be calculated. To obtain the empirical constant, $\bar{C}$, order of magnitude analysis was made utilizing test data from one of the runs of Rothe and Marscher's experiments [4] where photographs were available for estimate of the thickness of the stratified layer.

These pictures showed three different regions as illustrated in Fig. 1. First, in the HPI injection section (L1 in Fig. 1), the cold HPI flow forms a stably stratified flow. In this section, the flow is subcritical. Second, in the sloped section (L2 in Fig. 1), the stratified flow becomes supercritical. Finally, at the straight section of the cold leg (L3 in Fig. 1), a hydraulic jump was observed, indicating a transition to a subcritical flow. The critical flow, which corresponds to the condition of local flow velocity equal to the wave velocity, occurred at the junction of L1 and L2 and at the location of hydraulic jump in L3.

The HPI velocities in the three different sections, L_1, L_2, and L_3 were estimated using the HPI mass flow rate and the thickness of the stratified layers. The velocities in section L1 are on the order of 0.2 times their corresponding wave velocities, while those in section L2 are between 1 and 2 times the wave velocities.

For Rothe and Marscher's experiments [4], L_1 is 8.8 cm, L_2 is 83.1 cm, and L_3 is 30.5 cm. With these values and assuming the flow is critical in L_3, $\bar{C}$ as evaluated by equation (7) is about one. Thus, by setting $\bar{C}$ equal to one, a simple dimensionless correlation is obtained from equation (6) that is

$$\bar{t}_{CL} = t_{CL}j_{CL}/L = \mathrm{Fr}^{2/3} \quad (8)$$

Since the reactor cold leg geometry and that simulated in Rothe and Marscher's experiment are circular pipes, the channel height in equation (8) is replaced by the diameter for applications.

In the next section, this correlation is checked by comparison with the data of Rothe and Marscher [4].

Comparison with Data

The experiment of Rothe and Marscher [4] covered a wide range of test parameters; three different HPI geometries, a fortyfold variation of HPI flow rate, a tenfold variation of $\Delta\rho/\rho_c$, and a vent valve flow that was varied from zero to three times of the maximum HPI flow rate. The vent valve flow was injected near the top of the downcomer and was the source of warm water for the nonisothermal tests. Since the cold leg is blocked at the upstream end of the HPI injector section in these experiments, there was no net vent valve flow into the cold leg. Instead, the warm vent valve flow enters the cold leg as a countercurrent flow in the nozzle and leaves by entrainment in the cold HPI layer.

It is shown from equations (5) and (8) that L, D, g, are known quantities, j_{CL} and $\Delta\rho/\rho_c$ can be obtained from test parameters, and t_{CL} is measured from the experiment. Thus, equation (8) can be easily calculated. The comparison of data with prediction from equation (8), as indicated in Fig. 2, shows that data obtained from a wide range of test conditions can be correlated by a single dimensionless line.

Conclusions

A simple mechanistic correlation has been developed for the prediction of the transit time for a stably stratified flow in a channel with an inclined surface. The correlation is able to correlate the existing data of Rothe and Marscher [4] from their 1/5-scale model of a typical cold leg and downcomer of the Babcock and Wilcox reactors. The result of the study indicates that the Froude number, as defined in equation (5), is a governing parameter for the characterization of internal flow with a stratified layer.

References

1 Turner, J. S., "*Buoyancy Effects in Fluid*," Cambridge University Press, 1973.

2 Yih, C-S., "*Fluid Mechanics*," West River Press, 1977.

3 Chexal, B., Marston, T., and Sun, B. K. H., "Tackling the Pressurized Thermal Issue," *Nuclear Engineering International*, Vol. 27, No. 327, May 1982, p. 38.

4 Rothe, P. H., and Marscher, W. D., "Fluid and Thermal Mixing in a Model Cold Leg and Downcomer with Vent Valve Flow," EPRI Report NP-2227, Mar. 1982.

5 Benjamin, T. B., "Gravity Currents and Related Phenomena," *Journal of Fluid Mechanics*, Vol. 31, 1968, pp. 209-248.

6 Kao, T. W., "Density Currents and Their Applications," *ASCE Journal of the Hydraulics Division*, Vol. 103, No. HY5, May 1977, pp. 543-555.

7 Britter, R. E. and Linden, P. F., "The Motion of the Front of a Gravity Current Travelling Down an Incline," *Journal of Fluid Mechanics*, Vol. 99, 1980, pp. 531-543.

Cauchy Method for Solidification Interface Shape During Continuous Casting

R. Siegel[1]

Nomenclature

- A = dimensionless parameter and dimensionless length, $au\rho\lambda/k(t_f - t_c) = a/\gamma$
- a = half-width of slab ingot
- B_o, B_n = coefficients in Fourier series
- b = vertical distance from center of solidification interface to bottom edge of mold
- c = modulus of elliptic integral; $c' = \sqrt{1-c^2}$
- c_p = specific heat of solidified material

[1]National Aeronautics and Space Administration, Lewis Research Center, Cleveland, Ohio 44135, Fellow ASME

Contributed by the Heat Transfer Division for publication in the JOURNAL OF HEAT TRANSFER. Manuscript received by the Heat Transfer Division November 12, 1982.

$$V = CV_w = C(gh\Delta\rho/\rho_c)^{1/2} \quad (2)$$

where h is the height of the stratified layer, and C is an empirical constant.

The local velocity, V, is related to the HPI flow rate through the definition of a superficial velocity, j, and a mass balance consideration. As shown in Fig. 1, this is expressed as

$$Aj_{CL} = A_h V \quad (3)$$

The combination of equations (2) and (3) leads to the following form

$$V = C^{2/3}\mathrm{Fr}^{-2/3} j_{CL} \quad (4)$$

Where Fr, the Froude number corresponding to the HPI superficial velocity, is defined as

$$\mathrm{Fr} = j_{CL}(gD\Delta\rho/\rho_c)^{-1/2} \quad (5)$$

The transit time for the HPI water to flow from the injection location to the end of the cold leg, t_{CL}, can be obtained from equations (4) and (5) as follows

$$t_{CL} = \int_o^L dx/V = \mathrm{Fr}^{2/3}\left(\int_0^L C^{-2/3}dx\right)/j_{CL} = \bar{C}\mathrm{Fr}^{2/3}L/j_{CL} \quad (6)$$

where $\bar{C}$ is defined as

$$\bar{C} = \left(\int_o^L C^{-2/3}dx\right)/L \quad (7)$$

and L is the total length of the channel.

It is shown from equations (6) and (7) that L and j_{CL} are known parameters, and once the constant $\bar{C}$ is known, the transit time can be calculated. To obtain the empirical constant, $\bar{C}$, order of magnitude analysis was made utilizing test data from one of the runs of Rothe and Marscher's experiments [4] where photographs were available for estimate of the thickness of the stratified layer.

These pictures showed three different regions as illustrated in Fig. 1. First, in the HPI injection section (L1 in Fig. 1), the cold HPI flow forms a stably stratified flow. In this section, the flow is subcritical. Second, in the sloped section (L2 in Fig. 1), the stratified flow becomes supercritical. Finally, at the straight section of the cold leg (L3 in Fig. 1), a hydraulic jump was observed, indicating a transition to a subcritical flow. The critical flow, which corresponds to the condition of local flow velocity equal to the wave velocity, occurred at the junction of L1 and L2 and at the location of hydraulic jump in L3.

The HPI velocities in the three different sections, L_1, L_2, and L_3 were estimated using the HPI mass flow rate and the thickness of the stratified layers. The velocities in section L1 are on the order of 0.2 times their corresponding wave velocities, while those in section L2 are between 1 and 2 times the wave velocities.

For Rothe and Marscher's experiments [4], L_1 is 8.8 cm, L_2 is 83.1 cm, and L_3 is 30.5 cm. With these values and assuming the flow is critical in L_3, $\bar{C}$ as evaluated by equation (7) is about one. Thus, by setting $\bar{C}$ equal to one, a simple dimensionless correlation is obtained from equation (6) that is

$$\bar{t}_{CL} = t_{CL}j_{CL}/L = \mathrm{Fr}^{2/3} \quad (8)$$

Since the reactor cold leg geometry and that simulated in Rothe and Marscher's experiment are circular pipes, the channel height in equation (8) is replaced by the diameter for applications.

In the next section, this correlation is checked by comparison with the data of Rothe and Marscher [4].

Comparison with Data

The experiment of Rothe and Marscher [4] covered a wide range of test parameters; three different HPI geometries, a fortyfold variation of HPI flow rate, a tenfold variation of $\Delta\rho/\rho_c$, and a vent valve flow that was varied from zero to three times of the maximum HPI flow rate. The vent valve flow was injected near the top of the downcomer and was the source of warm water for the nonisothermal tests. Since the cold leg is blocked at the upstream end of the HPI injector section in these experiments, there was no net vent valve flow into the cold leg. Instead, the warm vent valve flow enters the cold leg as a countercurrent flow in the nozzle and leaves by entrainment in the cold HPI layer.

It is shown from equations (5) and (8) that L, D, g, are known quantities, j_{CL} and $\Delta\rho/\rho_c$ can be obtained from test parameters, and t_{CL} is measured from the experiment. Thus, equation (8) can be easily calculated. The comparison of data with prediction from equation (8), as indicated in Fig. 2, shows that data obtained from a wide range of test conditions can be correlated by a single dimensionless line.

Conclusions

A simple mechanistic correlation has been developed for the prediction of the transit time for a stably stratified flow in a channel with an inclined surface. The correlation is able to correlate the existing data of Rothe and Marscher [4] from their 1/5-scale model of a typical cold leg and downcomer of the Babcock and Wilcox reactors. The result of the study indicates that the Froude number, as defined in equation (5), is a governing parameter for the characterization of internal flow with a stratified layer.

References

1 Turner, J. S., "*Buoyancy Effects in Fluid*," Cambridge University Press, 1973.

2 Yih, C-S., "*Fluid Mechanics*," West River Press, 1977.

3 Chexal, B., Marston, T., and Sun, B. K. H., "Tackling the Pressurized Thermal Issue," *Nuclear Engineering International*, Vol. 27, No. 327, May 1982, p. 38.

4 Rothe, P. H., and Marscher, W. D., "Fluid and Thermal Mixing in a Model Cold Leg and Downcomer with Vent Valve Flow," EPRI Report NP-2227, Mar. 1982.

5 Benjamin, T. B., "Gravity Currents and Related Phenomena," *Journal of Fluid Mechanics*, Vol. 31, 1968, pp. 209-248.

6 Kao, T. W., "Density Currents and Their Applications," *ASCE Journal of the Hydraulics Division*, Vol. 103, No. HY5, May 1977, pp. 543-555.

7 Britter, R. E. and Linden, P. F., "The Motion of the Front of a Gravity Current Travelling Down an Incline," *Journal of Fluid Mechanics*, Vol. 99, 1980, pp. 531-543.

Cauchy Method for Solidification Interface Shape During Continuous Casting

R. Siegel[1]

Nomenclature

- A = dimensionless parameter and dimensionless length, $au\rho\lambda/k(t_f - t_c) = a/\gamma$
- a = half-width of slab ingot
- B_o, B_n = coefficients in Fourier series
- b = vertical distance from center of solidification interface to bottom edge of mold
- c = modulus of elliptic integral; $c' = \sqrt{1-c^2}$
- c_p = specific heat of solidified material

[1]National Aeronautics and Space Administration, Lewis Research Center, Cleveland, Ohio 44135, Fellow ASME

Contributed by the Heat Transfer Division for publication in the JOURNAL OF HEAT TRANSFER. Manuscript received by the Heat Transfer Division November 12, 1982.

H_1 = a Theta function (see [4])
h = height from bottom edge of mold to location where interface contacts mold surface; $H = h/\gamma$
$K(c)$ = complete elliptic integral of the first kind, $\equiv K$
$K(c')$ = associated complete elliptic integral of the first kind, $\equiv K'$
k = thermal conductivity of solidified material
n = normal to interface; $N = n/\gamma$
q = the quantity, $e^{-\pi K'/K}$
S = dimensionless coordinate along solidification interface
t = temperature
u = casting velocity of ingot
W = potential plane, $W = \Psi + i\Phi$
x,y = coordinates in physical plane; $X = x/\gamma$, $Y = y/\gamma$
Z = complex variable, $X + iY$

Greek Symbols

γ = length scale parameter, $k(t_f - t_c)/u\,\rho\lambda$
Θ,Θ_1 = Theta functions (see [4])
θ = angle between interface normal and ingot centerplane, Fig. 2
λ = latent heat of fusion per unit mass of solid
ξ = dummy integration variable
ρ = density of solidified material
τ = time
Φ = potential function, $(t_f - t)/(t_f - t_c)$
Ψ = heat flow function orthogonal to Φ
$\tilde{\nabla}^2$ = $\partial^2/\partial X^2 + \partial^2/\partial Y^2$

Subscripts

c = at cooled boundary
f = at solidification temperature
s = at solidification interface
0 = along $\Phi = 0$ boundary

Introduction

In [1], an analysis was made to obtain the two-dimensional interface shape of a slab ingot being cast continuously by withdrawing it from a mold. A complexity in this type of problem is that the interface shape depends on the heat transfer conditions, and hence when solving for the heat conduction within the ingot the region shape must be determined simultaneously as part of the analysis. A conformal mapping method was used, and this yielded an exact solution for the interface shape. The shape was found to depend on a single parameter combining the casting velocity, width of the ingot, and the temperature depression of the cooled sides of the ingot below the solidification temperature.

An alternative method for solving this type of problem is presented here. It is more compact than the conformal mapping method, and may be useful for other similar problems. The technique is an outgrowth of the method used in [2] for a free boundary analysis of a porous cooled medium.

The ingot in the present problem is bounded by two insulated boundaries and two constant temperature boundaries. A potential function that depends on temperature is defined along with a heat flow function orthogonal to it. As a result of the boundary conditions, the ingot occupies a rectangle when plotted in terms of these two functions. From symmetry this

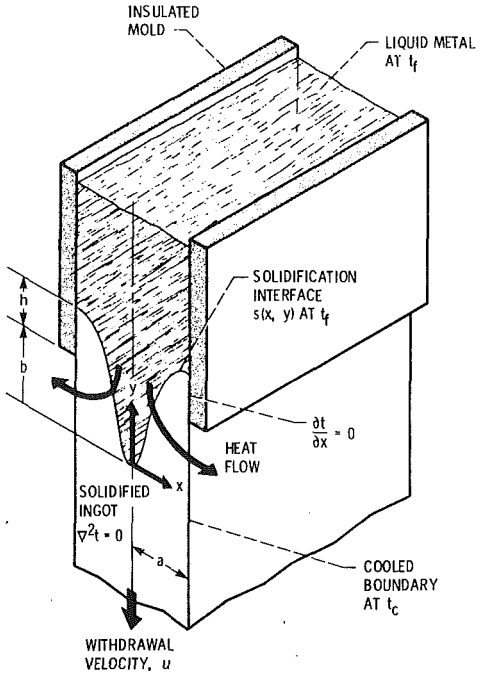

Fig. 1 Slab ingot being withdrawn from mold in continuous casting

rectangle is extended to occupy an infinite strip in the upper half plane. The solution can then be obtained as a Cauchy boundary value problem in the upper half plane, wherein the physical coordinates are treated as the dependent variables in terms of the potential and heat flow functions. This results in an infinite series solution that is summed into closed form to provide the same final expressions as in [1].

Analysis

A slab ingot is being formed by continuous casting at velocity, u (Fig. 1). The mold walls are of insulating material, and there is often poor contact of the walls with the ingot due to metal contraction. Hence, the heat flow associated with the phase change from liquid to solid at the solidification interface is transferred down and outward through the cooled sides of the ingot. These sides are cooled by a good heat-transfer medium, such as a liquid spray, so that the sides are essentially at a uniform temperature, t_c. As shown in [1], the boundary conditions along the solidification interface are

$$k \left.\frac{\partial t}{\partial n}\right|_s = \rho\lambda u \cos\theta \tag{1}$$

$$t(x_s, y_s) = t_f \tag{2}$$

Along the cooled boundaries of the ingot

$$t(x,y) = t_c \quad (x = \pm a, y < b) \tag{3}$$

and along the portion of the ingot sides that are within the mold

$$\frac{\partial t}{\partial x} = 0 \quad (x = \pm a, y > b) \tag{4}$$

As discussed in [1], there are many instances where energy transport by ingot motion is small relative to heat conduction so the temperature distribution within the solid is governed by

$$\frac{\partial^2 t}{\partial x^2} + \frac{\partial^2 t}{\partial y^2} = 0 \tag{5}$$

Ordinarily in the solution of Laplace's equation, either the temperature or temperature derivative is independently specified on each boundary. In the present situation, along

$s(x, y)$ there is specified both the temperature and the normal derivative; it is the unknown shape of the freezing interface that must be determined.

Region in Potential Plane. If a potential function is defined as $\Phi \equiv (t_f - t)/(t_f - t_c)$, then from equation (5), within the ingot

$$\tilde{\nabla}^2 \Phi = 0 \tag{6}$$

Along the solidification interface at t_f,

$$\Phi = 0 \tag{7}$$

and at the cooled boundaries, where $t = t_c$

$$\Phi = 1 \tag{8}$$

Equation (1) along the unknown interface becomes

$$-\frac{\partial \Phi}{\partial N} = \cos\theta \tag{9}$$

and along the insulated boundaries

$$\frac{\partial \Phi}{\partial X} = 0 \tag{10}$$

All lengths such as x are nondimensionalized by dividing by $\gamma = k(t_f - t_c)/u\rho\lambda$. The dimensionless width, $A = a/\gamma = au\rho\lambda/k(t_f - t_c)$ is a parameter in the solution.

Since lines of constant Φ correspond to constant temperature lines, a heat flow function, Ψ, can be defined normal to the constant Φ lines. From the Cauchy-Riemann equations, at the interface $\partial\Phi/\partial N|_s = -\partial\Psi/\partial S|_s$. Then, using equation (9)

$$\frac{\partial \Psi}{\partial X}\bigg|_s = \frac{\partial \Psi}{\partial S}\bigg|_s \frac{\partial S}{\partial X} = -\frac{\partial \Phi}{\partial N}\bigg|_s \left(-\frac{1}{\cos\theta}\right) = -1$$

so that along the solidification interface, if we let $\Psi = 0$ along the centerline $X = 0$

$$\Psi = -X \text{ along } \widehat{12} \text{ and } \widehat{89} \tag{11}$$

Then along $\widehat{23}$ and $\widehat{78}$, which are constant heat flow lines (constant Ψ lines) that join the interface at $X = -A$ and A,

$$\Psi = A \text{ along } \widehat{23},\ \Psi = -A \text{ along } \widehat{78} \tag{12}$$

The boundary conditions in terms of Φ and Ψ are summarized in Fig. 2.

From Fig. 2, it is evident that each portion of the ingot boundary is either a line of constant Φ or Ψ. The ingot region then forms a rectangle in the complex potential plane $W = \Psi + i\Phi$, Fig. 3. In the W-plane, the X, Y are dependent variables of Ψ and Φ. Since Ψ and Φ are analytic functions of X, Y, the X, Y are analytic functions of Ψ, Φ and satisfy

$$\frac{\partial^2 X}{\partial \Psi^2} + \frac{\partial^2 X}{\partial \Phi^2} = 0 \tag{13a}$$

$$\frac{\partial^2 Y}{\partial \Psi^2} + \frac{\partial^2 Y}{\partial \Phi^2} = 0 \tag{13b}$$

in the region bounded by $\Phi = 0$ and 1.

The insulated boundaries $\widehat{23}$ and $\widehat{78}$ in Fig. 3 can be considered as symmetry lines and the rectangular region repeated in a periodic fashion with Ψ to extend along the entire Ψ-axis of the upper half-plane. Then it follows from the results in [3] for a Cauchy boundary value problem that

$$Z(\Psi,\Phi) = X(\Psi,\Phi) + iY(\Psi,\Phi) = \Re e[X_0(\Psi + i\Phi)] + i\ \Re e[Y_0(\Psi + i\Phi)] + \frac{1}{2i}\int_{\Psi - i\Phi}^{\Psi + i\Phi}\left[\left(\frac{\partial X}{\partial \Phi}\right)_o(\xi) + i\left(\frac{\partial Y}{\partial \Phi}\right)_o(\xi)\right]d\xi \tag{14}$$

where the zero subscript corresponds to values along $\Phi = 0$.

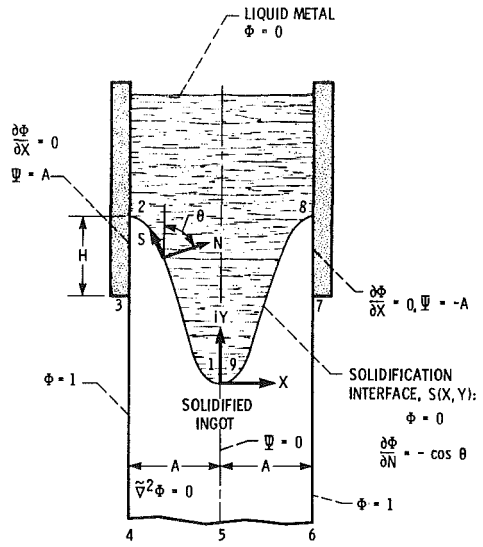

Fig. 2 Ingot geometry and boundary conditions in dimensionless physical plane, $Z = X + iY$

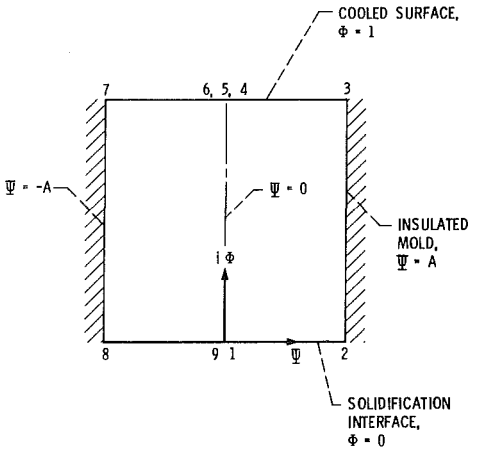

Fig. 3 Ingot in potential plane, $W = \Psi + i\Phi$

Using the Cauchy-Riemann equations, equation (14) is equal to

$$X(\Psi,\Phi) + iY(\Psi,\Phi) = \Re e[X_o(\Psi + i\Phi)] + i\ \Re e[Y_o(\Psi + i\Phi)] + \frac{1}{2i}\int_{\Psi - i\Phi}^{\Psi + i\Phi}\left[-\left(\frac{\partial Y}{\partial \Psi}\right)_o(\xi) + i\left(\frac{\partial X}{\partial \Psi}\right)_o(\xi)\right]d\xi \tag{15}$$

If the functions $X_o(\Psi)$ and $Y_o(\Psi)$ were known along the $\Phi = 0$ boundary in Fig. 3, then equation (15) yields by integration X and Y in the region in terms of known quantities

$$X(\Psi,\Phi) + iY(\Psi,\Phi) = \Re e[X_o(\Psi + i\Phi)] + i\ \Re e[Y_o(\Psi + i\Phi)] + \frac{1}{2i}\left[-Y_o(\xi) + iX_o(\xi)\right]_{\Psi - i\Phi}^{\Psi + i\Phi} = X_o(\Psi + i\Phi) + i\ Y_o(\Psi + i\Phi) \tag{16}$$

Then by separating real and imaginary parts

$$X(\Psi,\Phi) = \Re e\ X_o(\Psi + i\Phi) - \Im m\ Y_o(\Psi + i\Phi) \tag{17a}$$

$$Y(\Psi,\Phi) = \Im m\ X_o(\Psi + i\Phi) + \Re e\ Y_o(\Psi + i\Phi) \tag{17b}$$

As long as the solution is contained within a region in the upper half-plane in which Z is analytic, the X, Y coordinates can be determined from equations (17) if the functions $X_o(\Psi)$ and $Y_o(\Psi)$ are known along $\Phi = 0$. From equation (11), $X_o(\Psi) = -\Psi$. Then

$$X_o(\Psi+i\Phi) = -\Psi - i\Phi \tag{18}$$

and equations (17) become

$$X(\Psi,\Phi) = -\Psi - \mathfrak{Im}\ Y_o(\Psi+i\Phi) \tag{19a}$$

$$Y(\Psi,\Phi) = -\Phi + \mathfrak{Re}\ Y_o(\Psi+i\Phi) \tag{19b}$$

Let the unknown shape of the solidification interface be expressed as a Fourier cosine series where the B_o and B_n are unknown coefficients

$$Y_o(X) = B_o + \sum_{n=1}^{\infty} B_n \cos n\pi \frac{X}{A} \tag{20}$$

Using $X = -\Psi$ along the interface, this is inserted into equations (19) to obtain

$$X(\Psi,\Phi) = -\Psi + \sum_{n=1}^{\infty} B_n \sin n\pi \frac{\Psi}{A} \sinh n\pi \frac{\Phi}{A} \tag{21a}$$

$$Y(\Psi,\Phi) = -\Phi + B_o + \sum_{n=1}^{\infty} B_n \cos n\pi \frac{\Psi}{A} \cosh n\pi \frac{\Phi}{A} \tag{21b}$$

To obtain the B_n, it is noted that along $\widehat{34}$, $\Phi = 1$, $X = -A$, and Ψ varies from A to 0. Using these values in (21*a*) gives

$$\Psi - A = \sum_{n=1}^{\infty} B_n \sin n\pi \frac{\Psi}{A} \sinh \frac{n\pi}{A}$$

Then the B_n are found as Fourier coefficients from

$$B_n = \frac{2}{A \sinh \dfrac{n\pi}{A}} \int_0^A (\Psi - A) \sin n\pi \frac{\Psi}{A} d\Psi = -\frac{2A}{n\pi \sinh \dfrac{n\pi}{A}} \tag{22}$$

At the origin $\Phi = \Psi = 0$, and $Y = 0$, so from equation (21*b*) the B_o is

$$B_o = -\sum_{n=1}^{\infty} B_n = \frac{2A}{\pi} \sum_{n=1}^{\infty} \frac{1}{n \sinh \dfrac{n\pi}{A}} \tag{23}$$

The B values are substituted into equations (21) to yield the final expressions that map the rectangle of Fig. 3 into the ingot geometry in Fig. 2

$$X(\Psi,\Phi) = -\Psi - \frac{2A}{\pi} \sum_{n=1}^{\infty} \frac{1}{n} \sin n\pi \frac{\Psi}{A} \frac{\sinh(n\pi\Phi/A)}{\sinh(n\pi/A)} \tag{24a}$$

$$Y(\Psi,\Phi) = -\Phi - \frac{2A}{\pi} \sum_{n=1}^{\infty} \frac{1}{n} \frac{1}{\sinh \dfrac{n\pi}{A}} \left(\cos n\pi \frac{\Psi}{A} \cosh n\pi \frac{\Phi}{A} - 1\right) \tag{24b}$$

The heat flow condition at the interface was properly accounted for by use of equation (11).

The shape of the unknown interface is found by letting $\Phi = 0$ and $\Psi = -X$ (from equation (11)) in equation (24*b*) to yield

$$\frac{Y_s(X)}{A} = \frac{2}{\pi} \sum_{n=1}^{\infty} \frac{1}{n} \frac{1}{\sinh \dfrac{n\pi}{A}} \left(1 - \cos n\pi \frac{X}{A}\right) \quad -A \le X \le A \tag{25}$$

Although equation (25) gives the shape of the interface, the position of the interface must be located vertically in the mold. This is done by obtaining from equation (24*b*) the height, H, in Fig. 2 by using $H = Y_2 - Y_3 = Y(\Psi = A, \Phi = 0) - Y(\Psi = A, \Phi = 1)$. The resulting expression is placed in a more rapidly converging form by adding and subtracting the quantity

$$\frac{2}{\pi} \sum_{n=1}^{\infty} \frac{(-1)^n}{n} = -\frac{2}{\pi} \ln 2$$

to yield the final relation

$$\frac{H}{A} = \frac{1}{A} - \frac{2}{\pi} \ln 2 + \frac{4}{\pi} \sum_{n=1}^{\infty} \frac{-(-1)^n}{n} \frac{e^{-\frac{n\pi}{A}} - e^{-\frac{2n\pi}{A}}}{1 - e^{-\frac{2n\pi}{A}}} \tag{26}$$

The infinite series in equations (25) and (26) can each be summed into a closed form by use of Theta functions. From [4] (after correction of a typographical error), the logarithms of the three Theta functions, Θ, Θ_1, and H_1 yield

$$\ln\Theta_1(0) - \ln H_1(0) = -\ln(2q^{1/4}) + 2\sum_{n=1}^{\infty} \frac{-(-1)^n}{n} \frac{q^n - q^{2n}}{1 - q^{2n}} \tag{27}$$

$$\ln\left[\frac{\Theta(\zeta)}{\Theta(0)}\right] = 2\sum_{n=1}^{\infty} \frac{q^n}{n(1-q^{2n})} \left(1 - \cos n\pi \frac{\zeta}{K}\right) \tag{28}$$

where:

$$\Theta_1(0) = \sqrt{\frac{2K(c)}{\pi}}, \quad H_1(0) = \sqrt{\frac{2cK(c)}{\pi}}$$

$$\Theta(0) = \sqrt{\frac{2c'K(c)}{\pi}}, \quad q = e^{-\pi K'/K}$$

If we let $A = K(c)/K'(c)$ (this yields c corresponding to various values of the parameter A), then the series in equation (28) is the same as in equation (25) and $Y_s(X)$ becomes

$$\frac{Y_s(X)}{A} = \frac{2}{\pi} \ln \frac{\Theta\left[K(c)\dfrac{X_s}{A}\right]}{\Theta(0)} \tag{29}$$

The series in equation (27) is the same as in equation (26) so H/A reduces to

$$\frac{H}{A} = \frac{1}{2A} + \frac{1}{\pi} \ln\left(\frac{1}{c}\right) \tag{30}$$

Equations (29) and (30) are the same as the results obtained in [1] by a conformal mapping procedure.

Discussion

An alternate method is presented for the free boundary problem in continuous casting that was analyzed by conformal mapping in [1]. The analysis shows that the solidification interface shape during casting depends on only one parameter containing the casting velocity, width of the ingot, and the temperature of the boundary in contact with the coolant. Numerical results for interface shapes are not given here because they are already included in [1].

The present method treats the physical coordinates as dependent variables, with a temperature function and a heat flow function being independent variables. In this way the formulation is transformed into a Cauchy boundary value problem that directly yields the interface shape. The method is quite compact and may be useful for problems where the conformal mapping procedure is not convenient. The conformal mapping method requires using a temperature derivative plane in addition to the potential plane of the present formulation. The region in the derivative plane must be reasonably simple so that the necessary mapping transformations can be carried out. Since the derivative plane is not needed here, the present method can provide in some instances a means for treating more general heating conditions at the solidification interface.

References

1 Siegel, R., "Analysis of Solidification Interface Shape During Continuous Casting of a Slab," *International Journal of Heat and Mass Transfer*, Vol. 21, Nov. 1978, pp. 1421-1430.

2 Siegel, R., and Snyder, A., "Shape of Porous Region to Control Cooling Along Curved Exit Boundary," to be published in *International Journal of Heat and Mass Transfer*.

3 Morse, P. M., and Feshbach, H., *Methods of Theoretical Physics*, pt. I, McGraw-Hill, New York, 1953, p. 689.

4 Byrd, P. F., and Friedman, M. D., *Handbook of Elliptic Integrals for Engineers and Scientists*, 2d ed. (revised), Springer, Berlin, 1971.

Experimental Study of Solidification Heat Transfer in an Open Rectangular Cavity

C. J. Ho[1] and R. Viskanta[1, 2]

Nomenclature

AR = aspect ratio, H/W
c = specific heat
Fo = Fourier number, $\alpha_s t/H^2$
H = height of cavity
Δh_f = latent heat of fusion
S_h = superheating parameter, $c_l(T_o - T_f)/\Delta h_f$
Ste = Stefan number, $c_s(T_w - T_f)/\Delta h_f$
T = temperature
V = volume of solid frozen
W = width of cavity
α = thermal diffusivity
τ = dimensionless time, FoSte

Subscripts

f = fusion
l = liquid phase
o = initial
s = solid phase
w = wall

Introduction

This note describes solidification heat transfer experiments which were performed in a rectangular, two-dimensional, open cavity cooled from the vertial sides and the bottom. The focus in the paper is on the evolution of the solidification front and correlation of the frozen volume fraction of the phase change material with dimensionless time.

A search of archival heat transfer literature failed to unearth experiments or analyses of the type treated here. Solidification of liquids in rectangular cavities has received analytical [1-6] and experimental [1, 7] research attention, and an extensive and current literature review is available [8]. There are several effects which complicate realistic analyses of solid-liquid interface motion and heat transfer. Foremost is the fact that the solid-liquid interface position is not known *a priori* and must be determined from the solution of the problem. In addition, if the liquid is initially above its fusion temperature, natural convection will develop in the liquid, and also the difference in density between the solid and liquid phases will produce bulk motion in the fluid. Finally, in a test container that is open at the top, two moving boundaries will be formed: one at the solid-liquid interface and the other at the solid-gas interface at the top. In none of the aforementioned references have the combined effects of temperature and density difference (between solid and liquid phases) driven convection been studies.

[1]School of Mechanical Engineering, Purdue University, West Lafayette, Ind. 47907

[2]Fellow ASME

Contributed by the Heat Transfer Division for publication in the JOURNAL OF HEAT TRANSFER. Manuscript received by the Heat Transfer Division January 3, 1983.

Experiments

Solidification experiments with research grade (99 percent pure, $T_f = 27.4°C$, $\Delta h_f = 243.5$ kJ/kg) n-octadecane were performed in a rectangular test cell, 150-mm high, 80-mm wide, and 50-mm deep, open at the top. The upper surface of the material was bounded by an insulative air gap. Freezing occurred from the two vertical sides and the bottom of the cell. The front and back faces of the test cell were made from plexiglass to allow visualization, photographing, and optical measurements. To reduce natural convection from the test cell to the ambient laboratory environment, a second plexiglass plate was installed parallel to the first one. The thickness of the air gap between the two vertical plexiglass plates was chosen so as to minimize heat transfer between the test cell and the ambient environment. The vertical walls and the bottom surface of the test region could be cooled by circulating a working fluid from a constant temperature bath through multiple channels milled in a copper block to form a heat exchanger. The entire test cell was covered with removable insulation. A more detailed description of the test cell can be found in an earlier paper [9]. The thermophysical properties of n-octadecane are tabulated elsewhere [10].

To gain some insight into the effect of the initial liquid superheating on the solidification process, different initial temperature conditions in the liquid phase change material were studied. The solid-liquid interface motion was photographed using a 35-mm camera, and the tracing of the solid-liquid interface contours yielded the position and shape of the interface corresponding to the time of the experiment. The frozen fraction of the PCM was determined by measuring the area of the solid formed on the walls.

Results and Discussion

Whiskerlike (i.e., dendritic) growth was observed to form on the cooled surfaces and of the test cell. The physical processes involved are very complex and are not completely understood. A similar observation has been reported by others [11]. An examination of the photographs revealed that there was slightly more freezing at the edge near the free liquid surface. This is attributed in part to the heat loss from the free surface of the material to the ambient air across the air gap and insulation above the free surface.

Figure 1 illustrates the movement of the solid-liquid interface with time that was traced directly from the photographs. The contours displayed in the figure show that early in the process the solid layer was practically uniform in thickness over about 98 percent of the cavity height. As the liquid solidified, the liquid level dropped continuously during the course of the process. As a result, the shape of the in-

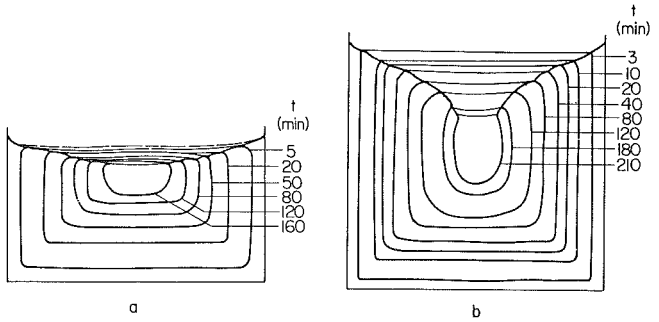

Fig. 1 Solid-liquid interface contours during freezing of n-octadecane in a rectangular cavity, Ste = 0.148, S_h = 0.010: (a) AR = 0.5 and (b) AR = 1.0

References

1 Siegel, R., "Analysis of Solidification Interface Shape During Continuous Casting of a Slab," *International Journal of Heat and Mass Transfer*, Vol. 21, Nov. 1978, pp. 1421-1430.

2 Siegel, R., and Snyder, A., "Shape of Porous Region to Control Cooling Along Curved Exit Boundary," to be published in *International Journal of Heat and Mass Transfer*.

3 Morse, P. M., and Feshbach, H., *Methods of Theoretical Physics*, pt. I, McGraw-Hill, New York, 1953, p. 689.

4 Byrd, P. F., and Friedman, M. D., *Handbook of Elliptic Integrals for Engineers and Scientists*, 2d ed. (revised), Springer, Berlin, 1971.

Experimental Study of Solidification Heat Transfer in an Open Rectangular Cavity

C. J. Ho[1] and R. Viskanta[1, 2]

Nomenclature

AR = aspect ratio, H/W
c = specific heat
Fo = Fourier number, $\alpha_s t/H^2$
H = height of cavity
Δh_f = latent heat of fusion
S_h = superheating parameter, $c_l(T_o - T_f)/\Delta h_f$
Ste = Stefan number, $c_s(T_w - T_f)/\Delta h_f$
T = temperature
V = volume of solid frozen
W = width of cavity
α = thermal diffusivity
τ = dimensionless time, FoSte

Subscripts

f = fusion
l = liquid phase
o = initial
s = solid phase
w = wall

Introduction

This note describes solidification heat transfer experiments which were performed in a rectangular, two-dimensional, open cavity cooled from the vertial sides and the bottom. The focus in the paper is on the evolution of the solidification front and correlation of the frozen volume fraction of the phase change material with dimensionless time.

A search of archival heat transfer literature failed to unearth experiments or analyses of the type treated here. Solidification of liquids in rectangular cavities has received analytical [1-6] and experimental [1, 7] research attention, and an extensive and current literature review is available [8]. There are several effects which complicate realistic analyses of solid-liquid interface motion and heat transfer. Foremost is the fact that the solid-liquid interface position is not known *a priori* and must be determined from the solution of the problem. In addition, if the liquid is initially above its fusion temperature, natural convection will develop in the liquid, and also the difference in density between the solid and liquid phases will produce bulk motion in the fluid. Finally, in a test container that is open at the top, two moving boundaries will be formed: one at the solid-liquid interface and the other at the solid-gas interface at the top. In none of the aforementioned references have the combined effects of temperature and density difference (between solid and liquid phases) driven convection been studies.

[1]School of Mechanical Engineering, Purdue University, West Lafayette, Ind. 47907

[2]Fellow ASME

Contributed by the Heat Transfer Division for publication in the JOURNAL OF HEAT TRANSFER. Manuscript received by the Heat Transfer Division January 3, 1983.

Experiments

Solidification experiments with research grade (99 percent pure, $T_f = 27.4°C$, $\Delta h_f = 243.5$ kJ/kg) n-octadecane were performed in a rectangular test cell, 150-mm high, 80-mm wide, and 50-mm deep, open at the top. The upper surface of the material was bounded by an insulative air gap. Freezing occurred from the two vertical sides and the bottom of the cell. The front and back faces of the test cell were made from plexiglass to allow visualization, photographing, and optical measurements. To reduce natural convection from the test cell to the ambient laboratory environment, a second plexiglass plate was installed parallel to the first one. The thickness of the air gap between the two vertical plexiglass plates was chosen so as to minimize heat transfer between the test cell and the ambient environment. The vertical walls and the bottom surface of the test region could be cooled by circulating a working fluid from a constant temperature bath through multiple channels milled in a copper block to form a heat exchanger. The entire test cell was covered with removable insulation. A more detailed description of the test cell can be found in an earlier paper [9]. The thermophysical properties of n-octadecane are tabulated elsewhere [10].

To gain some insight into the effect of the initial liquid superheating on the solidification process, different initial temperature conditions in the liquid phase change material were studied. The solid-liquid interface motion was photographed using a 35-mm camera, and the tracing of the solid-liquid interface contours yielded the position and shape of the interface corresponding to the time of the experiment. The frozen fraction of the PCM was determined by measuring the area of the solid formed on the walls.

Results and Discussion

Whiskerlike (i.e., dendritic) growth was observed to form on the cooled surfaces and of the test cell. The physical processes involved are very complex and are not completely understood. A similar observation has been reported by others [11]. An examination of the photographs revealed that there was slightly more freezing at the edge near the free liquid surface. This is attributed in part to the heat loss from the free surface of the material to the ambient air across the air gap and insulation above the free surface.

Figure 1 illustrates the movement of the solid-liquid interface with time that was traced directly from the photographs. The contours displayed in the figure show that early in the process the solid layer was practically uniform in thickness over about 98 percent of the cavity height. As the liquid solidified, the liquid level dropped continuously during the course of the process. As a result, the shape of the in-

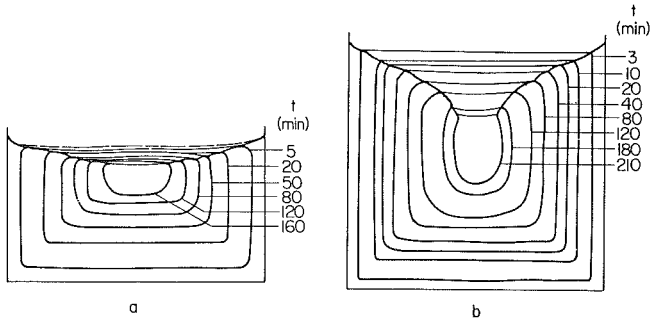

Fig. 1 Solid-liquid interface contours during freezing of n-octadecane in a rectangular cavity, Ste = 0.148, S_h = 0.010: (a) AR = 0.5 and (b) AR = 1.0

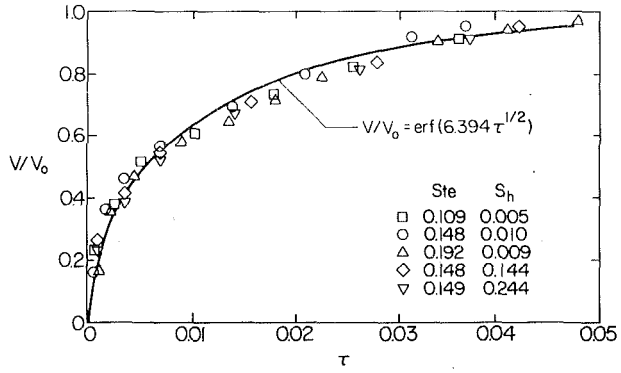

Fig. 2 Variation of frozen volume fraction with dimensionless time during freezing of n-octadecane

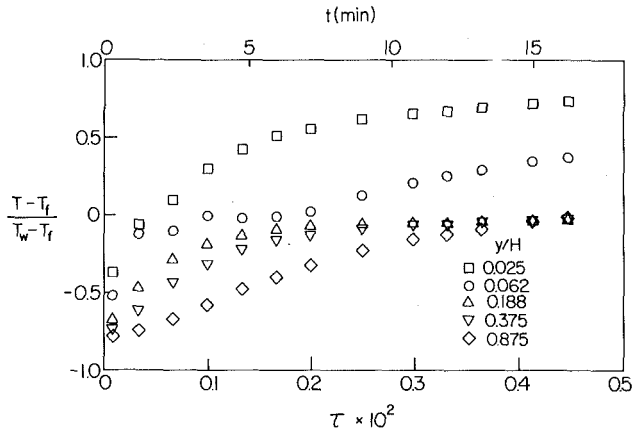

Fig. 3 Temperature history during freezing of n-octadecane in a rectangular cavity, Ste = 0.141, S_h = 0.110 and AR = 1.0

terface at the free surface became concave, and the free surface became nonplanar.

Figure 2 shows the variation of frozen fraction with dimensionless time τ (=FoSte) for different Stefan numbers (i.e., different temperatures imposed on the cavity walls) and different superheating parameters. The initial temperature of the liquid phase change material in some of the experiments was maintained nearly identical to the fusion temperature in order to eliminate the effect of the initial superheating on the solidification process. It is evident from the figure that the dimensionless time τ is appropriate time scale for the solidification process, since all the data appear to collapse into a single, unique, curve described by the empirical equation given on the figure. This equation was obtained by a least-squares fit of the experimental data for $S_h = 0$. Inspection of the figure reveals further that the slope of the curve decreases continuously with time, and this indicates gradual slowdown of the freezing rate during the cooling. This is due to the increase in the thermal resistance of the solid as a result of the growth in the thickness of the frozen layer.

In some of the experiments (Fig. 2), the Stefan numbers were kept nearly identical, but the initial superheating of the liquid was varied. It is clear from the figure that the initial superheating is of little significance in determining the rate of freezing during inward solidification in an isothermal wall cavity. The data points shown in the figure for initially superheated liquid conditions ($S_h > 0$) could be brought together more closely by defining an effective Stefan number such that $\mathrm{STE}_{\mathrm{eff}} = \mathrm{Ste}/(1 + S_h)$.

Several studies which have been reported demonstrate that natural convection in the liquid is significant during freezing [8]. The process can be drastically slowed down and ultimately terminated by natural convection during the outward solidification of a initially superheated liquid. However, there are some instances where the presence of temperature gradients in the liquid do not induce significant natural convection circulation, e.g., stably stratified liquid in which fluid of a lesser density is above fluid of a greater density. This situation is more likely to take place in an inward freezing problem of this study. In order to examine the significance of the effect of initial liquid superheating, several experiments were conducted with initial liquid temperatures greatly exceeding the fusion temperature of the material. A Mach-Zehnder interferometer was employed to construct interference fringe patterns in the liquid during solidification by using optical quality glass windows for the test cell. However, even for a relatively small temperture difference ($T_o - T_f$), the interference fringe density was very large, and the interferograms could not be used for quantitative measurements. The interference fringe patterns recorded showed that the initial superheating of the liquid was dissipated rapidly because energy required to cool the liquid to the fusion temperature, $c_l(T_o - T_f)$, is much smaller than the latent heat of fusion, Δh_f.

The temperature history in the liquid during the course of solidification (Fig. 3) was recorded by inserting a probe of five type-T thermocouples situated at different heights along the plane of symmetry of the cavity. It can be seen from the figure that the superheated liquid was cooled down to nearly its fusion temperature in a much shorter period of time (τ = 0.005, approximately 20 min) in comparison with the time period that spanned complete solidification (about 4 hrs). The finding indicates that the initial superheating of the liquid PCM was dissipated rapidly so that its effect on the solidification could be seen only early in the process.

The effect of the cavity aspect ratio on the solidification was also investigated. Owing to the small influence of the initial liquid superheating on the solidification in the cavity, no significant effect of the aspect ratio of the cavity was found.

Concluding Remarks

In contrast to outward solidification [8], the results of this study show that inward solidification of a superheated liquid (n-octadecane) contained in a rectangular cavity is affected little by fluid motion in the liquid melt.

Initial superheating of the liquid decreases the rate of solidification. The solidified volume fraction data were correlated using a dimensionless group that involves only dimensionless time, the product of Fourier and Stefan numbers.

Acknowledgments

This work was supported by the Heat Transfer Program of the National Science Foundation under Grant MEA-8014061.

References

1 Pehlke, R. D., Kirt, M. J., Marrone, R. E., and Cook, D. J., "Numerical Simulation of Casting Solidification," *CFS Cast Metals Research Journal*, Vol. 9, 1973, pp. 49–55.

2 Shamsundar, N., and Sparrow, E. M., "Analysis of Multidimensional Conduction Phase Change via the Enthalpy Model," ASME JOURNAL OF HEAT TRANSFER, Vol. 97, 1975, pp. 333–340.

3 Shamsundar, N., and Sparrow, E. M., "Effect of Density Change on Multidimensional Conduction Phase Change," ASME JOURNAL OF HEAT TRANSFER, Vol. 98, 1976, pp. 550–557.

4 Zavgorodnui, P. F., Povkh, I. L., and Sevost'yanov, G. M., "Concentration Convection in a Solidifying Melt," *High Temperature*, Vol. 14, 1976, pp. 728–732.

5 Saitoh, T., "Numerical Method for Multidimensional Freezing Problems in Arbitrary Domains," ASME JOURNAL OF HEAT TRANSFER, Vol. 100, 1978, pp. 294–299.

6 Sproston, J. L., "Two-Dimensional Solidification in Pipes of Rec-

tangular Section," *International Journal of Heat and Mass Transfer*, Vol. 24, 1981, pp. 1493-1501.

7 Patel, G. S., Goodling, J. S., and Khader, M. S., "Experimental Results of Two-Dimensional Inward Solidification," *Heat Transfer—1978*, Vol. 3, Hemisphere Publishing Corp., Washington, D.C., 1978, pp. 313-316.

8 Viskanta, R., "Phase-Change Heat Transfer," *Solar Heat Storage: Latent Heat Materials*, edited by G. A. Lane, CRC Press, Boca Raton, Fla., 1983.

9 Ho, C. J., and Viskanta, R., "Experimental Study of Melting in a Rectangular Cavity," *Heat Transfer—1982*, Vol. 2, edited by U. Grigull, et al., Hemisphere Publishing Corp., Washington, D. C., 1982, pp. 369-374.

10 Ho, C. J., "Solid-Liquid Phase Change Heat Transfer in Enclosures," Ph.D. thesis, Purdue University, 1982.

11 Sparrow, E. M., Ramsey, J. W., and Kemink, R. G., "Freezing Controlled by Natural Convection," ASME JOURNAL OF HEAT TRANSFER, Vol. 101, 1979, pp. 578-584.

Heat Transfer Through Thin Films: Approximate Analysis and Determination of Effective Heat Transfer Coefficient

L. E. Bobisud[1]

Introduction

The transfer of heat through the surface of a material is involved in many engineering problems, for example, the determination of the temperature distribution in a cooling fin. In practical situations the surface is often overlaid with a coating of another substance—scale, tarnish, oil, paint, etc.—possessing properties different from those of the underlying material and changing the heat transfer characteristics of the composite. Typically, this layer is both thin and a relatively poor conductor of heat. Although one can analyze the full problem of heat transfer through the base material, through the thin layer, and from the surface of this layer, such an analysis is more difficult than that involved in the textbook case of no surface layer. In this note we show how a related problem whose solution approximates the desired solution can be deduced when the surface layer is thin and poorly conducting, as is frequently the case. We also obtain low-order correction terms.

Analysis

For clarity we explore only a simple example that adequately illustrates the approach; the method can be employed in a much more general context, including time dependence, multiple layers, and more complex geometries. Thus, we consider the steady-state heat distribution within a semi-infinite flat plate occupying the region $x > 0$, $-L < y < L$, $-\infty < z < \infty$ with thin layers located in the regions $x > 0$, $-L-\epsilon < y < -L$, $-\infty < z < \infty$ and $x > 0$, $L < y < L+\epsilon$, $-\infty < z < \infty$. At the boundary $x = 0$ of the plate we impose the condition that the temperature be T_1, while far away from the plate the ambient temperature is T_0. We shall use lower case letters for properties of the thin layer and upper case for those of the base material:

K,k = thermal conductivity
h = coefficient of heat transfer between the thin layer and the ambient material
U,u = temperature

Taking advantage of the symmetries of the problem, we have at once the following formulation:

$$U_{xx}+U_{yy}=0, U_y(x,0)=0, U(0,y)=T_1 \quad (x>0, 0<y<L) \quad (1)$$

$$u_{xx}+u_{yy}=0, u(0,y)=T_1 \quad (x>0, L<y<L+\epsilon) \quad (2)$$

$$-ku_y(x,L+\epsilon)=h[u(x,L+\epsilon)-T_0] \quad (x>0) \quad (3)$$

$$U(x,L)=u(x,L), KU_y(x,L)=ku_y(x,L) \quad (x>0) \quad (4)$$

where we assume perfect thermal contact at the base material-thin layer junction.

The essence of our approach is the supposition that both the thermal conductivity, k, and the thickness, ϵ, of the coating layer not only approach zero, but do so in a related manner. The precise interrelationship determines the nature of the zeroth-order approximation [1]; this approximation should reflect as much of the physics of the situation as is possible in order that a minimal number of higher-order terms will be required. If we assume the simple relationship $k = \bar{k}\epsilon^\lambda$ for some constants, $\bar{k}$ and λ, then [1] for $\lambda > 1$ the zeroth-order approximation corresponds to treating the coating layer as an insulator, while for $\lambda < 1$ it corresponds to ignoring the presence of the thin layer. Since neither of these seem particularly good representations, we pursue here only the case $\lambda = 1$; i.e., we assume that

$$k=\bar{k}\epsilon \quad (5)$$

for some constant $\bar{k} \equiv k/\epsilon$.

We introduce a new independent variable, w, through $L + \epsilon w = y$ for $L < y < L+\epsilon$; then (2-4) can be written as

$$\epsilon^2 u_{xx}+u_{ww}=0, u(0,w)=T_1 \quad (x>0, 0<w<1) \quad (6)$$

$$-\bar{k}u_w(x,1)=h[u(x,1)-T_0] \quad (x>0) \quad (7)$$

$$U(x,L)=u(x,0), KU_y(x,L)=\bar{k}u_w(x,0) \quad (x>0) \quad (8)$$

Proceeding formally, we set $U = U^0 + \epsilon U^1 + \epsilon^2 U^2 + \ldots$, $u = u^0 + \epsilon u^1 + \epsilon^2 u^2 + \ldots$, where superscripts are used to avoid confusion with partial derivatives. Inserting these asymptotic expansions into (1), (6-8), using (5), and equating coefficients of like powers of ϵ, we get that

$$U^0_{xx}+U^0_{yy}=0, U^0_y(x,0)=0, U^0(0,y)=T_1 \quad (x>0, 0<y<L) \quad (9)$$

$$u^0_{ww}=0, u^0(0,w)=T_1 \quad (x>0, 0<w<1) \quad (10)$$

$$-\bar{k}u^0_w(x,1)=h[u^0(x,1)-T_0] \quad (x>0) \quad (11)$$

$$U^0(x,L)=u^0(x,0), KU^0_y(x,L)=\bar{k}u^0_w(x,0) \quad (x>0) \quad (12)$$

$$U^1_{xx}+U^1_{yy}=0, U^1_y(x,0)=0, U^1(0,y)=0 \quad (x>0, 0<y<L) \quad (13)$$

$$u^1_{ww}=0, u^1(0,w)=0 \quad (x>0, 0<w<1) \quad (14)$$

$$-\bar{k}u^1_w(x,1)=hu^1(x,1) \quad (x>0) \quad (15)$$

$$U^1(x,L)=u^1(x,0), KU^1_y(x,L)=\bar{k}u^1_w(x,0) \quad (x>0) \quad (16)$$

$$U^2_{xx}+U^2_{yy}=0, U^2_y(x,0)=0, U^2(0,y)=0 \quad (x>0, 0<y<L) \quad (17)$$

$$u^2_{ww}=-u^0_{xx}, u^2(0,w)=0 \quad (x>0, 0<w<1) \quad (18)$$

$$-\bar{k}u^2_w(x,1)=hu^2(x,1) \quad (x>0) \quad (19)$$

$$U^2(x,L)=u^2(x,0), KU^2_y(x,L)=\bar{k}u^2_w(x,0) \quad (x>0) \quad (20)$$

etc.

From the first equation of (10), we have that $u^0(x,w) = f^0(x)w + g^0(x)$ for some functions f^0 and g^0; substitution into (11) yields

$$u^0(x,w)=T_0+f^0(x)\left[w-1-\frac{\bar{k}}{h}\right]. \quad (21)$$

If we substitute this into the two equations of (12) and eliminate f^0 between them, there results

$$f^0(x)=\frac{K}{\bar{k}}U^0_y(x,L) \quad (22)$$

[1] Professor of Mathematics, University of Idaho, Moscow, Idaho 83843

Contributed by the Heat Transfer Division for publication in the JOURNAL OF HEAT TRANSFER. Manuscript received by the Heat Transfer Division September 22, 1982.

tangular Section," *International Journal of Heat and Mass Transfer*, Vol. 24, 1981, pp. 1493-1501.

7 Patel, G. S., Goodling, J. S., and Khader, M. S., "Experimental Results of Two-Dimensional Inward Solidification," *Heat Transfer—1978*, Vol. 3, Hemisphere Publishing Corp., Washington, D.C., 1978, pp. 313-316.

8 Viskanta, R., "Phase-Change Heat Transfer," *Solar Heat Storage: Latent Heat Materials*, edited by G. A. Lane, CRC Press, Boca Raton, Fla., 1983.

9 Ho, C. J., and Viskanta, R., "Experimental Study of Melting in a Rectangular Cavity," *Heat Transfer—1982*, Vol. 2, edited by U. Grigull, et al., Hemisphere Publishing Corp., Washington, D. C., 1982, pp. 369-374.

10 Ho, C. J., "Solid-Liquid Phase Change Heat Transfer in Enclosures," Ph.D. thesis, Purdue University, 1982.

11 Sparrow, E. M., Ramsey, J. W., and Kemink, R. G., "Freezing Controlled by Natural Convection," ASME JOURNAL OF HEAT TRANSFER, Vol. 101, 1979, pp. 578-584.

Heat Transfer Through Thin Films: Approximate Analysis and Determination of Effective Heat Transfer Coefficient

L. E. Bobisud[1]

Introduction

The transfer of heat through the surface of a material is involved in many engineering problems, for example, the determination of the temperature distribution in a cooling fin. In practical situations the surface is often overlaid with a coating of another substance—scale, tarnish, oil, paint, etc.—possessing properties different from those of the underlying material and changing the heat transfer characteristics of the composite. Typically, this layer is both thin and a relatively poor conductor of heat. Although one can analyze the full problem of heat transfer through the base material, through the thin layer, and from the surface of this layer, such an analysis is more difficult than that involved in the textbook case of no surface layer. In this note we show how a related problem whose solution approximates the desired solution can be deduced when the surface layer is thin and poorly conducting, as is frequently the case. We also obtain low-order correction terms.

Analysis

For clarity we explore only a simple example that adequately illustrates the approach; the method can be employed in a much more general context, including time dependence, multiple layers, and more complex geometries. Thus, we consider the steady-state heat distribution within a semi-infinite flat plate occupying the region $x > 0$, $-L < y < L$, $-\infty < z < \infty$ with thin layers located in the regions $x > 0$, $-L-\epsilon < y < -L$, $-\infty < z < \infty$ and $x > 0$, $L < y < L+\epsilon$, $-\infty < z < \infty$. At the boundary $x = 0$ of the plate we impose the condition that the temperature be T_1, while far away from the plate the ambient temperature is T_0. We shall use lower case letters for properties of the thin layer and upper case for those of the base material:

K,k = thermal conductivity
h = coefficient of heat transfer between the thin layer and the ambient material
U,u = temperature

Taking advantage of the symmetries of the problem, we have at once the following formulation:

$$U_{xx}+U_{yy}=0, U_y(x,0)=0, U(0,y)=T_1 \quad (x>0, 0<y<L) \quad (1)$$

$$u_{xx}+u_{yy}=0, u(0,y)=T_1 \quad (x>0, L<y<L+\epsilon) \quad (2)$$

$$-ku_y(x,L+\epsilon)=h[u(x,L+\epsilon)-T_0] \quad (x>0) \quad (3)$$

$$U(x,L)=u(x,L), KU_y(x,L)=ku_y(x,L) \quad (x>0) \quad (4)$$

where we assume perfect thermal contact at the base material-thin layer junction.

The essence of our approach is the supposition that both the thermal conductivity, k, and the thickness, ϵ, of the coating layer not only approach zero, but do so in a related manner. The precise interrelationship determines the nature of the zeroth-order approximation [1]; this approximation should reflect as much of the physics of the situation as is possible in order that a minimal number of higher-order terms will be required. If we assume the simple relationship $k = \bar{k}\epsilon^\lambda$ for some constants, $\bar{k}$ and λ, then [1] for $\lambda > 1$ the zeroth-order approximation corresponds to treating the coating layer as an insulator, while for $\lambda < 1$ it corresponds to ignoring the presence of the thin layer. Since neither of these seem particularly good representations, we pursue here only the case $\lambda = 1$; i.e., we assume that

$$k=\bar{k}\epsilon \quad (5)$$

for some constant $\bar{k} \equiv k/\epsilon$.

We introduce a new independent variable, w, through $L + \epsilon w = y$ for $L < y < L+\epsilon$; then (2-4) can be written as

$$\epsilon^2 u_{xx}+u_{ww}=0, u(0,w)=T_1 \quad (x>0, 0<w<1) \quad (6)$$

$$-\bar{k}u_w(x,1)=h[u(x,1)-T_0] \quad (x>0) \quad (7)$$

$$U(x,L)=u(x,0), KU_y(x,L)=\bar{k}u_w(x,0) \quad (x>0) \quad (8)$$

Proceeding formally, we set $U = U^0 + \epsilon U^1 + \epsilon^2 U^2 + \ldots$, $u = u^0 + \epsilon u^1 + \epsilon^2 u^2 + \ldots$, where superscripts are used to avoid confusion with partial derivatives. Inserting these asymptotic expansions into (1), (6-8), using (5), and equating coefficients of like powers of ϵ, we get that

$$U^0_{xx}+U^0_{yy}=0, U^0_y(x,0)=0, U^0(0,y)=T_1 \quad (x>0, 0<y<L) \quad (9)$$

$$u^0_{ww}=0, u^0(0,w)=T_1 \quad (x>0, 0<w<1) \quad (10)$$

$$-\bar{k}u^0_w(x,1)=h[u^0(x,1)-T_0] \quad (x>0) \quad (11)$$

$$U^0(x,L)=u^0(x,0), KU^0_y(x,L)=\bar{k}u^0_w(x,0) \quad (x>0) \quad (12)$$

$$U^1_{xx}+U^1_{yy}=0, U^1_y(x,0)=0, U^1(0,y)=0 \quad (x>0, 0<y<L) \quad (13)$$

$$u^1_{ww}=0, u^1(0,w)=0 \quad (x>0, 0<w<1) \quad (14)$$

$$-\bar{k}u^1_w(x,1)=hu^1(x,1) \quad (x>0) \quad (15)$$

$$U^1(x,L)=u^1(x,0), KU^1_y(x,L)=\bar{k}u^1_w(x,0) \quad (x>0) \quad (16)$$

$$U^2_{xx}+U^2_{yy}=0, U^2_y(x,0)=0, U^2(0,y)=0 \quad (x>0, 0<y<L) \quad (17)$$

$$u^2_{ww}=-u^0_{xx}, u^2(0,w)=0 \quad (x>0, 0<w<1) \quad (18)$$

$$-\bar{k}u^2_w(x,1)=hu^2(x,1) \quad (x>0) \quad (19)$$

$$U^2(x,L)=u^2(x,0), KU^2_y(x,L)=\bar{k}u^2_w(x,0) \quad (x>0) \quad (20)$$

etc.

From the first equation of (10), we have that $u^0(x,w) = f^0(x)w + g^0(x)$ for some functions f^0 and g^0; substitution into (11) yields

$$u^0(x,w)=T_0+f^0(x)\left[w-1-\frac{\bar{k}}{h}\right]. \quad (21)$$

If we substitute this into the two equations of (12) and eliminate f^0 between them, there results

$$f^0(x)=\frac{K}{\bar{k}}U^0_y(x,L) \quad (22)$$

[1] Professor of Mathematics, University of Idaho, Moscow, Idaho 83843

Contributed by the Heat Transfer Division for publication in the JOURNAL OF HEAT TRANSFER. Manuscript received by the Heat Transfer Division September 22, 1982.

$$-KU_y^0(x,L) = \frac{h\bar{k}}{h+\bar{k}}[U^0(x,L) - T_0] \tag{23}$$

(9) and (23) constitute a complete problem for U^0, the zeroth-order approximation to the temperature distribution in the base material. Once U^0 is determined, the rate of heat flow through the base of the fin can be obtained in the usual fashion. Note that the problem for U^0 does not depend on the heat distribution in the coating. The boundary condition (23) is of the convection type, but the heat transfer coefficient is no longer merely that for the coating-ambient material interface. To lowest-order terms the effect of the coating is replacement of the thermal conductivity k by K and reduction of the effective heat transfer coefficient by a factor $1 + \epsilon h/k$—compare (3) and (23). From an engineering standpoint, determination of this factor is the chief result of our calculations.

We consider in the same vein the problem (13–16) for the first-order correction. Equations (14–16) yield

$$-KU_y^1(x,L) = \frac{h\bar{k}}{h+\bar{k}} U^1(x,L) \tag{24}$$

Equations (13) and (24) determine the first-order correction term, U^1. (Since this problem happens to be homogeneous, we have $U^1 \equiv 0$ in this instance. In general, $U^1 \not\equiv 0$ for time dependent problems.)

Turning to (17–20), from (18, 19, 22) we find that

$$u_{ww}^2 = -\frac{K}{\bar{k}} U_{yxx}^0(x,L)\left[w - 1 - \frac{\bar{k}}{h}\right] \tag{25}$$

The right-hand side is a known function once U^0 has been found, provided U^0 is sufficiently smooth. Determination of the problem for U^2 now proceeds as before and results in a nonhomogeneous problem.

We have throughout ignored the boundary conditions $u^0(0,w) = T_1$, $u^i(0,w) = 0$ $(i = 1, 2, \ldots)$; moreover, it is obvious that the constructed functions cannot meet these requirements. It is clear on physical grounds that this failure results in only a small error, since the coating layer is a thin, poor conductor and the mismatch occurs along its edge. Detailed mathematical analysis, as in [1, 2], shows that low-order approximations are indeed not affected. If higher-order approximations are necessary, suitable correction terms must be introduced.

References

1 Bobisud, L. E., "Asymptotics of Heat Conduction in a Bar Capped With a Thin, Poorly Conductive Skin," *Applicable Analysis*, Vol. 14, 1982, pp. 43–54.

2 Bobisud, L. E., "Heat Conduction Through a Thin, Poorly Conductive Layer," *Quarterly of Applied Mathematics*, Vol. 41, 1983, pp. 85–97.

Heat Conduction in Anisotropic Wedge and Elliptic Cylinders[1]

S. C. Huang[2] and Y. P. Chang[3]

Nomenclature

c = specific heat
$\mathbf{e}_i$ = unit vectors of coordinates, $i = z, \zeta$
I_{s_n} = Bessel function of the second kind, order s_n
I_m = imaginary part
k_{ij} = thermal conductivity coefficients
q''' = rate of heat generation per unit volume
n^+ = outward conormal

$$\frac{\partial}{\partial n^+} = \frac{\partial}{\partial y} + \nu_{12}\frac{\partial}{\partial x} + \nu_{23}\frac{\partial}{\partial z}$$

T = temperature
t = time
x, y, z = rectangular coordinates
$\alpha_2 = k_{22}/(\rho c)$
ρ = density
$\nu_{ij} = k_{ij}/k_{22}$
$\beta_{ij} = (\nu_{ii}\,\nu_{jj} - \nu_{ij}^2)^{1/2}$
$\gamma = \nu_{13} - \nu_{12}\nu_{23}$
$\epsilon = \nu_{23} - \nu_{12}\gamma/\beta_{12}^2$
$\sigma = (\beta_{23}^2 - \gamma^2/\beta_{12}^2)^{1/2}$

Introduction

The study of heat conduction in anisotropic media has been of great interest in recent years due to the increasing use of crystals and laminated materials in industry [1–10]. For instance, graphite has been widely used in such diversified applications as structural furnace parts, nuclear control rods, heat shielding structures and electrical components. In spite of the importance, only a limited number of problems can be solved analytically. Even in numerical solution, an anisotropic problem is more difficult than its isotropic counterparts, because of the presence of cross-derivative terms in the differential equation [7].

This paper presents the analytical solution of heat conduction in a wedge and an elliptic cylinder of an anisotropic medium which is homogeneous in rectangular coordinates. Both steady and unsteady states are considered. By a number of coordinate transformations, these problems can be solved by many standard methods. Only the results obtained by the separation of variables are shown. The transformed equations are also useful for numerical solution.

To show how to use the transformed coordinates in practical calculation, the steady-state temperature distribution in a circular disk, which becomes an elliptic disk in the transformed coordinates, is calculated. Comparing the present exact solution with the approximate numerical solution [2, 10], we can conclude that those numerical methods yield fairly good results. The inconveience of using the principal coordinates for analytical as well as numerical solution is discussed.

1 Statement of Problems

Consider the heat conduction in an anisotropic medium which is homogeneous in rectangular coordinates (x, y, z). For unsteady state, the differential equation to be solved is

$$\upsilon_{ij}\frac{\partial^2 T}{\partial x_i \partial x_j} - \frac{1}{\alpha_2}\frac{\partial T}{\partial t} = -\frac{1}{k_{22}} q'''(x_i,t) \quad \text{in } \Omega, t>0 \tag{1}$$

along with the boundary and initial conditions

$$T = f(x_i, t) \qquad \text{on } S, t>0 \tag{2}$$

$$T = F(x_i) \qquad \text{in } \Omega, t=0 \tag{3}$$

where f and F are prescribed absolutely integrable functions and x_i with $i = 1, 2, 3$ designating x, y, z, respectively.

If the medium is anisotropic only in the z-plane and the problem depends only on x and y, we just omit the derivatives with respect to z and delete the variable z from the prescribed

[1] This study was supported in part by the National Science Foundation, ENG. 76-83367.

[2] Now at the Department of Mechanical Engineering, Southern Univesity, Baton Rouge, La.

[3] Faculty of Engineering and Applied Sciences, State University of New York at Buffalo, Buffalo, N.Y. 14260. Mem. ASME.

Contributed by the Heat Transfer Division for publication in the JOURNAL OF HEAT TRANSFER. Manuscript received by the Heat Transfer Division April 13, 1982.

$$-KU_y^0(x,L) = \frac{h\bar{k}}{h+\bar{k}}[U^0(x,L) - T_0] \tag{23}$$

(9) and (23) constitute a complete problem for U^0, the zeroth-order approximation to the temperature distribution in the base material. Once U^0 is determined, the rate of heat flow through the base of the fin can be obtained in the usual fashion. Note that the problem for U^0 does not depend on the heat distribution in the coating. The boundary condition (23) is of the convection type, but the heat transfer coefficient is no longer merely that for the coating-ambient material interface. To lowest-order terms the effect of the coating is replacement of the thermal conductivity k by K and reduction of the effective heat transfer coefficient by a factor $1 + \epsilon h/k$—compare (3) and (23). From an engineering standpoint, determination of this factor is the chief result of our calculations.

We consider in the same vein the problem (13–16) for the first-order correction. Equations (14–16) yield

$$-KU_y^1(x,L) = \frac{h\bar{k}}{h+\bar{k}} U^1(x,L) \tag{24}$$

Equations (13) and (24) determine the first-order correction term, U^1. (Since this problem happens to be homogeneous, we have $U^1 \equiv 0$ in this instance. In general, $U^1 \not\equiv 0$ for time dependent problems.)

Turning to (17–20), from (18, 19, 22) we find that

$$u_{ww}^2 = -\frac{K}{\bar{k}} U_{yxx}^0(x,L)\left[w - 1 - \frac{\bar{k}}{h}\right] \tag{25}$$

The right-hand side is a known function once U^0 has been found, provided U^0 is sufficiently smooth. Determination of the problem for U^2 now proceeds as before and results in a nonhomogeneous problem.

We have throughout ignored the boundary conditions $u^0(0,w) = T_1$, $u^i(0,w) = 0$ $(i = 1, 2, \ldots)$; moreover, it is obvious that the constructed functions cannot meet these requirements. It is clear on physical grounds that this failure results in only a small error, since the coating layer is a thin, poor conductor and the mismatch occurs along its edge. Detailed mathematical analysis, as in [1, 2], shows that low-order approximations are indeed not affected. If higher-order approximations are necessary, suitable correction terms must be introduced.

References

1 Bobisud, L. E., "Asymptotics of Heat Conduction in a Bar Capped With a Thin, Poorly Conductive Skin," *Applicable Analysis*, Vol. 14, 1982, pp. 43–54.

2 Bobisud, L. E., "Heat Conduction Through a Thin, Poorly Conductive Layer," *Quarterly of Applied Mathematics*, Vol. 41, 1983, pp. 85–97.

Heat Conduction in Anisotropic Wedge and Elliptic Cylinders[1]

S. C. Huang[2] and Y. P. Chang[3]

Nomenclature

c = specific heat
$\mathbf{e}_i$ = unit vectors of coordinates, $i = z, \zeta$
I_{s_n} = Bessel function of the second kind, order s_n
I_m = imaginary part
k_{ij} = thermal conductivity coefficients
q''' = rate of heat generation per unit volume
n^+ = outward conormal

$$\frac{\partial}{\partial n^+} = \frac{\partial}{\partial y} + \nu_{12}\frac{\partial}{\partial x} + \nu_{23}\frac{\partial}{\partial z}$$

T = temperature
t = time
x, y, z = rectangular coordinates
$\alpha_2 = k_{22}/(\rho c)$
ρ = density
$\nu_{ij} = k_{ij}/k_{22}$
$\beta_{ij} = (\nu_{ii}\,\nu_{jj} - \nu_{ij}^2)^{1/2}$
$\gamma = \nu_{13} - \nu_{12}\nu_{23}$
$\epsilon = \nu_{23} - \nu_{12}\gamma/\beta_{12}^2$
$\sigma = (\beta_{23}^2 - \gamma^2/\beta_{12}^2)^{1/2}$

Introduction

The study of heat conduction in anisotropic media has been of great interest in recent years due to the increasing use of crystals and laminated materials in industry [1–10]. For instance, graphite has been widely used in such diversified applications as structural furnace parts, nuclear control rods, heat shielding structures and electrical components. In spite of the importance, only a limited number of problems can be solved analytically. Even in numerical solution, an anisotropic problem is more difficult than its isotropic counterparts, because of the presence of cross-derivative terms in the differential equation [7].

This paper presents the analytical solution of heat conduction in a wedge and an elliptic cylinder of an anisotropic medium which is homogeneous in rectangular coordinates. Both steady and unsteady states are considered. By a number of coordinate transformations, these problems can be solved by many standard methods. Only the results obtained by the separation of variables are shown. The transformed equations are also useful for numerical solution.

To show how to use the transformed coordinates in practical calculation, the steady-state temperature distribution in a circular disk, which becomes an elliptic disk in the transformed coordinates, is calculated. Comparing the present exact solution with the approximate numerical solution [2, 10], we can conclude that those numerical methods yield fairly good results. The inconveience of using the principal coordinates for analytical as well as numerical solution is discussed.

1 Statement of Problems

Consider the heat conduction in an anisotropic medium which is homogeneous in rectangular coordinates (x, y, z). For unsteady state, the differential equation to be solved is

$$\upsilon_{ij}\frac{\partial^2 T}{\partial x_i \partial x_j} - \frac{1}{\alpha_2}\frac{\partial T}{\partial t} = -\frac{1}{k_{22}} q'''(x_i,t) \quad \text{in } \Omega, t>0 \tag{1}$$

along with the boundary and initial conditions

$$T = f(x_i, t) \qquad \text{on } S, t>0 \tag{2}$$

$$T = F(x_i) \qquad \text{in } \Omega, t=0 \tag{3}$$

where f and F are prescribed absolutely integrable functions and x_i with $i = 1, 2, 3$ designating x, y, z, respectively.

If the medium is anisotropic only in the z-plane and the problem depends only on x and y, we just omit the derivatives with respect to z and delete the variable z from the prescribed

[1] This study was supported in part by the National Science Foundation, ENG. 76-83367.

[2] Now at the Department of Mechanical Engineering, Southern Univesity, Baton Rouge, La.

[3] Faculty of Engineering and Applied Sciences, State University of New York at Buffalo, Buffalo, N.Y. 14260. Mem. ASME.

Contributed by the Heat Transfer Division for publication in the JOURNAL OF HEAT TRANSFER. Manuscript received by the Heat Transfer Division April 13, 1982.

functions. If the medium is fully anisotropic and the temperature is a function only of x and y, then [1]

$$\upsilon_{11}=k'_{11}/k'_{22}, i\,\upsilon_{12}=k'_{12}/k'_{22},\ \alpha_2=k'_{22}/\rho c$$

where

$$k'_{11}=(k_{11}k_{33}-k_{13}^2)/k_{33}, k'_{12}=k'_{21}=(k_{12}k_{33}-k_{13}k_{23})/k_{33},$$

$$k'_{22}=(k_{22}k_{33}-k_{23}^2)/k_{23}$$

For the steady state, we just delete the time derivative term from (1), the initial condition (3), and the time variable from (1) and (2).

To transform (1) into the canonical form, we may apply the Cartesian coordinates (ξ, η, ζ) [7] which can be considered as orthogonal with the domain deformed or nonorthogonal with the domain unaltered.

$$\xi=\frac{1}{\beta_{12}}(x-\upsilon_{12}y),\ \eta=y,$$

$$\zeta=\frac{1}{\sigma}\left(z-\epsilon y-\frac{\gamma}{\beta_{12}^2}x\right) \tag{4}$$

We now consider some specific problems whose solution can be readily obtained by the further transformation of the Cartesian coordinates (ξ, η, ζ).

2 Wedge of Angle θ_0

For this problem, we take the z-axis of the rectangular coordinates along the intersection of the two boundary planes and the x-axis on one of the boundary planes so that the wedge can be described by $0<\theta<\theta_0$ and $0\le\bar{r}<\infty$ where $x=\bar{r}\cos\theta$ and $y=\bar{r}\sin\theta$. The plane boundary at $\theta=0$ is transformed to the plane

$$\xi=\frac{\bar{r}}{\beta_{12}},\ \eta=0 \tag{5}$$

and the plane boundary at $\theta=\theta_0$ to the plane

$$\xi=\frac{\bar{r}}{\beta_{12}}(\cos\theta_0-\upsilon_{12}\sin\theta_0),\ \eta=\bar{r}\sin\theta_0 \tag{6}$$

We see from (5) and (6) that ξ and η are independent of ζ, i.e., the wedge angle in planes parallel to (ξ, η)-plane is invariant. Let $\xi=r\cos\phi$, $\eta=r\sin\phi$ where $0\le r<\infty$. We see from (5) that $\theta=0$ corresponds to $\phi=0$ and from (6) that $\theta=\theta_0$ corresponds to $\phi=\phi_0$ with $0<\phi_0<2\pi$ and

$$r\cos\phi_0=\frac{\bar{r}}{\beta_{12}}(\cos\theta_0-\upsilon_{12}\sin\theta_0),\ r\sin\phi_0=F\sin\theta_0 \tag{7}$$

which gives

$$r=\bar{r}\left[\frac{1}{\beta_{12}^2}(\cos\theta_0-\upsilon_{12}\sin\theta_0)^2+\sin^2\theta_0\right]^{1/2} \tag{8}$$

Thus the anisotropic wedge problem in rectangular coordinates is transformed into the problem described by the cylindrical coordinates (r, ϕ, ζ) with the Jacobian $r\beta_{12}\sigma$

$$\nabla^2 T-\frac{1}{\alpha_2}\frac{\partial T}{\partial t}=-\frac{1}{k_{22}}q'''(r,\phi,\zeta,t),$$

$$r>0,\ 0<\phi<\phi_0\ |\zeta|<\infty,\ t>0 \tag{9}$$

$$T=F(r,\phi,\zeta)\quad r>0,\ 0<\phi<\phi_0,\ |\zeta|<\infty,\ t=0 \tag{10}$$

$$T=f_1(r,\zeta,t)\quad r>0,\ \phi=0,\ |\zeta|<\infty,\ t>0 \tag{11}$$

$$T=f_2(r,\zeta,t)\quad r>0,\ \phi=\phi_0,\ |\zeta|<\infty,\ t>0 \tag{12}$$

$$T=0\quad r\to\infty \tag{13}$$

$$T=0\quad |\zeta|\to\infty \tag{14}$$

Where the ∇^2 is operated with respect to r, ϕ, and ζ. The Green's function associated with the problems (9)–(14) can be found by the image method aided by the concept of Riemann's space [1]

$$G(x,y,z,t|x',y',z',t')$$

$$=\frac{1}{\beta_{12}\sigma r'}G(r,\phi,\zeta;t'|r',\phi',\zeta',t')=\frac{1}{2\beta_{12}\sigma\phi_0\pi^{1/2}[\alpha_2(t-t')]^{3/2}}$$

$$\exp\left[-\frac{r^2+r'^2+(\zeta-\zeta')^2}{4\alpha_2(t-t')}\right]\sum_{n=1}^{\infty}\sin s_n\phi\,\sin s_n\phi'\,Is_n\left[\frac{rr'}{2\alpha_2(t-t')}\right] \tag{15}$$

Where $s_n=n\pi/\phi_0$. The corresponding Green's function in steady state can also be found by the Hankel transformation with respect to r, and periodic transform, with respect to ϕ

$$G(r,\phi,\zeta|r,'\phi',\zeta')$$

$$=\frac{1}{\phi_0}\sum_{n=1}^{\infty}\sin s_n\phi\,\sin s_n\phi'\int_0^{\infty}e^{-\lambda|\zeta-\zeta'|}J_{s_n}(\lambda r)J_{s_n}(\lambda r')d\lambda \tag{16}$$

When the Green's function is known, the temperature distribution can be obtained by the well-known formula [7].

3 Elliptic Cylinder

Consider first the two-dimensional heat conduction in an anisotropic plane whose boundary is an ellipse described in rectangular corrdinates (x, y) by

$$\frac{x^2}{a^2}+\frac{y^2}{b^2}=1 \tag{17}$$

Where a and b are the major and minor radii respectively. If the Cartesian coordinates (4) are employed, the major axis makes an angle with the positive ξ-axis at an angle ϕ_t, which can be found by geometry [11] as

$$\phi_t=\frac{1}{2}\tan^{-1}\frac{2\nu_{12}\beta_{12}}{\beta_{12}^2-\nu_{12}^2-\left(\frac{a}{b}\right)^2} \tag{18}$$

We now introduce a new set of coordinates (ξ_1, η_1) so that the major and minor axes of the ellipse coincide with ξ_1 and η_1

$$\frac{\xi_1^2}{A^2}+\frac{\eta_1^2}{B^2}=1 \tag{19}$$

where

$$\frac{1}{A^2}=\frac{1}{2}[I-\sqrt{(I^2-4D)^{1/2}}],\quad \frac{1}{B^2}=\frac{1}{2}(I+\sqrt{I^2-4D}),$$

$$I=\frac{\nu_{11}}{a^2}+\frac{1}{b^2},\quad D=\left(\frac{\beta_{12}}{ab}\right)^2 \tag{20}$$

It follows that we can use the elliptic coordinate system $(\xi_2\ \eta_2)$ defined by

$$\xi_1=C\cosh\xi_2\cos\eta_2$$

$$\eta_1=C\sinh\xi_2\sin\eta_2 \qquad C=(A^2-B^2)^{1/2} \tag{21}$$

or in complex variables

$$z_2\equiv\xi_2+i\eta_2=\cosh^{-1}\frac{z_1}{C},\quad z_1\equiv\xi_1+i\eta_1 \tag{22}$$

The elliptic domain is then transformed into the domain

$$0<\xi_2<\xi_0\quad 0<\eta_2<2\pi \tag{23}$$

where $\xi_0=\cosh^{-1}A/C$. The upper half plane $\eta_1>0$ corresponds to $0<\eta_2<\pi$ and the lower half plane to $\pi<\eta_2<2\pi$. Then (1) for the two-dimensional case takes the form

$$\frac{\partial^2 T}{\partial \xi_2^2}+\frac{\partial^2 T}{\partial \eta_2^2}-\frac{C^2}{2\alpha_2}\left[\cosh(2\xi_2)-\cosh(2\eta_2)\right]\frac{\partial T}{\partial t}$$

$$=-\frac{1}{k_{22}}q'''(\xi_2,\eta_2,t) \tag{24}$$

together with the initial and boundary conditions

$$T=F(\xi_2,\eta_2) \quad \text{in } \Omega_2, t=0 \tag{25}$$

$$T=f(\eta_2,t) \quad \text{on } \xi_2=\xi_0, t>0 \tag{26}$$

where Ω_2 is specified by (23). In order to obtain the unique solution of (24), we need additional conditions which can be determined as follows.

$\xi_2=0$ is a line segment of length $|\xi_1|<C$ in (ξ_1,η_1)-plane inside the domain in question. The two points η_2 and $2\pi-\eta_2$ on $\xi_2=0$ are the same point in (ξ_1,η_1)-plane. The continuity of temperature gives

$$T(\xi_2=0,\eta_2,t)=T(\xi_2=0,2\pi-\eta_2,t) \tag{27}$$

The continuity of heat flux at $\eta_1=0$ in (ξ_1,η_1)-plane requires that

$$\frac{\partial}{\partial \eta_1}T(\xi_1,\eta_1=0_+,t)=\frac{\partial}{\eta_1}T(\xi_1,\eta_1=0_-,t) \tag{28}$$

From (21), we obtain

$$\frac{\partial}{\partial \xi_2}\Big|_{\xi_2=0}=C\sin\eta_2\frac{\partial}{\partial \eta_1} \tag{29}$$

Since $0<\eta_2<\pi$ for which $\sin\eta_2>0$ corresponds to the upper half of (ξ_1,η_1)-plane and $\pi<\eta_2<2\pi$ for which $\sin\eta_2<0$ corresponds to the lower half of (ξ_1,η_1)-plane, (28) becomes

$$\frac{\partial}{\partial \xi_2}T(\xi_2=0,\eta_2,t)=-\frac{\partial}{\partial \xi_2}T(\xi_2=0,2\pi-\eta_2,t) \tag{30}$$

The Green's function associated with the problem (24–26), (27), and (30) for the elliptic disk can be readily written down by eigenfunction expansion as

$$G(\xi_2,\eta_2,t|\xi_2',\eta_2',t')$$

$$=\sum_{i=1}^{4}\sum_{n=1}^{\infty}e^{-\alpha_2[\lambda_n^{(i)}]^2(t-t')}\sum_{m=0}^{\infty}\Phi_{n,m}^{(i)}(\xi_2,\eta_2)\Phi_{n,m}^{(i)}(\xi_2',\eta_2') \tag{31}$$

where $\lambda_n^{(i)}=4k_{n,i}^2/C^2$ and $\Phi_{m,n}^{(i)}(\xi_2,\eta_2)$ are the orthonormal eigenfunctions with respect to $C^2/2[\cosh(2\xi_2)-\cosh(2\eta_2)]$ over $0<\xi_2<\xi_0$, $0<\eta_2<2\pi$:

$$\Phi_{n,m}^{(1)}=\frac{1}{N_1}Ce_{2m}(\xi_2,k_{n,1}^2)\,ce_{2m}(\eta_2,k_{n,1}^2)$$

$$\Phi_{n,m}^{(2)}=\frac{1}{N_2}Ce_{2m+1}(\xi_2,k_{n,2}^2)\,ce_{2m+1}(\eta_2,k_{n,2}^2)$$

$$\Phi_{n,m}^{(3)}=\frac{1}{N_3}Se_{2m+1}(\xi_2,k_{n,3}^2)se_{2m+1}(\eta_2,k_{n,3}^2)$$

$$\Phi_{n,m}^{(4)}=\frac{1}{N_4}Se_{2m+2}(\xi_2,k_{n,4}^2)se_{2m+2}(\eta_2,k_{n,4}^2) \tag{32}$$

in which *ce*'s and *se*'s are the Mathieu's functions, *Ce*'s and *Se*'s the modified Mathieu's functions: *N*'s the norms, and $k_{n,i}^2$ the eigenvalues determined by homogeneous boundary conditions [12, 13].

For an infinite elliptic cylinder, we just multiply the right-hand side of (31) by $G(\xi,t|\xi',t')$ defined by

$$G(\xi,t|\xi',t')=\frac{1}{2[\pi\alpha_2(t-t')]^{1/2}}e^{-\frac{(\xi-\zeta')^2}{4\alpha_2(t-t')}} \tag{33}$$

to obtain $G(\xi_2,\eta_2,\zeta,t|\xi_2',\eta_2',\zeta',t')$.

The three-dimensional Green's function in steady state can be easily obtained by setting $t'=0$ and integrating $G(\xi_2,\eta_2,\zeta,t|\xi_2',\eta_2',\zeta',0)$ with respect to t from $t=0$ to $t=\infty$. The Green's function for two-dimensional steady state is given in [12]. It should be remarked that the use of Green's function in elliptic coordinates is convenient for the solution of inhomogeneous differential equations, i.e., with distributed heat generation in the medium. If there is no heat generation, we had better solve the problem directly, since the conormal derivative of the Green's function is usually quite complicated in the transformed coordinate system.

4 Calculated Example – Circular Disk of Radius r_0

To show how to use the transformed coordinates, we consider the steady-state heat conduction in an anisotropic circular disk, which becomes an elliptic disk in the transformed coordinates, with the boundary condition

$$f(\theta)=\begin{cases}T_0\sin\theta & 0<\theta<\pi\\ 0 & \pi<\theta<2\pi\end{cases} \tag{34}$$

We seek the solution of this problem in the form

$$T(\xi_2,\eta_2)=\frac{a_0}{2}+\sum_{n=1}^{\infty}\left[a_n\frac{\cosh(n\xi_2)}{\cosh(n\xi_0)}\cos(n\eta_2)+b_n\frac{\sinh(n\xi_2)}{\sinh(n\xi_0)}\sin(n\eta_2)\right] \tag{35}$$

where a_n and b_n are coefficients. We assume the anisotropic property: $\nu_{11}=0.8333$ and $\nu_{12}=0.4167$ so that $\beta_{12}=0.8122$ and normalize T by T_0 and lengths by r_0. Then $a=b=1$ and $\phi_t=-0.4607$, $I=1.8333$, $D=0.6597$, $A=1.4261$, $B=0.8634$, and $C=1.1351$.

The determination of the coefficients a_n and b_n in (35) requires some deliberations. For simplicity, we may use the complex variables $z=x+iy$, $z_1=\xi_1+i\eta_1$ and $z_2=\xi_2+i\eta_2$. At the point $\theta=0$ on the boundary, $x=1$, $y=0$ and we get $z=z=1/\beta_{12}$, $z_1=e^{-i\phi_t}/\beta_{12}$ and $z_2=\cosh^{-1}(e^{-i\phi_t}/\beta_{12}C)$. At the point $\theta=\pi$ on the boundary, $x=-1$, $y=0$, and we get $z=-1/\beta_{12}$, $z_1=-e^{i\phi_t}/\beta_{12}$ and $z_2=\pi i+\cosh^{-1}(e^{-i\phi_t}/\beta_{12}C)$. Hence

$$a_n=\frac{T_0}{\pi}\int_{\eta_{2,i}}^{\eta_{2,f}}\sin\theta\cos(n\eta_2)d\eta_2,$$

$$b_n=\frac{T_0}{\pi}\int_{\eta_{2,i}}^{\eta_{2,f}}\sin\theta\sin(n\eta_2)d\eta_2 \tag{36}$$

where

$$\eta_{2,i}=Im\left[\cosh^{-1}(e^{-i\phi_t}/\beta_{12}C)\right],$$

$$\eta_{2,f}=Im\left[\pi i+\cosh^{-1}(e^{-i\phi_t}/\beta_{12}C)\right]$$

With the above data, we get $\eta_{2,i}=0.6867$ and $\eta_{2,f}=3.8283$ on the boundary where $\xi_0=0.7016$. The function $\sin\theta$ in (36) has to be transformed into the z_2-plane so that the integration can be performed. This can be done by substituting $x+iy=\beta_{12}\xi+\nu_{12}\eta+i\eta$, $\xi+i\eta=e^{i\phi_t}(\xi_1+i\eta_1)$, $\xi_1+i\eta_1=C\cosh(\xi_2+i\eta_2)$, where $\xi_2=\xi_0$, into the following formula

$$\sin\theta=\frac{y}{(x^2+y^2)^{1/2}}=\frac{\eta}{[(\beta_{12}\xi+\nu_{12}\eta)^2+\eta^2]^{1/2}} \tag{37}$$

in which $\xi+i\eta=Ce^{i\phi_t}\cosh(\xi_0+i\eta_2)$, so that (37) is a function of η_2 at the boundary.

When n is large, the intergrands in (36) are rapidly oscillatory functions and therefore the Filon's integration

Table 1 Steady-state isotherms in a unit circular plate with anisotropic properties $\nu_{11} = 0.8333$, $\nu_{12} - 0.4167$

	T/T_0								
y/r_0	0.1	0.2	0.3	0.4	0.5	0.6	0.7	0.8	0.9
−0.95	0.0450	0.173	0.298						
−0.80	−0.196	0.0659	0.227	0.350	0.472				
−0.60	−0.419	−0.124	0.0921	0.275	0.413	0.555	0.667		
−0.40	−0.538	−0.245	−0.0104	0.184	0.358	0.501	0.635	0.770	0.894
−0.20	−0.595	−0.306	−0.0723	0.129	0.304	0.463	0.612	0.746	0.869
x/r_0 0.00	−0.602	−0.323	−0.0892	0.108	0.283	0.444	0.599	0.739	0.868
0.20	−0.566	−0.288	−0.0670	0.118	0.295	0.452	0.594	0.734	0.875
0.40	−0.482	−0.220	−0.0104	0.166	0.329	0.474	0.619	0.754	0.893
0.60	−0.345	−0.111	0.0740	0.234	0.388	0.530	0.663		
−0.80	−0.147	0.0494	0.188	0.339	0.466				
0.95	0.0419	0.174	0.296						

formula should be used. The series (35) converges very fast when $\xi_2 << \xi_0$, but very slowly near the boundary $\xi_2 = \xi_0$. In order to speed up the convergence, we can use the Kummer's method by introducing the series

$$f_1(\eta_2) = \frac{a_0}{2} + \sum_{n=1}^{\infty} [a_n \cos(n\eta_2) + b_n \sin(n\eta_2)] \tag{38}$$

where a_0, a_n, b_n, $n = 1, 2, 3, \ldots$, are the same as those already defined. Clearly $f_1(\eta_2)$ is the Fourier series expansion of the boundary condition (34). Thus, for large ξ_2 we obtain

$$T(\xi_2, \eta_2) = f_1(\eta_2) + \sum_{n=1}^{\infty} \left\{ a_n \left[\frac{\cosh(n\xi_1)}{\cosh(n\xi_0)} - 1 \right] \cos(n\eta_2) + b_n \left[\frac{\sinh(n\xi_2)}{\sinh(n\xi_0)} - 1 \right] \sin(n\eta_2) \right\} \tag{39}$$

In the actual computation, (35) is used for $0 < \xi_2 < 1/2\ \xi_0$ and (39) is used for $1/2\ \xi_0 < \xi_2 < \xi_0$.

The calculated isotherms of (T/T_0) in the plane $(x/r_0, y/r_0)$ are shown in Table 1; this checks fairly well with those obtained by approximate numerical methods [2, 10].

5 Discussions

It is known that the numerical solution of either the generalized heat equation (i.e., with cross derivatives) and the generalized Laplace equation requires much more effort than that of the heat equation and Laplace equation [4, 14]. Therefore, it is always advantageous to transform the generalized equation into its canonical form for the purpose of either analytical or numerical analysis.

To transform the generalized heat equation, or the generalized Laplace equation, into its canonical form, the principal coordinates can be used, but more algebraic work will be involved. Firstly, we have to find the eigenvalues and eigenvectors of the square matrix $[\nu_{ij}]$. Second, none of the principal axis is, in general, along a desired direction, such as the axis of cylinder or the intersection of two plane surfaces. For instance, by either rotating the wedge or the cylinder with respect to the original rectangular coordinates or rotating the rectangular coordinates with respect to the region in question, the generalized heat equation is reduced to one for an orthotropic medium with the principal conductivity coefficients as the eigenvalues. The three eigenvalues are different in magnitude and rescaling is required to reduce the differential equation into that for an isotropic medium. Rescaling usually involves the change of the desired direction and the deformation of the region in question. After the rescaling, another rotation transformation is required in order to bring one of the coordinates along the desired direction [15]. Rather, the Cartesian coordinates defined in (4) involves very simple algebra. It can be easily shown that $\mathbf{e}_\zeta = \sigma \mathbf{e}_z$ [14] and hence the ζ-axis can always be aligned with the z-axis. Furthermore $y = \eta$ and $\partial T/\delta y = \partial T/\partial n^+$ provide an additional advantage which cannot be obtained for other transformed coordinate systems.

The calculation of Mathieu's functions and their eigenvalues is quite tedious and their programming is not available in most computer centers. Once they are known by special programming, the calculation for the temperature field becomes a routine matter. Nonetheless, the practical utility of Mathieu's function still survives by using their integral representation aided by the analytic continuation [12]. This, however, cannot be discussed in a paper like this.

The analytical solution of the infinite wedge problem is very useful. The Green's function given in (15) is useful for both small and large values of time. Numerical solutions for these two cases in an open region are usually quite time consuming in order to obtain a desired accuracy.

Analytical solutions of the two-dimensional problems in steady state for regions considered in this paper can also be solved by conformal mapping and potential theory of double layer, but the computation work requires more efforts than that obtained by the separation-variable technique [14].

References

1 Carslaw, H. S., and Jaeger, J. C., *Conduction of Heat in Solids*, Clarendon Press, Oxford, 1959.

2 Chang, Y. P., Kang, C. S., and Chen, D. J., "The Use of Fundamental Green's Functions for the Solution of Problems of Heat Conduction in Anisotropic Media," *International Journal of Heat and Mass Transfer*, Vol. 16, 1973, pp. 1905-1918.

3 Padovan, J., "Transient Temperature Distribution of an Anisotropic Half Space," *AIAA Journal*, Vol. 11, 1973, pp. 565-566.

4 Katayama, K., Saito, A., and Kobayshi, N., "Transient Heat Conduction in Anisotropic Solids," *Proceedings of the 5th International Heat Transfer Conference*, Tokyo, Cu. 1-4, 1974, pp. 137-141.

5 Sadd, M. H., and Miskioglu, I., "Temperatures in an Anisotropic Sheet Containing an Insulated Elliptical Hole," ASME JOURNAL OF HEAT TRANSFER, Vol. 100, 1978, pp. 553-555.

6 Cobble, M. H., "Nonlinear Anisotropic Temperature Distribution in a Wedge," *International Journal of Heat and Mass Transfer*, Vol. 17, 1974, pp. 379-380.

7 Chang, Y. P., "Analytical Solution for Heat Conduction in Anisotropic Media in Infinite, Semi-Infinite, and Two-Plane-Bounded Regions," *International Journal of Heat and Mass Transfer*, Vol. 20, 1977, pp. 1019-1028.

8 Poon, K. C., Tsou, R. C. H., and Chang, Y. P., "Solution of Anisotropic Problems of First Class by Coordinate Transformation," ASME JOURNAL OF HEAT TRANSFER, Vol. 101, 1979, pp. 340-345.

9 Clements, C. L., and Tauchert, T. R., "Stationary Heat Conduction in an Anisotropic Slab Containing a Crack," *International Journal of Engineering Science*, Vol. 17, 1979, pp. 1141-1149.

10 McWhorter, J. C., and Sadd, M. H., "Numerical Anisotropic Heat Conduction Solutions Using Boundary-Fitted Coordinate Systems," ASME JOURNAL OF HEAT TRANSFER, Vol. 102, 1980, pp. 308-311.

11 Korn, G. A., and Korn, T. M., *Mathematical Handbook for Scientists and Engineers*, McGraw Hill, New York, 1968.

12 Morse, P. M., and Feshback, H., *Methods of Theoretical Physics*, McGraw Hill, New York, 1953.

13 McLachlan, N. W., *Theory and Application of Mathieu Functions*, Clarendon Press, Oxford, 1951.

14 Huang, S. C., "Analytical Solution of Anisotropic Heat Conduction in Simple and Irregular Regions," PhD. Dissertation, Department of Mechanical Engineering, State University of New York at Buffalo, Apr. 1981.

15 Margenau, M., and Murphy, G. M., *Mathematics of Physics and Chemistry*, Van Nostrand, 1974.

Conductive Heat Transfer Between Eccentric Cylinders With Boundary Conditions of the Third Kind

R. F. DiFelice, Jr.[1] **and H. H. Bau**[2]

1 Introduction

We consider conductive heat transfer in an eccentric annulus (Fig. 1(*a*)), between a buried pipe and the surface of a semi-infinite medium (Fig. 1(*b*)), and between two pipes embedded in an infinite medium (Fig. 1(*c*)). Each of the above geometrical configurations is germane to various industrial problems, such as heat losses through eccentric insulations (Fig. 1(*a*)) and heat losses from buried pipes (Fig. 1(*b*)).

Approximate and exact steady-state heat transfer calculations are available in the literature only for cases with idealized boundary conditions such as isothermal surfaces [1-3]. The approximate solutions are based on superposition of infinite line heat source and sink solutions [1]. The exact solutions are obtained by the use of bicylindrical coordinates [2, 3].

Recently, Bau and Sadhal [4] solved analytically the case of a pipe, having convective boundary condition on its own surface, buried beneath an isothermal surface. In the above work, a simple, approximate expression accurate within 2 percent was obtained for the shape factor. Encouraged by this success, we use here a similar method for the cases described in Fig. 1, where convective boundary conditions are imposed on all the surfaces. The complicated geometries are handled through the use of the bicylindrical coordinate system. We obtain an exact solution for the foregoing cases and construct an approximate formula for the shape factor which is accurate within 5 percent for many cases of practical interest.

2 Formulation and Exact Solution

The problem involves essentially the solution of a heat equation with convective boundary conditions for the geometries described in Fig. 1. It is convenient to carry out the analysis by using the bicylindrical coordinate system (α, β) [5]. The transformation into this coordinate system is achieved by use of the formula

$$x+iy=a\,\mathrm{Tanh}\frac{\alpha+i\beta}{2} \qquad -\infty<\alpha<\infty \qquad -\pi<\beta<\pi \tag{1}$$

where constant α-coordinates describe the circles

$$(x-a\,\mathrm{Coth}\,\alpha)^2+y^2=\frac{a^2}{\mathrm{Sinh}^2\alpha} \tag{2}$$

Consequently, all the geometries depicted in Fig. 1 are defined by two constant α-coordinates: α_1 and α_2 ($\alpha_1 > \alpha_2$). In the case of the eccentric annulus, (Fig. 1(*a*)) $\alpha_1 > \alpha_2 > 0$; in the case of the buried pipe (Fig. 1(*b*)), $\alpha_2 = 0$; and in the case of the two cylinders (Fig. 1(*c*)), $\alpha_1 > 0$, $\alpha_2 < 0$.

We introduce nondimensional variables by scaling the length with R_1 (the radius of the inner cylinder) and the temperature with $(T_1 - T_2)$, where T_1 is the bulk temperature inside the inner pipe, and T_2 is the bulk temperature outside the outer pipe (Fig. 1(*a*)), above the surface (Fig. 1(*b*)), and inside the second pipe (Fig. 1(*c*)).

After this scaling, the radii ratio $R_1/R_2 = \mathrm{Sinh}\,\alpha_2/\mathrm{Sinh}\,\alpha_1$, the eccentricity (Fig. 1(*a*)) and 1(*c*)) $e = a(\mathrm{Coth}\,\alpha_2 - \mathrm{Coth}\,\alpha_1)$, the burial depth (Fig. 1(*b*)) $d = a\mathrm{Coth}\,\alpha_1$ and $a = \mathrm{Sinh}\,\alpha_1$.

The heat conduction equation is simply

$$\frac{\partial^2 T}{\partial\alpha^2}+\frac{\partial^2 T}{\partial\beta^2}=0 \tag{3}$$

The corresponding boundary conditions are

$$(\mathrm{Cosh}\,\alpha_1+\mathrm{Cos}\,\beta)\frac{\partial T}{\partial\alpha}=a\,\mathrm{Bi}\,(1-T) \quad \text{at } \alpha=\alpha_1 \tag{4a}$$

$$(\mathrm{Cosh}\,\alpha_2+\mathrm{Cos}\,\beta)\frac{\partial T}{\partial\alpha}=a\,\mathrm{Bi}\frac{h_2}{h_1}T \quad \text{at } \alpha=\alpha_2 \tag{4b}$$

and $T(\alpha, \beta+2\pi)=T(\alpha, \beta)$
where

$$\mathrm{Bi}=\frac{h_1 R_1}{k}$$

is the Biot number.
The solution of equation (3) is readily obtained in the form

$$T=\sum_{n=0}^{\infty}(A_n\,\mathrm{Sinh}\,n\alpha+B_n\,\mathrm{Cosh}\,n\alpha)\,\mathrm{Cos}\,n\beta+A_o\alpha \tag{5}$$

The coefficients A_n and B_n are to be established with the aid of the boundary conditions (4). For example, substitution of (5) into (4*a*) yields the following relationship

$$(\mathrm{Cosh}\,\alpha_1+\mathrm{Cos}\,\beta)\Big[A_o+\sum_{n=1}^{\infty}n(A_n\,\mathrm{Cosh}\,n\alpha_1 + B_n\,\mathrm{Sinh}\,n\alpha_1)\,\mathrm{Cos}\,n\beta=a\,\mathrm{Bi}\Big[1-A_o\,\alpha_1 - \sum_{n=0}^{\infty}(A_n\,\mathrm{Sinh}\,n\alpha_1+B_n\,\mathrm{Cosh}\,n\alpha_1)\mathrm{Cos}\,n\beta\Big] \tag{6}$$

The factor $(\mathrm{Cosh}\,\alpha_1 + \mathrm{Cos}\,\beta)$ causes some trouble, since we cannot equate the infinite series in equation (6) on a term by term basis. To overcome this difficulty, we use the trigonometric identity

$$\mathrm{Cos}\,\beta\,\mathrm{Cos}\,n\beta=\frac{1}{2}[\mathrm{Cos}\,(n+1)\beta+\mathrm{Cos}(n-1)\beta]$$

to obtain an infinite set of linear algebraic equations

$$A_o(\mathrm{Cosh}\,\alpha_1+\alpha\,\mathrm{Bi}\,\alpha_1)+\frac{1}{2}A_1\,\mathrm{Cosh}\,\alpha_1+B_o\,a\,\mathrm{Bi} + \frac{1}{2}\mathrm{Bi}\,\mathrm{Sinh}\,\alpha_1=a\,\mathrm{Bi}\,(n=0)$$

$$A_o+A_1\,(\mathrm{Cosh}^2\alpha_1+a\,\mathrm{Bi}\,\mathrm{Sinh}\,\alpha_1)+A_2\,\mathrm{Cosh}\,2\alpha_1 + B_1(\mathrm{Cosh}\,\alpha_1\,\mathrm{Sinh}\,\alpha_1+a\,\mathrm{Bi}\,\mathrm{Cosh}\,\alpha_1) + B_2\,\mathrm{Sinh}\,2\alpha_1=0 \qquad (n=1)$$

$$A_{n-1}\left(\frac{n-1}{2}\right)(\mathrm{Cosh}\,\alpha_1-\mathrm{Tanh}\,n\alpha_1\,\mathrm{Sinh}\,\alpha_1 + A_n\,(n\,\mathrm{Cosh}\,\alpha_1+a\,\mathrm{Bi}\,\mathrm{Tanh}\,n\alpha_1) + A_{n+1}\left(\frac{n+1}{2}\right)(\mathrm{Cosh}\,\alpha_1+\mathrm{Tanh}\,n\alpha_1\,\mathrm{Sinh}\,\alpha_1) + B_{n-1}\left(\frac{n-1}{2}\right)(\mathrm{Tanh}\,n\alpha_1\,\mathrm{Cosh}\,\alpha_1-\mathrm{Sinh}\,\alpha_1)+ + B_n[n\,\mathrm{Cosh}\,\alpha_1\,\mathrm{Tanh}\,n\alpha_1+a\,\mathrm{Bi}] + B_{n+1}\left(\frac{n+1}{2}\right)(\mathrm{Tanh}\,n\alpha_1\,\mathrm{Cosh}\,\alpha_1 + \mathrm{Sinh}\,\alpha_1)=0 \qquad (n>1) \tag{7}$$

A similar set of equations is obtained from the boundary condition (4*b*).

[1] General Electric Company, Philadelphia, Pa. 19101
[2] Department of Mechanical Engineering and Applied Mechanics, University of Pennsylvania, Philadelphia, Pa. 19104

Contributed by the Heat Transfer Division for publication in the JOURNAL OF HEAT TRANSFER. Manuscript received by the Heat Transfer Division November 5, 1982.

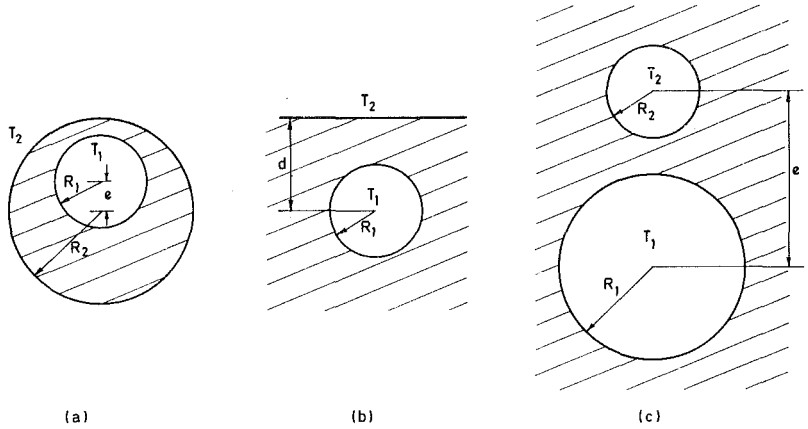

Fig. 1 The geometrical configurations considered: (a) eccentric annulus, (b) buried pipe, (c) two cylinders

Table 1 A few calculated values of the shape factor S. S_l, S, and S_u are, respectively, the lower bound, the exact value, and the upper bound. N is the number of equations used to obtain the exact value S.

α_1	α_2	Bi	h_1/h_2	S_l	S	S_u	N
0.2	0	100	1	3.5282	3.5287	4.7619	11
			10	1.9610	1.9675	4.7619	26
			100	.6972	.7222	4.7619	49
			1000	.2234	.2745	4.7619	147
0.2	−0.2	100	1	2.0350	2.0355	2.3809	18
			10	1.2721	1.2794	1.9608	48
			100	.4354	.4526	.7092	48
			1000	.0842	.0866	.0960	78
0.6	0.2	100	10	1.8101	1.8128	2.2648	11
			100	.7988	.8146	1.3769	26

This set of equations cannot be solved since any $2N$ equations involve $2N+2$ unknowns. However, A_n and B_n are decreasing sequences and can be truncated at some $n=N$. Should we set $A_{N+1} = B_{N+1} = 0$, the above $2N$ equations can be solved in a closed form for any N. The number of equations N is chosen in such a way as to satisfy the following criteria

$$\frac{{A_o}^{N+5} - {A_o}^{N}}{{A_o}^{N+5}} < 10^{-4} \tag{8}$$

where the superscripts indicate the number of coefficients calculated. The number of terms needed to achieve the above convergence criteria (8) increases with increasing $(\alpha_1 - \alpha_2)$, increasing $1/\text{Bi}(h_1/h_2)$ and decreasing α_1. A few representative examples are provided in Table 1.

Once the coefficients A_n, B_n are calculated we have a full description of the temperature field inside the medium and on the surfaces.

In many applications we are interested in the shape factor (S), which is defined by the ratio

$$S = \frac{Q^*}{2\pi k(T_1 - T_2)}, \tag{9}$$

where Q^* is the heat transfer per unit length. In accordance with (5), the exact value for S is

$$S = A_o \tag{10}$$

For this reason we have used A_o in our convergence criteria (8).

Results of a few calculations of the exact shape factor are exhibited in Fig. 2 (solid lines) for $\alpha_1 = 2$, Bi = 0.1, 1., and 10. We note that at low Bi and high h_1/h_2 ratio, the shape factor does not decrease monotonically with increasing distance between the cylinder centers $(\alpha_1 - \alpha_2)$ but rather picks up around $\alpha_2 = 0$. This is because the surface area of the cylinder associated with α_2 increases as $\alpha_2 \to 0$. The area of cylinder α_2 becomes actually infinite when $\alpha_2 = 0$.

3 Lower and Upper Bounds for the Shape Factor

In this section, following Yovanovich [6], we obtain lower (S_l) and upper (S_u) bonds for the shape factor.

The lower bound is obtained by considering a flux tube bounded by two constant β surfaces. This, in effect, is identical to the solution of the equation

$$\frac{\partial^2 T}{\partial \alpha^2} = 0 \tag{11}$$

with boundary conditions (4). The resulting expression is

$$S_l = \alpha\,\text{Bi}\,[(\text{Cosh}\,\alpha_1 + \frac{h_1}{h_2}\,\text{Cosh}\,\alpha_2 + a\,\text{Bi}(\alpha_1 - \alpha_2))^2 - (1 + h_1/h_2)^2]^{-1/2} \tag{12}$$

The upper bound (S_u) corresponds to a situation where the cylinders' surfaces are isothermal.

$$S_u = a\,\text{Bi}[a\,\text{Bi}(\alpha_1 - \alpha_2) + \text{Sinh}\,\alpha_1 + \frac{h_1}{h_2}\,\text{Sinh}\,|\alpha_2|]^{-1} \tag{13}$$

It is worth noting that for a variety of limiting cases the lower and upper bounds coincide (see Fig. 2). Clearly, the strategy to be adopted when one is solving a problem of this kind is first to calculate the lower and upper bounds for the shape factor. Only if those bounds are not sufficiently close need one seek an exact solution.

The exact shape factor together with the lower and upper bounds are depicted in Fig. 2. The solid line represents the exact solution, while the circles and crosses denote the lower and upper bounds, respectively.

We note that often the lower bound (S_l) is very close to the exact solution. We find that for $(a\text{Bi}\ h_2/h_1) \geq 1$, the

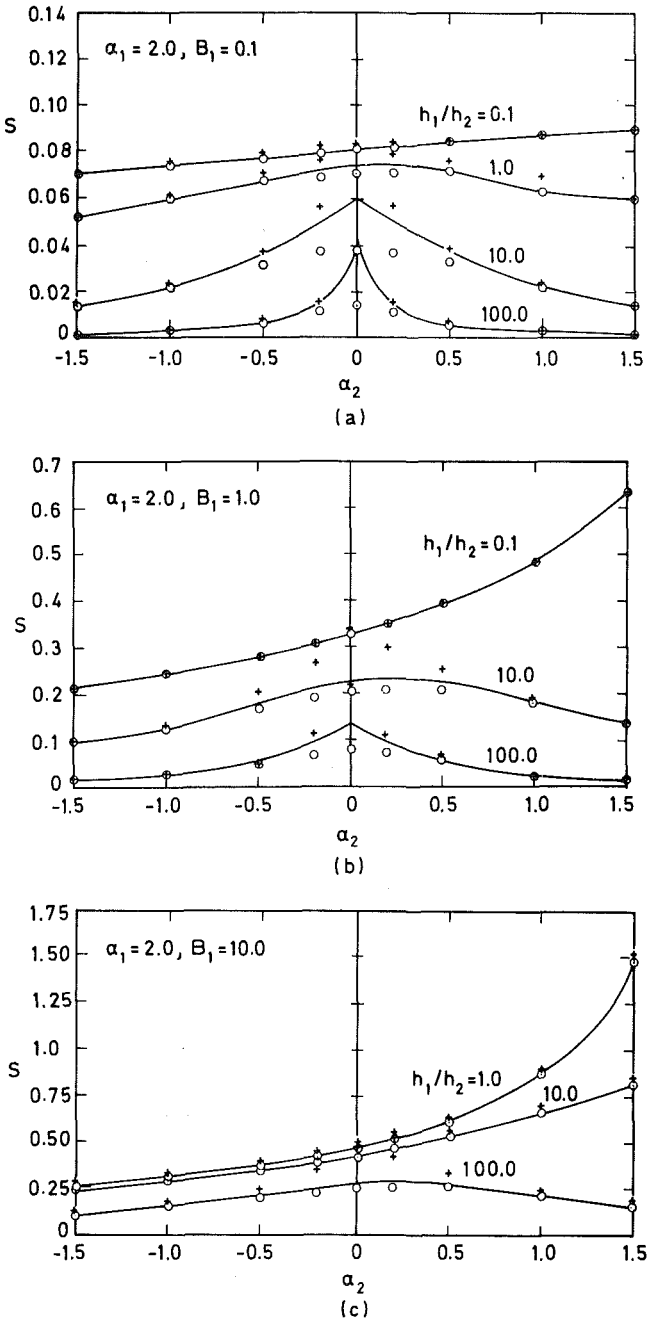

Fig. 2 The shape factor: (*a*) $\alpha_1 = 2$, Bi = 0.1; (*b*) $\alpha_1 = 2$, Bi = 1; (*c*) $\alpha_1 = 2$, Bi = 10

deviation between the lower bound, and the exact solution is well below 5 percent. For (aBi $h_2/h_1 \geq 0.1$, this deviation is smaller than 20 percent. These results have been confirmed in a large number of calculations which include the following range of parameters $0.1 \leq \alpha_1 \leq 2$, $-2 \leq \alpha_2 \leq 1.8$, $0.01 \leq$ Bi ≤ 100, $0.01 \leq h_1/h_2 < 1000$. A few representative results are exhibited in Table 1. As we have seen in section 2, the exact solution is relatively involved, and it is desirable to have a simple formula, such as equation (12), to calculate the shape factor.

The results just cited are in accord with a previous work [4], in which a pipe buried beneath an isothermal surface was considered. In the foregoing work [4], $h_2 \to \infty$; therefore, the criterion (aBi $h_2/h_1) \geq 1$ is always met and the lower bound is always an excellent approximation of the exact value of the shape factor.

4 Conclusions

We present a method to obtain an exact solution for conductive heat transfer between two eccentric cylinders with boundary conditions of the third kind. The exact solution is obtained in a series form where the evaluation of the coefficients requires the solution of a set of algebraic equations (section 2). To eliminate this difficulty, we present an approximate, easy-to-use formula for the shape factor (equation (12)). This approximation is good within 5 percent for (aBi $h_2/h_1) \geq 1$. Even if the foregoing criterion is not met, the approximation may yield a value of acceptable accuracy if the difference between the lower and upper bounds ($S_u - S_l$) is small enough.

References

1 Eckert, E. R. G., and Drake, R. M., *Analysis of Heat and Mass Transfer*, McGraw Hill, 1972, pp. 98-103.

2 Lebedev, N. N., Skalskaya, I. P., and Uflyand, Y. S., *Worked Problems in Applied Mathematics*, Dover, 1979, pp. 212-215.

3 Yovanovich, M. M., *Advanced Heat Conduction*, Hemisphere, 1984.

4 Bau, H. H., and Sadhal, S. S., "Heat Losses From a Fluid Flowing in a Buried Pipe," *International Journal of Heat and Mass Transfer*, Vol. 25, 1982, pp. 1621-1629.

5 Moon, P., and Spencer, D. E., *Field Theory Handbook*, Springer Verlag, 1971.

6 Yovanovich, M. M., personal communication, 1981.

Heat Transfer Behavior of Frozen Soils

H. Inaba[1]

Nomenclature

- C = specific heat
- E = water equivalent of calorimeter
- L_f = latent heat of fusion of ice at 0°C
- Q = heat flux per unit length of probe
- T = temperature
- ΔT = temperature difference
- t = time
- u = unfrozen water content per dry weight
- W = weight
- w = initial moisture content
- λ_{eff} = effective thermal conductivity
- γ = specific weight

Subscripts

- c = calorimeter and contents
- i = ice
- la = liquid added to calorimeter
- lc = liquid in calorimeter
- s = soil
- w = water
- wc = original calorimeter liquid
- wu = unfrozen water

Introduction

The freezing and thawing of water in soils at temperature below 0°C have important effects on those thermal

[1]Department of Mechanical Engineering, Kitami Institute of Technology, Kitami, Hokkaido 090, Japan

Contributed by the Heat Transfer Division for publication in the JOURNAL OF HEAT TRANSFER. Manuscript received by the Heat Transfer Division September 9, 1982.

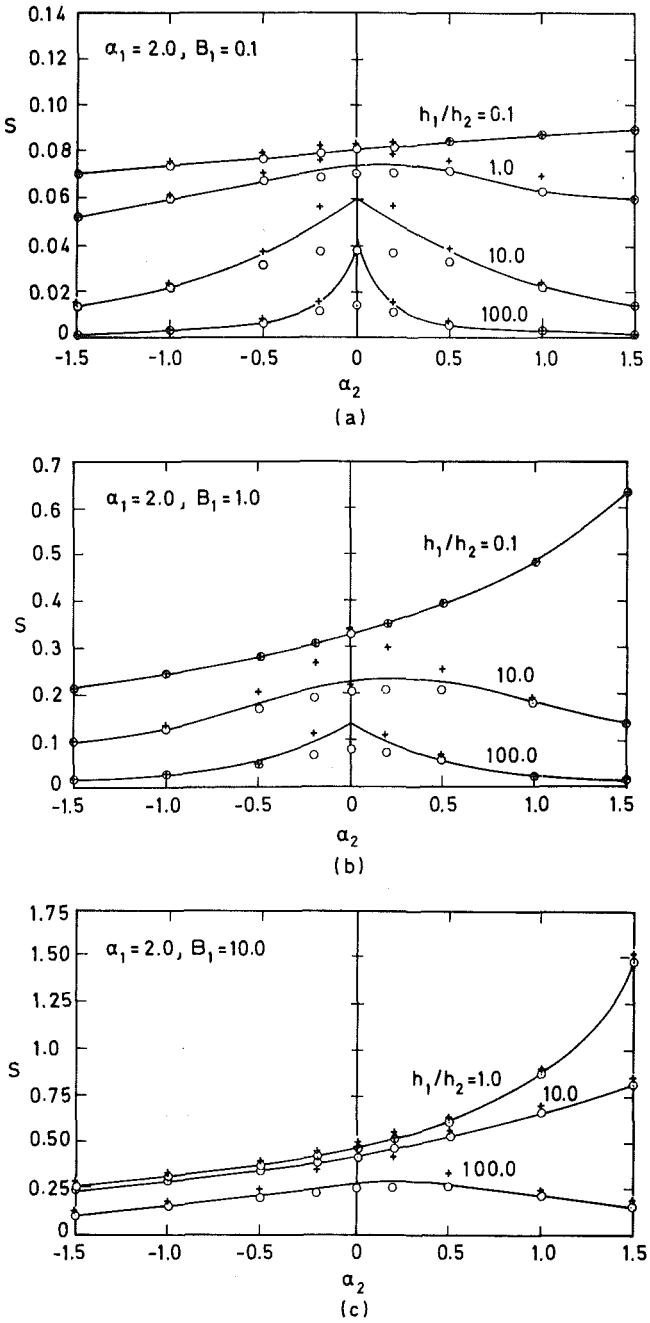

Fig. 2 The shape factor: (*a*) $\alpha_1 = 2$, Bi = 0.1; (*b*) $\alpha_1 = 2$, Bi = 1; (c) $\alpha_1 = 2$, Bi = 10

deviation between the lower bound, and the exact solution is well below 5 percent. For (aBi $h_2/h_1 \geq 0.1$, this deviation is smaller than 20 percent. These results have been confirmed in a large number of calculations which include the following range of parameters $0.1 \leq \alpha_1 \leq 2$, $-2 \leq \alpha_2 \leq 1.8$, $0.01 \leq$ Bi ≤ 100, $0.01 \leq h_1/h_2 < 1000$. A few representative results are exhibited in Table 1. As we have seen in section 2, the exact solution is relatively involved, and it is desirable to have a simple formula, such as equation (12), to calculate the shape factor.

The results just cited are in accord with a previous work [4], in which a pipe buried beneath an isothermal surface was considered. In the foregoing work [4], $h_2 \to \infty$; therefore, the criterion (aBi $h_2/h_1) \geq 1$ is always met and the lower bound is always an excellent approximation of the exact value of the shape factor.

4 Conclusions

We present a method to obtain an exact solution for conductive heat transfer between two eccentric cylinders with boundary conditions of the third kind. The exact solution is obtained in a series form where the evaluation of the coefficients requires the solution of a set of algebraic equations (section 2). To eliminate this difficulty, we present an approximate, easy-to-use formula for the shape factor (equation (12)). This approximation is good within 5 percent for (aBi $h_2/h_1) \geq 1$. Even if the foregoing criterion is not met, the approximation may yield a value of acceptable accuracy if the difference between the lower and upper bounds ($S_u - S_l$) is small enough.

References

1 Eckert, E. R. G., and Drake, R. M., *Analysis of Heat and Mass Transfer*, McGraw Hill, 1972, pp. 98-103.

2 Lebedev, N. N., Skalskaya, I. P., and Uflyand, Y. S., *Worked Problems in Applied Mathematics*, Dover, 1979, pp. 212-215.

3 Yovanovich, M. M., *Advanced Heat Conduction*, Hemisphere, 1984.

4 Bau, H. H., and Sadhal, S. S., "Heat Losses From a Fluid Flowing in a Buried Pipe," *International Journal of Heat and Mass Transfer*, Vol. 25, 1982, pp. 1621-1629.

5 Moon, P., and Spencer, D. E., *Field Theory Handbook*, Springer Verlag, 1971.

6 Yovanovich, M. M., personal communication, 1981.

Heat Transfer Behavior of Frozen Soils

H. Inaba[1]

Nomenclature

- C = specific heat
- E = water equivalent of calorimeter
- L_f = latent heat of fusion of ice at 0°C
- Q = heat flux per unit length of probe
- T = temperature
- ΔT = temperature difference
- t = time
- u = unfrozen water content per dry weight
- W = weight
- w = initial moisture content
- λ_{eff} = effective thermal conductivity
- γ = specific weight

Subscripts

- c = calorimeter and contents
- i = ice
- la = liquid added to calorimeter
- lc = liquid in calorimeter
- s = soil
- w = water
- wc = original calorimeter liquid
- wu = unfrozen water

Introduction

The freezing and thawing of water in soils at temperature below 0°C have important effects on those thermal

[1]Department of Mechanical Engineering, Kitami Institute of Technology, Kitami, Hokkaido 090, Japan

Contributed by the Heat Transfer Division for publication in the JOURNAL OF HEAT TRANSFER. Manuscript received by the Heat Transfer Division September 9, 1982.

properties. A knowledge of thermal properties of frozen soils has been highly desirable in the design and constructions of roads, buildings, and other structures in cold regions, and in the estimation of heat loss from underground power cables. A considerable amount of information on the thermal properties of frozen soils have been reported by many researchers. Specific heat and unfrozen water content of several frozen soils have been studied by calorimetric methods [1-3]. Anderson and Tice [4] predicted frozen water content in frozen soils from surface-area measurements. On the other hand, effective thermal conductivity has been measured by a transient heat flow method using a line heat source [5-7]. From the previous results, it has been known that those thermal properties of frozen soils are dependent on temperature, rate of freezing, initial moisture content, density, mineral type, and grain size. Very little seems to have been studied together on the measurements of specific heat, unfrozen water content, and effective thermal conductivity by the same researcher, especially under the small rate of freezing and thawing.

This paper deals with the measurements of thermal properties (specific heat, effective thermal conductivity) and unfrozen water content for several fine and coarse grain-sized soils over a range of above or below freezing temperature under a small rate of freezing. The effects of temperature, soil type, and initial moisture content on the thermal properties and unfrozen water content are examined experimentally by cooling cylindrical moist soil samples without access to additional water during the cooling process.

Experimental Apparatus and Procedure

A transient probe method utilizing a line heat source was employed to measure effective thermal conductivity. The line heat source is a hollow stainless steel probe with an outside diameter of 1.5 mm and 153 mm, as shown in Fig. 1. The thin wall stainless steel probe contains a uniformly spaced spiral manganin coil heater (0.2-mm in diameter) with a resistance of about 20 Ω. The d-c voltage (0.5-3 V) from a regulated power supply unit is supplied to the coil heater. Alumel-Chromel thermocouples (0.1 mm in diameter) are located inside the coil heater halfway along the probe. The probe is embedded into a tubular soil container with an inside diameter of D = 300 mm and a height of H = 400 mm, as can be seen in Fig. 1.Using the aforementioned finely calibrated thermocouples and a high-precision pen recorder (potentiometer), the reliability of the temperature measurements was considered to be within ± 0.04°C. The soil container is covered with insulating material, and placed into the cold room whose temperature can be controlled from 20°C to −25°C. The temperature difference in the soil container was controlled within 0.2°C.

The existence of air around the probe as a line heat source (the ratio of the length of the probe to the diameter l/d = 102) could be neglected since the soil sample was placed carefully into the container after the probe had been set in the container. If the measuring time, t, is larger than 3 min, the effective thermal conductivity of soils was calculated from the temperature rise of the probe, using the following simple equation [5-9]

$$\lambda_{\text{eff}} = \frac{Q}{4\pi\Delta T}(ln\ t_2/t_1) \tag{1}$$

where t_2 and t_1 are times corresponding to probe temperature change, ΔT. For a given soil, the value of λ_{eff} was obtained from the least squares fit to a plot of the temperature change versus the logarithm of the ratio of associated times. The measuring error for thermal conductivity with the transient probe method was estimated to be within ± 3 percent from the results in the preliminary experiments using ethylene-glycol and air.

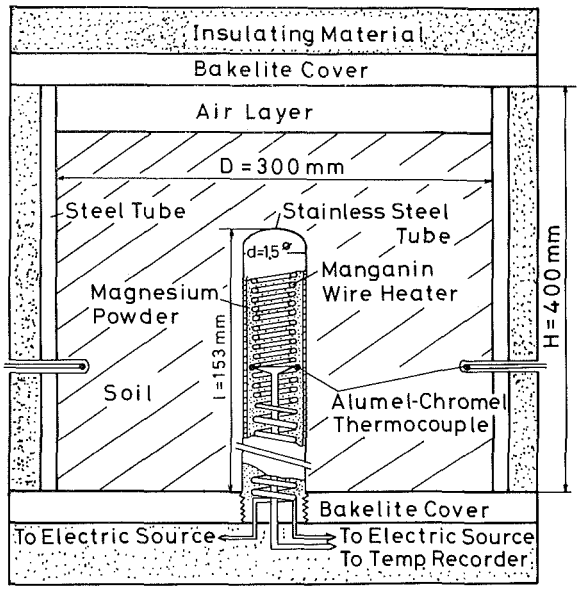

Fig. 1 Experimental apparatus for a transient probe method

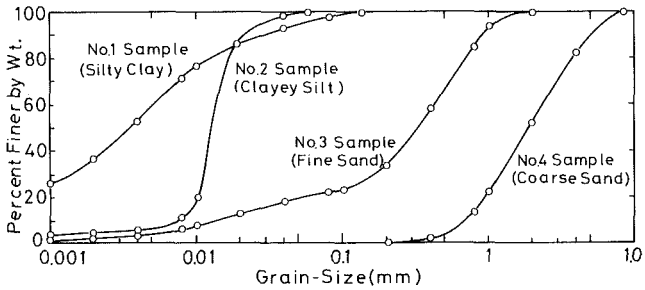

Fig. 2 Grain sized distributions for soil samples tested

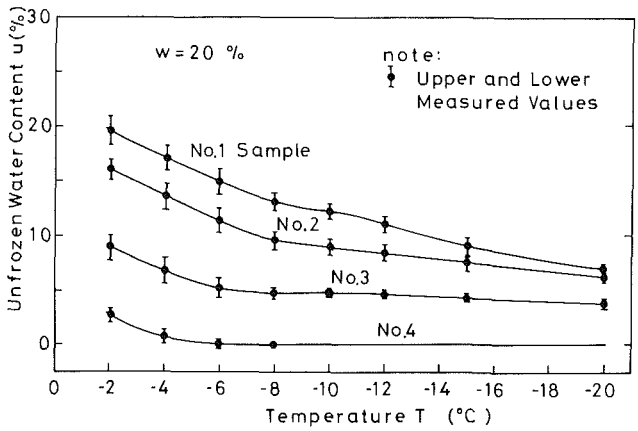

Fig. 3 The relationship between unfrozen water content, u, and temperature, T

The determination of specific heat of soils was performed by using calorimetric equipment and the general method of mixtures as reported by Williams [1] and Lovell [2]. The calorimeter consists of a large Dewar vessel with a silvered surface, an insulated cover with suitable openings for stirring, inserting a thermometer, and introduction of sample soil, and two thin-wall copper cups of approximately 200 ml capacity. Specific heat value, C_s, was determined by the following energy balance equation between heat gained by the calorimeter and its content and heat loss by the liquid (ethylene-glycol) added

$$C_s = \frac{-W_{la}C_{la}\Delta T_{la} + W_{lc}C_{lc}\Delta T_c + E\Delta T_c}{W_s \Delta T_s} \quad (2)$$

The measuring error for specific heat by the calorimeter was considered to be within ± 5 percent from the results in the preliminary experiments.

Unfrozen water content was determined by a calorimetric technique. That is, it was derived from the heat balance, including latent heat of fusion of ice, of the calorimeter and its contents when the temperature is raised above the freezing point from a subzero temperature, similar to that used by Lovell [2] as follows

$$W_s C_s \Delta T_s + (W_w - W_i) C_{wu} \Delta T_i + W_i C_i \Delta T_i + W_i L_f + W_w C_w \Delta T_w = E\Delta T_c + W_{wc} C_{wc} \Delta T_c \quad (3)$$

We can obtain W_i from equation (3). The unfrozen water content, u, is quotient of the weight of unfrozen water ($W_w - W_i$) by W_s. Values of the specific heat of water, ice, and latent heat of fusion of ice were taken from handbooks [10–12] for appropriate average or mid-range temperature.

Test samples in a wide range of grain-sized soils were selected to obtain the thermal properties and unfrozen water content. Grain-sized classification of the soil used was carried out with the Japanese Industrial Standard A1204T (1979). Grain-sized distributions from No. 1 (silty clay) to No. 4 (coarse sand) are presented in Fig. 2. Test samples were cooled automatically at a very slow cooling speed in the cold room by the cooling system. The time taken for cooling from −1°C to −5°C was varied from 30 to 40 hrs.

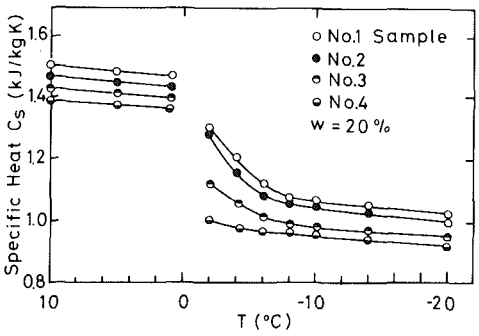

Fig. 4 The relationship between specific heat, C_s, and temperature, T

Results and Discussions

Figure 3 shows the relationship between the unfrozen water content, u, and subzero temperature, T, for various soils with initial moisture content w = 20 percent. The bar lines in the figure indicate the range of maximum and minimum values measured. From this figure, it would be understood that unfrozen water content is decreased with decreasing temperature, T. However, fine-grain size soils (No. 1 and No. 2 samples) still contain unfrozen-water content of about 7–8

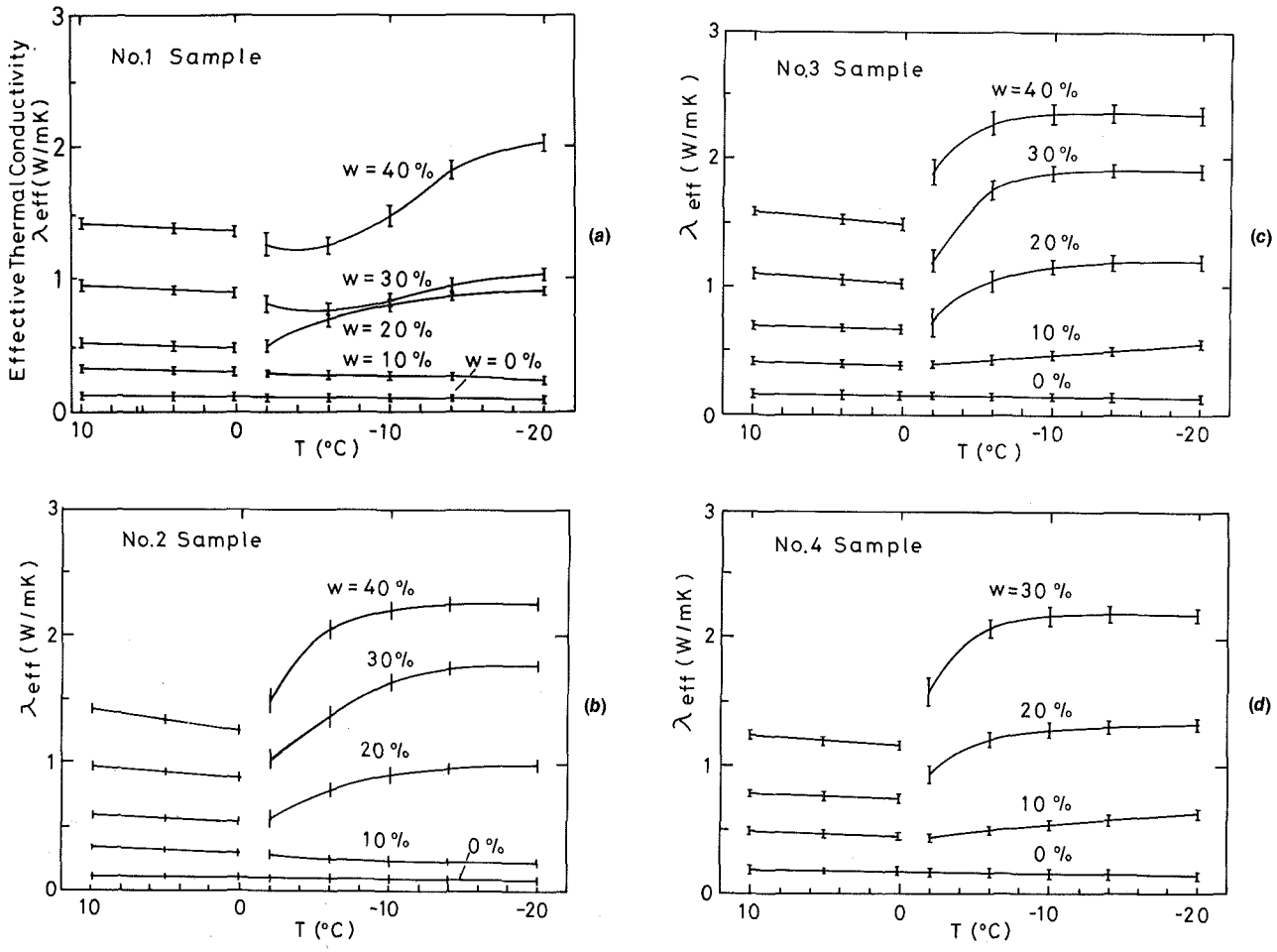

Fig. 5 The relationship between effective thermal conductivity, λ_{eff}, and temperature, T: (a) No. 1 sample, (b) No. 2 sample, (c) No. 3 sample, (d) No. 4 sample

percent at $T = -20°C$. As the grain size of soil becomes smaller from No. 4 sample (coarse sand) to No. 1 sample (silty clay), unfrozen-water content is increased over a wide range of subzero temperatures.

Figure 4 shows the relationship between specific heat, C_s, and subzero temperature for various soils and $w = 20$ percent. In this figure, it can be seen that the specific heat, C_s, of moist soil decreases linearly with decreasing temperature T above 0°C, while in the range of $T = 0$ to $-10°C$ it decreases curvedly and for $T < -10°C$ it is reduced linearly with decreasing temperature. These behaviors of C_s in the range of $T = 0$ to $-10°C$ might be explained by the fact that the amount of unfrozen water content in the soil changes according to the temperature as could be seen in Fig. 3.

Figures 5(*a*)-(*d*) for four soils indicate the relationship between effective thermal conductivity, λ_{eff}, and temperature, T, over the range of $T = 10°C$ to $-20°C$ for various initial moisture contents. From Figs. 5(*b*)-(*d*), it could be understood that the effective thermal conductivity, λ_{eff}, of moist soils is decreased with decreasing temeprature, T, above 0°C, while for $T < 0°C$ an increasing effective thermal conductivity with decreasing temperature is observed. This increasing effective thermal conductivity with decreasing temperature could be explained by the fact that the amount of ice, for which the thermal conductivity is more than four times greater than that of water, is increased in the frozen soil. An increasing rate of change of effective thermal conductivity to temperature varies according to the unfrozen-water content and initial moisture content in the soil. That is, for a given initial moisture content the effective thermal conductivity increases with decreasing unfrozen water content, depending on temperature as shown in Fig. 3. The rate of increase of λ_{eff} to temperature becomes larger as the initial moisture content, w, increases. However, in the case of fine grain-sized soil, as can be seen in Fig. 5(*a*), it is intriguing that the decreasing tendency of λ_{eff} to temperature, T, below 0°C is recognized for large initial moisture content $w = 30$–40 percent. This peculiar behavior of decreasing effective thermal conductivity of the frozen soil might be caused by the phenomenon of frost heaving of the frozen soil, that is, the movement of water in the moist soil to the freezing front existing in the neighborhood of the steel tube container, and by the containment of air having low thermal conductivity moving from the upper air layer in the test container into the frozen soil since the volume of the soils tested expands about 12–16 percent from the initial volume of moist soil before freezing.

Conclusions

The thermal properties and unfrozen water content of various soils were examined experimentally by the transient probe method and calorimetric technique. It could be seen that measured values of effective thermal conductivity and specific heat show a strong dependence on the temperature, initial moisture content, and grain size of soil in the temperature range of $T = 0°C$ to $-10°C$. Unfrozen water content of the frozen soil increases as the grain size of soil decreases. The peculiar behavior for fine grain-sized soil of decreasing effective thermal conductivity with decreasing temperature, T, below 0°C was observed for large initial moisture content $w = 30$–40 percent.

References

1 Williams, P. J., "Unfrozen Water Content of Frozen Soils and Soil Moisture Suction," *Geotechnique*, Vol. 14, No. 3, 1964, pp. 231–246.

2 Lovell, C. W., "Temperature Effects on Phase Composition and Strength of Partially Frozen Soils," Highway Research Board, Bulletin 168, 1957, pp. 74–95.

3 Dillon, H. B., and Andersland, D. B., "Predicting Unfrozen Water Contents in Frozen Soils," *Canadian Geotechnical Journal*, Vol. 3, No. 2, 1966, pp. 53–60.

4 Anderson, D. M., and Tice, A. R., "Predicting Unfrozen Water Contents in Frozen Soils from Surface Area Measurements," *Highway Research Record*, No. 343, 1972, pp. 12–18.

5 Penner, E., "Thermal Conductivity of Frozen Soils," *Canadian Journal of Earth Science*, Vol. 7, 1970, pp. 982–987.

6 Kersten, M. S., "Thermal Properties of Frozen Ground," *Proceedings of the Permafrost International Conference*, 1963, pp. 301–305.

7 Woodside, W., "Probe for Thermal Conductivity Measurement of Dry and Moisture Materials," ASHRAE *Journal of Piping and Air Conditioning*, Vol. 30, No. 9, 1958, pp. 163–170.

8 Flynn, D. R., and Watson, T. W., "High Temperature Thermal Conductivity of Soils," *Proceedings of the 8th Thermal Conductivity Conference*, Plenum Press, New York, 1969, pp. 913–939.

9 Mirkovich, V. V., ed., "Rocks and Soils," *Proceedings of Thermal Conductivity*, Session G, Vol. 15, Plenum Press, New York, 1978, pp. 263–313.

10 Clarks, S. P., *Handbook of Physical Constants*, Geol. Soc. Amer. Inc., 1966.

11 Dilland, D. S., and Timmenhause, K. D., "Low Temperature Thermal Conductivity of Solidification H_2O and D_2O," *Pure and Applied Cyrogenics*, Vol. 4, 1966, pp. 82–89.

12 *International Critical Table*, National Research Council of the U.S.A., McGraw Hill, 1962.

ERRATA

Corrections to "Effect of Fluid Carryover on Regenerator Performance," by P. J. Banks, published in the February 1982 issue of the ASME JOURNAL OF HEAT TRANSFER, pp. 215–217 (supplement to corrections given in November 1982 issue, p. 820):

1 In second line below Fig. 2, replace "II" by "II."
2 In second new paragraph on p. 217, replace second sentence with, "In this limiting case, the regenerator with carryover neglected is equivalent to a recuperator."